JOURNAL
OF
APPLIED PHYSICS

UNIVERSITY OF ILLINOIS
LIBRARY
JUL 17 1961
CHICAGO

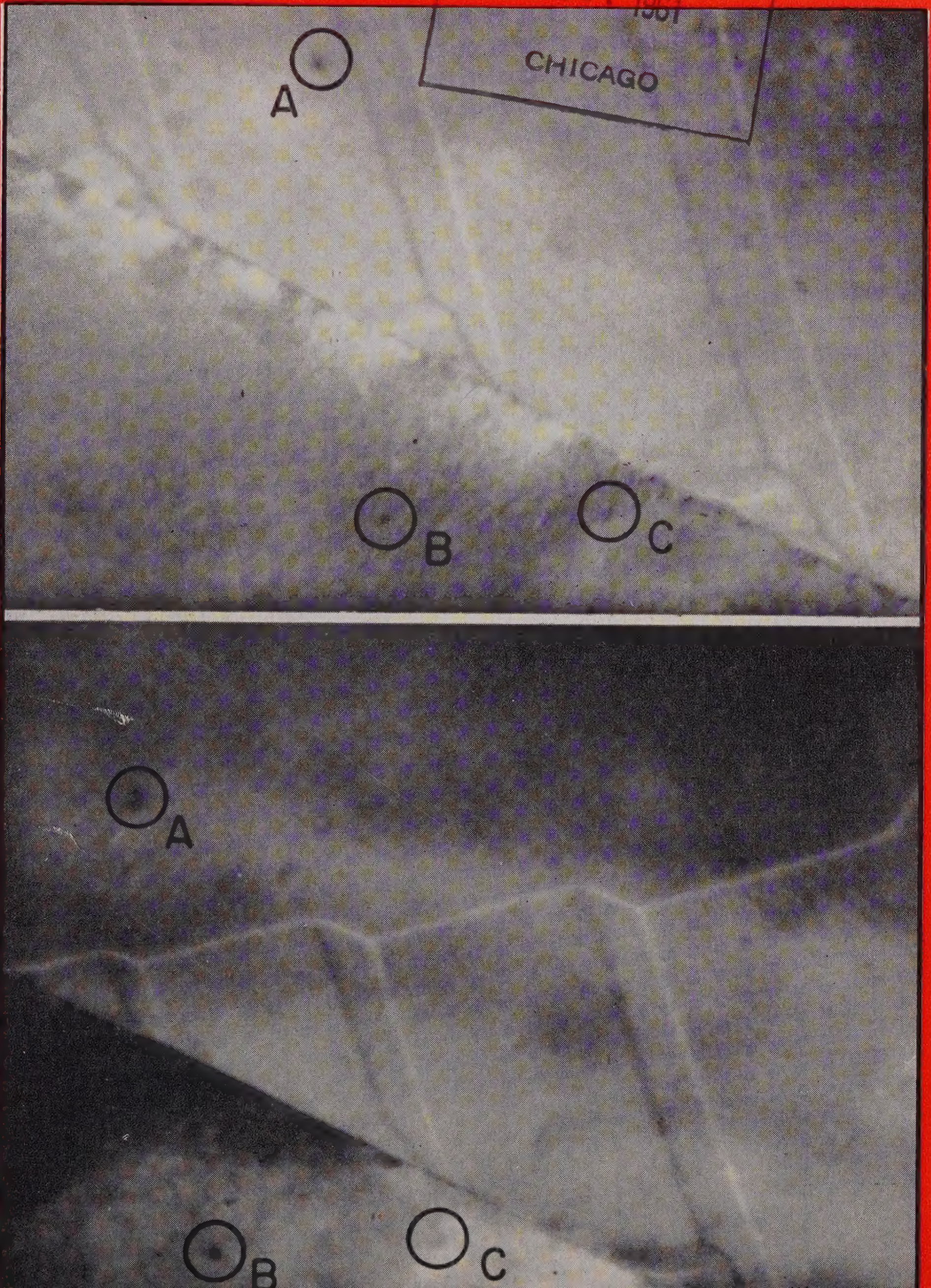

Movement
Domain Wa
for a Chan
in Magnet
Field

See Page 12

HARSHAW CRYSTALS are 1728
TIMES LARGER
than 25 years ago
with "Harshaw Quality" inherent in each crystal
1936
1"x 1"
1955
5"x 5"
1961
11½"x 11½"

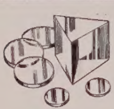

This year Harshaw's Crystal Division celebrates its Silver Anniversary. In these 25 years the "art" of growing crystals has given way to scientific procedures. With expanded crystal research and development laboratories, and recently doubled production facilities, Harshaw stands ready to produce your crystals—regardless of technical nature or production magnitude. Our physics, chemistry, and engineering departments enjoy the challenge of increasingly stringent demands from scientists and instrument manufacturers for infrared and ultraviolet optical crystals, and scintillation phosphors.

OPTICAL CRYSTALS

For Infrared and Ultra Violet Transmitting Optics

- **Sodium Chloride**
- **Sodium Chloride Monochromator Plates**
- **Potassium Bromide**
- **Potassium Bromide Pellet Powder (through 200 on 325 mesh).**
- **Potassium Chloride**
- **Optical Silver Chloride**
- **Thallium Bromide Iodide**
- **Lithium Fluoride**
- **Lithium Fluoride Monochromator Plates**
- **Calcium Fluoride**
- **Barium Fluoride**
- **Cesium Bromide**
- **Cesium Iodide**

SCINTILLATION

Mounted NaI (Tl) Crystals

Crystal detectors designed for your most sophisticated counting problems. Our physics and engineering groups are available to assist you.

- **Other Phosphors—Rough Cut Thallium Activated Sodium Iodide Crystal Blanks**
- **Europium Activated Lithium Iodide (Normal)**
- **Europium Activated Lithium Iodide (96% Li^6 Enriched)**
- **Thallium Activated Cesium Iodide**
- **Thallium Activated Potassium Iodide**
- **Anthracene**
- **Plastic Phosphors**

Write for our 36-page booklet "Synthetic Optical Crystals" or our 44-page booklet "Scintillation Phosphors"

The Harshaw Chemical Company
1945 East 97th Street • Cleveland 6, Ohio
Utrecht, Netherlands—Contact Harshaw-Van Der Hoorn N. V., Juffaseweg 186

HARSHAW

Crystal Division

JOURNAL OF APPLIED PHYSICS

Vol. 32, No. 7 JULY, 1961

In This Issue

Theory of Quantum Oscillators in a Multimode Cavity . . . . W. G. Wagner and G. Birnbaum 1185
Mass Spectrographic Analysis of Insulators Using a Vacuum Spark Positive Ion Source . . A. J. Ahearn 1195
Mass Spectrographic Detection of Impurities in Liquids . . . . A. J. Ahearn 1197
Electron Bombardment Damage in Silicon Esaki Diodes . . . . R. A. Logan, W. M. Augustyniak, and J. F. Gilbert 1201
On the Theory of Amplitude Distribution of Impulsive Random Noise . . . . K. Furutsu and T. Ishida 1206
Polygonization in Bent Zinc Crystals . . . . P. P. Sinha and Paul A. Beck 1222
Surface Layers on Barium Titanate Single Crystals above the Curie Point . . . ., H. Schlosser and M. E. Drougard 1227
Dangling Bonds in III–V Compounds . . . . Harry C. Gatos 1232
Observations of Cross-Tie Domain Walls by the Faraday Effect . . . . A. L. Houde 1234
Electrical Resistivity of Chromium in the Vicinity of the Néel Temperature . . . . M. J. Marcinkowski and H. A. Lipsitt 1238
Dissociation of Adsorbed CO by Slow Electrons . . . . George E. Moore 1241
Electric Breakdown Strength of Single and Laminated Films of Vinyl Chloride-Acetate . . . . Robert G. Greenler and Robert M. Kay 1252
Stress Distribution on the Boundary of an Elliptical Hole in a Large Plate during Passage of a Stress Pulse of Long Duration (Major Axis Normal to the Wave Front) . . . . . A. J. Durelli and W. F. Riley 1255
Transmission Electron Microscope Observations of Magnetic Domain Walls . . . . J. T. Michalak and R. C. Glenn 1261
Electrical Conductivity of NaCl during High-Temperature Creep . . R. W. Christy and W. E. Daniels, Jr. 1265
Magnetization Process in Small Particles of CrO_2 . . . . F. J. Darnell 1269
Electrically Imploded-Exploded Aluminum Tube . . . . Eugene C. Cnare 1275
Vapor-Phase Growth of Single Crystals of II–VI Compounds . . . . W. W. Piper and S. J. Polich 1278
Optical Properties of Oriented Polystyrene . . . . Richard S. Stein 1280
Corbino Disk Magnetoresistivity Measurements on InSb . . . . Milton Green 1286
***p*-Type Photoconductivity and Infrared Quenching in Electron-Bombarded CdS** . . . . B. A. Kulp and R. H. Kelley 1290
Magnetization of Nickel Single Crystals . . . . Lambros Tterlikkis and Alvin W. Jenkins, Jr. 1293
Hydromagnet: A Self-Generating Liquid Conductor Electromagnet . . . . Henry H. Kolm and Osman K. Mawardi 1296
Two-Phase Permalloy for High-Speed Switching . . . . E. A. Nesbitt and E. M. Gyorgy 1305
Helium Diffusion through Glass . . . . V. O. Altemose 1309
Temperature-Dependent Bismuth-Cesium Photosurfaces . . . . R. J. Zollweg and C. R. Taylor 1316
Nonohmic Behavior in Near-Stoichiometric Rutile (TiO_2) . . . . . E. H. Greener and D. H. Whitmore 1320
Analysis of Photojunctions Formed by Diffusing Copper into Insulating Cadmium Sulfide Crystals . . . . Robert R. Bockemuehl, James E. Kauppila, and David S. Eddy 1324
Formation Conditions and Structure of Thin Epitaxial Silver Films on Rocksalt . . . . Billy W. Sloope and Calvin O. Tiller 1331
Growth of Single-Crystal Calcium Fluoride with Rare-Earth Impurities . . . . H. Guggenheim 1337
Electroluminescence at *p-n* Junctions in Gallium Phosphide . . . . M. Gershenzon and R. M. Mikulyak 1338
Propagation in Periodic Electron Beams . . . . W. M. Mueller 1349
Anodic Oxidation of Germanium . . . . T. Gabor 1361
Proposed Method of Measuring Thermal Diffusivity at High Temperatures . . . . . Robert D. Cowan 1363
Paramagnetic Maser Oscillator Analysis . . . . S. Wang and J. R. Singer 1371
Spectral Response of Solar Cells . . . . Brian Dale and F. P. Smith 1377
Perfection of the Lattice of Dislocation-Free Silicon, Studied by the Lattice-Constant and Density Method . . . . M. E. Straumanis, P. Borgeaud, and W. J. James 1382
Charged Cylindrical Tube . . . . T. R. Ferguson and R. H. Duncan 1385
Piezoelectricity of Quartz for Finite Strain . . . . S. Machlup and M. E. Christopher 1387
Texture Transition in High-Purity Silver and Its Correlation with Stacking Fault Frequency . . . . Hsun Hu, R. S. Cline, and S. R. Goodman 1392

Letters to the Editor:

Guidance and Collimation of Sputtered Tungsten Particles . . . . Carl A. Ludeke 1400
Multiple Shock Wave Structures in Polycrystalline Ferroelectrics . . . . C. E. Reynolds and G. E. Seay 1401
New, Thermally Variable Bead Resistor . . . . Victor J. Tennery and Russell G. West 1402
Field-Enhanced Donor Diffusion in Degenerate Semiconductor Layers . . . . W. Shockley 1402
Deformation-Produced Point Defects . . . . Howard K. Birnbaum and Floyd R. Tuler 1403
Nuclear Magnetic Resonance in Flowing Fluids . . . . Louis R. Hirschel and Louis F. Libelo 1404
Useful Technique for Growing Large, Single-Crystal YIG . . . . Don Barry and Roy W. Roberts 1405
Elastic Constants of TiC and TiB_2 . . . . J. J. Gilman and B. W. Roberts 1405
Erratum: Oblique-Incidence Anisotropy in Evaporated Films . . . M. S. Cohen, D. O. Smith, and G. P. Weiss 1405
Errata: Microwave Propagation through a Magnetoplasma . . R. L. Phillips, R. G. De Losh, and D. E. White 1406
Erratum: Growth Twins in Indium Antimonide . . . . R. K. Mueller and R. L. Jacobson 1406
Announcements 1406
Index to Advertisers xxxiii

JOURNAL OF APPLIED PHYSICS

A journal of general physics and its applications to other sciences and to industry

Published by the
American Institute of Physics

GOVERNING BOARD

Members

Ralph A. Sawyer, *Chairman*
James G. Baker
R. H. Bolt
Wallace R. Brode
Harvey Brooks
Dirk Brouwer
J. H. Elliott
Herbert A. Erf
N. S. Gingrich
S. A. Goudsmit
W. W. Havens, Jr.
W. V. Houston
Winston E. Kock
R. Bruce Lindsay
David L. MacAdam
H. Victor Neher
Leonard O. Olsen
C. J. Overbeck
Ray Pepinsky
S. L. Quimby
Ralph A. Sawyer
Francis W. Sears
Frederick Seitz
C. Guy Suits
Mary E. Warga
William R. Willets

ADMINISTRATION

Elmer Hutchisson
Director

Wallace Waterfall
Secretary and Treasurer

Henry A. Barton
Administrative Consultant

W. C. Kelly
Director of Education

Eugene H. Kone
Director of Public Relations

Hugh C. Wolfe
Director of Publications

Kathryn Setze
Assistant Treasurer

James E. Mills
Supervisor, Editorial Department

Sistina Greco
Circulation Manager

Edward Tober
Manager, Production and Distribution

Theodore Vorburger
Advertising Manager

Emily Wolf
Manager, Special Services

Editor
J. H. Crawford, Jr.

Assistant Editor
Ethel McMillan

Editorial Board

J. E. Goldman
J. L. Tuck
C. A. Wert
Herman A. Haus
C. Lester Hogan
R. S. Rivlin
Henry Hurwitz
James A. Krumhansl
C. P. Slichter

THE JOURNAL OF APPLIED PHYSICS is devoted to general physics and its applications to other sciences, to engineering, and to industry. Previous to 1937, this journal was called PHYSICS.

The JOURNAL OF APPLIED PHYSICS welcomes articles of two distinct kinds: (1) Descriptions of new results in experimental or theoretical physics which are of general interest to physicists. The author should explain his contribution in such a way that a physicist or engineer in another field of specialization can appreciate its objectives and essential features. (2) Critical reviews of particular areas of physics or surveys of extensive investigations at a single laboratory. Authors contemplating writing such should correspond with the Editor before they begin writing.

The JOURNAL OF APPLIED PHYSICS welcomes Letters to the Editor which are short [approximately four (4) typewritten pages] communications without abstracts. Timeliness, briefness, and degree of current importance of the subject matter will be of primary concern in the publication of Letters. Letters should not be looked upon as partial publication or announcement of more comprehensive work, but rather self-contained presentations in themselves.

Manuscripts should be submitted to the Editor, J. H. Crawford, Jr., Solid State Division, Oak Ridge National Laboratory, Oak Ridge, Tennessee. Authors should read the "Information for Contributors," facing page 1 of the January issue, before writing articles or letters. The *Style Manual* of the American Institute of Physics is also helpful to writers preparing manuscripts for journals published by the American Institute of Physics. It can be obtained for $1.00 from the American Institute of Physics, 335 East 45 Street, New York 17, New York.

Corrected proofs and all correspondence concerning papers in the process of publication should be addressed to the Supervisor, Editorial Department, American Institute of Physics, 335 East 45 Street, New York 17, New York.

Subscriptions, renewals, and orders for back numbers should be addressed to the American Institute of Physics, 335 East 45 Street, New York 17, New York.

Subscription Price	U.S. and Canada	Elsewhere
To members of member organizations of the American Institute of Physics and Affiliated Societies ..	$12.00	$13.00
To all others	14.00	16.00

Back Number Prices

Yearly back number rate when complete year is available: $17.00.
Single copies: $1.75 each (exception: March, 1958—$3.00 each).

Changes of address should be sent to the American Institute of Physics.

Advertising rates supplied on request. Orders, advertising copy, and cuts should be sent to the American Institute of Physics.

The Journal of Applied Physics is published monthly at Prince and Lemon Streets, Lancaster, Pennsylvania.
Second-class postage paid at Lancaster, Pa.

NOW...

AUTOMATIC VACUUM EVAPORATION SYSTEMS

with VacIon® electronic pumps

Varian announces a fully-automatic vacuum evaporation system, available from stock and employing the famous VacIon all-electronic vacuum pump.

Applications include film deposition and crystal plating. A servo-mechanism feedback circuit provides automatic control of the vacuum cycle, with maximum operating speed and minimum pumpdown time.

The 400 litre/second VacIon pump included in the system is a revolutionary development in vacuum pumping. VacIon pumps employ no moving parts, no fluids, no refrigerants. There is no danger of oil contamination in the vacuum chamber. VacIon pumps are fail-safe —if power failure occurs, vacuums are not compromised.

Other components of this completely-integrated system include a Pyrex vacuum bell jar, base plate, roughing pump, instrumentation, and controls. Shipped ready for operation, after connection to power and compressed air sources.

For full technical data on this and other Varian high-vacuum systems, write Vacuum Division.

- FULLY AUTOMATIC
- PROMPT DELIVERY
- PRESSURES BELOW 5×10^{-8} mm Hg WITHOUT BAKEOUT
- TIME, PRESSURE, TEMPERATURE CONTROLLED
- ALL-ELECTRIC HIGH-VACUUM PUMP

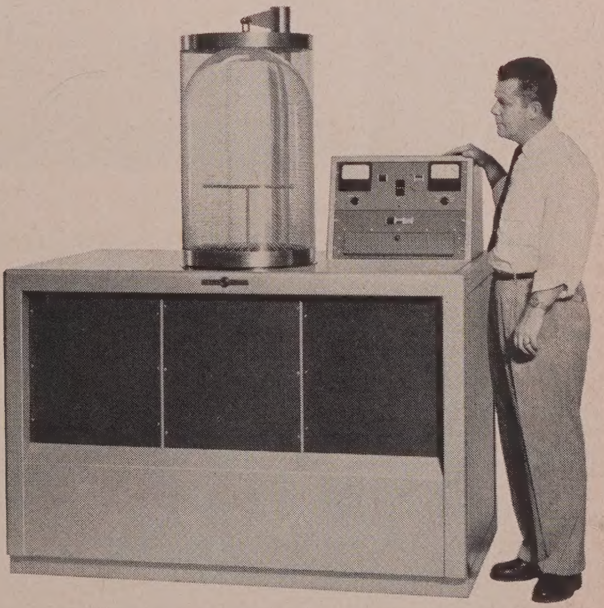

VARIAN associates
PALO ALTO 36, CALIFORNIA
Subsidiaries:
BOMAC LABORATORIES, INC.
VARIAN ASSOCIATES OF CANADA, LTD.
S-F-D LABORATORIES, INC.
SEMICON ASSOCIATES, INC.
SEMICON OF CALIFORNIA, INC.
VARIAN A. G. (SWITZERLAND)

research in a unique environment

The scientists of Aerospace Corporation's Laboratories are in the forefront of research in the space sciences. They provide broad scientific eadership to the scientific-industrial team developing space systems and ballistic missiles. With the advantages of stable funding and a stimulating environment, Aerospace Corporation scientists are conducting basic and applied research and experimental investigations on a broad spectrum of problems selected by staff members on the basis of their intrinsic scientific interest, as well as on problems arising directly from space systems in development. Their singular role within this leadership group nstalls the scientists of Aerospace Corporation in a position to make real progress toward advancing the space sciences. Now, as new areas of research are being considered, more men of high caliber are needed. Such men who hold advanced degrees are urged to direct their inquiries and resumes to Mr. George Herndon, Aerospace Corporation, Room 123, P. O. Box 95081, Los Angeles 45, California.

Organized in the public interest and dedicated to providing objective leadership in the advancement and application of space science and technology for the United States Government.

AEROSPACE CORPORATION

PIONEERING

AT BELL TELEPHONE LABORATORIES

In such an open field as this Dr. Karl Jansky of Bell Laboratories opened the way to radio astronomy. His search for a mysterious source of radio noise led him—and us—to the stars for our answer.

Today Bell scientists continue their pioneering in many fields—among them the transmission of human voices on beams of coherent light. Bell Laboratories' revolutionary Optical Maser foreshadows the use of light as a whole new medium of telephone, TV and data communications.

These are but two of the many fundamental advances which have come from breaking fresh ground at the world center of communications research and development.

Massachusetts Institute of Technology

OPERATIONS EVALUATION GROUP

Venturing Beyond the Confines of Your Discipline

The ultimate argument of the diplomat is still the threat of force; the conduct of war is still the business of the soldier and sailor. But in this era of sensitive political situations and nuclear peril, the immense complexities of armed combat have placed a few scientists in positions of uncommon responsibility.

Imaginative scientists and mathematicians with advanced degrees are invited to share in this uncommon responsibility with the staff of the Operations Evaluation Group of the Massachusetts Institute of Technology. Specifically you will provide the Chief of Naval Operations and Fleet commanders with an analytical basis for decision making on matters of tactics, strategy, composition of forces, employment of weapons and equipment, and research and development needs.

The appointments are permanent and well remunerated, and the peripheral benefits are indeed worth exploring.

Positions available in Cambridge.
Direct your inquiry to:
Dr. Jacinto Steinhardt, Director.

M.I.T.
OPERATIONS EVALUATION GROUP
Washington 25, D. C.
292 Main St., Cambridge 42, Mass.

All applicants will receive consideration for employment without regard to race, creed, color or national origin.

-RAY DIFFRACTION AND SPECTROSCOPY

NEW

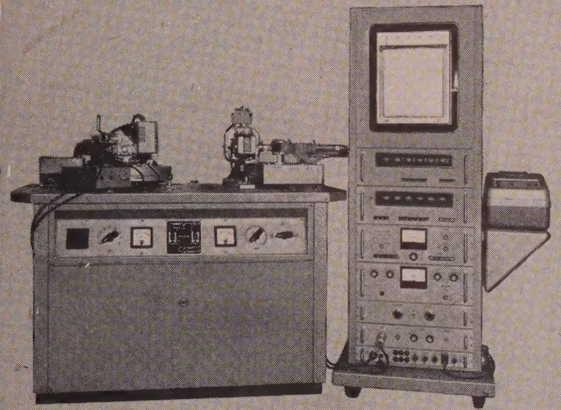

```
 No. of     No. of      Recording
 Events     Counts       Time in
                         Minutes

4559     10000       0.100  ┐
4560     10000       0.100  │
4561     10000       0.100  │
4562     10000       0.100  │
4563     10000       0.100  │
4564     10000       0.100  │ SEPARATE
4565     10000       0.100  │ RECORDING
4566     10000       0.100  │
4567     10000       0.100  │
4568     10000       0.100  │
4569     10000       0.100  │
4570     10000       0.100  ┘

4571     10000       0.100  ┐
4572     20000       0.200  │
4573     30000       0.300  │
4574     40000       0.400  │
4575     50000       0.500  │
4576     60000       0.600  │ CUMULATIVE
4577     70000       0.700  │ RECORDING
4578     80000       0.800  │
4579     90000       0.900  │
4580    100000       1.000  │
4581    110000       1.100  │
4582    120000       1.200  ┘
```

AUTOMATIC PRINTER

another time-saving device from RCA

This new RCA Printer automatically records events, counts, and time, thus freeing the researcher for other duties while this information is being accumulated. It also provides an accurate and convenient means of checking the stability of the counting, timing and recording circuits—a valuable advantage for spectroscopists in quantitative work and for diffractionists in line profile studies. The unit can be used with scintillation, proportional and Geiger-Mueller counter tubes in conjunction with the RCA Electronic Circuit Panel.

The Printer is the latest addition to the wide range of attachments and accessories available for RCA X-Ray Diffraction and Spectroscopy apparatus which contribute to its outstanding flexibility. Others include an X-Ray Vacuum Spectrometer for analysis of both light and heavy elements, a versatile horizontal goniometer which, with RCA accessories, performs six functions, and a Table Model Generator, available complete with cameras, for as little as $4000.

Installation supervision and contract service are available through the RCA Service Company.

Leasing Plan

RCA X-ray diffraction and spectroscopy equipment, as well as electron microscopes, can be leased directly from RCA, with no down payment, low monthly rates and a favorable option to buy.

For details on RCA's complete line of X-Ray Diffraction and Spectroscopy apparatus or Electron Microscopes, write to RCA, Dept. X-65, Bldg. 15-1, Camden, N. J.

RCA®

The Most Trusted Name in Electronics

RADIO CORPORATION OF AMERICA

Increased technical responsibilities in the field of range measurements have required the creation of new positions at the Lincoln Laboratory. We invite inquiries from senior members of the scientific community interested in participating with us in solving problems of the greatest urgency in the defense of the nation.

RADIO PHYSICS and ASTRONOMY

RE-ENTRY PHYSICS

PENETRATION AIDS DEVELOPMENT

TARGET IDENTIFICATION RESEARCH

SYSTEMS: Space Surveillance
Strategic Communications
Integrated Data Networks

NEW RADAR TECHNIQUES

SYSTEM ANALYSIS

COMMUNICATIONS: Techniques
Psychology
Theory

INFORMATION PROCESSING

SOLID STATE Physics, Chemistry,
and Metallurgy

A more complete description of the Laboratory's work will be sent to you upon request.

All qualified applicants will receive consideration for employment without regard to race, creed, color or national origin.

Research and Development
LINCOLN LABORATORY
Massachusetts Institute of Technology
BOX 33
LEXINGTON 73, MASSACHUSETTS

HIGH-RESOLUTION, ALL-PURPOSE JEM-6A ELECTRON MICROSCOPE FROM FISHER

Now, Fisher Scientific is your exclusive United States and Canadian ource for electron microscopes, related instruments manufac-ured by Japan Electron Optics Laboratory Co., Ltd. Model JEM-6A ives you resolving power up to 8 Angstroms for physical, chem-cal and metallurgical work . . . 12 A is routine. **Direct magnification:** ontinuously variable from 600X to 200,000X, providing photo-raphic magnifications above 1,000,000X. **Accelerating voltages** of 0, 80 and 100 KV are extremely stable. With accessories, you heat pecimens to 1000° C; cool them to −140° C; put them under ten-ile stress while inside the JEM-6A. A 16-mm camera films changes n crystal structure. You can record electron diffraction patterns of -micron fields . . . make direct-reflection photographs of surface tructure. **For full details,** call your Fisher branch, or write Fisher Scientific Company, 151 Fisher Building, Pittsburgh 19, Pa.

F-195

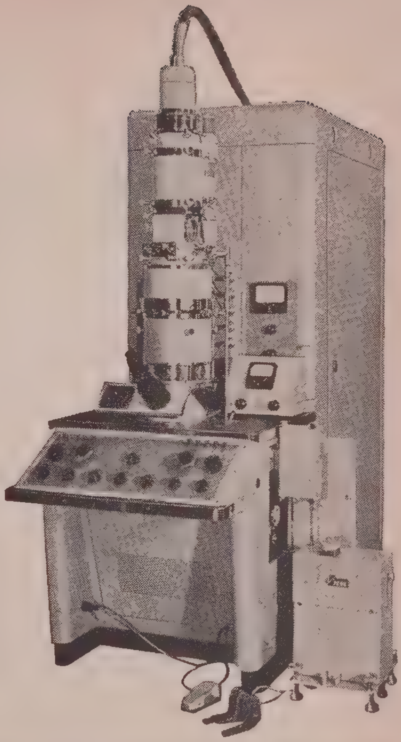

INC OXIDE SMOKE 80,000X

FISHER SCIENTIFIC

World's Largest Manufacturer-Distributor of Laboratory Appliances & Reagent Chemicals

Boston • Chicago • Ft. Worth • Houston • New York • Odessa • Philadelphia • Pittsburgh • St. Louis • Washington • Montreal • Toronto

signal hide and seek...

planned through advanced communication techniques at Amherst Laboratories

Signal transmission can be protected and hidden from interception by using natural or man-made disturbances. Locating such a signal in intelligible form at a designated point has been accomplished by scientists at Amherst Laboratories.
These and other accomplishments are a result of long-range experimental investigation currently in progress. We are concerned with wave propagation and properties of the propagation medium, as applied to advanced Ground, Air and Space Communications.

PROFESSIONAL STAFF AND MANAGEMENT OPPORTUNITIES *are unlimited for Physicists, Mathematicians and Electronic Engineers with advanced degrees and creative desire. All qualified applicants will receive consideration for employment without regard to race, creed, color or national origin. You are invited to direct inquiries in confidence to Mr. H. L. Ackerman, Professional Employment,*

AMHERST LABORATORIES • 1184 WEHRLE DRIVE • WILLIAMSVILLE, NEW YORK

SYLVANIA ELECTRONIC SYSTEMS
Government Systems Management
for GENERAL TELEPHONE & ELECTRONICS

GENERAL SYSTEM

A SEVEN INCH ELECTROMAGNET SYSTEM WITH A CHOICE OF CUSTOM POWER SUPPLIES

L-75A ELECTROMAGNET

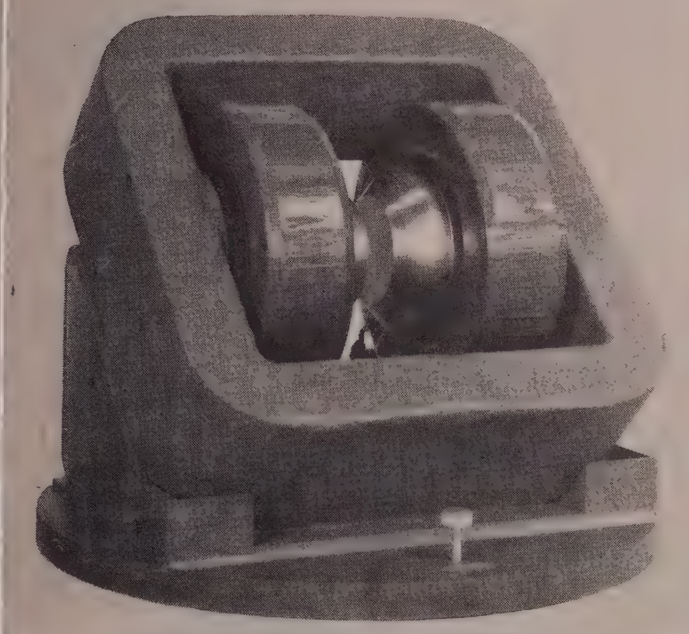

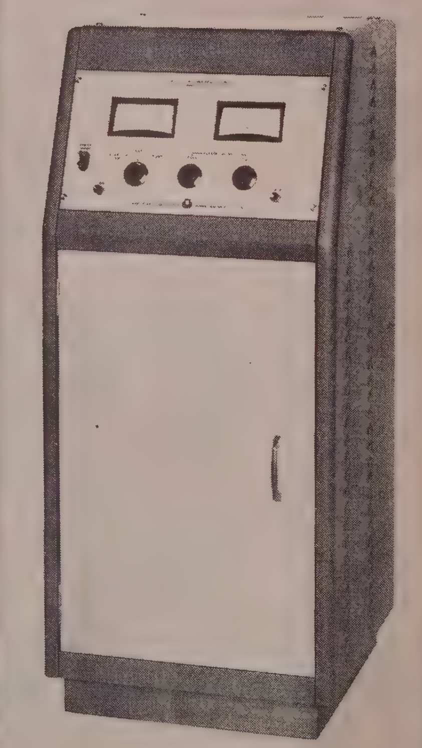

HS-1050 POWER SUPPLY

The Model L-75A Electromagnet and the Model HS-1050 Power Supply combine to produce a precision electromagnet system for a wide range of laboratory applications.

The L-75A Electromagnet can produce homogeneous fields in the order of one part in 10^5.

Standard gap width of 1.25 inches across a seven inch diameter pole face produces 10,000 gauss, with higher field strength possible by use of tapered pole faces.

Model HS-1050 Power Supply is a completely transistorized unit designed specifically for magnet users requiring an extremely stable (one part in 10^5 or better, short term). d.c. power source.

Maximum power is 5 kilowatts, 100 volts, at 50 amperes. Current adjustment is achieved by a continuous one-knob control. rather than a series of critical range adjustments normally encountered. An input connector on the control panel allows for electronic sweeping of the supply as well as NMR field control. Field reversal is available as an accessory when required.

The combination of a high homogeneity, medium-high field strength seven inch magnet, and a compact highly stable, solid state power supply, makes Harvey-Wells the logical choice. Send for complete specifications.

Alternate Power Supplies for use with the L-75A or L-128 electromagnets are available with either 0.1% regulation at intermediate cost or no regulation at low cost where high stability is not required.

Like the Model HS-1050, both of the above produce 5 kilowatts, 100 volts at 50 amperes.

UR-1050 POWER SUPPLY

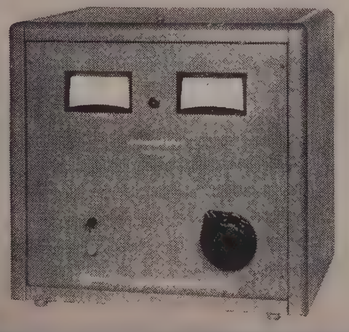

HARVEY-WELLS CORPORATION
Magnetics Division, 43 Kendall St., Framingham, Mass.

Please send complete data on the L-75A and HS-1050.

I am also interested in ☐ A 0.1% regulated power supply
☐ An unregulated power supply

NAME ______________________

POSITION ______________________

COMPANY ______________________

ADDRESS ______________________

CITY ______________________

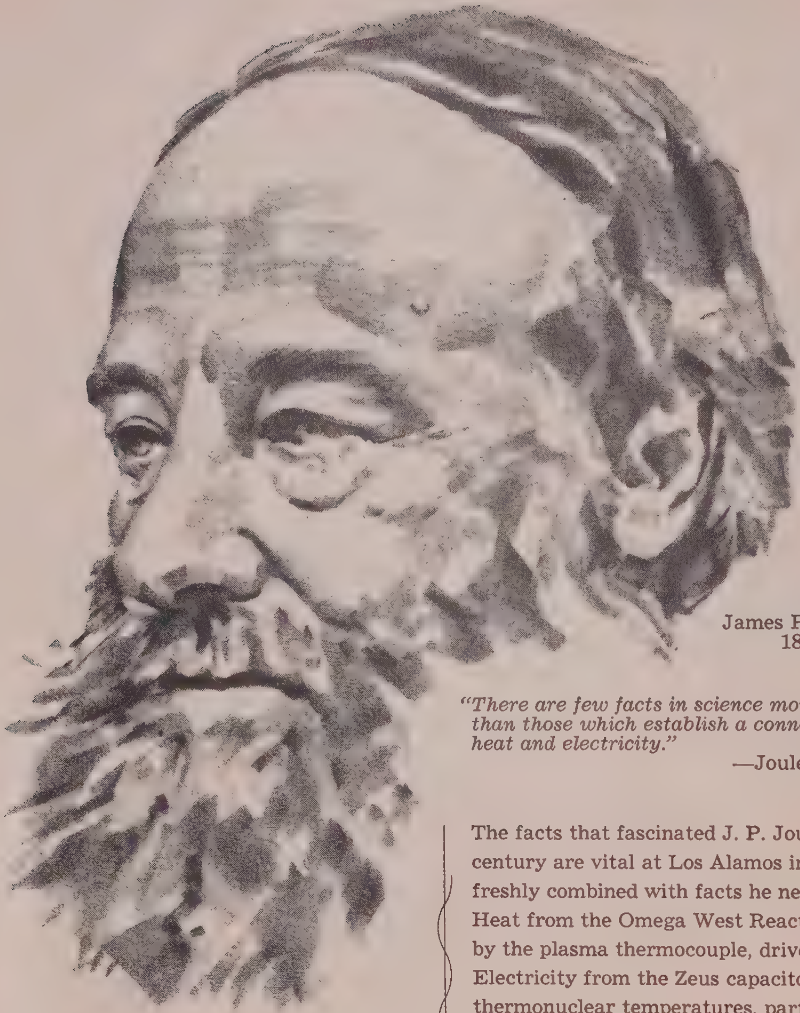

James Prescott Joule
1818-1889

"There are few facts in science more interesting than those which establish a connection between heat and electricity."
—Joule

The facts that fascinated J. P. Joule in the nineteenth century are vital at Los Alamos in the twentieth—freshly combined with facts he never dreamed of. Heat from the Omega West Reactor, directly converted by the plasma thermocouple, drives electric motors. Electricity from the Zeus capacitor bank produces thermonuclear temperatures, partly by the familiar process called joule heating. The Los Alamos Scientific Laboratory is proud to acknowledge its debt to great men who have found facts "interesting."

For employment information write:
Personnel Director, Division 61-58

los alamos
scientific laboratory
OF THE UNIVERSITY OF CALIFORNIA
LOS ALAMOS, NEW MEXICO

ILIKON MEANS MATERIAL

ILIKON CORPORATION is a research and development company founded for the purpose of contributing solutions to problems in the fields of materials science and engineering. The demands which today's Space Age technology places on materials have been so severe that materials scientists cannot satisfy these demands by simply improving upon existing conventional materials. ILIKON was created to meet these demands. At ILIKON scientists and engineers are searching for new materials, unique methods of fabrication, and devices based on the development of new materials and fabrication techniques.

To complement ILIKON's Space Age research and development activities an Applied Physics department was founded. This department specializes in outer space simulation testing, ultrahigh vacuum research and technology; and high energy particle physics. The coordination of these areas enables ILIKON to solve some of the most difficult problems which today's Space Age places on technology.

R & D PROJECTS IN THE FOLLOWING PROBLEM AREAS ARE NOW IN PROGRESS.

MATERIALS FOR HIGH TEMPERATURE APPLICATION • HIGH ENERGY PARTICLE PHYSICS
ELECTRO-CHEMISTRY AND CORROSION • PHYSICAL PROPERTY MEASURING DEVICES
NEW MATERIAL SHAPING AND FORMING TECHNIQUES • ULTRAHIGH VACUUM TECHNOLOGY
OUTER SPACE SIMULATION TECHNIQUE • PHYSICAL AND MECHANICAL METALLURGY

FOR FURTHER INFORMATION CONCERNING OUR TECHNICAL PROGRAM WRITE TO:

ILIKON CORPORATION
NATICK INDUSTRIAL CENTRE • NATICK, MASSACHUSETTS • CEDAR 5-8220

TESLA ELECTRON MICROSCOPE—Desk Model BS242

Guaranteed
Local Service

Installation
and
Instruction
Included in Price

TESLA

The Little
Giant
60 kV
30,000X
30Å

TESLA

FEATURES

- Resolving power 30Å to 50Å in routine operation, optimal resolution 25Å
- Magnification 1,000X to 30,000X, adjustable in steps
- Accelerating voltage 60 kV ±0.01%
- High-voltage stability better than 10^{-4}, ripple less than 2.5×10^{-5}
- Specimen inserted under vacuum
- Specimen motion controlled from microscope platform
- Microscope may be tilted for stereo-photography
- Viewing port usable for diffraction patterns
- Uses standard 35 mm film (36 pictures) or ten 2″ x 2″ plates
- Dimensions of basic instrument:
  14½″ wide, 18″ deep, 34½″ high
- Low initial cost and minimal maintenance

Made in
Czechoslovakia

Worldwide
Distribution
by

KOVO

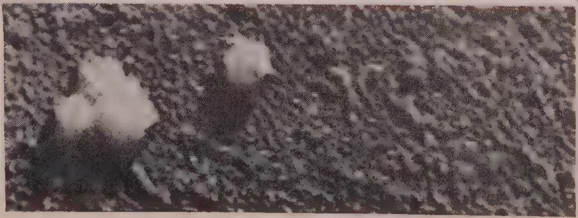

For complete
description, technical
data, and ordering
information, write for
BULLETIN 8-2000

Exclusive Sales and Service in U.S.A.

NATIONAL INSTRUMENT LABORATORIES, Inc.

828 Evarts St., Washington 18, D.C.
Tel. NOrth 7-7582

A complete range of the Tesla products will be shown at the Brno International Trade Fair,

HIGH PURITY ELEMENTS

SOUTH PLAINFIELD, N. J., July 1 -- ASARCO'S CENTRAL RESEARCH LABORATORIES ANNOUNCED THAT HIGH PURITY ELEMENTS ANTIMONY, ARSENIC, BISMUTH, CADMIUM, GOLD, INDIUM, SELENIUM AND TELLURIUM ARE NOW AVAILABLE IN COMMERCIAL QUANTITIES FOR EXPANDING PRODUCT APPLICATIONS. SINCE THESE AND OTHER ELEMENTS ARE PRODUCED FROM MATERIALS BASIC TO ASARCO'S DAILY OPERATIONS, CUSTOMERS ARE ASSURED OF CONTINUOUS SUPPLIES.

ASARCO HIGH PURITY ELEMENTS ANALYSES as of JULY 1, 1961

Impurities sometimes found at maximum levels in parts per million
(< denotes less than ppm indicated)

Element and Grade		Bi	Cu	Fe	As	Pb	Ag	Tl	Sn	Te	Au	Na	Cl	Cd
ANTIMONY	A-60	<1	<1	<1	2	<1								
✓ ARSENIC	A-60		<1											
BISMUTH	A-58		2	1		1	2						<1	
CADMIUM	A-60		<1	<1		1								
COPPER	A-58	No Impurities Detectable by Spectrographic Analysis												
GOLD	A-59		<1	<1		<1	1							
INDIUM	A-58		<1			1		<1	1					
LEAD	A-59	<1	<1	<1										
SELENIUM	A-58		<1		<1					1			<1	
SILVER	A-59		<1	<1		<1								
SULFUR	A-58											1	1	
TELLURIUM	A-58		<1	<1										
✓ THALLIUM	A-60		1	1		<1	<1					2	<1	
ZINC	A-59		<1	<1		<1								<1

✓ *Denotes element improved since last published analyses.*

ASARCO

The analyses above are among pertinent data compiled by Asa
Central Research Laboratories in an up-to-date catalogue now avai
to users of high purity elements. For a copy, write on
company letterhead to American Smelting and Refining Com
120 Broadway, New York 5,

ELECTRONICS PHYSICIST

Ultra Microwave Tubes

We are expanding our company supported program of basic research on mechanisms for generating, amplifying and detecting coherent radiation in the millimeter and sub-millimeter region of the electromagnetic spectrum. Research is carried out on unconventional vacuum tubes and masers, supported by basic paramagnetic materials, studies and investigations into bulk and surface semiconductor properties at extremely high frequencies.

A position has become available for an Electronics Physicist or Microwave Tube Engineer with an extensive theoretical background to participate with a well-established group of theoreticians and experimentalists in a new phase of research on ultra microwave tubes. The position requires a high level of competence in the execution of analytical studies on interaction processes between electron streams and electromagnetic fields. We are particularly interested in applicants who have had at least several years of experience in this area at a university or in industry. A PhD or MS degree in Physics or Electrical Engineering is required.

We are seeking a scientist who enjoys the stimulation and challenge of theoretical, creative research, supported by a group of experimentalists working in a modern, well-equipped laboratory. Salary offered will be commensurate with academic training and scientific accomplishment in this field.

Please submit resume to F. J. Loyer

GENERAL TELEPHONE
& ELECTRONICS LABORATORIES

Subsidiary of **GENERAL TELEPHONE & ELECTRONICS** GENERAL SYSTEM

208-20 Willets Point Boulevard
Bayside, LI, New York

All qualified applicants will receive consideration for employment without regard to race, creed, color or national origin.

UNIQUE...

mple and versatile underwater manipulation

Central Research Laboratories'

model B
canal manipulator

If your operation has required grappling and shing at the bottom of a canal or pool, Central Research Laboratories' Model B Canal Manipulator may be the new tool for you. Master-Slave Manipulator type ambidextrous handle, wrist joints, and tongs are coupled by alloy tapes passing through a cross-over housing and long vertical ube. This makes possible dexterous underwater manipulation. All submerged components are tainless steel for maximum corrosion resistance.

Wrist Joint and Tong Motions

The wide range of wrist-joint and tong motions nsures deft and adroit handling of large and mall objects. Squeeze motion is 3½ inches with n elevation rotation of 168° going from 38° back of vertical to 40° above horizontal. Twist rotation is 360° minimum at ends of elevation range, 720° when the tong is pointed 45° downward.

Azimuth rotation and X, Y, and Z translations are provided by gross movement of the vertical support tube. A constant force spring suspension supports the manipulator in the canal or pool.

For further versatility, the Model B Canal Manipulator may be equipped with standard or special purpose interchangeable tongs of either he RCD-447-100 or SRL-IIA type. Vertical ubes of desired length are available to meet most requirements.

CENTRAL RESEARCH . . .
MANIPULATORS FOR EVERY NEED

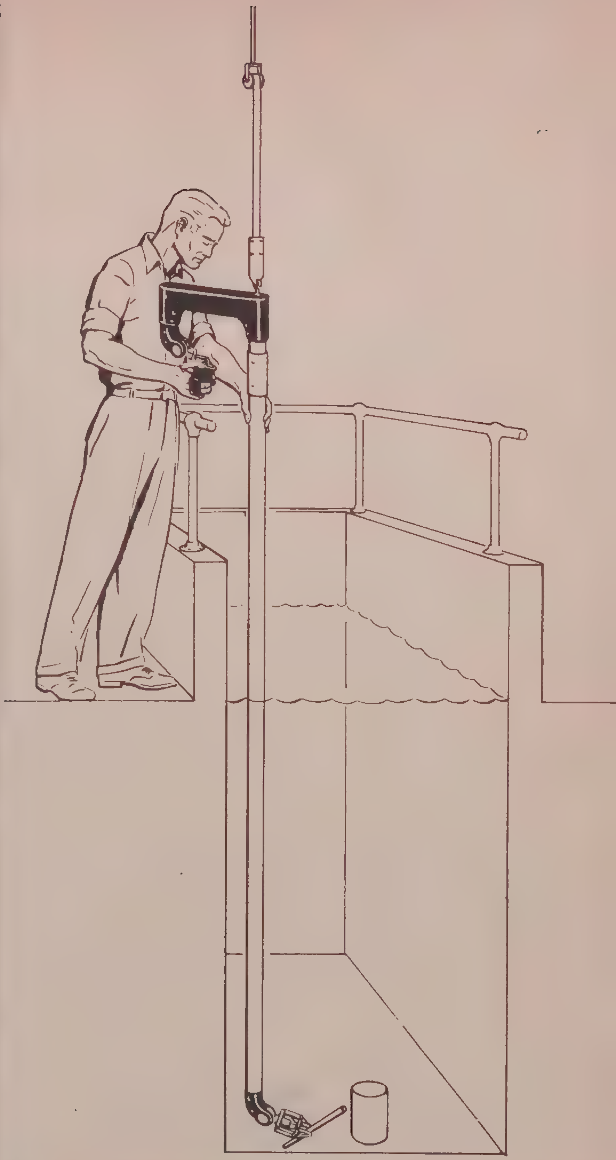

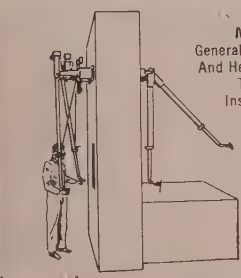

Model 8
General Purpose
And Heavy Duty
Thru-Wall
Installations

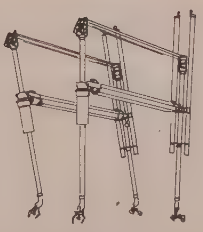

Model 7
Restricted Space Installations

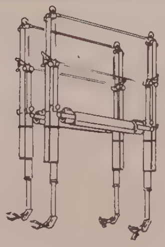

Model 4
Over-Wall Installations

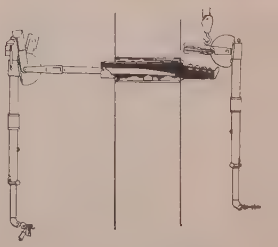

Model A Sealed

For further information on Central Research manipulators, accessories, or hot cell design problems, write: Dept. 311

Central Research
laboratories, inc.
Red Wing, Minnesota

Corporate Associates

American Institute of Physics

The Corporate Associates of the American Institute of Physics are a group of corporations, institutions, and laboratories who believe it is valuable to them and to America to maintain a vigorous advance in the physical sciences. By their membership dues they aid the Institute significantly in carrying out its purpose: the advancement and diffusion of knowledge of the science of physics and its application to human welfare. The Institute is grateful for their assistance.

CORPORATE ASSOCIATES OF THE INSTITUTE

Abbott Laboratories
Academic Press Inc.
Acoustica Associates, Inc.
Aerospace Corporation
Airborne Instruments Laboratory
Air Products, Inc.
Allegheny Ludlum Steel Corporation
Allen-Bradley Company
Allied Research Associates, Inc.
Allis-Chalmers Manufacturing Co.
Aluminum Company of America
American Can Company
American Cyanamid Company
American Machine & Foundry Co.
American Oil Company
American Optical Company
American Radiator & Standard Sanitary Corp.
American Viscose Corporation
Ansco Div. of General Aniline & Film Corp.
Applied Physics Corporation
Armco Steel Corporation
Armour Research Foundation
Armstrong Cork Company
The Atlantic Refining Company
Atomics International Division North American Aviation, Inc.
Automatic Electric Laboratories, Inc.
Avco-Everett Research Laboratory
Avco Research & Advanced Development
Baird-Atomic, Inc.
Ball Brothers Research Corporation
Barnes Engineering Company
Basic Books, Inc.
Battelle Memorial Institute
Bausch & Lomb Incorporated
Beckman Instruments, Inc.
Bell & Howell Research Center
Bell Telephone Laboratories, Inc.
Bendix Corporation
Bethlehem Steel Company, Inc.
Bodine Soundrive Company
Boeing Airplane Company
Bolt Beranek and Newman Inc.
Borg-Warner Corporation
The Budd Company
Bulova Research and Development Laboratories, Inc.
Burroughs Corporation
California Research Corporation
The Carborundum Company
Carrier Corporation
Caterpillar Tractor Company
CBS Laboratories
Celanese Corporation of America
Central Scientific Company
Chance Vought Aircraft, Inc.
Chemstrand Research Center, Inc.
Chrysler Corporation
The Cincinnati Milling Machine Company
Clevite Corporation
Collins Radio Company
Combustion Engineering, Inc.
Continental Can Company, Inc.
Continental Oil Company
Cornell Aeronautical Laboratory, Inc.
Corning Glass Works
Crane Company
The Detroit Edison Company
Douglas Aircraft Co., Inc.
The Dow Chemical Company
E. I. du Pont de Nemours & Co., Inc.
Eastman Kodak Company
Thomas A. Edison Research Laboratory
The Eppley Laboratory, Inc.
Esso Research & Engineering Company
Fairchild Camera & Instrument Corp.
Farrand Optical Co., Inc.
The Firestone Tire & Rubber Co.
Ford Motor Company
The Foxboro Company
General Dynamics Corporation
General Electric Company
General Motors Corporation
General Precision, Inc.
General Radio Company
General Telephone & Electronics Laboratories, Inc.
The Gillette Company
The B. F. Goodrich Company
The Goodyear Tire & Rubber Co.
W. R. Grace & Co.
Grinnell Corporation
Grumman Aircraft Engineering Corp.
Gulf Research & Development Co.
Haller, Raymond and Brown, Inc.
Halliburton Oil Well Cementing Co.
Haloid Xerox Inc.
Hercules Powder Company
Hewlett-Packard Company
High Voltage Engineering Corp.
Hughes Aircraft Co.
Humble Oil & Refining Company
International Business Machines Corp.
International Harvester Company
International Minerals & Chemical Corp.
International Nickel Co., Inc.
Itek Corporation
ITT Federal Laboratories
Joslyn Mfg. & Supply Co.
Knowles Electronics, Inc.
Koppers Company, Inc.
Lear, Incorporated
Leeds & Northrup Company
Libbey-Owens-Ford Glass Co.
Arthur D. Little, Inc.
Litton Industries, Inc.
Lockheed Aircraft Corporation
McGraw-Hill Book Company, Inc.
The Magnavox Company
The Martin Company
Massachusetts Institute of Technology
Merck Sharp & Dohme Research Labs.
Minneapolis-Honeywell Regulator Co.
Minnesota Mining & Manufacturing Co.
Monsanto Chemical Company
Motorola Semiconductor Products Division
The National Cash Register Company
National Research Corporation
Northrop Corporation
Nuclear Development Corporation of America
The Ohio Oil Company
Olin Mathieson Chemical Corp.
Operations Research Incorporated
Outboard Marine Corporation
Owens-Corning Fiberglas Corporation
Owens-Illinois Glass Co.
Pacific Semiconductors, Inc.
Page Communications Engineers, Inc.
Pergamon Press, Inc.
The Perkin-Elmer Corp.
Philco Corporation
Philips Laboratories, Div. of North American Philips Co., Inc.
Phillips Petroleum Company
Pilkington Brothers Limited
Pitney-Bowes, Inc.
Pittsburgh Corning Corp.
Pittsburgh Plate Glass Company Glass Division
Polaroid Corporation
The Procter & Gamble Company
The Pure Oil Company
Radio Corporation of America
Ramo-Wooldridge Division Thompson Ramo Wooldridge Inc.
The Rand Corporation
Raytheon Company
Republic Aviation Corporation
Republic Steel Corporation
Sangamo Electric Company
Schering Corporation
Schlumberger Well Surveying Corp.
Scientific American
Shell Development Company
Shockley Transistor Corporation
Smyth Research Associates
Socony Mobil Oil Company, Inc.
Space Technology Laboratories, Inc.
Sperry Rand Corporation
Sprague Electric Company
A. E. Staley Manufacturing Co.
Sun Oil Company
Technical Operations, Inc.
Texaco, Inc.
Texas Instruments, Inc.
TRG, Incorporated
Tung-Sol Electric Inc.
Union Carbide Corporation
Union Oil Company of California
Union Switch & Signal Div. of Westinghouse Air Brake Co.
United Aircraft Corporation
United Gas Corporation
United States Rubber Company
United States Steel Corp.
Universal Oil Products Company
The Upjohn Company
Vacuum-Electronics Corp.
Varian Associates
Vitro Laboratories Division of Vitro Corp. of America
Western Union Telegraph Company
Westinghouse Electric Corporation
Whirlpool Corporation
Wyandotte Chemicals Corporation
Zenith Radio Corporation

The American Institute of Physics cordially invites interested corporations and institutions to make application for Corporate Associate membership and will welcome their inquiries addressed to the Secretary.

AMERICAN INSTITUTE OF PHYSICS *335 East 45 Street, New York 17, New Y*

Physicists

The Hughes Research Laboratories offer an outstanding professional environment to Scientists with an interest in basic and applied research. At these exceptional facilities you can realize maximum professional growth through programs including:

SOLID STATE PHYSICS RESEARCH
Microwave and millimeter wave magnetic resonance
Optical and infrared spectroscopy
Solid state masers
Semiconductor physics

MATERIALS RESEARCH
Crystal growing
Crystal growth mechanisms
Crystal perfection

SURFACE PHYSICS
Low work function surfaces
Thermionic electron emission
Thermionic ion emission

MATERIALS STUDIES
Molecular design
Chemical synthesis

PLASMA PHYSICS
Thermionic energy conversion
Microwave plasma devices

ION PROPULSION

The facilities of the Hughes Research Laboratories are located in Malibu, California, overlooking the Pacific Ocean—immediately adjacent to major academic institutions—with programs of academic support and participation. These facilities were specifically designed for effective research efforts with private offices and complete research laboratories. In this uniquely creative atmosphere, Hughes scientists are continually adding to their record of accomplishments in electronics and physics research.

Your inquiry may be directed in strict confidence to: Mr. D. A. Bowdoin, Hughes Research Laboratories, Malibu, California.

All qualified applicants will receive consideration for employment without regard to race, creed, color or national origin.

creating a new world with electronics

HUGHES

HUGHES AIRCRAFT COMPANY
RESEARCH LABORATORIES

New High Performance 22" Magnet System from Va

UP TO 50 KG

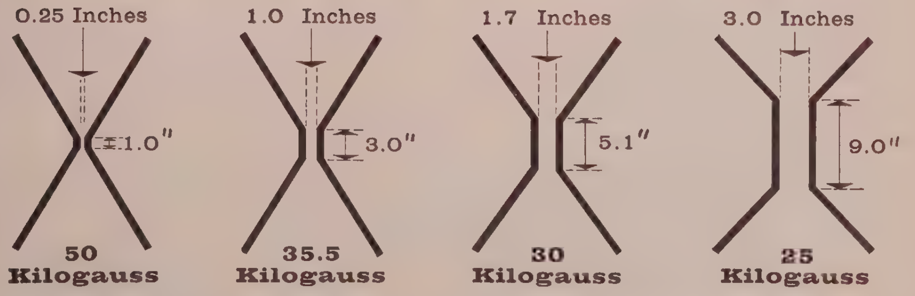

The achievement—an extension of Varian performance

Highly homogeneous and stable magnetic fields at previously unavailable intensities up to 50 KG are made possible by Varian's new V-3100/V-2400 electromagnet/power supply system. The Key: uncompromising design standards and Varian's traditional painstaking care. This performance is delivered with only modest power and cooling requirements through integrated *system design.* And a high degree of usefulness has been attained without sacrificing performance capabilities:

Alignment of magnetic fields in most specified air gaps is assured by Varian *nuclear-magnetic-resonance* techniques.

Stability of one part in 10^5 against ± 10% line voltage change is achieved by the 40 KW regulated power supply. Optimum regulation against slow *and* fast line changes is accomplished.

Engineered feature by feature for maximum usefulness

In addition to the basic characteristics enumerated, the V-3100/V-2400 system incorporates both conventional and outstanding new design features:

- Massive yoke and 22" diameter pole pieces allow steep pole tapering to achieve extremely high fields.
- Magnetic field may be rotated 225° about the vertical axis; field polarity is reversible by switch circuit.
- Air gap accessibility is assured by the 8" coil separation and 45° yoke angle. A 1"-diameter axial hole is provided through yoke and pole pieces permitting sample irradiation when special axial-hole pole caps are used. Air gap is 36⅝" above bottom of magnet base.
- Economy of operation, achieved by system design, is shown by low input requirements: a nominal 45.5 KW of power (3-phase, 480V/60 cps or 380V/50 cps) and cooling water at 20 gpm—60 psi differential pressure.
- Compact, all-transistorized power supply stands at convenient operating height, and rests on only 3' x 3' of floor space.
- System is completely protected by safety interlocks.
- Interchangeable pole caps and adapter plates, and a field-sweep system, are optional at extra cost.
- World-wide field engineering service is available at all times from Varian.

For further details write,
Instrument Division.

VARIAN associates
PALO ALTO 36, CALIFORNIA

INSTRUMENT DIVISION REGIONAL OFFICES

EASTERN OFFICE: *12 South Michigan Avenue*
Kenilworth, New Jersey • CHestnut 1-0200

MIDWESTERN OFFICE: *517 Talcott Road*
Park Ridge, Illinois • TAlcott 5-6686

THINNER THAN EVER!

Sanyo Electric Co., Ltd. now announces the achievement in dramatically reducing thickness of *thermo module* element down to 2/3 of others, without sacrificing its performances in any way. Our exhaustive study reveals possibility of still reducing its thinness for applying to limit installing space of scientific and electronics equipments.

SPECIFICATIONS

Type	Couple	Optimum Current (amp)	Optimum Voltage (volt)	T (1) (°C)	Insulation Voltage (volt) (2)	Dimensions mm (inch)
STM-1025	10	25	0.9	55	50	57 × 43 × 9.5 (2.24 × 1.69 × 0.374)
STM-1025V	10	25	0.9	55	1500	57 × 43 × 10.5 (2.24 × 1.69 × 0.413)
STM-1012	10	12	0.9	55	50	41 × 32.5 × 8.5 (1.62 × 1.28 × 0.334)
STM-1012V	10	12	0.9	55	1500	41 × 32.5 × 9.5 (1.62 × 1.28 × 0.374)
*STM-1006	10	6	0.9	55	50	36 × 29 × 6.5 (1.42 × 1.14 × 0.256)
*STM-1006V	10	6	0.9	55	1500	36 × 29 × 7.5 (1.42 × 1.14 × 0.295)

Subject to change without notice

Note: (1) No heat load T_h is 27°C

(2) Voltage applied between circuit and hot or cold plate.

* Being marketed soon.

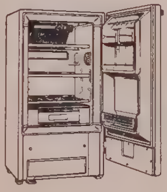
Thermo-electric Refrigerator

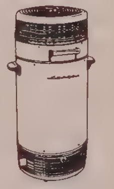
Thermo Electric Jar

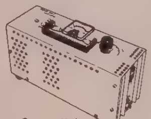
Power Unit

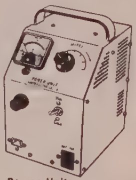
Power Units

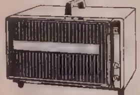
Thermo Pac

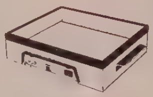
Thermo Processing Tray

Apply for further details to:

SANYO

SANYO ELECTRIC CO., LTD. OSAKA, JAPAN
INTERNATIONAL DIVISION SANYO ELECTRIC TRADING CO., LTD.

the first portable, "desk-top" 400-channel pulse height analyzer

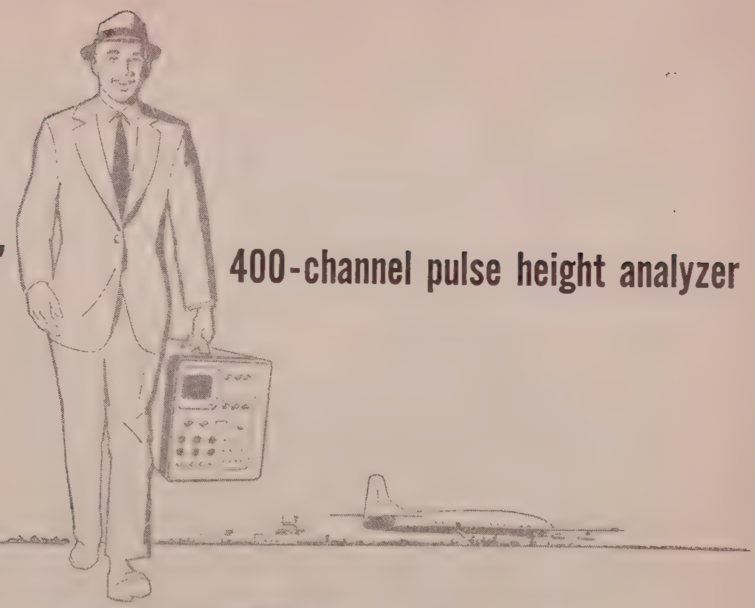

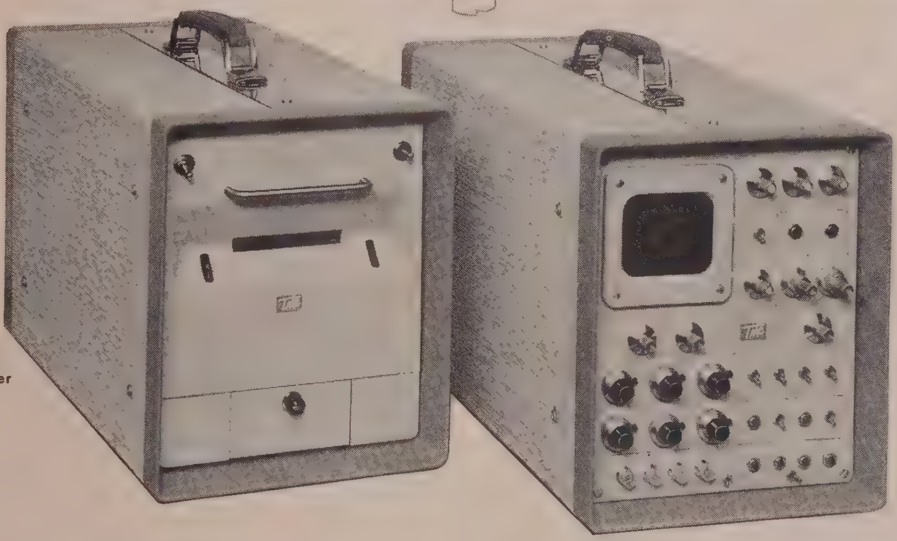

Model 500
decimal printer

Model 404
pulse height analyzer

— the TMC Model 404

The new TMC Model 404 is the most portable pulse height analyzer you can own. Take it and use it anywhere. With its all-transistor, printed circuitry and 400-channel memory in a package just over a cubic foot, this analyzer is small enough to operate on your desk. *All* the instruments needed for an experiment can be carried easily by one person.

The Model 404 has a magnetic core memory that can be used in sub-groups of two or four; four separate inputs and associated amplifiers; internal pulse routing circuitry; pushbutton data transfer and display overlap; very low power requirements and many "system" advantages. And it can be used with the new solid state detectors.

For readout, use its companion unit, the Model 500 Decimal Printer; a high speed paper tape punch; strip chart or X-Y recorders; or an IBM electric typewriter.

LITERATURE ON REQUEST

TMC TECHNICAL MEASUREMENT CORPORATION
441 WASHINGTON AVENUE NORTH HAVEN, CONNECTICUT

Large Capacity—High Vacuum

Welch TWO-STAGE DUO-SEAL VACUUM PUMP *with* VENTED-EXHAUST

PATENT NO. 2,885,143

Eliminates Condensed Vapor Problems

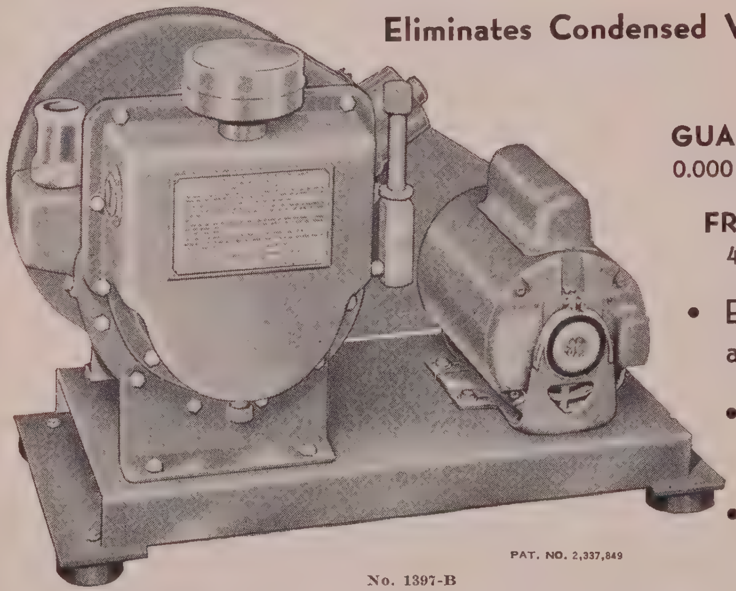

PAT. NO. 2,337,849

No. 1397-B

GUARANTEED VACUUM
0.0001 mm Hg. or 0.1 Micron

FREE AIR CAPACITY
425 Liters Per Minute

- Eliminates oil filters and separators
- Reduces pumpdown time
- Fewer oil changes required

The Welch vented exhaust pump has provision for adjusting the amount of air introduced to meet various conditions of temperature and vapor concentration. The design is such that the air admitted through the exhaust vent cannot return to the system, so ultimate vacuum attainable approaches that of the same pump with the exhaust vent closed.

Thus the vented exhaust enables these Duo-Seal pumps to remove both permanent and condensable gases from a system without contamination of the oil. This means in practice that these pumps will be able to reach lower total pressures in shorter periods of time, and good vacuum performance will be possible for long periods without the bothersome trapping and excessive number of oil changes formerly necessary.

1397B. DUO–SEAL VACUUM PUMP, Motor Driven.
For 115 Volts, 60 Cycles, A.C. **Each, $645.00**

1397C. DUO–SEAL VACUUM PUMP, Motor Driven.
For 230 Volts, 60 Cycles, A.C. **Each, $645.00**

1397D. DUO–SEAL VACUUM PUMP, Motor Driven.
For 115 Volts, D.C. **Each, $749.00**

A belt guard is included with the mounted pumps.

1397. DUO–SEAL VACUUM PUMP, Unmounted.
With pulley, but without motor, belt or base.
Each, $525.00

Pump Revolutions – 365 RPM
Motor – 1 HP – 1725 RPM
Tubing Required – 1⅝-inch i.d.
Over-all Dimensions of Mounted Pump
25⅝ x 14¾ x 18¾ inches high
Belt-tightening Provision
Extra Supply of Duo-Seal Oil

THE WELCH SCIENTIFIC COMPANY

ESTABLISHED 1880

1515 Sedgwick Street, Dept. C-1 Chicago 10, Illinois U. S. A.

Manufacturers of Scientific Instruments and Laboratory Apparatus

Journal
of
Applied Physics

Volume 32, Number 7 July, 1961

Theory of Quantum Oscillators in a Multimode Cavity

W. G. Wagner and G. Birnbaum
Hughes Research Laboratories, A Division of Hughes Aircraft Company, Malibu, California

(Received February 1, 1961)

The spectrum of power radiated by a solid-state optical maser in steady-state operation is obtained by considering each atomic system to be a source of randomly fluctuating dipole moment which drives every mode of the cavity. The nonlinear behavior of the collection of atomic systems is treated in such a way that a detailed examination of the distribution of power in the various modes is possible. A number of examples are considered which show how critically dependent on the relative loss rates of the various modes are the characteristics of the output from a multimode oscillator. An interesting result of this calculation is the appearance in some cases of an abrupt transition as the pumping power is increased: above this point a large fraction of energy goes into the mode which is resonant with the atomic transition and which has the lowest loss rate. Another case is studied which does not have this feature, but which could be useful in analyzing the behavior of solid-state optical masers which have substantial scattering due to crystal imperfections.

I. INTRODUCTION

WITH the realization of the optical maser by Maiman[1] and soon after by Collins *et al.*,[2] it became important to consider the theory of this device. Schawlow and Townes[3] have already discussed the extension of maser techniques to the optical region by using a resonant cavity having a great many modes, in particular, a Fabry-Perot interferometer. Although they discuss in detail how a single mode may be selected, they give only a qualitative account of the spectral distribution of the output radiation. It is the purpose of this paper to study this question by developing a theory of quantum oscillators coupled to a multimode cavity.

It is to be noted that in practice the wall losses could be so great that the use of the independent mode concept may be untenable. This also may be the case if the material in the cavity is so inhomogeneous that interference effects are obliterated; i.e., that mode coupling becomes important. For these reasons, care must be taken in attempting to analyze experiments by comparison with the theory for an ideal case. Our primary purpose here is to understand in detail the behavior of a multimode oscillator rather than to explain the details of optical maser action in practice. However, it is hoped that this study of an ideal case will help in analyzing the properties of a real optical maser.

In the case of the ammonia beam maser, Gordon, Zeiger, and Townes[4] analyzed the spectrum of the oscillations by considering the device as a linear amplifier driven by circuit or thermal noise. In the optical region, where thermal noise is inconsequential compared with the spontaneous emission from the maser material, it is natural to consider the maser as an amplifier driven by its own internal noise. In this paper, however, the nonlinear behavior of the atomic system is treated, thus allowing a detailed examination of the distribution of power in the various modes.

In the region below oscillation, the optical maser may be operated as an amplifier or used as a very narrow band filter. These cases can be treated by a straightforward extension of the theory developed here.

II. DESCRIPTION OF THE MASER SYSTEM

Let us consider a fluorescent substance which ideally has just three energy levels ($E_3 > E_2 > E_1$) and behaves in the following way: Atomic systems in levels 2 and 3

---

[1] T. H. Maiman, Phys. Rev. Letters 4, 564 (1960); Nature **187**, 493 (1960); Brit. Communs. Electronics **7**, 674 (1960).

[2] R. J. Collins, D. F. Nelson, A. L. Schawlow, W. Bond, C. G. B. Garrett, and W. Kaiser, Phys. Rev. Letters **5**, 303 (1960).

[3] A. L. Schawlow and C. H. Townes, Phys. Rev. **112**, 1940 (1958).

[4] J. P. Gordon, H. J. Zeiger, and C. H. Townes, Phys. Rev. **99**, 1264 (1955).

Copyright © 1961 by the American Institute of Physics.

decay to the ground level solely by radiative transitions. On the other hand, the transition from level 3 to level 2 is nonradiative and, compared with the other transitions, infinitely rapid. This implies that the probability of a system being in the third level is negligible and that there can be no saturation of the pumping transition 1 to 3. We desire to compute the spectral properties of the power emitted in the radiative transition from the second to the first level subject to a given amount of pumping radiation. The output results from spontaneous emission which is amplified (or absorbed) by the optically excited maser material.

Broadening of the lines plays a very important role in determining the properties of the output. Here, however, we shall be occupied with setting up a formalism to describe the steady-state oscillation of an optical maser (or laser) and thus shall not consider the effect of various types of broadening. We shall treat the simple case in which the second level is homogeneously broadened and assume a Lorentz shape with a full width at half-maximum of $2/T$. Furthermore, we shall make the simplifying assumption that $2/T$ is much larger than any of the radiative transition rates that occur in our problem so that we may neglect the additional broadening caused by the latter.

It is important to realize that in absorption experiments the broadening resulting from saturation is not caused by an intrinsic modification of a line shape, but rather by the alteration of the populations in the two states as a result of the high rate of induced transitions.[5] In absorption experiments, the change in populations depends strongly on the frequency of the imput radiation. It is common practice to combine this function of frequency with the intrinsic absorption line shape, calling the product the saturation shape factor. In the problem we consider, the relative population of the levels is determined by the pumping rate and the rates of spontaneous and induced transitions. The latter does not depend on frequency because there is no monochromatic input radiation in this case. Thus, we never encounter the so-called saturated line shape. By the uncertainty principle, high transition rates resulting from the pumping radiation and the cavity radiation must give rise to additional broadening since they shorten the lifetimes of the states, but we shall explicitly neglect this effect by the assumption that the substance is not pumped so hard that any of the radiative transition rates becomes comparable to $2/T$.

The conceptual idea we shall employ to compute the spectrum of power radiated is to consider each system to be a source of a randomly fluctuating dipole moment which drives every mode of the cavity. It will be demonstrated that this approach leads to a power output which equals that from spontaneous plus induced emission. Our principal approximation in this treatment of multiple modes will be to neglect the coupling between the cavity modes as a result of the losses in the walls and the material in the cavity.

Since the second level is homogeneously broadened, the state of the large number of systems in the cavity and the radiation density in the steady state can be specified by giving the relative number of systems in the second level, N_2/N. This makes the problem much simpler compared with one in which the width of the second level is caused by inhomogeneous broadening. There the state of the N atomic or molecular systems and the radiation density depends on the function $N_2(\omega_a)/N(\omega_a)$, which gives the relative number of systems in the second level for each packet of homogeneously broadened lines characterized by having its absorption line centered at ω_a.

The crux of the problem is to determine the relation between N_2 and the pumping rate $\Gamma_{31}{}^i$, since N_2 determines the spectrum of the power output. That relation can be obtained most simply by equating the total power output to the power input less the power loss in the transition from level 3 to level 2, neglecting the small uncertainty in the energy of the photon emitted in the transition from 2 to 1. Stated in equivalent terms, we just equate the number of systems being pumped out of level 1 per second to the net number returning from level 2 by means of induced and spontaneous transitions.

III. CALCULATION OF THE RADIATION SPECTRUM

Every system in an excited state is able to drive another system if the two are coupled. In our case, the various dipoles drive each cavity mode. When the phase of the excited system is unspecified, however, we are unable to predict, even classically, its effect or "force" upon the second system and instead characterize its effect by giving the spectral density of that statistically fluctuating force. The spectral density of noise fluctuations in the dipole moment of the ith system is given by[6]

$$|\mu_s{}^i(\omega)|^2 = \sum_{m,n} 2\rho_m |\langle n|\mu|m\rangle|^2 \delta(\omega-\omega_{mn}), \quad \text{for } \omega>0, \quad (1)$$

where ρ_m is the density matrix, under the assumption that the excited states are sharply defined in energy. Actually, they are broadened because they have finite lifetimes, and thus we should replace the δ function by a resonance function reflecting the widths of the states involved. For our case, therefore, the total noisy dipole moment per unit frequency of all the atomic systems in the cavity is

---

[5] R. Karplus and J. Schwinger, Phys. Rev. **73**, 1020 (1948).

[6] This formula is a modification of a result obtained by H. Ekstein and N. Rostocker, Phys. Rev. **100**, 1023 (1955); see Eqs. (13) and (15). It differs from theirs by a factor of 2, which arises because in our analysis the frequency variable takes on only positive values, and by the deletion of the term $\delta(\omega+\omega_{nn'})$. The latter modification is due to the fact that only downward transitions are effective in driving another system. Our formula has been derived by Hellwarth in an unpublished report [R. W. Hellwarth (private communication)].

$$|\mu_s(\omega)|^2=2\mu^2N_2\{T/\pi[1+T^2(\omega-\omega_a)^2]\}, \tag{2}$$

where $\mu^2=|\langle 1|\mu|2\rangle|^2$ and N_2 is the number of systems in the second level.

Let us turn now to a consideration of the behavior of the electromagnetic field in the cavity. In a lossless cavity, the field can be expanded in terms of normal modes:

$$\begin{aligned}\mathbf{E}&=\textstyle\sum_m q_m(t)\omega_m\mathbf{N}_m(\mathbf{x})\\ \mathbf{B}&=\textstyle\sum_m p_m(t)\nabla\times\mathbf{N}_m(\mathbf{x})/\omega_m,\end{aligned} \tag{3}$$

where $\int_V\mathbf{N}_m(\mathbf{x})\cdot\mathbf{N}_n(\mathbf{x})d^3\mathbf{x}=\delta_{mn}$. The Hamiltonian, which is the energy in the field, can be expressed in terms of the normal coordinates as

$$\tfrac{1}{2}\int_V(E^2+B^2)d^3x=\tfrac{1}{2}\sum_m(p_m{}^2+\omega_m{}^2q_m{}^2). \tag{4}$$

The equations of motion are simply those of an uncoupled collection of harmonic oscillators:

$$\dot{q}_m=p_m;\quad \dot{p}_m=-\omega_m{}^2q_m. \tag{5}$$

The introduction of wall losses and holes in the cavity couples these modes; the effect of this coupling will be mentioned later. We shall neglect this here, however, and take the equations of motion to be

$$\ddot{q}_m+\gamma_m\dot{q}_m+\omega_m{}^2q_m=\textstyle\sum_i\mu^if_m{}^i\omega_m, \tag{6}$$

where $\mu^if_m{}^i=\langle\boldsymbol{\mu}_i\rangle\cdot\mathbf{N}_m(\mathbf{x}_i)$ and γ_m is the damping rate in the *m*th normal mode. The dipole moment μ^i is the sum of an induced part $\mu_i{}^i$ and a spontaneous part $\mu_s{}^i$.

The response of each mode to the spontaneous moments must be calculated. The first step is to calculate the dipole induced in each of the systems because of the oscillating electric field. From lowest-order perturbation theory, including damping, for a field oscillating as $e^{-i\omega t}$ we have

$$\langle\mu_i{}^i(\omega)\rangle=\sum_n\frac{-\omega_nf_n{}^iq_n(\omega)}{\hbar}\sum_{\alpha,\beta}\rho_\alpha|\langle\beta|\mu|\alpha\rangle|^2Z, \tag{7}$$

where

$$Z=\{[(\omega-\omega_{\beta\alpha})+i\Gamma/2]^{-1}-[(\omega+\omega_{\beta\alpha})+i\Gamma/2]^{-1}\}.$$

Equation (7), for two levels, reduces to

$$\langle\mu_i{}^i(\omega)\rangle=\sum_n i\omega_n\frac{\mu^2}{\hbar}q_nf_n{}^iT\frac{(N_1-N_2)}{N}\times\left[\frac{1}{1-iT(\omega-\omega_a)}-\frac{1}{1-iT(\omega+\omega_a)}\right]. \tag{8}$$

Note that $\langle\mu_i{}^i\rangle$ is the Fourier transform of $\langle\mu_i{}^i(\omega)\rangle$. The second term in the bracket is negligible, since we do not consider frequencies far from the resonance frequency. With this result we can eliminate the induced dipole variables from the equations for the forced oscillation of the electromagnetic modes. On doing so, we obtain the following set of coupled equations:

$$\begin{aligned}-\omega^2q_m-i\omega\gamma_mq_m+\omega_m{}^2\left\{1-\frac{i\mu^2T\langle(f_m{}^i)^2\rangle(N_1-N_2)}{\hbar[1-iT(\omega-\omega_a)]}\right\}q_m\\ =\sum_{n\neq m}i\omega_m\omega_n\mu^2\frac{T\langle f_m{}^if_n{}^i\rangle(N_1-N_2)q_n}{\hbar[1-iT(\omega-\omega_a)]}\\ +\sum_i\mu_s{}^i(\omega)f_m{}^i\omega_m,\end{aligned} \tag{9}$$

where

$$\langle(f_m{}^i)^2\rangle=\textstyle\sum_i(f_m{}^i)^2/N.$$

Now we cannot handle this coupling between the modes and so in order to proceed we are forced to neglect it. We can see, however, that this neglect is justified. Whereas $\langle(f_m{}^i)^2\rangle$ cannot be discarded, $\langle f_m{}^if_n{}^i\rangle$ can be if the optical sites are distributed randomly, because the normal modes are orthogonal. Thus, to a good approximation the material in the cavity does not couple the modes, and hence the admittance of each mode to the spontaneous dipole of the *i*th system is

$$\frac{q_m(\omega)}{\mu_s{}^i(\omega)}=\frac{-\omega_mf_m{}^i}{\omega^2-\omega_m{}^2+i\omega\gamma_m+i\omega_m{}^2\{\mu^2T\langle(f_m{}^i)^2\rangle(N_1-N_2)/\hbar[1-iT(\omega-\omega_a)]\}}. \tag{10}$$

We shall be concerned with only those modes near the molecular resonance, and so we shall approximate this admittance by

$$\frac{q_m(\omega)}{\mu_s{}^i(\omega)}=\frac{-f_m{}^i}{2(\omega-\omega_m)+i\gamma_m+i\omega_m\mu^2T\xi_m(N_1-N_2)/\hbar V[1-iT(\omega-\omega_a)]}\equiv\frac{-f_m{}^i}{z_m(\omega)}, \tag{11}$$

where $\langle(f_m{}^i)^2\rangle=\xi_m/V$ and V is the cavity volume.

The spectral density of radiation from the fluctuating dipoles in the cavity is given by the following expression:

$$E(\omega)=\textstyle\sum_m\omega_m{}^2|q_m(\omega)|^2. \tag{12}$$

Using the formulas for the admittance of each mode and for the "noisy" dipole moments which drive each mode, we find that the frequency distribution of electromagnetic energy from Eqs. (11) and (2) must be

$$E(\omega)=\sum_m\frac{\omega_m{}^22\mu^2N_2T\xi_m}{\pi[1+T^2(\omega-\omega_a)^2]V|z_m(\omega)|^2}. \tag{13}$$

IV. CHECK ON CONSISTENCY OF THE FORMALISM

To demonstrate that Eq. (13) does indeed imply that the power output equals the input less the loss in the transition from level 3 to level 2, let us digress. This adjusted power input must be equal to

$$P=\hbar\omega_a N_1\Gamma_{31}{}^{i},\qquad(14)$$

under the approximation that the energy of all the photons emitted in the jump from 2 to 1 is given by $\hbar\omega_a$, since $N_1\Gamma_{31}{}^{i}$ gives the number of systems per second being pumped from the first to the third level. In equilibrium, that number must equal the net number returning to 1 from 2 as a result of induced and spontaneous transitions. Thus, the adjusted power input is

$$P=\hbar\omega_a[N_2\Gamma_{12}{}^{s}+(N_2-N_1)\Gamma_{12}{}^{i}].\qquad(15)$$

Now the rate of induced transitions between the two levels is given by[7]

$$\frac{\pi\mu^2}{\hbar^2}\int U_i(\omega)\frac{Td\omega}{\pi[1+T^2(\omega-\omega_a)^2]},\qquad(16)$$

where $U_i(\omega)$ is the energy density at the ith system and is given by $\sum_m E_m(\omega)(f_m{}^{i})^2/\langle(f_m{}^{i})^2\rangle V$. On averaging this rate over all the systems and inserting the density of radiation in the cavity, we find that

$$\Gamma_{12}{}^{i}=\sum_m\int\frac{2\omega_m{}^2\xi_m{}^2\mu^4N_2T^2d\omega}{\hbar^2V^2\pi[1+T^2(\omega-\omega_a)^2]^2|z_m(\omega)|^2}.\qquad(17)$$

The rate of spontaneous transitions between two levels is determined essentially by the density and the response of the electromagnetic modes. It therefore may depend in a pronounced way on the state of the maser material. For the ith system, the rate is given by[8]

$$\sum_m\frac{2}{\hbar}\mu^2\int\frac{T\,\mathrm{Im}[\omega_m q_m(\omega)f_m{}^{i}/\mu_s{}^{i}(\omega)]d\omega}{\pi[1+T^2(\omega-\omega_a)^2]}.\qquad(18)$$

On averaging over all the systems, we obtain

$$\Gamma_{12}{}^{s}=\sum_m\int\frac{2\mu^2\omega_m\xi_m\{\gamma_m+\mu^2\xi_m\omega_mT(N_1-N_2)/\hbar V[1+T^2(\omega-\omega_a)^2]\}Td\omega}{\hbar V\pi[1+T^2(\omega-\omega_a)^2]|z_m(\omega)|^2}.\qquad(19)$$

It is not necessary to use Eqs. (17) and (19) for the rates in the solution of our problem. We have presented them only to substantiate that our method of calculating the power output gives exactly what should be expected when the energies of all photons emitted can be approximated by $\hbar\omega_a$; viz., $P=\hbar\omega_aN_1\Gamma_{31}{}^{i}$. Upon substituting the expressions for the induced and spontaneous transition rates, we see that

$$\begin{aligned}P&=\hbar\omega_a[N_2\Gamma_{12}{}^{s}+(N_2-N_1)\Gamma_{12}{}^{i}]\\&=\sum_m\int\gamma_m\omega_m\omega_a\frac{2\mu^2\xi_mN_2Td\omega}{\pi V[1+T^2(\omega-\omega_a)^2]|z_m(\omega)|^2}\\&\approx\sum_m\int\gamma_m\omega_m{}^2|q_m(\omega)|^2d\omega\equiv P_0,\end{aligned}\qquad(20)$$

where P_0 is clearly the power output since $\omega_m{}^2|q_m(\omega)|^2$ is the energy and γ_m the loss rate in the mth mode.

V. DETERMINATION OF $(N_2-N_1)/N$

The output spectrum depends only on the relative populations and is a function of the pumping rate. The relation $P=P_0$, or equivalently the condition that the populations be in equilibrium, $N_1\Gamma_{31}{}^{i}=N_2\Gamma_{12}{}^{s}+(N_2-N_1)\Gamma_{12}{}^{i}$, determines $(N_2-N_1)/N$ as a function of the pumping rate $\Gamma_{31}{}^{i}$. To put it into a more convenient form, let us set $x=T(\omega-\omega_a)$ and $y_m=T(\omega_m-\omega_a)$ and approximate ω_m by ω_a, except in the resonance difference. Then from Eqs. (14) and (20),

$$\Gamma_{31}{}^{i}N_1/N_2=\frac{2\mu^2T^2\omega_a}{\hbar V}\sum_m\int\frac{dx\gamma_m\xi_m}{\pi(1+x^2)|2(x-y_m)+i\gamma_mT-i\omega_aTK_m/(1-ix)|^2},\qquad(21)$$

where $K_m=\mu^2(N_2-N_1)T\xi_m/\hbar V$ and $-K_m{}^{-1}$ is the material Q for the mth mode. Each of the integrands is proportional to the energy spectrum and/or power output spectrum of one of the modes. The specialization of Eq. (21) for the single mode case is discussed in Appendix A.

The integrals in Eq. (21) are evaluated in Appendix B with the result that

$$\Gamma_{31}{}^{i}\frac{N_1}{N_2}=\frac{\mu^2\omega_aT}{\hbar V}\sum_m\frac{\xi_m}{1-K_mQ_m+y_m{}^2},\qquad(22)$$

where $Q_m=\omega_a/\gamma_m$. Let us denote by w the pumping rate in units of the rate of spontaneous emission in the empty cavity:

$$w=(3\pi\hbar c^3/\mu^2\omega_a{}^3\xi)\Gamma_{31}{}^{i},\qquad(23)$$

where ξ is the average of $3\xi_m$ over all the modes. Then

$$w\frac{N_1}{N_2}=\frac{\pi c^3T}{V\omega_a{}^2}\sum_m\frac{3\xi_m/\xi}{1-K_mQ_m+y_m{}^2}.\qquad(24)$$

This equation determines $(N_2-N_1)/N$ as a function of w and applies when $w>1$. Given any spectrum of modes with arbitrary decay rates, we could perform the sum on a machine and plot w vs $(N_2-N_1)/N$. For the optical case, however, it is sufficient to treat the modes as belonging to a continuum (i.e., approximate the sum by a set of integrals), except possibly for a few modes having frequencies near resonance and low loss rates.[9]

---

[7] W. Heitler, *Quantum Theory of Radiation* (Oxford University Press, New York, 1954).

[8] J. Weber, Phys. Rev. **108**, 537 (1957).

VI. EXAMPLES

A. Fabry-Perot Interferometer Cavity

The next step is to sum over the modes; to do this we must specify the nature of the cavity. The maser cavities used thus far are made of a cylindrical ruby rod whose end walls are plated with a highly reflecting metal. The field patterns of the resonant modes of such a cavity will be described by a complicated combination of Bessel functions, but we shall not consider these in detail. It will suffice to remark that the modes with the lowest loss rates should be closely related to the TE_{01q} or TEM_{00q} configurations.

The field pattern and the loss rates for these axial high-Q modes have been investigated recently by Fox and Li.[10] Their results show that in a Fabry-Perot interferometer-type cavity, a couple of discrete modes do exist which have significantly lower loss rates than all the others. This feature is the essential characteristic of our first example.

To determine the loss rates of all the resonant modes would require a large amount of computation which is actually unnecessary. It will be seen that the maser oscillates in the highest Q mode and that all the other modes contribute to the background noise. We shall estimate the loss rates by employing a photon model. Since the essential features of our analysis do not depend on the geometry, and since the photon model is more easily related to the modes in a rectangular cavity, for ease of exposition we shall take the cavity to be a rectangular solid of length D and square cross section with an area equal to L^2. The sides perpendicular to the axial direction are plated with a highly reflecting metal, whose reflection coefficient is denoted by r, while that of the parallel sides is r' (independent of the angle of incidence). For $r'=0$, the rectangular cavity becomes the Fabry-Perot interferometer.

The modes of such a cavity are taken to be standing waves with wave numbers $q\pi/D$, $m\pi/L$, $p\pi/L$ in the axial and perpendicular directions, respectively; q, m, p are positive integers. It is assumed that the cavity is tuned so that some of the modes with the smallest losses are exactly on resonance. In this case, there will be four such modes, if we remember the polarization degeneracy, characterized by $q=q_a\approx\omega_a D/\pi c$,[11] $m=1$, $p=0$, or $m=0$, $p=1$.

As is well known, inside a rectangular cavity each mode can be represented as a superposition of eight plane waves with wave vector components

$$(k_x,k_y,k_z)=[\pm(\pi m/L),\ \pm(\pi p/L),\ \pm(\pi q/D)]. \quad (25)$$

Now using the concepts of geometrical optics, we regard each of the packets as a photon in the box moving in a direction specified by θ and ϕ, where the z axis is the polar axis. These angles are given by $\cos\theta=ck_z/\omega$ and $\tan\phi=k_y/k_x$. The average time this photon stays in the box will be

$$(1/c)\int_0^\infty \alpha s ds e^{-\alpha s}$$

$$=1/\alpha=[\gamma_0\cos\theta+\gamma_1\sin\theta(|\cos\phi|+|\sin\phi|)]^{-1}, \quad (26)$$

where

$$\gamma_0=[2c/D(1-r)/(1+r)]$$

and

$$\gamma_1=(2c/L)[(1-r')/(1+r')].$$

We shall neglect the variation with ϕ and investigate the case in which the loss rate is assumed to be

$$\gamma(\theta)=\gamma_0(1+a\sin\theta)\equiv\gamma_0/f(\theta), \quad (27)$$

where

$$a=(D/L)[(1+r)/(1+r')][(1-r')/(1-r)]. \quad (28)$$

When $D=L$, $r=0.98$, and $r'=0$, then $a=10^2$.

At this point, it is quite beneficial to describe the physics qualitatively in order to determine what approximations in the mathematical analysis should be made. For $N_1=N_2$, there are no net induced transitions between the two levels and the admittances of the cavity modes are the same as those in the absence of any optically active maser material; thus, $w=1$. We shall study the situation when we have a population inversion $N_2>N_1$ or $w>1$. For w near unity, the output is distributed among the various modes with the spectrum of the natural line, its width being $2/T$. As w increases, those modes near resonance with the lower loss rates deliver more of the output, and the width of the energy distribution shrinks. For a certain range of w, the dominant fraction of the energy goes into a large number of modes, and we may treat this situation mathematically by assuming that the spectrum of modes in continuous, the density of modes being

---

[9] In most physical systems, the atoms will be able to relax from the excited states through nonradiative transitions. At these optical energies, only downward transitions need to be accounted for in the low temperature range. Let $\Gamma_{12}{}^l$ be the rate for a nonradiative transition from level 2 to 1 and let $\Gamma_{13}{}^l$ be that from level 3 to the ground state; only the ratio $\Gamma_{13}{}^l/\Gamma_{23}{}^l=L$ is significant. The rate equation becomes $N_1\Gamma_{31}{}^i(1+L)^{-1}=N_2\Gamma_{12}{}^l+N_2\Gamma_{12}{}^s+(N_2-N_1)\Gamma_{12}{}^i$, and our basic equation (24) must be modified to read:

$$w(1+L)^{-1}\frac{N_1}{N_2}-M=\frac{\pi c^3T}{V\omega_a{}^3}\sum_m\frac{3\xi_m/\xi}{1-K_mQ_m+y_m{}^2},$$

where $M=(3\pi\hbar c^3/\mu^2\omega_a{}^3\xi)\Gamma_{12}{}^l$, and the normalized power output is the left side of the equation multiplied by N_2.

[10] A. G. Fox and T. Li, Proc. I.R.E. 48, 1904 (1960).

[11] c is the velocity of light. If the material in the cavity other than the flourescent ions has a dielectric constant ϵ, the following substitutions should be made in all equations: $f_m{}^i\rightarrow f_m{}^i/\epsilon^{\frac{1}{2}}$, $\xi_m\rightarrow\xi_m/\epsilon$, $\xi\rightarrow\xi/\epsilon$, and $c\rightarrow c/\epsilon^{\frac{1}{2}}$.

$dn/d\omega = L^2\omega/\pi c^2$ for those modes with a given q. At a certain value of w, however, there is a rather abrupt change in behavior. Above this point, the dominant fraction of the energy goes to a small number of modes which have the lowest loss rates and are closest to the molecular resonance. This transition is the exact analog of the condensation in the theory of an ideal Bose gas. In the case where the loss rate varies rapidly from mode to mode near the optimal modes, as compared with the frequency variations, the existence of such a transition is demanded because the amount of power delivered by the continuum of modes has a finite upper limit. The difference between the adjusted power input and this upper limit must be delivered by the small number of optimal modes. Until the transition is passed, the spectrum of the power output has essentially the same width as the neutral line; the decrease in the width of the spectrum arising from the continuum of modes is very slight. As w increases from unity, however, the energy spectrum in the optimal modes sharpens very rapidly. Therefore, as w passes the transition, a very sharp spike in the output spectrum appears. As w increases, this spike grows taller and narrower.

The treatment of the continuum of modes is carried out in Appendix C, with the result that Eq. (24) reduces to

$$\frac{N_1}{N_2}w = \frac{\epsilon}{1-s} + \int_0^1 \frac{dx}{[1-sf(x)]^{1/2}}, \tag{29}$$

where $\epsilon = 4c^2T/L^2\omega_a q_a$ is the number of axial modes at resonance divided by the total number of modes in the line width $2/T$, $s = K\omega_0/\gamma_0$ is the ratio of cavity Q for the most favored mode to material Q, $x = \cos\theta$ where $\cos\theta = \omega_q/\omega$, and $f(x)$ expresses the way in which the mode Q varies with θ. The first term arises from the most favored modes, and the integral closely approximates the contribution of all the other modes. This equation determines s as a function of w. Knowing $s(w)$, we essentially have determined the degree of the inversion as a function of the pumping rate:

$$(N_2 - N_1)/N = (3\hbar\gamma_0 V s/\mu^2\omega_a T N \xi). \tag{30}$$

For our optical case, $f(x) = [1 + a(1-x^2)^{1/2}]^{-1}$, where

$$a = (D/L)[(1+r)/(1+r')][(1-r')/(1-r)]$$

as before. It is evident that the last integral is bounded above if we transform variables by setting $y = (1-x^2)^{1/2}$ and thereby put it in the form (for $s=1$)

$$\int_0^1 \frac{y^{1/2}(a^{-1}+y)^{1/2}dy}{(1-y^2)^{1/2}}, \tag{31}$$

which is certainly less than $(\pi/2)(a^{-1}+1)^{1/2}$. For $a>1$, it is possible to show that the integral is less than

$$1 + \pi/4a + [(1-1/a^2)^{1/2} - 1]/a^2. \tag{32}$$

Typical values of the parameters for ruby entering the theory are the following: $\omega_a = 3\times 10^{15}$ sec^{-1}, $T = \frac{4}{3}10^{-12}$ sec corresponding to a linewidth of $3\frac{1}{2}$ A at 7000 A. If we take the cavity to be a cube with a side of 1 cm, $N = 10^{19}$ cm^{-3}, $r' = 0$, $r = 0.98$, $\mu^2 = e^2\, 10^{-21}$ cm^2, we find that $\gamma_0 = 6\times 10^8$ sec^{-1}, $a = 100$, $s = 50(N_2 - N_1)/N$, and $\epsilon = 6\times 10^{-11}$. Since s ranges from 0–1 as w increases from 1 to ∞, N_1 is very nearly equal to N_2, and we may replace the ratio by unity in Eq. (29).[12]

In units of $\frac{1}{2}N\hbar\omega_a\xi\mu^2\omega_a{}^3/3\pi\hbar c^3$, all the modes other than the axial resonant modes deliver a power output which ranges from 1–1.01 as w increases from unity. This power has a broad spectrum; its width is essentially $2/T$. If $w>1.01$, there is a spike in the power spectrum at the resonant frequency. The power in the spike is, of course, $w-1.01$. For example, if $w\approx 2$, 50% of the output will be very monochromatic. If w is increased by a factor of ten, then 95% of the output will be coherent radiation. The spike will be Lorentzian in shape and will have a width of

$$\tfrac{1}{2}\gamma_0 T(1-s) = \tfrac{1}{2}\gamma_0 T\epsilon/(w-1.01) \approx 10^{-14}/(w-1.01) \tag{33}$$

in units of the natural width $2/T$. The gain (defined as the ratio of the power out when the material is in the cavity to the power out when $N_2 = N_1$) in the optimal modes is

$$G = 1/(1-s) = (w-1.01)/\epsilon. \tag{34}$$

The extreme narrowness of the spike at such low pumping rates is a consequence of the fact that the losses are assumed to increase so rapidly away from the favored mode. The population increase in the upper level is limited by the requirement that the gain in the optimal modes must remain finite under steady-state operation. In the model studied here, when the gain in the most favored modes approaches infinity, the gain in the nearest modes cannot be more than about 300; that in the next nearest modes is less than 200, for example, and so on. There are of the order of $1/\epsilon\sim 10^{11}$ modes within the bandwidth $2/T$, but only 10^{-6} of these can have gains greater than 100 and only 10^{-4} of them have gains greater than 10 when the emission into the optimal mode approaches infinity. Thus, it can be seen that the power output in the most favored modes can completely dominate the output arising from all the other modes even at not very large values of w.

---

[12] It is easy to remove the approximation $N_1\approx N_2$ since the quantity $N_1 w/N_2$ appears as a unit. Since, whenever there is a coherent output, $N_1/N_2 \approx (1-\alpha)/(1+\alpha)$, where $\alpha = (N_2 - N_1)_{s=1}/N = 3\hbar\gamma_0 V/N\mu^2\omega T\xi = \gamma_0\omega_a{}^2/N\pi c^3\Gamma_{21}{}^3 T$, the prescription amounts to the substitution: $w \to [(1-\alpha)/(1+\alpha)]w$. The results obtained in this paper also apply to those four-level systems which can be described by two population variables. Consider, for example, the case where $3\to 2$ is the maser transition, and levels 4 and 2 rapidly relax, so that $N_4\approx N_2\approx 0$. Obviously, one need only replace N_2 by N_3, $(N_2 - N_1)$ by N_3, and the unit $N_1 w/N_2$ by $[(1/\alpha)-1]w$.

B. Case of Equal Loss Rates

At the other extreme, if all the modes had the same losses, there would be no condensation. This is conceivably the model when $r' \approx r \approx 1$ and much scattering in the dielectric tends to equalize the nearly equal cavity Q's. In this case, where $f(x)=1$,

$$\int_0^1 [1-sf(x)]^{-\frac{1}{2}} dx = (1-s)^{-\frac{1}{2}}.$$

It is possible in this case to sum over modes before performing the integration over frequency to find that the spectrum would be Lorentzian with a width equal to $(1-s)^{\frac{1}{2}}=1/w$ in units of $2/T$. The gain is

$$G=1/(1-s)^{\frac{1}{2}}=w. \qquad (35)$$

C. Case of Equal Loss Rates but an Angular-Dependent Transition Probability

We consider now the case where the transition probability varies with respect to a preferred direction such as a crystal axis. In particular, we suppose that the axis in question is along the z axis of the cavity and that the coupling varies as $\cos^2\theta$. This functional dependence on θ is far too small compared with the angular variation of Q considered in case A to be significant in that case.

When the reciprocal of the material Q varies as $\cos^2\theta$, $f(x)=x^2$ and

$$\begin{aligned} w &= \frac{\epsilon}{1-s} + \int_0^1 \frac{3x^2 dx}{(1-sx^2)^{\frac{1}{2}}} + \frac{3}{\pi q_a}\int_{y_1}^{\infty} \frac{dy}{1-sx^2+y^2} \\ &= \frac{\epsilon}{1-s} + \frac{3}{2}\frac{1}{s^{\frac{3}{2}}}[\sin^{-1}s^{\frac{1}{2}} - s^{\frac{1}{2}}(1-s)^{\frac{1}{2}}] \\ &\qquad + \frac{3}{\pi q_a}\int_{y_1}^{\infty} \frac{dy}{1-sx^2+y^2}. \qquad (36) \end{aligned}$$

It can be shown that the integral over y is bounded, the limit being about $\frac{1}{2}$. Consequently, from Eq. (36) we find that condensation into the highest Q cavity modes occurs when $w > (3\pi/4)+(1/2)$, in which case the peaked output spectrum has a width given by

$$3\epsilon(\gamma_0 T/2)[w-(3\pi/4)-(1/2)]^{-1}.$$

As might be expected, with a weaker angular dependence, condensation into the highest Q modes occurs at greater pumping power.

D. Intermediate Case

Let us treat the case where a reasonably large fraction of the modes have the same Q and the rest have a much smaller Q, conceivably a model when there is light trapping in a dielectric rod. For this case, $f(x)=1$ for $x>x_0$ and $f(x)\ll 1$ for $x<x_0$. Then Eq. (29) gives

$$w=[(1-x_0)/(1-s)^{\frac{1}{2}}]+x_0$$
$$\text{or} \quad 1-s=[(1-x_0)/(w-x_0)]^2. \qquad (37)$$

By using Eq. (13) in this case, it is easy to exhibit the output spectrum explicitly:

$$\begin{aligned} P_0(\omega,w) = \frac{N\hbar\omega_a}{2\tau}\Bigg[& x_0\frac{(\pi T)^{-1}}{T^{-2}+(\omega-\omega_a)^2} \\ & + \frac{(1-x_0)/\pi T}{(1/T^2)[(1-x_0)/(w-x_0)]^2+(\omega-\omega_a)^2}\Bigg], \qquad (38) \end{aligned}$$

which is the sum of two normalized Lorentzian terms multiplied by x_0 and by $w-x_0$. The width of the first term is $2/T$ and that of the second is $(2/T)(1-x_0)/(w-x_0)$. The quantity τ is the lifetime of the fluorescent level, and $1-x_0=\delta$ is the fractional number of modes which have a high Q. When $x_0=0$, Eq. (38) gives the result for equal loss rates; i.e., case B.

From this relation we see that the width of the coherent radiation is essentially inversely proportional to the pumping rate. If we use the natural units, the coefficient is just the ratio of the number of modes which have a high Q to the total number of modes in the natural bandwidth. Since the angular distribution of the power output from a given mode is peaked at the angle $\theta=\cos^{-1}(\omega_q/\omega)$, δ is related to the beam angle θ_B of the coherent radiation. If the optical material is isotropic, $\xi=1$, then $\delta=1-\cos\theta_B \simeq \theta_B^2/2$. In ruby, $\xi=\cos^2\theta=x^2$, then $\delta \simeq (3/2)\theta_B^2$. The factional number of modes which are on resonance and coherently excited is $\delta^2/(w-1)=(9/4)\theta_B^4/(w-1)$.

VII. DISCUSSION

The examples serve to show how critically dependent on the relative loss rates are the characteristics of the output from a multimode oscillator. In fact, it is this dependence rather than the condition that material Q equal cavity Q which determines how hard the system has to be pumped in order for it to oscillate. A principal result of the analysis is that very intense line narrowings occur in a multimode resonator when only a small fraction of the modes participate in the oscillation. We have shown in cases A and C, where there is sufficient discrimination among the modes, that above a certain condensation point, an exceedingly narrow spike in the output spectrum develops. This feature, however, is very delicately dependent on the independence of the modes.

It is certainly of interest to consider the modifications in the properties of the output in cases A and C when the axial mode is not on the atomic resonance. As is shown in Appendix D, these modifications depend critically on the degree to which the loss spectrum or molecular coupling favors the axial modes. In case A, the axial mode remains dominant, and the frequency of the spike is pulled. In case C, if the axial mode is sufficiently removed from the atomic resonance, the spike remains at the resonance frequency but is broadened substantially. In addition, the output would not be peaked in the forward direction, but would form a ring, so that there would be a dark spot on the axis.

In a real optical maser system the coupling between the modes, which serves to scatter radiation from one mode into others, resulting from inhomogeneities in the material and wall losses, would certainly be important. This means that in attempting to use the concepts of this multimode resonator theory to understand aspects of experimental results, we should employ models in which not an unreasonably small fraction of the modes participate in the oscillation. It may be expected that the principal effect of strong mode couplings among a group of modes may be simulated by equalizing the Q's of those modes. Thus a case such as our intermediate case D, where a packet of modes rather than a few preferred modes are important, may be useful in correlating optical maser data.

We wish to comment briefly here on some of the experimental results using our intermediate case. A moderate degree of narrowing has been observed in experiments by Maiman[1] and Collins *et al.*[2] The narrowing, however, is nowhere near as great as predicted by the intermediate case. This is obvious from the following considerations. The coherent radiation is reported to be confined in angle to within $\theta_B=1°$ of the cavity axis, which means that less than $(1-\cos\theta_B)\approx 1/7000$ of the modes have a high Q. In the intermediate case, therefore, the line should be narrowed by a factor of order $(w-x_0)/(1-x_0)\sim 10^4$, but the reported narrowings are at least two orders of magnitude smaller than 10^4. Recently, Maiman *et al.*[13] have reported much sharper spikes in the output which have widths narrowed by a factor of 10^3.

The conditions of these experiments are such that a pulsed output is obtained. The theory presented here describes the properties of the steady-state operation of an ideal multimode oscillator. Until a careful investigation of the transient behavior is made, it is not at all certain that the huge frequency narrowings characteristic of the steady-state solutions would also be obtained for the pulsing solutions. Therefore, the discrepancy elucidated above could well be nonexistent. However, if it turns out that the line narrowing is much the same for the pulsing solutions, the discrepancy might imply that the observed linewidth is to be attributed to magnetic and thermal effects.

In some unpublished work of Maiman, various ring structures in the output from an optical ruby maser have been found. It is interesting to note that such angular distributions are predicted in the intermediate case. The ring pattern is described in Appendix D.

ACKNOWLEDGMENTS

The authors wish to acknowledge stimulating discussions with Dr. T. H. Maiman and Dr. R. W. Hellwarth.

APPENDIX A. SINGLE MODE CASE

It is instructive to examine the case where the optical resonator is supposed to support only a single mode. Equation (21) then reduces to

$$\Gamma_{31}{}^{i}N_1=\frac{2\mu^2N_2T^2\omega_a\gamma\xi}{\pi\hbar V}\times\int\frac{dx}{4x^2(1+\gamma T/2)^2+(\gamma T-K\omega_aT)^2},\qquad(39)$$

provided that $\gamma T-K\omega_aT\ll 1$. Upon performing the integration, we obtain for the output power resulting from spontaneous emission

$$P=\frac{\mu^2T\omega_a{}^2\xi N_2}{V(1-KQ)(1+\gamma T/2)}.\qquad(40)$$

When the bandwidth of the circuit is large compared with the width of resonance of the material, i.e., $\gamma T\gg 1$, Eq. (40) reduces to Pound's result,[14] which was restricted, however, to the small-signal or linear amplification region. As may be seen from the more general analysis given here, this restriction is unnecessary. The induced and spontaneous transition rates given by Eqs. (17) and (19) are valid for any level of radiation in the cavity.

The spectral width of the output radiation $\Delta\omega_a$ is easily obtained from Eq. (39):

$$\Delta\omega_a=[\gamma(1-KQ)/(1+\gamma T/2)].\qquad(41)$$

By calling $(1-KQ)^{-1}$ the gain, we see that this expression is the usual gain-bandwidth product. On obtaining $(1-KQ)^{-1}$ from Eq. (40), Eq. (41) becomes

$$\Delta\omega_a=\frac{\gamma\mu^2N_2T\omega_a{}^2\xi}{PV(1+\gamma T/2)^2}.$$

If we re-express this in terms of the degree of inversion $(N_2-N_1)_{\mathrm{th}}$ required for the gain to become infinite; i.e.,

$$(N_2-N_1)_{\mathrm{th}}=\hbar\gamma V/\mu^2\omega_aT\xi,$$

we have

$$\Delta\omega_a=\frac{N_2}{(N_2-N_1)_{\mathrm{th}}}\,\frac{\hbar\omega_a}{P}\,\frac{\gamma^2}{[1+(\gamma T/2)]^2},$$

which is somewhat more general than the results of Townes and Schawlow[3]; i.e., their Eq. (17). Their expression may be obtained in the limiting case where (a) the response of the cavity mode is broad compared to the natural width of the resonance; i.e., $\gamma T/2 \gg 1$; and (b) the dominant fraction of the molecules are in the upper state; i.e., $N_1/N_2 \ll 1$.

---

[13] T. H. Maiman, R. H. Hoskins, I. J. D'Haenens, C. K. Asawa, and V. Evtuhov, Phys. Rev. (to be published).

[14] P. V. Pound, Ann. Phys. 1, 24 (1957).

APPENDIX B. EVALUATION OF INTEGRALS IN EQ. (21)

To evaluate the integrals in Eq. (21), let us investigate the integrands in some detail. In a given mode, the energy spectrum is proportional to

$$\{4[x(1+\gamma_m T/2)-y_m]^2 + [\gamma_m T - K_m\omega_a T - 2x(x-y_m)]^2\}^{-1}. \tag{42}$$

The maximum in this spectrum occurs at a value of x satisfying the relation

$$x=(1+\gamma_m T/2)^{-1}\left\{y_m+\frac{x-y_m/2}{1+\gamma_m T/2}\times[\gamma_m T-K_m\omega_a T-2x(x-y_m)]\right\}. \tag{43}$$

For those modes not far removed from the resonance, a single iteration of this equation gives for the location of the peak

$$x=\frac{\gamma_m}{1+\gamma_m T/2}\left\{1+\frac{1-\gamma_m T/2}{2(1+\gamma_m T/2)^2}\times\left[\gamma_m T-K_m\omega_a T+\frac{\gamma_m T y_m{}^2}{(1+\gamma_m T/2)^2}\right]\right\}. \tag{44}$$

The frequency pulling of the spectral line is described by the preceding formulas. Now $\gamma_m T/2$ is the width of the mode in units of the width of the line, or $\gamma_m T/2 = \Delta\omega_m/\Delta\omega_a$, and thus the first approximation to the last formula yields

$$y_m - x = x\gamma_m T/2$$

or

$$(\omega-\omega_a)/\Delta\omega_a=(\omega_m-\omega)/\Delta\omega_m. \tag{45}$$

a well-known result in the theory of maser oscillations.

The total power output from a given mode is proportional to

$$\int \{4[x(1+\gamma_m T/2)-y_m]^2 + [\gamma_m T-K_m\omega_a T-2x(x-y_m)]^2\}^{-1}dx. \tag{46}$$

For $\gamma_m T - K_m\omega_a T \ll 1$, which holds once there is a population inversion, the integrand is approximately Lorentzian and centered at x given by Eq. (43). Expanding about this value of x, we find that the integral is very closely equal to $\pi\{(2+\gamma_m T)[\gamma_m T - K_m\omega_a T + y_m{}^2\gamma_m T/(1+\gamma_m T/2)^2]\}^{-1}$. In the optical case, $\gamma_m T \ll 1$, so that the basic equation (21), which equates the power out to the adjusted power input, reduces to

$$\Gamma_{31}{}^{\gamma}\frac{N_1}{N_2}=\frac{\mu^2\omega_a T}{\hbar V}\sum_m \frac{\xi_m}{1-K_m Q_m + y_m{}^2}, \tag{47}$$

where $Q_m = \omega_a/\gamma_m$.

APPENDIX C. EVALUATION OF THE MODE CONTINUUM

To treat the continuum for a given q in evaluating Eq. (24), let us employ the variable θ; as before, $\omega_q = \omega \cos\theta$, where $\omega_q = \pi c q/D$. The density of modes is

$$dn/d\theta=(L^2\omega/\pi c^2)\sec\theta\tan\theta \approx (L^2\omega_a/\pi c^2)\tan\theta \tag{48}$$

in the region of the spectrum which is important. In terms of θ, $y_m = (\omega_a T/q_a)(q\sec\theta - q_a)$. For simplicity, we shall treat the isotropic case where $\xi_m = \xi/3$. Introducing the symbols $b = q_a/\omega_a T$, $K\omega_a/\gamma_0 = s$, where s is the ratio of cavity to material Q for the most favorable mode, and $\epsilon = 4c^2T/L^2\omega_a q_a$, where ϵ is the number of axial modes at resonance divided by the total number of modes in the linewidth $2/T$, we arrive at the following equation for w:

$$w=\epsilon\sum_{q=1}^{\infty}\frac{b^2}{(1-s)b^2+(q-q_a)^2} + \frac{1}{\pi b}\int_0^{\pi/2}\sum_{q=1}^{\infty}\frac{b^2\cos^2\theta\tan\theta d\theta}{[1-sf(\theta)]b^2\cos^2\theta+(q-q_a\cos\theta)^2}, \tag{49}$$

where the first term represents the contributions from the axial modes and the second term represents the contributions from the off-axis continuum of modes. For $q_a\cos\theta - 1 \gg b\cos\theta[1-sf(\theta)]^{\frac{1}{2}}$, the lower limit on the summation integer can be replaced by $-\infty$, in which case the sum may be done in closed form, the result being

$$\frac{\pi b\cos\theta\sinh\{2\pi b\cos\theta[1-sf(\theta)]^{\frac{1}{2}}\}}{[1-sf(\theta)]^{\frac{1}{2}}\{\cosh[2\pi b\cos\theta(1-sf)^{\frac{1}{2}}]-\cos[2\pi q_a\cos\theta]\}}. \tag{50}$$

For large angles, i.e., for $1-q_a\cos\theta \gg b\cos\theta$, the sum tends to $(\pi^2/6)b^2\cos^2\theta$, which vanishes as $\theta \to \pi/2$. The integrand is very sharply peaked at $x = \cos\theta = q/q_a$, for $q = 1 \to q_a$, if $2\pi bx(1-sf)^{\frac{1}{2}} \ll 1$. Since $2\pi b \gg 1$ and $(1-sf)^{\frac{1}{2}} > \frac{1}{2}$ for $x < (q_a-1)/q_a$, the peaks appear only at small values of x. There we may neglect the variation in $(1-sf)^{\frac{1}{2}}$; the height of the peak becomes

$$\begin{aligned}H(x)&=\{[1-sf(x)]^{\frac{1}{2}}\tanh[\pi bx(1-sf)^{\frac{1}{2}}]\}^{-\frac{1}{2}}\\&\approx\{\pi bx[1-sf(x)]\}^{-1},\end{aligned} \tag{51}$$

and the width is $W(x) = 2bx[1-sf(x)]^{\frac{1}{2}}/q_a$. Since the peaks are nearly Lorentzian in shape, the area under them is approximately

$$A(q)=\frac{1}{q_a}\frac{1}{[1-sf(x)]^{\frac{1}{2}}}. \tag{52}$$

Noticing that $A(q)$ is also given by

$$\int_{(q-\frac{1}{2})/q_a}^{(q+\frac{1}{2})/q_a}[1-sf(x)]^{-\frac{1}{2}}dx, \tag{53}$$

and that where no peaks occur the integrand is also

$$[1-sf(x)]^{-\frac{1}{2}}, \tag{54}$$

we are led to approximate the contribution to w from the continuum simply by

$$\int_0^1[1-sf(x)]^{-\frac{1}{2}}dx. \tag{55}$$

The basic equation of the theory has thus been reduced to the simple form

$$\frac{N_1}{N_2}w=\frac{\epsilon}{1-s}+\int_0^1\frac{dx}{[1-sf(x)]^{\frac{1}{2}}}. \tag{56}$$

APPENDIX D. SPECTRUM IN OFF-RESONANCE CASE

Suppose the spacing of the plates is such that no axial mode is on resonance. Then there will be a competition between modes for the power output, the winner being that mode for which

$$1-sf(\theta)+y_m^2$$

is a minimum. This mode, in general, will be a function of s, and thus a function of the pumping rate. But, as we shall see, the dependence on s is weak for the cases we have studied.

Let $\Delta=(\omega_a-\omega_{q_a})T$ measure the amount by which the axial modes are off resonance. Clearly, $2|\Delta|$ must be less than the separation between axial modes:

$$|\Delta|<(\omega_aT/2q_a)=(\pi cT/2D)\approx\tfrac{1}{16}.$$

Since the modifications will occur only at small angles, for $\theta\ll1$, let us expand

$$f(\theta)=1-\sigma_1\theta-\tfrac{1}{2}\sigma_2\theta^2+\cdots,$$
$$y_\theta^2=[\Delta-\omega_aT(\theta^2/2)]^2+\cdots.$$

In case A where $\sigma_1=a\approx10^2$, $1-sf(\theta)+y_\theta^2$ takes its minimum value at $\theta=0$ for

$$s>\tfrac{4}{3}(\Delta/\sigma_1)(\tfrac{2}{3}\omega_aT\Delta)^{\frac{1}{2}}<0.02,$$

because for such an s

$$s[\sigma_1+\sigma_2\theta]-2[\Delta-\omega_aT(\theta^2/2)]\omega_aT\theta=0,\quad\theta>0, \tag{57}$$

then has no solution. The only changes are that the condensation point is raised slightly and the spike will be pulled from ω_a to ω_{q_a}, the frequency of the nearest axial mode.

In case B, there is of course no change because no angular discrimination exists. In case C, $\sigma_1=0$, $\sigma_2=2$. The angle of the dominant modes is determined from Eq. (57) to be

$$\theta=\left(\frac{2\Delta}{\omega_aT}-\frac{\sigma_2s}{(\omega_aT)^2}\right)^{\frac{1}{2}}\approx\left(\frac{2\Delta}{\omega_aT}\right)^{\frac{1}{2}}$$
$$\text{for }\frac{\Delta}{s}\gtrsim\frac{10}{2\omega_aT}\approx10^{-3}. \tag{58}$$

If Δ is large, the angular distribution of the output radiation will have a minimum in the forward direction, so the output would form a ring when photographed. The frequency width of the power in the ring will be

$$\delta\omega\simeq\frac{2}{T}\frac{3}{q_a}\frac{1}{w-(3\pi/4)} \tag{59}$$

for $w>3\pi/4$, which is very large compared to the width when $\Delta=0$.

In case D, the coherent output is distributed among several rings centered at the angles

$$\theta_n=\left(\frac{2\Delta}{\omega_aT}+\frac{2n}{q_a}\right)^{\frac{1}{2}}$$
$$n=0,\,1,\,2\leq q_a(1-x_0). \tag{60}$$

Since $\omega=\omega_q\sec\theta$, the angular width of the rings is determined by

$$\delta[\omega_{q_n}\sec\theta]=\delta\omega=(2/T)[(1-x_0)/(w-x_0)]. \tag{61}$$

When $\delta\theta_n\ll\theta_n$, this condition gives

$$\delta\theta_n\approx\frac{\delta\omega}{\omega_a\tan\theta_n}\approx\frac{2(1-x_0)}{(w-x_0)(2\Delta\omega_aT+2n\omega_a^2T^2/q_a)^{\frac{1}{2}}}. \tag{62}$$

JOURNAL OF APPLIED PHYSICS VOLUME 32, NUMBER 7 JULY, 1961

Mass Spectrographic Analysis of Insulators Using a Vacuum Spark Positive Ion Source

A. J. Ahearn
Bell Telephone Laboratories, Inc., Murray Hill, New Jersey

(Received March 10, 1961)

Serious limitations are encountered in the analysis of insulators when conducting tubes packed with the powdered insulator are the electrodes of the vacuum spark. A general method of forming a vacuum spark directly between a conductor and a slab of insulator, which removes the above limitations, is presented. Mass spectral data of the insulators steatite and quartz are presented showing the presence of bulk impurities and surface contamination.

INTRODUCTION

SEVERAL years ago a mass spectrograph was designed and built for the analysis of trace impurities in solids.[1] Its positive ion source was a vacuum spark between electrodes of the sample under test. The performance and calibration of the instrument for the detection of trace impurities either within or on the surface of metals and semiconductors have been described.[2]

The analysis of a solid insulator is also outlined.[2] Two short metal tubes were completely filled with the insulator after the latter had been ground up into a powder. The mass spectrum of the insulator along with that of the metal was recorded when a vacuum spark between the tube ends was formed. The spectrum of the insulator could be isolated from that of the metal by suitable control tests.

This method of analyzing powdered insulator has three limitations: (a) The danger of contamination of the sample during the powdering process is great, in cases where the sample must be ground up. (b) Surface contamination cannot be distinguished from bulk impurities. (c) The contribution of the powder to the spark, and therefore to the spectrum, is erratic: it varies appreciably with time. This limitation means that the sensitivity with which trace impurities in the powder are detected would vary erratically.

METHOD

The above limitations inherent in this powder technique for analyzing insulators led to the methods sketched in Fig. 1. When the conductor electrode is brought near the insulator with the usual spark voltage applied (50–100 kv), a vacuum spark between the two is produced. Its mass spectrum is a mixture of the conductor and the insulator. By means of the electrode positioners,[1] a spark can also be formed between the two conductor electrodes in order to obtain the spectrum of the conductor alone along with the background characteristic of the instrument. The difference between these spectra yields the spectrum of the insulator.

The presence of impurities in the conductor would hinder the detection of the same impurities in the insulator. Therefore a metal whose impurity content is too low in concentration to be detected should if possible be used. For this reason the conductor electrodes were cut from high-resistivity silicon semiconductor, which show no detectable impurities.

RESULTS

Figure 2 presents photographs of typical mass spectra obtained for steatite using the geometry of Fig. 1(a). The Fig. 2 (a) spectrum was obtained from the spark between the two high-purity silicon electrodes. Little appears in this spectrum beyond the silicon mass lines and the usual background lines of carbon, nitrogen, oxygen, etc. The (b) spectrum was recorded when the spark was first passed between the steatite and the silicon. The (c) spectrum was recorded immediately after the (b) one. In all three, the total number of ions to the photographic plate was the same.

The major components of this particular steatite were barium oxide (16%), magnesium oxide (26%), silicon oxide (49%), and aluminum oxide (8%). The sum of all other components was less than 1% of the mixture.

The seven isotopes of barium with positive charges ranging up to seven electronic units, along with similar multiply charged ions of the aluminum and the three isotopes of silicon, magnesium, and oxygen, account for most but not all of the many lines in the (b) spectrum.

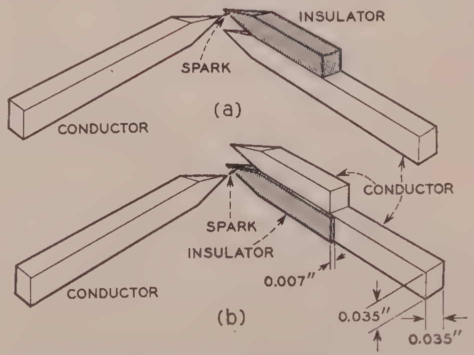

FIG. 1. Electrodes for vacuum spark positive ion source for mass spectrographic studies of insulators.

---

[1] N. B. Hannay, Rev. Sci. Instr. **25**, 644 (1954).
[2] N. B. Hannay and A. J. Ahearn, Anal. Chem. **26**, 1056 (1954).

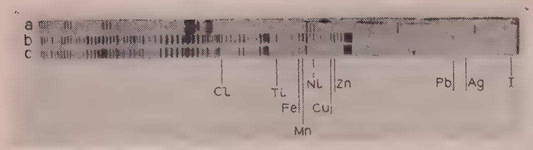

(a) SILICON—SILICON
(b, c) SILICON—STEATITE

FIG. 2. Mass spectra for analysis of steatite. (a) Vacuum spark between silicon electrodes. (b) Initial vacuum spark between silicon and steatite. (c) Subsequent vacuum spark between silicon and steatite.

Lines that are stronger in (b) than in (c) indicate surface contamination[3] by iodine, silver, lead, zinc, copper, nickel, manganese, iron, titanium, and chlorine. Lines that are the same in (c) as in (b) indicate the presence of phosphorus, sodium, potassium, calcium, and strontium as bulk impurities in the steatite.

The spectra of Fig. 2 were part of a study of the efficiency of different chemical treatments in cleaning steatite that had been heavily contaminated with perspiration. Before the (b) spectrum was recorded, the steatite had been treated successively in petroleum ether, ammonium hydroxide, distilled water, and ethyl alcohol.

In the absence of standard samples of steatite containing impurities at known concentrations, the sensitivity for the detection of bulk impurities remains unknown. However, since the contribution of the insulator to the spectrum is large, the sensitivity is probably comparable to that for semiconductors where impurities at concentrations below 10^{-7} atom fraction are detected.[2]

A 10-monolayer film of indium deposited on steatite was readily revealed by the indium mass 113 isotope on the spectrum of the steatite. Since this isotope comprises only 4% of the indium, it is the equivalent of 0.4 monolayer. Probably the sensitivity for detection of surface contaminants on steatite and other insulators is as great as with semiconductors where the equivalent of 0.01 monolayer has been detected.[3]

Figure 3 contains density records from portions of the mass spectra for quartz obtained using the method of Fig. 1(b). The top record represents high-resistivity silicon and reveals little besides silicon and the usual background lines, carbon, oxygen, etc. The lower record is from the spectrum obtained when the spark passes between the high-resistivity silicon and the quartz wafer.

This wafer was cut from a natural crystal of Brazilian quartz. Impurities in this quartz revealed in Fig. 3 include phosphorus, sulfur, magnesium, aluminum, iron, fluorine, nickel, calcium, and copper.

As in the case with steatite, the sensitivity is assumed to be about the same as with semiconductors. On this basis, the concentration of aluminum, the most abundant impurity, was about 10 parts per million.

An example of the analysis of a powdered sample by first sintering the material and then sparking by the methods of Fig. 1 was represented by the analysis of yttrium oxide. A direct comparison showed that there was a significant difference in the amount of rare-earth impurities in two samples. Since only these rare-earth impurities were of primary interest in this comparison, the sintering of the powder samples into a suitable slab was undertaken without fear of introducing relevant impurities.

DISCUSSION

The methods of Fig. 1 for analyzing insulators[4] represents a substantial improvement over the powder method tried earlier.[1,2] Sufficiently high-purity semiconductors are readily available to spark to the insulator. Surface contaminants can be distinguished from bulk impurities just as with metals and semiconductors. The insulator current to the photographic plate could be satisfactorily monitored by measurement of the total current before mass separation,[1] since measurements indicate that the insulator contributes a fixed fraction of the ion current.

The vacuum spark source used by James and Williams[5] employed auxiliary conducting electrodes each of which had a piece of the insulator sample in contact with its sparked end. With this arrangement the relative amounts of insulator and conductor ionized could be varied by sidewise movement of the electrodes. The main constituent of the insulator current had to be

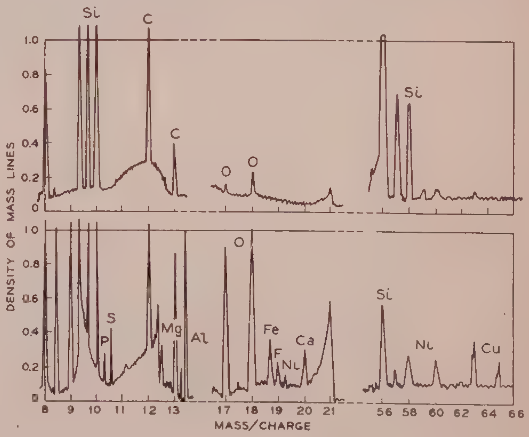

FIG. 3. Mass line density records showing impurities in natural crystal of Brazilian quartz.

---

[3] A. J. Ahearn, *1959 Sixth National Symposium on Vacuum Technology Transactions* (Pergamon Press, New York, 1960). Some of the material in this 1959 paper is included in the current paper by courtesy of the American Vacuum Society.

[4] A. J. Ahearn, Am. Soc. Testing Materials, Committee E14 on Mass Spectrometry, Cincinnati, Ohio, May 28–June 1, 1956.

[5] J. A. James and J. L. Williams, *Advances in Mass Spectrometry*, edited by J. D. Waldron (Pergamon Press, New York, 1959).

monitored after mass separation. This procedure imposed a limitation that only impurities of lower mass than this main constituent could be recorded on the photographic plate.

ACKNOWLEDGMENT

The author gratefully acknowledges the collaboration of W. R. Sinclair in part of this work, and the continued interest and support of N. B. Hannay.

JOURNAL OF APPLIED PHYSICS VOLUME 32, NUMBER 7 JULY, 1961

Mass Spectrographic Detection of Impurities in Liquids

A. J. Ahearn
Bell Telephone Laboratories, Inc., Murray Hill, New Jersey

(Received March 10, 1961)

The mass spectrograph with the vacuum spark positive ion source distinguishes between bulk impurities in the electrodes and contaminants present on their surface. Surface contamination can be detected and identified when it is the equivalent of less than 0.01 monolayer in thickness. Impurities in liquids are studied by exposing an electrode to the liquid, thereby contaminating its surface. Two ways of contaminating an electrode surface are described: (a) electroplating of impurities onto the electrode, and (b) evaporation leaving residue on the electrode. Experiments with doped water demonstrate that impurities at a concentration of 10^{-9} atom fraction can be detected. Only about 10^{-10} g of impurity is needed for detection using the evaporation technique. Some applications are discussed.

INTRODUCTION

THE design, construction, and performance of a mass spectrograph for the study of trace impurities in solids has been described in two papers.[1,2] This instrument uses a vacuum spark between electrodes of the sample as its positive ion source. This source enables the mass spectrograph to distinguish between bulk impurities homogeneously distributed through the sample and those impurities that are present largely as contamination on the surface of the sample electrode.[2] This differentiation arises since the vacuum spark first samples the surface of the electrodes before it consumes the interior of the sample. Consequently, impurity mass lines due to surface contamination decay in intensity as the spark erodes into the electrode, whereas bulk impurity mass lines do not decrease.

This is illustrated in Fig. 1. Three successive photographs of the mass spectrum from nickel electrodes were made. The photographic plate received the same number of ions from the spark in each case. A, B, and C are density records of the aluminum doubly charged ion mass line obtained, A being that from the initial sparking of the electrodes. These data indicate that the aluminum is present in the nickel as a bulk impurity since the density (A) of the aluminum line during the initial sparking of the nickel electrodes is no greater than that subsequently obtained (B and C).

In Fig. 1, D, E, F are density records of a magnesium doubly charged ion mass line that appeared in the spectrum of silicon. This data indicates that the magnesium is present as a surface contaminant on the silicon since the density of the magnesium line during the initial sparking (D) of the silicon electrodes is about 10 times greater than that subsequently obtained (E), which in turn is greater than (F).

In the early work with this instrument, with the use of a pair of pointed electrodes, surface contaminants were detected and identified when they were equivalent to 0.1 monolayer. The film thickness that can be detected by this means clearly is determined by the surface area that the vacuum spark explores. Figure 2

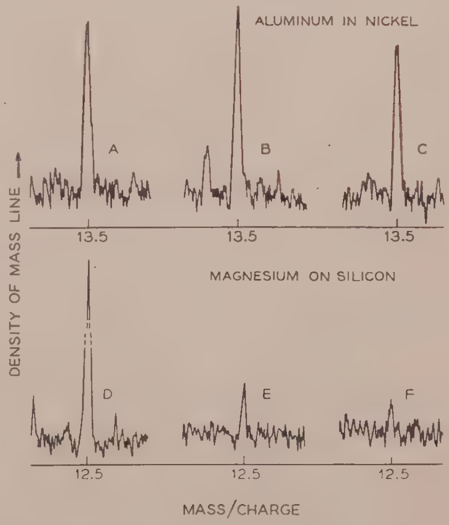

Fig. 1. Density records for mass line of bulk impurity vs surface contaminant. A, B, C: Aluminum as bulk impurity in nickel. Mass line 13.5 (Al^{2+}) in successive spectra. D, E, F: Magnesium as surface contaminant on silicon. Mass line 12.5 (Mg^{2+}) in successive spectra.

---

[1] N. B. Hannay, Rev. Sci. Instr. **25**, 644 (1954).

[2] N. B. Hannay and A. J. Ahearn, Anal. Chem. **26**, 1056 (1954).

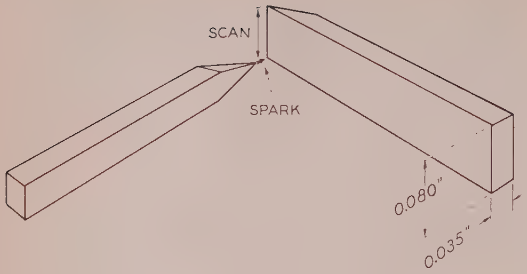

Fig. 2. Electrodes for surface contamination studies in which area explored by spark is increased by manual scanning.

illustrates a simple way to increase the area scanned by the spark. The pair of pointed electrodes referred to above and ordinarily used for bulk impurity studies is replaced by one pointed and one wedge-shaped electrode. The electrode positioners enable the operator to move the pointed electrode along the entire 2-mm width of the wedge.

By evaporation in vacuum, a single monolayer of indium was deposited on such a pair of point-wedge electrodes of germanium. Figure 3 presents the density record of the mass lines for the two isotopes of indium from the spectrum photographed during the initial sparking of the electrodes.

Since the mass 113 isotope is 4% abundant, the mass 113 line is the response from the equivalent of 0.04 monolayer of indium. It is quite evident that the equivalent of less than 0.01 monolayer could be detected by visual examination of the photographic plate.

Although this mass spectrograph was designed primarily with studies of bulk impurities in solids in mind, the investigation of surface impurities forms an important type of study to which the instrument is applied.[3] It is almost unique in its ability to detect and identify surface contaminants where these films are the equivalent of less than a monolayer in thickness.

In this paper methods and results are reported in which this surface contamination sensing ability of the vacuum spark is employed to study trace impurities in liquids. This is done by exposing a suitable surface to the liquid and its impurities in one of two ways. It is best done with high-purity electrode material, the surface of which is initially clean. Control tests justify the assignment of detected surface contamination to the liquid in question.

EXPERIMENTAL METHODS

A. Contamination of Surface by Electroplating

Experiments suggested that the presence and identity of impurities in low-conductivity water might be revealed by electroplating onto suitable electrodes. The impurities thus deposited subsequently would appear as surface contaminants in the mass spectra of the electrodes.

Table I. Mass spectrographic detection of impurities electroplated from deionized water.

cadmium
lead
arsenic
zinc
copper
nickel
iron
manganese
aluminum
beryllium

Six electrodes of high-purity silicon were prepared from the same crystal, etched in the usual nitric hydrofluoric acid solution, and washed in the deionized water (of a conductivity less than 0.1 μmho/cm) to be tested. Two were set aside to serve as controls, two were used as cathode, and two were used as anode in the electroplating setup of Fig. 4. For calibration purposes this deionized water was doped with beryllium nitrate and arsenic oxide (As_2O_3) to give a concentration of 10^{-9} atom fraction for beryllium and for arsenic.

With the anode and cathode about $2\frac{1}{2}$ in. apart, a potential difference of about 565 v was applied for about 10 min, giving a current of about 4 ma. This conductivity was achieved by bubbling carbon dioxide through the water.

Mass spectra of the two silicon electrodes that served as cathode, along with the control silicon electrodes,[4] were then recorded on the same photographic plate.

The densities of the mass lines in two regions of the spectrum where significant differences occurred are plotted in Fig. 5. Impurities on the electroplated silicon that are either absent or much weaker on the control silicon are listed in Table I.

The beryllium and arsenic were chosen for calibration purposes because neither one was detected in the water

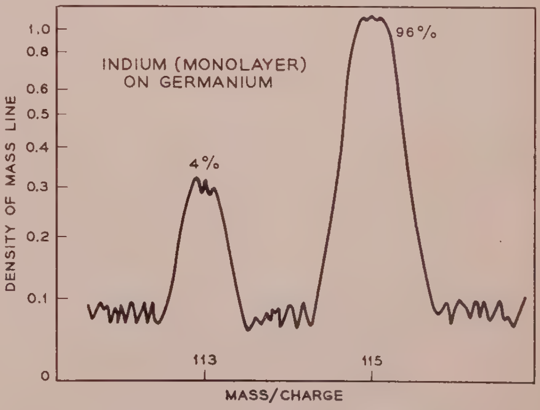

Fig. 3. Density record for indium mass lines from one monatomic layer deposited on germanium surface.

---

[3] A. J. Ahearn, *1959 Sixth National Symposium on Vacuum Technology Transactions* (Pergamon Press, New York, 1960). Some of the material in this 1959 paper is included in the current paper by courtesy of the American Vacuum Society.

[4] Two pairs of electrodes can be mounted in the mass spectrograph.

in preliminary tests. The appearance of arsenic and beryllium in the electroplated silicon spectrum clearly demonstrates that these impurities can be detected by this technique at concentrations as low as 10^{-9} atom fraction. Many of the impurities in the water were accumulated on the silicon in amounts far greater than needed for detection by this method. The data of Fig. 5 show that under the conditions of the experiment, impurities are readily detected by this technique in deionized water of very low conductivity. These impurities presumably are simply the residue remaining after the water passed through the deionizer. On the other hand, they could result from subsequent contamination of the deionized water from the air, from the walls of the polyethylene container, or from the carbon dioxide used.

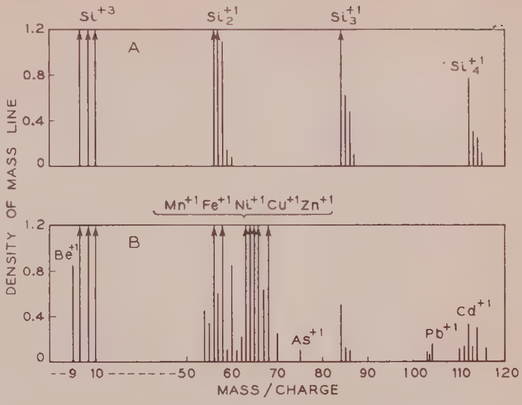

FIG. 5. Density of mass lines from contaminated surfaces of silicon. Arrow indicates density greater than 1.2. (A) Silicon washed in deionized water. (B) Silicon electroplated in deionized water.

B. Contamination of Surface by Evaporation of Liquid

Experiments reported elsewhere[3] were made in which electrode surfaces were contaminated merely by dipping into a sodium hydroxide solution. Surface contaminants subsequently detected and identified included boron, sulfur, sodium, magnesium, aluminum, copper, zinc, nickel, iron, chromium, calcium, and chlorine. These elements came from the solution in question, since they were not detected in control tests.

These experiments suggested that impurities at very low concentrations might be detected if a mass of liquid was deposited on an electrode surface and allowed to evaporate. The impurities in the liquid would be left contaminating the surface, provided the liquid evaporated more rapidly than the impurities.

Preliminary tests were made by putting a drop of doped water at the junction of electrodes like those shown in Fig. 2, allowing it to evaporate, and then recording the mass spectrum of the electrodes. In repeated experiments with the same doped water, the density of the doping impurity mass line varied greatly. Since the spark samples only the extreme tips of the electrodes, this is where the residue from the evaporation must be deposited in order to be detected. The large variation in line density encountered clearly indicated considerable variation in the drying pattern.

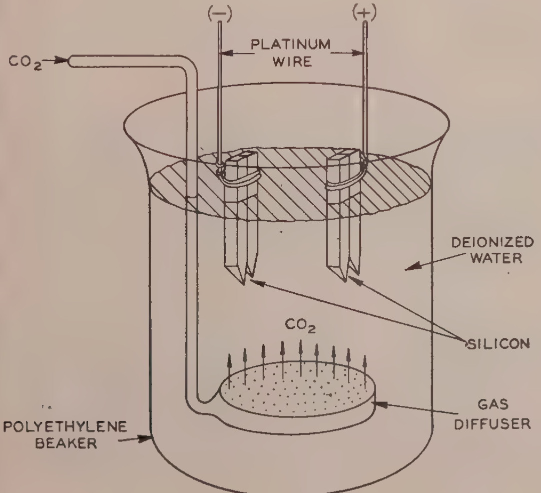

FIG. 4. Apparatus for contaminating silicon surfaces by electroplating impurities from deionized water.

In order to confine the water drop to the tip end of the electrode throughout the evaporation, particularly during its last stage, the arrangement shown in Fig. 6 was used. This shows a photograph of a silicon electrode held in a pin vise only a little of which is included in the picture. Originally, the electrode was square in cross section throughout its length, this cross section being about 1 mm². Over a length of several millimeters, this cross section was decreased as shown, but at the extreme tip it flared out to the original dimensions.

If the mass of a drop of water is the maximum that the tip can support, the drop will hang from the electrode tip. Larger drops fall off, and smaller ones tend to creep up the electrode. However, by applying an electric field, indicated in Fig. 6, these smaller drops can be pulled down toward the tip. With the flared tip end, the integrated contact force increases as the drop is pulled down. Consequently, by increasing the field the drop can be pulled well down to the electrode tip without pulling it off. As evaporation proceeds the remaining drop can be held at the tip by appropriately increasing the electric field, the needed value of which may reach several kilovolts per centimeter.

This localization of the water drop is illustrated by the photographs of Fig. 7. In (a), with zero electric field, the drop, being less than the critical mass, has crept up the electrode. By applying an appropriate electric field it was pulled down to the tip as shown in (b). Parts (c), (d), (e), and (f) show the remaining drop held in posi-

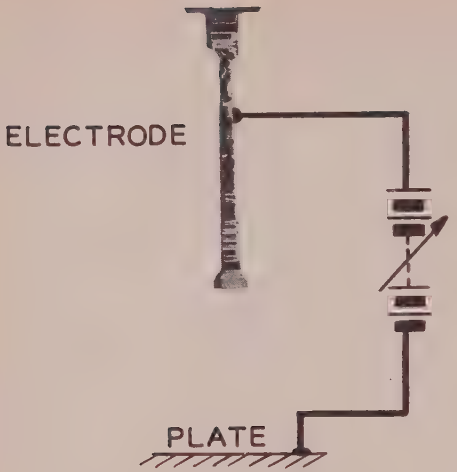

FIG. 6. Electrode tip on which liquid drop can be confined by electric field.

tion by progressive increase in the voltage as the water evaporated.

With a pointed electrode like that shown in Fig. 2, much of the tip end of this specially shaped electrode of Fig. 6 can be scanned with the vacuum spark.

The method outlined above yields satisfactorily reproducible results. In 10 tests on deionized water doped with beryllium at a concentration of 10^{-9} atom fraction, the density of the beryllium mass line varied from 0.35–0.80 with an average value of 0.55. Half of the density values fell within $0.55\pm 30\%$.

A deionized water sample was doped simultaneously with beryllium, sulfur, chromium, copper, arsenic, silver, and lead.[5] One drop of this multiply doped water sample was dried on an electrode, as shown in Fig. 7. All were detected in the mass spectrum subsequently recorded.

Table II lists the concentration of a specific isotope of each of these doped impurities along with the density of the corresponding mass line used for detection of this impurity. Where the singly charged ion mass lines were employed, concentrations as low as 1×10^{-9} atom fraction were detected. The density of the doubly charged mass line of lead suggests that its singly charged ion would be detected at about 1×10^{-9} atom fraction if the latter were recorded. Similarly, the density of the sulfur triply charged line suggests that if the singly charged line were resolved from the oxygen background line, it too could be detected at about 1×10^{-9} atom fraction.

TABLE II. Mass spectrographic detection of impurities introduced into deionized water.

Impurity	Isotope	Mass line m/e	Density of mass line	Concentration, atom fraction
Beryllium	9	9	0.44	1.1×10^{-9}
Chromium	53	53	0.12	1.0×10^{-9}
Copper	65	65	0.06	0.9×10^{-9}
Arsenic	75	75	0.33	1.0×10^{-9}
Silver	107	107	<0.02[a]	1.2×10^{-9}
Lead	207	103.5	0.04	5.8×10^{-9}
Sulfur	32	10.67	0.11	22.0×10^{-9}

[a] Visually detected.

DISCUSSION

The data in Table II indicate that, with the technique of Fig. 6, impurities in water can be detected at or below a concentration of 10^{-9} atom fraction. Table II indicates that beryllium and arsenic should be detectable at a concentration probably as low as 10^{-10} atom fraction.

The data of Table II were obtained using one drop of water about 3 mm in diameter.. This drop contained about 7×10^{-12} g of beryllium and 8×10^{-11} g of silver. These small quantities of impurity needed for detection by this mass spectrographic technique compare favorably with the quantity of about 10^{-7} g needed for detection by spectrophotometric methods at optimum sensitivity.

This method of detecting impurities is not limited to the case of water but should be applicable to any liquid which evaporates more rapidly than do the impurities in solution in the liquid. Many laboratory chemicals could be tested. Body fluids including blood serum should be amenable to analysis for trace impurities by this method. Trace impurities in gasoline and other petroleum products might be detected by this technique.

By bubbling an air sample through water or another suitable liquid, inorganic impurities in the air that go into solution should be detectable.

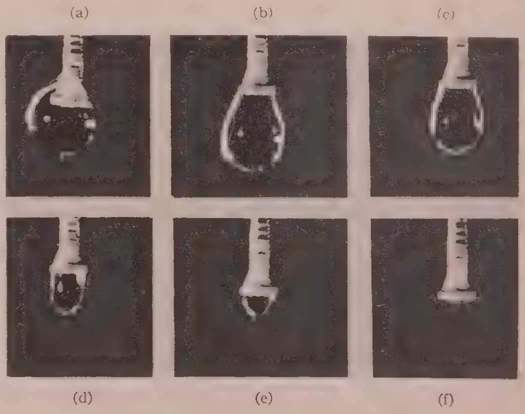

FIG. 7. Evaporation of water drop confined to electrode tip by electric field.

---

[5] Among the reasons for selecting these particular doping impurities was the observation that they were not being detected in the undoped deionized water used in the current tests. This statement is not inconsistent with the impurities detected in deionized water as listed in Table I, since the tests of Table I were made four years earlier.

When it is not feasible to study contamination by sparking directly to a surface, the contamination could be dissolved from the surface and the solvent then tested. In specific instances the area of contamination might be small. In such a case it should be quite feasible to put as little as a few drops of liquid on a contaminated surface and then transfer the equivalent of one drop to the electrode in the Fig. 6 setup. This technique, with its high sensitivity and low total mass requirement, would be employed to full advantage in a case like this where the total impurity mass available for detection could be very small.

ACKNOWLEDGMENTS

It is a pleasure to acknowledge the collaboration of D. MacNair and T. M. Buck in different phases of this work, and the continuous advice and criticism of N. B. Hannay.

JOURNAL OF APPLIED PHYSICS VOLUME 32, NUMBER 7 JULY, 1961

Electron Bombardment Damage in Silicon Esaki Diodes*

R. A. Logan, W. M. Augustyniak, and J. F. Gilbert
Bell Telephone Laboratories, Inc., Murray Hill, New Jersey

(Received March 3, 1961)

The excess current in silicon Esaki diodes has been shown to be a sensitive indicator of the density and distribution of states intorduced into the forbidden gap by electron bombardment. Both the effects of bombardment and the annealing properties of the radiation damage have been found to depend upon the specific donor in the n-type region of the diode. The average bombardment dose of 1-Mev electron/cm^2 needed to increase the excess current density by 1 amp/cm^2 at a bias of 0.3 v is 1.2×10^{16} for P-doped diodes and 0.8×10^{16} for Sb- or As-doped diodes. Upon annealing in an inert atmosphere, at temperature in the range 300°–400°C, the bombarded diode is restored to its original characteristics. While the annealing studies reveal novel interactions, they show considerable similarity with other work where the radiation damage was monitored by carrier lifetime or conductivity measurements. Structures observed in the I–V characteristics during the annealing indicate that the bombardment-induced levels at $E_v+0.27$ and $E_v+0.06$ are due to pairing of a primary defect (probably a vacancy) with an arsenic and a phosphorus impurity atom, respectively.

INTRODUCTION

IN studies of silicon which had been irradiated with high-energy electrons, much of the early investigation centered on the measurements of the positions of defect energy levels in the forbidden band. In the earlier studies,[1] the effects of irradiation were observed by lifetime and conductivity measurements as a function of temperature. The positions of the levels were also deduced[2] from the rate of carrier removal as a function of the position of the Fermi level and by Hall effect measurements. From all of these studies it is concluded that electron bombardment of silicon introduces levels at 0.03, 0.17, and 0.4 ev below the conduction band and at 0.055 and 0.27 ev above the valence band. Extensive studies[3] of electron bombardment damage by simultaneously measuring carrier lifetime, concentration, mobility, and the conductivity as a function of temperature indicated a model of paired defects for the levels at $E_c-0.17$ ev and $E_v+0.27$ ev. More recently,[4,5] spin resonance studies have shown that the level at $E_c-0.17$ ev is formed by the association of oxygen and a primary defect (probably a vacancy). The observation[5] that the introduction rate of this level is very small at low temperature is interpreted to imply that diffusion of the primary defect is necessary to produce the level. Similar studies[5] indicated that the level at $E_c-0.4$ ev is due to the association of a phosphorus impurity atom and a vacancy. These results have been confirmed by Hall effect and conductivity studies.[6]

The present work describes the effects of electron bombardment damage and their annealing upon the electrical characteristics of Esaki diodes. Since the excess current portion of the characteristic is very sensitive to the density and distribution of states in the forbidden gap, it has been suggested[7] that the Esaki diode serves as a novel tool to study radiation damage. The results

---

* This work was supported in part by the Electronic Technology Laboratory of the Wright Air Development Division.

[1] G. K. Wertheim, Bull. Am. Phys. Soc. **1**, 295 (1956).

[2] D. E. Hill, Bull. Am. Phys. Soc. **1**, 321 (1956); Phys. Rev. **114**, 1414 (1959).

[3] G. K. Wertheim, Phys. Rev. **105**, 1730 (1957); **110**, 1272 (1958).

[4] G. Bemski, J. Appl. Phys. **30**, 1195 (1959).

[5] G. D. Watkins, J. W. Corbett, and R. M. Walker, J. Appl. Phys. **30**, 1198 (1959).

[6] G. K. Wertheim and D. N. E. Buchanan, J. Appl. Phys. **30**, 1232 (1959).

[7] T. A. Longo, Bull. Am. Phys. Soc. **5**, 160 (1960); R. S. Claasen, *ibid.* **5**, 406 (1960).

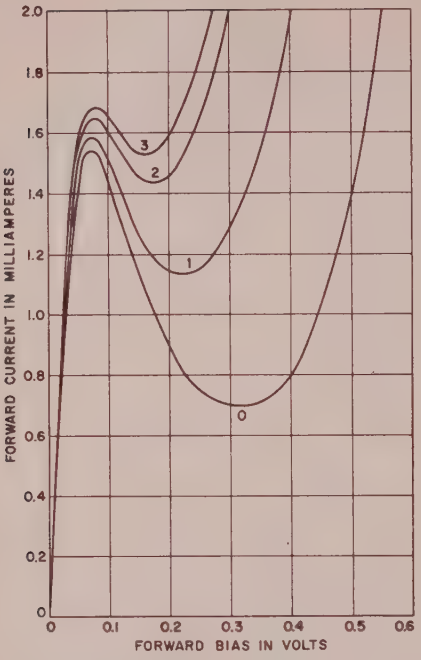

FIG. 1. Bombardment-induced changes in the Esaki characteristic of a silicon Esaki diode with the *n* region doped with Sb. Curve 0 refers to the junction before bombardment, and the other curves show the effects of three successive bombardments with 1-Mev electrons.

described here give new information about bombardment-induced energy levels. In particular, an identification is suggested for other levels described above, and the role played by dopant impurities in defect formation is emphasized.

EXPERIMENTAL PROCEDURE

The Esaki diodes used in this study were made by alloying aluminum wire containing 1% boron onto *n*-type silicon, heavily doped with either As, P, or Sb. Ohmic contact to the *n*-type wafer was made by alloying a gold wire to the wafer. The average junction area formed in this way was 3.5×10^{-4} cm^2. The diode was then mounted in a Van de Graaff accelerator such that the wafer was clamped onto a copper block which served as a heat sink. The bombardments with 1-Mev electrons were performed in vacuum at either 300° or 78°K, and they were halted at frequent intervals while the forward bias characteristics were traced on an X-Y recorder.

The annealing of the damage introduced by the bombardment was studied by heating the sample in a hydrogen atmosphere in a furnace of low heat capacity so that the time taken to go to or from the annealing temperature was about 1 min. The sample was held by its two wires in a jig so that during the annealing the sample was not mechanically disturbed. At frequent intervals, the annealing was interrupted and the forward-bias, V-I characteristics were recorded on an X-Y recorder, first with the sample at room temperature and then immersed in liquid nitrogen. It was ascertained that the heating of unbombarded samples in this way produced negligibly small changes in their I-V characteristics, so that in annealing of bombarded samples only the radiation-induced properties were changed.

TABLE I. Bombardment dose.[a]

Dopant	No. of diodes	$\varphi/\Delta\times10^{-16}$ amp^{-1}	$N\varphi/\Delta\times10^{-35}$ (amp cc)$^{-1}$
P	14	1.2 ±28%	8.2±31%
As	16	0.80±30%	5.5±30%
Sb	8	0.84±39%	2.8±20%

[a] φ/Δ is bombardment flux per unit increase in excess current density at a bias of 0.3 v, and N is the *n*-type dopant density.

RESULTS

The effects of bombardment upon the diode characteristics have been described in previous work.[8] However, in the more extensive study described here, an attempt was made to investigate the effect of specific dopant and of dopant density upon the radiation damage, using a large sampling of diodes. The diodes, made from pulled silicon crystals doped with As, P, or Sb, with peak

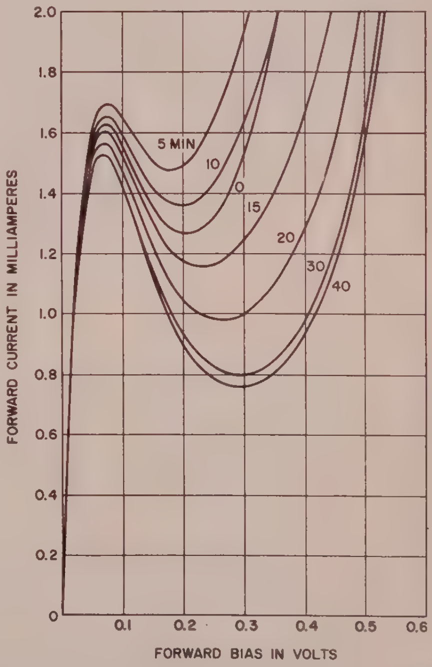

FIG. 2. Room-temperature I–V characteristics of the Esaki diode of Fig. 1 obtained by interrupting the annealing at 380°C at the times shown.

---

[8] A. G. Chynoweth, W. L. Feldmann, and R. A. Logan, Phys. Rev. **121**, 684 (1961).

currents varying from 0.15–15 ma, were bombarded with 1-Mev electrons until the valley current was increased in magnitude to approximately that of the original peak current. A typical result is shown in Fig. 1, which shows the effect of four successive bombardments upon the I-V characteristics of an Sb-doped diode. It has been found that at any bias, the excess current increases linearly with the bombardment dose, the constant of proportionality varying exponentially with the bias in accordance with a detailed model proposed for the effect of the bombardment introduced states upon the excess current.[8] A summary is presented in Table I of the average bombardment dose φ/Δ required to increase the excess current density by 1 amp/cm^2 at a bias of 0.3 v. It is seen that this dose is about 50% higher in diodes made using P than in those made using As or Sb. The mean deviations of the average doses φ/Δ are also listed; and while they are large, $\sim\pm30\%$, they are perhaps typical of the variation in rate of damage encountered in other similar studies; e.g., the rate of introduction of the level at $E_c-0.17$ ev in As-doped silicon.[3] The mean deviation of φ/Δ for Sb diodes is significantly larger than for those of the other diodes. It was noted that the dose φ/Δ for Sb diodes was relatively large for lightly doped diodes, and vice versa for heavily doped diodes. Since this suggested a primary defect formation by the incident beam involving the Sb impurity atoms, the product $N\varphi/\Delta$ was computed, and is listed in Table I together with its mean deviation. For the Sb-doped diodes the mean deviation of $N\varphi/\Delta$ is reduced by a factor of 2 from that for φ/Δ, whereas for the As- and P-doped diodes no such effect is evident.

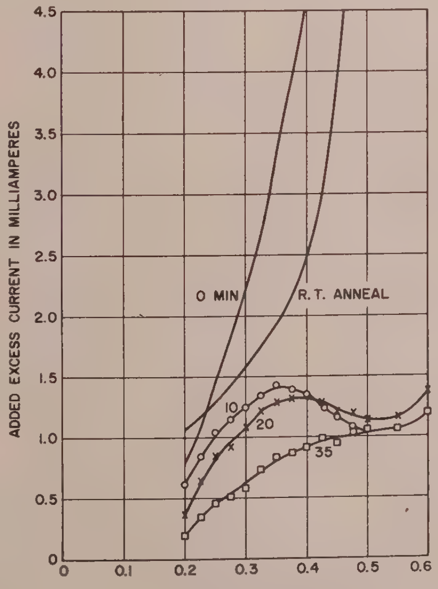

Fig. 3. Bombardment-induced excess current measured at 78°K vs forward bias for a silicon Esaki diode with the *n* region doped with As. The curves show the annealing which occurred at room temperature and that after various times of heating at 360°C.

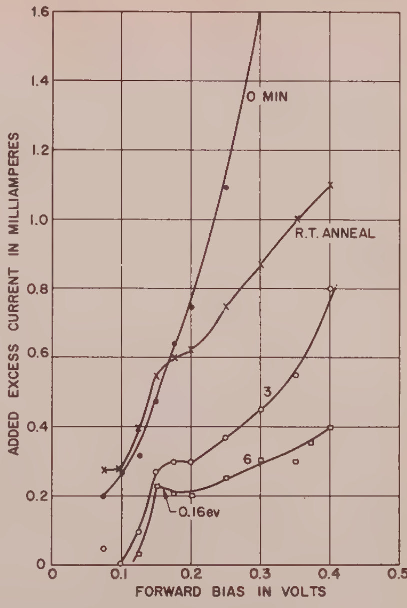

Fig. 4. Bombardment-induced excess current measured at room temperature vs forward bias for a silicon Esaki diode with the *n* region doped with P. The curves show the annealing which occurred at room temperature and that after various times of heating at 360°C.

Several bombardments were performed while the sample was cooled to liquid nitrogen temperature. The quantity φ/Δ measured for these diodes in terms of the excess current change observed at room temperature is the same as for those diodes bombarded at room temperature. Since the time taken to raise the sample temperature from 78° to 300°K was much shorter than the time of bombardment, this result indicates that the differences, described above, in bombardment dose are not due to any significant annealing at room temperature during the bombardment.

Upon heating in the range 360°–400°C, the room-temperature V-I characteristics of a bombarded diode are returned to their initial values. Typical annealing data for Sb-doped diodes are shown in Fig. 2, where some general features of the annealing may be noted. In general, annealing occurs at room temperature as evidenced by a decrease in the excess current which is perceptible after only a few minutes at room temperature. The extent of this anneal varies from diode to diode, but as much as 50% of the added excess current has been found to have annealed out after a few days at room temperature. Upon annealing at elevated temperature, the excess current observed at room temperature (or lower) typically increases to values near that observed immediately after bombardment and then decreases monotonically until the I-V characteristic is nearly that of the prebombarded diode. During a given

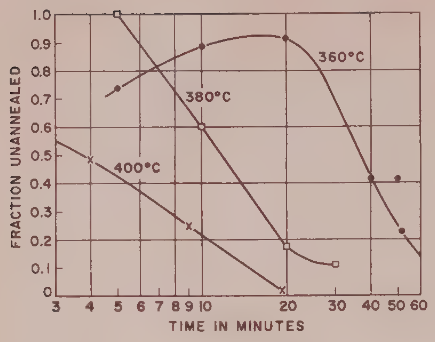

FIG. 5. Fraction of unannealed excess current measured at room temperature at $V=0.35$ v vs the logarithm of the time of heating at the temperatures indicated.

period of annealing, the percentage decrease in excess current is about the same at all biases.

There were other characteristics of the annealing behavior of the diodes which varied with the dopant used.

Figure 3 shows typical annealing data of a diode doped with As, where the bombardment-induced excess current alone is plotted vs the bias. In this case a marked maximum centered about a bias of 0.37 v is developed in the excess current during the annealing. These data were obtained at 78°K, where the maximum is somewhat more pronounced than at room temperature. Similar data for a P-doped diode, taken at room temperature, are shown in Fig. 4, where the maximum is developed at about 0.16 v and forms during the initial room temperature annealing. The I-V characteristics were examined at forward biases up to 1 v, and the only secondary current maxima observed were those described above at 0.37 v and 0.16 v in As- and P-doped diodes, respectively. It should also be noted that the annealing time in P-doped diodes, as shown in Fig. 4, is much shorter than in the As or Sb diodes at the same annealing temperature. With identical heat treatment, the As and Sb diodes anneal completely to their original I-V characteristic, whereas the current maximum in the P diodes does not anneal out.

The only annealing data to which our results can be compared are those of Bemski and Augustyniak,[9] which were obtained in the studies of bombardment-induced recombination centers. In that work, for As-doped samples of Si, the fraction of recombination centers remaining in the bombarded sample plotted against the logarithm of the time of annealing had a characteristic shape. The effect of increasing the annealing temperature in the range 220°–400°C was to shift the curves to shorter times. For a diffusion-limited process, the factor by which the time scale shifts is the factor by which the diffusion constant has increased if the sample contains equal numbers of annealing centers. The plot of the time scale shift against the reciprocal of annealing temperature had a slope of 1.3 ev. This value is interpreted as the activation energy for diffusion of the annealing species.

To compare the annealing kinetics here with those obtained in recombination studies, the remaining fraction of the bombardment-induced excess current at a bias of 0.35 v was plotted aginst the time of annealing; typical results for As-doped diodes are shown in Fig. 5. The particular bias used is not critical, as curves of similar shape are obtained at other biases. The usual increase in excess current during the initial annealing is a point of marked distinction to that of the recombination studies. However, there is some similarity in the annealing beyond this initial rise. Since the initial excess current increase obscures the shape of the curve of the later decrease, a plot is made in Fig. 6 of the time $t_{\frac{1}{2}}$ at which half of the increase in excess current has annealed ($t_{\frac{1}{2}}$ is proportional to the time scale shift) vs the reciprocal of the annealing temperature. The resulting data are consistent with the activation energy of 1.3 ev observed in the recombination studies. Moreover, the annealing of phosphorus-doped diodes occurred in relatively shorter times than those of As or Sb, the time constant $t_{\frac{1}{2}}$ being ~2 min at all temperatures in the range 360°–400°C. In recombination studies, phosphorus-doped samples also annealed more rapidly than those doped with arsenic.[10] Using vacuum floating zone cyrstals doped with phosphorus, the level introduced at 0.4 ev has been observed[11] to anneal rapidly (but not to completion) at 145°C with $t_{\frac{1}{2}}=3$ min.

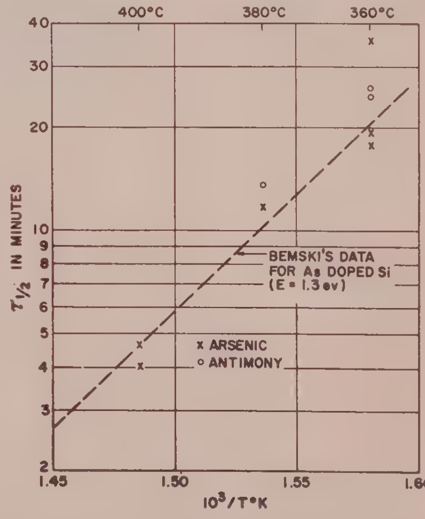

FIG. 6. Logarithm of the time required to anneal one-half of the bombardment-induced excess current at $V=0.35$ v vs the reciprocal of the annealing temperature.

---

[9] G. Bemski and W. M. Augustyniak, Phys. Rev. **108**, 645 (1957).

[10] G. Bemski (private communication).

[11] G. Wertheim (private communication).

DISCUSSION AND CONCLUSIONS

It has been shown[8] that the excess current is caused by electrons tunneling to or from states within the forbidden energy gap. The states serve as a mechanism to remove the energy unbalance caused by the applied bias which makes band-to-band tunneling energetically impossible. Since the tunneling probability is a smooth function of applied bias, the appearance of secondary maxima in the excess current curve implies a large increase in the local density of states in the gap at position corresponding to the bias. The fact that the maxima are broad in energy, and that structure is not observed in these diodes after fabrication but only after deliberately increasing the deep level density by doping[12] or irradiation, suggests that in the excess current flow, carriers with considerable energy differences take part. Nevertheless, the changes produced in the excess current by irradiation are such as to produce structure in the I-V characteristics which give important information about the deep states which are introduced into the gap. The curves of added excess current vs bias as shown in Figs. 3 and 4 are essentially those of the product of the state density and tunneling probability vs position in the gap, within the limitations discussed above. In addition, there is some uncertainty as to the bias at which the transition occurs from mainly direct tunneling across the gap (which is predominantly responsible for the peak current) to the tunneling mainly via intermediate states, which is denoted as excess current.

In arsenic-doped silicon, the secondary current maximum occurs at a bias of 0.37 v. Since the states which give rise to this maximum are formed upon annealing and there is some identification of the annealing kinetics with those of Bemski and Augustyniak[9] for As-doped silicon, it follows that these levels may be those which give rise to the recombination properties. Wertheim[3] has identified this recombination center at 0.27 v above the valance band. The difference in energy between the bias at which the current maximum occurs and that of the deep level (0.1 ev) would then be the transition point at which the bands uncross and the excess current flow begins to dominate. This result would also imply that the current maximum in P-doped diodes which occurs at 0.16 v is due to levels at 0.06 ev above the valence band. Even though levels have been formed at $E_v+0.06$ ev by electron bombardments,[2] the dopant used was not ascertained so that the association of this level with phosphorous impurities is not unambiguously confirmed.

These results imply that the bands uncross at a fixed voltage ($\sim$0.1 ev) rather than at a bias determined[13] by the penetration of E_F, the Fermi level, into the conduction or valence bands. This finding, though unexpected, is consistent with the fact that theory[13] also does not predict the observed variation of the peak voltage with junction doping in the diodes studied here. The donor concentration varied from 3×10^{19} cm^{-3} to 1.5×10^{20} cm^{-3}, while the estimated acceptor concentration in the boron regrowth region was 3×10^{20} cm^{-3}. From these concentrations, it is found[14] that E_F-E_C varied from 0.037 ev to 0.11 ev and $E_v-E_F=0.31$ ev. The observed peak voltage for these diodes varied from 0.062 to 0.080 v, whereas theory[13] predicts that they should be $\simeq E_F-E_C$. The identification of the current maxima with states above the valence band also implies that current flow is dominated by tunneling from the conduction band to the deep states above the valence band in silicon, so that with this technique it is not possible to examine the deep states near the conduction band introduced by electron bombardment in silicon.

The association of deep levels above the valence band with As and P requires the presence of these impurities near the *p*-type edge of the space-charge region. Since the diodes were formed by an alloy process, it seems likely that some donors are left in the *p*-type region during the crystal regrowth on the cooling portion of the heat cycle. One might therefore infer that the irradiation characteristics would be very different in Esaki diodes formed by alloying donor-rich metals into boron-doped silicon if the *p*-type portion of the diode were sufficiently uncompensated. In addition, the correlation of the rate of damage introduction with dopant concentration N may have been obscured by small variations in the heat cycle in the alloy process. The degree of homogeneity in the alloy and the rate of cooling would alter the effective distribution coefficient and thus cause N to vary in a random way. Although the rate of change of excess current with bombardment flux increased with dopant concentration for Sb diodes, there was no correlation with the P or As concentrations. A correlation has been observed[3] between the rate of introduction of the level at $E_c-0.17$ ev and arsenic concentration. This is a somewhat suprising result since this level has been shown[4,5] to consist of an oxygen atom and a primary defect (vacancy).

P-doped diodes required about a 50% greater bombardment dose to produce unit excess current change than did those doped with As or Sb. Since more rapid annealing was observed in P-doped diodes, one might speculate that the increase in φ/Δ was due to low-temperature annealing during the bombardment. This interpretation seems unlikely however, since φ/Δ was unchanged in low-temperature bombardments (78°K), where annealing effects would be markedly reduced.

---

[12] C. T. Sah, Bull. Am. Phys. Soc. 5, 507 (1960).

[13] E. O. Kane, J. Appl. Phys. 32, 83 (1961).

[14] W. Shockley, *Electrons and Holes in Semiconductors* (D. Van Nostrand Company, Inc., Princeton, New Jersey, 1950), p. 241, Eq. (15b). Note that the numerical factor is misprinted there and should read $E_F-E_C=38\times10^{-16}\,n^{\frac{2}{3}}$ ev.

JOURNAL OF APPLIED PHYSICS VOLUME 32, NUMBER 7 JULY, 1961

On the Theory of Amplitude Distribution of Impulsive Random Noise

K. Furutsu and T. Ishida
Radio Research Laboratories, Kokubunji, Kitatama-gun, Tokyo, Japan

(Received August 8, 1960; in final form, February 13, 1961)

Two phenomenological models are considered by which impulsive random noises can be described: (a) *Poisson noise*, consisting of the superposition of independent, randomly occurring elementary impulses. Much electronic noise belongs to this type and the familiar physical examples are precipitation noise, ignition noise, and solar "static." (b) *Poisson-Poisson noise*, consisting of the superposition of independent, randomly occurring Poisson noise, each type of Poisson noise forming a wave packet of some duration. Atmospheric noise is a representative example of the latter type. The attempt at first is made to deduce the general amplitude distribution for each model; then, because the noise sources in nature are spatially distributed and noise strength decreases with distance so that the amplitude of the received noise sometimes depends seriously on this spatial distribution of noise sources, the amplitude probability distributions are considered according to the two typical cases of the discrete and continuous spatial distributions, and are compared with those of actual atmospherics. Moments of even order and correlation functions are also calculated for each model. Finally, the dependence of the assumptions used on amplitude probability distribution are discussed. The distributions obtained are, in some cases, found to be independent of the adopted models and some of the used assumptions in a wide range of noise amplitude.

I. INTRODUCTION

THE statistical treatment of impulsive random noise has been treated by many authors, and recently by Rice[1] and Middleton.[2] The latter, especially, analyzed the problem qualitatively according to the order of magnitude of $\gamma=$ (average number of impulses/sec) × (mean duration of the pulses), and treated the problem from the normal random noise of $\gamma\gg 1$ (large overlapping of basic impulses) to the impulsive, random noise of $\gamma\lesssim 1$ in unified form. He limited himself mainly to the formulation of the general theory for Poisson noise and, though he presented the amplitude distribution in the case of nearly normal random noise, he did not extend his work to show an amplitude distribution to be compared with such actual impulsive, random noise as atmospherics.

One of the most typical examples of impulsive random noise in nature is the atmospheric radio noise. In 1937, the statistical characteristics of atmospherics were measured first by Maeda *et al.*[3] But the data were not sufficient to determine the amplitude probability distribution. Later on, the amplitude distribution of atmospherics was extensively measured in the narrow frequency band by Hoff and Johnson,[4] Horner and Harwood,[5] Hersperper *et al.*,[6] and J. I. Likhter.[7] The latter three proposed, respectively, as results the following cumulative amplitude probability distribution from the amplitude R to ∞ for atmospherics:

(a) $$[1+(R/M)^q]^{-1};$$

(b) $$\frac{1}{(2\pi)^{\frac{1}{2}}\sigma}\int_R^\infty \exp\left[-\frac{1}{2\sigma^2}(\log R/M)^2\right]d(\log R);$$

(c) $$(1-C)\exp(-aK^2)+C\exp(-bR^2).$$

The ordinary method used by these investigaters for measuring the cumulative probability distribution is first to take out the noise envelope through the second detector having some time constant, and slice the output by an amplitude discriminator whose sensing level is slid up, or by several discriminators whose sensing levels are preset according to the dynamic range of the noise envelope. The output through the discriminators is then formed into the rectangular waves of definite amplitude; their durations are the time intervals to be obtained in which the amplitude exceeds the reference levels. Finally, the durations of every rectangular wave are summed up by the use of a capacitor and resistor integrating circuit (CR circuit). However, the errors due to the use of a CR circuit of some proper time constant are unavoidable when the durations of the impulses change in a very wide range. Watt[8] improved the method by the use of the mechanical digital counter for summing up the rectangular waves, and found the deviations of the above-proposed three distributions from the actual atmospherics in the parts of high and low probabilities, respectively. He proposed the following distribution:

(d) $$\exp(-y^2),$$

where

$$R=a_1y+a_2y^{(b+1)/2}+a_3y^b,$$
$$b=0.6(20\log_{10}E_{\mathrm{rms}}/E_{\mathrm{av}}).$$

In 1956, Yuhara *et al.*[9] took into account that the wave envelope obtained by the second detector might not be correct because of the use of the CR circuit, and extensively improved the measuring method in those points such that any device using a nonlinear circuit, such as the second detector, and a CR circuit, were completely excluded except for the first heterodyne detector to give rise to the i.f. noise waves; the durations of i.f. pulse waves above the reference levels were directly measured by the use of the electric digital counters, as will be explained in Sec. V. As the result of observation by this equipment, Ishida proposed the following distribution[10]:

---

[1] S. O. Rice, Bell System Tech. J. **23**, 282 (1944); **24**, 46 (1945); **27**, 10 (1948). See also E. N. Gilbert and H. G. Pollak, *ibid.* **39**, 333 (1960).

[2] D. Middleton, J. Appl. Phys. **22**, 1143, 1153 (1950).

[3] K. Maeda and H. Yokoyama, Rept. Radio Research Japan **7**, 153 (1937).

[4] R. S. Hoff and R. C. Johnson, Proc. I. R. E. **40**, 185 (1952).

[5] F. Horner and J. Harwood, Proc. Inst. Elec. Engrs. (London) **B103**, 743 (1956).

[6] S. P. Hersperper, W. J. Kessler, A. W. Sullivan, and J. D. Wells, Univ. Florida Progr. Rept. **5**, (1954).

[7] J. I. Likhter, Radiotekh. i Electron. **1**, 1295–1302 (1956).

[8] A. D. Watt and E. L. Maxwell, Natl. Bur. Standards (U. S.) Rept. 3586 (1956).

[9] H. Yuhara, T. Ishida, and M. Higashimura, J. Radio Research Lab. (Japan), **3**, 101 (1956).

(e) $$(1-c)\exp(-aR^2)+c\frac{1}{(2\pi)^{\frac{1}{2}}\sigma}\int_R^\infty \exp\left[-\frac{1}{2\sigma^2}(\log R/M)^2\right]d(\log R).$$

All of these proposed amplitude distributions except (c) are experimental formulas, of course, and thus lack their physical grounds. On the other hand, distribution (c) is simply a combination of two Rayleigh distributions of different mean amplitudes and is also poor in agreement with the practice.

Anyway, in the narrow band case, the actually observed probability will not be that of noise itself but of the output through a rectifier, and thus the probability density of the envelope will be of most importance. In this paper, we shall investigate exclusively the probability of this kind.

In nature, Poisson-Poisson noise also seems to exist: Schonland[11] has shown that, in the case of atmospheric lightning discharge, the discharge is initiated by a weakly ionized slow moving pilot streamer. This pilot is followed by a highly ionized leader, which travels at approximately 200 ft/μsec, producing a current pulse in the order of 300 amp whose length is approximately 1 μsec. The pilot again moves forward and the process repeats itself every 25–100 μsec. These short pulses, and the branch leaders, radiate energy known as predischarge which has a total length of the order of 1 msec. These pulse currents are believed to occur according to the Poisson law,[12] and thus the radio noise due to the predischarge forms a Poisson noise of an approximately 1-msec duration and consisting of the basic impulses of the order of 1-μsec duration. Since the atmospheric lightning discharge itself would also be repeated according to the Poisson distribution of some time rate, the kind of noise like atmospherics may be called Poisson-Poisson noise. The contribution to the atmospherics in Mc bands is almost due to this kind of noise.

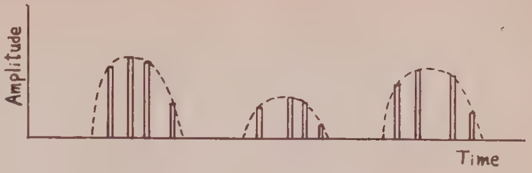

FIG. 1. Amplitude and occurrence time of the original elementary impulses in Poisson-Poisson noise.

In Sec. II, the probability density of the noise envelope is first formulated for Poisson noise. The i.f. circuit response for the elementary impulse is put in the form of $r=r(t,a)\cos(\omega t-\psi)$, where t is the time length from the time of pulse occurrence to the time of observation, the envelope $r(t,a)$ is, of course, a time function changing very slowly in the period $2\pi/\omega$ in the narrow-band case with which we are concerned, and a denotes any other parameters specifying the amplitude. Here, the pulses are considered to occur uniformly in the observation time of the length T, and the phase ψ also distributes uniformly in the range 2π. Thus the distribution function $w(a,\psi,t)$ for a, ψ, and t is assumed to take the form $w(a,\psi,t)=w(a)/2\pi T$. The probability $w(n)_T$ that exactly n impulses occur in the time interval T is of course assumed to follow the Poisson law, Eq. (8). After the formulation of the integral representation of amplitude distribution on these assumptions, the explicit form of $r(t,a)$ is tentatively assumed to be

$$r(t,a)=ae^{-\alpha t}, \tag{1}$$

which has the definite mean duration α^{-1}; the integral is actually evaluated for arbitrary distribution of $w(a)$.

The amplitude distribution of Poisson-Poisson noise is then evaluated in the same way. One of the essential differences from Poisson noise is that the amplitude of the basic impulse depends on the time length from the time t at which the "elementary Poisson noise packet" (e.g., the predischarge of an atmospheric discharge) begins to occur, to the time of occurrence t' of the basic elementary impulse in question in the same packet (Fig. 1). Correspondingly, the i.f. circuit response $r(t',a;t)$ for the basic elementary impulse generally takes the form

$$r(t',a;t)=A(a,t-t')B(t'). \tag{2}$$

Here, the time axis is taken in the direction of past and the origin at the time of observation. $A(a,t-t')$ represents the amplitude of the input impulse, and $B(t')$ the i.f. circuit response for the impulse of the unit strength. In the case of atmospherics, the duration of the basic impulse is of the order of 1 μsec, as stated above, and is thus very small as compared with the reciprocal of the bandwidth of the i.f. circuit in the usual equipment. Thus, in the simplest case of one resonant circuit, we may safely put $B(t')=e^{-\alpha t'}$. Moreover in this paper, the amplitude A is assumed to take the form $A=ae^{-\beta(t-t')}$, which means the "elementary packet" of the definite mean duration β^{-1}.

---

[10] T. Ishida, Bulletin (in Japanese) of the XIth Symposium of Radio Research Lab. (held on October 23–24, 1956, at Kokubunji, Tokyo), pp. 113–120.

[11] B. F. Schonland, Proc. Roy. Soc. (London), **A220**, 25 (1953). See also A. D. Watt and E. L. Maxwell, Proc. I. R. E. **45**, 787–794 (1957).

[12] This situation might be understood by considering the simple model of stationary discharge; "stationary" here means that the circumstance is the same before and after the discharge. Let t be the time length from the time of "switching in" the electric field to start the discharge, and $P_0(t)$ the probability that any discharge does not occur yet in the time interval t after the switching. Then the relation $P_0(t_1+t_2)=P_0(t_1)P_0(t_2)$ holds for arbitrary t_1 and t_2 on account of the stationary assumption. The general solution is readily found to be $P_0(t)=(\alpha)^{-1}e^{-\alpha t}$ with the correct normalization. The Poisson law of distribution is readily derived from this distribution successively; e.g., let $P_1(t)$ be the probability that the discharge occurs only once in the time interval t after the switching; then the relation $P_1(t_1+t_2)=P_1(t_1)\times P_0(t_2)+P_0(t_1)P_1(t_2)$ holds for arbitrary t_1 and t_2 to give $P_1(t)=\alpha te^{-\alpha t}$, etc.

The spatial distribution of noise source seriously affects the amplitude distribution in many cases since the noise strength decreases with the distance from the source. In Sec. IV, the amplitude distributions are evaluated according to the spatial distributions in the two typical cases of the discrete case and the continuous case. In Sec. V, the results are numerically compared with the actual atmospherics. The used equipment for measuring the cumulative amplitude distribution is also displayed there in some detail.

In Sec. VI, the amplitude moments of even order and the correlation functions are calculated for each model without any assumption about the spatial distribution of noise source. Finally, in Sec. VII, the dependence of the used assumptions on the probability densities is discussed.

II. PROBABILITY DENSITIES

A. Poisson Noise

Poisson noise, as is well known, consists of the superposition of independent, randomly occurring elementary pulses which may overlap each other. The waveforms of these elementary pulses are assumed to be identical, and their amplitudes, phases, and even their durations can vary in a random way; their times of occurrence are independent, purely random quantities. The observed particular wave forms, of course, depend on the frequency response of the circuits or the selective properties of the medium through which the disturbance quantities eventually pass. We here only consider the narrow-band noise of the middle frequency ω. Thus the response of the i.f. circuit for the elementary pulse takes the form

$$r=r(t,a)\cos(\omega t-\psi)=r(t,a)(\cos\psi\cos\omega t+\sin\psi\sin\omega t), \quad (3)$$

where $r(t,a)$ $(=0, t<0)$ is a function changing very slowly in the period $2\pi/\omega$, and a denotes any other parameters specifying the amplitude. As usual, we may represent this wave by the vector $\mathbf{r}(t,a,\psi)$, having the two components with the factors $\cos\omega t$ and $\sin\omega t$:

$$\mathbf{r}(t,a,\psi)=[r(t,a)\cos\psi,\ r(t,a)\sin\psi]. \quad (4)$$

We hereafter take the time axis in the direction of past and the origin at the time of observation. Thus the t in Eq. (4) expresses the time interval from the time of pulses occurrence to the time of observation. Let $w(a,\psi,t)$ be the distribution function of a, ψ, t, and $P_n(\mathbf{R})d\mathbf{R}$ be the probability that the total vector sum $\mathbf{R}$ of the exactly n elementary wave vectors $\mathbf{r}=\mathbf{r}(a_i,\psi_i,t_i)$ $(i=1, 2, 3, \cdots, n)$ in the time interval $(0,T)$ is in the range $(\mathbf{R}, \mathbf{R}+d\mathbf{R})$. Then the probability density $P_n(\mathbf{R})$ is given by

$$P_n(\mathbf{R})=\int\delta[\mathbf{R}-(\mathbf{r}_1+\mathbf{r}_2+\cdots+\mathbf{r}_n)]$$

$$\times\prod_{i=1}^{n} w(a_i,\psi_i,t_i)da_id\psi_idt_i, \quad (5)$$

$$2\pi\geqq\psi_i\geqq 0,\quad T\geqq t_i\geqq 0.$$

Here, $\delta(x)$ is the ordinary Dirac δ function in two-dimensional space. In the following, we assume uniform distribution in the phase ψ and the time t, and thus put

$$w(a,\psi,t)=w(a)/2\pi T,\quad \int w(a)da=1. \quad (6)$$

On the other hand, let $w(n)_T$ be the probability that exactly n impulses occur in the interval $(0,T)$; then the probability density $P(\mathbf{R})$ with which the total wave vector takes the value $\mathbf{R}$ is given by

$$P(\mathbf{R})=\sum_{n=0}^{\infty} w(n)_TP_n(\mathbf{R}). \quad (7)$$

Here, for the stationary random impulses occurring in the definite rate ν, $w(n)_T$ might be assumed to follow the Poisson distribution

$$w(n)_T=\frac{(\nu T)^n}{n!}e^{-\nu T}. \quad (8)$$

By the use of the integral representation

$$\delta(\mathbf{r})=\frac{1}{(2\pi)^2}\int\int_{-\infty}^{\infty}(d\lambda)\exp[i(\lambda\mathbf{r})],$$

$$(d\lambda)=d\lambda_1d\lambda_2,\quad (\lambda\mathbf{r})=\lambda_1r_1+\lambda_2r_2,$$

Eq. (5) gives us the representation

$$P(\mathbf{R})=\frac{1}{(2\pi)^2}\int\int_{-\infty}^{\infty}(d\lambda)\exp[i(\lambda\mathbf{R})]\sum_{n=0}^{\infty} w(n)_T$$

$$\times\prod_{i=0}^{n}\int\exp[-i(\lambda\mathbf{r}_i)]w(a_i,\psi_i,t_i)da_id\psi_idt_i. \quad (9)$$

Here, from Eqs. (4) and (6),

$$\int_0^T dt\int_0^{2\pi}d\psi\int\exp[-i(\lambda\mathbf{r})]w(a,\psi,t)da$$

$$=\frac{1}{T}\int_0^T dt\int J_0[\lambda r(t,a)]w(a)da. \quad (10)$$

Hence, using the Poisson distribution, Eq. (8), Eq. (9) takes the form

$$P(\mathbf{R})=\frac{1}{(2\pi)^2}\iint_{-\infty}^{\infty}(d\boldsymbol{\lambda})\exp[i(\boldsymbol{\lambda}\mathbf{R})]f(\lambda,T).$$

Here

$$f(\lambda,T)=\sum_{n=0}^{\infty}\frac{1}{n!}\left\{\nu\int_0^T dt\int J_0[\lambda r(t,a)]w(a)da\right\}^n e^{-\nu T}$$

$$=\exp\left\{\nu\int_0^T dt\int daw(a)[J_0(\lambda r)-1]\right\}, \qquad (11)$$

which depends only on λ. Thus, using the cylindrical coordinates $\boldsymbol{\lambda}=(\lambda,\varphi)$, $\mathbf{R}=(R,\phi)$ with $(d\boldsymbol{\lambda})=\lambda d\lambda d\varphi$ and $(d\mathbf{R})=RdRd\phi$, we have after the integration with respect to φ

$$P(\mathbf{R})=\frac{1}{2\pi}\int_0^{\infty}\lambda J_0(\lambda R)f(\lambda,T)d\lambda,$$

or the amplitude density $P(R)=2\pi RP(R)$:

$$P(R)=\int_0^{\infty}\lambda RJ_0(\lambda R)f(\lambda,T)d\lambda. \qquad (12)$$

The cumulative probability density $F(R)$ that the amplitude lies in the range up to R then becomes

$$F(R)=\int_0^R P(R)dR=R\int_0^{\infty}J_1(\lambda R)f(\lambda,T)d\lambda. \quad (13)$$

In the same way, the second-order amplitude probability density $P(R_1,R_2)$ that R takes the values R_1 at the time t_1, and R_2 at the time t_2, is given by the integral

$$P(R_1,R_2)=\iint_0^{\infty}[\lambda_1R_1J_0(\lambda_1R_1)][\lambda_2R_2J_0(\lambda_2R_2)]$$
$$\times f(\lambda_1,\lambda_2;T)d\lambda_1d\lambda_2. \quad (14)$$

Here

$$f(\lambda_1,\lambda_2;T)=\frac{1}{2\pi}\int_0^{2\pi}d\varphi\exp\Bigl(\nu\int_0^T dt\int daw(a)$$
$$\times\{J_0[(\lambda_1r_1)^2+(\lambda_2r_2)^2+2(\lambda_1r_1\lambda_2r_2)\cos\varphi]^{\frac{1}{2}}-1\}\Bigr). \quad (15)$$

For further discussion, the form of the wave envelope $r(t,a)$ should be specified. We assume for a moment that

$$r(t,a)=ae^{-\alpha t}, \quad t>0, \quad \infty>a>0. \qquad (16)$$

When the duration of the original elementary pulse is sufficiently small as compared with the reciprocal of the i.f. bandwidth, the wave envelope of the i.f. circuit response for the pulse would actually take the form of Eq. (16) in the simplest case of a single-resonance i.f. circuit. Hence, the α^{-1} in this case represents the duration of the i.f. response for the basic pulse or, since the duration depends directly on the resistance part of the i.f. circuit which is also closely connected with the frequency bandwidth, the α generally might be thought to represent the bandwidth of the i.f. circuit.

The characteristic function $f(\lambda,T)$ defined in Eq. (11) then takes the form

$$f(\lambda,T)=\exp\{(\nu/\alpha)[W(\lambda a_0)-W(\lambda a_0e^{-\alpha T})]\}, \quad (17)$$

where

$$W(\lambda a_0e^{-T})=\int_T^{\infty}dx\int_0^{\infty}[J_0(\lambda ae^{-x})-1]w(a)da, \quad (18)$$

and a_0 is any constant having the dimension of r. For later convenience, we shall take it as

$$a_0=\exp(\langle\log a\rangle+\gamma), \quad \gamma=0.5772=\text{Euler's const.} \quad (19)$$

We have, especially,

$$f(\lambda,\infty)=\exp[(\nu/\alpha)W(\lambda a_0)]. \qquad (20)$$

Here, from Eq. (18), the series expansion of $W(\lambda a_0)$ becomes

$$W(\lambda a_0)=\sum_{n=1}^{\infty}\frac{(-)^n}{2n(n!)^2}\langle(\lambda a/2)^{2n}\rangle \qquad (21)$$

or, using the Barnes method,[13]

$$W(\lambda a_0)=\frac{-1}{2\pi i}\int_{\epsilon-i\infty}^{\epsilon+i\infty}\frac{\Gamma(1-s)}{2s^2\Gamma(1+s)}\langle(a/a_0)^{2s}\rangle$$
$$\times\left(\frac{\lambda a_0}{2}\right)^{2s}ds, \quad 1>\epsilon>0. \quad (22)$$

B. Poisson-Poisson Noise

As is stated in the introduction, the predischarge in an atmospheric discharge consists of many random elementary impulses of the order of the duration of 1 μsec, each of which occur successively in the time interval of 25–100 μsec. Since the elementary pulses would occur in time according to the Poisson distribution, the predischarge, so to speak, forms a wave packet of Poisson noise as a whole. In atmospherics, such predischarge repeats itself in every stroke presumably according to the Poisson law of some rate. Thus we may call the noise of this kind Poisson-Poisson noise; that is, the basic elementary impulses of Poisson noise, stated in Sec. II A, are simply replaced here by the basic elementary packets of Poisson noise; their forms are assumed to be identical, and their amplitudes and durations can vary in a random way; their times of occurrence are independent, purely random quantities. In the case of the narrow band of the middle frequency of megacycles, the noise of this kind contributes most to atmospherics.

---

[13] As the residue of $\Gamma(1-s)$ at $s=n$ is $(-)^n/\Gamma(n)$, the integral representation, Eq. (22), can be readily deduced, provided the integrand decreases sufficiently rapidly as $|s|\to\infty$ on the right side of the imaginary axis.

The characteristic function in this case, as will be explained subsequently, is replaced by $f'(\lambda,T)$ with a form similar to Eq. (11):

$$f'(\lambda,T)=\sum_{n=0}^{\infty} w'(n)_T\left[\frac{1}{T}\int_0^T f(\lambda,t)dt\right]^n. \tag{23}$$

Here

$$w'(n)_T=\frac{(\nu'T)^n}{n!}e^{-\nu'T}$$

is the probability that exactly n wave packets of Poisson noise occur in the time interval T, and $f(\lambda,t)$ is the characteristic function for the elementary Poisson noise packet; it thus takes the same form as given by Eq. (11) except that the i.f. circuit response r for the basic impulse depends on the time length from the time t at which the "elementary Poisson noise packet" (e.g., the predischarge of an atmospheric discharge) begins to occur, to the time of occurrence t' of the basic elementary impulse in the same packet:

$$f(\lambda,t)=\exp\left\{\nu\int_0^t dt'\int da w(a)[J_0(\lambda r)-1]\right\}, \tag{24}$$
$$r=r(t',a;t).$$

The wave packets are assumed to be distributed uniformly in the interval T. Hence, the characteristic function for one packet becomes $T^{-1}\int_0^T f(\lambda,T)dt$. Thus the characteristic function for the probability that exactly n wave packets occur in the interval T becomes the term $[T^{-1}\int_0^T f(\lambda,t)d\lambda]^n$ in Eq. (23).

Summing up the series of Eq. (23),

$$f'(\lambda,T)=\exp\left\{\nu'\int_0^T [f(\lambda,t)-1]dt\right\}. \tag{25}$$

We may assume the rectangular form for the elementary pulse packet. In this paper, we adopt instead the following packet form of exponential decrease:

$$r(t',a;t)=ae^{-\beta(t-t')-\alpha t'},\quad t\geqq t'\geqq 0. \tag{26}$$

Here, $\alpha\gg\beta$ of course, $ae^{-\beta t}$, giving the envelope of the packet (Fig. 2).

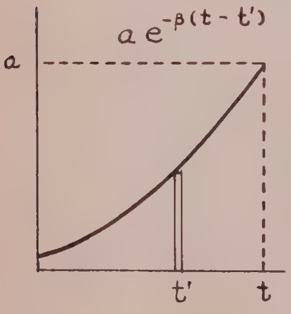

FIG. 2. Amplitude-occurrence time relation of the elementary impulse for Eq. (26).

Using Eq. (26) in Eq. (24), we have

$$f(\lambda,t)=\exp\left\{\frac{\nu}{\alpha-\beta}\int_{\beta t}^{\alpha t}dx\int_0^{\infty}[J_0(\lambda ae^{-x})-1]w(a)da\right\},$$

which gives, by the use of Eq. (18),

$$f(\lambda,t)=\exp\left\{\frac{\nu}{\alpha-\beta}[W(\lambda a_0e^{-\beta t})-W(\lambda a_0e^{-\alpha t})]\right\}. \tag{27}$$

By the substitution of Eq. (27),

$$\int_0^T[f(\lambda,t)-1]dt=\int_0^T \exp\left[\frac{\nu}{\alpha-\beta}W(\lambda a_0e^{-\beta t})\right]$$
$$\times\left\{\exp\left[\frac{-\nu}{\alpha-\beta}W(\lambda a_0e^{-\alpha t})\right]-1\right\}dt$$
$$+\int_0^T\left\{\exp\left[\frac{\nu}{\alpha-\beta}W(\lambda a_0e^{-\beta t})\right]-1\right\}dt.$$

Here, in the case of $\nu/(\alpha-\beta)\lesssim 1$, the integrand of the first integral is different from zero only in the range of t where $\lambda a_0e^{-\alpha t}\gtrsim 1$ or $\beta t\lesssim(\beta/\alpha)\log\lambda a_0$, as is seen from the series expansion of Eq. (21). Hence, taking into account that $\alpha\gg\beta$, we may put $e^{-\beta t}\simeq 1$ in the necessary range of values of λa_0. Thus, we have from Eq. (25)

$$f'(\lambda,T)\simeq\exp\{(\nu'/\alpha)\exp[(\nu/\alpha)W(\lambda a_0)]W_{\alpha T}'(-\nu/\alpha;\lambda a_0)$$
$$+(\nu'/\beta)W_{\beta T}'(\nu/\alpha;\lambda a_0)\},\quad \alpha\gg\beta. \tag{28}$$

Here

$$W_T'(b;x)=\int_0^T\{\exp[bW(xe^{-t})]-1\}dt. \tag{29}$$

It may be noted that, when $\nu'/\beta\lesssim 1$, it follows that $\nu'/\alpha\ll 1$, and the first term in the exponential of Eq. (28) can be neglected in many important cases (Secs. IV C and VI).

Even when we assumed the rectangular form of the elementary pulse packet of the duration $\Delta\tau$, Eq. (28) still remains valid by the simple replacements of β^{-1} by $\Delta\tau$ and $W_T'(b;x)$ by

$$W_T'(b;x)$$
$$=\{\exp[bW(x)]-1\}\times\begin{cases}T/\Delta\tau, & \Delta\tau>T>0\\ 1, & T>\Delta\tau.\end{cases} \tag{30}$$

III. EVALUATION OF INTEGRAL

We here assume the special distribution

$$w(a)=(a_0)^{-1}e^{-a/a_0},\quad \langle a\rangle=a_0 \tag{31}$$

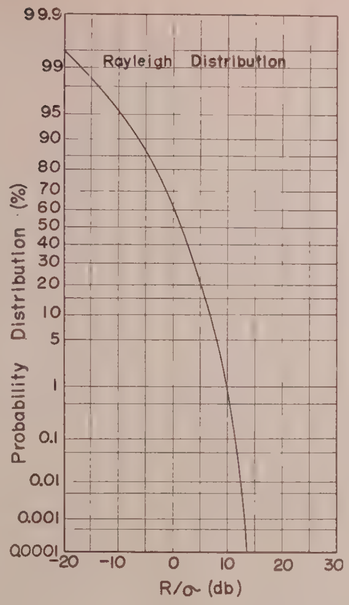

Fig. 3. Rayleigh distribution of Eq. (38).

and evaluate the integrals in Sec. II A. This assumption, however, is not essential in many cases, as will be seen later.

We first note that the definition of a in Eq. (19) agrees with that of Eq. (31), and

$$\int_0^\infty J_0(\lambda a e^{-x})w(a)da = 1/[1+(\lambda a_0)^2 e^{-2x}]^{\frac{1}{2}}. \qquad (32)$$

Hence, from Eq. (18), we have by elementary calculation,

$$W(\lambda a_0 e^{-T}) = \log(2/\{1+[1+(\lambda a_0 e^{-T})^2]^{\frac{1}{2}}\}). \qquad (33)$$

Thus, from Eq. (20)

$$f(\lambda,\infty) = \{2/1+[1+(\lambda a_0)^2]^{\frac{1}{2}}\}^{\nu/\alpha}, \qquad (34)$$

and finally from Eq. (13),

$$F(R) = R\int_0^\infty J_1(\lambda R)\left\{\frac{2}{1+[1+(\lambda a_0)^2]^{\frac{1}{2}}}\right\}^{\nu/\alpha} d\lambda, \quad T\to\infty$$

$$= (R/a_0)\int_0^\infty J_1[(R/a_0)\lambda]\left\{\frac{2}{1+(1+\lambda^2)^{\frac{1}{2}}}\right\}^{\nu/\alpha} d\lambda \qquad (35)$$

$$= 1-(R/a_0)\frac{2}{\pi}\int_1^\infty K_1[(R/a_0)\lambda]$$

$$\times \mathrm{Im}\left[\frac{2}{1-i(\lambda^2-1)^{\frac{1}{2}}}\right]^{\nu/\alpha} d\lambda. \qquad (36)$$

Here, Im denotes the imaginary part (Appendix A).

The representations (35) and (36) are especially convenient for $R/a_c \ll 1$ and $R/a_0 \gg 1$, respectively.

On the other hand, when $\nu/\alpha \gg 1$, the integral (35) is decisively determined by the integration in the range of $\lambda^2 \ll 1$, in which

$$f(\lambda,\infty) \simeq \exp[-(\nu/4\alpha)\lambda^2]. \qquad (37)$$

Hence, it follows that

$$F(R) \simeq 1-\exp[-\tfrac{1}{2}(R/\sigma)^2], \quad \sigma^2 = \tfrac{1}{2}(\nu/\alpha)a_c^2, \qquad (38)$$

which gives the ordinary Rayleigh distribution of Fig. 3, as is expected.

IV. EFFECT OF SPATIAL DISTRIBUTION OF NOISE SOURCES

The noise source generally has a distribution in space, and the strength decreases with the distance from the source. Hence, the spatial distribution of the source sometimes gives a serious effect to the amplitude distribution of noise.

Using the spatial coordinates (x), the characteristic function $f(\lambda,\infty)$ of Eq. (20) then should be replaced by

$$\Pi_i e^{(\nu/\alpha)_i W(\lambda a_0)} = \exp\left[\int (\nu/\alpha)W(\lambda a_0)dx\right], \qquad (39)$$

where $\nu_i = \nu\delta x_i$ is the average time rate of impulse occurrence in the ith segment of space in the range $(x_i, x_i+\delta x_i)$, and ν and a_0 are generally functions of space coordinates. Hence, on using Eq. (33), the characteristic function $f(\lambda,\infty)$ becomes

$$f(\lambda,\infty) = \exp\left(\int \frac{\nu}{\alpha}\log\left\{\frac{2}{1+[1+(\lambda a_0)^2]^{\frac{1}{2}}}\right\}dx\right). \qquad (40)$$

In the following, we shall consider the two typical cases of space distribution.

A. Noise by Strong Local Source

This is the case where there exists locally a strong noise source in a short distance (Fig. 4) and also a continuous noise source distributed far distant from the former in such a way that the noise strength is sufficiently small as compared with that at a short distance. As the noise from the latter will effectively act as a white noise, the whole noise will be observed as the ordinary noise mixed with strong random impulsive noise.

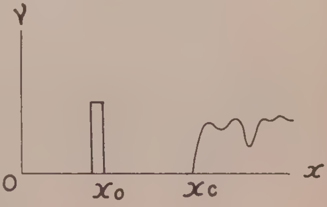

Fig. 4. Spatial distribution of $\nu(x)$ for Eq. (41).

In Eq. (40), we thus put

$$\nu(x) \to \nu\delta(x-x_0)+\nu(x), \quad x_0 \ll x_c. \tag{41}$$

Here, x simply denotes the distance from the receiver; $\nu(x)=0$ for $x<x_c$, and

$$a_c = a_0\big|_{x=x_0} \gg a_0\big|_{x=x_c}. \tag{42}$$

Thus, we may use Eq. (37) for the continuous distribution part, and we have

$$f(\lambda,\infty)=\left\{\frac{2}{1+[1+(\lambda a_0)^2]^{\frac{1}{2}}}\right\}^{\nu/\alpha}\exp(-\tfrac{1}{2}\sigma^2\lambda^2),$$
$$\sigma^2=\tfrac{1}{2}\int_{x_c}^{\infty}(\nu/\alpha)a_0^2dx. \tag{43}$$

Eq. (43) will be valid for the range of $\lambda\sigma \lesssim 1$ in which the integral for the probability density is decisively determined, because, generally, $\sigma \gg a_0|_{x=x_c}$.

In the case of atmospherics, it usually holds that $\nu/\alpha \ll 1$. Thus, when $R/a_0 \ll 1$ in the integral representation of $F(R)$ of Eq. (13), the characteristic function $f(\lambda,\infty)$ only in the range of $\lambda a_0 \gg 1$ becomes most important for the integration. By the use of the asymptotic form of Eq. (43),

$$f(\lambda,\infty)\sim(2/\lambda a_0)^{\nu/\alpha}\exp(-\tfrac{1}{2}\sigma^2\lambda^2), \tag{44}$$

we have thus

$$F(R) \simeq R\int_0^\infty J_1(\lambda R)(2/\lambda a_0)^{\nu/\alpha}\exp(-\tfrac{1}{2}\sigma^2\lambda^2)d\lambda, \qquad R/a_0 \ll 1,$$
$$=(\sigma/a_0)^{\nu/\alpha}\Gamma(1-\nu/\alpha)(R/\sigma)^2$$
$$\times {}_1F_1(1-\nu/2\alpha;2;-(R/\sigma)^2). \tag{45}$$

Here, ${}_1F_1$ is the confluent hypergeometric function.

On the other hand, for $R/a_0 \gg 1$, the integral representation similar to Eq. (36) is convenient to use, and gives the result (Appendix B)

$$F(R) \simeq 1-(\nu/\alpha)2^{\nu/\alpha}(R/a_0)^{-1}$$
$$\times\exp[-(R/a_0)+\tfrac{1}{2}(\sigma/a_0)^2], \tag{46}$$
$$R/a_c \gg 1, \quad a_0/\sigma \gtrsim 1.$$

Hence, $1-F(R)$ effectively decreases exponentially with R/a_0 for $R/a_c \gg 1$, and thus the rate of decrease is very slow as compared with the Rayleigh distribution of the form of Eq. (38).

The range of R in which the approximation (44), and thus Eq. (45), is valid is fairly large and covers the important part of $F(R)<0.98$ or more for $a_0/\sigma>100$ and $\nu/\alpha<0.02$.

In Fig. 5(a) and (b), the numerical values of $1-F(R)$ are displayed as a function of R/σ for several values of ν/α and a_0/σ in decibels. These are obtained by the use of Eq. (45) for $R/a_0<0.1$ and by numerical calculation of the integral (B.4) for $5>R/a_0>0.2$.

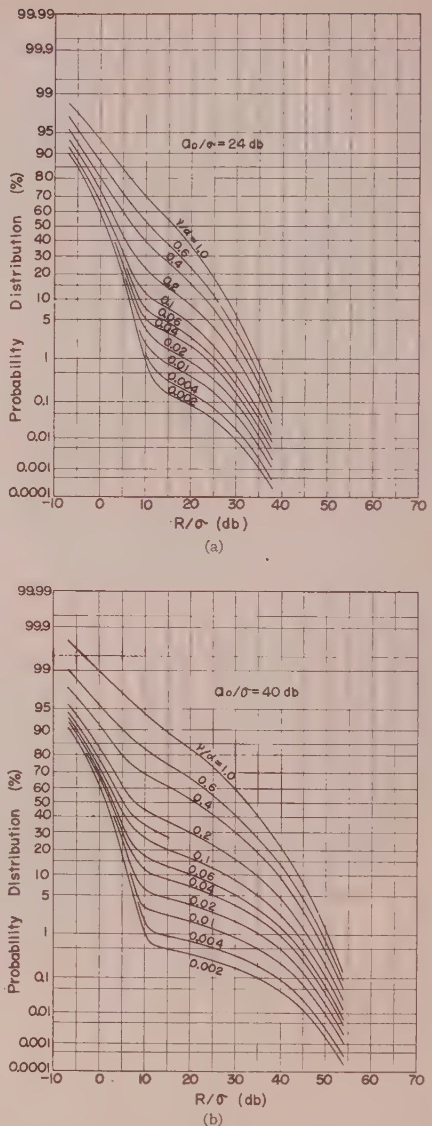

(a)

(b)

FIG. 5. Cumulative amplitude distributions from R to ∞ by Eq. (43) as a function of R/σ for several values of ν/α and a_0/σ. (a) $a_0/\sigma=24$ db, (b) $a_0/\sigma=40$ db.

B. Noise by Sources of Continuous Distribution

This is the case in which the noise sources are continuously distributed as illustrated in Fig. 6. In the case of atmospherics, this condition is frequently realized in midnight when the wave propagation loss is so small that waves from long distances are uniformly received.

We shall here consider the problem in one-dimensional distribution and assume that ν per unit distance is constant from the point x_0 to ∞, and a_0 decreases with

x in proportion to $1/x$. Then, Eq. (40) gives

$$f(\lambda,\infty)=\left\{\frac{1+[1+(\lambda a_0)^2]^{\frac{1}{2}}}{2}\right\}^{(\nu x_0/x)}$$
$$\times\exp((\nu x_0/\alpha)\{1-[1+(\lambda a_0)^2]^{\frac{1}{2}}\}) \quad (47)$$
$$\sim(\lambda a_0/2)^{\nu x_0/\alpha}e^{(\nu x_0/\alpha)(1-\lambda a_0)}, \quad \lambda a_0\gg 1. \quad (48)$$

Here, a_0 is the value of a_0 at the point x_0.

By the use of the asymptotic form (48), we have for $R/a_0\ll 1$

$$F(R)\simeq\tfrac{1}{2}\Gamma(2+\rho)e^{\rho(1-\log 2\rho)}(R/a_0\rho)^2$$
$$\times{}_2F_1[1+(\rho/2),\tfrac{3}{2}+(\rho/2);2;-(R/a_0\rho)^2], \quad (49)$$
$$\rho=\nu x_0/\alpha, \quad R/a_0\ll 1,$$

in the same way as in Sec. IVB while, for $R/a_0\gg 1$, it is found from Eq. (B.7) that

$$F(R)\simeq 1-\rho e^{\rho(1-\log 2)}[(R/a_0)^2]^{-1}e^{-R/a_0}, \quad R/a_0\gg 1. \quad (50)$$

Hence, as in Eq. (46), $1-F(R)$ decreases almost exponentially with R/a_0 for $R/a_0\gg 1$.

By the use of Eqs. (49) and (50) for $R/a_0\ll 1$ and $R/a_0\gg 1$, respectively, and by the numerical calculation of the integral (B.6) for the intermediate range, the values of $1-F(R)$ are displayed as functions of $R/a_0\rho$ and ρ in Fig. 7.

The feature of these curves may be the linearity in a wide range of R in this scale of representation, and it implies the validity of the approximate log-normal distribution of the noise.

C. Poisson-Poisson Noise

The characteristic function in this case is given by Eq. (28). Here, using Eq. (33) for $W(xe^{-t})$ in Eq. (29) we have

$$W_\infty'(b;x)=\int_0^\infty\left(\left\{\frac{2}{1+[1+(xe^{-t})^2]^{\frac{1}{2}}}\right\}^b-1\right)dt, \quad (51)$$

which has the asymptotic form (Appendix C) of

$$W_\infty'(b;x)\sim\log(2/x)+b^{-1}[1-(2/x)^b]$$
$$-\tfrac{1}{2}[\Gamma'(1+b)+\gamma]+0(x^{-1}), \quad (52)$$

with

$$\Gamma'(z)=(\partial/\partial z)\Gamma(z), \quad x\gg 1, \quad b>0,$$

and

$$W_\infty'(b;x)\sim -b^{-1}(x/2)^{-b}, \quad x\gg 1, \quad b<0. \quad (53)$$

FIG. 6. Spatial distribution of $\nu(x)$ for Eq. (47).

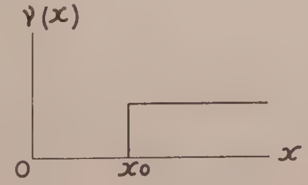

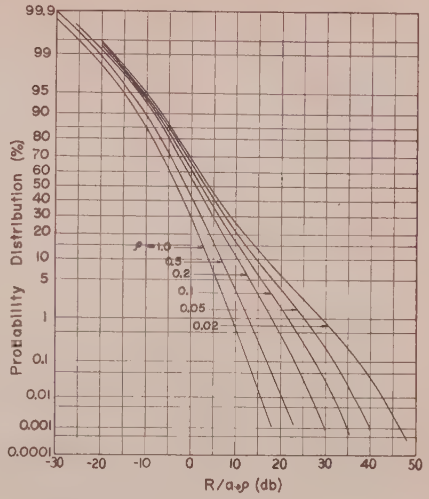

FIG. 7. Cumulative amplitude distributions from R to ∞ by Eq. (47) for several values of ρ.

Hence, the asymptotic form of the characteristic function $f'(\lambda,\infty)$ takes the form

$$f'(\lambda,\infty)\sim\exp\,[(\nu'/\nu)+(\nu'/\beta)$$
$$\times(\log(2/\lambda a_0)+\alpha/\nu-\tfrac{1}{2}\{\Gamma'[1+(\nu/\alpha)]+\gamma\})\,]$$
$$=(2/\lambda a_e)^{\nu'/\beta}, \quad (\lambda a_0/2)^{\nu/\alpha}\gg 1. \quad (54)$$

Here

$$a_e=a_0\exp(-(\alpha+\beta)/\nu+\tfrac{1}{2}\{\Gamma'[1+(\nu/\alpha)]+\gamma\}), \quad (55)$$

which means the effective value of a_C.[14] Of course, the term $(\alpha+\beta)/\nu$ in Eq. (55) can be replaced by α/ν on account of $\alpha\gg\beta$, and this fact simply implies that the first term in the exponent of Eq. (28) can be neglected.

On the other hand, the approximate form at $\lambda^2 a_0^2\ll 1$ is simply

$$f'(\lambda,\infty)=\exp[-(\nu'\nu/8\beta\alpha)a_0^2\lambda^2]. \quad (56)$$

It is also interesting to consider the case of $\nu/\alpha\gg 1$, in which the overlapping of the elementary pulse waves is very large in the basic Poisson noise packet. In the limit of $\nu/\alpha\longrightarrow\infty$ and $a_0^2\longrightarrow 0$ with a finite value of $(\nu/\alpha)a_0^2$, the asymptotic form of $f'(\lambda,\infty)$ at $(\nu/\alpha)a_0^2\lambda^2\gg 1$ is proven by Eqs. (C.8) and (C.9) to be

$$f'(\lambda,\infty)\bigg|_{\substack{\nu/\alpha\to\infty\\ a_0^2\to 0}}\sim(2/\lambda a_e)^{\nu'/\beta}, \quad (\nu/\alpha)a_0^2\lambda^2\gg 1,$$
$$a_\varepsilon=(\nu/\alpha)^{\frac{1}{2}}a_0e^{\frac{1}{2}\gamma}, \quad (57)$$

being the same form as that of Eq. (54), while the approximate form at $(\nu/\alpha)a_0^2\lambda^2\ll 1$ becomes the same as Eq. (56). Hence, the analytical properties of the function $f'(\lambda,\infty)$ in both cases are found to be very similar to each other and also to those of the original characteristic function $f(\lambda,\infty)$ of Eq. (34) with the replacements of ν/α by ν'/β and a_0 by a_e, respectively. Their asymptotic forms, especially, are the same.

---

[14] The difference due to the frequency bandwidth of the receiver will appear only through Eq. (55); as is noted in the text following Eq. (16), the α in Eq. (55) could represent the frequency bandwidth of the receiver.

Hence, it follows that the asymptotic form of a characteristic function such as that of Eq. (44) is valid also in the case of Poisson-Poisson noise with the replacement of σ^2 in Eq. (43) by

$$\sigma^2=\frac{1}{4}\int_{x_c}^{\infty}\frac{\nu\nu'}{\alpha\beta}a_0^2dx. \qquad (58)$$

Thus, the distribution (45) is found to be true also in this case of Poisson-Poisson noise in the range of about $R/a_0<0.1$ with the suitable replacements stated above.

On the other hand, for $R/a_0\gg1$, Eq. (46) is replaced by

$$F(R)\simeq1-f'(ia_0,\infty)\left(\frac{\nu\nu'}{\alpha\beta}\right)\frac{1}{(R/a_0)^2}e^{-R/a_0}, \qquad (59)$$

$$f'(ia_0,\infty)\sim1,\quad R/a_0\gg1,\quad \nu/\alpha\lesssim1,$$

which is obtained by the use of the formula (A.5) and the calculation similar to Eq. (B.5). Thus, $1-F(R)$ effectively decreases exponentially with R/a_0 as in Eq. (46) but not with R/a_e, a_0 being the internal structure constant of the elementary Poisson noise packet, while a_e is the effective amplitude of the packet as an elementary impulse of Poisson noise. It has also the factor ν'/β explicitly besides ν/α. Thus, we may say that the probability distribution in the range of $R/a_0\gg1$ depends explicitly on the fine structures of i.f. circuit response for the original elementary impulse. These facts are in contrast to the range of $R/a_0\ll1$, where the amplitude probability distribution takes the same form as Eq. (45) and depends on the fine structure constants of the internal pulse waves, such as ν and α, only through a_e.

The above result might be expected because, for such large value of R of $R/a_0\gg1$, the greatest contribution is due to the peak parts of the elementary pulse waves, and the overlapping will become so poor that the structure of the pulse waves determines explicitly the amplitude probability distribution.

The fact that the amplitude distribution of Poisson-Poisson noise (except for the case of $\nu/\alpha\ll1$) becomes the same as that of Poisson noise in the range of $R/a_0\ll1$ or $R/[(\nu/\alpha)^{\frac{1}{2}}a_0]\ll1$ when $\nu/\alpha\rightarrow\infty$ and $a_0{}^2\rightarrow0$ would be explained in the following way: The amplitude distribution is decisively controlled only by the form of the elementary noise packet but not explicitly by the internal structures of the packet because of the large overlapping of the elementary pulse waves of which the packet consists.

We can draw a similar conclusion also for the continuous spatial distribution case of Sec. IV B. However, the range of R in which the approximate distribution, Eq. (49), is valid is not so wide as to cover the whole practical important values of $F(R)$. Therefore, the dependence of the amplitude probability distribution on the fine structures of the elementary pulse waves is in principle unavoidable, though it might probably be small, as is expected from the analytical properties of the characteristic function $f'(\lambda,\infty)$ very similar to those of $f(\lambda,\infty)$ [Eqs. (34), (54)–(57)].

V. COMPARISON WITH ACTUAL ATMOSPHERICS

In Figs. 8 and 9, and the two theoretical distributions obtained in Secs. IV A and IV B are compared with several examples of the actual atmospheric noise measured at the Ohira station (long. 35° 37′N, lat. 140° 30′E) in Japan.

The spots are the observational values and the solid lines are the theoretical distributions, whose parameter values are chosen to give the best agreement with the former. It may be remarked that the so chosen values of parameters are found to be consistent with those determined directly from the photograph of the noise waves (Sec. V A).

The measurement is made by the use of the equipment of which the block diagram is shown in Fig. 10.[9] In order to avoid the distortion of the envelope of noise amplitude caused by the circuit nonlinearity and also by the time constant of the detector, the noise output from the i.f. amplifier is directly sliced by the five amplitude discriminators of which the sensing levels are each set beforehand at intervals of 10 db. The following five counters count the output pulses of intermediate frequency, the counting time interval being set for 100 sec in general cases. But, in the case where the dynamic range of noise intensity is large, after the measurement of the first portion of low level for 100 sec, the next portion is measured for the same interval, with the 5~25 db attenuator inserted at the head of the five discriminators and so on, according to the dynamic range of noise intensity. The value of inserted attenuation is set so that the succeeding portion is overlapped with a part of the preceding portion.

Though the time interval of 100 sec is the value decided empirically, but not theoretically, the sample for this time interval is long enough to represent the whole atmospheric noise, first and last, for about an hour, except for the time toward morning and evening, when atmospheric noise intensity varies rapidly according to the propagation condition of the ionosphere and, also for the time where there are some local thunders, of which the occurrence frequency is very low.

Moreover, it may be useful to give a notice that in the low-level range of noise there exist, in addition to atmospheric noise, receiver noise, man-made noise, and galactic noise. However, the intensities of the latter two are expected to be sufficiently lower than the former to be neglected at least in these examples. For reference, the receiver noise measured just before the measurement of the external noise is indicated by the dotted lines.

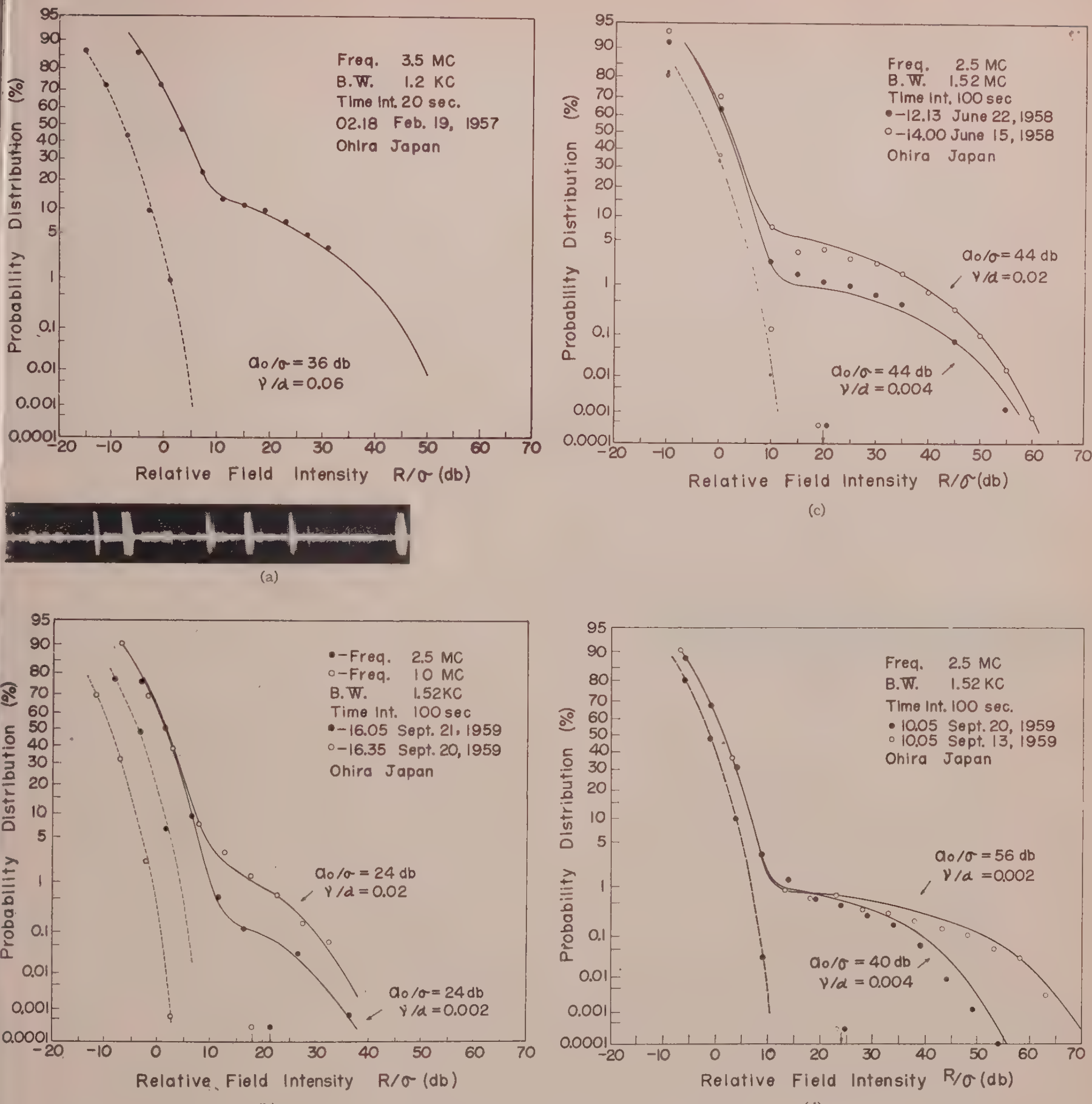

(a) (c) (b) (d)

FIG. 8. Comparison of the theoretical distributions by Eq. (43) with those of atmospheric noise.

The abscissa shows the relative intensity in db, and the arrow on the abscissa indicates the level of absolute field intensity of 1 μv/m.

A. Local Noise Source Predominant (Fig. 8)

These phenomena can be observed in the day time and the afternoon when the attenuation of the ionosphere is large and the noises of local thunders at a short distance are predominantly received.

The photograph in Fig. 8(a) shows a part of the waveform of atmospheric noise during the measurement of the distribution in Fig. 8(a). Time marks under the waveform indicate a half-second interval.

It is interesting to deduce the approximate value of ν/α from such a photograph as that of Fig. 8 (a). From Eqs. (8) and (16) and the discussion of Sec. IV C, we have ν/α (or ν'/β)$=\sum_i \tau_i/T$, where τ_i is the mean duration of the ith impulse; therefore the value of ν/α can be deduced from the photograph by summing up all the impulse durations (τ_i's) and dividing by the total observation time T. Thus we have 0.1 as ν/α from the photograph, though the theoretical distribu-

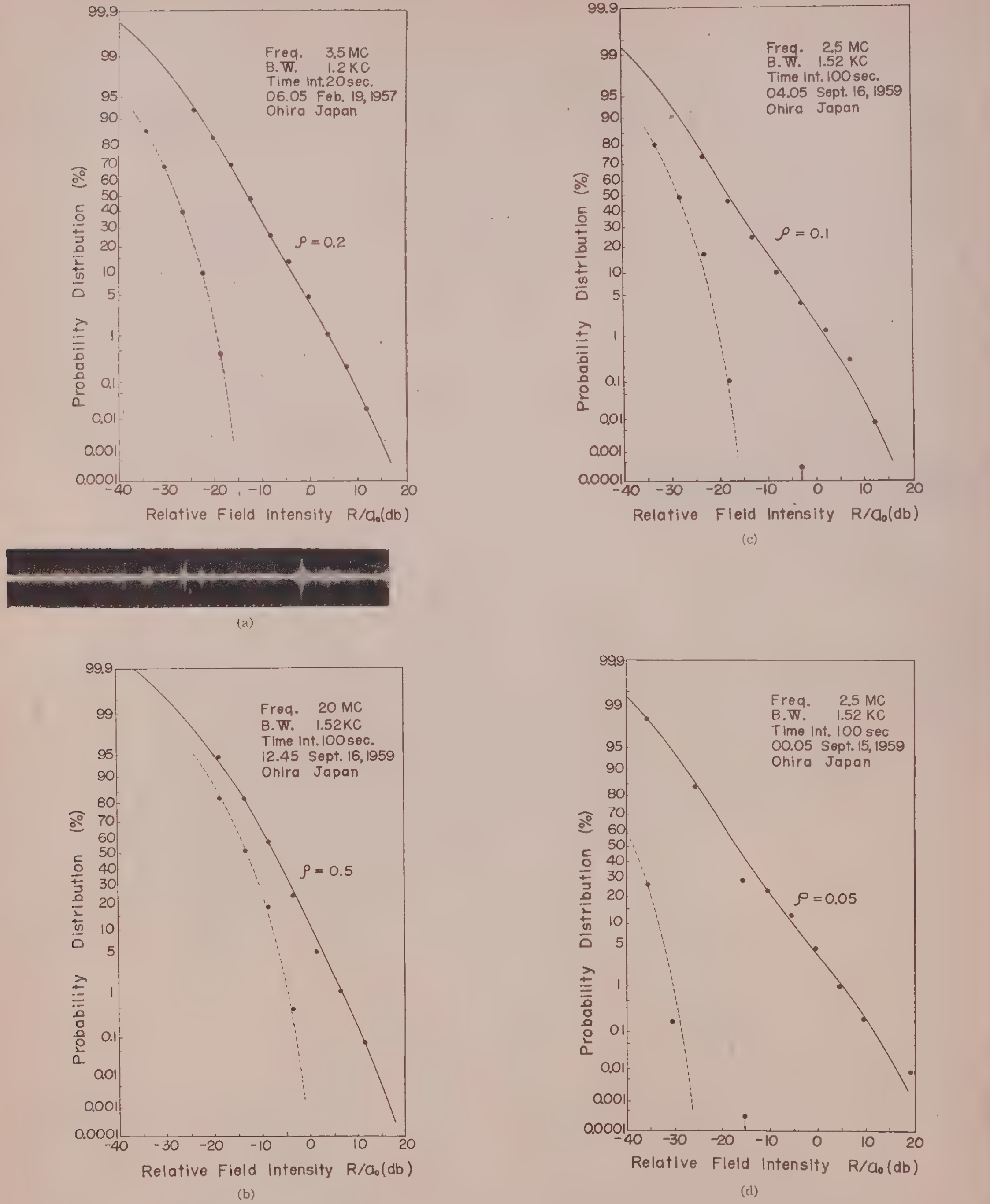

(a)

(c)

(b)

(d)

FIG. 9. Comparison of the theoretical distributions by Eq. (47) with those of atmospheric noise.

tion curve shows 0.06 as ν/α. However, if we took account of the waveform of the photograph, which was cut at the high level due to the poor linearity of the oscilloscope used, a smaller value might be expected for each *mean* duration of τ_i's. Hence the more exact value of ν/α would be fairly smaller than 0.1.

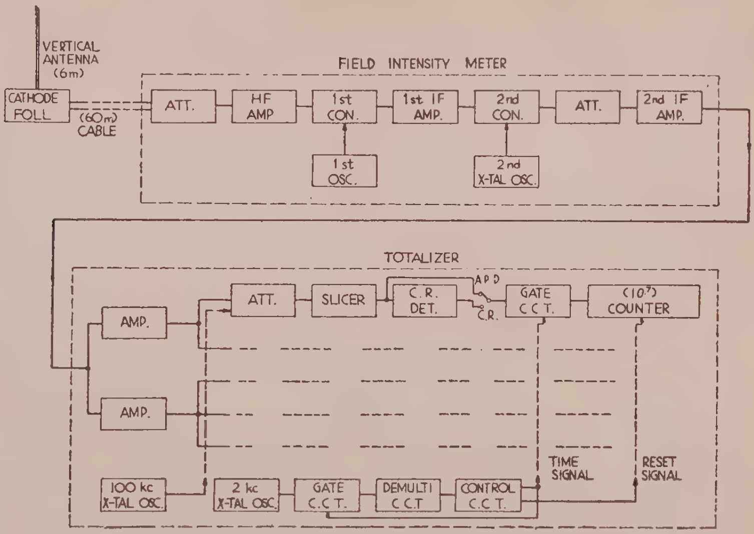

FIG. 10. Block diagram for measurement of the cumulative amplitude distribution of the atmospheric noise.

B. Noise Sources Continuously Distributed (Fig. 9)

These amplitude distributions can be observed at night when the condition of ionospheric propagation improves and a large number of atmospheric noises at long distances arrive at the receiver uniformly, as seen in the photograph of Fig. 9(a).

In the case where the observed frequency is high enough, these amplitude distributions appear even in the daytime because of the low attenuation of the ionosphere.

The feature of this distribution may be the linearity of the curve in the scale of representation adopted, and it implies the validity of the approximate log-normal distribution, as Hersperper *et al.*[6] have insisted.

VI. MOMENTS AND CORRELATION FUNCTIONS

From Eq. (12), we have

$$\langle J_0(zR)\rangle=\int\int_0^\infty \lambda R J_0(zR)J_0(\lambda R)f(\lambda,T)dRd\lambda$$
$$=f(z,T), \quad (60)$$

which gives the generating function for $\langle R^{2n}\rangle$. Thus, by expanding both sides in the power series of z^2, we get

$$\langle R^{2n}\rangle=(-4)^n(n!)^2f_T(n). \quad (61)$$

Here, $f_T(n)$'s are defined by

$$f(z,T)=1+\sum_{n=1}^{\infty} f_T(n)z^{2n}. \quad (62)$$

In the same way, from Eq. (14),

$$\langle J_0(z_1R_1)J_0(z_2R_2)\rangle=f(z_1,z_2;T), \quad (63)$$

which gives

$$\langle R_1^{2m}R_2^{2n}\rangle=(-4)^{m+n}(m!n!)^2f_T(m,n). \quad (64)$$

Here

$$f(z_1,z_2;T)=1+\sum_{m,n=1}^{\infty} f_T(m,n)z_1^{2m}z_2^{2n}. \quad (65)$$

Applying the formula (61) to the three cases of Secs. IV A–C, we have, respectively,

$$\langle R^2\rangle=\begin{cases}2\sigma^2+(\nu/\alpha)a_0^2\\ \frac{1}{2}\int_{x_0}^{\infty}\frac{\nu}{\alpha}\langle a^2\rangle dx\\ \frac{1}{4}\int\frac{\nu\nu'}{\alpha\beta}\langle a^2\rangle dx,\end{cases}$$
$$\langle R^4\rangle=\begin{cases}2\langle R^2\rangle^2+6(\nu/\alpha)a_0^4\\ 2\langle R^2\rangle^2+\frac{1}{4}\int_{x_0}^{\infty}\frac{\nu}{\alpha}\langle a^4\rangle dx\\ 2\left[1+\frac{\alpha\beta}{(\alpha+\beta)\nu'}\right]\langle R^2\rangle^2+\frac{1}{16}\int\frac{\nu\nu'}{\alpha\beta}\langle a^4\rangle dx.\end{cases} \quad (66)$$

In the same way, by the use of Eq. (15) and the formula (64), it can be shown that

$$\langle R_1^2R_2^2\rangle=\begin{cases}\langle R^2\rangle^2(1-e^{-2\alpha\tau})+\langle R^4\rangle e^{-2\alpha\tau}\\ \qquad\text{for Poisson noise}\\ \langle R^2\rangle^2\left[1-\frac{(\beta)^{-1}e^{-2\beta\tau}-(\alpha)^{-1}e^{-2\alpha\tau}}{(\beta)^{-1}-(\alpha)^{-1}}\right]\\ \qquad+\langle R^4\rangle e^{-2\alpha\tau}\quad\text{for P}-\text{P noise,}\end{cases} \quad (67)$$

where τ is the time difference between R_1 and R_2.

VII. EXAMINATION OF ASSUMPTIONS

We shall here investigate the dependences of the assumptions used in preceding sections on the characteristic functions $f(\lambda,\infty)$ and $f'(\lambda,\infty)$, especially on their asymptotic forms.

A. Dependence on the Distribution of $w(a)$

From Eq. (22),

$$W(a_0\lambda)=\frac{-1}{2\pi i}\int_{\epsilon-i\infty}^{\epsilon+i\infty}\frac{\Gamma(1-s)}{2s^2\Gamma(1+s)}\times\langle(a/a_0)^{2s}\rangle\left(\frac{\lambda a_0}{2}\right)^{2s}ds. \quad (68)$$

Here, on account of the definition, Eq. (19), of a_0,

$$\begin{aligned}\frac{\Gamma(1-s)}{\Gamma(1+s)}\langle(a/a_0)^{2s}\rangle&=1+[-\Gamma'(1)+\langle\log(a/a_0)\rangle]2s+0(s^2)\\&=1+0(s^2),\quad -\Gamma'(1)=\gamma.\end{aligned} \quad (69)$$

Hence, the residue of the integrand at $s=0$ is simply $\log(\lambda a_0/2)$. Thus, by the use of the ordinary method,[15] the asymptotic expansion of the integral for $\lambda a_0\gg1$ becomes

$$W(\lambda a_0)\sim-\log(\lambda a_0/2)+0[(\lambda a_0)^{-2\delta}],\quad \delta>0, \quad (70)$$

which takes just the same asymptotic form as that of Eq. (33). Hence, it is concluded that, with the definition (19) for a_0, the distribution (45) is valid irrespective of the distribution $w(a)$. This conclusion is true also for Poisson-Poisson noise as shown in Sec. VII B.

B. Asymptotic Form of Characteristic Function of Poisson-Poisson Noise

From Eq. (29),

$$W_\infty'(b;x)=\int_0^\infty\{\exp[bW(xe^{-t})]-1\}dt, \quad (71)$$

which gives, putting $xe^{-t}=y$,

$$\begin{aligned}W_\infty'(b;x)&=\int_0^x(e^{bW(y)}-1)\frac{dy}{y}\\&=-\int_0^1(1-e^{bW})\frac{dy}{y}+\int_1^x e^{bW}\frac{dy}{y}-\log x.\end{aligned} \quad (72)$$

Here, $e^{bW(x)}$ tends to 1 as $x\rightarrow0$ and to 0 as $x\rightarrow\infty$ for $b>0$. Hence, the second integral on the right side of Eq. (72) takes a finite value as $x\rightarrow\infty$. Thus, from Eq. (28),

$$f'(\lambda,\infty)\simeq\exp[(\nu'/\beta)W_\infty'(\nu/\alpha;\lambda a_0)]\sim(2/\lambda a_e)^{\nu'/\beta},\quad \lambda a_0\gg1, \quad (73)$$

which again takes the same asymptotic form as that of Eq. (33). Here

$$a_e=2a_0\exp\left[\int_0^1(1-e^{(\nu/\alpha)W(y)})\frac{dy}{y}-\int_1^\infty e^{(\nu/\alpha)W(y)}\frac{dy}{y}\right], \quad (74)$$

and the first term in the exponent of Eq. (28) is proved to be ν'/ν ($\ll1$) and can be neglected (Appendix D).

C. Dependence on the Waveform of the Elementary Impulse

From Eq. (11),

$$f(\lambda,\infty)=\exp\left\{\nu\int da\,w(a)\int_0^\infty dt[J_0(\lambda r)-1]\right\}. \quad (75)$$

Here, $r=r(a,t)$ is the wave envelope of circuit response due to the original elementary impulse and thus might take various forms, depending on the frequency bandwidth of the i.f. circuit. Our interest is to know how the asymptotic form of $f(\lambda,\infty)$ for $\lambda a_0\gg1$ does depend on the form of $r(a,t)$.

In the integral (75),

$$\int_0^\infty[J_0(\lambda r)-1]dt=\int_{\lambda r<1}[J_0(\lambda r)-1]dt+\int_{\lambda r>1}J_0(\lambda r)dt-\int_{\lambda r>1}dt. \quad (76)$$

Here, in the simplest case of a single-resonance i.f. circuit, $r(a,t)$ will have the form of $ae^{-\alpha t}$, the duration of the original pulse being assumed to be very small as compared with the reciprocal of the i.f. bandwidth. The first and second integrals on the right side then take definite constant values, and the third integral takes the form of $\alpha^{-1}\log\lambda+$const. Hence, the asymptotic form of $f(\lambda,\infty)$ is readily found to be of the form of Eq. (73).

On the other hand, when $r(a,t)$ (>0) is a slowly oscillating function whose mean value tends to vanish in the form of $ae^{-\alpha t}$ as $t\rightarrow\infty$ (Fig. 11), the first two integrals on the right side of Eq. (76) will take, as $\lambda\rightarrow\infty$, fluctuating values of the order of magnitude 1.

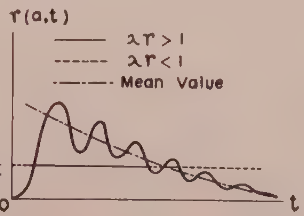

FIG. 11. Form of the wave envelope $r(a,t)$ for Eq. (76).

---

[15] See, for example, G. N. Watson, *Theory of Bessel Functions* (Cambridge University Press, London, 1952), Sec. 7.5, p. 220.

he last integral also takes indefinite values whose ean value tends to grow in the form of $\alpha^{-1}\log\lambda+\text{const}$ s $\lambda\rightarrow\infty$. Thus the asymptotic function of the charcteristic function takes indefinite values whose mean alue tends to vanish in the form of $(2/\lambda a_e)^{\nu/\alpha}$ as $\rightarrow\infty$. Since any circuit has a resistance part and nce, therefore, the assumed attenuation form $ae^{-\alpha t}$ f the mean wave envelope for $t\rightarrow\infty$ will be natural, he conclusion derived above about the asymptotic orm of characteristic function $f(\lambda,\infty)$ seems to be eneral.

VIII. SUMMARY

The amplitude probability distributions of impulsive, andom noise are evaluated according to the two hodels of Poisson noise and Poisson-Poisson noise; representative example of the latter type of noise is tmospheric radio noise. The spatial distribution of oise sources is also taken into account, and the robability distributions are calculated according to he two typical spatial distributions of the discrete ase and the continuous case. In the discrete case, the mplitude probability distribution does not depend xplicitly, in the useful range of the amplitude, on he assumption we have used about the amplitude listribution $w(a)$ of the elementary impulses, nor on the dopted different models of Poisson and Poisson-Poisson oises. In the latter type of noise, it depends only on he form of the envelope of the elementary Poisson noise acket but not explicitly on the internal structure onstants of the noise packet, such as the mean time ate of occurrence of the elementary impulse in the acket ν, the impulse duration α^{-1}, and the impulse mplitude distribution $w(a)$. These nondependencies may correspond in this case to the situation in which the Rayleigh distribution is valid (in the useful range of the amplitude) irrespective of the details of the elementary wave structure when the overlapping of the elementary waves is sufficiently large. On the other hand, in the continuous case of spatial distribution, the situation stated above is not always true and depends on the internal structure or on the fine structures of noise, though to a small extent in the useful range of the amplitude. The more the amplitude increases, the more the probability density depends on the noise structure in detail. This increase of the dependence on elementary pulse wave structure with the amplitude, of course, would be the general tendency due to the poor overlapping of elementary pulse waves at the large amplitude.

The most typical example of impulsive, random noise in nature would be atmospheric noise, for which the cumulative amplitude probability distributions from ∞ to R measured at the Ohira station up to now are compared with the theoretical distributions derived from the characteristic functions (43) and (47), and rather surprising good agreement is found between them.

APPENDIX A

$$F(R)=R\int_0^\infty J_1(\lambda R)f(\lambda,\infty)d\lambda. \tag{A.1}$$

Here, $f(\lambda,\infty)$ is assumed to be an even real function of λ having the branch points at $\lambda=\pm i$ and no other singularity in the finite plane, such as those functions of Eqs. (34), (43), and (47). By the use of

$$J_1(\lambda R)=\tfrac{1}{2}[H_1^{(1)}(\lambda R)+H_1^{(1)}(\lambda Re^{i\pi})],$$

the integral (A.1) can be represented by

$$F(R)=\frac{R}{2}\left\{\int_{-\infty}^{\infty}H_1^{(1)}(\lambda R)f(\lambda,\infty)d\lambda\right.$$
$$\left.+i\pi\,\mathrm{Res}_{\lambda=0}[H_1^{(1)}(\lambda R)f(\lambda,\infty)]\right\}. \tag{A.2}$$

Here, the path contours the origin on the upper side. Thus, by the use of

$$\mathrm{Res}_{z=0}[H_1^{(1)}(z)]=-i2/\pi,\quad f(0,\infty)=1, \tag{A.3}$$

Eq. (A.2) takes the form

$$F(R)=1+\frac{R}{2}\int_{-\infty}^{\infty}H_1^{(1)}(\lambda R)f(\lambda,\infty)d\lambda. \tag{A.4}$$

Here, the integration path can be deformed to the contour path around the branch cut in the upper plane, as is shown in Fig. 12.

Putting $\lambda\rightarrow i\lambda$ and using the relation

$$H_1^{(1)}(iz)=-(2/\pi)K_1(z),$$

Eq. (A.4) finally takes the form

$$F(R)=1-i\frac{R}{\pi}\int_{+1}^{\infty}K_1(\lambda R)f(i\lambda,\infty)d\lambda$$
$$=1-\frac{2R}{\pi}\int_1^\infty K_1(\lambda R)\,\mathrm{Im}f(i\lambda,\infty)d\lambda, \tag{A.5}$$

provided the integrand tends to zero sufficiently

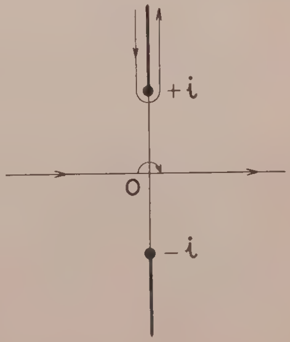

FIG. 12. Integration path for Eq. (A.4).

rapidly as $\lambda \to \infty$, and the contour integral around the branch point of $\lambda=1$ vanishes. Here Im denotes the imaginary part, and

$$(1-\lambda^2)^{\frac{1}{2}}=-i(\lambda^2-1)^{\frac{1}{2}},\quad \lambda>1. \tag{A.6}$$

APPENDIX B

By the substitution of $a_0\lambda \to \lambda$ in Eq. (43), $F(R)$ is here evaluated by the use of the formula (A.5). Thus,

$$F(R)=1-\frac{i}{\pi}(R/a_0)\int_{+1}^{\infty} K_1[\lambda(R/a_0)]\left[\frac{2}{1+(1-\lambda^2)^{\frac{1}{2}}}\right]^{\nu/\alpha} \times\exp[\tfrac{1}{2}(\sigma/a_0)^2\lambda^2]d\lambda, \tag{B.1}$$

whose integrand diverges badly as $\lambda \to \infty$. Hence, the path should be taken as in Fig. 13, where the points $\lambda_\pm$ are the saddle points of the integrand (existing on the real axis) to be determined later. On dividing the integral into the two parts of the contributions due to the paths C_1 and C_2+C_3, respectively, the integral takes the form

$$F(R)=1-(R/a_0)\frac{2}{\pi}\int_{1}^{\lambda+} K_1[\lambda(R/a_0)] \times\mathrm{Im}\left[\frac{2}{1-i(\lambda^2-1)^{\frac{1}{2}}}\right]^{\nu/\alpha}\exp[\tfrac{1}{2}(\sigma/a_0)^2\lambda^2]d\lambda -i(R/a_0)\frac{1}{\pi}\int_{C_2+C_3}. \tag{B.2}$$

Here

$$\left[\frac{2}{1-i(\lambda^2-1)^{\frac{1}{2}}}\right]^{\nu/\alpha}=(2\cos\theta)^{\nu/\alpha}e^{i(\nu/\alpha)\theta},\quad \lambda=\sec\theta. \tag{B.3}$$

On using the asymptotic form of $K_1(z)$ for $z\gg 1$, it is found that $\lambda_\pm=Ra_0/\sigma^2$, at which the integrand is of the order of magnitude of $\exp(-\frac{1}{2}R^2/\sigma^2)$, being very small as compared with the integrand in the first integral in Eq. (B.2) in so far as $\lambda_\pm\gg 1$. Thus, the second integral can be neglected as compared with the first. Using Eq. (B.3),

$$F(R)\simeq 1-(R/a_0)\frac{2}{\pi}\int_{1}^{Ra_0/\sigma^2} K_1[\lambda(R/a_0)](2\cos\theta)^{\nu/\alpha} \times\sin(\theta\nu/\alpha)\exp[\tfrac{1}{2}(\sigma/a_0)^2\lambda^2]d\lambda, \tag{B.4}$$

$$\theta=\cos^{-1}\lambda^{-1},\quad Ra_0/\sigma^2\gg 1.$$

In the case of $R/a_0\gg 1$ and $a_0/\sigma\gtrsim 1$, the integral (B.4) takes the simple form of

$$F(R)\simeq 1-\frac{\nu}{\alpha}2^{\nu/\alpha}\left(\frac{2R/a_0}{\pi}\right)^{\frac{1}{2}}\exp[-R/a_0+\tfrac{1}{2}(\sigma/a_0)^2] \times\int_0^\infty \theta^2\exp\{-(R/2a_0)\theta^2\}d\theta$$

$$=1-(\nu/\alpha)2^{\nu/\alpha}\frac{1}{R/a_0}\exp[-R/a_0+\tfrac{1}{2}(\sigma/a_0)^2]. \tag{B.5}$$

On the other hand, for the characteristic function of Eq. (47), the formula (A.5) can be simply used, and gives

$$F(R)=1-(R/a_0)\frac{2}{\pi}e^{(1-\log 2)\rho}\int_1^\infty K_1[\lambda(R/a_0)] \times\sin[\rho(\tan\theta-\theta)]\cos\theta^{-\rho}d\lambda, \tag{B.6}$$

$$\rho=\nu x_0/\alpha,$$

which gives, for $R/a_0\gg 1$ and $\rho\lesssim 1$,

$$F(R)\simeq 1-\frac{\rho}{3}e^{(1-\log 2)\rho}\left(\frac{2R/a_0}{\pi}\right)^{\frac{1}{2}}e^{-R/a_0}\int_0^\infty \theta^4 \times\exp\{-\tfrac{1}{2}[(R/a_0)-\rho]\theta^2\}d\theta$$

$$=1-\rho e^{(1-\log 2)\rho}\frac{(R/a_0)^{\frac{1}{2}}}{(R/a_0-\rho)^{\frac{5}{2}}}e^{-R/a_0},\quad R/a_0\gg 1. \tag{B.7}$$

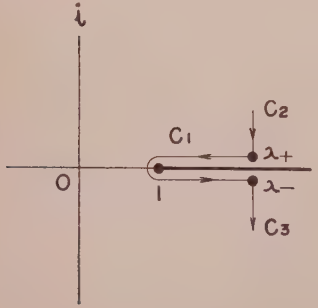

FIG. 13. Integration path for Eq. (B.1).

APPENDIX C

By the change of variable of

$$y=\tfrac{1}{2}\{1+[1+(xe^{-t})^2]^{\frac{1}{2}}\}, \tag{C.1}$$

the integral (51) takes the form

$$W_\infty'(b;x)=\frac{1}{2}\int_{1+\epsilon}^{K}\frac{2y-1}{y^{b+1}(y-1)}dy-T,\quad T\to\infty,$$

with

$$\epsilon=\tfrac{1}{4}x^2e^{-2T},\quad K=\tfrac{1}{2}[1+(1+x^2)^{\frac{1}{2}}] \tag{C.2}$$

or

$$W_\infty'(b;x)=\frac{1}{b}(1-K^{-b})-T+\frac{1}{2}\int_{1+\epsilon/2}^{K}\frac{dy}{y^{b+1}(y-1)}. \tag{C.3}$$

Here, in the last integral, $y^{-(b+1)}$ can be expanded in power series of $y-1$, and thus the last integral becomes

$$\frac{1}{2}\left[\log(y-1)\Big|_{1+\epsilon}^{K}\right.$$
$$\left.+\sum_{n=1}^{\infty}(-)^n\frac{\Gamma(b+1+n)}{\Gamma(b+1)n!n}(K-1)^n\right]. \quad \text{(C.4)}$$

By the substitution of ϵ of Eq. (C.2), Eq. (C.3) finally becomes

$$W_\infty'(b;x)=\frac{1}{b}(1-K^{-b})-\frac{1}{2}\log K$$
$$+\sum_{n=1}^{\infty}\frac{(-)^n\Gamma(b+1+n)}{2\Gamma(b+1)n!n}(K-1)^n. \quad \text{(C.5)}$$

In order to get the asymptotic form for $K\gg1$, it is convenient to use Barnes' representation for the last series in Eq. (C.5): On the condition of $b+1>0$,

$$\sum_{n=1}^{\infty}=\frac{-1}{2\pi i}\int_{\epsilon-i\infty}^{\epsilon+i\infty}\frac{\Gamma(b+1+s)\Gamma(1-s)}{2\Gamma(b+1)s^2}(K-1)^s ds, \quad \text{(C.6)}$$
$$|\arg(K-1)|<\pi, \quad 1>\epsilon>0, \quad b+1>0,$$

which, taking the residues of $\Gamma(b+1+s)$ and that at $s=0$, gives the power series of $(K-1)^{-1}$:

$$\sum_{n=1}^{\infty}=-\frac{1}{2}[\log(K-1)+\Gamma'(b+1)-\Gamma'(1)]$$
$$+\sum_{n=0}^{\infty}\frac{(-)^n\Gamma(b+2+n)(K-1)^{-(n+b+1)}}{2\Gamma(b+1)(n+b+1)^2 n!}, \quad \text{(C.7)}$$
$$\Gamma'(z)=(\partial/\partial z)\Gamma(z), \quad |K-1|>1, \quad |\arg(K-1)|<\pi,$$

which is also valid in the range of $b+1<0$ by the theory of analytical continuation. Thus the asymptotic forms of Eqs. (52) and (53) are obtained.

In the limit case of $b\rightarrow\infty$ and $x^2\rightarrow0$ with a finite value of bx^2, it follows that $K-1\rightarrow\frac{1}{4}x^2$, and Eq. (C.5) becomes

$$W_\infty'(b;x)\Big|_{\substack{b\to\infty\\x\to0}}=\sum_{n=1}^{\infty}\frac{(-)^n}{2n!n}[b(K-1)]^n$$
$$=-\frac{1}{2}\int_0^{\frac{1}{4}bx^2}(1-e^{-t})\frac{dt}{t} \quad \text{(C.8)}$$
$$\simeq-bx^2/8, \quad bx^2\ll1,$$

which, by the same method as in Eq. (C.7), gives the asymptotic form

$$W_\infty'(b;x)\Big|_{\substack{b\to\infty\\x\to0}}\sim-\log[(b)^{\frac{1}{2}}x/2]+\tfrac{1}{2}\Gamma'(1),$$
$$bx^2\gg1. \quad \text{(C.9)}$$

APPENDIX D

From Eq. (70), $e^{-bW(x)}\sim e^{b\log x/2}$ tends to zero as $x\rightarrow\infty$ ($b<0$). Hence, by the use of Eq. (72),

$$e^{-bW(x)}W_\infty'(b;x)\sim e^{-bW(x)}\int_1^x e^{bW(y)}\frac{dy}{y}, \quad \text{(D.1)}$$

which gives, by the change of variable from y to W,

$$e^{-bW(x)}\int_{W(1)}^{W(x)}e^{bW}\left(\frac{d}{dW}\log y\right)dW,$$

which gives by partial integration

$$e^{-bW(x)}\left[\frac{1}{b}e^{bW}\frac{d}{dW}\log y\Big|_{W(1)}^{W(x)}-\frac{1}{b^2}e^{bW}\left(\frac{d}{dW}\right)^2\log y\Big|_{W(1)}^{W(x)}\right.$$
$$+\cdots+\frac{(-)^n}{b^{n-1}}e^{bW}\left(\frac{d}{dW}\right)^{n-1}\log y\Big|_{W(1)}^{W(x)}$$
$$\left.-\frac{(-)^n}{b^{n-1}}\int e^{bW}\left(\frac{d}{dW}\right)^n\log y\,dW\Big|_{W(1)}^{W(x)}\right], \quad \text{(D.2)}$$

which tends to $-1/b$ for $x\gg1$, since $W\sim-\log y/2$ or $\log y\sim-W+\log2$ for $y\gg1$ and therefore $(d/dW)(\log y)=-1+0(W^{-1})$. Hence,

$$W_\infty'(b;x)\sim-\frac{1}{b}e^{bW(x)}\simeq-\frac{1}{b}\left(\frac{x}{2}\right)^{-b}, \quad x\gg1, \quad b<0, \quad \text{(D.3)}$$

which is proved quite generally irrespective of the distribution $w(a)$, and of course agrees with Eq. (53). Thus, the first term in the exponent of Eq. (28) becomes ν'/ν as $\lambda a_0\rightarrow\infty$, and can be neglected as compared with the second term.

JOURNAL OF APPLIED PHYSICS VOLUME 32, NUMBER 7 JULY, 1961

Polygonization in Bent Zinc Crystals

P. P. SINHA AND PAUL A. BECK
Department of Mining and Metallurgical Engineering, University of Illinois, Urbana, Illinois

(Received November 17, 1960)

High-purity zinc crystals were grown from the melt by the soft mold technique, and bent in such a way that $[0\bar{1}10]$ was parallel to the bending axis and the $[21\bar{1}0]$ slip direction enclosed approximately 45° with the bending radius. A dislocation etching technique was developed, which reveals the edge dislocations introduced on bending, without the necessity of decoration. It was found that crystals bent either at room temperature or at liquid nitrogen temperature had approximately two-thirds of the edge dislocations arranged in low-angle tilt boundary segments. The fact that no observable change occurred in the dislocation structure on annealing up to 225°C for 5000 min suggests that the observed low-angle boundaries were formed directly on bending rather than by a thermally activated polygonization process, which might have been thought to take place at room temperature in the interval between bending and etching.

EARLIER results obtained with zinc crystals[1] by means of the Lambot x-ray technique[2] indicated that during plastic bending at room temperature, low-angle boundaries are formed, which are similar to those known to result from the thermally activated rearrangement of individual dislocations on annealing of bent crystals, i.e., from polygonization, in the original sense of this term.[3] The conclusion was reached[1] that an edge dislocation gliding above or below an immobile parallel edge dislocation of the same sign, located on a nearby slip plane, may "stick on" by virtue of the interaction between the stress fields of the two dislocations. As other parallel dislocations of the same sign are successively added in the same way in the course of further slip, dislocation walls may be formed essentially without dislocation climb, or other thermally activated process. Consequently, the formation of low-angle boundaries by this essentially athermal mechanism may be designated as "mechanical polygonization," to distinguish it from polygonization in the usual sense of the term,[3] which may now be designated as "thermal polygonization."

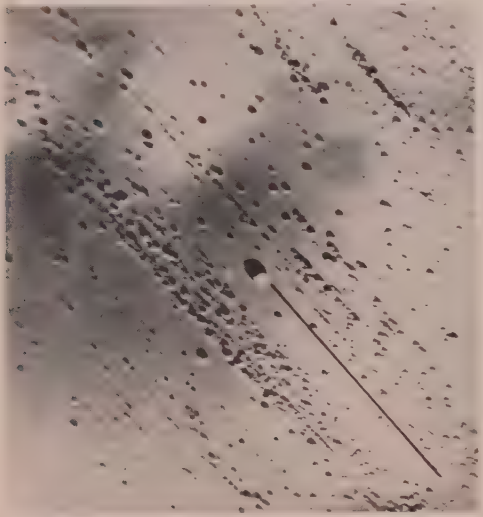

FIG. 1. (0110) face of a zinc crystal as grown, polished, and etched. Etch pits at dislocations. Line shows [2110] direction. Oblique illumination. 375×.

In a study of polygonization in bent zinc crystals by optical microscopy, Gilman[4] found no evidence for the formation of low-angle boundaries on bending, without annealing. By means of dislocation etching, Dunn and Hibbard showed[5] that in bent silicon-iron crystals the dislocations are arranged along slip planes, and that they rearrange themselves into low-angle boundaries only on annealing, by the classical "thermal polygonization" process. Merlini noted the discrepancy between

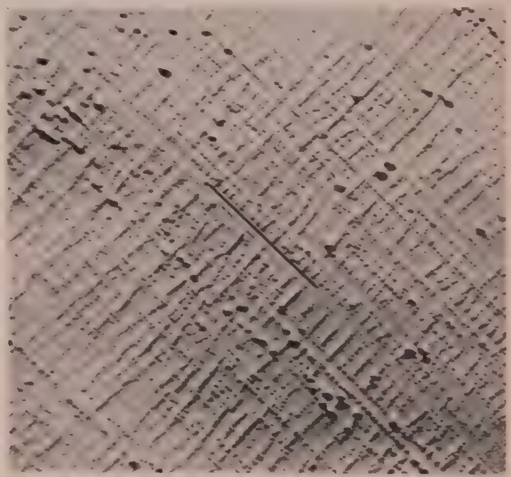

FIG. 2. (0110) face of zinc crystal bent to 2 cm radius at room temperature, polished, and etched. Etch pits at dislocations. Line shows $[21\bar{1}0]$ direction, approximately perpendicular to low-angle boundary segments. 750×.

---

[1] C. T. Wei and Paul A. Beck, J. Appl. Phys. **27**, 1508 (1956).

[2] H. Lambot, L. Vassamillet, and J. Dejace, Acta Met. **1**, 711 (1953).

[3] E. Orowan, Communication to the Congrès de la Société Francaise de la Metallurgie, October, 1947; R. W. Cahn; J. Inst. Metals **76**, 121 (1949).

[4] J. J. Gilman, Acta Met. **3**, 277 (1955); Trans. Am. Inst. Elec. Engrs. **206**, 998 (1956).

[5] C. G. Dunn and W. R. Hibbard, Jr., Acta Met. **3**, 409 (1955).

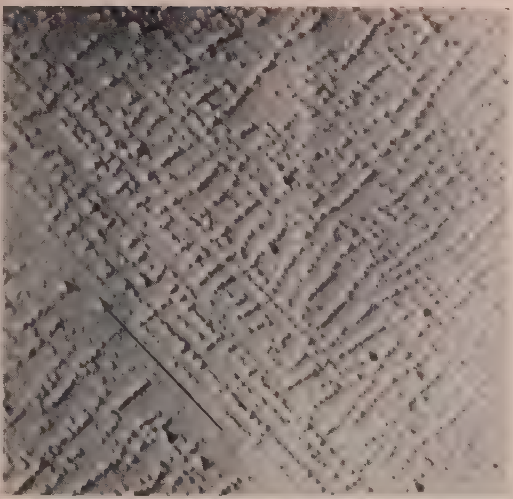

FIG. 3. $(0\bar{1}10)$ face of a zinc crystal bent to 2-cm radius at 78°K. Line shows $[21\bar{1}0]$ direction, approximately perpendicular to low-angle boundary segments. 750×.

the results of the optical and the x-ray investigations and, on the basis of an x-ray study,[6] he concluded that the striations observed in the Lambot patterns of bent crystals may result not from subboundary formation during plastic bending, but from variations on a microscopic scale of the reflecting power for x-rays (extinction) of the crystal.[7]

In order to test whether or not in bent zinc crystals the "mechanical polygonization" mechanism may nevertheless play a role in determining the dislocation arrangement, the following investigation was carried out, using a dislocation etching method.

EXPERIMENTAL PROCEDURE

Plate-shaped crystals of zinc of 99.999% purity were grown by solidification from the melt, using the soft mold technique.[8] The crystals were cut into plate-like specimens approximately 0.075 in. thick, $\frac{1}{4}$ in. wide, and 1 in. long by means of an acid saw. The specimens were oriented so that their length direction bisected [0001] and $[21\bar{1}0]$, while $[0\bar{1}10]$ was parallel to the face of the plate, and they were bent around a mandrel so that $[0\bar{1}10]$ was parallel to the bending axis. Microscopic observations were made on a face of the specimen approximately perpendicular to the $[0\bar{1}10]$ bending axis.

The specimens were polished in a solution having the following composition:

32 g of Cr_2O_3,
4 g of Na_2SO_4, 10 H_2O,
2 g of $Cu(NO_3)_2$,
100 cc of deionized water.

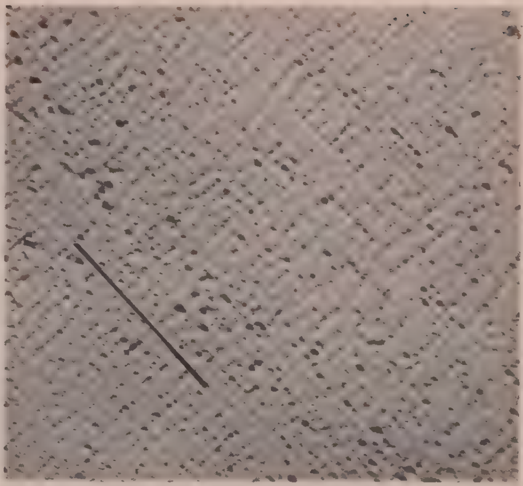

FIG. 4. $(0\bar{1}10)$ face of a zinc crystal bent to 2-cm radius at room temperature and annealed 6000 min at 100°C. Same area as in Fig. 2. Line shows $[21\bar{1}0]$ direction, approximately perpendicular to low-angle boundary segments. 750×.

Polishing was carried out by immersion for one minute at room temperature, followed by rinsing in deionized water. The following etchant was used since it revealed undecorated dislocations as etch pits:

4 cc concentrated HNO_3,
100 cc deionized water.

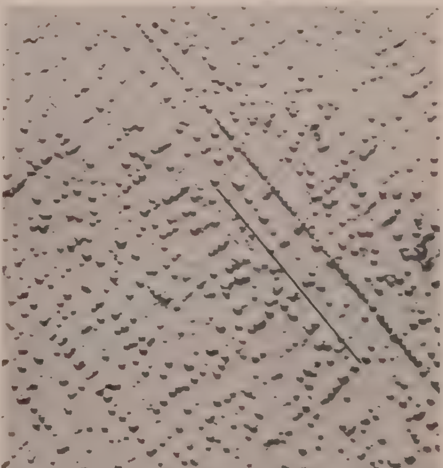

FIG. 5. $(\bar{1}010)$ face of a zinc crystal bent to 2-cm radius at room temperature and annealed 5000 min at 225°C. Line shows $[21\bar{1}0]$ direction, approximately perpendicular to low-angle boundary segment. 750×.

---

[6] A. Merlini and A. Guinier, Bull. soc. franç. mineral. et crist. **80**, 147, 261 (1957).
[7] A. Merlini, Acta Met. **6**, 19 (1958).
[8] T. S. Noggle, Rev. Sci. Instr. **24**, 184 (1953).

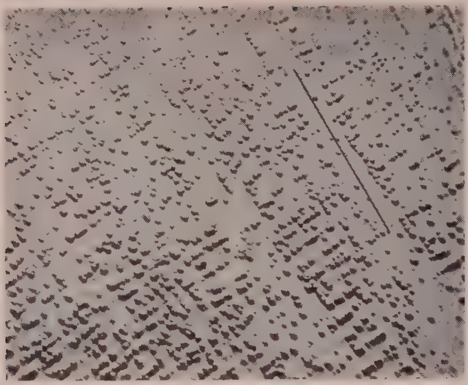

FIG. 6. (0$\bar{1}$10) face of a zinc crystal bent to 2-cm radius at room temperature and annealed 1000 min at 245°C. Line shows [21$\bar{1}$0] direction, approximately perpendicular to low-angle boundary segments. 375×.

The specimens were etched for 15 sec at room temperature, then rinsed in water and finally in methyl alcohol, and then dried in a stream of air. The time of etching was found to be very critical. An etching period less than 15 sec does not reveal all dislocations. On etching longer than 15 sec, the pits become larger and they may overlap one another.

The specimens were bent to 2-, 5-, or 9-cm radius of curvature by wrapping them around appropriate mandrels at room temperature. One specimen was bent to 2-cm radius at liquid nitrogen temperature. In addition to the dislocation etching method, the structure of this crystal was also examined by using the Lambot x-ray diffraction method, in order to compare the two methods.

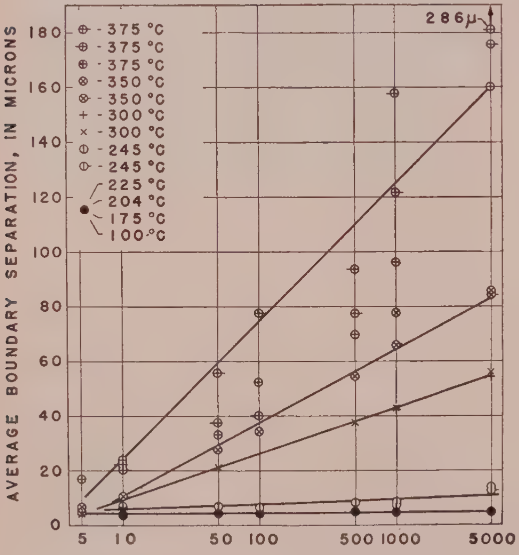

FIG. 7. Average boundary separation in bent zinc crystals after various annealing treatments.

At 100° and 204°C, the specimens were annealed in boiling deionized water and benzyl alcohol, respectively, in a flask fitted with a reflux condenser. Annealing at 175°, 225°, and 245°C was carried out in a silicone oil bath (Down Corning Fluid No. 702). At 300°, 350°, and 375°C, the specimens were annealed in a muffle furnace with a temperature fluctuation of not more than ±2°C. During annealing, the bent specimens were supported by means of an aluminum block having the same radius of curvature as the bent specimen in order to prevent the latter from deforming at elevated temperatures under its own weight.

The average spacing of the polygonized boundaries was measured by counting at a magnification of 375× the number of boundaries intersected by a perpendicular line of known length. At least 50 boundaries were counted after each annealing treatment.

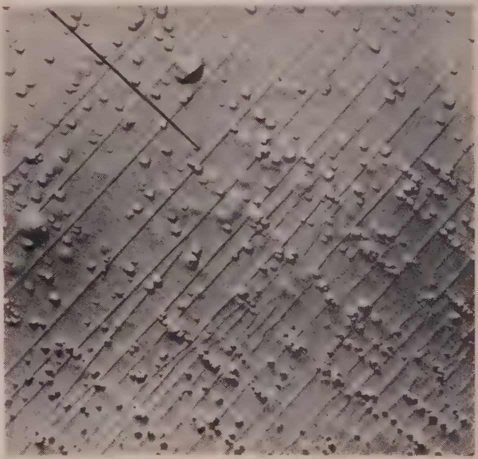

FIG. 8. Same specimen as in Fig. 6, but annealed 5000 min at 245°C. 375×.

EXPERIMENTAL RESULTS

A crystal, which was not bent, showed on etching the structure seen in Fig. 1. The dislocation etch pits were lined up parallel to the basal plane; their average density was 3.5×10^6/cm^2. The typical dislocation arrangement observed in bent but not annealed zinc crystals is shown in Fig. 2. The dislocation density was approximately 2.6×10^7/cm^2. Approximately one-third of the dislocations were aligned along slip planes, and most of the other two-thirds formed low-angle boundary segments approximately perpendicular to the sli planes. These boundary segments were not connected into a continuous interface system and, hence, did no enclose subgrains (Figs. 2 and 3). The structure wa similar to that observed in silicon-iron crystals afte partial thermal polygonization.[5]

The average boundary separation at the oute cylindrical surface of a crystal bent to 2-cm radius a liquid nitrogen temperature was calculated fro measurements made at the $(0\bar{1}10)$ face using dislocation etching. The resulting value of $7.5\,\mu$ agreed within a factor of 2.5 with that $(17.7\,\mu)$ determined for the same specimen by means of the Lambot x-ray technique in the manner previously described.[1] The difference undoubtedly arose from the fact that, at these small boundary separations, the resolution of the dislocation etching method is better than that of the x-ray diffraction method.

Figure 4 shows the dislocation arrangement in a specimen bent to 2-cm radius at room temperature and annealed for 600 min at 100°C. The area shown in this micrograph corresponds to that in Fig. 2. The boundary segments remained disconnected even after annealing for 5000 min at 225°C, or for 1000 min at 245°C (Figs. 5 and 6). No increase in average boundary separation took place with increasing annealing time up to 225°C within the experimental accuracy. But a slight increase, which is probably real, was noted between 1000 min and 5000 min at 245°C. Since the average distance between adjacent subboundaries did not change on annealing for 5000 min at 225°C (Fig. 7), it is safe to conclude that no thermal polygonization took place at room temperature, even during a period of many days. The fact that dislocation climb cannot play a significant role in the formation of subboundary segments during plastic bending is further strongly supported by the microscopically observed uniformity of the separation of dislocations in these wall segments, Figs. 2 and 3. As pointed out by Friedel (Les Dislocations, 1956), the stresses acting on dislocations closest to the edge of a wall segment are different from those on dislocations further away; as a result, the separation of dislocations increases near the edge, if climb is possible. This configuration has been in effect observed in the present work, but only after annealing for 5000 min at 245°C. Consequently, the low-angle boundaries found in the specimens immediately after bending at room temperature (Fig. 2) or at liquid nitrogen temperature (Fig. 3) must have formed *during* the plastic deformation, most likely by the postulated mechanical polygonization mechanism not involving climb.

Fig. 9. $(0\bar{1}10)$ face of a zinc crystal bent to 2-cm radius at room temperature and annealed 50 min at 300°C. Line shows $[21\bar{1}0]$ direction, approximately perpendicular to tilt boundaries. 375×.

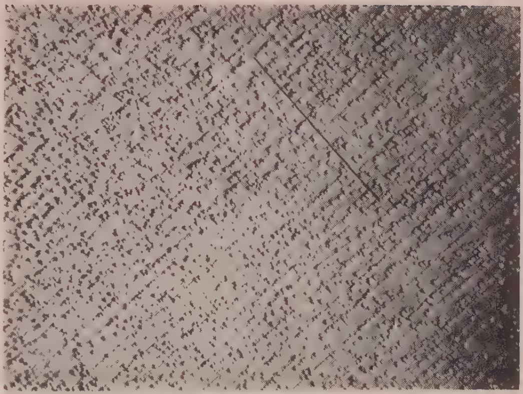

Fig. 10. $(0\bar{1}10)$ face of a zinc crystal bent to 2-cm radius at room temperature and annealed 10 min at 350°C. Line shows $[21\bar{1}0]$ direction, approximately perpendicular to tilt boundaries. 375×.

Thermal polygonization during annealing of the bent crystals resulted in the formation of a continuous low-angle boundary network. Annealing treatments which were found to accomplish this were 5000 min at 245°C (Fig. 8), 50 min at 300°C (Fig. 9), 10 min at 350°C (Fig. 10), or 5 min at 375° (Fig. 11). Further annealing

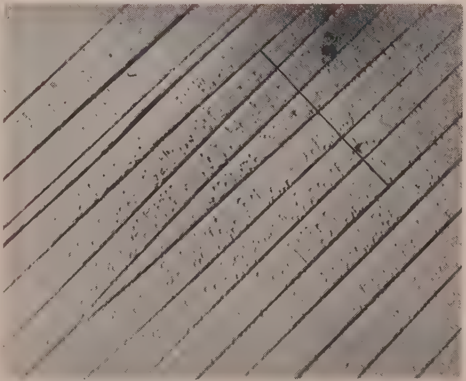

Fig. 11. $(0\bar{1}10)$ face of zinc crystal bent to 2-cm radius at room temperature and then annealed 5 min at 375°C. Line shows $[21\bar{1}0]$ direction, approximately perpendicular to tilt boundaries. 375×.

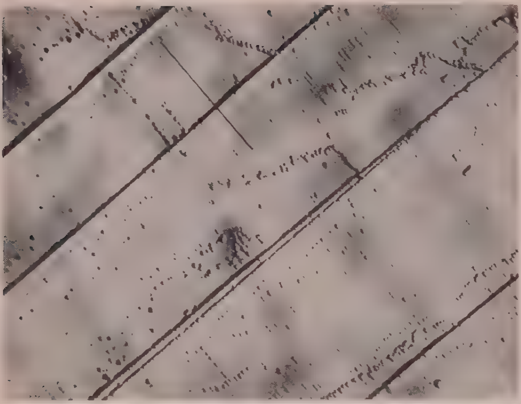

FIG. 12. Same specimen as in Fig. 10, but annealed 500 min at 350°C. 375×.

at each of these temperatures brought about subgrain growth by the usual mechanism of *Y*-junction migration (Figs. 10, 12, and 13). However, even after long periods at the highest annealing temperatures, there were still many dislocations within the subgrains. Some of these even remained aligned along the former slip planes (Figs. 8, 12, and 13). It is possible that these dislocations became immobilized by decoration with impurity atoms.

The average boundary separation measured after various annealing treatments is given in Fig. 7. The data points for 375°C do not follow a regular pattern. In order to test whether or not these apparent irregularities were reproducible, two repeat runs were made at 375°C. These results are also shown in Fig. 7. It is clear that the reproducibility of the subboundary separation data for 375°C is not good and that the irregularities observed in duplicate runs did not coincide. At lower temperatures, the reproducibility was fairly good.

One cannot meaningfully assign an activation energy to the process of subgrain growth since the slopes of the subgrain size vs log time lines in Fig. 7 corresponding to different temperatures are not the same. A rough estimate of the activation energy for thermal polygonization can be made from the observed annealing periods necessary for the formation of a continuous subboundary network at various annealing temperatures. This gives a range of values between 23 and 47 kcal/g atom.

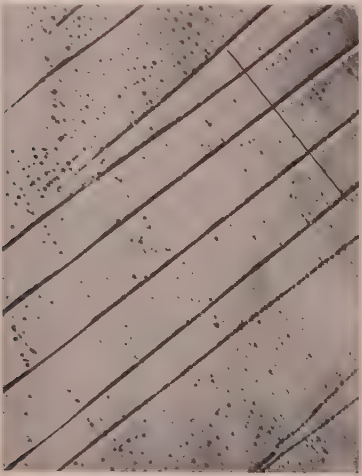

FIG. 13. Same specimen as in Fig. 10, but annealed 50 min at 350°C. 375×.

Mechanical polygonization entirely analogous to that observed in crystals bent to a radius of 2 cm was also observed in crystals bent to 5- and 9-cm radii. The average separation of the subboundaries was approximately 6 μ for 5-cm radius and 7 μ for 9-cm radius.

DISCUSSION

The present work verifies the conclusion, previously arrived at[1] on the basis of x-ray diffraction results, that low-angle boundaries are formed on bending in suitably oriented zinc crystals. This mechanical polygonization mechanism, which does not depend on thermal activation, was not noted by Gilman in his work with zinc, using dislocation etching,[4] because of the unavailability at that time of an effective etching reagent capable of showing undecorated dislocations.

Mechanical polygonization phenomena were also observed earlier by means of the Lambot technique in copper crystals of certain orientations bent at room temperature and not annealed.[9] For these crystals, thermal polygonization was found to be very slow even at 800°C. The occurrence of mechanical polygonization in copper crystals bent at room temperature was recently confirmed by means of dislocation etching.[10] Mechanical polygonization is thus seen to take place in metals of widely varying stacking fault energies, and correspondingly different from each other in regard to the temperatures they require for thermal polygonization. Although mechanical polygonization appears to be essentially absent in silicon-iron crystals bent at room temperature,[5] subgrain formation in iron on severe plastic deformation at room temperature has been well substantiated.[11,12] It appears very likely that the formation of subgrains on plastic deformation of varying severity is a process fundamentally closely related to mechanical polygonization in bent single crystals.

ACKNOWLEDGMENTS

The authors wish to express their appreciation to Professor B. G. Ricketts for helpful advice and to Harold Korte for assistance with the experiments. The high-purity zinc was furnished by the New Jersey Zinc Company, through the courtesy of Dr. A. E. Anderson. This work was supported by the U. S. Atomic Energy Commission, under contract.

---

[9] C. T. Wei, M. N. Parthasarathi, and P. A. Beck, J. Appl. Phys. **28**, 874 (1957).

[10] J. D. Livingston, J. Appl. Phys. **31**, 1071 (1960).

[11] P. Gay and A. Kelly, Acta Cryst. **6**, 165 (1953).

[12] Unpublished results obtained by B. G. Ricketts with transmission electron microscopy.

JOURNAL OF APPLIED PHYSICS VOLUME 32, NUMBER 7 JULY, 1961

Surface Layers on Barium Titanate Single Crystals above the Curie Point

H. Schlosser* and M. E. Drougard
IBM Research Center, Yorktown Heights, New York

(Received April 8, 1960; and in final form, March 13, 1961)

Dielectric dispersion measurements have been carried out on barium titanate single crystals of different thicknesses at temperatures above the Curie point ranging up to 180°C. In the high-frequency range of the measurements (100 kc), the measured dielectric constant of thin crystals is consistently much smaller than that of thick samples. The effect is ascribed to the presence of a layer of low dielectric constant on the surface of the crystals, with a capacitance of the order of 0.5 μf/cm^2 in the temperature range explored. The relaxation time of this surface layer is found to be at least 10^{-4} sec at 120°C on crystals which have not been "aged" recently.

I. INTRODUCTION

THE dependence of the switching time of ferroelectric barium titanate on the crystal thickness was first observed experimentally by Merz,[1] who also suggested that it might be due to the presence of an anomalous surface layer. The effect of such a layer on switching has been analyzed recently,[2] with the conclusion that Merz' experimental results can be predicted if we assume the existence near each electrode of a surface layer having a capacitance of 10 μf/cm^2. This conclusion applies either to a completely anomalous layer (having no spontaneous polarization) or to a barrier layer in which the space-charge fields are strong enough to prevent reversal of the spontaneous polarization. The conductivity of the layer has only to be smaller than some reasonable value (see Discussion).

Prior to the work quoted in the preceding paragraph, Känzig[3] found that a surface layer of tetragonal symmetry and with a thickness of about 100 A exists on small particles of BaTiO$_3$ far above the Curie point. He suggested later[4] that the tetragonal symmetry of this layer could be caused by strong space-charge fields. Such a layer would have a practically irreversible polarization in the ferroelectric phase, since the space-charge fields would be of the order of 10^6 v/cm. More recently, Chynoweth[5] has found evidence for the presence of a space-charge surface layer above the Curie point.

As mentioned above, Känzig's observations were made on small particles, and his results may not be valid for single crystals. Chynoweth's work[5] does not tell us anything about the barrier capacitance, and it was thought desirable to obtain more information about the characteristics of surface layers on single crystals. We have attempted to measure these characteristics by studying the frequency dependence and the thickness dependence of the complex dielectric constant of single crystals.

To interpret the experimental results, we shall compare them with the behavior of the network shown in Fig. 1, consisting of a capacitance C_l shunted by a resistance R_l (representing the surface layer) in series with a capacitance C_b shunted by a resistance R_b. The analysis of the frequency dependence of the complex admittance of this network is sketched in the Appendix, in terms of an equivalent capacitance C_p shunted by a resistance R_p. Similarly, the results of the measurements are expressed in terms of an equivalent parallel combination of a resistance and a capacitance. The most obvious feature of this network (and perhaps the most interesting) is that the equivalent capacitance C_p decreases with frequency, having a high-frequency limit which is the capacitance of the series combination of C_b and C_l.

II. EXPERIMENTS

The investigations have been carried out only above the Curie point because at such temperatures the capacitance of the bulk crystals becomes very high, so that any capacitance in series with it should be most easily detectable. (The range of temperatures just below 5°C would also be very favorable for the same reason.[6]) The frequency range was limited from 50 cps to 100 kc for convenience, with only a few measurements being taken up to 1 Mc. The measurements were taken on a 716C General Radio capacitance bridge, at 120°, 150°, and 180°C.

The thickness of the samples ranged from a few tenths of a millimeter down to about one hundredth of a millimeter. Two series of samples were investigated. The first series had undergone a phosphoric acid etch to smooth the surface (15 min to 1 hr at about 140°C), and also a brief hydrochloric acid etch; the other had not been submitted to any etching. A total of 18 crystals

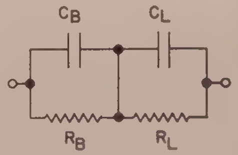

Fig. 1. The equivalent circuit for a crystal with two identical surface layers (one near each electrode).

---

[*] Present address: General Telephone and Electronics Laboratories, Inc. Work performed at IBM as a summer employee.

[1] W. J. Merz, J. Appl. Phys. **27**, 938 (1956).

[2] M. E. Drougard and R. W. Landauer, J. Appl. Phys. **30**, 1663–1668 (1959).

[3] M. Anliker, H. R. Brugger, and W. Känzig, Helv. Phys. Acta **27**, 99 (1954).

[4] W. Känzig, Phys. Rev. **98**, 549 (1955).

[5] A. G. Chynoweth, Phys. Rev. **102**, 705 (1956).

[6] W. J. Merz, Phys. Rev. **75**, 687 (1949).

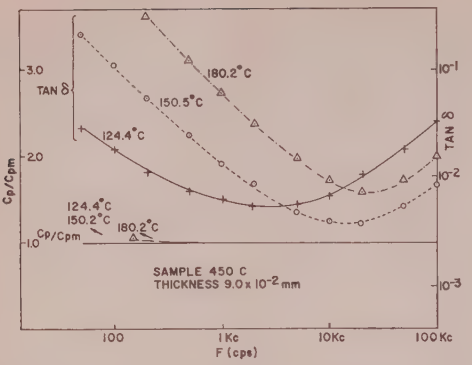

FIG. 2. The equivalent parallel capacitance and loss factor of a thick sample as a function of frequency at different temperatures (C_{pm} is the value of C_p at 100 kc).

were studied. Nine samples had undergone the chemical treatment just described, and most of those had been "aged" (that is, a 60-cps voltage largely sufficient to reverse the polarization has been applied to them) previously though not recently. One of these etched samples was investigated before aging and shortly after aging. The other nine samples were simply rinsed in distilled water before evaporation and were investigated prior to any aging. The electrodes in all cases were of evaporated gold. The large faces of the samples were entirely covered by the electrodes; their area was between 0.5 mm² and 1 mm².

We have also measured the dc conductivity of our samples. The thinnest crystals exhibit a slight nonlinearity in the range of voltages used in the ac measurements (approx 1 v), but in all cases the dc conductivity in the range 120°–180°C may be described within a factor of 2 by the equation

$$\sigma = 5.0 \exp(-\Delta E/kT) \text{ mho cm}^{-1}, \tag{1}$$

with $\Delta E = 0.71$ ev. This is the same result that Nishioka *et al.*[7] obtained on samples containing about 2% added iron. (No iron, however, was intentionally added to our crystals.)

III. RESULTS

In all cases but one, the measured equivalent parallel capacitance at 100 kc was found to represent a fairly well-defined high-frequency limit. Accordingly, this value C_{pm} was taken as a reference; the plots in Figs. 2 and 3 show the frequency dependence of C_p/C_{pm}. Also plotted in Figs. 2 and 3 in the loss factor $D = (R_p\omega C_p)^{-1}$.

Figures 2 and 3 relate to two crystals which exhibited the most typical and extreme behaviors. The crystal of Fig. 2 is characterized by a definite minimum in the loss factor and no visible relaxation of the capacitance. The measurements were extended to 1 Mc for a few samples of this type, and it was found that the loss factor kept increasing continuously. The sample of Fig. 3 is characterized by a minimum followed by a maximum in the plot of loss factor vs frequency with a relaxation of the equivalent parallel capacitance at a slightly higher frequency than the maximum of the loss factor. These frequencies increase rapidly with increasing temperature.

About one-half the crystals investigated yielded plots very similar to either Fig. 2 or Fig. 3. The other crystals exhibited the same general features, but the minima and maxima were less clear.

It is worth noting that no crystal thicker than 0.03 mm was found to exhibit the features of Fig. 3 (hump in loss factor, with relaxation of C_p). Among the thinnest crystals (thinner than 3×10^{-2} mm), about one-third were similar to that of Fig. 2 and two-thirds to that of Fig. 3. This remark holds for etched or raw crystals.

If the network of Fig. 1 is representative of the real crystals, we should expect the high-frequency limit of the dielectric constant ϵ_{pm} to be thickness dependent. More precisely, if t is the thickness of the crystal, δt the thickness of the layer, and ϵ_b and ϵ_l the dielectric constant of the bulk and layer respectively, we have, under the assumption that δt be much smaller than t,

$$\epsilon_{pm}^{-1} = (\epsilon_b)^{-1} + (\delta t/\epsilon_l) \times (t)^{-1}. \tag{2}$$

We have plotted in Fig. 4 the inverse of the high-frequency dielectric constant against the inverse thickness for the different temperatures at which the data were taken. Since all measurements could not be made at exactly the same temperature, we have used the relation

$$[\epsilon_{pm}(T_1)]^{-1} = [\epsilon_{pm}(T_2)]^{-1} + (A/2\pi)(T_1 - T_2), \tag{3}$$

where A is the coefficient of the p^2 term in Devonshire's expansion of the free energy. We have used for A an average of values determined by previous workers[8] and

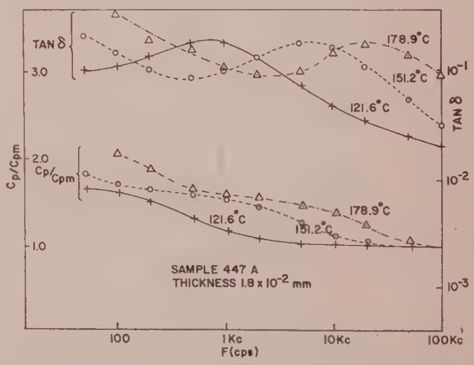

FIG. 3. The equivalent parallel capacitance and loss factor of a thin sample as a function of frequency at different temperatures (C_{pm} is the value of C_p at 100 kc).

---

[7] A. Nishioka, K. Sekikawa, and M. Owaki, J. Phys. Soc. Japan **11**, 180 (1956).

[8] W. J. Merz, Phys. Rev. **91**, 513 (1953); M. E. Drougard, R. Landauer, and D. R. Young, *ibid.* **98**, 1010 (1955).

avoided the use of the coefficient T_0, which seems to be much more variable (see, however, the remark at the end of Sec. IV). It is seen that there is much more scatter in the points corresponding to etched crystals. This scatter (which bears no relation to the exact duration or temperature of the etch) is the only qualitative difference we have found between the etched and raw samples.

Since the dielectric constant ϵ_{pm} at 100 kc is always smaller than the value extrapolated to infinite thickness, and since the corresponding difference increases with decreasing thickness, we consider that we have here a proof of the existence of a surface layer having a dielectric constant lower than that of the bulk. There is nothing in our experiments that allows us to make any statement as to the magnitude of this dielectric constant nor as to the layer thickness. All we can do is to compute from our plots the capacitance of the layer per unit area. We find that, at 120°C, the average value of C_l corresponds to about 0.7 $\mu f \times cm^2$. The temperature dependence is very weak, the value of C_l at 150°C being about 1.2 times its value at 120°C.

Before discussing the behavior of the loss factor, we shall need some results which are derived in the Appendix concerning the network shown in Fig. 1. The values of C_l quoted above are such that, except for five crystals at 120°C, we have $C_l > C_b$. Under those conditions, we may find maximum in the plot of log tanδ versus logω if the inverse time constants ω_l and ω_b are sufficiently different. If $\omega_l < \omega_b$, and if there exists a maximum in the loss factor plot, this maximum will occur for an angular frequency which will always be smaller than ω_b. Now, from our dc measurements, summarized by Eq. (1), we can compute the relaxation frequencies of the bulk to be 3, 5, and 200 sec^{-1} at temperatures 120°, 150°, and 180°C, respectively. Hence, since the lowest frequency in our measurements is 200 cps, we can hardly expect to be able to detect the possible existence of such a maximum. If, on the other hand, we have $\omega_l > \omega_b$, there may exist a maximum, and if so, this maximum occurs at an angular frequency which is within a factor of about 2 below ω_l.

In the cases where $C_l < C_b$, the conclusions quoted above remain, provided we exchange the subscripts l and b. This would tend to make it more difficult to observe the relaxation of the surface layer since the corresponding maxima could be displaced towards lower frequencies by a factor of $(C_b/C_l)^{\frac{1}{2}}$ (actually at most a factor of 2 in our experiments).

We now examine the actual behavior of tanδ. In Fig. 2, the magnitude of the loss factor at low frequencies is in good agreement with the bulk relaxation frequencies just quoted. At high frequencies, if the crystal were correctly represented by the network shown in Fig. 1, we would predict a maximum of loss factor somewhere beyond 100 kc. Measurements up to 1 Mc for two such samples show, however, that the loss factor keeps increasing continuously. In addition, the dielectric constant ϵ_{pm} at 100 kc is sufficiently lower than that of thicker crystals that we can be sure it is above the relaxation frequency of the surface layer. The reason for the increase of tanδ is certainly the finite resistance of the silver paint dots which hold the leads to the electrodes. This resistance has been measured by making two contacts to the same electrode and found to be as high as 100 Ω, which agrees well with the highest loss factor found for similar crystals at 100 kc.

The network of Fig. 1 should therefore be completed by the addition of a series resistance R_c of a few tens of ohms. The presence of this resistance should have no effect on the existence of a maximum in tanδ as long as R_l is much larger than 100 Ω; that is, as long as $\omega_l \ll 10^{+6}$ (Our samples are at most 1 mm^2 in area). It would probably wash out a maximum of tanδ occurring above 100 kc, but its presence should not affect a possible relaxation of C_p.

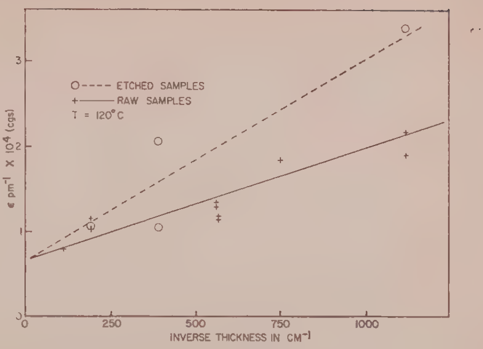

FIG. 4. The difference Δ between the inverses of the apparent and theoretical dielectric constants vs the inverse thickness at 120°C for raw and etched samples. A cluster of points near the origin, corresponding to etched samples, has been omitted.

The plots such as that shown in Fig. 3 are in very good agreement with the results obtained for the network of Fig. 1, completed by the addition of the series resistance R_c. The inflection point in the C_p plot occurs as it should at a frequency slightly higher than the maximum of tanδ. The failure of the loss factor to fall down like ω^{-1} at high frequencies is due to the resistance of the silver paint dot.

It is obvious, from the shift with temperature of the loss factor maxima in Fig. 3, that the surface layer conductivity is much more sensitive to temperature than its capacitance. The maximum relaxation frequency observed at 120°C was 1 kc, corresponding to a relaxation time of roughly 10^{-4} sec, except for the one sample mentioned before.

The case of this sample was particularly interesting, for it was the only one to exhibit a surface layer relaxation at or above 100 kc at 120°C. It was also the only sample which was investigated shortly after aging. Before aging, it had yielded plots very similar to Fig. 2,

IV. DISCUSSION

The magnitude of the surface layer capacitance found above the Curie point is smaller by at least a factor of 10 than that inferred[2] from the switching behavior at room temperature. Of course, it might be that this capacitance is larger below the Curie point, although we have found it to increase slightly with temperature. It is much more likely that the layer breaks down during switching in the presence of the strong fields involved.

We want to emphasize that our measurements do not tell us anything about the lower limit of the relaxation time of the surface layers. Since we did not go below 50 cps, all we can say is that in the majority of unaged samples (or in samples that have not been aged recently), this time constant must be at least 5×10^{-2} sec.

In the case of the crystal which was investigated shortly after aging, the relaxation time was found to be 10^{-6} sec. In view of the marked temperature dependence of the layer relaxation time, one would expect to find a much larger value at room temperature. It is interesting, however, to wonder how short the relaxation time could be without making the layer ineffective for low af switching. The switching process is still not very well understood, but we can attempt to answer the question as follows: Based on the analysis mentioned before,[2] we expect the layer to be effective as long as $lv^{-1}\tau_l^{-1}<1$, where l is the layer thickness and v the domain wall velocity. At 60 cps, the switching time may not be much larger than 10^{-3} sec if a reasonably square hysteresis loop is to be obtained. From other work on crystals with metal electrodes,[9] it can be estimated that the average domain expands in radius from 1 to at least 10 μ, indicating an average domain wall velocity of at least 1 cm/sec. If we now take for l the value of 10^{-6} cm observed by Känzig (though on small particles), we see that the relaxation time of the layer may be as small as 10^{-6} sec and still the layer will be almost completely effective in slowing down the switching process. If the density of nuclei or nucleation sites becomes very low, as in Miller's experiments,[10] such a layer may be completely effective even for very slow switching.

We have tried to detect a correlation between the conductivity and capacitance of the surface layer, but without any success. It seems, however, that there exists a correlation between the layer conductivity and the thickness of the crystal. For instance, the crystal of Fig. 2 is characterized by the parameters (see Appendix) $c=2$, $g=4\times10^3$. If the surface layers of the two crystals of Figs. 2 and 3 were identical, the ratio g/c would be the same. Now, for the case of Fig. 3, $c=10$, and we would have $g=2\times10^4$, which largely satisfies the condition (A.8) (sufficient in this case). Yet, no sample thicker than 0.03 mm exhibits any surface layer relaxation in the frequency range involved. Perhaps this dependence of layer characteristics upon thickness is due to the difference in growth conditions, which difference is evidenced by the fact that the same crucible may yield crystals of very different thicknesses. The influence of exact growth conditions may also explain that, out of three crystals coming from the same butterfly, one behaved like the sample of Fig. 3 while the two others, though prepared in exactly the same conditions, yielded plots similar to Fig. 2. It may also well be that the two surface layers on opposite sides of the same crystal do not have identical characteristics.

We would like to mention here that the deviations from a straight line which are observed on many Curie-Weiss plots may be explained by the presence and characteristics of the surface layer. Even if the measurements are taken well above the relaxation frequency of the surface layer, there may be a bending downwards due to the temperature dependence of the layer capacitance. If the measurements are taken at too low a frequency, a strong bending downwards may be observed due to the shift of the relaxation frequency of the layer with temperature. A surface layer of constant capacitance and perfectly insulating would give a straight line on a Curie-Weiss plot parallel to that obtained for an ideal crystal with no surface layer, but displaced towards low temperatures. This can be seen immediately from the following equation:

$$C^{-1}=K(T-T_0)+(C_l)^{-1}=K\{T-[T_0-(KC_l)^{-1}]\}.$$

This shift of the Curie-Weiss plot to low temperatures is probably one of the reasons why the parameter T_0 is much more poorly known than the parameter A.

ACKNOWLEDGMENTS

The authors are much indebted to Miss Marie Whitehill for her wonderful help in the preparation of the samples. They would also like to thank Dr. D. R. Young and Dr. S. Triebwasser for their encouragement and for many stimulating discussions.

APPENDIX

Using the notations of Sec. III, it is easily shown that, if we let $1/R_b=G_b$, $1/R_l=G_l$:

$$D=\frac{G_b(G_l^2+\omega^2C_l^2)+G_l(G_b^2+\omega^2C_b^2)}{\omega[C_b(G_l^2+\omega^2C_l^2)+C_l(G_b^2+\omega^2C_b^2)]}; \quad (A.1)$$

$$C_p=\frac{C_bG_l^2+C_lG_b^2+\omega^2C_bC_l(C_b+C_l)}{(G_b+G_l)^2+\omega^2(C_b+C_l)^2}. \quad (A.2)$$

We can simplify these expressions by letting

$$C_l/C_b=c, \quad G_l/G_b=g, \quad w=\omega C_b/G_b=R_bC_b\omega. \quad (A.3)$$

---

[9] A. G. Chynoweth, Phys. Rev. **110**, 1316 (1958); M. E. Drougard, J. Appl. Phys. **31**, 352–355 (1960).

[10] R. C. Miller, Phys. Rev. **111**, 736 (1958); R. C. Miller and A. Savage, *ibid.* **112**, 755 (1958).

We obtain

$$D=\frac{(g^2+g)+w^2(c^2+g)}{w[g^2+c+w^2(c^2+c)]}=\frac{c^2+g}{c^2+c}$$
$$\times\frac{w^2+(g^2+g)/(c^2+g)}{w^3+w(g^2+c)/(c^2+c)}\equiv\frac{c^2+g}{c^2+c}\times\frac{w^2+x}{w^3+yw}, \qquad \text{(A.4)}$$

where we have set $x=(g^2+g)/(c^2+g)$, $y=(g^2+c)/(c^2+c)$, and

$$C_p=C_b\frac{g^2+c+w^2(c^2+c)}{(g+1)^2+w^2(c+1)^2}. \qquad \text{(A.5)}$$

To find the maxima and minima of D, we differentiate Eq. (A.4), and obtain

$$\frac{dD}{dx}=-\frac{c^2+g}{c^2+c}\times\frac{w^4+(3x-y)w^2+xy}{w^2(y+w^2)^2},$$

so that there may exist a maximum for w_M such that

$$w_M{}^2=\tfrac{1}{2}\{y-3x+[(y-3x)^2-4xy]^{\frac{1}{2}}\}, \qquad \text{(A.6)}$$

provided that

$$(y-3x)^2-4xy\geqslant 0 \text{ and that } y>3x,$$

from which we obtain that a maximum will exist provided $y>9x$. Using the definition of xy, Eq. (A.4), this reads

$$(g^2+c)/(c^2+c)>9(g^2+g)/(c^2+g).$$

Let us first assume $C_l>C_b$; that is $c>1$. If $g=c$, we have a balanced network, with constant C_p and R_p throughout the frequency range.

If $g>c$, we may write Eq. (A.7) as

$$(c^2+g)/(c^2+c)>9(g^2+g)/(g^2+c)>9,$$

hence a necessary, though not sufficient condition (except if $g\gg 1$, in which case the condition is sufficient to a very good approximation):

$$g>8c^2+9c. \qquad \text{(A.8)}$$

From Eq. (A.6) we also have the following inequalities:

$$y>w_M{}^2>\tfrac{1}{3}y. \qquad \text{(A.9)}$$

If $g>c$, Eq. (A.8) shows that c is negligible compared to g^2, and we obtain

$$g^2/c^2>y>g^2/2c^2, \quad g/c>w_M>6^{-\frac{1}{2}}\times g/c,$$

which, in terms of angular frequencies, reads

$$\omega_l>\omega_M>6^{-\frac{1}{2}}\omega_l \qquad (\omega_l>\omega_b). \qquad \text{(A.10)}$$

Turning now to the case $g<c$, we make use again of Eq. (A.9) and of the inequalities

$$1>y>(2c)^{-1}$$

to obtain

$$\omega_b>\omega_M>(6c)^{-\frac{1}{2}}\omega_b \qquad (\omega_b>\omega_l). \qquad \text{(A.11)}$$

We note that, if in addition $g<1$, we have $y<1/c$, so that in this case

$$\omega_b c^{-\frac{1}{2}}>\omega_M>(6c)^{-\frac{1}{2}}\omega_b.$$

To treat the case where $C_l<C_b$, it is obvious from the symmetry of the network that all we have to do is to exchange the subscripts l and b.

The point of inflection of the C_p vs logω plot occurs at the point defined by

$$\frac{d^2C_p}{d(\log w)^2}=w^2\frac{dC_p}{dw}+w^2\frac{d^2C_p}{d^2w^2}=0,$$

which yields

$$w_i=(g+1)/(c+1)$$

or, in terms of angular frequencies,

$$\omega_i=(G_l+G_b)/(C_l+C_b).$$

JOURNAL OF APPLIED PHYSICS VOLUME 32, NUMBER 7 JULY, 1961

Dangling Bonds in III–V Compounds

HARRY C. GATOS
Lincoln Laboratory, Massachusetts Institute of Technology, Lexington 73, Massachusetts*

(Received March 2, 1961)

The model proposed by Gatos and Lavine [H. C. Gatos and M. C. Lavine, J. Electrochem. Soc. **107**, 427 (1960)] for the dangling bonds of III–V compounds is discussed in the context of the available experimental facts and the objection advanced by Holt [D. B. Holt, J. Appl. Phys. **31**, 2231 (1960)]. It is shown that the model as originally proposed is consistent with basic principles and experimental observations.

GATOS and Lavine[1] have proposed an atomic model for the $\{111\}$ surfaces of the III-V compounds (zinc-blende structure). These surfaces terminate either with group III atoms triply bonded to the crystal (A or $\{111\}$ surfaces) or with group V atoms triply bonded to the crystal (B or $\{\bar{1}\bar{1}\bar{1}\}$ surfaces). According to the model, the B-surface atoms have a dangling bond with two unshared electrons; to a first approximation, they retain the tetrahedral configuration of the bulk. The A-surface atoms, on the other hand, have no unbonded electrons and presumably acquire a configuration intermediate between planar and tetrehedral leading to significant surface distortion. Similar electronic configurations must be assumed for the triply bonded A atoms along an edge dislocation line consisting of a row of A atoms (α dislocation) and for the triply bonded B atoms along an edge dislocation line consisting of B atoms (β dislocation). Although certain simplifications are inherent in this model, it has been found to be consistent with experimentally observed differences between the A and B surfaces with respect to etching behavior,[1] crystal growth,[2] surface perfection,[3] and resistance to cold-work penetration.[3] The model also accounts satisfactorily for the observed differences in the chemical and electrical properties of the α and β dislocations.[1,4]

Recently, Holt[5] has raised objections to the model as applied by Gatos *et al.*[2] to crystal growth, while admitting that it is consistent with experimental observations. Holt maintains that in the III-V compounds the group V atoms contribute 5/4 electrons to each of the four tetrahedral bonds, and that the group III atoms contribute 3/4 of an electron. According to his reasoning, the dangling bond of a group V atom has on an average 5/4 and not two electrons, and the group III surface atom has a dangling bond with 3/4 electron. Thus, any perturbation of the bonds due to the termination of the crystal lattice is precluded. Holt further concludes that the presence of electron pairs in the dangling bonds of the B surfaces and the absence of electron dangling bonds at A surfaces, as proposed by Gatos and Lavine, would result in a dipole moment through the entire crystal in the $\langle 111 \rangle$ direction for a $\{111\}$-oriented wafer.

In the Gatos-Lavine model it is implicitly assumed that the probability of occurrence of electron dangling bonds at the group III surface atoms is very small. Rather, the group III surface atoms contribute one electron to each of the three bonds to underlying group V atoms. For bookkeeping purposes, a group V atom in the second layer may be considered to have contributed one electron to each of its three bonds with group III surface atoms and the remaining two valence electrons to the bond with a group III atom below.[6] This assignment is entirely consistent with Holt's statement that a group V atom contributes an average of 5/4 electrons to each of its four bonds. It is clear that in any model the bonds in the interior of the crystal must be considered equivalent. Since, for steric reasons, the bond configuration of the group III surface atoms cannot be planar, the bond moments will add up to give a net surface dipole moment. However, this moment cannot conceivably extend through the whole crystal. At the worst one can expect, for semiconductor crystals, the induction of a space charge in the surface region. Although it is not clear as to how far this surface distortion extends into the bulk, it must be limited to a depth of the order of tens of Angstrom units. Beyond this depth the crystal assumes its normal configuration.

In the case of the group V atoms of the $B\{\bar{1}\bar{1}\bar{1}\}$ surfaces it is believed that the probability for the dangling bonds to contain two electrons is much greater than the probability for containing less than two electrons. Depending upon the relative electronegativities of the bonded atoms, the moment due to the lone pair of electrons on a group V surface atom will be augmented to an extent determined by the moments of the underlying bonds. Here again, however, the influence of a net moment at the surface would not be felt very far into

---

* Operated with support from the U. S. Army, Navy, and Air Force.

[1] H. C. Gatos and M. C. Lavine, J. Electrochem. Soc. **107**, 427 (1960).

[2] H. C. Gatos, P. L. Moody, and M. C. Lavine, J. Appl. Phys. **31**, 212, 1696 (1960).

[3] E. P. Warekois, M. C. Lavine, and H. C. Gatos, J. Appl. Phys. **31**, 1302 (1960).

[4] H. C. Gatos, M. C. Finn, and M. C. Lavine, J. Appl. Phys. **32**, 1174 (1961).

[5] D. B. Holt, J. Appl. Phys. **31**, 2231 (1960).

[6] The model is also applicable to the II-VI and I-VII compounds with the zinc-blende structure. The group II and group I atoms of the $\{111\}$ surfaces have no electron-dangling bonds. Thus, the group II atoms may be considered as forming two covalent bonds and one coordinate bond with the underlying group VI atoms; similarly the group I atoms may be considered as forming one covalent bond and two coordinate bonds. The group VI (or group VII) atoms of the $\{\bar{1}\bar{1}\bar{1}\}$ surfaces have two-electron dangling bonds.

the crystal. The configurations of the two surfaces of a {111}-oriented wafer of any reasonable thickness could not conceivably exhibit a mutual interdependence.

The Gatos and Lavine model thus leads to a net moment at the *A* surfaces with the positive ends of the dipoles directed out of the crystal, and a moment at the *B* surfaces, with the negative ends directed outwards (Fig. 1). Indirect evidence for the foregoing is provided by the observation that positive ions in aqueous solution (substituted ammonium ions) appear to adsorb preferentially on the *B*{111} surfaces.[7]

While surface dipoles are of universal occurrence, Holt's particular assignment of electrons to surface atoms leads to real surface charges of $-\frac{3}{4}$ per group III atom and $+\frac{3}{4}$ per group V atom. This can be illustrated by use of a molecular analogy as follows: Allow reaction to take place between a molecule of boron trimethyl, $(CH_3)_3B$, and one of ammonia, $:NH_3$, forming the compound $(CH_3)_3B:NH_3$, in which the four boron and four nitrogen bonds are tetrahedral bonds.[8] Now sever the B:N bond so that 5/4, rather than two, electrons go with the nitrogen; the result is $[(CH_3)_3B]^{-\frac{3}{4}}$ and $(NH_3)^{+\frac{3}{4}}$, as is schematically represented in Fig. 2. The concept of resonance may be invoked, but these would be unusual structures nonetheless. The analogy with III-V surfaces is obvious. Real surface charges can certainly exist, resulting for example, from adsorption of ions and occupancy of surface traps, but the densely charged surfaces obtained on literal interpretation of Holt's remarks make his proposal untenable.

Pursuing the above molecular analogy further, we note that $(CH_3)_3B$ is a planar molecule, whereas $:NH_3$ is pyramidal with a lone pair of electrons in an approximately tetrahedral orbital.[9] (These structures have implications for the growth of III-V crystals in the ⟨111⟩ direction.[2]) In the boron-nitrogen compound molecule, however, the boron atom no longer lies in the plane of the methyl groups, but forms four tetrahedrally directed covalent bonds. It is thus apparent that the surface rearrangements (distortion) in the III-V intermetallic compounds on the basis of the Gatos-Lavine model must be far greater on the *A* than on the *B* surfaces.[10] This conclusion is entirely consistent with the fact that the crystalline perfection of *B* surfaces was found by x-ray diffraction techniques to be greater than that of *A* surfaces for the same crystal and treatment.[3] Similarly, it has been shown that the resistance of the *A* surfaces to cold work is much greater, indicating that there is a greater inherent strain in the *A* surfaces than in the *B* surfaces of a given crystal. Such pronounced differences should not be expected if the tetrahedral configurations were maintained at both the surfaces.

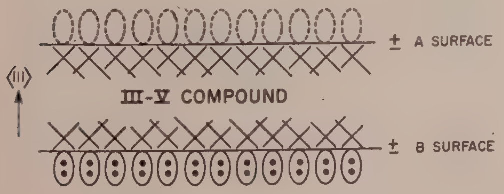

FIG. 1. Schematic representation of the dangling bonds on the *A* and *B* surfaces of III-V compounds and the associated surface dipole moments.

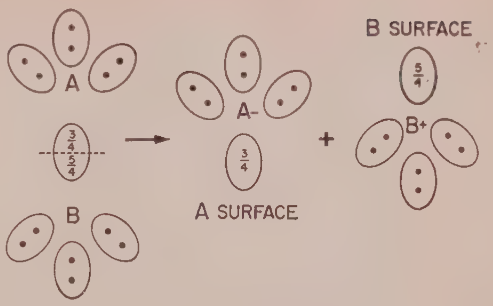

FIG. 2. Schematic representation of the formation of *A* and *B* surfaces with real electrical charges (see text).

Holt attempts to explain the behavior of α and β dislocations by suggesting that the dangling bonds of the group III atoms are formed up by resonance between zero- and one-electron tetrahedral orbitals and that the group V dangling bonds are made up by resonance between two-electron and one-electron tetrahedral orbitals. On that basis, an α edge dislocation should acquire a stronger line charge, and therefore a larger surrounding positive space charge region, than the β dislocation. This, he claims, is the reason for the appearance of only α dislocations in ordinary etching media. This reasoning again is contrary to the experimental results, which have shown that the appearance of dislocation etch pits is based on the different chemical reactivity of the group III and the group V atoms with the etching media; in fact, β dislocations have been revealed by simply adding surface active agents in the etching solutions.[4] Finally, the Gatos-Lavine model is consistent with the experiments suggesting that α dislocations serve as acceptors, whereas β dislocations serve as donors. According to Holt's reasoning both α and β dislocations should exhibit different electron trapping tendencies.

In concluding, it can be stated that the model proposed by Gatos and Lavine, although it involves certain approximations and is admittedly somewhat heuristic, is consistent with a host of experimental results obtained with various III-V intermetallic compounds in connection with the etching and adsorption behavior of the *A* and *B* surfaces, crystal growth along the ⟨111⟩ directions, and chemical and electrical characteristics of the α and β dislocations. Holt's objection that the Gatos-Lavine model leads to a dipole moment across a III-V crystal is shown to be unfounded and his proposed modifications are inconsistent with the experimental facts.

---

[7] H. C. Gatos and M. C. Lavine, J. Phys. Chem. Solids 14, 169 (1960).

[8] L. Pauling, *The Nature of the Chemical Bond* (Cornell University Press, Ithaca, New York, 1960), 3rd ed., p. 124.

[9] G. W. A. Fowles, J. Chem. Educ. 34, 187 (1957).

[10] Accordingly, the α dislocations are expected to be more energetic than the corresponding β dislocations.

Discussions we had with Dr. W. W. Harvey have been very profitable.

JOURNAL OF APPLIED PHYSICS VOLUME 32, NUMBER 7 JULY, 1961

Observations of Cross-Tie Domain Walls by the Faraday Effect

A. L. Houde
Aeronutronic Division, Ford Motor Company, Newport Beach, California

(Received February 13, 1961)

A microscopic Faraday effect apparatus is described by means of which the fine structure of the domain configurations in thin Permalloy films has been observed. The direction of the magnetization in cross-tie domain walls and other domain configurations has been deduced from their light, dark, or gray appearance and known polarizer angles. Faraday effect hysteresis loops are presented in support of a proposal that domain walls at 45° to the easy direction represent an intermediate demagnetized state in films having a high degree of uniaxial anisotropy.

I. INTRODUCTION

THE gross appearance of the domain structure in thin ferromagnetic films as observed by the Faraday magneto-optic effect has already been reported.[1–3] The fine structure of the domain walls in these films may also be observed directly by this technique, and conclusions may be drawn as to the direction of magnetization in the cross-tie walls and in various domain configurations.

For oblique transmission of polarized light through semitransparent Permalloy films below 1000 A in thickness, a rotation of the polarized light occurs which is proportional to the magnitude and direction of the component of magnetization along the transmitted beam. This rotation is many times that obtained by the reflection of polarized light in the magneto-optic Kerr effect so that much improved contrast is available. For such thin films it does not seem energetically possible for volume domains to occur; therefore, the same domain structure exists all the way through the film.

This method for observing domain structure has some advantages over the well known Bitter pattern technique. The collection of colloidal magnetite particles at domain walls depends on flux leakage whereby the magnetic particles provide flux closure for components of magnetization normal to the plane of the film. The Bitter technique does not give an indication of the direction of magnetization in the plane of the film unless a field is applied normal to the domain wall, in which case the colloidal pattern is displaced.[4,5] Furthermore, it requires a moment or so for the Bitter pattern to appear after the magnetic configuration in the film has been changed. In the Faraday method the direction of the magnetization in the various parts of the domain structure can be deduced from their light, dark, or gray appearance and the known polarizer angles. Also, continuous and immediate observations of the domain structure are available.

The fine structure of domain walls in thin ferromagnetic films has been observed at high resolution and magnification using electron microscopy.[6–8] Electron microscopy gives an orthogonal mapping of the magnetization distribution in the specimen which does not differentiate magnetization directions in the defocused method,[7] or if it does, requires a knife edge to be

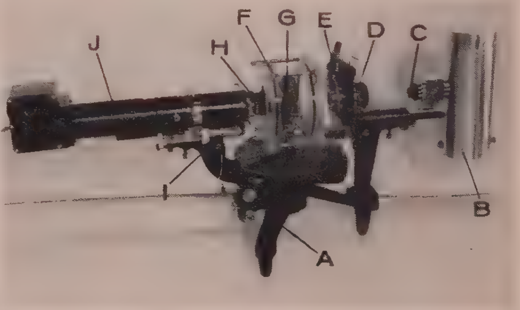

Fig. 1. Microscopic Faraday effect apparatus. A, spectrometer base; B, light source; C, first image-forming lens; D, diaphragm and second image-forming lens; E, polarizer manipulator; F, Helmholtz pair; G, inclined film; H, objective and analyzer; I, focus manipulator; J, photomultiplier.

---

[1] C. A. Fowler and E. M. Fryer, J. Appl. Phys. **24**, 104 (1956).

[2] M. E. Hale, *1958 Fifth National Symposium on Vacuum Technology Transactions* (Pergamon Press, New York, 1959), p. 212.

[3] H. Boersch and M. Lambeck, Z. Physik **159**, 248 (1960).

[4] E. E. Huber, D. O. Smith, and J. B. Goodenough, J. Appl. Phys. **29**, 294 (1958).

[5] R. M. Moon, J. Appl. Phys. **30**, 82S (1959).

[6] M. E. Hale, H. W. Fuller, and H. Rubinstein, J. Appl. Phys. **30**, 789 (1959).

[7] H. W. Fuller and M. E. Hale, J. Appl. Phys. **31**, 238 (1960).

[8] H. W. Fuller and M. E. Hale, J. Appl. Phys. **31**, 1699 (1960).

brought into the electron beam parallel to a domain wall.[8] The knife-edge method utilizes an electrostatic-focusing microscope to overcome the difficulty of perturbing low coercive field films by the magnetic lenses of a magnetic-focusing microscope.

II. EXPERIMENTAL

The apparatus used for microscopic Faraday observations is similar to that described by Fowler *et al.*[9] for magneto-optic Kerr observations of domains in iron whiskers; it is shown in Fig. 1. The photomultiplier shown in the photograph is used for obtaining optical hysteresis loops as described below, and is interchangeable with eyepiece or camera. The present apparatus does not compensate for the difficulty of photographing an inclined plane, so that schematic reconstructions of magnetization directions were made on the basis of the more satisfactory visual observations at a magnification of 100×.

The film was inclined at an angle of 45° to the vertical axis, and polarizer angles were measured with a precision of ±2 min of arc. The photographs presented were all taken on one 5-mm film spot; however, the features described are representative of those found in 50 or more such films. The thickness of this particular film spot (81 Ni–19 Fe Permalloy) was measured by the Tolansky interference method using a very narrow line filter (15-A half-width) and found to be 490±20 A.

The procedure by which domains were introduced was as follows: With the film spot in a single-domain state and the easy axis horizontal, a small permanent magnet was approached at an angle of about 45° to the easy direction until the film broke up into an interesting domain structure. The magnet was then removed so that the domain structure represented a relatively stable demagnetized state under the influence of stray fields at the most. The effect of these stray fields was negligible because the film could then be rotated freely without disturbing the domain configuration under observation.

III. CROSS-TIE DOMAINS

If the analyzer prism is set at about 35 min from extinction with respect to the vertical polarizer and the film is rotated so that the domain walls are horizontal, there is maximum contrast between the areas on both sides of the domain wall and cross ties cannot be seen. However, as the film is rotated towards the position where the domain walls are vertical, the cross-ties appear to "grow" out of the wall. Figure 2 is a photograph made when the domain wall direction was 32° from the vertical. In this position, the cross ties are almost fully developed in length.

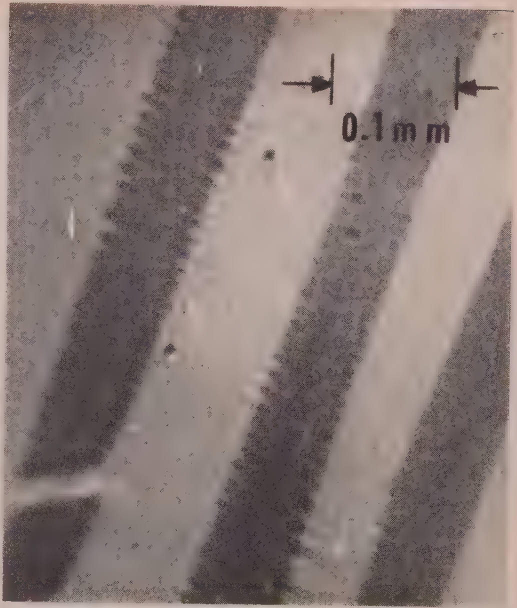

FIG. 2. Typical appearance of cross-tie domain walls inclined at 32° to the vertical polarizer prism.

The direction of the magnetization in the cross ties may be deduced from the fact that the more nearly the magnetization is directed to the horizontal, the greater will be its component in the direction of the light, and the darker (or lighter) will that region be. Particularly in the upper left region of Fig. 2, periodic contrast along the wall of regions which are very dark and very light seems to indicate that the magnetization is rotating

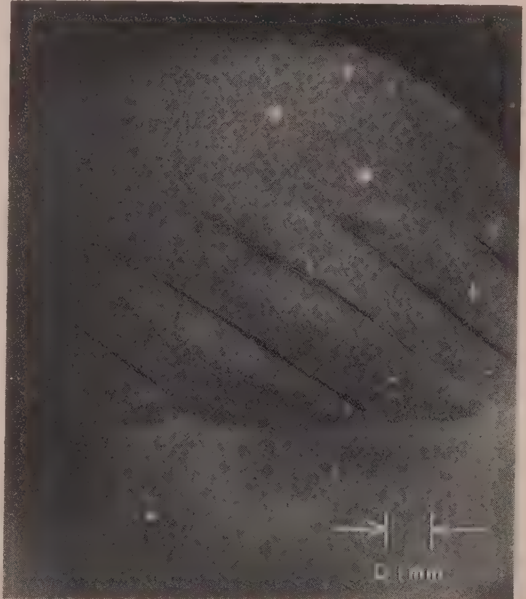

FIG. 3. "Candy-cane" domain configuration resulting from a combination of easy-direction domains and those at 45° to the easy direction. Polarizer and analyzer are set at extinction and the easy direction is parallel to the page horizontal.

---

[9] C. A. Fowler, E. M. Fryer, and D. Treves, J. Appl. Phys. **31**, 2267 (1960).

towards the horizontal direction. This periodic rotation of the magnetization around the cross ties can be interpreted in terms of the model proposed by Huber *et al.*[3]

As shown in Fig. 2, the films were observed to break up into narrow domains at about 45° on either side of the easy direction. The large easy-direction domains show a cross-tie structure similar to that shown here for the domains at 45° to the easy direction. The domain configuration shown in Fig. 3 is a combination of easy-direction domains and domains at 45° to the easy direction.

Figure 4 shows quasiperiodic intensity variations due to "magnetization ripple" in domains inclined at 45° to the easy direction as viewed by the Faraday effect. These have been observed by the Bitter technique[10] and by electron microscopy.[6,7] They appear to be produced by the uniaxial anisotropy in this film which is directed at about 45° to the domain wall.

IV. NÉEL WALLS

Figures 3 and 5 are photographs of domain walls as they appear when the vertical polarizer and analyzer are set almost at extinction (within 2 min) and the domain walls are horizontal. Under these conditions the domains on either side of the wall appear almost equally gray, because they produce equal and opposite rotations of the polarized light.

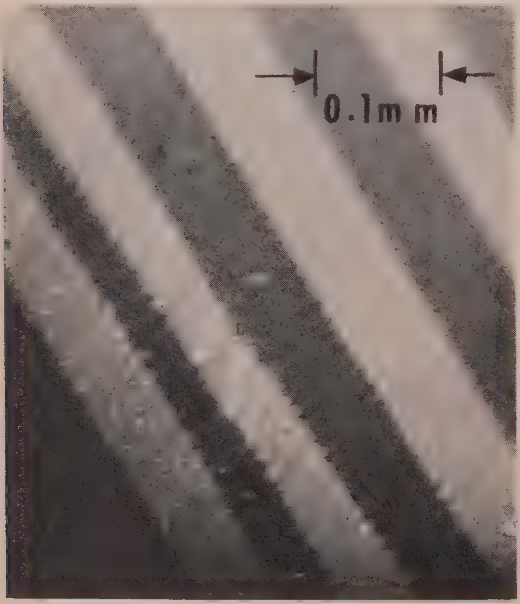

FIG. 4. Magnetization ripple in domains at 45° to the easy direction. The domains are inclined at 32° to the vertical polarizer prism.

The walls, however, appear as dark or light lines of the same appearance as that observed by electron microscopy.[5,6] In the references just quoted, the authors explained the alternation of dark and light wall images as being due to the divergence or overlap of the beam of electrons after passing through the deflecting magnetization of the specimen. There is much evidence, both theoretical and experimental[3,4,9] for the existence of Néel wall segments alternating in direction at right angles to the domain wall in these thin (500-A) films. If this condition is presumed to exist in the same way in the walls on both sides of a domain, then nonparallel light must strike one wall at a different angle than the next one with a corresponding change in refringence. By the Faraday effect, in the simple manner in which it is interpreted here, vertical magnetization directions in the wall would result always in a dark line only for light which is perfectly parallel.

Due to the limited resolving power of the Faraday microscope (numerical aperture 0.1), the width of the Néel wall could not be measured with any great accuracy. The width of the wall in Fig. 5 is approximately 30 000 A, twice the resolving power of the objective which compares favorably with the calculated width of a Néel wall for a film of this thickness.[11]

V. COMBINATION DOMAINS

Figure 3 is a photograph of a "candy-cane"-type domain structure which is interpreted as a combination

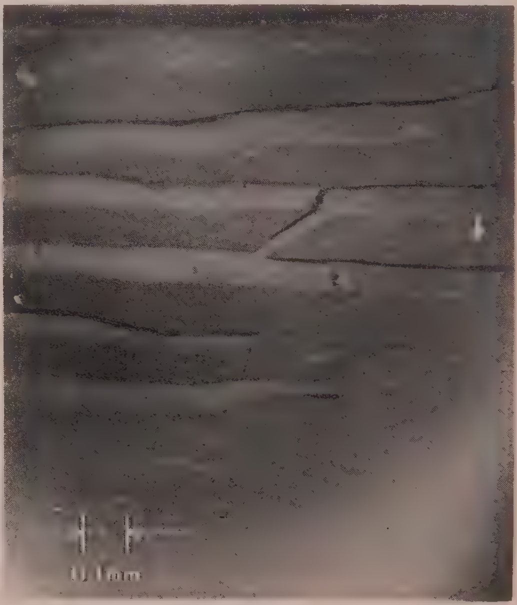

FIG. 5. Appearance of any type of domain walls when the vertical polarizer and analyzer are set at extinction and the domain walls are horizontal.

---

[10] H. W. Fuller and H. Rubinstein, J. Appl. Phys. **30**, 84S (1959).

[11] M. Prutton, Phil. Mag. 5, **54**, 625 (1960).

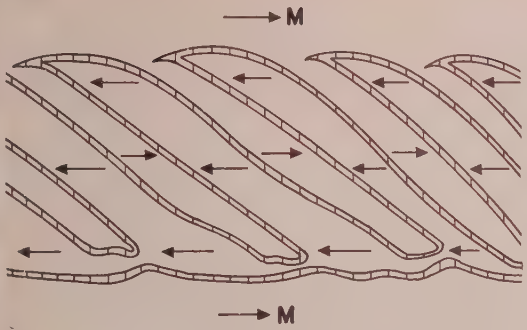

Fig. 6. Schematic representation of the direction of magnetization in the combination of easy-direction domains and those at 45° to the easy direction as shown in Fig. 3.

of easy direction domains and those at 45° to the easy direction which is parallel to the page horizontal. Figure 6 is a schematic representation of the direction of magnetization in this domain structure. The domain walls again appear as dark or white lines. These lines are interpreted as Néel walls in which the magnetization direction is vertical.

VI. FARADAY EFFECT HYSTERESIS LOOPS

A switching field was applied to the film by means of the Helmholtz coils shown in Fig. 1, and the resulting change in light intensity was detected with a photomultiplier. After suitable amplification, hysteresis loops were displayed on an x-y recorder. This method has been used by Reimer[12] and Boersch *et al.*[13] Figure 7 shows the easy direction loop and the transverse loop for the film spot described in this article. They show that this film spot has a well-defined easy direction, and the loop taken at 45° to the easy direction shows no anomaly. It seems, therefore, that the ability to form domains at 45° to the easy direction is due to a low-energy demagnetized state in these thin films. The coercive field of this film spot (2.1 oe) is about double that usually found for films of this thickness.

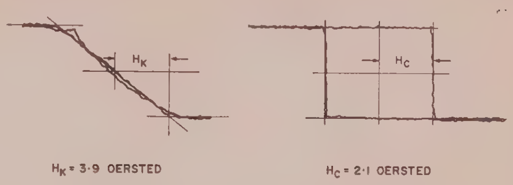

Fig. 7. Faraday effect hysteresis loops taken on a 1-mm² area of the film spot described in this article. $Hc=2.1$ oe, $Hk=3.9$ oe. The thickness was 490±20 A.

Faraday hysteresis loops are felt to be more representative of the dc switching conditions in a magnetic film for the following reasons: Unlike the ordinary hysteresis loop apparatus, there is no perturbation or uncertainty due to a pickup coil, nor are there time delays and phase difficulties due to integration circuitry. The effect of phase differences is apparent in obtaining easy-direction loops, in which case the Faraday apparatus gives coercive field values consistently lower than those provided by the pickup method. The linear variation in the transverse loops gives the same value for the anisotropy field by both methods.

A further advantage of the Faraday apparatus is its ability to probe small areas on a film spot. The area on which the hysteresis loops were made in Fig. 7 was about 1 mm².

VII. CONCLUSION

A microscopic Faraday apparatus has proved to be a useful tool in the study of the static domain characteristics of thin Permalloy films below 1000 A in thickness, which is a range of thickness of interest to those who would use small spots of such films as high-speed and high-density computer storage devices.

ACKNOWLEDGMENTS

The author wishes to thank Dr. H. Wieder of the Naval Ordnance Laboratory at Corona, California for providing experimental details in obtaining the Faraday hysteresis loops. The help of L. Lambert, A. Renard, and E. Saller is also gratefully acknowledged.

---

[12] L. Reimer, Z. Physik **148**, 527 (1957).

[13] H. Boersch, M. Lambeck, and W. Raith, Naturwissenschaften **21**, 595 (1959).

JOURNAL OF APPLIED PHYSICS VOLUME 32, NUMBER 7 JULY, 1961

Electrical Resistivity of Chromium in the Vicinity of the Néel Temperature

M. J. MARCINKOWSKI
Edgar C. Bain Laboratory for Fundamental Research, United States Steel Corporation Research Center, Monroeville, Pennsylvania

AND

H. A. LIPSITT
Metallurgy and Ceramics Research Branch, Aeronautical Research Laboratories, Wright-Patterson Air Force Base, Dayton, Ohio

(Received February 13, 1961)

Previous work by other investigators has shown that a sharply cusped minimum occurs in the resistivity-temperature relationship for fully recrystallized chromium at the Néel temperature, i.e., 35°C. Plastic deformation, on the other hand, eliminates this minimum, and in addition gives rise to a pronounced change in the resistivity-temperature relationship over a wide range of temperatures centered about the Néel temperature. These results have been corroborated in the present paper. Furthermore, this behavior has been analyzed and interpreted in terms of the strong dependence of the Néel temperature on hydrostatic stresses which are thought to arise from the presence of dislocations in the deformed material.

A NUMBER of previous investigations have established the existence of a cusped minimum in the resistivity-temperature relationship for pure chromium[1–7] lying in the temperature interval 12°–41°C. Furthermore, de Morton[7] has shown that cold work eliminates the cusp. Thus far, no satisfactory explanation has been given to account for these phenomena. Because of the discrepancies in the position of the cusped minimum, it was decided to reinvestigate its behavior in somewhat more detail than had been done previously for both a fully recrystallized sample, i.e., one that was given a half-hour anneal at 1050°C, and for one that had been heavily deformed plastically, i.e., 96% reduction in area at 350°C. Figure 1 shows the results obtained from both these specimens.

Considering first the results obtained with the recrystallized sample, it is noted that a sharp cusped minimum appears at a temperature of 35±1°C. It has been suggested previously[6] that this minimum may be associated with the antiferromagnetic transition in chromium; however, Shull and Wilkinson[8] found from neutron diffraction analysis with powders that the Néel temperature was about 175°C, or 140°C above the observed minimum in resistivity. Because of the greater intensities obtained from single crystals, attempts were made to prepare single-crystal specimens suitable for neutron diffraction experiments. Five samples were annealed for 46 hr at 1500°C in a purified argon atmosphere, after which time two of them were found to be single crystals. These specimens were in turn investigated by Corliss *et al.*[9] and, among other things, were found to show a well-defined Néel temperature of 35±2°C. It is concluded therefore that the cusped minimum observed in the present resistivity measurements, with the same material, is indeed associated with the Néel temperature T_N. On the other hand, Corliss *et al.* were able to verify the previous results of Shull and Wilkinson[8]; i.e., that powder samples showed a Néel temperature of 175°C. A possible reason for the high value of the Néel temperature obtained from the powders will be discussed in a later section. In addition, previous work by other investigators has shown that the cusped minimum in resistivity is not only peculiar to

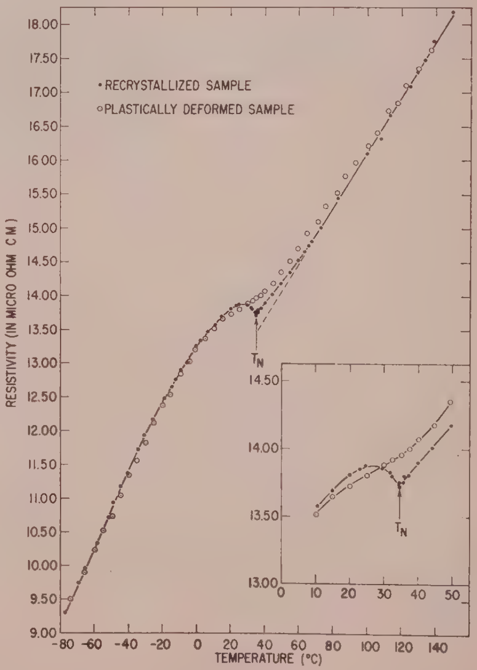

FIG. 1. Variation of electrical resistivity with temperature for both recrystallized and plastically deformed chromium.

---

[1] P. W. Bridgman, Proc. Am. Acad. Arts Sci. **68**, 37 (1932–33).
[2] H. Söchtig, Ann. Physik **38**, 695 (1941).
[3] M. E. Fine, E. S. Greiner, and W. C. Ellis, Trans. AIME **191**, 56 (1951).
[4] A. H. Sully, E. A. Brandes, and K. W. Mitchell, J. Inst. Metals **81**, 585 (1952–53).
[5] R. W. Powell and R. P. Tye, J. Inst. Metals **85**, 185 (1956–57).
[6] H. Pursey, J. Inst. Metals **86**, 362 (1957–58).
[7] M. E. de Morton, Nature **181**, 477 (1958).
[8] C. G. Shull and M. K. Wilkinson, Revs. Modern Phys. **25**, 100 (1953).
[9] L. M. Corliss, J. M. Hastings, and R. J. Weiss, Phys. Rev. Letters **3**, 211 (1959).

chromium, but occurs at the Néel temperatures in Mn,[10] Tb, Dy, Ho, Er, and Tm.[11] A similar type minimum appears in the resistivity-temperature curves of the beta phase of Li-Pb alloys near 150°C,[12] indicating that it may also exhibit antiferromagnetism.

Another important feature of Fig. 1 pertaining to the recrystallized specimen is that, below 35°C, the resistivity begins to increase and reaches a maximum at 27°C. Ordinarily, it might be expected that below T_N, the spin-disorder scattering would be greatly reduced so that the resistivity should decrease instead of increase. On the other hand, Corliss *et al.*[9] have shown that below T_N, 180° spin reversals occur every 14 unit cells, giving, in effect, an antiphase arrangement of the magnetic spins. It is conceivable that these small domains could give rise to an increased scattering of electrons in a manner similar to that observed for small, chemically ordered domains.[13] Of further interest in Fig. 1 is the observation that unlike most other antiferromagnetic substances,[10,11] the slopes of the resistivity-temperature curves below and above T_N are not very much different, indicating that the spin-disorder scattering in chromium is quite small. Still another feature to be noted from this figure is that from about 65°C down to T_N, the curve obtained from the recrystallized specimen shows a marked departure from linearity, as can be seen by comparison with that portion of the dotted curve extrapolated from higher temperatures. This departure from linearity is quite likely associated with short-range magnetic order that may be present above T_N.

Perhaps the most interesting aspect of this investigation concerns the manner in which the resistivity-temperature relationship is affected by plastic deformation. This is shown by the open-circle data in Fig. 1. It will be noted first that the cusped minimum is completely eliminated, and instead there now remains only a smooth inflection at T_N. These same general results have been recently obtained by de Morton.[7] Furthermore, between −55° and 30°C, the resistivity of the deformed specimen is lower than that of the recrystallized one, while between 30° and 130°C, the resistivity of the deformed specimen is higher than that of the recrystallized specimen. From these results one is tempted to suggest that the Néel temperature originally present at 35°C in the recrystallized specimen is now, as a result of plastic deformation, smeared out over a range of temperatures above and below 35°C. This would account for the increase in resistivity of the deformed sample above T_N, and the decrease below T_N ,with respect to the sample that had been recrystallized.

In order to account for the smearing out of the resistivity near 35°C in the plastically deformed sample, it is instructive to consider the curve of Fig. 2. This curve was constructed from those of Pursey,[6] who in turn replotted the original data of Bridgman.[14] Specifically, it was found that the temperature at which the cusped minimum appeared decreased with increasing pressure. Since this minimum has now been definitely established to occur at the Néel temperature, it has been labeled as such in Fig. 2. Bridgman's results, however, are about 22°C lower than those obtained in the present investigation and may have been due to a greater impurity content in his sample, along with some uncertainty in T_N due to a relatively small number of data points. It is expected, however, that the same general tendency would be obtained for the present specimen; i.e., the Néel temperature would decrease roughly linearly with increasing hydrostatic pressure. It is also anticipated that the Néel temperature would be increased with increasing hydrostatic tension, perhaps in a manner such as shown by the dotted-line extrapolation in Fig. 2. No attempt will be made to account for the mechanism by which T_N is affected by stress in this paper, but presumably it is related to the changes in interatomic distance brought about by the hydrostatic stresses.

With the above observations, it is now merely necessary to account for the manner in which these stresses could arise in the plastically deformed crystal. The simplest assumption is that they arise from the relatively high density of dislocations resulting from the 96% reduction in area at 350°C. Furthermore, it appears reasonable to consider only the hydrostatic stress components of these dislocations, since the shear components would not contribute to any dilatation. For simplicity then, we will consider the hydrostatic stress field σ around a pure edge dislocation in chromium. In polar coordinates this is given, using the appropriate expressions obtained from isotropic elastic theory,[15] by the following relation:

$$\sigma=\tfrac{1}{3}(\sigma_{xx}+\sigma_{yy}+\sigma_{zz}) \\ =-[(1+\nu)Gb\sin\theta/(1-\nu)3\pi r], \quad (1)$$

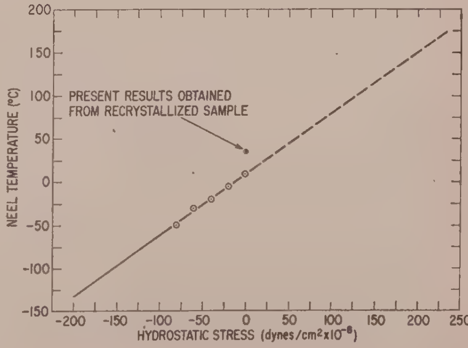

FIG. 2. Variation of Néel temperature with hydrostatic stress.

---

[10] G. K. White and S. B. Woods, Can. J. Phys. **35**, 346 (1957).

[11] R. V. Colvin, S. Legvold, and F. H. Spedding, Phys. Rev. **120**, 741 (1960).

[12] T. C. Wilson, J. Chem. Phys. **8**, 13 (1940).

[13] F. P. Burns and S. L. Quimby, Phys. Rev. **97**, 1567 (1955).

[14] P. W. Bridgman, Proc. Am. Acad. Arts Sci. **68**, 27 (1932–33).

[15] A. H. Cottrell, *Dislocations and Plastic Flow in Crystals* (Clarendon Press, Oxford, England, 1953), p. 57.

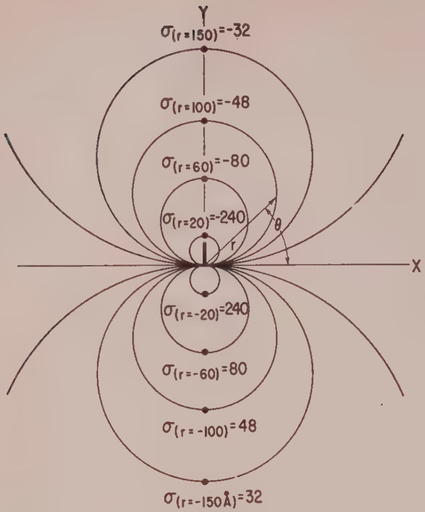

FIG. 3. Hydrostatic stress field around an edge dislocation in chormium. Stresses in units of $d/cm^2 \times 10^{-8}$, indicated at $\theta=90$.

where σ_{xx}, etc. are the normal components of stress in the x, etc. directions; b is the Burgers vector of the dislocation or 2.49×10^{-8} cm; ν is Poisson's ratio and is taken to be approximately 0.22 at 25°C,[6] while the shear modulus G at this same temperature, as cacluated from the elastic modulus[3] ($E=28.2 \times 10^{11}$ d/cm^2), is found to be 11.6×10^{11} d/cm^2. Both θ and r are as shown in Fig. 3. It can be seen from Eq. (1) that the curves of constant σ are circles passing through the origin of the dislocation and centered on the y axis. Several such equistress curves are shown in Fig. 3, and for convenience are labeled with respect to their r values on the y axis. For distances smaller than $r=20$ A, i.e., in the core of the dislocation, Eq. (1) is not applicable because linear elastic theory breaks down at these small distances. However, we note that at $r=20$ A in the y direction, $\sigma=-240 \times 10^8$ d/cm^2, and is -32×10^8 d/cm^2 at $r=150$ A in the y direction. The negative signs refer to compressive stresses, while below the x axis, the stresses are all positive or tensile but symmetrical to those above the x axis. Referring to Fig. 2, it is obvious that the range of stresses produced by the stress field of the edge dislocation in Fig. 3 is of the right magnitude to cause a variation in Néel temperature over the temperature interval shown in Fig. 2. In many cases, the stress fields around dislocations are expected to be somewhat more complicated than that shown in Fig. 3, since there will be a certain degree of cancellation of these stresses by neighboring random dislocations. Furthermore, the stress fields in certain regions may be greater than that shown in Fig. 3 due to groups of closely spaced dislocations. It is also conceivable that the stress fields associated with other types of imperfections such as vacancies or clusters of vacancies may also be important. In any event, the simple picture presented above is compatible with the present results. Specifically, the varying stress fields around edge dislocations give rise to both a continuous increase as well as a continuous decrease in the Néel temperature from its value of 35°C in the perfect lattice. In effect, the Néel temperature is smeared out over a range of temperatures, and so correspondingly is the cusped minimum in the electrical resistivity.

Having developed what appears to be a reasonable model to explain the present experimental results, we are now in a position to discuss, somewhat more intelligently, the observed difference between the Néel temperatures obtained from single crystals and from powders. As mentioned earlier, there appears to be little doubt that the Néel temperature of the single crystals is the one associated with a relatively perfect crystal lattice. It must therefore be assumed that the Néel temperature obtained from the powder is representative of an imperfect lattice, and from the above discussion, may arise from the internal stresses associated with dislocations. The powders examined by Shull and Wilkinson[8] were obtained by grinding electrolytic flake chromium, and it is quite likely that this procedure introduced a very high density of dislocations, perhaps even higher than that introduced into the resistivity sample, since the grinding was carried out at room temperature. It is conceivable that this plastic deformation smeared the Néel temperature of the powdered samples over a range of temperatures to the extent that the sample possessed antiferromagnetism up to 175°C, in good agreement with what is to be expected from Figs. 2 and 3. Of further significance in this respect is that the half-hour anneal at 1050°C given to the resistivity sample was found to be the minimum condition under which complete recrystallization of the sample could be obtained. Laue x-ray back reflection techniques showed that lower temperatures or shorter times were insufficient to remove completely the residual stresses within the specimen imparted by cold work. This difficulty in attaining complete recrystallization may also account in part for the discrepancies in the position of the Néel temperature observed by previous investigators.

The authors would like to express their appreciation to E. J. Hassel and A. M. Adair of the Aeronautical Research Laboratory, and to D. S. Miller and J. C. M. Li of the Edgar C. Bain Laboratory for Fundamental Research for their many helpful suggestions during the course of this investigation. In addition they would also like to thank G. Asai of the U. S. Bureau of Mines, Albany, Oregon, for supplying chromium specimens.

JOURNAL OF APPLIED PHYSICS VOLUME 32, NUMBER 7 JULY, 1961

Dissociation of Adsorbed CO by Slow Electrons

GEORGE E. MOORE
Bell Telephone Laboratories, Inc., Murray Hill, New Jersey

(Received December 17, 1960)

We have investigated ions emitted from molybdenum and tungsten surfaces in CO when the surfaces are bombarded by electrons. The surfaces, in the form of ribbons, can be cleaned at will by heating, and bombarded by an electron stream in which current and energy are controlled separately. The product ions are observed in a mass spectrometer whose envelope contains the experimental filament. Electron bombardment liberates only the O^+ ion from adsorbed CO with any abundance; it may be 50–100 times more abundant from the surface than from space. No CO^+ nor C^+ ions are detected nor any negative ions of CO or its fragments. Carbon atoms remain on the surface. Significant amounts of F^+ and Cl^+ are also liberated from new filaments; these diffuse from the interior and are more tightly bound than CO, and disappear only after prolonged heating. Their surface abundance is so slight that they do not interfere with the O^+ process. The threshold electron energy for liberation of O^+ ions and the dependence of O^+ ion current on electron current and energy are given. The method might be useful for studying kinetics of complex adsorption phenomena, although precautions are necessary to avoid perturbing the adsorbed film by the incoming electrons. The following phenomena are readily observed and probably understood: (a) The growth of a monomolecular film of CO from the ambient following a flash of the filament. (b) Competition for available sites by chlorine, fluorine, carbon, and CO. (c) Poisoning of the surface, for adsorption of CO, by carbon atoms freed by departure of O^+ ions. A simple theory reproduces the experimental kinetics of adsorption and poisoning semiquantitatively.

INTRODUCTION

VERY little has been published on the behavior of adsorbed gas under electron bombardment. If the gas or its fragments leave the surface as ions, the mass spectrometer should be an ideal method for study. Such experiments were reported briefly by Dempster[1] and by Plumlee[2] as incidents in other work. Other papers[3] discuss the phenomenon in more detail, although their author simply studied pressure changes, making no identification of products.

EXPERIMENTAL

In our system (Fig. 1), the metal surface S was a wide filament much like those used by Hagstrum.[4] (Four different Mo filaments and one W were used. Except as noted, results are given only for Mo; any difference between results for the two metals will be mentioned.) The filament was mounted directly behind the open-type[5] ionization chamber IC in the stainless steel envelope. Gas molecules or ions from S readily enter IC. Ions are processed through the slits S_1, S_2, S_3 and are measured. Electrons drawn from F_1 or F_2 into IC can ionize ambient molecules in IC. These ions give a measure of the partial pressure of each ambient gas; Ne and CO were admitted and used for calibration.[6]

The principal measurements were made by directing a stream of electrons into S from F_3 and F_4 (F_{34}) which were enclosed by grids. When these electrons excite adsorbed molecules to unstable electronic states of sufficient energy, the system ejects ions or excited atoms. Ejected ions are drawn toward IC by a field of proper polarity, and a sample is processed through the mass spectrometer and measured essentially like the ions produced in IC from ambient gas. Uncharged atoms or molecules liberated from S can also diffuse toward IC. A small fraction of these could then be ionized by electrons from F_{12} and a fraction of this fraction would be processed through the mass spectrometer. Because the first fraction is small (~ 0.0001), the method is much more sensitive to ions leaving S than to uncharged particles.

RESULTS

O^+ Ion Peak from S

The measurements must distinguish between ions formed by electrons striking adsorbed molecules on S and those formed by electrons striking gaseous mole-

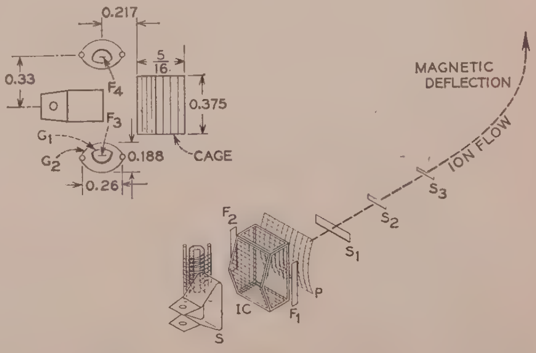

FIG. 1. Schematic of experiment. Dimensions in inches. Flat part of S "seen" by IC is experimental surface; effective area is 0.30 cm^2. Cage or IC is the open-type ionization chamber for ready entry of ions produced on S. F_3 omitted in isometric view.

---

[1] A. J. Dempster, Phys. Rev. **11**, 316 (1918).

[2] R. H. Plumlee and L. P. Smith, J. Appl. Phys. **21**, 811 (1950).

[3] Y. Ishikawa, Rev. Phys. Chem. Japan **15**, 83, 117 (1942); Proc. Imp. Acad. (Tokyo) **19**, 380 (1943).

[4] H. D. Hagstrum, Rev. Sci. Instr. **24**, 1122 (1953).

[5] G. E. Moore, J. Appl. Phys. **30**, 1086 (1959).

[6] For neon, the calibration was 7.0×10^{-4} amp of Ne^{+}_{20} ions collected per mm of pressure, and for CO^+, 2.5×10^{-3} amp of CO^{+}_{28} per mm of pressure. These calibrations are for 1-ma, 80-v energy electron currents into the cage. Variations of $\pm 50\%$ result from small variations in magnet positions or electrode potentials. The sensitivity could also be increased by other means, such as adding magnetic shields, but these introduced some instability. The limiting slits were 0.010 in. wide, and the radius of the analyzer was 4.5 cm.

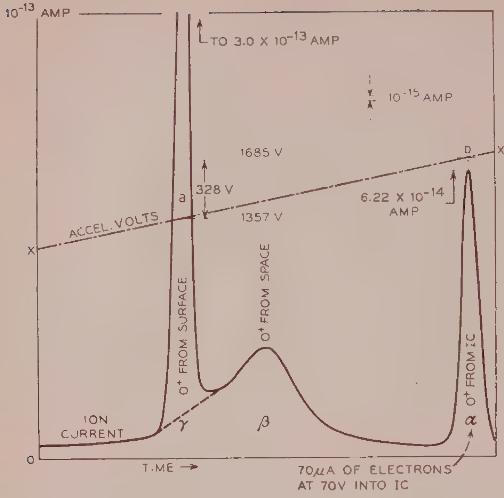

FIG. 2. Voltage displacement method for determining origin of O^+ ions. This and most succeeding drawings are tracings of experimental chart recordings. Peak α measures O^+ ions produced from gaseous CO molecules in *IC*, using 70 μamp of 70-v electrons from F_{12}. The dot-dash curve XX shows the voltage which accelerates ions from *IC* through slit and analyzer system; α appears at 1685 v, proper for O^+ in the magnetic field used. Peaks β and γ represent O^+ ions produced by an electron current of 4.20 ma from F_{34} flowing to *S* through 300-v potential difference. Peak β is for ions produced in the ambient gas and is therefore nearly 300 v wide. Peak γ for ions liberated from *S* appears at 328±5 v below peak α. The theoretical difference is 328.5 v, composed of 300 v between F_{34} and *S* and 28.5 v between F_{34} and *IC*, to draw ions into *IC*. Peaks β and γ can be moved at will with respect to peak α by varying these voltages. Because G_1 is negative, it attracts positive ions from inside G_2 and hence decreases peak β with respect to α.

cules en route from F_{34} to *S*. Figure 2 illustrates one method of distinction for O^+ ions; we note three peaks. The sharp peak α represents O^+ from gaseous[7] CO. The O^+ ions are formed in *IC* by impact of electrons from F_{12}.

The O^+ ions of peak β, also from gaseous CO, are formed by electrons flowing from F_{34} toward *S*; these ions arrive at *IC* with velocity corresponding to the potential difference between *IC* and their point of formation, and thus require less acceleration through the slits than ions formed in *IC*. Hence they produce a broad peak which appears at positions along XX corresponding to lower accelerating voltage than for peak α.

Peak γ shows ions liberated from *S*. Because *S* is equipotential, all O^+ ions originating on its surface arrive at *IC* with the same energy and form a sharp peak. Figure 3 shows that peak γ for O^+ is actually considerably higher than the peak for CO^+ ions formed in space, although CO is the parent molecule for O^+ ions.

Comparison of O^+ with Other Ions and Effect of Temperature

Figure 3 shows three charts, all taken with 300-v electrons bombarding *S*. *S* was operated at 1250°K for the top chart, at 1700°K for the center, and at 950°K for the bottom. The ion responsible for each peak is indicated as well as the proper position for that ion, if liberated only from *S*. No peaks corresponding to α on Fig. 2 appear in Fig. 3, because no electrons from F_{12} flow into *IC*.

On the upper two charts, the peaks for C^+ and O^+ are diffuse, corresponding to β of Fig. 2; neither indicates liberation of ions from *S*. Substantially all of the C^+ structure occurs at voltages too high for the C^+ to have come from *S*, but the diffuse structure on the left portion of the O^+ peak, labeled crest No. 1, was probably caused by dissociation of CO from the region between G_2 and *S* which has the same potential as *S*. Because this crest relative to background is unchanged for two temperatures differing by 450°C, we believe that there is no CO on *S* at either 1250° or 1700°K, and that the C^+ and O^+ are produced by dissociation, on electron bombardment, of CO in the space between G_2 and *S*. The C^+ peaks on all three charts are alike, but the O^+ peak on the bottom chart resembles its γ peak of Fig. 2, and represents O^+ ions originating *on S*.

Peaks for thermal ions of Na^+ and of $K_{39}{}^+$ and $K_{41}{}^+$ are apparent in Fig. 3. Thermal Rb^+ ions were also observed occasionally. Thermal ions were especially prominent when *S* was new, but disappeared on prolonged heating. They had no observable effect on O^+ ions liberated from *S* by electron impact on adsorbed CO.

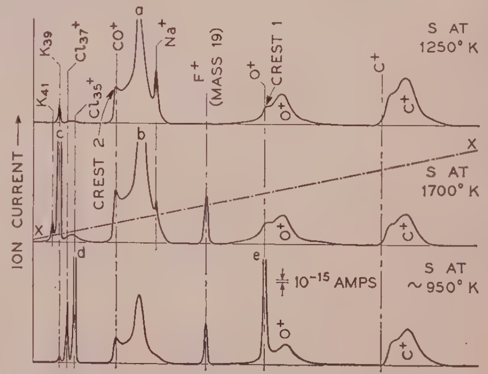

FIG. 3. Temperature method for determining origin of ions. Ion currents are plotted on a linear scale. Curve XX, indicated on center spectrogram, again gives the voltage which accelerates ions through the slits. The vertical dot-dash lines indicate the proper position of a given peak if the ion producing that peak was formed on *S*; thus O^+ ions come from *S* at ~950°K, as in bottom spectrogram, but not at higher temperatures. Several peaks are open at their top, indicating extension above the chart from which spectrogram was traced. Currents for these peaks, measured at lower gain, are $a=1.02\times10^{-13}$ amp, $b=1.6\times10^{-13}$ amp, $c=3.5\times10^{-13}$ amp, $d=2.15\times10^{-13}$ amp, $e=2.9\times10^{-13}$ amp.

---

[7] H. D. Hagstrum, Revs. Modern Phys. **23**, 185 (1951).

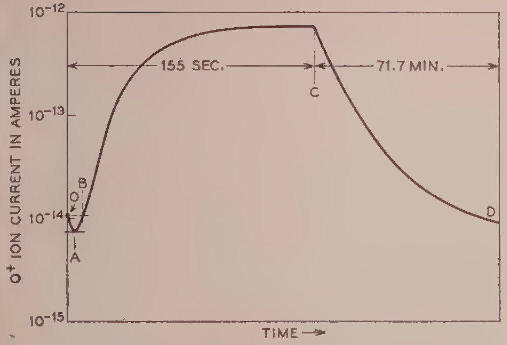

FIG. 4. Behavior of the $O^+\gamma$ peak with time. O^+ ion current is plotted on logarithmic scale. Time begins at instant when flashing current is extinguished. Incoming electron current flowed continuously. The curve breaks at 155 sec only because of the change in time scale. Flash 76 sec at 1785°K before curve begins. $E_s=253$ v; $I_s=2.60$ ma; $I_{G_2}=3.25$ ma; $Pr=7.0\times10^{-8}$ gauge.

The peaks shown for Cl_{35}^+, Cl_{37}^+ and F^+ were liberated from *S* only by electron bombardment. These ions were also prominent when *S* was new, but had no observable influence on the O^+ yield from *S*. F^+ and Cl^+ are apparently liberated about tenfold more efficiently than O^+ ions; this and other results on F^+ and Cl^+ are presented in the Appendix.

The abundance relative to background of crest No. 2 on the left, or low-voltage side, of the complex including masses 23 to 28 seems independent of temperature. The location and approximate independence of temperatures suggests that this CO^+ peak represents CO molecules from the space between G_2 and *S*.

OH^+, but not H_2O^+, is also liberated from *S* whenever H_2O (and OH) are observed in the ambient, but it was not studied because its occurrence and abundance were erratic.

Note that no peak occurs for O_2 or CO_2; this was true at the highest gains used, unless O_2 was admitted.

Behavior of the $O^+\ \gamma$ Peak with Time

Figure 4 illustrates the time dependence of the $O^+\ \gamma$ peak, following a flash of filament *S*. We distinguish three regions; the first extends to point *B*. Flashing terminates at time zero, *S* is too hot for adherence of CO, and the ordinate represents ions formed in space, on the left side of the broad peak β of Fig. 2. As *S* cools, CO molecules become less abundant near *S*, in part because they can now adhere, and the O^+ ion current consequently decreases to point *A* and then increases as CO builds up on *S*. The width of the pocket to *B* is roughly inversely proportional to the pressure of CO, for given flashing procedure. Its width increases with temperature and time of flash, probably because the heavy supports become hot during flash and then conduct heat to *S*.

In the second region, from *B* to *C*, the CO film builds up to a monolayer; the γ peak of Fig. 2 was taken with the surface in the condition near *C*. To reach point *C* required 155 sec, and time is plotted on a uniform scale.

In the third region, from *C* to *D*, the time scale is slower by a factor of 30 to illustrate the gradual decline, which continued to *D*; the ion current then approximated its value at time zero. The ability to produce O^+ ions at the previous abundance is then fully recovered only on flashing at high temperatures, and is only partially recovered by extinguishing the incoming electron current; the electrons thus decrease the ability of *S* to emit O^+ ions.

Temperature of *S* is therefore a second method to identify the source of ions. Henceforth we treat the O^+ ion yield from *S* as a measure of the CO adsorbed.

Behavior of the O^+ Ion Peak on Pulsing the Incoming Electron Current

Figure 5 shows three sets of typical results when the incoming electron current was pulsed. We consider here only section (a); during the first four pulses the electron current flowed for 30 sec and was extinguished for 30 sec; for the next four pulses, the "on" period was decreased to 2 sec. During a pulse, the amplitude of the ion current falls off exponentially. For the first and fourth pulses the points, plotted from the indicated

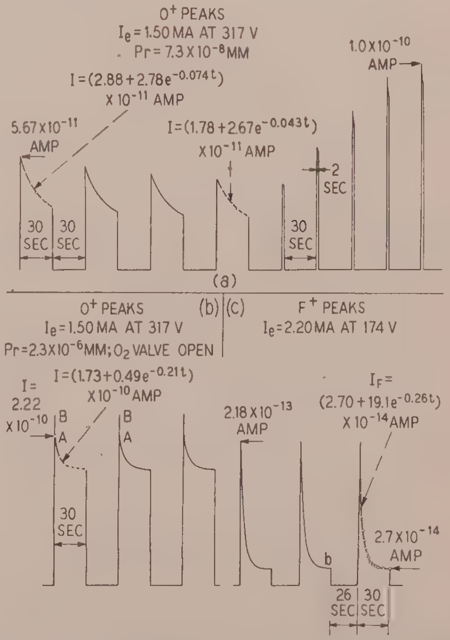

FIG. 5. Ion current from *S* as incoming electron current is pulsed. Ion currents are plotted on a linear scale. Electron current is uniform during a pulse, but ion current from *S* declines; recovery occurs during idle interval. (a) Recovery is greater for active pulse duration of 2 sec than for 30 sec. No oxygen was admitted and O_2^+ peak was 0.009 of CO^+ peak. (b) The oxygen valve was open and the O_2^+ peak was 0.78 of the CO^+ peak. Note that amplitude of O^+ ion pulses is about fourfold the value in (a), and that the percentage decline is much less. (c) F^+ peaks from *S*.

(purely empirical) decay equation, fit the experimental curves, although the slow decay from pulse to pulse causes the equations to differ. But much more important, the ability to emit ions recovers during the idle period of 30 sec almost to the initial level of the preceding pulse. In the last four pulses, the active periods were only 2 sec; the amplitude of ion current increased to a new level approximately 25% higher than for the fourth pulse of 30-sec duration. So the *decay* occurs only while electrons flow, and some *recovery* mechanism obviously acts during the idle period and also probably acts while electrons flow into *S*.

For threshold measurements and other observations, Ne or CO were admitted. Their ions and those of C^+ fragments of CO were produced by electrons en route to *S*. No decay such as that shown in Fig. 5 occurs during a pulse for molecules ionized only in the gas phase; their pulses were rectangular. The short-time decay during a pulse is therefore a third method to distinguish ions originating on *S* from those produced in gas by electrons en route to *S*.

Temperature of *S*

A ribbon duplicating *S* was mounted on similar supports in a glass bulb for optical pyrometer measurements above incandescence. Lower temperatures were estimated from the energy radiated by *S* in the mass spectrometer. With no heating current flowing, bombarding electrons and energy radiated from the emitting filaments heat *S*. When electrons flowed into *S* continuously, it could reach 950°K or more, depending on the power delivered by the incoming electrons. This temperature would permit only the double-bonded β phase (stable at 960°–1400°K) of absorbed CO defined by Redhead[8] and by Hickmott and Ehrlich[9]; the single-bonded α phase (stable at 450–600°K) would disappear during continuous bombardment except at very low energy input. We probably deal primarily with the β phase, although some α phase may be present at the beginning of each pulse; this may cause the very rapid decay indicated during the 2-sec pulses of Fig. 5 if electrons dissociate the α phase more efficiently than the β phase. Significant tests with the α phase would require cooling *S* below 400°K, which seemed impractical.

Experiments on Decay

Decay probably occurs as follows: Adsorbed CO, struck by electrons, gives up an O^+ ion and leaves a carbon atom. Because no evidence was ever found that C evaporated, as such, at rates significant in the present work, the adsorbed carbon atom can pursue one of three courses:

(1) hold its site tenaciously,[10] preventing a new CO molecule from occupying that space;
(2) diffuse into the volume of the metal;
(3) meet some molecule with which it can combine, forming a volatile compound and thus leave the surface.

The following indicates that processes (2) and (3) occur:

(a) After decay is nearly complete, the heating of *S* can cause a net increase of surface CO by increasing the inward diffusion of C. Sudden increase to this temperature would thus produce some rejuvenation. We show such results following point *a* for curve *A* on the right side of Fig. 6, using an expanded time scale for this region of curve *A* only. *S* was suddenly heated at *b* to 1050°K; this increased the O^+ current by more than 50%. Heating current was eliminated at *c*; the ion current again increased by about 50%. While not large, these effects are reproducible with Mo (but not observed with W). Temperatures appreciably above about 1050°K decrease or eliminate the effect.

(b) One can follow the growth and decay curves approximately as well by pulsing the electron current to *S* as by continuous flow. Decay occurs only during bombardment, and both recovery mechanisms (diffusion of C into *S*, or removal of C from *S* by chemical reaction) operate continuously. One might even avoid observable decay by sufficiently long idle intervals. For curve B, shown dotted, the incoming electron current flowed 3 sec and was off 59 sec. Pressure was 3×10^{-9} mm, as distinguished from 8.0×10^{-8} mm for curve A. Because of lower pressure, curve B exhibits much slower growth than A and a wider pocket. But the maximum O^+ yield is almost tenfold higher than in A, and there is no decline. These effects of pulsing and pressure are reproducible.

(c) To cause departure of carbon by forming a gaseous product, the reaction

$$C+\tfrac{1}{2}O_2 \rightarrow CO$$

was tried, by admitting small quantities of O_2 with results shown in curve C. The incoming electron current was not pulsed. Note that the maximum O^+ yield from *S* is now about 30 times that shown in curves A and B. However, when the mass spectrometer was used for analysis, the CO^+ peak was 35 times larger than the O_2^+ peak; apparently the O_2 which entered the system encountered C on most collisions with surfaces and formed CO. By heating *S* for about 16 hr under these conditions, the O^+ ion effect increased by a factor of 40 or more, and additional heating gave no additional improvement. Most important, the small amount of O_2 present essentially prevented decay of the O^+ effect. The slow time scale was continued to the end of the

---

[8] P. A. Redhead, Conference on Physical Electronics, M.I.T., March, 1960. Dr. Redhead has also kindly allowed me to read his manuscript for formal publication of this work.

[9] T. W. Hickmott and G. Ehrlich, J. Chem. Phys. **24**, 1263 (1956); **5**, 57 (1958).

[10] Prolonged treatment of *S* using a low pressure of O_2 causes adsorption of O, which can also hold its sites tenaciously.

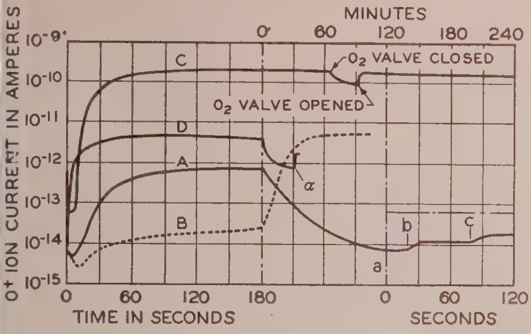

FIG. 6. Growth and decay curves under various conditions. Note that ion currents are plotted on a very condensed logarithmic scale. Curve A: O^+ ions; incoming electron current 2.60 ma at 253 v, not pulsed. *Pr* of $CO = 8.0 \times 10^{-8}$ mm. Note that time scale, for this curve only, in region *abc* is the same as for first 180 sec. For all other curves, time scale after 180 sec is condensed by a factor of 60 and given at top of curve. O_2 valve closed. Curve B: O^+ ions. Incoming electron current 0.87 ma at 33.6 v, *pulsed*: on 3 sec and off 59 sec. *Pr* of $CO = 3 \times 10^{-9}$ mm. Note that there is no decline. O_2 valve closed. Curve C: O^+ ions. Incoming electron current 0.85 ma at 100 v, *not* pulsed. Oxygen valve open. CO pressure is 1.05×10^{-7} mm; ion gauge pressure $= 1.00 \times 10^{-6}$ mm. Note that no appreciable decay occurs until O_2 valve is closed, and recovery is almost immediate on reopening valve. Curve D: Cl^+ ions. Incoming electron current 1.75 ma at 175 v, not pulsed. Note absence of any pocket at beginning of curve. At α, temperature of *S* increased from 950° to 1050°K.

figure. The O_2 valve was closed at the point indicated, giving an immediate decay which in 25 min amounted to a factor of 2. On then reopening the valve, the O^+ quickly reached its former magnitude.

Figure 5(b) shows that some fast decay occurs in the presence of O_2 when the incoming electrons flow in pulses.

Ratio of Detected Ion Current to Incoming Electron Current

The previously stated results suggest that perturbation of the adsorption system by incoming electrons must be minimized in any significant measurements. This requires using low electron currents pulsed with a large ratio of idle-to-active durations, together with an appreciable oxygen content for the system whenever *S* contains carbon. These conditions were used for the tests described in this and the two following sections.

Figure 7 shows the behavior of O^+ from *S* as incoming electron current is varied, using two different electron energies. Both coordinates are logarithmic, and the best 45° straight line was drawn through the points of each curve. The satisfactory fit over about five orders of magnitude indicates that the yield of O^+ ions is directly proportional to incoming electron current. The liberation of an ion is therefore a single-step process, involving only one electron.

The black dots at the upper end of the 85-v curve represent measurements at electron currents sufficiently high to decrease the ion yield during the response time of the amplifier-recorder system. Each open dot above the corresponding black dot represents the reading corrected for that decline. All other open dots represent actual readings and the points were reproducible.

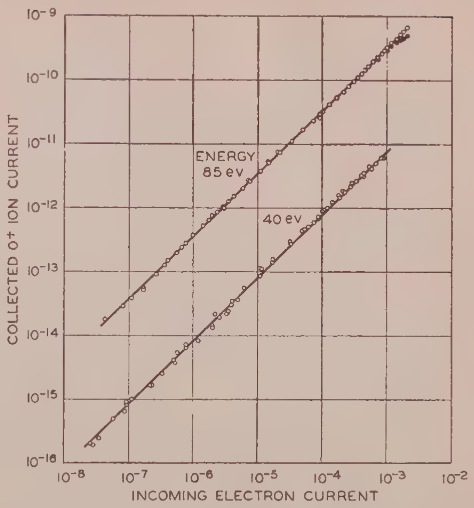

FIG. 7. Collected O^+ ion current is directly proportional to incoming electron current. This is a necessary and probably sufficient condition that the emission of each emitted O^+ ion result from a single incoming electron.

The probability that a liberated ion passes through the spectrometer to the collector is about 0.005, so the efficiency of liberation is about 6×10^{-5} O^+ ions per incoming electron at 85-v energy, for what was presumably a monolayer of CO on *S*; 1×10^{-4} was the maximum efficiency obtained.

Effect of Electron Energy

The four curves of Fig. 8 show specific O^+ ion current collected plotted logarithmically against electron energy. In all cases the incoming current was pulsed. Data for curve A were taken before admitting O_2. Curve B represents the first run in the presence of O_2, and gives a yield about 50 times higher than curve A. Curve C was taken with O_2 in the spectrometer, and after *S* had been heated for some hours in its presence in an effort to remove carbon from the interior. This maximum yield was the highest yet attained and was quite reproducible. Curve D was taken after closing the O_2 valve and pumping out the system.

Curves A, C, and D were continued to low energies; points for the three runs in this region follow the same path, indicating that the threshold is approximately unchanged under variations that altered the upper sections of the curves by orders of magnitude. Oxygen thus apparently increases the maximum without affecting the threshold appreciably.

In all these curves, the points were often taken in random order and were usually reproducible. The two points labeled *a*, associated with curve C, represent the poorest reproducibility encountered. Reproducibility

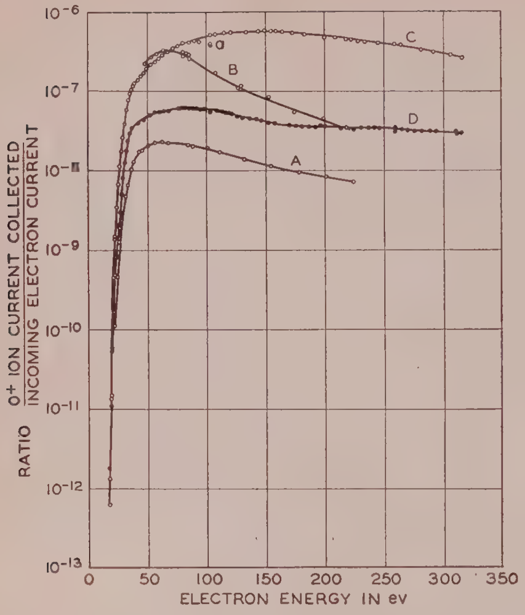

Fig. 8. Effect of electron energy on O^+ ion emission. Curve A was taken before O_2 had been admitted to burn carbon out of filament. O_2 in ambient gas was not observable, so was less than 10^{-3} as abundant as CO. Curve B: O_2 flowing into system 0.14 as abundant as CO. Curve C: O_2 flowing into system and about 0.90 as abundant as CO. Curve D: O_2 valve closed following curve B, and several treatments in CO. O_2 was 1.6×10^{-3} as abundant as CO in ambient.

from curve to curve in the horizontal portions is apparently affected by events during a flash.

Measurements of Threshold

We first state the results of the threshold measurements and then discuss the technique. Figure 9 gives three curves for O^+ from *S* and two for Ne^+ from the gas phase. The ordinates express efficiency in terms of "collected ion current divided by incoming electron current" on a logarithmic scale, and the abscissas are "electron energies" as measured by an external voltmeter. The latter scale is expanded by a factor of 15 over the corresponding scale of Fig. 8. True electron energies corrected for surface potentials, thermal energies, and errors in the voltmeter are obtained by using the well-established first ionization potential of Ne, 21.53 v. Any ordinate in the region for which the Ne^+ curves and the O^+ curves are parallel to within our experimental precision is adequate for comparison; we use the undrawn 2×10^{-12} ordinate. One of the Ne^+ curves crosses this ordinate 1 v higher, and the other 0.9 v higher, than 21.53 v. We emphasize the former, and therefore subtract 1.0 v as the correction to be applied to the voltage at which the O^+ curves cross the same ordinate. The latter three curves cross between 19.3–18.0 v, and the corrections bring these to 18.3 and 17.0 v as limits on the threshold energy for producing O^+.

We next compare these numbers with Hagstrum's evaluation[7] of the threshold for fragmentation of gaseous CO into gaseous C and O^+ with neither fragment having kinetic energy. He designates this as A_0 and gives 23.2 v, which is 4.9–6.2 v above our result for fragmentation of adsorbed CO into gaseous O^+ and adsorbed C. This large difference is believed real, and is discussed later.

The ionization potential of a noble gas is often used similarly to calibrate thresholds in experiments on the fragmentation of gaseous molecules; validity depends on the assumption, also used in our measurement, that the intensity of the calibrated process falls off with dedecreasing electron energy in just the same way as the current of rare-gas atomic ions. This assumption has never been justified from first principles for fragmentation of gaseous molecules, but seems warranted by years of favorable experience. Its extension to the case of adsorbed molecules in the present work is rather adventurous. We merely mention the additional assumption, required in the present work but not in fragmentation of gaseous molecules, that if Ne is adsorbed to any surface, its liberation by electron bombardment makes no contribution to the Ne^+ current.

In making these measurements, we admitted Ne, together with CO and/or O_2, to a gauge pressure of about 10^{-5} mm each and measured the O^+ and Ne^+ (mass 20) ion currents at frequent small steps of electron energy from 50 v downward. *IC* was 90 v negative with respect to *S*, giving a drawout field of about 100 v per cm. The observed threshold was independent of this field from above 90 v to below 10 v. *S* was 1.5 v positive with respect to G_2, making *S* the most positive surface, so that electrons passing G_2 have their maximum energy as they strike *S*. Therefore the threshold for Ne^+ involves electrons adjacent to *S* and should be directly comparable to the threshold for O^+ from adsorbed CO.

Repeated runs with Ne agreed, in the region used for calibration, about as well as the two shown in Fig. 9. Ion currents above this region are proportional to Ne pressure; difference in this pressure causes the divergence shown in the two curves at higher electron energies. Reproducibility of 15 independent runs for O^+ ions, all at the same electrode potentials, is indicated by the separation between the three curves. For reasons not understood, flashing *S* may start the curve for O^+ on a new track which can differ appreciably from the preceding track. However, on any one curve, reproducibility is good, as indicated by lack of scatter in the points associated with each curve. All 15 runs for O^+ ions from *S* gave thresholds within the range covered by the three curves shown, regardless of pressure or admission of O_2.

The vertical dot-dash lines indicate established thresholds for various processes in the gas phase which

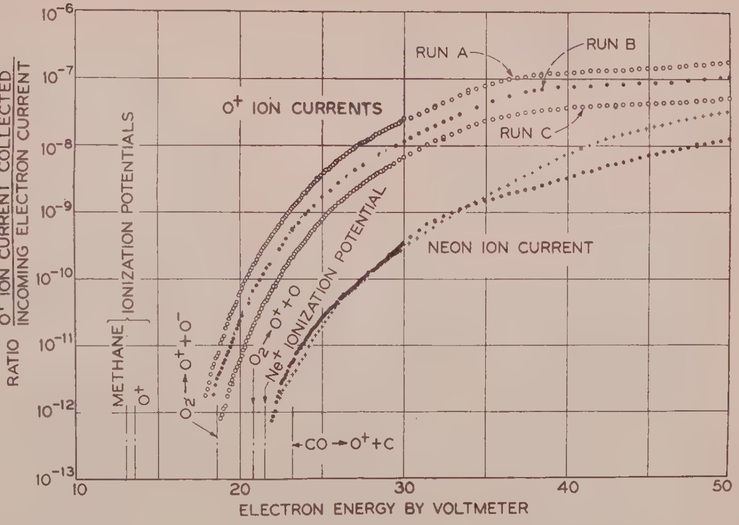

FIG. 9. Tests for threshold of O^+ ion emission. Three curves (A, B, and C) of O^+ ion yield from S vs electron energy in vicinity of threshold, and two curves of Ne^+ ion yield in gas phase. The curve for O_2^+ peak in ambient gas about 0.14 of CO^+ peak. For the two runs, A and C, of O^+ from S, the O_2^+ peak in the ambient was only 1.8% of the CO^+ peak.

could be relevant. These include the previously mentioned ionization potential of Ne and the threshold for O^+ and C as fragments of CO. Several conceivable difficulties have probably been avoided. First, if methane or atomic oxygen were present in the ambient, they would cause the curves to flatten out and head toward the 13.1- and 13.6-v energies of ionization (indicated at the left of the figure), respectively; no such flattening occurred. If O^+ from gaseous CO were important, an abrupt nearly vertical drop should occur near 23.2 v, its threshold; it was never observed.

Because the experimental threshold was unchanged whether O_2 was absent or abundant in the ambient gas, we conclude that the ion current near threshold involved only O^+ ions from adsorbed CO and not from adsorbed O_2, even though the published dissociation potentials of O_2 (shown in Fig. 9) are suggestively close to our experimental values. We also conclude that the threshold for liberation of O^+ from *adsorbed* CO measured in this way is about 6 v below the threshold for the corresponding process in the gaseous phase.

DISCUSSION

Analysis of Growth and Decay Curves

These can be reproduced reasonably well by a theory mentioned above: Following Langmuir, assume that an incoming CO molecule is reflected if it strikes a site already occupied either by a CO molecule or a C atom, and call β the probability that any vacant site will become occupied per second. Adsorption of CO with removal of C atoms as fast as they are formed is most simply considered, and is probably nearly realized, for curve C of Fig. 6. Here the scarcity of carbon inside S probably permits rapid diffusion inward from the surface; oxidation of surface C atoms also helps. For this situation, CO fills

$$dn/dt=\beta[N-n] \tag{1}$$

sites per second, where n is the number of sites occupied by CO and N is the total number of sites on $S(=1.11\times10^{14})$; the number of vacant sites is then $N-n$. β is the number of CO molecules colliding with a site per second, times the probability that a molecule adheres. Because $(1.05\times10^6 P_{\text{mm}})$ CO molecules collide[11] with a site per second, one can compute an adhering probability from experimental values of β. For this simple situation, Eq. (1) gives

$$n=N(1-e^{-\beta t})$$

or, in terms of ion current,

$$I=I_{\max}(1-e^{-\beta t}). \tag{2}$$

The ratio of the asymptote and half-maximum ion currents for curve C in Fig. 6 gives $\beta=0.025$ without regard to absolute magnitude of ion current. Curve C is replotted in Fig. 10, and the dots give values of I computed from Eq. (2), assuming time to begin 13 sec after extinguishing the flashing current. Complications during cooling are minimized simply by assuming that the zero of theoretical time occurs a few seconds after that of the experimental curve. Any realistic choice will not affect β critically nor the fit of the points to the curve. The points plotted agree satisfactorily over the upper two orders of magnitude. Comparison of the ambient CO peak in the present situation with that observed when CO was admitted at a known pressure gives $P=1.05\times10^{-7}$ mm; with $\beta=0.025$, the adhering

---

[11] See, for example, S. Dushman, *Scientific Foundations of Vacuum Technique* (John Wiley & Sons, Inc., New York, 1949), p. 17.

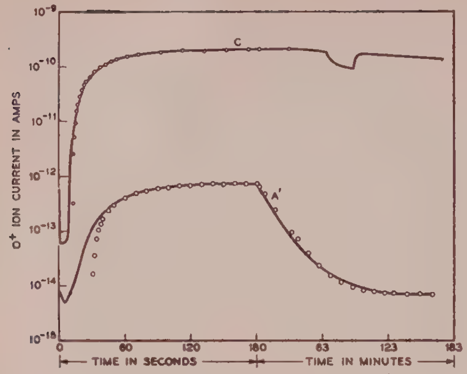

FIG. 10. Tests of theory in predicting growth and decay curves. The curves are tracings of experimental chart recordings and the points are theoretical, using constants given in Tables I and II.

probability is 0.22.[12] We note that the ionization gauge pressure was 1.0×10^{-6} mm, but the mass spectrometer showed components other than CO, and the composition of gas undoubtedly differed in gauge and spectrometer. We believe that the agreement of 0.22 with the 0.2 published by Eisinger[12] illustrates the desirability of using the spectrometer, rather than the gauge, to measure the abundance of any gas.

To include the destruction of adsorbed CO molecules and diffusion of carbon into the body of S, the two differential equations are:

$$dn/dt=\beta[N-n-c]-\alpha n \tag{3}$$

and

$$dc/dt=\alpha n-k(c-c_0), \tag{4}$$

where β, N, and n have the meanings given above. α is the probability that an adsorbed CO molecule will be split into a free O^+ ion and an adsorbed C atom during 1 sec. It is the product of the number of incoming electrons striking a site and the reaction probability; Fig. 8 gives the relative dependence of this probability on electron energy. Then αn is the number of CO molecules converted per second. Similarly, c is the number of adsorbed C atoms at any time, and c_0 is the number at completion of the flash. Since relatively few C atoms evaporate during a flash, c_0 is approximately the number in equilibrium[13] with the concentration in the volume. k is the probability that an adsorbed carbon atom in excess of this equilibrium will disappear each second and thus make the vacated site available for CO; so $k(c-c_0)$ is the number of sites thus made available per second.

These equations can be solved by standard methods. Using the facts that at $t=0$, $c=c_0$ and $n=0$, n is given by

$$n=\frac{k\beta(N-c_0)}{\alpha\beta+\alpha k+\beta k}\left[\frac{m_2(m_1+k)}{k(m_1-m_2)}e^{m_1t}+\frac{m_1(m_2+k)}{k(m_2-m_1)}e^{m_2t}+1\right], \tag{5}$$

where

$$m=-\frac{(\alpha+\beta+k)}{2}\pm\frac{[\alpha^2+\beta^2+k^2-2(\alpha\beta+\beta k+\beta k)]^{\frac{1}{2}}}{4} \tag{6}$$

the positive sign being associated with m_1. Since α, β, and k are positive quantities, m_1 and m_2 are inherently negative and m_2 is always greater in absolute value than m_1. Therefore, after a sufficiently long time, the exponential in m_2 becomes negligible compared to that in m_1; furthermore, if the coefficient of the m_1 exponential is A, that of the m_2 is $-(A+1)$. If we take n proportional to I, the coefficient of the bracketed term in Eq. (5) is proportional to I_∞, which is readily evaluated in Fig. 6 or Fig. 4. One can then choose a time sufficiently large on the decline that the m_2 exponential can be neglected, giving the product of A and the m_1 exponential. A table of corresponding pairs of values for A and m_1 was then made. For each pair, values of m_2 were chosen to give the maximum value of I and the time at which the maximum current occurred was also computed. These comparisons determined m_1, m_2, and A, and thus k, α, and β. Computed ion currents using these graphically determined values are shown by points in Fig. 10 associated with the corresponding experimental tracing. The agreement is satisfactory, except for the initial chaotic period.

Table I gives values of α, β, and k determined graphically from Eqs. (3) and (4) as indicated, using curves of collected ion current vs time. These are consistent internally and with published results. The "fraction of the sites clean at $t=0$" was computed from the amplitudes of O^+ ion current curves, relative to curve C, assuming that all sites were clean as curve C began. Derived values in Table I such as α, β, k, etc., thus generally depend only on the *shapes* and relative magnitudes of these curves, and not on absolute magnitudes. Of the *fundamental* constants, the "adhering probability" alone depends only on shape and is computed from β and CO pressure, as indicated.

To compute "reaction probability," we must use the transmission of the spectrometer to convert the collected ion current to rate of liberation of O^+ ions from S. Since α is not involved in Eqs. (1) and (2), which govern the behavior of O^+ ion current for curve C, the transmission is also necessary to convert the observed collected current to the liberated current for this curve in order to evaluate α. Measurements indicate that roughly one ion passes through the spectrometer for

---

[12] J. Eisinger [J. Chem. Phys. **27**, 1206 (1957)] obtained 0.2 for the probability that a CO molecule adheres to the 133 face of W; Eisinger assumed a somewhat different mechanism and made his tests at a lower temperature than was possible by our method.

[13] Build-up and decay curves taken immediately after flash essentially duplicate those taken after holding S at 1050°–1300°K for about 20 hr following flash but before permitting adsorption to begin. This result suggests that the equilibrium distribution of carbon between surface and volume, which is approximately achieved during flash, is probably not very sensitive to temperature.

TABLE I. Values of α, β, and k determined graphically from Eqs. (3) and (4).

Curve	P_{CO}(mm)	E(v)	I_{ma}	α	β	k	Fraction clean at $t\equiv 0$	Adhering probability	Reaction probability
C	1.05×10^{-7}	100	0.85	0.0025	0.025	...	1.00	0.22	2.2×10^{-6}
A	8.00×10^{-8}	253	2.60	0.0011	0.021	9.32×10^{-6}	0.0079	0.25	7.8×10^{-6}
P	2.10×10^{-8}	250	2.70	0.0085	0.0066	28.3×10^{-6}	0.026	0.30	3.5×10^{-5}

each 200 leaving S, but this is uncertain to ±50%. Using this value, the listed reaction probabilities for all curves were computed, as well as α for curve C.

Although the reaction probability depends on electron energy as indicated relatively in Fig. 8, the actual spread is probably less than indicated in Table I because of errors in fitting curves. Most derived parameters in Table I are fairly consistent internally, but α introduces some diffculty. It was computed above, simultaneously with other constants, from the shape of growth and decay curves; it can be estimated independently of other constants from the pulses of Fig. 5. From Eq. (3), if one assumes that the O^+ ion current is directly proportional to n, then α should be greater than, or equal to, $-(dI/dt)/I$, the percentage decay rate. In Table II, we tabulate α and the reaction probability for the beginning and end of the first pulse of Fig. 5(a) and for the beginning of the first pulse in Fig. 5(b).

These values tend to be greater than those of Table I, especially at the beginning of the pulse, but the discrepancy is not extreme and we have the possibility of the α phase as mentioned earlier. But, except for the third entry, the values so computed are minima; for the other entries, the term in Eq. (3) containing β has some value, which would increase both α and the reaction probability so computed.

The recovery mechanism, attributed primarily to diffusion of carbon residue atoms into S, produced values of k on fitting the *shape only* of the curves. We must compare implications of these values to any independent published diffusion data since k was defined as the probability that a carbon atom diffused from the surface during 1 sec. We have assumed that the carbon atoms formed during run C (Figs. 6 and 11) diffused essentially as fast as formed into molybdenum free of C. This would require a k of about 0.5 for the maximum diffusion rate. In atomic terms, the diffusion[14] constant $D=\lambda^2\nu$, where λ is the distance between successive interstitial positions of the carbon atom, or about 3.5×10^{-8} cm in Mo, and ν is the frequency at which the diffusing atom jumps from one position to the next; ν and k are thus approximately the same and $D=6\times10^{-16}$ on this basis. For C in[15] Ni, $D=0.909\times\exp(-20\,200/T)$. These two values of D are equal at 578°K; the temperature of S as curve C was taken is at least this high. The rate of interstitial diffusion of carbon in molybdenum is probably intermediate between the rates in Ni and W; for the latter, two sets[16,17] of data are available. The first gives $D=0.31\times\exp(-29\,700/T)$ and our experimental value of D would then occur at 880°K; probably this slower diffusion rate explains the fact that when S is of tungsten we have been unable to observe effects similar to those shown in Fig. 6 by points b and c. Keimer *et al.*[17] give $D=2750\exp(-56\,200/T)$ for diffusion of C in W; our experimental value would then occur at 1300°K. The latter equation suggests that diffusion of C could not be important in our experiments with tungsten. Because the decay and recovery behavior of W and Mo are essentially alike, we believe that the equation of Pirani and Sandor is more accurate. This view is supported by the abnormally large value of 2750 for D_0 in Keimer's equation. If this last equation is neglected, our interpretation does no violence to published diffusion data.

The data permit an estimate of the transmission of the spectrometer for comparison with the measured value of $5\times10^{-3}\pm50\%$. For Fig. 5(b), the O^+ pulses are horizontal at the end of each pulse, signifying that O^+ ions leave the surface at the same rate as CO molecules are adsorbed. At the beginning of each pulse nearly every site on S is occupied by CO molecules and at the end only 78% of the sites are occupied, judged by relative height. From the height of the CO peak in the ambient, its pressure was 1.2×10^{-8} mm, and so $\beta=1.26\times10^{-2}$. So with an adhering probability of 0.25, we have 0.315×10^{-2} molecules adhering to a site per second, or a total of 7.7×10^{10} on S. The same number of O^+ ions leave and carry a charge of 1.24×10^{-8} amp; we measure 1.73×10^{-10} amp, so that the com-

TABLE II. α and reaction probability under pulsed operation.

Experimental condition	α	Reaction probability
At beginning of first pulse, Fig. 5(a)	0.036	4.2×10^{-5}
At end of first pulse, Fig. 5(a)	0.0071	4.1×10^{-6}
At beginning of first pulse, Fig. 5(b)	0.046	2.1×10^{-4}

---

[14] See, for example, S. Glasstone, K. Laidler, and H. Eyring, *The Theory of Rate Processes* (McGraw-Hill Book Company, Inc., New York, 1941), p. 518. ν is the temperature-sensitive term and is *not* the frequency of oscillation of the diffusing atom in an interstitial pocket.

[15] J. J. Lander, H. E. Kern, and A. L. Beach, J. Appl. Phys. **23**, 1305 (1952). We know of no published data for C in Mo.

[16] M. Pirani and J. Sandor, J. Inst. Metals **73**, 385 (1947). $T=1780°\text{–}2070°$K.

[17] G. S. Keimer, L. D. Efros, and E. A. Voronova, Zhur. Tekh. Fiz. **22**, 858 (1952).

puted transmission is 1.4×10^{-2}, or about 2.8 times that measured; considering the assumptions involved and the difficulty in measuring transmission, the discrepancy is not alarming.

Comparison of Products in Gaseous and Adsorbed Phases

When electrons strike gaseous CO, the following reactions have been demonstrated[18,19]:

$$\begin{aligned} &\rightarrow CO^{+}+2e && 14.1\text{ ev}=\text{threshold } A\\ &\rightarrow C^{+}+O+2e && 22.8\text{ ev}=\text{threshold } B\\ &\rightarrow C^{+}+O^{-}+e && 20.9\text{ ev}=\text{threshold } C\\ CO+e&\rightarrow C+O^{+}+2e && 23.2\text{ ev}=\text{threshold } D\\ &\rightarrow C+O^{-} && 9.5\text{ ev}=\text{threshold } E\\ &\rightarrow C^{-}+O && 23.65\text{ ev}=\text{threshold } F. \end{aligned}$$

These were not all discovered with equal ease; D came[18] considerably later than A, B, C, and E, while F was discovered[19] still later.

Our own examination of the products from CO adsorbed to Mo disclosed only O^+; any other ionized products are certainly far less abundant. Un-ionized products were not found and probably do not leave the system, although their absence is less certain. The strong tendency of the experiment to exclude all analogs of the many reactions in the gaseous phase except D suggests that adsorption either orients the CO to favor D, and/or that energy considerations suppress the others. The work function of the surface is higher than the electron affinity of C or O; this may explain the absence of C^- and O^-.

Adsorption of CO increases[12] the photoelectric work function of W, implying that CO is absorbed with negative polarity outward. This, and the preponderance of O^+ as the major product in the present experiments, suggest that CO adsorbs with the negative end of the dipole residing in the O atom,[20] and the C atom adjacent to the Mo, the orientation proposed by Redhead.[8] Such orientation might explain the absence of C^+ ions in the product, but would not explain the absence of CO^+ or O^-, which are observed dissociation products in the gaseous phase. However, D is the only reaction in the gaseous phase in which the products leave with appreciable kinetic energy at the experimental threshold. Presumably any particle observed in the present experiments must have come from a molecule excited to an electronic state which dissociates to give kinetic energy to the product atoms. Uncharged carbon, the other product of the state giving D, probably remains on the Mo because the CO molecule is oriented as indicated. We hope to determine whether such selectivity is followed in the release of ions from other adsorbed molecules. Since the β phase of adsorbed CO involves a double bond from carbon to the adsorbing metal, the additional bond between C and O is probably double,[2 resembling the bond in gaseous CO_2 more than that in CO. Published work[22] on fragmentation in gaseous CO_2 dealt only with positively ionized fragments, so that significant comparison of our results with fragmentation in CO_2 is not possible.

Heat of Adsorption of Carbon Atom

The fact that treatment of S for hours at high temperatures in vacuum removes only insignificant amounts of carbon from the surface implies a large heat of adsorption. We attempted to estimate a minimum value using a cycle-type argument. The argument presented[23] neglected the energies lost after collision by the incoming electron and by the electron liberated in forming the O^+ ion. Probably each electron enters the metal and loses energy equal to the work function. When this loss of energy is considered, the computed heat of adsorption of the carbon atom would depend critically on the kinetic energy possessed by the O^+ ions liberated at threshold. Our efforts to measure this kinetic energy were not successful.

CONCLUSIONS

The only dissociation product of any abundance when CO molecules adsorbed to Mo or W are struck by electrons of roughly 10^2-ev energy is the O^+ ion. Since this will drift toward electrodes of negative polarity, the process may be of some importance in contaminating oxide-coated cathodes. The kinetics of the O^+ liberation process agree with some simple equations given, liberation being first order in the electron current. The fact that O^+ is the only product liberated in the process stands in strong contrast to the variety of products in the fragmentation of gaseous molecules of CO or CO_2

ACKNOWLEDGMENTS

F. C. Unterwald gave valuable help in the experimental work. Discussion with several colleagues, especially H. D. Hagstrum, E. Helfand, A. R. Hutson, P. P. Kisliuk, and Howard Reiss are gratefully acknowledged.

APPENDIX

Behavior of Cl^+ and Fl^+

Figure 11 shows peaks for F^+ and Cl^+; the corresponding negative ions were never observed. F^+ is prominent for 950° and 1700°K but absent at 1250°K. Its behavior was erratic and it frequently disappeared but with a new S filament, heating to 1600°K or above usually revived the F^+ peak. Its amplitude then usually persisted for a few hours. The Cl^+ peaks are sharp and have high amplitude on the chart for 950°K, but have very low amplitude and are diffuse when S is hot. Their behavior is much more reproducible than that of F, but both F and Cl gradually disappear after repeatedly heating S. Both were much more prominent in each of the four molybdenum filaments than in the one tungsten filament examined.

---

[18] H. D. Hagstrum and J. T. Tate, Phys. Rev. **59**, 354 (1951).

[19] C. R. Lagergren, Ph.D. thesis, University of Minnesota. Minneapolis, Minnesota (1955, unpublished).

[20] B. Rosenblum, A. H. Nethercot, Jr., and C. H. Townes [Phys. Rev. **109**, 400 (1958)] show that the negative charge of the CO dipole in the *gaseous* phase resides in the carbon atom. Conditions in the adsorbed phase could be entirely different, however.

[21] See, for example, L. Pauling, *The Nature of the Chemical Bon* (Cornell University Press, Ithaca, New York, 1960), 3rd ed.

[22] H. D. Smyth and E. C. G. Stueckelberg, Phys. Rev. **36**, 4 (1930).

[23] G. E. Moore, Bull. Am. Phys. Soc. **5**, 380 (1960).

Mayer and Kimball and their students have shown[23,24] that monatomic films of F on W are stable beyond 2600°K; we believe, therefore, that F tends to have the same abundance on S at 950° and 1700°K. Because the thermionic emission of electrons is approximately that of clean Mo, the coverage with F must be less than monatomic. Apparently S contained initially a small quantity of F and Cl which comes to the surface more readily at 1700°K than at 1250°K and is stable even above 1700°K. Nothing yet published gives the stability of Cl on Mo or W, but our results suggest that a Cl partial layer is stable at 1050°K but completely disappears in a few minutes at 1250°K. The present method, however, gives no method for determining θ for such a layer unless it is much the most abundant species. Nor do we know the chemical form for Cl and F on S. Although Cl^+ and F^+ ions readily left S under electron bombardment, they were never observed in the ambient gas. In several, but not all, respects the behavior of these ions from S resembled that of O^+ ions. Curve D of Fig. 6 shows growth and decay of Cl_{35}^+ ions from S under electron bombardment, for comparison with similar curves of O^+.

Figure 11 shows three growth curves for Cl_{35}^+, the dotted curve being taken first with continuous flow of electrons into S, which operated at 950°K. A slow decay became evident after about 80 sec; the time scale was then slowed. Most of the decay was recovered at the point indicated, on heating S to 1050°K; higher temperatures were usually still more effective, especially with S new. For the two solid-line curves, the incoming electron current was pulsed as indicated. For the lower curve, S operated at 950°K and for the upper, at 1050°K. As with the curves for O^+ ions from S, no slow decay is observed when the incoming electron current is pulsed. For Cl^+ and F^+, no "pocket" similar to AB of Figs. 4 and 5 was ever observed; it would not be expected for any species arriving at the surface of S by outward diffusion.

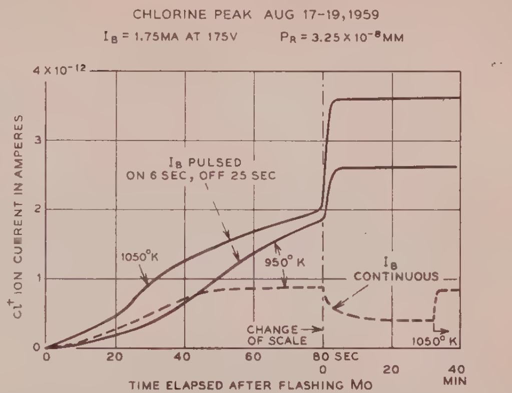

FIG. 11. Effect of temperature and pulsing on Cl^+ ion current from S. Ion currents are plotted on a linear scale. Dotted curve taken under same conditions as curve D of Fig. 6, with incoming electron current not pulsed. For both curves drawn by solid lines, electron current was pulsed as indicated. For upper curve, S was held at 1050°K, which is 100° hotter than for lower curves. Note that no decline occurs when electron current is pulsed with S at either temperature.

A *short-time* decay is always observed during each pulse for both Cl^+ and F^+. This is very similar to that for O^+ ions. Figure 5(c) shows this for F^+; Cl^+ behaves similarly with an exponential decay. We believe that the cause is disappearance of the Cl and F from the surface, but the carbon residue from CO may also be a factor. The yield of Cl^+ from S was directly proportional to the incoming electron current, resembling the yield of O^+ ions shown in Fig. 7, but the experimental points scattered more than for O^+. Measurements for liberation of F^+ ions also suggest the same relationship, but the scatter was even greater. The portion of the surface covered by Cl and F is unknown but small, and its variation with time probably caused the scatter. No measurements of threshold or of the effect of voltage were made.

For the three pulses of F^+ current of Fig. 5, the curves begin at point a and end at c, where they are horizontal. We believe that the number of F-containing molecules at c bears the same relationship to those at a as the F^+ currents which are in the ratio 0.124 to 1. At the horizontal section, F-containing molecules form on S at the same rate as they are destroyed. Since about 200 ions are liberated from S for each collected, this rate is 3.4×10^7 F-containing molecules per second. Neglecting any arrival of F, we obtain the minimum amount on the surface. Integrating the area under a pulse shows that we collect 1.87×10^9 ions, and in so doing reduce the occupancy to 0.124 of its value at the beginning of a pulse. So the original occupancy was 2.14×10^9 F-containing molecules. F therefore occupies, at the beginning of a pulse, only one site in 52 000 of the 1.11×10^{14} available. Since this same fraction represents the relative number of F to O-containing molecules struck by incoming electrons, comparison of the ratio of O^+ to F^+ currents produced shows that the yield of F^+ per electron striking an F-containing molecule is more than 10 times the yield of O^+ per electron striking an adsorbed CO molecule. If we assume that F diffuses to the surface to build up the deposit during the idle period, these figures are not changed greatly.

---

[23] M. Metlay and G. E. Kimball, J. Chem. Phys. **16**, 779 (1948).
[24] T. L. Bailey, J. Chem. Phys. **28**, 792 (1958).

JOURNAL OF APPLIED PHYSICS VOLUME 32, NUMBER 7 JULY, 1961

Electric Breakdown Strengths of Single and Laminated Films of Vinyl Chloride-Acetate

Robert G. Greenler and Robert M. Kay
Research Laboratories, Allis-Chalmers Manufacturing Company, Milwaukee 1, Wisconsin

(Received January 20, 1961)

The electric breakdown strengths of thin, unsupported vinyl chloride-acetate films in the thickness range of 1200 to 50 000 A have been measured. No dependence of breakdown strength on thickness is found in this region. Composite films composed of alternate layers of plastic film and thin conducting layers of silver show essentially the same breakdown strength as do single films. Five and six layer laminates which do not contain metal layers show a breakdown strength greater by a factor of 2 than that of single films of the same total thickness.

INTRODUCTION

THE electric breakdown strengths of some dielectric materials have been reported to increase for samples which are sufficiently thin.[1–5] The thickness at which this effect occurs varies for different materials, but is the order of a few thousand angstroms. The two approaches to a theory of dielectric breakdown which have been most fruitful are those ascribed to Frölich[6] and von Hippel.[7–9] Both of these theories account, at least qualitatively, for the observed rise in breakdown strength for thin samples although their assumptions differ. Because of the prominent place in these theories occupied by the prediction of this effect, measurements on the variation of breakdown strength with thickness of thin crystalline films and thin amorphous films are of interest.

EXPERIMENTAL TECHNIQUES AND APPARATUS

Standard techniques for preparing thin plastic films and for measuring electrical properties were found to be unsatisfactory for films ranging in thickness from 1200 to 50 000 A. The following satisfactory methods were developed for the investigation.

Film Preparation

Films are made of vinyl chloride-acetate copolymer[10] dissolved in dichloroethane. The films are produced by letting a few drops of the solution spread on the surface of water and remain till the solvent has evaporated, leaving the plastic film floating on the water. This film is picked up on a glass ring which has been coated with the same plastic material. The entire operation is carried out in a box which is nearly saturated with an atmosphere of dichloroethane to slow the rate of evaporation of the solvent from the plastic solution. The lower evaporation rate allows the film to spread to a more uniform thickness before it hardens and also eliminates many of the streaks of nonuniformity caused by evaporation from the surface of the drop of solution while it is being transferred from the bottle to the water surface. This procedure results in the production of films which are considerably more uniform than those made in a room atmosphere.

Fresh films are successfully laminated by putting them in contact with each other in vacuum. With this treatment the bonding is such that the resultant composite film has the appearance of a single film.

Since measurements indicate that electric strength is affected by moisture, the freshly made films are stored in a desiccator overnight and are removed immediately prior to testing.

Measurement of Electric Breakdown Strength

Figure 1 shows the test device used for making electric strength measurements. The film, affixed to its glass ring, is mounted on an adjustable, calibrated microscope stage. This stage is removable and is also used to position the film in the thickness-measuring optical system. By means of the calibrated screw motion of the stage, the same points of the film can be accurately located for breakdown testing as were previously located for thickness measurements.

Electrical contact is made to the film through mercury electrodes. The lower electrode is a pool of mercury about 1 cm in diameter while the upper electrode consists of a drop of mercury contained in a hollow-tip copper electrode. The diameter of the contact area of the upper mercury electrode is less than a millimeter The mercury electrodes may conveniently be freed of dust particles by passing a piece of Scotch tape over the surface. The use of these mercury electrodes solves many problems which make other (more standard) techniques unsuitable for thin films. The advantages of mercury

---

[1] A. E. W. Austen and W. Hackett, Nature **143**, 637 (1939).

[2] A. E. W. Austen and S. Whitehead, Proc. Roy. Soc. (London) **A176**, 33 (1940).

[3] K. W. Plessner, Proc. Phys. Soc. (London) **B60**, 243 (1948).

[4] A. E. W. Austen and H. Pelzer, J.I.E.E. **93**, 525 (1946).

[5] S. Whitehead, in *Dielectric Breakdown of Solids* (Clarendon Press, Oxford, 1951), gives a critical review of data and theories of dielectric breakdown.

[6] H. Fröhlich, Proc. Roy. Soc. (London) **A160**, 230 (1937); **172**, 94 (1939); **178**, 493 (1941); **188**, 521, 532 (1947).

[7] A. von Hippel, J. Appl. Phys. **8**, 815 (1937).

[8] R. J. Seeger and E. Teller, Phys. Rev. **54**, 515 (1939); **56**, 352 (1939).

[9] F. Seitz, Phys. Rev. **76**, 1376 (1949).

[10] VYNS-3, produced by Bakelite Company, 30 East 42nd Street, New York 17, New York, contains approximately 90% vinyl chloride.

electrodes for this problem are:

(1) They provide an intimate contact with the film without the danger of applying localized high pressure or doing mechanical damage to the film, as for example, with solid electrodes.

(2) They produce no thermal or chemical damage to the film as might be expected to result from the deposition of thin metal films by thermal evaporation, sputtering, or chemical methods.

(3) The electrodes have no sharp edges which tend to give high local values of the electric field and cause premature breakdown.

(4) After breakdown, the mercury shorts out through the film giving a positive indication that the breakdown has occurred. With other electrodes this has been a difficult problem for testing very thin films.

The electrical breakdown tests were made by applying a linearly increasing voltage across the film until breakdown occurred. Figure 2 shows the circuit which was used to apply and measure the breakdown voltage. Resistance R_1 and capacitance C_1 were adjusted to give approximately the same rise time to breakdown (5 to 8 sec) for films of various thicknesses. Keeping the rate of increase of the electric field constant in this manner should avoid the slow variation of breakdown strength with pulse duration which is described by Inuishi and Powers.[11] Breakdown voltage is read from the electronic voltmeter. To facilitate reading, maximum voltage across the voltmeter is temporarily maintained after breakdown by capacitor C_2 which is blocked from discharge through the film by the diode D.

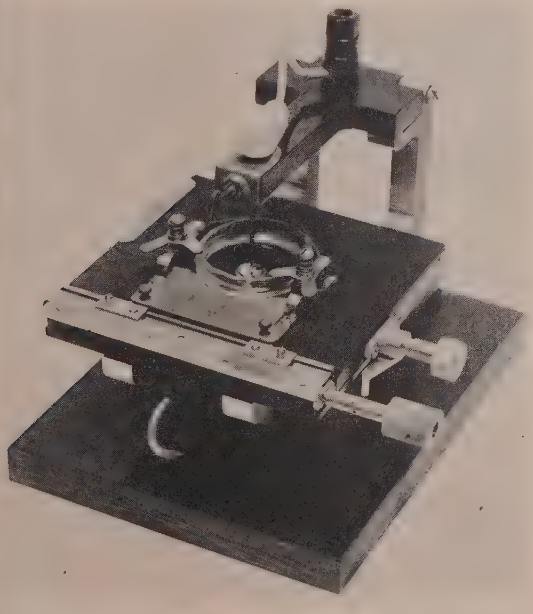

FIG. 1. Test device for measuring the electrical breakdown strengths of thin plastic film.

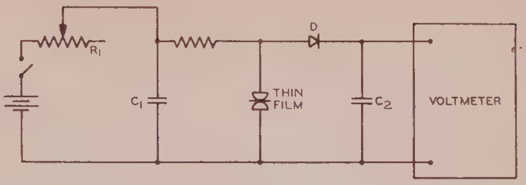

FIG. 2. Circuit diagram for electric breakdown measurements.

Measurement of Film Thickness

The thicknesses of most of the films were measured using the interference fringes of equal chromatic order which have been described by Tolansky.[12] The thickness of a film can be calculated from the position of the interference maxima (or minima) in the spectrum of white light reflected from the film. The method as applied to this problem generally gave thickness measurements which are reproducible to within 1%. This method of determining thickness works very well for films which are as thick as a wavelength of light or thicker, but for films thinner than about 2500 A it proved to be easier to determine the thickness by comparison with a barium stearate stepgauge.[13] Ambiguity in the order of interference can be removed by noting the position of the broad interference maximum which occurs in the visible or near infrared. With the approximate thickness determined, the step gauge yielded thickness measurements accurate to about 5% on films as thin as 1200 A.

RESULTS

Figure 3 shows the results of breakdown tests on 50 areas sampled from 37 different single plastic films, ranging in thickness from 1200 to 50 000 A. These data are plotted as open circles. Each point represents the mean of about 25 separate breakdown tests in a small area surrounding the point at which the thickness measurement was made. Occasionally the breakdown voltage of a particular spot on a thin film is zero or a few volts when most of the other values are much higher. It seems reasonable to assume that such values result from faults in the form of holes or bubbles in the film. Since the object of these measurements is not to determine the fault count of the films, but rather to measure the breakdown strength of those areas of the film where there are no faults, it seemed desirable to accept some criterion which would reject these particularly low values. The criterion which was adopted rejected all values below one-half of the accepted average of the set

---

[11] Y. Inuishi and D. A. Powers, J. Appl. Phys. 28, 1017 (1957).

[12] S. Tolansky, *Multiple Beam Interferometry* (Clarendon Press, Oxford, 1948).

[13] A stepgauge for the range 2 to 16 μin. is made by the General Electric Company.

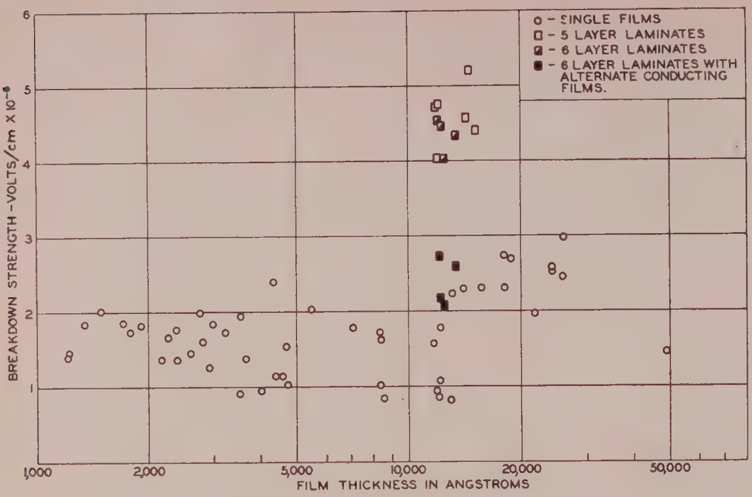

FIG. 3. Breakdown strength of vinyl chloride-acetate films.

of values. This resulted in discarding approximately 1 point in 14 of all the measurements made on single films.

Also shown in Fig. 3 are the test results of six composite films, each consisting of five laminated layers. These data are plotted as open squares.

Another set of composite films was prepared in which half of each film was given a light coating of silver by thermal evaporation of silver in a high-vacuum system, while the other half of the film was left uncoated. Six of these films were laminated to form a single composite film. Half of the composite film then consisted of six laminated plastic layers interleaved with five thin conducting layers of silver while the other half consisted of the same films without the conducting layers. Four such composite films were made. The test results on the region which contains the conducting layers are shown in Fig. 3 as the solid squares, while the data on the other side without the conducting layers are shown by the half-solid squares.

The following conclusions may be drawn from the data shown in Fig. 3.

(1) There appears to be no dependence of electric breakdown strength on thickness in the range 1200 to 50 000 A for these vinyl chloride-acetate single films.

(2) The laminated films which contain alternate layers of plastic and thin conducting layers of silver exhibit breakdown strengths which are not significantly higher than the single plastic films of the same thickness.

(3) Composite films composed of five or six thin plastic films laminated together show a breakdown strength which is higher by a factor of two than for single films of the same thickness.

The data on the composite films come from 10 composites, each consisting of five or six laminated films. Since these films were made in five different batches, it seems quite unlikely that the high breakdown values are the result of any pecularity of technique in making the films. Single films, made by the identical method, were cycled in vacuum simulating the treatment received by the films during lamination. The data on these films fall in the region of other single films indicating that the high-breakdown values of the composites were not a result of the special handling the films received during lamination, but are actually a property of the composite films.

It is of interest to note the effect of lamination on the number of low-value breakdowns attributed to the existence of faults in the films. The number of breakdown values rejected according to the previously described criterion averages 1 in 14 for the single films tested, whereas it is only 1 in 60 for the laminated films (which do not contain metal layers). No great effort was made to control the number of faults in the films once a technique was worked out which produced films of a reasonable quality for testing purposes. This comparison does illustrate the expected lowering of fault count of composite films.

DISCUSSION

The average coefficient of variation of a group of breakdown measurements, represented by one point in Fig. 3, is about 4%, much less than the magnitude of scatter between different points. This would seem to rule out the statistical nature of the breakdown phenomenon as the cause of scatter and would rather indicate that some variable characteristic of the films (other than thickness) is responsible for the data spread. It may be that the scatter of data between different films is the result of different degrees of orientation of molecules in the polymer film. Such difference in orientation might result from mechanical stress while handling the film or from surface contamination of the water or which the films were spread. An oriented polymer would be expected to have a longer mean free path for electrons than would an amorphous polymer and, hence, a lower breakdown strength according to Frölich's theory.

It is possible that films thinner than the 1200-A films investigated here may still show a rise in breakdown strength; however, the increase in breakdown strength of the laminated films is quite surprising since the thin films which were laminated to produce the composite films showed no increase in strength over the thicker films. The higher breakdown strength for laminated films than for the individual films from which they were made does not appear to be readily explainable in terms of difference of mean free path.

JOURNAL OF APPLIED PHYSICS VOLUME 32, NUMBER 7 JULY, 1961

Stress Distribution on the Boundary of an Elliptical Hole in a Large Plate during Passage of a Stress Pulse of Long Duration (Major Axis Normal to the Wave Front)

A. J. Durelli and W. F. Riley
Illinois Institute of Technology and Armour Research Foundation, Chicago 16, Illinois

(Received November 4, 1960)

A solution to the problem of the stress distribution on the boundary of an elliptical hole in a large plate during passage of a compressive stress pulse of relatively long duration is presented. The major axis of the ellipse is normal to the wave front. The solution was experimentally obtained by using a low modulus model material in a combined photoelasticity and moiré analysis. The long-duration stress pulse was applied by loading a small region on an edge of the plate with a falling weight. The results of the investigation indicate that the falling weight loading generates a biaxial state of stress at every point in the plate, which varies with time. The maximum dynamic compressive stresses on the hole boundary can be computed with a fair degree of accuracy by using: (a) the equation of Inglis for the static stress distribution on the boundary of an elliptical hole in any two-dimensional uniform and axial system of combined stress and (b) the biaxial stresses, at the same instant of time, that would have been present at the center of the ellipse if there had been no hole (free-field stresses). The maximum dynamic tensile stresses on the hole boundary were always smaller than the values computed using this same procedure.

I. INTRODUCTION

THE experimental results presented in this paper were obtained in a program similar to the ones conducted by the authors in determining the stress distribution on the boundary of (a) a circular hole in a large plate during passage of a stress pulse of long duration[1] and (b) a circular hole in a large plate during passage of a stress pulse of short duration.[2] The discontinuity was always centered at a point 4 in. from the point of load application on a radial line making 30° with the center line of the plate (line of loading). In all of these programs, dynamic photoelasticity methods were used in conjunction with low-modulus model materials. Both embedded-grid techniques and moiré techniques have been used previously to measure strains at a free-field point symmetric with respect to the center of the hole. In the current program, however, moiré methods were used exclusively for these determinations.

II. THEORETICAL CONSIDERATIONS

When a time-dependent load is applied at a point on one edge of a semi-infinite plate, two basic waves are produced; namely, dilatational waves and distortional waves. These waves propagate radially from the point of load application with velocities C_1 and C_2, respectively. Theoretically, the dilatational wave is produced by radial displacements which occur at the point of load application. The maximum shearing stresses associated with this wave, at every point in the field, make an angle of 45° to the wave front. This maximum shear is independent of θ (angular position of the point, measured with respect to a line perpendicular to the edge of the plate at the point of load application) and as a consequence, the photoelastic fringes associated with the dilatational wave form circular lines with the point of load application at the center.

Theoretically, the distortional wave is produced by transverse or circumferential displacements; therefore, the maximum shearing stresses at every point in the field are in the plane of the wave front. It can be expected that the photoelastic pattern associated with a distortional wave will be quite complex since the magnitude of the maximum shear will be zero at the boundaries and axis of the plate, and a function of the angular position at the other points.

III. EXPERIMENTAL METHODS

The photoelastic method employed in this program utilized a low-modulus model material in conjunction

---

[1] A. J. Durelli and W. F. Riley, J. Appl. Mech. (to be published).

[2] W. F. Riley and A. J. Durelli, J. Mech. Eng. Sci. 3, 62–68 (1961).

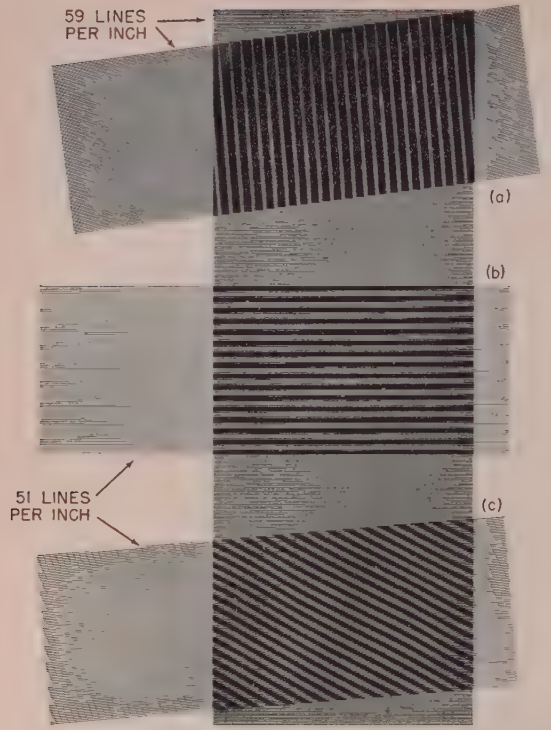

FIG. 1. Mechanism of formation of moiré fringes. (a) Fringes due to rotation alone. (b) Fringes due to difference in spacing alone. (c) Fringes due to a combination of rotation and a difference in spacing.

with: (a) a 16-mm Fastax camera for recording the over-all fringe patterns and (b) a microflash unit for obtaining fringe patterns in the immediate vicinity of the hole. These photoelastic techniques have been described in previous papers by the authors,[3–5] and will not be repeated here. The interested reader can refer to those papers.

The use of the moiré method for determining strains in two-dimensional problems is not so well known, but has found increasing application in recent years. The moiré effect is an optical phenomenon observed when two arrays of lines are superimposed. If the arrays consist of opaque parallel lines which are not identical in spacing or orientation, then moiré fringes will form as the lines of one array alternately fall on or between the lines of the other array (see Fig. 1). Measurement of the spacing and direction of the fringe gives sufficient information for determining differences between the arrays. In a recent paper by one of the authors, the techniques and equations needed to determine strains from moiré fringes are developed.[6] These relationships were used in determining strains in the present study.

IV. TEST PROCEDURE

A large plate with dimensions 0.37×12×12 in. was machined from a sheet of urethane rubber (Hysol 8705). An elliptical hole with major and minor axes 1.35 and 0.70 in., respectively, was machined in the plate. The location and orientation of the hole is shown in Fig. 2. The location of the hole was chosen to allow maximum time for study before reflections return from the boundary. Also, the 30° orientation provides a symmetric point in the same model where free-field stresses can be simultaneously determined. The symmetric point is far enough removed from the hole so that any disturbances produced by the presence of the hole do not interfere appreciably with the free field stress distribution. The 30° orientation also places the hole in a location where the influences of both the dilatational and distortional waves are felt. If the hole were located on the center line of the plate, the distortional wave influence would be smaller.

The loading of the model was accomplished by dropping a weight (108 g) from a height of 16 in. on a hard plastic striker which was permanently positioned on the model (see Fig. 2). A complete record of the photoelastic fringes produced by the impact was obtained by using a 16-mm Fastax camera operating at 6900 frames per sec. The first 20 frames of this record, together with five additional frames, are shown in Fig. 3.

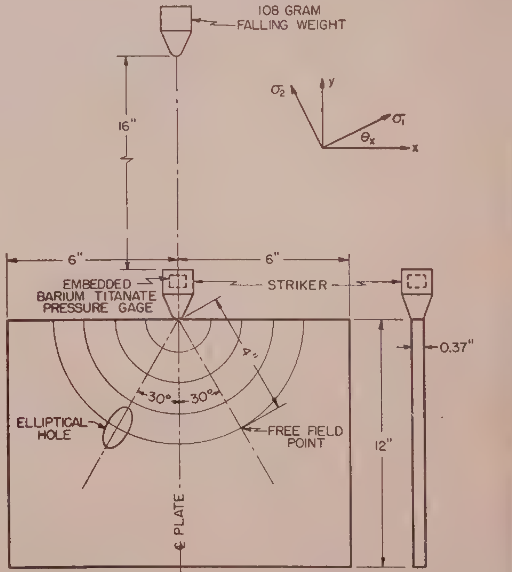

FIG. 2. Sketch of the model illustrating the loading, the location and orientation of the hole, and the symmetric free-field point.

---

[3] A. J. Durelli and W. F. Riley, J. Appl. Mech. **24**, 69–76 (1957); Trans ASME **79**, 69–76 (1957).

[4] J. W. Dally, W. F. Riley, and A. J. Durelli, J. Appl. Mech. **26**, 613–620 (1959).

[5] J. W. Dally, A. J. Durelli, and W. F. Riley, Proc. Soc. Exptl. Stress Anal. **17**, 33–50 (1960).

[6] S. Morse, A. J. Durelli, and C. A. Sciammarella, Proc. Am Soc. Civil Engrs. **86**, No. EM4, 105–126 (1960).

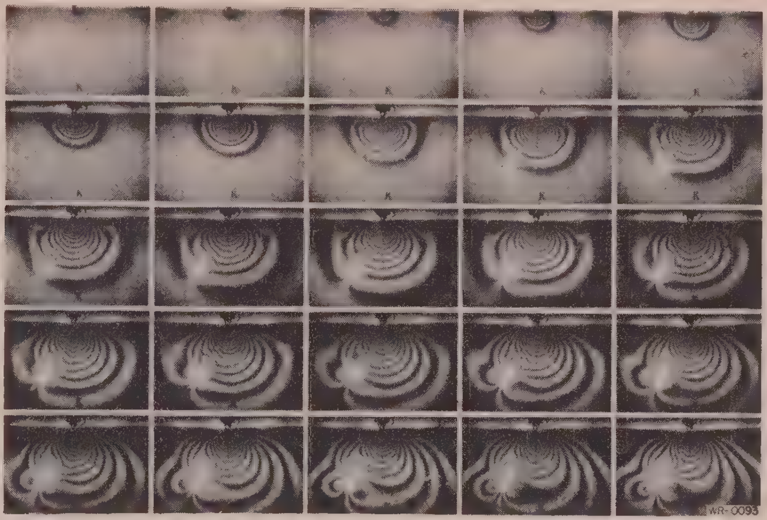

Fig. 3. Series of 25 photographs showing a compressive stress wave of long duration propagating past an elliptical hole in a large plate of Hysol 8705. Photographs taken with a Fastax camera at 6900 frames per sec.

The time period covered by these frames is approximately 4000 μsec. The total time duration of the pulse applied by the falling weight was approximately 12 000 μsec.

This corresponds to a pulse having a length approximately 35 times the length of the major axis of the elliptical hole. The portion of the pulse which could be considered as the front (rise from zero to peak) was approximately 12 times the length of the major axis.

Similar Fastax records were also obtained of the moiré fringes in the region of the free-field symmetric point. The printed grid used in obtaining the moiré fringes had 1000 lines per in. Typical records are shown in Fig. 4.

The photoelastic fringe patterns obtained with the Fastax camera were suitable for studying the over-all wave propagation phenomena, but were not suitable for precise fringe order determinations at the hole boundary. In order to obtain photographs suitable for these determinations, a series of 20 microflash photographs were obtained at approximately 200-μsec intervals after impact. The microflash photographs were sequenced by using a specially built timer unit which was triggered with a barium titanate pressure gauge embedded in the striker. Two representative photographs of the fringe distribution around the hole are shown in Fig. 5. It can readily be seen from these photo-

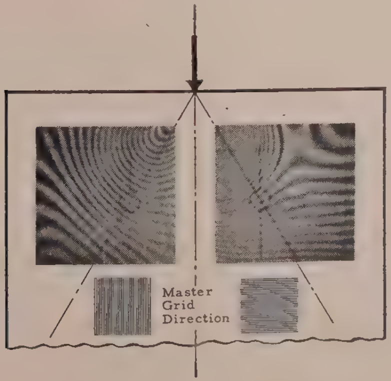

Fig. 4. Typical dynamic moiré patterns.

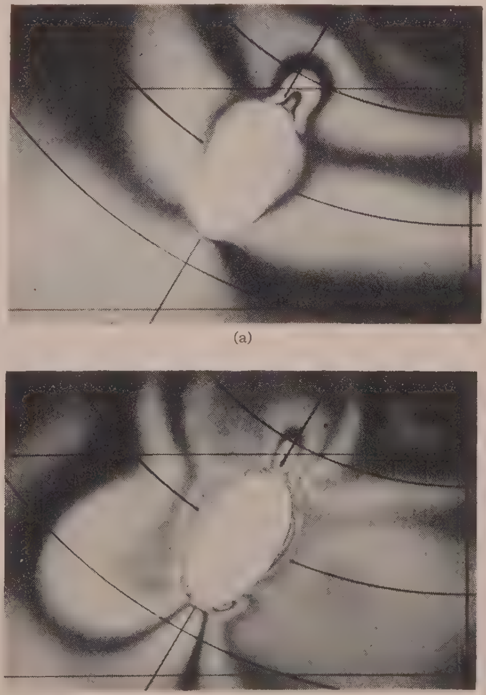
(a)

(b)

Fig. 5. Microflash photographs showing the fringe order distribution around the boundary of the hole (a) 1578 μsec and (b) 3173 μsec after impact.

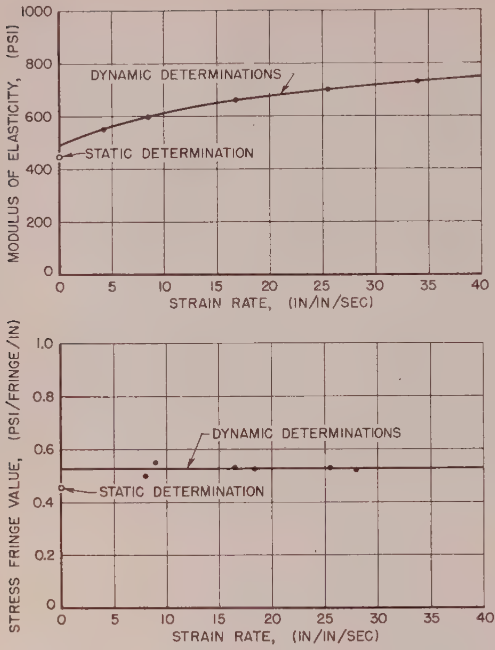

FIG. 6. Curves showing the modulus of elasticity and stress fringe value as a function of strain rate.

graphs that the fringe order at the boundary of the hole can be accurately determined.

V. MODEL MATERIAL PROPERTIES

As stated previously, the material used for the model was a low-modulus urethane rubber known commercially as Hysol 8705. Curves showing the modulus of elasticity and stress fringe value as a function of strain rate are presented in Fig. 6. The data from which these curves were obtained indicate that the modulus of elasticity and stress fringe value are independent of stress level over the range normally encountered in photoelasticity determinations (0–20 psi). For higher stress levels this may not be true. Additional properties of the material which are independent of strain rate are as follows:

$\nu = 0.46$ (Poisson's ratio);

$\rho = 0.000103$ lb sec^2/in.^{4} (mass density).

The method used in determining these material properties together with complete stress strain curves at a number of loading rates were presented in a previous paper by the authors.[4]

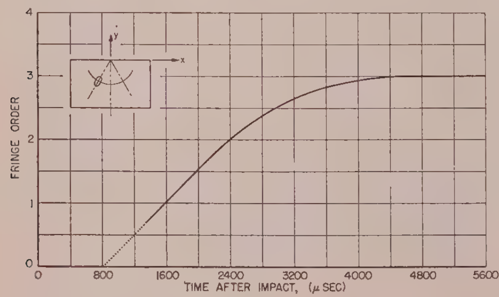

FIG. 7. Fringe order at the symmetric free-field point as a function of time after impact.

VI. ANALYSIS OF DATA

The microflash photographs used for analysis covered the interval of time from 1200 μsec after impact until 4600 μsec after impact. The beginning of the time interval was chosen when the 0.5-order fringe reached the symmetric point in the field (the wave front reached this point about 800 μsec after impact). This was the first instant at which the response around the hole boundary was sufficient to make fringe order determinations. The end of the interval was chosen to ensure that reflections were not influencing the distribution around the hole.

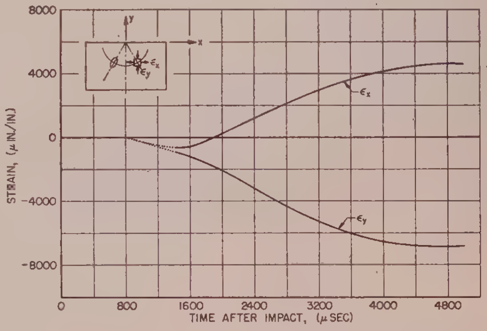

FIG. 8. Horizontal strain ϵ_x and vertical strain ϵ_y at the symmetric free-field point as a function of time after impact.

The Fastax and microflash records were then used to obtain the fringe order distribution around the hole, the fringe order at the symmetric point in the free field, and the two strains ϵ_x and ϵ_y at the symmetric point in the free field. The experimentally determined values for the fringe order as a function of time at the symmetric free field point are shown in Fig. 7. Similar curves for the two strains ϵ_x and ϵ_y are shown in Fig. 8. It was possible to make very accurate fringe order determinations. It is estimated that the two strain curves, however, may be in error by as much as 10%. The data shown in Figs. 7 and 8 were then used to obtain the two principal stresses and their directions. This was accomplished through the use of equations developed in a previous paper.[1]

In all of the determinations the effect of strain rate on the modulus of elasticity at the free-field point at the particular instant under study was considered.

VII. DYNAMIC STRESS DISTRIBUTION

The dynamic stresses around the hole were computed directly from the photoelastic data since the radial component of the boundary stress vanishes. An equivalent static stress distribution around the hole was then computed by using the Inglis solution[7] for an elliptical hole in an infinite plate under any system of combined stress. A stress field equivalent to the biaxial stress field at the symmetric point at the same instant of time was used in these calculations. The results of the static and dynamic stress determinations for several representative times after impact are shown in Figs. 9–11. At the center of each of these figures the magnitudes and directions of the free field stresses are plotted for the same instant of time.

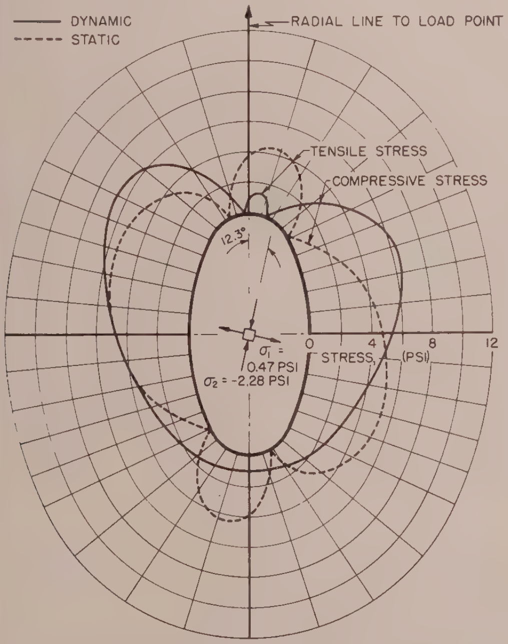

FIG. 9. Static and dynamic stress distributions on the hole boundary 1578 μsec after impact.

It can readily be seen from these figures that the compressive stresses on the hole boundary develop ahead of the tensile stresses. It should also be noted that the location of the maximum compressive stress shifts as the stress pulse moves past the hole. The first indication of the development of a tensile stress can be seen in Fig. 9 on the portion of the boundary nearest the point of load application. The tensile stress on the opposite side of the hole develops much later. As the peak of the stress pulse passes the hole the dynamic stress distribution begins to approach the static distribution.

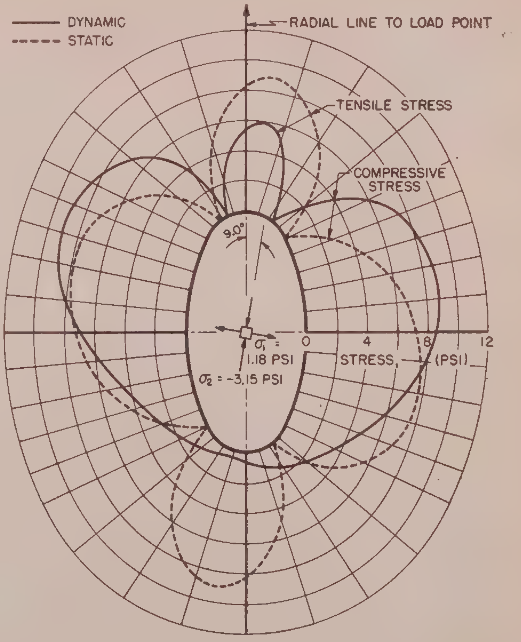

FIG. 10. Static and dynamic stress distributions on the hole boundary 1995 μsec after impact.

While the individual values of stress at all points on

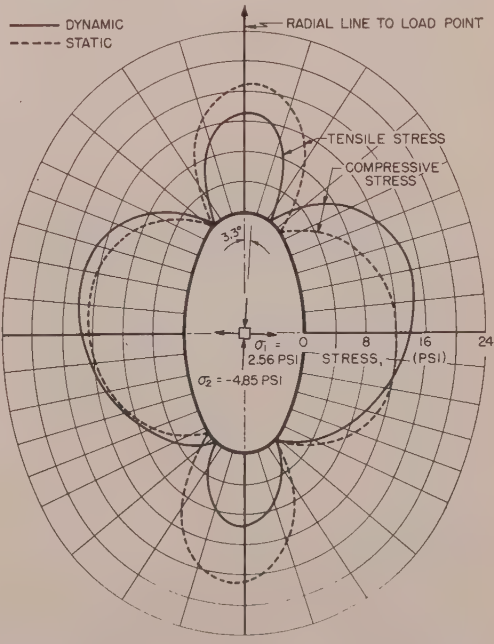

FIG. 11. Static and dynamic stress distributions on the hole boundary 3173 μsec after impact.

---

[7] C. E. Inglis, Trans. Inst. Naval Architects (Engl.) **55**, 219 (1913); Engineering **95**, 315 (1913).

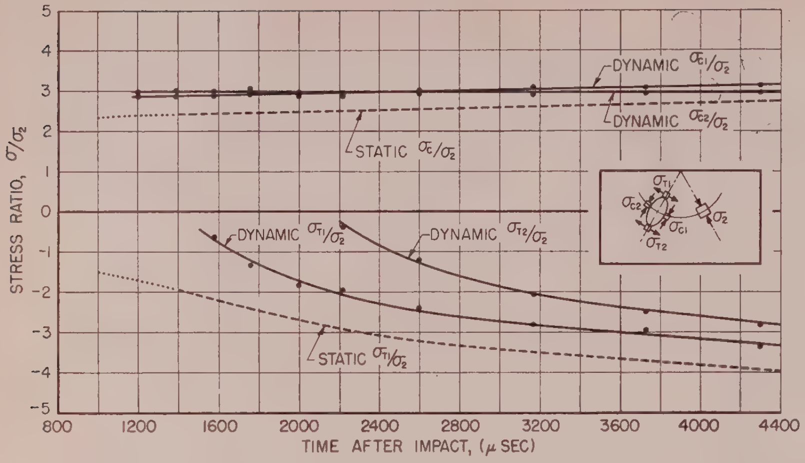

FIG. 12. Maximum tensile and compressive stresses on the boundary of the hole compared to the maximum compressive stress (σ_2) which occurs at the symmetric point in the free field at the same instant of time.

the boundary are of considerable significance, the maximum compressive and tensile stresses which develop are of greatest importance to the designer. In Fig. 12 the maximum tensile and compressive stresses on the boundary of the hole are compared to the maximum compressive stress (σ_2) which occurs at the symmetric point in the free field at the same instant of time. The static values of stress in this figure have been computed for the biaxial condition of stress which exists at the free-field symmetric point at the same instant of time. It can readily be seen from this figure that the dynamic compressive stresses on the hole boundary are only slightly larger than they would be in an equivalent static field. The differences are probably not significant. The tensile stresses developed on the hole boundary are always smaller under dynamic loading than predicted.

VIII. CONCLUSIONS

The results of this investigation indicate that the maximum compressive stresses on the hole boundary can be computed with a fair degree of accuracy by employing the Inglis solution for an elliptical hole in an infinite plate and considering the free-field biaxial stress conditions. It was also established that the maximum tensile stresses are always smaller than predicted In drawing conclusions based on this work, it should be remembered that the stress pulse employed had a length approximately 35 times the length of the major axis of the hole. The front of the pulse was not very steep; therefore, the gradient of stress along a portion of the pulse equal in length to the major axis of the hole was small. The results of this current study agree in general with the results obtained previously for the case of a circular hole and for the case of an elliptical hole oriented 90° to the one currently used. More recently, some work has been conducted on a similar problem using a circular hole and a short-duration pulse generated by detonating a small explosive charge of lead azide. The results of this study also are in agreement with the current work.

ACKNOWLEDGMENTS

The research reported in this paper was part of a project conducted at the Armour Research Foundation under the sponsorship of the U. S. Air Force Special Weapons Center, Air Research and Development Command. The authors wish to express their appreciation to E. H. Wang, Chief, Structures Division, and Capt. J. T. Pantall for their encouragement and support.

JOURNAL OF APPLIED PHYSICS VOLUME 32, NUMBER 7 JULY, 1961

Transmission Electron Microscope Observations of Magnetic Domain Walls

J. T. MICHALAK AND R. C. GLENN
Edgar C. Bain Laboratory for Fundamental Research, United States Steel Corporation Research Center, Monroeville, Pennsylvania

(Received January 25, 1961)

Ferromagnetic domain wall images have been observed in a variety of ferromagnetic materials by an electron transmission technique employing defocusing of the objective lens. Image formation and contrast effects are interpreted on the basis of charged particle motion through a magnetic field and electron microscope imaging. Observations are consistent with magnetic domain theory; domain sizes and wall geometry have been confirmed by the Bitter pattern technique.

INTRODUCTION

FERROMAGNETIC domains and domain walls have been observed by a variety of experimental techniques employing (a) the magnetic powder method (Bitter patterns),[1,2] (b) Kerr and Faraday magneto-optic effects,[3,4] (c) x-ray diffraction,[5] and (d) deflection of electrons.[6–8] Fuller and Hale[9] have recently demonstrated a transmission electron microscope technique which allows observation of high-resolution images of the domain walls in thin films of 50-50 Fe-Ni. The method utilizes the deflection of the electron beam caused by direct interaction of the electrons with the magnetization of the thin film specimen as the electrons pass through the specimen. The authors have successfully employed a similar technique for the observation of domain walls in high-purity alpha iron and several iron base alloys.

MATERIAL AND PROCEDURE

The purified iron (99.97% Fe) was zone melted by the Battelle Memorial Institute, and was processed by several cold reductions and intermediate anneals at 600°C in flowing wet hydrogen. The recrystallization anneal following the final cold reduction to 0.010-in. thickness was for 6 hr at 600°C or 900°C in flowing wet hydrogen followed by slow furnace cooling in dry hydrogen. The resulting average grain size was about 0.10 mm for the 600°C anneal and 2.0 mm for the 900°C anneal. Foils suitable for examination by electron transmission in the electron microscope were prepared from the 0.010-in. sheet by first chemically polishing to 0.002-in. in a 2:1 mixture of phosphoric acid and hydrogen peroxide (50%) and then electropolishing in the standard chromic oxide–glacial acetic acid electrolyte. The average thickness of the foils was about 1500–2000 A.

The foils were examined by transmission on an RCA-EMU-3 electron microscope operating at 100 kv under normal conditions except for a very slight defocusing of the objective lens; that is, the condenser, intermediate, and projector lens currents were maintained at their proper values for a given magnification. The objective lens current was varied by approximately ±1% of the current required for in-focus operation.

Other materials examined by this method included Fe-0.017% C, Fe-14.0% Al, Fe-3.6% Si, Fe-3.9% Au, Cu, and an 18% Cr-8% Ni austenitic stainless steel. Foils of these materials were prepared by the recommended techniques.[10]

Bitter patterns of the domain wall traces were obtained for several of the coarse-grained, high-purity iron foils which were previously examined in the electron microscope.

RESULTS

Domain wall images were observed in all of the materials examined, with the obvious exceptions of copper and austenitic stainless steel which are nonferromagnetic. Figures 1, 2, and 3 (a) are examples of domain walls in high-purity iron as seen by transmission electron microscopy. The characteristic features apparent for all of the wall images observed are the very nearly straight line traces and the alternating light and dark traces. Figure 1 is an electron micrograph of the

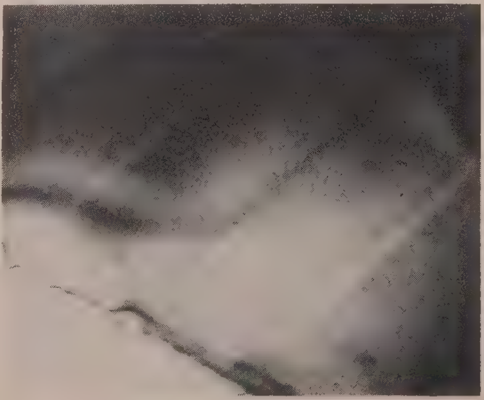

FIG. 1. Domain wall images in high-purity iron at edge of foil. 4480×. Overfocus.

---

[1] H. J. Williams, R. M. Bozorth, and W. Shockley, Phys. Rev. **75**, 155 (1949).
[2] R. W. DeBlois and C. D. Graham, J. Appl. Phys. **29**, 931 (1958).
[3] C. A. Fowler and E. M. Fryer, Phys. Rev. **100**, 746 (1955).
[4] B. W. Roberts and C. P. Bean, Phys. Rev. **96**, 1494 (1954).
[5] K. M. Merz, J. Appl. Phys. **31**, 147 (1960).
[6] L. Marton, Phys. Rev. **73**, 1475 (1948).
[7] L. Mayer, J. Appl. Phys. **28**, 975 (1957).
[8] M. E. Hale, H. W. Fuller, and H. Rubinstein, J. Appl. Phys. **30**, 789 (1959).
[9] H. W. Fuller and M. E. Hale, J. Appl. Phys. **31**, 238 (1960).
[10] P. M. Kelly and J. Nutting, J. Inst. Metals **87**, 385 (1958–59).

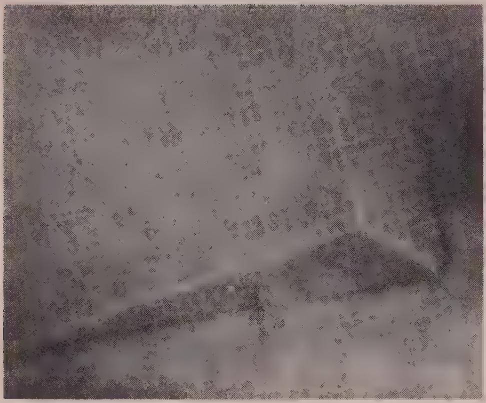

Fig. 2. Tapered domain in high-purity iron. 4480×. Overfocus.

domain wall images at the edge of the thin foil, and shows familiar closure domains with a constant angular relation among the three walls. The tapered domains of Fig. 2 are exceptional in that domains of this configuration were very rarely observed. They are probably associated with an inclusion which was not observed due to the thickness of the foil.

Figure 3(a) shows the domain wall images of a region removed from the edge of the foil, and Fig. 3(b) shows the Bitter patterns obtained on the same foil, although not necessarily in the same region, as Fig. 3(a). The wall arrangements of Fig. 3 were observed in several areas of this particular single-crystal foil specimen. Measurements of domain widths were made on electron micrographs and on light micrographs of Bitter patterns taken from the same foil samples. In the case of the Bitter patterns, measurements were restricted to areas within 0.02 mm of the edge of the foil, since it is believed that all electron micrographs were obtained from regions no further than 0.02 mm from the edge. Domain widths from both measurements agreed quite well with each other and were within the range of 1×10^{-4} cm to 5×10^{-4} cm. Domains in the thicker portion of the foil, away from the edge, were found to be 10^{-3}–10^{-2} cm in width as measured by the Bitter pattern technique.

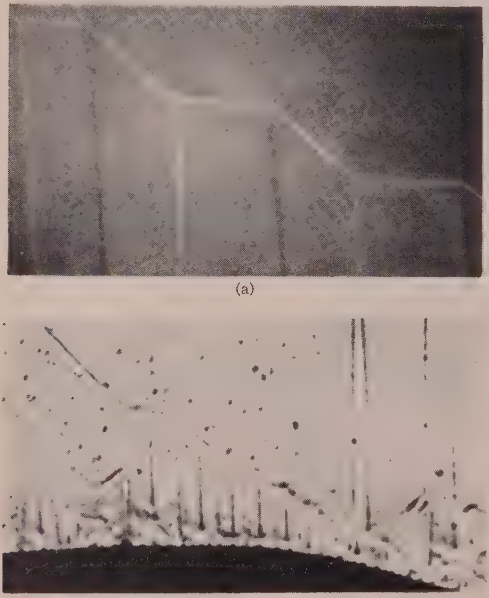

(a)

(b)

Fig. 3. (a) Electron transmission micrograph of domain wall images in high-purity iron. 4480×. Overfocus. (b) Bitter pattern of domain boundaries in same specimen. 480×.

The angles between domain wall traces were also measured on both types of micrographs, and very good agreement was obtained for similar arrangements of traces. For example, for the similar arrangement shown in Fig. 3(a) and (b), the average angles, measured clockwise from the horizontal domain wall, were 87°, 133°, and 140° on the electron micrograph, and 89°, 133°, and 138° on the light micrograph.

Figure 4(a) and (b) shows another general character-

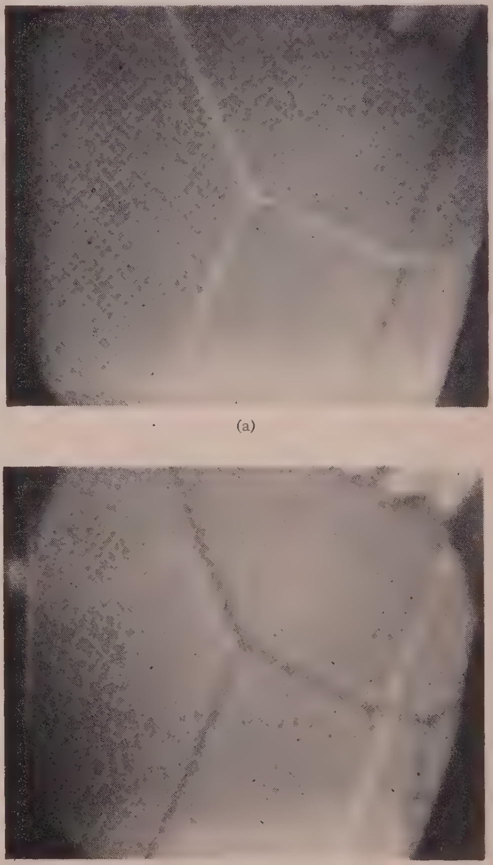

(a)

(b)

Fig. 4. Domain wall images in Fe-3.9% Au: (a) 6400×, overfocus; (b) 6400×, underfocus.

istic of domain wall images as seen by electron microscopy; namely, the reverse in contrast of the wall image when going from overfocus to underfocus (and vice versa) of the objective lens. Overfocus is the condition of increased current of the objective lens such that its first focal plane is moved below the in-focus plane. Underfocus is the condition of reduced current of the objective lens such that its first focal plane is now moved above the in-focus plane. Since the specimen and the first focal plane of the objective lens are almost coincident for the in-focus condition, the first focal plane is below the specimen for overfocus and above the specimen for underfocus. The defocusing is slight and, since the intermediate lens has a large depth of focus, the observed image does not appear to be too much out of focus.

The orientations of several foils were obtained by electron diffraction, and a trace analysis of domain wall images revealed that the plane of the wall was in most cases (001) or (011). Other walls, not parallel to either (001) or (011) planes, were found to be (012) or (013) planes parallel to the [001] direction.

Figure 5(a) shows the effect of inclusions on the domain geometry, and provides further confirmation of the proposals of Néel[11] that domains are formed around a hole or inclusion in such a way that no free poles exist at the free surfaces or interfaces. Figure 5(b) is a schematic representation of the resolvable domains indicating assumed directions of magnetization to coincide with the domain pattern of Fig. 5(a).

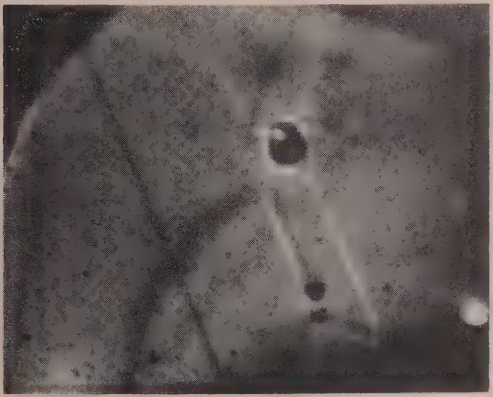

(a)

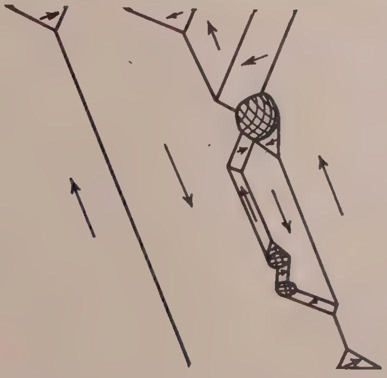

(b)

FIG. 5. (a) Domain wall images in Fe-3.9% Au around inclusions. 4480×. Underfocus. (b) Suggested interpretation of (a).

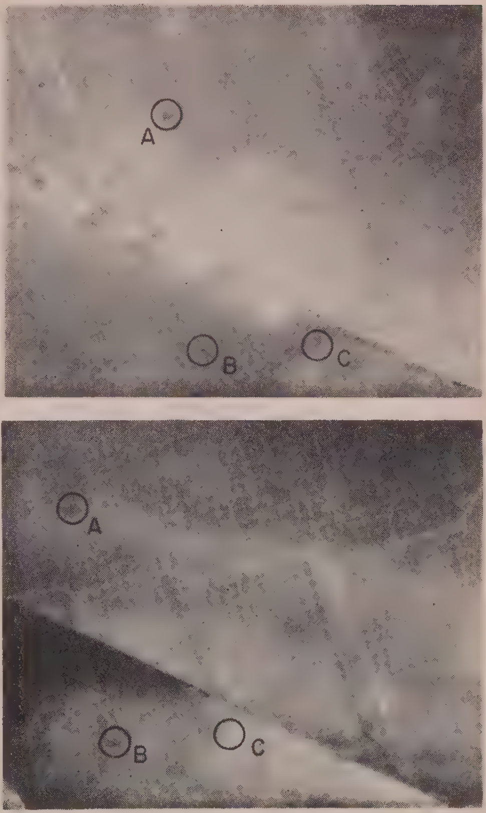

FIG. 6. Domain wall images in high-purity iron showing movement as result of change in magnetic field of objective lens. 4480×. Overfocus.

Domain wall motion due to changes in the magnetic field of the objective lens was rarely observed even with relatively large changes in field. When such movement did occur, the motion was jerky although the change in field was continuous. Figure 6 is an example of movement caused by an alteration of the objective lens field. The reference marks *A*, *B*, and *C* indicate that the micrographs are from the same area, and the very small change in the distances between these reference marks suggests only a slight variation of the objective lens field. From these same reference marks it is apparent that motion has been parallel to the direction of the grain boundary and also parallel to the length of the thin domains. In some cases, the movement of domain walls was completely reversible, so that a particular domain configuration could be altered by a change in the magnetic field, and the initial configuration regained by an equal opposite change in the field.

---

[11] L. Néel, from R. M. Bozorth, *Ferromagnetism* (D. Van Nostrand Company, Inc., Princeton, New Jersey, 1959).

DISCUSSION

The foregoing results are all consistent with the conclusion that these traces observed by out-of-focus operation of the objective lens of an electron microscope are the images of magnetic domain walls. These images have been observed only in ferromagnetic materials as straight line traces with regular repeated angular relations. The size of domains and angular relations between traces in electron micrographs have been verified by Bitter patterns. The discontinuous motion of these images in a changing magnetic field and their configuration around an inclusion are consistent with domain theory.

Other aspects of these observations which are also in agreement with the images being domain walls are (a) the out-of-focus requirement of the objective lens, (b) the alternate light and dark contrast of parallel traces, and (c) the contrast reversal in going from overfocus to underfocus or vice versa.

Fuller and Hale[9] have adequately considered the interaction of the electrons with the magnetic field of the specimen and the out-of-focus requirement of the objective lens which give rise to the electron intensity variation at the observation plane and make the domain wall images visible. In this study, however, it was found that operation of the objective lens at a reduced current was not necessary and that, in fact, wall images could be obtained at an increased objective lens current. The high coercive force of the materials examined prevents the elimination of the domain walls by the objective lens field. Thus it was possible to produce a contrast reversal in going from overfocus to underfocus or vice versa. The contrast reversal is readily explained by reference to Fig. 7, a schematic representation of the electron intensity at the various positions of the objective focal plane which is projected to the observation plane. The figure indicates that for the overfocused condition, a convergent wall (A) will appear as a narrow bright line and a divergent wall (B) as a broad dark line, and vice versa for the underfocused condition. Measurements of image width have substantiated this concept. The imaging of domain walls in a defocused condition is analogous to the imaging by fringe effects and changes in index of refraction as discussed by Hall.[12]

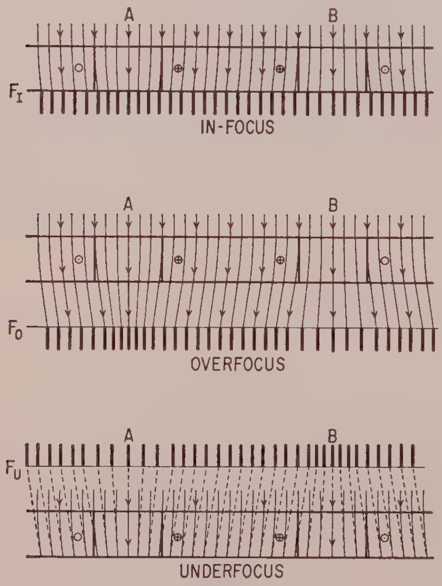

Fig. 7. Projected electron intensity observed at fluorescent screen for the three positions of the objective focal plane.

An evaluation of the domain wall width may be obtained from measurements of the widths of images of parallel convergent and divergent walls. It is assumed that the magnetic field of a domain is parallel to the specimen surface and to the domain walls, reverses 180° through a wall, and that the walls are normal to the specimen surface. The deflection of electrons by a wall is then of the same magnitude, but in the opposite sense for the two types of walls; therefore, the average of the width of parallel bright and dark traces measured on the same electron micrograph will be the width of the domain wall. Measurements of this kind made on various micrographs at various conditions of defocusing and magnification yield a 180° domain wall width of about 1400 A. This width is probably somewhat less than the true domain wall width because of difficulty in accurate measurement of the width of contrast change through the images. It is a reasonable value in fair agreement with theoretical estimates of about 2000 A for a 180° wall in iron.[13]

CONCLUSION

The observation of magnetic domain walls by transmission electron microscopy provides an experimental technique for domain studies to complement other techniques, and is especially valuable for investigations on magnetic films. However, the domain walls observed in a thin foil prepared from a bulk sample are probably not a true picture of domain structures in the bulk material. The preparation of a thin foil sample by electropolishing may very well change the domain configurations, at least in a pure material. The variation in domain size with thickness of sample has been mentioned. Nevertheless, this technique would be suited to a study of the interaction of domain walls with dislocations produced by straining a thin foil in the electron microscope. Effects of temperature might also be investigated by hot-stage electron microscopy, and the technique should be very useful in studies of magnetic aging. Results of such investigations could properly be extended to reactions in a bulk material with the reservation that what is observed in a thin foil may not be the same for a bulk sample.

---

[12] C. E. Hall, *Introduction to Electron Microscopy* (McGraw-Hill Book Company, Inc., New York, 1953).

[13] R. M. Bozorth, *Ferromagnetism* (D. Van Nostrand Company, Inc., Princeton, New Jersey, 1959).

ACKNOWLEDGMENTS

The authors wish to thank E. Hornbogen, A. S. Keh, W. C. Leslie, and M. J. Marcinkowski for providing thin foils of certain of the alloy materials examined and for helpful discussion. They are indebted also to P. R. Swann for stimulating discussion. D. W. Stevens performed some of the experimental work.

JOURNAL OF APPLIED PHYSICS VOLUME 32, NUMBER 7 JULY, 1961

Electrical Conductivity of NaCl during High-Temperature Creep*

R. W. Christy and W. E. Daniels, Jr.
Dartmouth College, Hanover, New Hampshire

(Received February 20, 1961)

In view of recent interest in the effect of creep on the coefficient of self-diffusion, measurements have been made on the electrical conductivity of NaCl in the intrinsic range during and after deformation by creep. The conductivity is proportional to the diffusion coefficient for Na. At about 550°C, no change in conductivity was observed, even at steady state creep rates approaching 10%/min. This negative result is shown to be in accord with theoretical estimates.

I. INTRODUCTION

EVER since Buffington and Cohen[1] reported large increases in the diffusion coefficient of iron during creep at high temperatures, there has been considerable interest in this effect, although further work[2] indicated that the original observations had overestimated the magnitude of the increases. Lee and Maddin[3] also found large increases in silver between 600°–800°C; on the other hand, Darby *et al.*[4] observed no enhancement during deformation of silver single crystals above 800°C. Although these experiments did not completely establish the conditions for an enhancement of diffusion coefficient during creep, a relationship between creep at high temperatures and diffusion, involved in the control of the creep rate by diffusion-limited dislocation climb,[5] has been generally recognized. A calculation[6] of the enhancement of diffusion to be expected because of this mechanism suggests, however, that it should be rather small.

On the other hand, there are other mechanisms which could possibly lead to an increase in diffusion during creep. Seitz proposed[7] that the production of vacancies by intersecting dislocations could explain the enhancement of ionic conductivity observed following cold work of NaCl crystals.[8] Since ionic conductivity is proportional to the diffusion coefficient in ionic crystals,[9] this mechanism also would lead to increased diffusion. Seitz's interpretation has more recently been confirmed by the observation that the effect occurs only in squat crystals where multiple slip is produced,[10] and not in tall crystals, which deform by single slip. Further evidence that vacancies are dynamically produced by cold work is given by the direct observation of expansion of the specimen following cold work.[11] Although the production of vacancies by colliding dislocations is well confirmed, one can estimate that its effect during high-temperature creep is quite small,[6] because of the relatively large equilibrium number of vacancies already present.

Forestieri and Girifalco[12] have made more extensive measurements of the self-diffusion coefficient of silver, over the temperature range 540°–900°C, under constant strain rates. They find that above about 800°C, the deformation has no effect on the diffusion rate, but below this temperature there is an enhanced diffusion, proportional to strain rate, which appears to become independent of temperature below about 540°C. The authors ascribe the effect to the mechanisms mentioned above but we believe, as will be discussed in Sec. IV, that the observed effect is too large to be accounted for in this way.

---

* Supported by the National Science Foundation.

[1] F. S. Buffington and M. Cohen, J. Metals **4**, 859 (1952).

[2] N. Ujiiye, B. L. Averbach, M. Cohen, and V. Griffiths, Acta Met. **6**, 68 (1958).

[3] C. H. Lee and R. Maddin, J. Metals **10**, 93 (1958).

[4] J. B. Darby, Jr., C. T. Tomizuka, and R. W. Baluffi, J. Appl. Phys. **30**, 104 (1959).

[5] N. F. Mott, Proc. Phys. Soc. (London) **B64**, 729 (1951).

[6] R. W. Christy, J. Appl. Phys. **30**, 760 (1959).

[7] F. Seitz, Phys. Rev. **80**, 239 (1950).

[8] Z. Gyulai and D. Hartly, Z. Physik **51**, 378 (1928); D. B. Fischbach and A. S. Nowick, J. Phys. Chem. Solids **5**, 302 (1958).

[9] N. F. Mott and R. W. Gurney, *Electronic Processes in Ionic Crystals* (Oxford University Press, London, 1948), 2d ed., Chap. II.

[10] A. Taylor and P. L. Pratt, Phil. Mag. **3**, 1051 (1958).

[11] W. H. Vaughan, W. J. Leivo, and R. Smoluchowski, Phys. Rev. **110**, 652 (1958).

[12] A. F. Forestieri and L. A. Girifalco, J. Phys. Chem. Solids **10**, 99 (1959).

Finally, diffusion could be enhanced by increasing the mobility, rather than the number, of the vacancies during deformation. Dislocations can provide high-mobility pathways for vacancy migration, and therefore the production of new dislocations increases the average diffusion coefficient. This effect has been studied near room temperature in silver bromide[13] and at somewhat higher temperatures in potassium chloride,[14] but again it becomes less effective at high temperatures where the volume diffusion coefficient is larger.

In order to contribute to the clarification of the relations between diffusion and creep, we have measured the ionic conductivity of NaCl crystals, in the intrinsic conductivity range above 550°C, during deformation by compressive creep. Since the conductivity in the alkali halides is proportional to the self-diffusion coefficient for the alkali metal ions, the results bear on the above problem.[15] In fact, the ionic conductivity measurement has a number of advantages over direct diffusion measurements: (a) The accuracy obtainable in conductivity measurements is about an order of magnitude higher than in diffusion measurements. (b) It is easy to use single crystals, thus eliminating grain boundary effects which are important in both diffusion and creep. (c) The observed effect is a volume effect, averaged over the entire crystal; diffusion of radioactive tracers occurs entirely in a very thin layer near a free surface. (d) The time dependence of the effect can be observed during the deformation and during annealing after the deformation; the diffusion measurement is integrated over the entire high-temperature history of the sample. (e) Since the measurement is instantaneous, creep rates may be studied which are many orders of magnitude greater than those which will give a reasonable total deformation during the course of a diffusion run.

Both the electrical conductivity[16] and steady state creep rate[17] have previously been measured in NaCl. Here we report on simultaneous measurements of the two effects.

II. EXPERIMENTAL PROCEDURE

The apparatus used to deform the specimens in compression at high temperatures while measuring the conductivity is a modification of one described previously.[18] As shown in Fig. 1, the specimen is placed on a stainless steel plug which is supported by a rigidly mounted length of $\frac{1}{2}$-in. thin wall stainless steel tubing. The specimen is loaded by a similar plug and tube, which rests on the crystal and carries a platform for the load at its upper end. The deformation is measured by a dial strain gauge actuated by the platform. The creep process can be stopped after the desired deformation by removing the load, since the creep rate due to the weight of the platform assembly is entirely negligible.

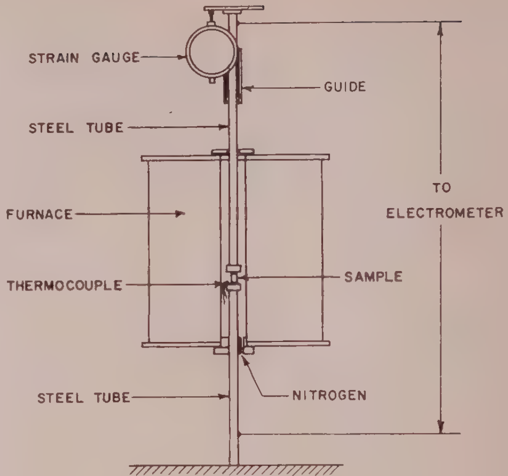

Fig. 1. Apparatus for deforming crystal by compressive creep, while simultaneously measuring the electrical resistance.

The upper and lower pieces of stainless steel tubing also form the electrical leads to the sample. It is important that these be identical in order to eliminate thermal emf's. The upper ram is electrically isolated from the rest of the apparatus; a length of glass tubing near room temperature is used as a guide, and the strain gauge is isolated with Teflon. This arrangement gives a leakage resistance greater than 10^9 ohm when the apparatus is at high temperature, compared with a typical specimen resistance of not more than 10^6 ohm. The two stainless steel plugs are faced with silver sheet soldered to them, in order to have noncorroding surfaces which will provide good electrical contact.

The samples were cleaved from single crystals obtained from the Harshaw Chemical Company. They were from 5–10 mm high and slightly smaller in the other dimensions. Graphite electrodes were painted on top and bottom of the specimen. Pieces of platinum foil were placed between the sample and the silver-faced platens, so that the platens would not stick to the specimen and so that silver would not diffuse into the specimen. Even though the crystal was not in contact with the silver, some silver was detected in the sample by uv optical absorption measurements. Since this contamination was mainly on the exposed lateral surfaces of the crystal, it probably occurred by a vapor phase mechanism whereby free chlorine reacted with the silver, which was transported to the crystal as AgCl vapor. The high-temperature conductivity was not affected by this surface contamination.

---

[13] W. G. Johnston, Phys. Rev. **98**, 1777 (1955).

[14] J. Burmeister, Z. Physik **148**, 402 (1957).

[15] It is possible that migration of neutral anion-cation vacancy pairs could contribute to diffusion but not to conductivity. This effect is known not to occur, however, at high temperatures [D. Mapother, H. N. Crooks, and R. J. Maurer, J. Chem. Phys. **18**, 1231 (1950)].

[16] H. W. Etzel and R. J. Maurer, J. Chem. Phys. **18**, 1003 (1950).

[17] R. W. Christy, Acta Met. **4**, 441 (1956).

[18] R. W. Christy, Acta Met. **2**, 284 (1954).

The specimen was surrounded by a furnace, whose temperature was kept constant to within 1°C by a proportioning controller. The temperature of the specimen was measured to within 0.2°C by a Chromel-Alumel thermocouple soldered to the lower silver plate. Dry nitrogen was run slowly through the furnace in order to prevent oxidation of the graphite electrodes and contamination of the crystal by oxygen or water vapor.

The resistance of the crystal was measured with a General Radio type 1230-A electrometer-amplifier. The measurement with this instrument is unaffected by presence of a thermal emf; nevertheless the furnace was positioned so as to minimize the thermal emf, and therefore the temperature gradient across the sample. The output of the amplifier was recorded during the rapid deformations.

III. RESULTS

Before the deformation, the conductivity of all the NaCl specimens was within about 10% of the formula given by Etzel and Maurer[16]:

$$\sigma = 3.72\times10^8/T \exp(-21\,600/T) \text{ (ohm-cm)}^{-1}.$$

Our values were consistently somewhat higher, and were further increased by a slight compression, presumably because the contacts were improved. The activation energy, however, was in excellent agreement with the above value, both before and after the creep experiments. It was confirmed that the resistance remained constant over periods of time much longer than the duration of the creep and recovery experiments. It did not depend on the polarity of the applied voltage.

All the specimens were loaded in the (001) direction during creep, with a constant load rather than with constant stress. Slip appeared to occur entirely on the (011) planes. The specimens were purposely made not too tall compared to their diameter, so that not much barrelling would occur. Assuming the specimen volume remains constant during the deformation, the conductivity is

$$\sigma = (L_0/A_0R)(L/L_0)^2,$$

where L_0 and A_0 are the initial height and cross-sectional area of the specimen, L is the deformed height, and R is the measured resistance. This formula is accurate if the specimen does not barrel out. The resistance R was corrected for temperature fluctuations during a run by using the above activation energy.

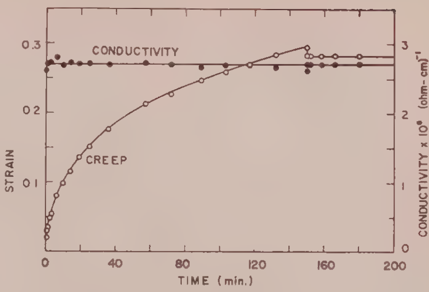

FIG. 2. Creep and conductivity of an NaCl crystal at 555°C. The final stress was 144 g/mm². The conductivity remained constant for 18 hr after this experiment.

The temperature for the experiments was chosen to be just over 550°C. All experimental evidence and theoretical predictions indicate a larger effect the lower temperature. Below about 550°C, however, NaCl enters the extrinsic conductivity region, where the behavior is determined by the relatively large and constant number of impurity-controlled vacancies. We therefore chose the lowest possible temperature in the intrinsic region.

The results were that during the entire course of the creep deformation, and during recovery periods up to 10 times longer after the deformation, there was no change in the electrical conductivity. Although the resistance of the samples decreased by factors of 2 or 3 as a result of the large total compressions applied, when the conductivity was calculated taking into account the measured change in dimensions of the sample, the result was constant to within a few percent.

The results of one run are plotted in Fig. 2. The deformation occurred at a temperature of 555°C. The stress, initially 203 g/mm², decreased to 144 g/mm² as the specimen cross-sectional area increased. The final creep rate of 7×10^{-4} min^{-1} appears to be nearly constant. An extrapolation from the previously measured[17] steady state creep rate of NaCl gives 1×10^{-4} min^{-1}. Since the present stress is 50% greater than the largest stress previously used, and since the stress range covered then was not large enough to determine the stress dependence unambiguously, it is quite possible that the steady state was reached here, or at least closely approached. After the deformation, the conductivity was followed for 18 hr, and it remained constant to within 1%.

In another run, a very much higher creep rate was obtained. A total deformation of 42% occurred in 20 sec, at a stress which varied from 680 to 390 g/mm². The final creep rate of the order of 3×10^{-1} min^{-1} was probably close to the steady state rate. The deformation was too rapid to permit recording of the strain gauge deflections during the deformation, but again the conductivity values before and up to 5 hr after the deformation were constant to within 2%.

The measured variations in conductivity, of the order of a few percent, appeared to be random rather than systematic, and were extremely small compared to the geometrical corrections of the order of 200–300%. We therefore conclude that the conductivity of NaCl, and therefore the diffusion coefficient for Na, is unaffected by creep down to temperatures 250° below the melting point, even at steady state creep rates as large as about 10%/min.

IV. DISCUSSION

It appears difficult to reconcile the reported large effects of creep on the diffusion coefficient in metals with the absence of any effect in NaCl, since in general the plastic behavior of ionic crystals is rather similar to that of metals. It is easier, on the other hand, to understand the lack of an observable effect in NaCl, on the basis of a theoretical estimate of the magnitude of the increase to be expected. Therefore the latter point will be discussed first.

In NaCl, the Na ion diffuses much more rapidly than the Cl ion, except at temperatures just below the melting point. Consequently, it is the Na diffusion coefficient which is related to the conductivity; on the other hand, it is the more slowly diffusing Cl which limits the rate of dislocation climb and the steady state creep rate. Since Schottky disorder predominates in NaCl, the numbers of Na vacancies and Cl vacancies are equal in the intrinsic region, in order to have charge neutrality. Taking these facts into consideration, the increased diffusion coefficient for Na, $\mathbf{D}'$, which accompanies a steady state creep rate $\dot{\gamma}$ limited by a dislocation-climb mechanism, has been estimated to be[6]

$$\mathbf{D}'=D'[1+(hd^2/L)(\dot{\gamma}/D)],$$

where D' is the normal diffusion coefficient for Na and D that for Cl. The other quantities are related to the dislocation climb mechanism: L is the average length of the edge component of the climbing dislocations, h is the distance the dislocations have to climb, and d is the distance excess vacancies have to diffuse before being annihilated. The latter quantities are not well known, but the ratio (hd^2/L) was estimated to be from 10^{-11}–10^{-10} cm^2 in order to give agreement with creep data.

The highest final creep rate attained in our experiments was about 5×10^{-3} sec^{-1}, and this value was probably not far from the steady state rate; in any case, the steady state rate could not have been higher. The diffusion coefficient for Cl at the same temperature of 555°C would be[19] about 1.5×10^{-12} cm^2/sec. Thus $(\dot{\gamma}/D)$ was about 3×10^9 cm^{-2}, and if (hd^2/L) were 10^{-11} cm^2, the predicted conductivity increase would be 3%. As this increase is just about at the limit of detectability, our experiment is consistent with this prediction, assuming the smaller value for (hd^2/L). It would be quite difficult to achieve a larger steady state creep rate, or to decrease D by going to lower temperatures in the intrinsic region.

The largest creep rate attained in the experiments on silver[12] was about 1.5×10^{-6} sec^{-1}. A constant strain rate was imposed, but it is probable that the real steady state rate (with constant stress) was not achieved, since at low temperatures the transient creep is likely to be much more than 10%, the total strain in these experiments. The diffusion coefficient for Ag, extrapolated to the lowest temperature of 538°C, was 5×10^{-13} cm^2/sec. Thus the ratio $(\dot{\gamma}/D)$ could not have been greater than 3×10^6 cm^{-2}, about 1000 times smaller than in our experiment on NaCl. With the larger estimate of $(hd^2/L)\approx10^{-10}$ cm^2, the predicted increase in diffusion coefficient would be 0.03%. As the observed increase was about a factor of 100, we conclude that it is unlikely that the mechanism under consideration could have accounted for it.

The mechanism proposed by Seitz, the production of vacancies by intersecting dislocations, could probably give no greater an effect,[6] again on the basis of data measured in NaCl at lower temperatures. The experiments on AgBr and KCl[13,14] suggest that the increase of vacancy mobility afforded by an enhanced dislocation concentration would also be negligible at high temperatures. Therefore we believe that the explanation of the large diffusion increases measured in metals during creep (about a million times larger than the calculated increase) should be sought in effects which occur near the surface, where the diffusion measurement is made.

---

[19] M. Chemla, Compt. rend. **234**, 2601 (1952).

JOURNAL OF APPLIED PHYSICS VOLUME 32, NUMBER 7 JULY, 1961

Magnetization Process in Small Particles of CrO_2

F. J. Darnell
Central Research Department, E. I. du Pont de Nemours and Company, Wilmington, Delaware

(Received December 5, 1960)

Initial magnetization curves, remanence, coercivity, reversible susceptibility, and rotational hysteresis have been measured for CrO_2 in the form of small particles. The measurements allow rough division into three types of behavior with decreasing particle size: multidomain, or bulk behavior, for $\sim$100-μ particles; few-domain behavior for $\sim$1–10-μ particles; and single-domain behavior for particles with a length/diameter ratio $\sim$5 and a diameter ≤ 0.2 μ. The smaller particles studied were acicular and showed coercivity dominated by shape anisotropy.

I. INTRODUCTION

THE possibility of comparing experiment with theory in the magnetic behavior of single-domain particles has given encouragement to many investigations.[1] Of particular interest have been the separation of shape and crystalline anisotropy contributions to particle coercivity[2–4] and determinations of magnetization reversal mechanisms.[5,6] In the range of particle sizes in which there occurs a transition from single-domain to multidomain behavior, three types of behavior may be studied. In the smallest particles which contain only a single domain, the sources of anisotropy and magnetization mechanisms may be determined. In few-domain particles, i.e., those with less than four or five domains, one may hope to observe domain wall motion limited by the magnetostatic effects discussed by Amar.[7] Finally, in larger multidomain particles, one expects to see behavior characteristic of bulk material exhibiting domain wall motion.

In the present studies, the ferromagnetic oxide of chromium having the rutile structure, here referred to as CrO_2,[8] was available in a range of particle sizes which included that expected for the transition from single to multidomain. This paper reports magnetic measurements on small particles of CrO_2 and their interpretation in terms of particle size effects, origin of coercivity, and magnetization reversal mechanism.

II. SAMPLE PREPARATION AND EXPERIMENTAL METHODS

CrO_2 particles prepared by hydrothermal synthesis[8] or by vapor deposition (from chromyl chloride) were used. Roughly equiaxed particles of dimension approximately 1 μ were obtained from the former method when no chemical modifier was used. Acicular particles 1×0.2 μ or smaller were obtained by use of antimony oxide modifier in this process. Either of these particle sizes could be built up by vapor deposition of CrO_2 achieved by thermal decomposition of CrO_2Cl_2. Table I gives particle sizes and synthesis methods for samples used in the present study. Particle sizes were measured by electron microscopy at magnifications of 2000–50 000 times and by optical microscopy for the largest particles. Dimensions are given as an average diameter and a length-to-diameter ratio since these are convenient parameters for later calculations of coercivity and the width is an important factor in the determination of single-domain size for acicular particles. The dimensions quoted represent average values for unfortunately broad size distributions.

TABLE I. Chromium dioxide samples.

Sample	Particle Width (μ)	Particle Length/width	Bulk coercivity (oe)	Synthesis	Modifier
A	3	1.5	21	vapor deposition	···
B	1	1.5	38	vapor deposition	···
C	2	2	38	hydrothermal	···
D	0.6	2	138	vapor deposition	···
E	0.2	5	224	hydrothermal	Sb
F	0.1	4	166	hydrothermal	Sb
G	10	2	14	vapor deposition	···
H	0.1	5	382	hydrothermal	Sb
J	0.1	4	234	hydrothermal	Sb
K	0.1	5	393	hydrothermal	Sb
L	0.1	5	297	hydrothermal	···

As reported by Arthur *et al.*,[8] chemical modification has little or no effect on the Curie temperature, but decreases the saturation magnetization by an amount greater than can be accounted for by nonmagnetic dilution alone. While magnetization and coercivity are affected to a small extent by the synthesis method and modifier, the strictly chemical effects will be neglected here in considering the larger effect of particle size changes. The magnetic properties were found to correlate well with particle size regardless of

---

[1] For a review see E. P. Wohlfarth, Advances in Phys. **8**, 87–224 (1959).

[2] L. Néel, Compt. rend. **224**, 1488–90 (1947).

[3] E. C. Stoner and E. P. Wohlfarth, Phil. Trans. Roy. Soc. London **240**, 599–642 (1948).

[4] F. E. Luborsky, E. F. Fullam, and D. S. Hallgren, J. Appl. Phys. **29**, 989–93 (1958).

[5] I. S. Jacobs and C. P. Bean, Phys. Rev. **100**, 1060–67 (1955).

[6] I. S. Jacobs and F. E. Luborsky, J. Appl. Phys. **28**, 467–73 (1957).

[7] H. Amar, J. Appl. Phys. **28**, 732 (1957); Phys. Rev. **111**, 149 (1958).

[8] P. Arthur, N. L. Cox, J. N. Ingraham, A. L. Oppegard, T. J. Swoboda, and M. S. Sadler, J. Phys. Chem. Solids (to be published).

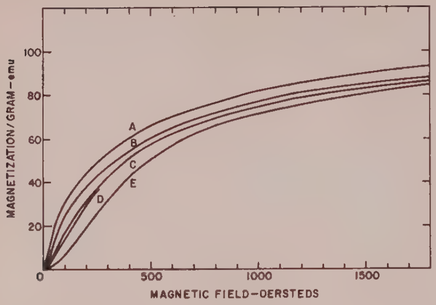

Fig. 1. Initial magnetization vs field for several particle sizes. See Table I for sample descriptions.

the synthesis method in the critical transition region from multidomain to single domain.

Selected area electron diffraction pictures showed the smaller particles to be single crystals. The larger particles could not be studied by this technique. The structure and basic magnetic properties of CrO_2 are described by Cloud *et al.*[9] This oxide exists in the tetragonal rutile structure and exhibits a room temperature volume saturation magnetization of $I_S = 490$ gauss. The crystalline anisotropy is positive uniaxial, the actual easy directions lying at $\sim 40°$ to the tetragonal axis, with $K_1 = 3 \times 10^5$ erg/cm^3. X-ray studies on oriented particles showed that the tetragonal axis lay along the acicular particle axis.

Samples were prepared in the shape of bars and cylinders. Bars $2 \times 2 \times 38$ mm were pressed at 3 atm using 2% ether resin or "Lucite" acrylic resin as a binder. The volume fraction of magnetic material in the resulting bar was approximately 0.4. Cylinders 7 mm high by 8 mm in diameter were pressed with no binder at 21 000 atm and 400°C. The volume fraction of magnetic material in these cylinders ranged from 0.95–0.98. Crystals as large as $0.2 \times 0.2 \times 0.3$ mm were also available. Table I lists some properties of representative samples studied.

Magnetization was measured by moving the sample in the normal induction technique[10] with fields up to 4000 oe provided by a solenoid. Temperatures from $-196°$ to 150°C were obtained by cooling with liquid nitrogen and heating with a resistance glass tube.

Reversible susceptibility, defined as the limit, for changes in internal field ΔH approaching zero, of the ratio $\Delta I/\Delta H$, where I is the volume magnetization, was measured as a function of field by the change in inductance of a resonant circuit coil upon insertion of a cylidrical sample. A Boonton 160A Q meter was used to provide the alternating field at 2 Mc and to measure the inductance change. A solenoid provided fields to 2000 oe.

Rotational torque measurements were carried out on a magnetometer designed after that of Byrnes and Crawford.[11] By using transducers of several sensitivities a torque range of 80–80$\times 10^3$ d-cm could be measured. Fields up to 26 000 oe were obtained with a Varian 4-in. electromagnet. Since samples of random particle alignment were used, orientation or single-crystal effects could not be measured, and torque curves were used only to obtain rotational hysteresis as a function of field.

Domain patterns were examined on natural faces of larger crystals by the Bitter technique using colloidal dispersions of magnetite prepared according to Kittel and Galt.[12]

III. RESULTS AND DISCUSSION

A. Particle Size Effects

Magnetization as a function of field is shown in Fig. 1 for five samples of different particle size. As the particles become smaller, the initial rapid rise in magnetization due to domain wall motion is lost and the data approach the limiting behavior of sample E. Samples with particles smaller than 0.2 μ in diameter by 1 μ in length dropped only slightly below the curve of sample E. There thus appeared to be a break in behavior at this particle size. For multidomain particles, almost all of the irreversible magnetization is associated with domain wall motion. The value of remanent magnetization as a function of field, obtained by measuring the remanence after incremental increases in the applied field starting from a demagnetized initial state, should then approach saturation in the case of randomly oriented particles of uniaxial anisotropy at fields approximately one-half those required for saturation of magnetization. In the case of randomly oriented single-domain particles, application of the magnetic field will cause irreversible changes in magnetization by reversing the spin direction in the particle. This irreversible process, and hence the remanence, will

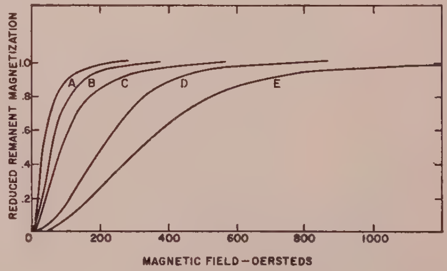

Fig. 2. Reduced remanent magnetization vs field for samples of Fig. 1.

---

[9] W. H. Cloud, M. S. Sadler and H. S. Jarrett, J. Phys. Chem. Solids (to be published).

[10] A. Arrott and J. E. Goldman, *Methods of Experimental Physics* (Academic Press, Inc., New York, 1959), Vol. 1, p. 535.

[11] W. S. Byrnes and R. G. Crawford, J. Appl. Phys. **29**, 493–95 (1958).

[12] C. Kittel and J. K. Galt in *Solid State Physics*, edited by F. Seitz and D. Turnbull (Academic Press, Inc., New York, 1956), Vol. 3, p. 492.

continue to increase almost to the fields required for saturation of magnetization. Figure 2 shows remanence curves for the samples of Fig. 1. Again it was found that for particles smaller than those of sample E the remanence curve changed only slightly.

The relationship between the magnetization and remanence curves may be shown by plotting for several samples the field required to saturate remanence vs the field required to half-saturate magnetization. Such a plot, Fig. 3, demonstrates that the largest particles behave as multidomain, while smaller particles achieve half-saturation in fields considerably less than those required to complete processes which introduce remanence. The steep rise in the plotted points above the dotted line of slope 1 is attributed to both single-domain behavior with irreversible magnetization reversals, and to the effect of magnetostatic energy in few-domain particles which increases the fields necessary to complete wall motion above those fields at which appreciable rotation can take place. For single-domain particles smaller than those of E, the latter effect is no longer present and the data lie in the region of E. There is considerable error in the determination of the remanence saturation field due to the slow approach to saturation.

In both the magnetization and remanence results, the break at a critical particle size is not so sharp as might be expected. This is attributed to the effect of particle size distribution. In particular, the presence of a few large particles can increase the low-field part of the magnetization curve to a considerable extent and may not contribute appreciably to the remanence curve. It is concluded that CrO_2 particles of size smaller than $0.2\,\mu$ in diameter with a length-to-diameter ratio of ~ 5 show single-domain behavior.

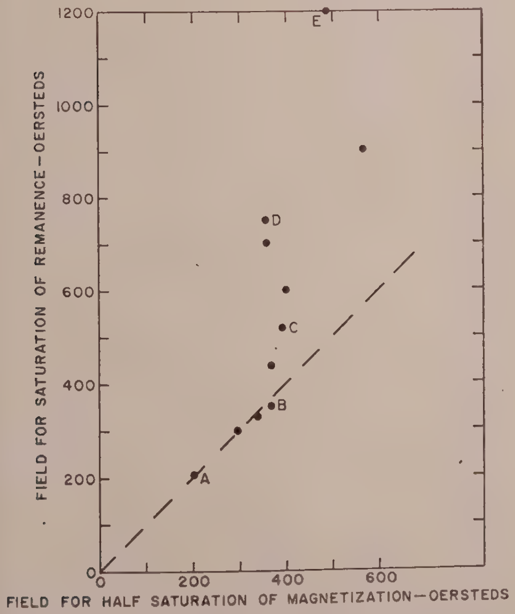

FIG. 3. Field required to saturate remanence vs field required to half-saturate magnetization. Particle size decreases from A to E.

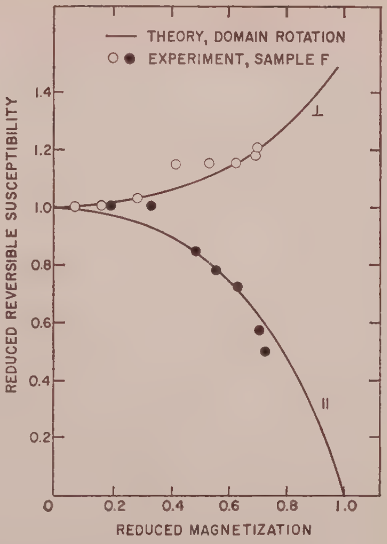

FIG. 4. Reduced reversible susceptibility vs reduced magnetization for small particles (sample F). Orientation of susceptibility field with respect to biasing field denoted as perpendicular ($\perp$) or parallel ($\|$).

A critical size for single-domain ellipsoids of CrO_2 may be calculated by balancing the magnetostatic energy of a single-domain particle against the wall energy required for a two-domain particle.[13] For a prolate ellipsoid of major semiaxis a and minor semiaxis b, with the easy axis of magnetization along the major axis, the wall energy for a two-domain particle is

$$W_w = \pi ab\sigma_w = \pi ab[2(\pi^2 JS^2K/a_0)^{\frac{1}{2}}],$$

where σ_w is wall energy in erg/cm², J is the exchange integral, S is the atomic spin, K is the crystalline anisotropy constant, and a_0 is the effective distance between magnetic ions. The magnetostatic energy for a single domain is

$$W_m = \tfrac{1}{2}NI_S^2(\tfrac{4}{3}\pi ab^2),$$

where N is the demagnetization coefficient and I_S is the volume saturation magnetization. By equating the two energies and using the values $I_S = 490$, $K = 3.0 \times 10^5$, $a_0 = 4 \times 10^{-8}$, and $\pi^2 JS^2 = kT_c = 400\ k$, where $k = 1.38 \times 10^{-16}$ erg/deg, a critical size $b_c = 0.16\ N\mu$ is obtained. For a ratio a/b of 5, $N = 0.7$, giving $2b_c = 0.46\,\mu$ as the largest minor axis for a single domain. It would then be predicted that the transition from single- to few-domain particles would occur in the range of samples examined here, as concluded from the measured magnetic properties. The difference between prediction and experiment may be attributed to the approximate

---

[13] See p. 504 ff. of reference 12.

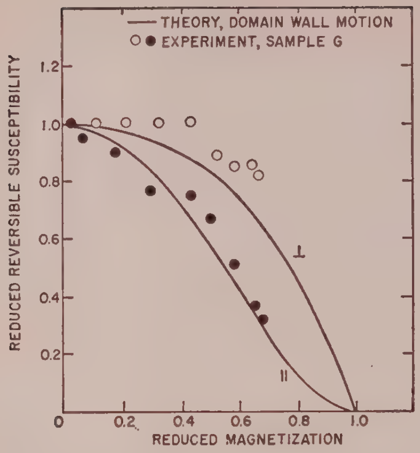

Fig. 5. Reduced reversible susceptibility vs reduced magnetization for large particles (sample *G*). Notation as in Fig. 4.

nature of the calculation and to the size and shape distributions which can give an effective N different from that of the average particle.[14]

Further evidence for the interpretation of the present magnetization studies in terms of a transition from few-domain to single-domain particles was found in measurements of the reversible susceptibility. Grimes[15] has shown that the expected behavior of the reversible magnetic susceptibility associated with domain rotation is quite different from that due to wall motion. His theoretical curves are given in Fig. 4 for the expected variation of susceptibility with magnetization measured parallel or perpendicular to the magnetizing field for domain rotation, and in Fig. 5 for domain wall motion. Assumptions made in deriving these curves are that interparticle effects may be described by an effective field, and that the magnetic material is polycrystalline and unoriented. In addition, interpretation of inductance changes as reversibility susceptibility requires the assumption that the natural frequencies of the magnetization processes were sufficiently above the 2 Mc used in measurement so that no resonance effects would be observed. Results for a sample of small particles are shown in Fig. 4, and agree with the predictions for pure domain rotation. Results for a larger-particle sample in Fig. 5 show both wall motion and rotation, with a larger contribution from the former. Samples of intermediate particle size showed behavior intermediate to those of the above examples. These results again indicate a transition from single to multidomain behavior for 5:1 acicular particles of $\sim0.2\mu$ diam.

Visual studies of domain wall motion at low applied fields were made by the Bitter technique on crystals $0.2\times0.2\times0.3$ mm. The patterns observed showed uniaxial anisotropy with a value of $K\sim3\times10^5$ erg/cm^3 calculated from domain dimensions. Domain walls were found to move easily and magnetization was one-half saturated for fields of 20–40 oe. This field strength is about one-fifth that required for one-half saturation of few-domain particles in the 1–5-μ size. The larger fields required for comparable magnetization of the few-domain particles is presumably due to the important role of magnetostatic energy,[7] as well as to the presence of single-domain particles even in those samples with the largest average particle size. Rotation of magnetization away from the easy direction was observed only for small closure regions at crystal edges. From the visual observations and reversible susceptibility measurements, it is concluded that the fields required for domain wall motion in few-domain particles are comparable to those required for domain rotation, and that only in larger, multidomain particles does the initial magnetization process become one primarily of wall motion.

B. Source of Coercivity

The origin of the coercivity may be determined by study of its variation with temperatures and comparison with the dependence on temperature expected for shape and crystalline anisotropy fields. The coercivity for randomly oriented single-domain particles can be calculated as follows: for crystalline anisotropy, an average coercivity given by[16] $\langle H_c\rangle=0.96K/I_S$ would equal 585 oe for CrO$_2$; for shape anisotropy, $\langle H_c\rangle=0.48(N_t-N_l)I_S$, according to the Stoner-Wohlfarth[3] uniform rotation model, or $\langle H_c\rangle=0.18\pi I_S(6K_N-4L_N)$, according to the Jacobs-Bean[5] chain-of-spheres model. For an a/b ratio of 5, the coercivities for these two

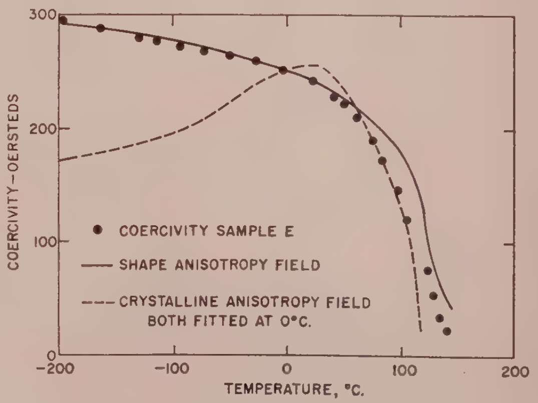

Fig. 6. Coercivity vs temperature for compact of single-domain particles (sample *E*), with theoretical shape and crystalline anisotropy fields adjusted to fit at 0°C.

---

[14] E. P. Wohlfarth, Research **7**, 518–20 (1954); Sci. J. Roy. Coll. Sci. **26**, 19–43 (1956).

[15] D. M. Grimes, Univ. Michigan Eng. Research Inst., Solid State Devices Lab., Dept. Elec. Eng., Tech. Rept. No. 1, December, 1956 (ASTIA AD97082); Proc. Second Conf. Magnetism and Magnetic Materials, AIEE Publ. **T91**, 570–575 (1957).

[16] See p. 507 ff. of reference 12.

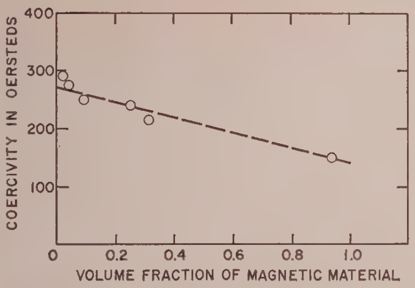

FIG. 7. Coercivity vs volume fraction of magnetic material.

models are 1230 and 590 oe, respectively, at room temperature. Both of these later coercivities should be decreased by an appropriate packing factor.[17] Figure 6 shows experimental data for a high-coercivity, single-domain particle sample together with theoretical curves fitted at 0°C for I_S and for K/I_S. The coercivity appears to arise primarily from a shape dependence. Coercivity-temperature data for larger few-domain particles also show agreement with temperature dependence of magnetization, again indicating a dominant contribution from shape anisotropy.

The coercivities for the smallest particles, measured on compacts with random particle orientation (Table I), are smaller than the expected values for either shape or crystalline anisotropy even when packing effects are taken into consideration. The primary cause of this discrepancy is believed to arise from the presence of a small number of large particles or masses which contribute to the magnetization and have a very low effective coercivity. Further development of synthesis methods has given samples of similar but much more uniform particle size, and these do show larger coercivities, in the range 350–450 oe. Any shape and size distribution, even if rather narrow, will give a coercivity lower than that of the average particle.[14]

An experimental study of the effect of packing on coercivity for single-domain particles is shown in Fig. 7. The dependence is considerably less than the $1-p$ behavior expected from simple considerations[17] and found for a number of materials.[18–20] Although it has been shown[17] that particle interactions can lead to dependences other than $1-p$, it is believed that additional effects may cause the slow change in coercivity with packing found here. These include the lack of true dispersion at low packing, the reduction of particle size due to crushing at high packing, and any crystalline anisotropy contributions to coercivity, all of which would have the effect of making $H_c(p)$ more independent of packing than a $1-p$ relationship. In addition, the application of extreme pressure to achieve densities above 90% may introduce an additional source of coercivity, that arising from magnetostrictive effects in the strained particles.

From the temperature dependence of coercivity, the crystalline anisotropy is found to contribute little. From the rough estimates above, however, this anisotropy would be expected to contribute an appreciable part of the total coercivity if shape and crystalline effects are additive. Although the macroscopic easy direction of magnetization appears to lie along the CrO_2 tetragonal axis, neutron diffraction and magnetization experiments show the moments to lie at ~40° to this axis in (110) planes. Calculations were carried out to estimate the effect of such an anisotropy on the coercivity of randomly oriented single-domain particles.

The total energy for an acicular particle was written as

$$E=I_SH_0\cos(\psi+\alpha)+K_1\sin^2\psi+K_2\cos^2(\beta-\psi)\sin^2(\beta-\psi),$$

where ψ, β, and $(180-\alpha)$ are the angles between the particle axis and the magnetization I_S, the crystalline anisotropy direction, and the applied field H_0, respectively, and K_1 and K_2 are the shape and crystalline energy coefficients, the former of the form $\langle N\rangle(I_S^2/2)$. Taking the derivative of E with respect to ψ and solving for a maximum value of H_0 gives the field required to reverse the particle magnetization against the anisotropies K_1 and K_2.[16] After determining H_0 for values of $0\leq\alpha\leq 90°$, a coercivity for random particles is calculated as that field required to reverse magnetization in one-half the particles; it can be shown that the actual coercivity will be less. The ratio of anisotropies is

$$\frac{K_2}{K_1}=\frac{K_2}{(\langle N\rangle I_S^2/2)}=\frac{2\times3\times10^5}{\langle N\rangle(490)^2}=\frac{2.5}{\langle N\rangle}.$$

For randomly oriented particles with a length/diameter ratio of 5:1, $\langle N\rangle=0.48(N_t-N_l)=2.5$, a value which should be decreased by some packing factor to account

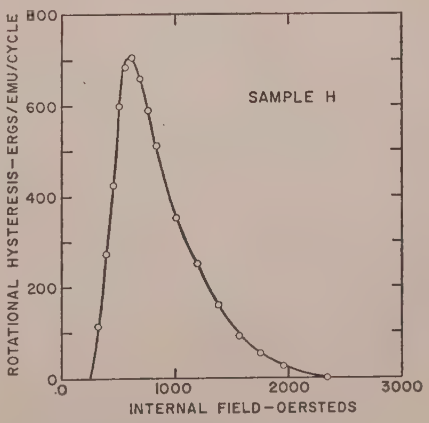

FIG. 8. Rotational hysteresis vs internal field for sample H.

---

[17] E. P. Wohlfarth, Proc. Roy. Soc. (London) **A232**, 208 (1955).

[18] L. Weil, Compt. rend. **225**, 229–30 (1947); **227**, 1347–49 (1948).

[19] F. E. Luborsky, J. Phys. Chem. **61**, 1336–40 (1957).

[20] A. H. Morrish and S. P. Yu, J. Appl. Phys. **26**, 1049–55 (1955).

TABLE II. Rotational hysteresis data.

Sample	$\int \frac{W_R}{I_S} d\left(\frac{1}{H}\right)$	$H_{\max}$[a]	Disk coercivity
H	1.10	2220	382
J	1.22	2380	234
K	1.33	2180	393
L	1.36	2500	297

[a] Applied field, corrected for disk demagnetization factor, at which rotational hysteresis becomes zero.

for interparticle interactions. For $K_2=K_1$ and $\beta=40°$, the reduced coercivity $h_0=H_0I_S/K_1$ is 1.58, compared to 1.10 for $K_2=0$. The value of β turns out not to be critical; for $\beta=0$, $h_0=1.68$.

The calculations have assumed I_S constant; i.e., a coherent rotation model. It appears that a crystalline anisotropy at an angle to the particle axis should favor fanning, curling, or buckling modes of magnetization reversal, and might even decrease the coercivity from that expected for shape anisotropy alone. It is concluded that simple addition of shape and crystalline anisotropies is not valid, but that the present calculations have not shown why crystalline anisotropy should be ineffective in contributing to coercivity.

One way to avoid corrections for random particle orientations and to measure the maximum internal fields directly is by use of rotational torque.[6] The rotational hysteresis is defined as $W_R= \int_0^{2\pi} Ld\theta$, where $I(H,\theta)$ is the torque on a sample slowly rotated in a magnetic field. Figure 8 shows rotational hysteresis as a function of internal field for a disk with a measured bulk coercivity of 382 oe (sample H). The hysteresis becomes zero at 2200 oe, showing maximum internal fields of this magnitude. Comparison of the curve with the sharp rise expected theoretically at the low-field side shows that a particle size distribution is present. In particular, contributions from low-coercivity particles are evident. Similar curves for other samples of CrO_2 showed maximum anisotropy fields from 2180–2500 oe. The origin of internal fields higher than 2000 oe must be ascribed to shape anisotropy, since the maximum contribution of crystalline anisotropy would be $2K/I_S=1200$ oe. The maximum value for shape anisotropy according to the Stoner-Wohlfarth model for an a/b ratio of 5 would be $(N_t-N_l)I_S=2560$ oe. With the temperature dependence described earlier, these results support the conclusion that the coercivity is determined almost entirely by shape for single-domain particles.

C. Magnetization Reversal Mechanism

Two aspects of rotational hysteresis measurements may be used to distinguish between different models for the magnetization reversal process in shape-dominated particles. The first of these is estimation of the maximum particle fields by determination of the field at which hysteresis disappears. Table II shows maximum fields so determined for several samples, all of single-domain particles. For coherent or parallel rotation with an ellipsoid of axial ratio 5, the effective field 2560 oe is predicted as noted above. For coherent rotation with a chain of five spheres, a maximum value $\pi I_S K_N=1370$ oe is predicted. The experimental maximum values are in better agreement with the Stoner-Wohlfarth model.

The rotational hysteresis integral $R= \int_0^\infty W_R/I_S \times d(1/H)$ gives a number which is independent of particle interactions but which depends on the magnetization reversal mechanism.[6] For random orientation of particles, coherent rotation in either an ellipsoid or chain of spheres gives a value $R=0.38$, while the chain of spheres with fanning gives 1.02. Values of R shown in Table II vary from 1.10–1.36. These all lie between the values 1.02 and 1.54 predicted for chains of spheres with random and planar alignment, respectively. In low fields magnetization changes occur by incoherent rotation, while in high fields the behavior is coherent and governed by shape anisotropy of the prolate ellipsoid type.

IV. CONCLUSIONS

Magnetic measurements on samples compacted from elongated particles of chromium dioxide over a range of sizes show a transition from few-domain to single-domain behavior for diameters $\approx 0.2\ \mu$ and a length/diameter ratio ≈ 5. Coercivity of both single-domain and few-domain particles is controlled by shape anisotropy, as evidenced by temperature dependences. Maximum particle fields of 2500 oe, determined by rotational hysteresis, are in agreement with shape anisotropy calculated by the Stoner-Wohlfarth uniform rotation model; coercivities of particle compacts are much lower due to particle interactions, the presence of particles larger than single domain, and incoherent rotation processes. The observed dependence on packing is much less than $1-p$, believed due primarily to lack of particle dispersion in low-density samples.

Measurements of the rotational hysteresis integral give values in agreement not with a uniform rotation model, but with the Jacobs-Bean chain of spheres.

Few-domain particles exhibit wall motion only in fields considerably higher than those required for comparable movement in bulk multidomain material. This effect is ascribed to the importance of surface magnetostatic energy for the small particles.

ACKNOWLEDGMENTS

The author wishes to thank M. S. Sadler for helpful discussions and interest. The materials studied were furnished by N. L. Cox, and electron microscopy was carried out by J. F. Godlewski. Anisotropy data were provided by W. H. Cloud and D. S. Schreiber. Many of the measurements were made by J. F. Yeninas.

OURNAL OF APPLIED PHYSICS VOLUME 32, NUMBER 7 JULY, 1961

Electrically Imploded-Exploded Aluminum Tube*

Eugene C. Cnare
Sandia Corporation, Albuquerque, New Mexico

(Received February 27, 1961)

A high-energy exploding wire facility has been used to investigate pinch effects in thin-walled aluminum tubing. The experiments carried out consisted of subjecting the tubing to the discharge of a 141-kj capacitor bank and observing its motion by flash radiography and by high-speed sequential photography. Each tube first imploded uniformly, then broke down into an arc discharge in a manner similar to that of solid exploding wires. The implosion or pinch phase is adequately accounted for by the magnetic forces of the current discharge first acting against the mechanical strength of the tube walls and then, after melting, against the wall inertia and the retarding force of the air being compressed within the tube.

INTRODUCTION

In the continuing study of the phenomena associated with electrically exploded metallic elements of various geometries, a thin-walled aluminum tube was observed to first implode uniformly and then to explode in a manner similar to that of an exploding wire. A capacitor bank discharged through the aluminum tube established the self-magnetic pinch force for the implosion phase. This phase is accounted for by the magnetic force of the discharge current first acting against the mechanical strength of the tube walls and then, after melting, acting against the wall inertia and the retarding force of the air being compressed within the tube. The other portions of the phenomenon are described qualitatively to maintain continuity in the discussion.

EXPERIMENTAL SYSTEM

The capacitor bank energy source stored 141 kj at 20 kv and was discharged by a spark gap through the aluminum tube test specimen. The aluminum tubes studied in the experiment described here had the following physical characteristics: (a) 19.0-cm length, (b) 0.476-cm radius, (c) 0.01-cm wall thickness. The tube, mounted at the capacitor bank terminals, is shown in Fig. 1. Flash radiography, high-speed sequential photography, and measurement of the discharge current contributed to the data presented in the next section.

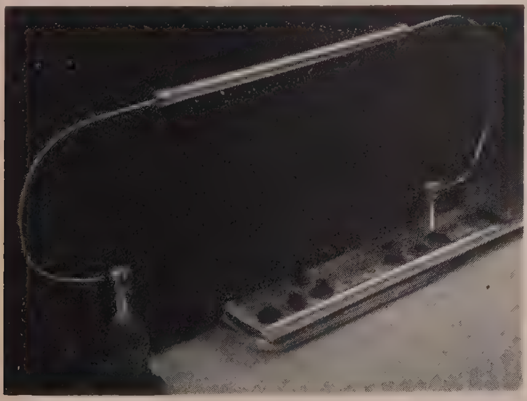

Fig. 1. Aluminum tube assembly mounted at test location.

RESULTS

A reproduction of the initial portion of the current-time measurement, as obtained from a Park current shunt,[1] is shown in Fig. 2. The flash x rays of Fig. 3 illustrate the tube appearance corresponding to the times indicated in Fig. 2 with a flash x-ray pre-exposure for comparison. Since the implosion was observed to be repeatable electrically, the outer radius of the tube vs

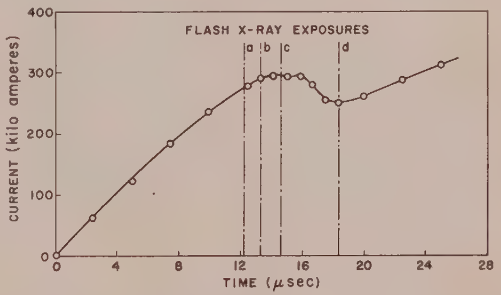

Fig. 2. Current vs time waveform of capacitor bank discharge through an aluminum tube.

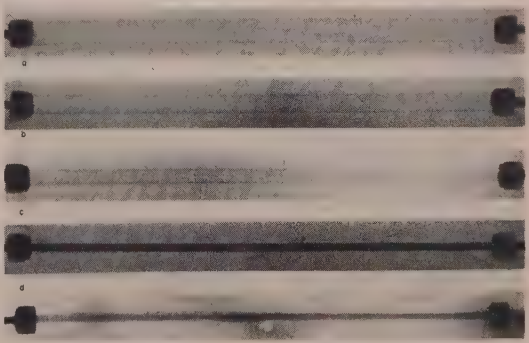

Fig. 3. Flash x rays (pre-exposure) of imploding-exploding aluminum tube.

---

* This work was done under the auspices of the U. S. Atomic Energy Commission.

[1] J. H. Park, J. Natl. Bur. Standards (U. S.) 39, 191 (1947).

time was measured from the flash x rays of several tests wherein the time of exposure was synchronized to different times in the implosion and explosion phases. The curve resulting from these tests is plotted in Fig. 4 and is separated into four regions to facilitate the discussion.

No measurable motion of the tube wall is to be expected until the magnetic pinch pressure on the wall exceeds the ultimate strength of the tube material. The time at which this pressure is reached can be calculated, and has been chosen as the time separating regions 1 and 2. The calculation is as follows: the magnetic pressure on the thin-walled tube in the emu system of units is given by

$$P=i^2/2\pi r^2, \qquad (1)$$

where i=instantaneous current, r=tube radius, and the tangential stress in a thin-walled cylinder is given by

$$S_t=Pr/T, \qquad (2)$$

where P=pressure, r=radius of cylinder, and T=wall thickness. By assuming a linear current-time dependency, and inserting the ultimate stress S_u for S_t, one can combine Eqs. (1) and (2) to obtain the time as

$$t=k^{-1}(2\pi rTS_u)^{\frac{1}{2}}=3.72\times10^{-6}\text{ sec}, \qquad (3)$$

where $k=2.22\times10^9$ (abamp/sec) and $S_u=2.28\times10^9$ (d/cm²).[2] Since it was reasonable to expect no appreciable tube wall motion until this time, the initial portion of Fig. 4 was drawn accordingly.

The second portion of the radius-time curve is a gradual decrease in radius with time. Since wall heating causes a temperature-dependent variation in the mechanical strength of the tube, a mathematical treatment during this portion of the collapse has not been attempted.

The third portion of the collapse is a rapid decrease in radius with time. On the suspicion that the tube material had received sufficient energy to reach the liquid phase, a plot of the action integral $\int i^2dt$ experienced by the tube vs time, Fig. 5, was made to determine the time at which the transition from solid to liquid was accomplished. The action to complete melt, indicated in the figure, was calculated with the aid of small exploding-wire data[3] and high-temperature heat content tables.[4] Scaling to large cross sections from small-wire data has been found, in previous comparisons,[5] to be accurate to within 10%. From Fig. 5, it can be seen that at $t=10.5$ μsec, the tube should be completely liquified.

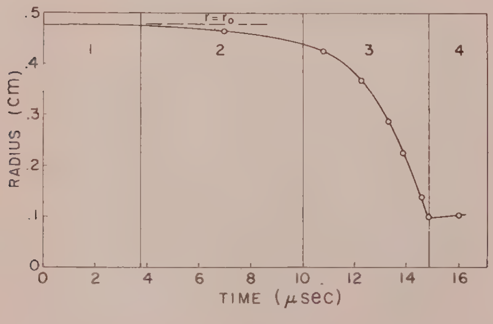

FIG. 4. Tube radius vs time as measured from flash x rays.

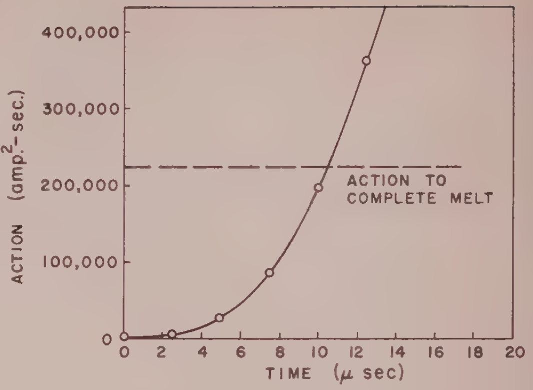

FIG. 5. Action experienced by the aluminum tube vs time.

Therefore, the third portion of the collapse is presumed to be the fluid motion of the tube walls driven by the magnetic pinch pressure and resisted by the pressure due to the adiabatic compression of the air inside the tube. Assuming uniform current distribution in a uniform tube wall, the following equation describing the tube wall motion was derived[6]:

$$\rho\frac{d[V_e r_e(r_e-r_i)]}{dt}=\frac{-2i^2(r_e+2r_i)}{3\pi(r_e+r_i)^2}+P_0r_i\left(\frac{r_{i0}}{r_i}\right)^{2\gamma}, \qquad (4)$$

where ρ=tube material density,

d/dt=total derivative with respect to time,

V_e=velocity of external tube radius,

r_e=external tube radius,

r_i=internal tube radius,

i=instantaneous current,

P_0=initial internal pressure,

r_{i0}=initial internal radius,

γ=ratio of specific heats, assumed equal to 1.4.

---

[2] *Handbook of Chemistry and Physics*, edited by D. Hodgman, R. C. Weast, and S. M. Selby (Chemical Rubber Publishing Company, Cleveland, Ohio, 1958), 40th ed., p. 2122.

[3] T. J. Tucker and F. W. Neilson, Sandia Corporation Tech. Memo. 334-59(51). Available from Office of Technical Services, Department of Commerce, Washington 25, D. C.

[4] K. K. Kelley, U. S. Bur. Mines, Bull. 476 (1949).

[5] E. C. Cnare and F. W. Neilson in *Exploding Wires*, edited by W. G. Chace and H. K. Moore (Plenum Press, Inc., New York. 1959), p. 83.

[6] Derived by J. R. Banister, Sandia Corporation, Albuquerque, New Mexico.

and with the restraint that $\pi(r_e^2-r_i^2)$ remains constant. The left-hand side of Eq. (4) is the time rate of change of momentum of a sector of the tube which has a unit length and an angular width of 1 rad. The right-hand side includes the net force on the angular sector resulting from the inward magnetic pinch force and the outward force caused by the adiabatic compression of the gas, atmospheric air, in the tube. The last term in Eq. (4) expressing the effect of air compression is not significant until the implosion is nearly complete. However, it does affect the minimum diameter to which the tube can be driven.

This equation was programed into an analog computer to determine the earliest time on the experimental radius-vs-time curve for which the equation was applicable. A computer solution beginning at $t=10$ μsec is shown in Fig. 6 with the experimentally obtained curve for comparison. This is the computer solution for which an excellent agreement with the experimental results and a small t_0, the time at which the computer solution of the problem is begun, occur together. This earliest time of agreement confirms the time of complete liquification, 10.5 μsec, predicted in connection with Fig. 5.

It is interesting to note that the smallest radius observed during the implosion, 0.098 cm, is very nearly identical to the radius of a solid rod having the same cross-sectional area as the original tube. This indicates that little or no vaporization has taken place through the completion of the implosion, justifying the constant area constraint used with Eq. (4).

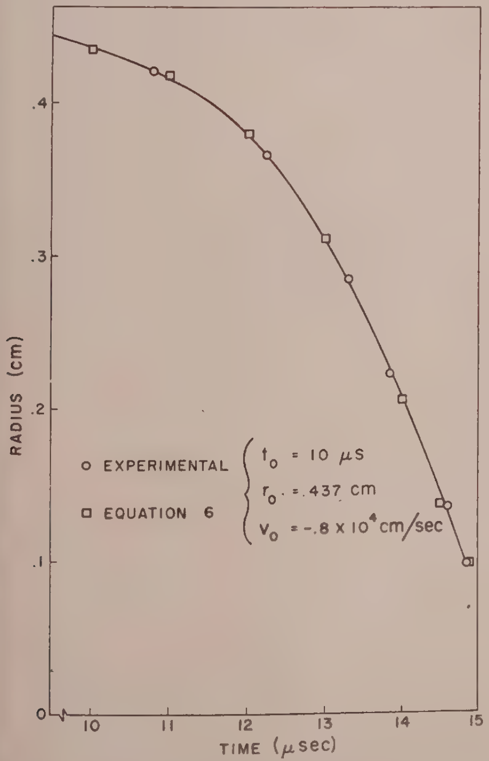

Fig. 6. Comparison of experimental results with computer solution of Eq. (6).

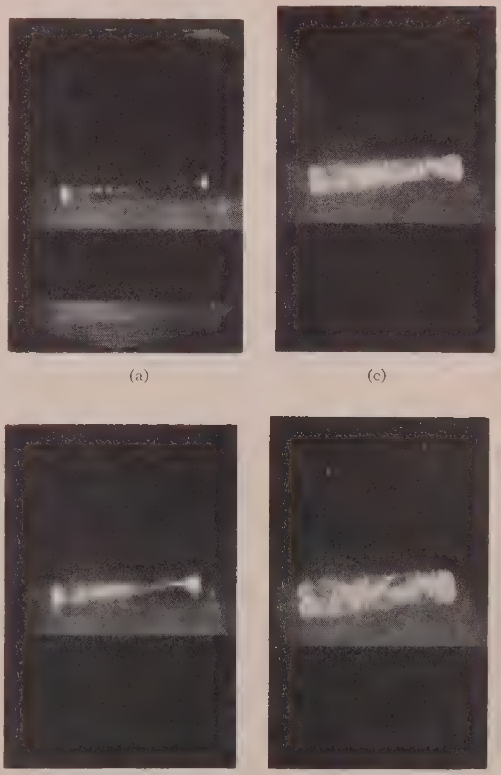
(a) (c)

(b) (d)

Fig. 7. Selected frames from a framing camera sequence of the explosion phase of the aluminum tube; 2 μsec between frames.

During the final portion of the radius-vs-time curve, Fig. 4, the imploded tube becomes unstable and forms a striated appearance, Fig. 3(d), similar to that which has been observed in connection with exploding wires.[7] Arcs form between these striations and progress rapidly to a single arc through the metallic vapor being emitted from the imploded tube. Selected frames from a framing camera sequence, Fig. 7, illustrate the optical appearance of the arc breakdown discussed above. The first frame corresponds in time to the flash x ray of Fig. 3(d). Subsequent frames showing the complete arc breakdown are at 2-μsec intervals.

SUMMARY

A model of the aluminum tube implosion-explosion has been deduced from the experimental results by considering the state of the material under test, the magnetic pressure on the tube walls due to current conduction, and the pressure of the air trapped inside the tube impeding the implosion. The mathematical descriptions of the implosion indicate that the salient effects governing the tube wall motion are indeed these. A more sophisticated treatment than has been advanced here would be required to account for the solid to liquid transition portion of the implosion.

---

[7] W. Müller in *Exploding Wires*, edited by W. G. Chase and H. K. Moore, (Plenum Press, Inc., New York, 1959), p. 186.

ACKNOWLEDGMENTS

The author wishes to thank James E. Van Meter for his able assistance in the experimental phase of this study.

JOURNAL OF APPLIED PHYSICS VOLUME 32, NUMBER 7 JULY, 1961

Vapor-Phase Growth of Single Crystals of II–VI Compounds

W. W. Piper and S. J. Polich
General Electric Research Laboratory, Schenectady, New York

(Received March 6, 1961)

A method of growing doped single crystals of II–VI compounds a few cm^3 in size is described. The crystal is grown from the vapor phase in a closed moving crucible which permits an efficient utilization of the charge and flexibility in the dimensions of the crystal.

Recently several investigators have reported on methods for growing large single crystals of CdS and other II–VI compounds which sublime easily from either the liquid phase[1,2] or the vapor phase.[3–7] Growth from the melt is encumbered by the high melting point and a vapor pressure of several atmospheres at that temperature. Earlier vapor phase techniques have been limited to single crystals of a few cubic millimeters or less in size. Greene *et al.*[3] have reported the growth of single crystals of CdS as large as 20 cm^3. The method described below differs in that often one single crystal is grown from the powdered charge, that a relatively small charge is needed, and that the length of the crystal is not limited by the temperature profile of the furnace.

A cross-sectional view of the furnace and crucible are shown in Fig. 1. Below this sketch is a typical temperature profile used for CdS. A similar profile increased by approximately 300C° is appropriate for ZnS. Other II–VI compounds have different optimum growing temperatures. In each case it is estimated that the vapor pressure is approximately 0.1 atm. The furnace is heated by a tapped helix of platinum–10% rhodium wire externally wound around an Alundum muffle. Within the muffle is shown a mullite tube which is gas-tight. The tube is closed at one end and sealed at the other end with a tapered glass joint to permit evacuation of the tube or injection of a slow flow of an inert gas at atmospheric pressure.

A CdS charge is sintered by packing CdS powder into a quartz tube open at both ends. The charge is vacuum baked at 500°–700°C for approximately 1 hr, then fired in a stream of H_2S at 900°–1000°C for 10 hr. This procedure serves to purify and to concentrate the charge. The density is increased from about 25% to about 80% of the crystal density. The shorter charge then required eliminates an early problem of the charge

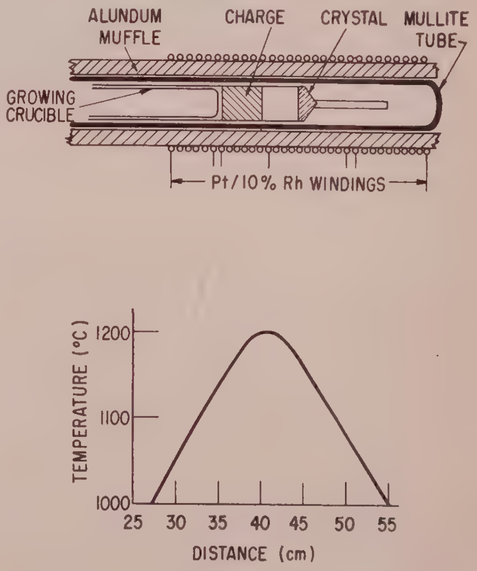

Fig. 1. Furnace cross section and temperature profile used fo growing CdS. The cross section is drawn to the same scale as th profile.

---

[1] A. Addamiano and P. A. Dell, J. Phys. Chem. **61**, 1020 (1957).

[2] W. E. Medcalf and R. H. Fahrig, J. Electrochem. Soc. **105**, 719 (1958).

[3] L. C. Green, D. C. Reynolds, S. J. Czyzak, and W. M. Baker, J. Chem. Phys. **29**, 1375 (1958).

[4] H. Yamashita and S. Ibuki, J. Phys. Soc. Japan **13**, 226 (1958).

[5] D. R. Boyd and Y. T. Sihvonen, J. Appl. Phys. **30**, 176 (1959).

[6] J. Nishimura and Y. Tanabe, J. Phys. Soc. Japan **14**, 850 (1959).

[7] S. Devlin, J. M. Jost, and L. R. Shiozawa, WADD Tech. Rept. 60-11 (June, 1960).

shrinking out of the hot zone. In preparing doped charges, an aqueous solution of the impurity is stirred into a slurry of the powdered compound. The powder is dried, mechanically mixed, and then sintered.

The crucible itself is made from standard clear quartz tubing. The outer tube is sealed off with a blunt conical tip. A quartz rod is joined to the tip end of the crucible. This aids in conducting the heat of sublimation axially down the crystal as it is growing. A charge of CdS is placed in the crucible as is shown in Fig. 1 and is backed up with a closed quartz tube which fits snugly into the crucible. The mullite protection tube containing the quartz crucible is evacuated and slowly heated up to 500°C. After a 1-hr bakeout to remove volatile impurities, a slow stream of argon at 1 atm is injected and escapes by bubbling through a bottle containing dibutyl phthalate. The furnace temperature is increased to the operating temperature and 1 atm of argon is maintained throughout the run.

The initial position of the crucible is such that the tip is near the maximum temperature. The entire mullite protection tube, containing the crucible, is mechanically pushed so that the tip moves into a cooler region at the rate of 0.3–1.5 mm/hr. The crucible velocity is constant during a particular run, but the optimum velocity will depend upon the temperature profile.

Although some vapor escapes past the inner quartz tube, this tube extends far enough into the cooler part of the furnace that the vapor condenses and seals off the crucible thus confining the rest of the charge. An equilibrium vapor pressure of the compound being grown is then established. Since the self-sealing of the crucible occurs near the final temperature configuration, the pressure difference stressing the quartz tube is approximately the vapor pressure of the compound.

As the tube moves, the supersaturation at the tip increases until nucleation occurs. Usually one seed crowds all others out and a single crystal grows out from the tip at approximately the rate at which the tube is being pushed. The growing surface is approximately 30C° below the temperature of the charge. Fig. 2 shows a single crystal of CdS as it was taken from the crucible. The diameter of the crystal is 13 mm. In principle one should not be limited in the length of the crystal to be grown.

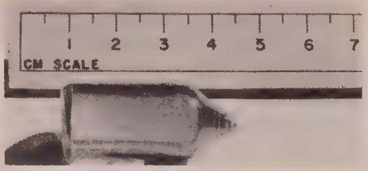

FIG. 2. Single crystal of CdS.

To the extent that the entire crucible is in thermal equilibrium, and therefore that the vapor contains the proper partial pressure of each constituent, any impurity in the charge should transfer to the crystal without segregation. For the system CdS:Ga, it has been noted that over a concentration range of 10–10^4 ppm of Ga in the charge, the impurity concentration in the crystal is equal to that of the charge within ±30%.

This method has been used successfully to grow crystals of ZnS and CdSe of similar size in the same furnace. The ZnS crystals exhibited well developed {11.0}, {10.0}, and {00.1} faces in several cases. Crystal orientation with the c axis parallel to and perpendicular to the growth axis has been noted on different runs.

Dr. M. Aven of the General Electric Research Laboratory using similar equipment has succeeded in growing crystals of comparable size of ZnSe and ZnTe. Furthermore he has grown mixed crystals of $Zn_xCd_{1-x}S$ and $ZnSe_xTe_{1-x}$ with virtually no evidence of segregation of any of the constituents. This is in marked contrast to the strong segregation of the components for the case of growth from the melt.

JOURNAL OF APPLIED PHYSICS VOLUME 32, NUMBER 7 JULY, 1961

Optical Properties of Oriented Polystyrene*

RICHARD S. STEIN
Department of Chemistry, University of Massachusetts, Amherst, Massachusetts

(Received October 13, 1960)

The orientation of a monomer unit of a polystyrene molecule is specified in terms of seven orientation functions, of which five are independent in the general case. The birefringence and infrared dichroism are expressed in terms of these orientation functions. The expression for infrared dichroism is dependent on the angle which the direction of dipole moment change for the normal mode of vibration concerned makes with the axes of the molecule. Experimental possibilities for determining these orientation functions are discussed.

INTRODUCTION

THE relationship between the birefringence and the infrared dichroism of a polyethylene crystal and the orientation functions for this polyethylene crystal have been discussed in previous publications.[1] The orientation function description has recently been extended to the specification of the accessible orientation states of biaxially oriented films.[2] It was pointed out that in the case of polystyrene, the benzene ring could rotate about the bond connecting it with the main chain, and that it was necessary to specify an additional function which characterized this rotation. The equations defining the optical properties would then also contain this function. In this paper, these equations will be formulated for the birefringence and the infrared dichroism of films subjected to a general three-dimensional orientation.

COORDINATE SYSTEM FOR A SEGMENT OF A POLYSTYRENE MOLECULE

The monomer unit of a polystyrene molecule will be located by means of the coordinate system shown in Fig. 1. The c axis is in the chain direction. It bisects the carbon-carbon bond of the main chain at the angle $(180°-\theta_T)/2$. The a axis is perpendicular to the c axis and coplanar with it and the C$-$C bond. The b axis is perpendicular to the a axis and the c axis, and forms a right-handed coordinate system. Three more axes, d, e, and f are introduced to define the orientation of the benzene ring. The d axis is perpendicular to the ring; the e axis is perpendicular to the d axis and in the plane of the ring; the f axis is also in the plane of the ring and perpendicular to the d and e axes, and is parallel to the C$-$C bond which connects the ring to the main chain. The angle between the d axis and the plane defined by the a and c axes is designated by ω. This angle characterizes the state of rotation of the benzene ring about the C$-$C bond. The a, b, and c axes are located with respect to the coordinate system of the film by the angles defined in previous publications and shown in Fig. 2. The orientation functions associated with these angles are summarized in the following equations:

$$f_\alpha=\frac{3\langle\cos^2\alpha\rangle_{\mathrm{av}}-1}{2} \qquad (1)$$

$$f_\beta=\frac{3\langle\cos^2\beta\rangle_{\mathrm{av}}-1}{2} \qquad (2)$$

$$f_\epsilon=\frac{3\langle\cos^2\epsilon\rangle_{\mathrm{av}}-1}{2} \qquad (3)$$

$$f_\delta=2\langle\cos^2\delta\rangle_{\mathrm{av}}-1 \qquad (4)$$

$$f_\gamma=2\langle\cos^2\gamma\rangle_{\mathrm{av}}-1 \qquad (5)$$

$$f_\sigma=2\langle\cos^2\sigma\rangle_{\mathrm{av}}-1 \qquad (6)$$

$$f_\omega=2\langle\cos^2\omega\rangle_{\mathrm{av}}-1. \qquad (7)$$

These angles and functions are not all independent, but are interrelated by constraining equations.[2] Unit vectors along the a, b, c, d, e, and f axes may be expressed in terms of $\mathbf{i}$, $\mathbf{j}$, and $\mathbf{k}$, the unit vectors along the x, y, and z axes, respectively, according to the following notation:

$$\mathbf{a}=(\sin\alpha\,\sin\delta)\mathbf{i}+(\sin\alpha\,\cos\delta)\mathbf{j}+(\cos\alpha)\mathbf{k}; \qquad (8)$$

$$\mathbf{b}=(\sin\beta\,\sin\gamma)\mathbf{i}+(\sin\beta\,\cos\gamma)\mathbf{j}+(\cos\beta)\mathbf{k}; \qquad (9)$$

$$\mathbf{c}=(\sin\epsilon\,\sin\sigma)\mathbf{i}+(\sin\epsilon\,\cos\sigma)\mathbf{j}+(\cos\epsilon)\mathbf{k}; \qquad (10$$

$$\mathbf{d}=[\sin\omega\,\sin(\theta_T/2)]\mathbf{a}+[\pm\sin\omega\,\cos(\theta_T/2)]\mathbf{b}+(\cos\omega)\mathbf{c}; \qquad (11$$

$$\mathbf{e}=[\cos\omega\,\sin(\theta_T/2)]\mathbf{a}+[\pm\cos\omega\,\cos(\theta_T/2)]\mathbf{b}+(\sin\omega)\mathbf{c}; \qquad (12$$

$$\mathbf{f}=[\cos(\theta_T/2)]\mathbf{a}+[\pm\sin(\theta_T/2)]\mathbf{b}. \qquad (13$$

The ± which appears in the b component in Eqs (11)–(13) is related to the tacticity of the polymer a previously discussed.[2] In all cases of practical interest the + and − should be chosen in this term with equa probability. θ_T is the tetrahedral angle. The expression

---

[*] Supported in part by a contract from the Office of Naval Research and in part by grants from the National Science Foundation and the Plax Corporation, and assistance from the Monsanto Chemical Company.

[1] R. S. Stein, ONR Tech. Rept. No. 8, Project NR 356-378, University of Massachusetts, Amherst, Massachusetts (1958); J. Pol. Sci. **31**, 327, 335 (1958).

[2] R. S. Stein, ONR Tech. Rept. No. 21, Project NR 356-378, University of Massachusetts, Amherst, Massachusetts (1960).

For **a**, **b**, and **c** in Eqs. (9) and (10) may be substituted into Eqs. (11)–(13) to give such equations as:

$$\mathbf{d}=[\sin\omega\,\sin(\theta_T/2)\sin\alpha\,\sin\delta\pm\sin\omega\,\cos(\theta_T/2)\sin\beta\,\sin\gamma+\cos\omega\,\sin\epsilon\,\sin\sigma]\mathbf{i}+[\sin\omega\,\sin(\theta_T/2)\sin\alpha\,\cos\delta\pm\sin\omega\,\cos(\theta_T/2)\sin\beta\,\cos\gamma+\cos\omega\,\sin\epsilon\,\cos\sigma]\mathbf{j}+[\sin\omega(\sin\theta_T/2)\cos\alpha\pm\sin\omega\,\cos(\theta_T/2)\cos\beta+\cos\omega\,\cos\epsilon]\mathbf{k}. \quad (14)$$

CALCULATION OF BIREFRINGENCE

Two components of birefringence must be specified in order to describe a three-dimensionally oriented film:

$$\Delta_x=n_z-n_y, \quad (15)$$

$$\Delta_z=n_x-n_y, \quad (16)$$

where n_x, n_y, and n_z are the refractive indices for polarized light having its electrical vector along the x, y, and z axes, respectively, of the film. The refractive index differences may be related to the polarizability differences in these directions by the differentiated Lorentz-Lorenz equation[3]:

$$(n_z-n_y)=(2/9)\pi[(n^2+2)^2/n](P_z-P_y). \quad (17)$$

P_y, for example, is in this equation the polarizability of the material per unit volume for light polarized with its electric field in the y direction. n is the average refractive index of the polymer. P_y may be resolved in two parts, as expressed in

$$P_y=n_m[(P_y)_m+(P_y)_b]. \quad (18)$$

$(P_y)_m$ is the polarizability of the monomer unit, not including the benzene ring, for light polarized in the y direction. This is expressed in units of polarizability per monomer unit. Similarly, $(P_y)_b$ is the polarizability for light polarized in the y direction per benzene ring. n_m is the number of monomer units per unit volume, and is given in

$$n_m=[\rho N_0/M_m], \quad (19)$$

where ρ is the density of the polymer and M_m is the molecular weight of the monomer unit including the benzene ring. N_0 is Avogadro's number. The polarizabilities of the monomer units and the benzene rings may be expressed in terms of their polarizabilities along their principal axes and the angle between these principal axes in the y direction, as expressed in

$$(P_y)_m=P_a\langle(\mathbf{a}\cdot\mathbf{j})^2\rangle_{\mathrm{av}}+P_b\langle(\mathbf{b}\cdot\mathbf{j})^2\rangle_{\mathrm{av}}+P_c\langle(\mathbf{c}\cdot\mathbf{j})^2\rangle_{\mathrm{av}}, \quad (20)$$

$$(P_y)_b=P_d\langle(\mathbf{d}\cdot\mathbf{j})^2\rangle_{\mathrm{av}}+P_e\langle(\mathbf{e}\cdot\mathbf{j})^2\rangle_{\mathrm{av}}+P_f\langle(\mathbf{f}\cdot\mathbf{j})^2\rangle_{\mathrm{av}}. \quad (21)$$

P_a is the polarizability along the a axis of the monomer, P_b the polarizability along the b axis, etc., and $\langle(\mathbf{a}\cdot\mathbf{j})^2\rangle_{\mathrm{av}}$ is equal to the square of the cosine of the angle between the z axis and the y axis. For example, such terms as $\langle(\mathbf{a}\cdot\mathbf{j})^2\rangle_{\mathrm{av}}$ may be obtained from Eqs. (8)–(10) which give, for example,

$$\langle(\mathbf{a}\cdot\mathbf{j})^2\rangle_{\mathrm{av}}=\langle(\sin^2\alpha\,\cos^2\delta)\rangle_{\mathrm{av}}. \quad (22)$$

If there is no correlation between the uniaxial and biaxial orientation functions, this may be expressed in terms of the appropriate orientation functions, as in

$$\langle(\mathbf{a}\cdot\mathbf{j})^2\rangle_{\mathrm{av}}=\tfrac{1}{3}(1-f_\alpha)(1+f_\delta). \quad (23)$$

On substituting results of this type into Eq. (20), one

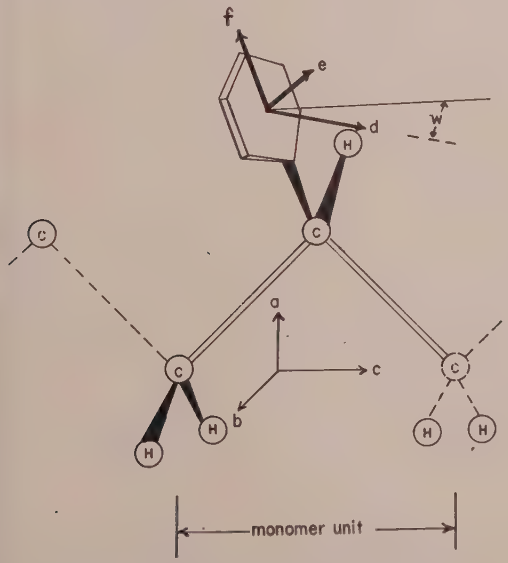

FIG. 1. Coordinate system for a monomer unit of a polystyrene molecule.

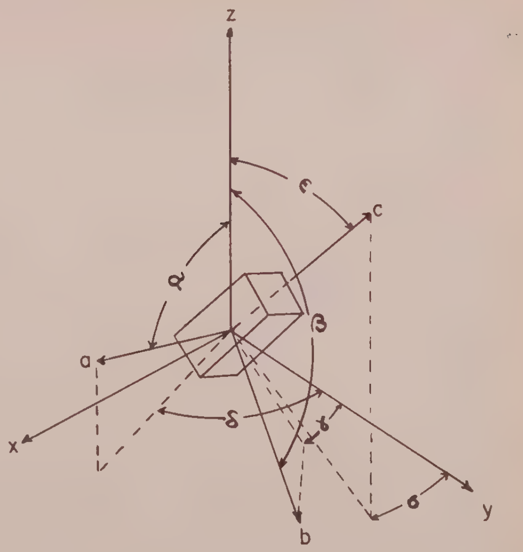

FIG. 2. Angle between the a, b, and c axes and the coordinate system of the film. The Z axis is the unique (machine) direction of the film. The x axis is the normal to the plane of the film (yz).

---

[3] R. S. Stein and F. H. Norris, J. Polymer Sci. 21, 381 (1956).

obtains

$$\begin{aligned}(P_y)_m=\tfrac{1}{3}[&P_a(1-f_\alpha)(1+f_\delta)+P_b(1-f_\beta)(1+f_\gamma)\\&+P_c(1-f_\epsilon)(1+f_\sigma)].\end{aligned}\qquad(24)$$

Similarly,

$$\begin{aligned}(P_x)_m=\tfrac{1}{3}[&P_a(1-f_\alpha)(1-f_\delta)+P_b(1-f_\beta)(1-f_\gamma)\\&+P_c(1-f_\epsilon)(1-f_\sigma)],\end{aligned}\qquad(25)$$

$$(P_z)_m=\tfrac{1}{3}[P_a(2f_\alpha+1)+P_b(2f_\beta+1)+P_c(2f_\epsilon+1)]\qquad(26)$$

are obtained for the x and z components of the polarizability of the monomer unit. To obtain the term $\langle(\mathbf{d}\cdot\mathbf{j})^2\rangle_{\text{av}}$ in Eq. (21) for the y component of the polarizability of the benzene ring, one uses Eq. (14) for the unit vector **d** to give

$$\begin{aligned}\langle(\mathbf{d}\cdot\mathbf{j})^2\rangle_{\text{av}}\\=&\langle\sin^2\omega\,\sin^2(\theta_T/2)\sin^2\alpha\,\cos^2\delta\rangle_{\text{av}}\\&+\langle\sin^2\omega\,\cos^2(\theta_T/2)\sin^2\beta\,\cos^2\gamma+\cos^2\omega\,\sin^2\epsilon\,\cos^2\sigma\rangle_{\text{av}}\\&+\langle 2\,\sin\omega\,\cos\omega\,\sin(\theta_T/2)\sin\alpha\,\sin\epsilon\,\cos\delta\,\cos\sigma\rangle_{\text{av}}.\end{aligned}\qquad(27)$$

The cross products involving the ± term disappear if the positive and negative contributions occur with equal frequency. If, as is most probable, the angular rotation of the benzene ring is symmetrical, the $\langle\sin\omega\,\cos\omega\rangle_{\text{av}}$ [appearing in the last term of Eq. (27)] is 0, so that this term vanishes. If there is no correlation between the uniaxial and biaxial orientation angle, and with the angle characterizing rotation of the benzene ring, then orientation functions may be substituted into Eq. (27) to get

$$\begin{aligned}\langle(\mathbf{d}\cdot\mathbf{j})^2\rangle_{\text{av}}=\tfrac{1}{6}[&(1-f_\alpha)(1+f_\delta)(1-f_\omega)\sin^2(\theta_T/2)\\&+(1-f_\beta)(1+f_\gamma)(1-f_\omega)\cos^2(\theta_T/2)\\&+(1-f_\epsilon)(1+f_\sigma)(1+f_\omega)].\end{aligned}\qquad(28)$$

By treating the vectors **e** and **f** in a similar manner,

$$\begin{aligned}\langle(\mathbf{e}\cdot\mathbf{j})^2\rangle_{\text{av}}=\tfrac{1}{6}[&(1-f_\alpha)(1+f_\delta)(1+f_\omega)\sin^2(\theta_T/2)\\&+(1-f_\beta)(1+f_\gamma)(1+f_\omega)\cos^2(\theta_T/2)\cos^2(\theta_T/2)\\&+(1-f_\epsilon)(1+f_\sigma)(1-f_\omega)]\end{aligned}\qquad(29)$$

$$\begin{aligned}\langle(\mathbf{f}\cdot\mathbf{j})^2\rangle_{\text{av}}=\tfrac{1}{3}[&(1-f_\alpha)(1+f_\delta)\cos^2(\theta_T/2)\\&+(1-f_\beta)(1+f_\gamma)\sin^2(\theta_T/2)]\end{aligned}\qquad(30)$$

are obtained. By substituting these into Eq. (21), one obtains

$$\begin{aligned}(P_y)_b=\tfrac{1}{6}P_d[&(1-f_\alpha)(1+f_\delta)(1-f_\omega)\,\sin^2(\theta_T/2)\\&+(1-f_\beta)(1+f_\gamma)(1-f_\omega)\cos^2(\theta_T/2)\\&+(1-f_\epsilon)(1+f_\sigma)(1+f_\omega)]\\&+\tfrac{1}{6}P_e[(1-f_\alpha)(1+f_\delta)(1+f_\omega)\sin^2(\theta_T/2)\\&+(1-f_\beta)(1+f_\gamma)(1+f_\omega)\cos^2(\theta_T/2)\\&+(1-f_\epsilon)(1+f_\sigma)(1-f_\omega)]\\&+\tfrac{1}{3}P_f[(1-f_\alpha)(1+f_\delta)\sin^2(\theta_T/2)\\&+(1-f_\beta)(1+f_\gamma)\cos^2(\theta_T/2)].\end{aligned}\qquad(31)$$

The equation for the x component of the polarizability of the benzene ring is similar, except that the signs of f_δ, f_γ, and f_σ are reversed. The z component is given by

$$\begin{aligned}(P_z)_b=\tfrac{1}{6}P_d[&1+2f_\alpha)(1-f_\omega)\sin^2(\theta_T/2)\\&+(1+2f_\beta)(1-f_\omega)\cos^2(\theta_T/2)+(1+2f_\epsilon)(1+f_\omega)]\\&+\tfrac{1}{6}P_e[(1+2f_\alpha)(1+f_\omega)\sin^2(\theta_T/2)\\&+(1+2f_\beta)(1+f_\omega)\cos^2(\theta_T/2)+(1+2f_\epsilon)(1-f_\omega)]\\&+\tfrac{1}{3}P_f[(1+2f_\alpha)\sin^2(\theta_T/2)\\&+(1+2f_\beta)\cos^2(\theta_T/2)].\end{aligned}\qquad(32)$$

By combining the above relationships and using

$$f_\alpha+f_\beta+f_\epsilon=0\qquad(33)$$

$$f_\delta(1-f_\alpha)+f_\gamma(1-f_\beta)+f_\sigma(1-f_\epsilon)=0,\qquad(34)$$

we obtain

$$\begin{aligned}P_z-P_y=n_m\Big\{&[P_e-P_c+(\tfrac{1}{2})\langle P_d(1-f_\omega)+P_e(1+f_\omega)\rangle\\&\times\sin^2(\theta_T/2)-\tfrac{1}{2}\langle P_d(1+f_\omega)+P_e(1-f_\omega)\rangle\\&+P_f\cos^2(\theta_T/2)]\left[f_\alpha-\frac{f_\delta(1-f_\alpha)}{3}\right]\\&+[P_b-P_c+\tfrac{1}{2}\langle P_d(1-f_\omega)+P_e(1+f_\omega)\rangle\\&\times\cos^2(\theta_T/2)-\tfrac{1}{2}\langle P_d(1+f_\omega)+P_e(1-f_\omega)\rangle\\&+P_f\sin^2(\theta/2)]\left[f_\beta-\frac{f_\gamma(1-f_\beta)}{3}\right]\Big\}.\end{aligned}\qquad(35)$$

As can be seen from Eqs. (15) and (17), this quantity (P_z-P_y) is proportional to the x component of the birefringence of the polymer. (P_x-P_y), which is proportional to the z component of the birefringence, is obtained in a similar manner and given by

$$\begin{aligned}P_x-P_y=\tfrac{2}{3}n_m\{&[P_c-P_a-\tfrac{1}{2}\langle P_d(1-f_\omega)+P_e(1+f_\omega)\rangle\\&\times\sin^2(\theta_T/2)+\tfrac{1}{2}\langle P_e(1+f_\omega)+P_e(1-f_\omega)\rangle\\&-P_f\cos^2(\theta_T/2)]f_\delta(1-f_\alpha)+[P_c-P_b\\&-\tfrac{1}{2}\langle P_d(1-f_\omega)+P_e(1+f_\omega)\rangle\cos^2(\theta_T/2)\\&+\tfrac{1}{2}\langle P_d(1+f_\omega)+P_e(1-f_\omega)\rangle\\&-P_f\sin^2(\theta_T/2)]f_\gamma(1-f_\beta)\}.\end{aligned}\qquad(36)$$

This component is only different from zero in the case of biaxial orientation where f_δ or f_γ are nonzero. For the tetrahedral angle, $\sin^2(\theta_T/2)=\tfrac{2}{3}$ and $\cos^2(\theta_T/2)=\tfrac{1}{3}$. On substituting these values into Eqs. (35) and (36), one obtains

$$\begin{aligned}P_z-P_y=n_m\Big\{&[P_a-P_c-\tfrac{1}{6}\langle P_d(1+5f_\omega)+P_e(1-5f_\omega)\\&-2P_f\rangle]\left[f_\alpha-f_\delta\frac{(1-f_\alpha)}{3}\right]\\&+[P_b-P_c-\tfrac{1}{3}\langle P_d(1+2f_\omega)+P_e(1-2f_\omega)\\&-2P_f\rangle]\left[f_\beta-f_\gamma\frac{(1-f_\beta)}{3}\right]\Big\},\end{aligned}\qquad(37)$$

$$P_x-P_y=\tfrac{2}{3}n_m\{[P_c-P_a+\tfrac{1}{6}\langle P_d(1+5f_\omega)+P_e(1-5f_\omega)-2P_f\rangle]f_\delta(1-f_\alpha)+[P_c-P_b+\tfrac{1}{3}\langle P_d(1+2f_\omega)+P_e(1-2f_\omega)-2P_f\rangle]f_\gamma(1-f_\beta)\}. \tag{38}$$

For uniaxial orientation, f_δ and $f_\gamma=0$ and $f_\alpha=f_\beta = -f_\epsilon/2$. Then Eq. (37) reduces to

$$P_z-P_y=n_mf_\epsilon\left\{P_c-\left(\frac{P_a+P_b}{2}\right)+\frac{1}{2}\left[\frac{P_d(1+3f_\omega)}{2}+\frac{P_e(1-3f_\omega)}{2}-P_f\right]\right\}. \tag{39}$$

Under these conditions, the birefringence is a function of only two orientation functions, f_ϵ for the chain and f_ω for the rotation of the benzene ring. The special case for free rotation of the benzene ring where $f_\omega=0$ is given by

$$P_z-P_y=n_mf_\epsilon\left[P_c-\left(\frac{P_a+P_b}{2}\right)+\frac{1}{2}\left(\frac{P_d+P_e}{2}-P_f\right)\right]. \tag{40}$$

If the benzene ring is restricted to being perpendicular to the chain, $f_\omega=1$, and

$$P_z-P_y=n_mf_\epsilon\left[P_c\left(\frac{P_a+P_b}{2}\right)+P_d-\left(\frac{P_e+P_f}{2}\right)\right] \tag{41}$$

results. The effect of rotation of the benzene ring on the birefringence of polystyrene has been discussed by Gurnee.[4] Following his approach, f_ω may be expressed as a function of $V(\omega)$, the potential energy characterizing the rotation of the benzene ring:

$$f_\omega=\frac{2\int_0^{2\pi}\cos^2\omega\, e^{-V(\omega)/kT}d\omega}{\int_0^{2\pi}e^{-V(\omega)/kT}d\omega}-1. \tag{42}$$

Gurnee has discussed various special cases for the potential function $V(\omega)$. The values of the polarizabilities P_a through P_f may be obtained using the assumption of additivity of bond polarizabilities.[5–7] By this approach, the polarizability in a particular direction P_k may be obtained by the equation

$$P_k=\textstyle\sum_i[(b_1-b_2)_i\cos^2\theta_{ik}+b_{2i}], \tag{43}$$

TABLE I. Polarizabilities of bonds.

Bond	Polarizability (cm³×10²⁵) Denbigh b_1	b_2	Δ	b	Bunn and Daubeney b_1	b_2	Δ	b
C−C	18.8	0.2	18.6	6.40	9.68	2.63	7.05	4.98
C−H	7.9	5.8	2.1	6.50	7.82	5.73	2.09	6.43

where b_1 and b_2 are the polarizabilities of the ith bond, parallel to and perpendicular to the axis of the bond. θ_{ik} is the angle between the axis of the ith bond in the k direction. $\sum_i$ is over all bonds, constituting the segment whose polarizability is being calculated. The equations

$$P_a=2(b_1-b_2)_{\mathrm{CC}}\cos^2(\theta_T/2)+2b_{2\mathrm{CC}}+3(b_1-b_2)_{\mathrm{CH}}\cos^2(\theta_T/2)+3b_{2\mathrm{CH}} \tag{44}$$

$$P_b=2b_{2\mathrm{CC}}+3(b_1-b_2)_{\mathrm{CH}}\sin^2(\theta_T/2)+3b_{2\mathrm{CH}} \tag{45}$$

$$P_c=2(b_2)_{\mathrm{CC}}\sin^2(\theta_T/2)+2b_{2\mathrm{CC}}+3b_{2\mathrm{CH}} \tag{46}$$

give P_a, P_b, and P_c obtained in this way. The subscript CC designates the carbon-carbon bond and CH the carbon-hydrogen bond. On substituting the bond angles, these equations reduce to

$$P_a=\bar{P} \tag{47}$$

$$P_b=\bar{P}+\tfrac{2}{3}\Delta_{\mathrm{CC}}+\Delta_{\mathrm{CH}} \tag{48}$$

$$P_c=\bar{P}+\tfrac{2}{3}\Delta_{\mathrm{CC}}-\Delta_{\mathrm{CH}}. \tag{49}$$

$\bar{P}$, Δ_{CC}, and Δ_{CH} are defined by

$$\bar{P}=2\frac{(b_1+2b_2)_{\mathrm{CC}}}{3}+3\frac{(b_1+2b_2)_{\mathrm{CH}}}{3} \tag{50}$$

$$\Delta_{\mathrm{CC}}=(b_1-b_2)_{\mathrm{CC}} \tag{51}$$

$$\Delta_{\mathrm{CH}}=(b_1-b_2)_{\mathrm{CH}}. \tag{52}$$

Two differing set of bond polarizabilities are reported in the literature.[5,6] These are given in Table I. By using these two sets of values, P_a, P_b, and P_c may be obtained, values for which are summarized in Table II. To obtain the principal polarizabilities of the benzene

TABLE II.

Polarizability	Denbigh cm³×10²⁵	Bunn and Daubeney cm³×10²⁵
P_a	32.3	29.3
P_b	22.2	26.6
P_c	42.6	31.8
P_d	54.6	54.9
P_e	116.4	116.3
P_f	138.3	138.6

---

[4] E. F. Gurnee, J. Appl. Phys. **25**, 1232 (1954).

[5] K. G. Denbigh, Trans. Faraday Soc. **36**, 936 (1940).

[6] C. W. Bunn and R. de P. Daubeney, Trans. Faraday Soc. **50**, 1173 (1954).

[7] R. P. Smith and E. Mortensen, J. Chem. Phys. **32**, 502, 508 (1960).

TABLE III. Variation of the maximum birefringence of uniaxially oriented polystyrene with f_ω.

f_ω	Δ_x (at $f_\epsilon=1$)
+1	−0.276
0	−0.161
−1	+0.195

ring, we shall follow Gurnee,[4] and use the principal polarizabilities for the toluene molecule reported by Stuart and Volkmann.[8] Using our notation, these are $b_d=74.8\times10^{-25}$ cm³ per molecule, $b_e=136.6\times10^{-25}$ cm³ per molecule, and $b_f=156.4\times10^{-25}$ cm³ per molecule. One should, however, subtract the contribution of the three carbon-hydrogen bonds of the methyl group of the toluene from the polarizabilities, as follows:

$$\begin{aligned}P_d&=b_d-3[(b_1-b_2)_{\mathrm{CH}}\cdot\tfrac{1}{2}\sin^2\theta_T+b_{2\mathrm{CH}}]\\&=b_d-\tfrac{4}{3}\Delta_{\mathrm{CH}}-3b_{2\mathrm{CH}}\end{aligned}\tag{53}$$

$$P_e=b_e-\tfrac{4}{3}\Delta_{\mathrm{CH}}-3b_{2\mathrm{CH}}\tag{54}$$

$$\begin{aligned}P_f&=b_f-3[(b_1-b_2)_{\mathrm{CH}}\cos^2\theta_T+b_{2\mathrm{CH}}]\\&=b_f-\tfrac{1}{3}\Delta_{\mathrm{CH}}-3b_{2\mathrm{CH}}.\end{aligned}\tag{55}$$

On substituting bond polarizabilities, the values for P_d, P_e, and P_f, included in Table II, are obtained. If these polarizabilities are substituted, for example in Eq. (39), and this is combined with Eqs. (15) and (17), one obtains

$$\Delta_x=[0.075(1+3f_\omega)+0.160(1-f_\omega)-0.296]f_\epsilon\tag{56}$$

for the x component of birefringence. A value of 1.59 for the average value of the refractive index of polystyrene, and 1.06 for its density, was used. The Denbigh polarizability values were used in this equation. In Table III the maximum possible birefringence of uniaxially oriented polystyrene, that is with $f_\epsilon=1$, is listed for some limiting values of f_ω. The values are somewhat higher than those reported by Gurnee,[4] probably because of his neglect of the monomer bond contribution and the contribution due to the CH bond in the toluene.

INFRARED DICHROISM

Consider a normal mode of vibration of a portion of a molecule, where in the course of the vibration the dipole moment varies in the direction indicated by the unit vector **M**. A beam of polarized infrared radiation, having a frequency equal to that of the normal mode, passes through the sample. The direction of polarization of the electrical field of this beam is indicated by **O**. The absorbency of this infrared beam will then be given by

$$A=K\langle(\mathbf{M}\cdot\mathbf{O})^2\rangle_{\mathrm{av}},\tag{57}$$

where K is a constant which is independent of orientation but dependent upon the particular infrared band. The direction of $\mathbf{M}_m$ is specified with respect to the coordinate system of the monomer unit by the angles μ and ω (Fig. 3), and may be expressed in the terms of unit vectors **a**, **b**, and **c** by

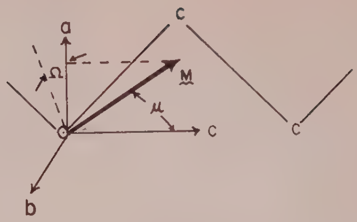

FIG. 3. Orientation of the dipole moment change vector of the monomer unit $\mathbf{M}_m$ with respect to the monomer axes.

$$\mathbf{M}_m=(\sin\mu\cos\Omega)\mathbf{a}+(\sin\mu\sin\Omega)\mathbf{b}+(\cos\mu)\mathbf{c}.\tag{58}$$

If the infrared beam is polarized along the z direction of the sample, it is said to be vertically polarized; **O** is then indicated by $\mathbf{O}_v$ and is equal to **k**. If the infrared beam is polarized perpendicular to the z direction, **O** is indicated by $\mathbf{O}_h$, which is given in

$$\mathbf{O}_h=(\sin\phi)\mathbf{i}+(\cos\phi)\mathbf{j},\tag{59}$$

where ϕ is the angle which the direction of polarization of the infrared beam makes with respect to the plane of the sample. This would correspond to having the infrared beam pass through a sample which is tilted about its z axis away from the normal to the beam through the angle ϕ (Fig. 4). Then, for example, $(\mathbf{O}_h\cdot\mathbf{M}_m)$ is given by

$$\begin{aligned}(\mathbf{O}_h\cdot\mathbf{M}_m)=&\sin\mu\cos\Omega(\sin\phi\sin\alpha\sin\delta+\cos\phi\sin\alpha\cos\delta)\\&+\sin\mu\sin\Omega(\sin\phi\sin\beta\sin\gamma+\cos\phi\sin\beta\cos\gamma)\\&+\cos\mu(\sin\phi\sin\epsilon\sin\sigma+\cos\phi\sin\epsilon\cos\sigma),\end{aligned}\tag{60}$$

and A_h, the absorbency for horizontally polarized light, is given by

$$\begin{aligned}A_h=K[&\sin^2\mu\cos^2\Omega(\sin^2\phi\langle\sin^2\alpha\sin^2\delta\rangle_{\mathrm{av}}\\&+\cos^2\phi\langle\sin^2\alpha\cos^2\delta\rangle_{\mathrm{av}})\\&+\sin^2\mu\sin^2\Omega(\sin^2\phi\langle\sin^2\beta\sin^2\gamma\rangle_{\mathrm{av}}\\&+\cos^2\phi\langle\sin^2\beta\cos^2\gamma\rangle_{\mathrm{av}})+\cos^2\mu(\sin^2\phi\langle\sin^2\epsilon\sin^2\sigma\rangle_{\mathrm{av}}\\&+\cos^2\phi\langle\sin^2\epsilon\cos^2\sigma\rangle_{\mathrm{av}})+\text{cross-product terms}].\end{aligned}\tag{61}$$

By assuming no correlation between uniaxial and biaxial orientation functions and substituting these for the trigonometric expressions in Eq. (61), one obtains

$$\begin{aligned}A_h=(K/3)\{&\sin^2\mu\cos^2\Omega[\sin^2\phi(1-f_\alpha)(1-f_\delta)\\&+\cos^2\phi(1-f_\alpha)(1+f_\delta)]+\sin^2\mu\sin^2\Omega[\sin^2\phi\\&\times(1-f_\beta)(1-f_\gamma)+\cos^2\phi(1-f_\beta)(1+f_\gamma)]\\&+\cos^2\mu[\sin^2\phi(1-f_\epsilon)(1-f_\sigma)+\cos^2\phi(1-f_\epsilon)(1+f_\sigma)]\\&+\text{cross products}\}.\end{aligned}\tag{62}$$

---

[8] H. A. Stuart and H. Volkman, Z. Physik **80**, 107 (1933).

Orientation functions cannot be readily used in the cross-product terms which should also be included in Eq. (61), since this would involve severe limitation on correlations between orientation functions. Consequently, this formalism will not be useful unless these cross-product terms vanish. This will occur if $\sin\mu=0$ or $\cos\mu=0$ and simultaneously $\sin\omega$ or $\cos\omega=0$. This corresponds to **M** being parallel to one of the vectors **a**, **b**, or **c**. It is only in this case that the infrared dichroism may be interpreted simply in terms of orientation functions. For example, if **M** is parallel to the ϵ axis,

$$A_h=(K/3)[\sin^2\phi(1-f_\epsilon)(1-f_\sigma)+\cos^2\phi(1-f_\epsilon)(1+f_\sigma)] \quad (63)$$

for A_h results. If A_μ is the absorbency for the unoriented sample, where all of the f's equal 0, then the constant $K=3A_\mu$. For normal incidence of the infrared beam where $\phi=0°$, Eq. (63) becomes

$$A_h(\phi=0°)/A_\mu=(1-f_\epsilon)(1+f_\sigma). \quad (64)$$

For $\phi=45°$, $\cos^2\phi=\sin^2\phi=\frac{1}{2}$, and Eq. (63) becomes

$$A_h(\phi=45°)/A_\mu=(1-f_\epsilon). \quad (65)$$

Thus, we see that a measurement of A_h at $\phi=0°$ and $\phi=45°$ will serve to characterize both f_ϵ and f_σ. The equation for the vertical component of absorbency is given by

$$A_v/A_\mu=(1+2f_\epsilon). \quad (66)$$

This is a function of only f_ϵ and is independent of the tilt angle ϕ. Consequently, this equation may be combined with Eq. (64) to characterize both functions.

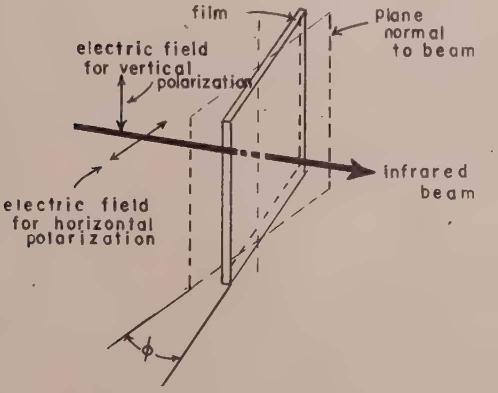
film
Plane normal to beam
electric field for vertical polarization
infrared beam
electric field for horizontal polarization
ϕ

FIG. 4. Horizontally polarized infrared with a tilted film.

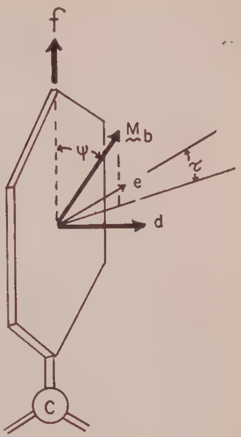

FIG. 5. Orientation of the dipole moment change vector of the benzene ring $\mathbf{M}_b$ with respect to the benzene ring axes.

In a similar manner, for an absorption band for which the dipole moment change M_m is along the a axis, one obtains

$$A_h(\phi=0°)/A_\mu=(1-f_\alpha)(1+f_\delta), \quad (67)$$

$$A_h(\phi=45°)/A_\mu=(1-f_\alpha), \quad (68)$$

$$A_v/A_\mu=(1+2f_\alpha), \quad (69)$$

which may be used to determine f_α and f_δ. For absorption bands of the benzene ring, a unit vector $\mathbf{M}_b$ is defined by

$$\mathbf{M}_b=(\sin\psi\,\sin\tau)\mathbf{d}+(\sin\psi\,\cos\tau)\mathbf{e}+(\cos\psi)\mathbf{b}, \quad (70)$$

which is in the direction of the dipole moment change of the vibration of the ring (see Fig. 5). We shall assume that the ring rotation orientation functions are not correlated with the others, and that the potential energy function characterizing ring rotation is symmetrical with respect to the **a**, **b**, and **c** coordinate axes. Consider the special case in which $\mathbf{M}_b$ is perpendicular to the benzene ring and we wish to determine the vertical component of absorbency. Then $\langle(\mathbf{M}_b\cdot\mathbf{k})\rangle_{\text{av}}$ is given by

$$\langle(\mathbf{M}_b\cdot\mathbf{k})\rangle_{\text{av}}=[\sin\omega\,\sin(\theta_T/2)\cos\alpha \pm\sin\omega\,\cos(\theta_T/2)\cos\beta+\cos\omega\,\cos\epsilon] \quad (71)$$

and A_v by

$$A_v=K\langle(\mathbf{M}_b\cdot\mathbf{k})^2\rangle_{\text{av}}=K[\langle\sin^2\omega\,\sin^2(\theta_T/2)\cos^2\alpha\rangle_{\text{av}} +\langle\sin^2\omega\,\cos^2(\theta_T/2)\cos^2\beta\rangle_{\text{av}}+\langle\cos^2\omega\,\cos^2\epsilon\rangle_{\text{av}} +\langle\sin\omega\,\cos\omega\,\sin(\theta_T/2)\cos\alpha\,\cos\epsilon\rangle_{\text{av}}]. \quad (72)$$

The last term of Eq. (72) averages to zero because of the symmetry in ω. The other cross-procuct terms are also zero because of the ± in Eq. (71). On substituting orientation functions, one obtains

$$A_v=(K/9)[3-f_\alpha-2f_\beta-f_\omega(5f_\alpha+4f_\beta)]. \quad (73)$$

If f_α and f_β are known from measurement on absorption bands of the monomer chain section, the f_ω may be calculated from this. For the simpler case of uniaxial orientation, Eq. (73) reduces to

$$A_v/A_\mu=[1+\tfrac{1}{2}f_\epsilon(1+3f_\omega)]. \quad (74)$$

In the limiting case of perfect chain orientation where $f_\epsilon=1$, A_v/A_μ will vary from 3 for $f_\omega=1$ to 0 for $f_\omega=0$. The former case corresponds to perfect alignment of the normal to the benzene ring along z, the polarization direction, where the latter corresponds to alignment of this normal perpendicular to the polarization direction.

CONCLUSION

Equations are obtained for calculating the birefringence of polystyrene in terms of bond and benzene ring polarizabilities and the five orientation functions necessary to characterize the structure. The absorbency with polarized infrared may also be expressed in terms of these orientation functions, providing one is dealing with an absorption band giving its dipole moment change parallel to one of the principal axes. By proper choice of absorption bands, it should be possible to individually measure the various orientation functions.

JOURNAL OF APPLIED PHYSICS VOLUME 32, NUMBER 7 JULY, 1961

Corbino Disk Magnetoresistivity Measurements on InSb

MILTON GREEN*
U. S. Army Signal Research and Development Agency, Fort Monmouth, New Jersey

(Received September 22, 1960)

Magnetoresistivity measurements employing "Corbino disk" geometry have been made, at temperatures of 77°, and 203°K, and at approximately room temperature, on a slice of fairly high-purity, single-crystal, n-type InSb (probably compensated) with excess impurity concentration N_D-N_A of about 7×10^{15}. In a series of measurements the ratios of the resistance at 20 kgauss to that at zero field, for the temperatures and in the order listed above, were found to be approximately 23, 23, and 33. The maximum magnetic coefficients of resistance, in the same order, were approximately 0.87, 0.70, and 0.50 per kgauss occurring approximately at fields of 0.7, 1.0, and 2.6 kgauss, respectively. Mobilities were determined by both Hall effect and low-field magnetoresistivity, and were found to agree within a few percent. The values were, in the same temperature order, 7.3, 5.3, and 4.5 m^2/v sec. Temperature cycling and aging appear to cause a reduction in area of soldered contacts to the specimen. Very slight variations of magnetoresistance with the polarity of current through the specimen were observed. An explanation is given; calculations are of the same order of magnitude as experimental observations.

INTRODUCTION

WEISS and Welker[1] have demonstrated that, for high-motility materials ($\mu_0\geq10^4$ cm^2/v sec), the magnetoresistivity is very dependent upon the geometry of the sample, and that the effect is maximum for circular geometry with radial flow (Corbino disk). For InSb samples having room temperature mobilities of 43 000 and 63 000 cm^2/v sec, they have obtained increases in resistance of 18.7 and 24.6 fold, respectively, in a magnetic field of 10 kgauss relative to the resistance at zero magnetic field. Since then, others[2] have obtained equivalent results and, in some cases, material has been produced which gives a slightly better performance.

For magnetoresistance amplifiers and oscillators,[3–5] a high magnetoresistance effect is required. In particular, near the operating point, the percentage change in resistance per gauss should be as high as possible; that is, the slope of the logarithm of the resistance vs magnetic field should be very high. For this reason, we decided to investigate the shapes and the effect of temperature upon the magnetoresistance curves, employing disks of high-purity InSb.

EXPERIMENTAL

A slice of fairly high-purity InSb, obtained from the National Bureau of Standards,[6] $\frac{1}{16}$ in. thick and $\frac{5}{8}$ in. in diameter, was used as the Corbino disk. The leads were soldered to the sample with indium metal, except for one series of measurements at room temperature. In the latter case, a low melting point alloy (cerrocast of composition: 60% Sn, 38% Bi, 2% Pb) was used. The center electrode was attached to a soldered area, approximately 1 mm^2.

Solder for the periphery electrode was placed on the crystal along the circumference of a circle approximately 13 mm in diameter. The solder was spaced so that alternate arcs were covered for distances of about 3 mm, leaving 3 mm between soldered arcs uncovered. A flexible copper wire was connected by solder to the crystal at the points of the crystal covered with solder. This method of attaching the periphery electrode was used in order to reduce the mechanical stress on the crystal, resulting from the attached electrodes, at reduced temperatures.

The resistance of the sample was measured with a Wheatstone bridge. The bridge was keyed when obtaining balance in order to prevent heating of the specimen. The magnitude and polarity of the measuring current were variable. The magnetic field was measured with a rotating coil gaussmeter.

---

* Present address: Burroughs Research Center, Paoli, Pennsylvania.

[1] H. Weiss and H. Welker, Z. Physik **138**, 322–329 (1954).

[2] R. K. Willardson and A. C. Beer, Elec. Mfg. **57**, 79–84 (1956).

[3] H. I. Thuy, Arch. Elek. Übertragung **8**, 269 (1954).

[4] M. Green, I.R.E. Trans. on Electron Devices **ED-3**, 133 (1956).

[5] A. Aharoni and E. Frei, Bull. Research Council Israel **5A**, 240 (1956).

[6] I am indebted to Dr. Hans Fredrickse of the National Bureau of Standards for the sample.

RESULTS

Characteristic curves are shown in Fig. 1 for temperatures of 283°, 203°, and 77°K. The slopes of the curves of Fig. 1 are of particular interest since the power gain of a galvanomagnetic amplifier[4] (gaussistor) is proportional to its square. It will be observed that the maximum slope $S_{\max}$ increases with decreasing temperature.[7]

Low-Field Quadratic Variation in Resistance

For Corbino disk geometry and weak magnetic induction B, theory predicts a quadratic variation in the magnetoresistance $\Delta R/R_0$. Equations of Weiss and Welker[8] give (neglecting a higher order term)

$$\Delta R/R_0 = \Delta\mu/\mu_B + [(3\pi/8)\mu_B B 10^{-8}]^2, \qquad (1)$$

where μ_B is the conductivity mobility in transverse magnetic induction B (in gauss). The term $\Delta\mu/\mu_B$ in Eq. (1) represents the ordinary, or physical, transverse magnetoresistance; it is known to be quadratic[9] in B.

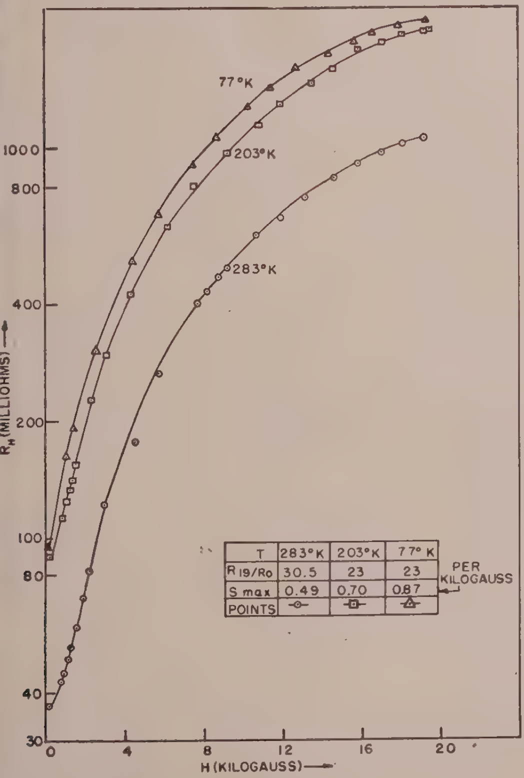

FIG. 1. Characteristic curves of Corbino disk magnetoresistance in n-type InSb. Semilog plots, three different temperatures.

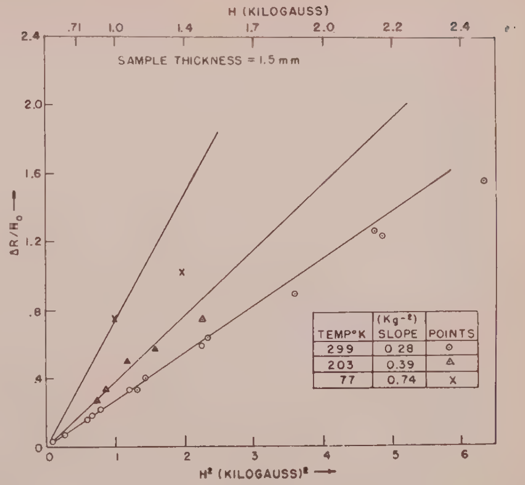

FIG. 2. $\Delta R/R_0$ vs B^2 curves. This graph confirms low-field quadratic dependence of magnetoresistance on magnetic field. Slopes were used in calculating μ_0 from Eq. (1) of text. Specimen thickness, 1.5 mm.

Beer *et al.*[10] give a low-field equation somewhat different from Eq. (1), but still quadratic in μH.

Figure 2 shows curves of $\Delta R/R_0$ vs B^2 for the specimen of Fig. 1. The curves are linear in the vicinity of the origin, and pass through it. The departure from linearity occurs at lower field strengths as the temperature is reduced. This observation would indicate that the magnetic field dependence of μ, i.e., μ_B, increases more rapidly with decreasing temperature.

Low-Field Mobilities by Hall and Magnetoresistance Measurements

Actually, the expression $3\pi/8\mu_B B$ in Eq. (1) is the tangent of the Hall angle, and $3\pi/8\mu_B = \sigma_B R_H$ is the Hall mobility μ_H (assuming isotropic conduction), where σ_B is the transverse conductivity for magnetic induction B and R_H is the corresponding Hall coefficient. The use of the factor $3\pi/8$ by Weiss and Welker to relate conductivity mobility to Hall mobility assumes spherical energy surfaces and nondegenerate semiconductor and lattice scattering.[11] At room temperature and for a sample of InSb of purity comparable to the one of this paper, Weiss and Welker[12] get fairly good agreement between experiment and theory using the equation

$$R_B/R_0 = (\mu_0/\mu_B)[1 + (3\pi\mu_B B 10^{-8}/8)^2]. \qquad (2)$$

This would indicate that at room temperature the factor $3\pi/8$ cannot be too far off. At lower temperatures,

---

[7] The slope does not increase as fast at reduced temperatures as it does in the case of bismuth.

[8] See reference 1, Eqs. (11) and (12).

[9] H. P. R. Frederikse and W. R. Hosler, Phys. Rev. **108**, 1136 (1957).

[10] A. C. Beer, J. A. Armstrong, and I. N. Greenberg, Phys. Rev. **107**, 1510 (1957), Eq. (11).

[11] W. Shockley, *Electrons and Holes in Semiconductors* (D. Van Nostrand Company, Inc., New York, 1950), p. 215.

[12] See Table I of reference 1.

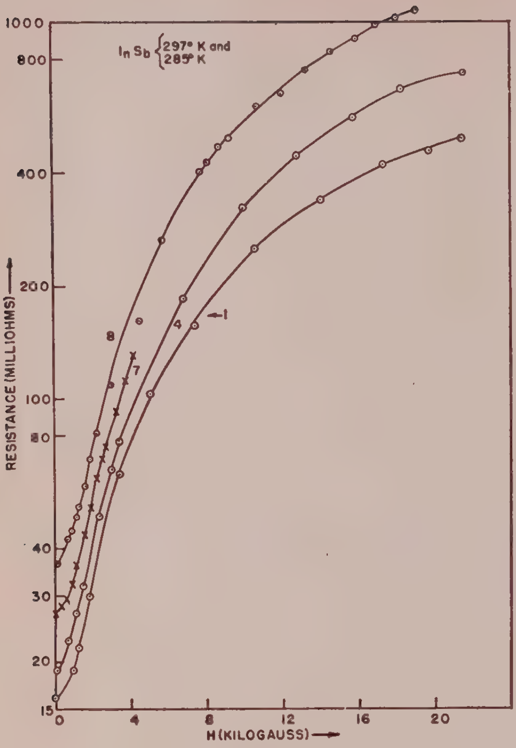

FIG. 3. Corbino disk characteristics demonstrating effect of temperature cycling and aging. Curves taken in time sequence in the order as numbered; i.e., 1, 4, 7, and 8. Curve 8 taken six weeks after curve 1. Specimen had been lowered to dry-ice and liquid-nitrogen temperatures several times between the measurements of curves 1 and 8. Most of the change is probably due to temperature cycling.

however, where impurity scattering is more effective, Eq. (2) may be in considerable error.[10] For the present, we will assume it is correct, pointing out the influence it has on any results presented.

Low-field mobilities were determined from the initial slopes of the curves of Fig. 2, using Eq. (1) but neglecting the term $\Delta\mu/\mu_0$. (Experimental data on the "ordinary" transverse magnetoresistivity[1,9] indicate that, in this case, this procedure leads to mobility values which are *at most* 5% too high.) The values determined by this method are listed in column 6 of Table I, and values determined from Hall constant and resistivity measurements are listed in column 5. (The Hall mobilities are greater than the ones listed in Table I by a factor of $3\pi/8$.) The agreement between the two sets of measurements, column 5 and column 6, is good. This is to be expected because in essence both the methods measure the Hall mobility.

TABLE I. Results of measurements on N-type InSb.

Temp. (°K)	Resistivity (ohm cm)	Hall const. (cm³/coul)	Carrier density (electron/cm³)	Mobility[a] (cm²/v sec)	Mobility[b] (cm²/v sec)
296	0.0049	241	31×10^{15}	42 000	45 000
203	0.0108	720	10×10^{15}	56 000	53 000
77	0.0122	975	7.5×10^{15}	73 000	73 000

[a] Determined from Hall constant (R_H) and resistivity (e.g., $\mu=8R_H/3\pi\rho$).
[b] Determined from initial slope of $\Delta R/R_0$ vs B^2 curve employing Eq. (1), but neglecting the term $\Delta\mu/\mu_B$.

TABLE II. Effects of magnitude and polarity of current on magnetoresistance.

Temp. (°K)	Measuring current (ma)	Polarity of center electrode	Resistance (ohm)	Magnetic field strength (k gauss)	ΔR (ohm) calculated from Eq. (3)
296	800	+	0.877	18.2	+0.0016[a]
296		−	0.876	18.2	−0.0016
296	100	−	0.882	18.2	+0.0002
		−	0.882	18.2	−0.0002
203	650	+	+2.027	18.6	+0.0075[b]
		−	−2.007	18.6	−0.0075
203	300	+	2.034	18.4	+0.0035
		−	2.020	18.4	−0.0035
203	150	+	2.038	18.4	+0.0017
		−	2.029	18.4	−0.0017
203	75	+	2.034	18.4	+0.0008
		−	2.029	18.4	−0.0008
203	40	+	2.032	18.4	+0.0004
		−	2.029	18.4	−0.0004
203	20	+	2.029	18.4	+0.0002
		−	2.029	18.4	−0.0002

[a] For 296°K, $H=18.2$ kgauss, $\partial R/\partial H=0.038$ ohm/kgauss, $\mu_B=2250$ cm²/v sec, $d=0.06$ cm, $p=13$. Values of μ_B calculated with the use of Eq. (2); values of μ_0 taken from column 6 of Table I.
[b] For 203°K, $H=18.4$ kgauss, $\partial R/\partial H=0.11$ ohm/kgauss, $\mu_B=4350$ cm²/v sec, $d=0.06$, $p=13$. Values of μ_B calculated using Eq. (2); values of μ_0 taken from Table I, column 6.

Effect of Temperature Cycling and Aging on Magnetoresistance

The magnetoresistance measurements were repeated periodically at the three different temperatures, the last measurements having been made seven weeks after the first. In successive measurements, we found that R_0, the zero-field resistance, increased with age. The effect is probably due mostly to temperature cycling. Starting with a value of 0.016 ohm at room temperature, R_0 increased to 0.037, a factor of 2.3, after the eighth room temperature measurement six weeks later. Similarly, at the lower temperatures R_0 also increased from 0.052 to 0.89 ohm at 203°K and from 0.055 to 0.092 ohm at 77°K. The approximate net effect upon the log$R$ vs H characteristic curves is to shift them parallel to themselves in the direction of increasing log$R$ (Fig. 3). These latter results indicate that the increase in resistance as a result of aging cannot be due to the introduction of a series resistance insensitive to magnetic fields. The only plausible explanation for this type of resistance increase is that there is a reduction with age of electrode contact area to the crystal, particularly for the center electrode where most of the effective resistance is located.

Effects of the Magnitude and the Polarity of the Current on the Magnetoresistance

The effects of the magnitude and polarity of the measuring current on the magnetoresistance are shown in Table II. The results indicate that a slight current-polarity effect does exist, particularly at 203°K, and that it increases with increasing current.[13] Such polarity effects could arise from the following causes: (a) the magnetic field associated with the angular current in the disk, (b) small-area vs large-area injection,[14] and (c) a slight inhomogeneity in the impurity distribution in the crystal. There is every indication that the third possibility cited above does not exist in this particular crystal. The magnetic effect, (a) above, *does* exist, and most likely the injection effect does too. The magnitude of the magnetic effect for n-type crystal is approximately

$$\Delta R = \frac{-\partial R}{\partial H} \frac{\mu_B B_z I}{0.2d} \left[\frac{(p^2+1)\ln p}{(p^2-1)} - 1 \right] 10^{-8}, \qquad (3)$$

where ΔR is the resistance change, I the total current flow into the crystal (positive when radially outwards), $\partial R/\partial H$ the slope of the Corbino magnetoresistance curve, μ_B the electron mobility at magnetic induction of magnitude B_z, p the ratio of the outside to the inside radius of the contact electrodes, and d the thickness of the specimen. Magnitudes of ΔR calculated from Eq. (3) are shown for comparison in Table II. The difference in the experimental values of R_B between $I+$ and $I-$ for 300 ma and at 203°K is 0.014 ohm; the corresponding calculated difference is 2×0.0035 ohm or 0.007. For 150 ma the comparison is: experimental $\Delta R = 0.009$ ohm; calculated $\Delta R = 0.0034$ ohm. At 296°K the values for 800 ma are 0.001 ohm vs 0.0032 ohm. The comparison indicates that the experimental and calculated values are of the same order of magnitude, so that if injection is involved, it must also be of the same order of magnitude or else much smaller. The measurement is approaching the limit of accuracy by the method used (approximately one part in 2000) with some difficulty entering into the measurement due to heating effects and keying. The measurements of the effect at 77°K were somewhat unsteady and hence are not shown.

Crystal Orientation

The two circular surfaces of the Corbino disk were found to be within 5.6° of the [001] direction by x-ray diffraction. At the center electrode, conduction would be taking place in nearly all crystallographic directions; at the periphery, the current flows parallel to the above surfaces.

CONCLUSIONS

On the basis of Eq. (2) the experimental curves, Fig. 2, indicate that the mobility decreases with increasing Hall angle, $\theta = \tan^{-1}(3\pi/8)\mu_B B$. For Hall angles less than 35° ($\tan\theta < 0.7$), the mobility at each temperature is approximately constant.

The curves of Fig. 1, in connection with data[1,9] on transverse magnetoresistivity, indicate that in a magnetic induction of approximately 20 kgauss, a larger Hall angle—hence a greater mobility—exists in the disk at room temperature than at 78°K.

Mobilities as determined by weak-field Corbino disk measurements and Hall and conductivity measurements are apparently in good agreement with each other.

Other things being equal, the magnetic field associated with the angular current in the disk produces a slight current-rectification effect.

---

[13] Since the time this paper was submitted, a theoretical paper concerning this effect has been published [D. A. Kleinman and A. L. Schawlow, J. Appl. Phys. 31, 2176 (1960)].

[14] W. C. Dunlap, Jr., *An Introduction to Semiconductors* (John Wiley & Sons, Inc., New York, 1957), p. 130.

JOURNAL OF APPLIED PHYSICS VOLUME 32, NUMBER 7 JULY, 1961

p-Type Photoconductivity and Infrared Quenching in Electron-Bombarded CdS

B. A. Kulp and R. H. Kelley*
Aeronautical Research Laboratory, Wright-Patterson Air Force Base, Ohio

(Received November 16, 1960; and in final form, February 3, 1961)

A platelet-type crystal of pure cadmium sulfide 46 μ thick was irradiated first with 100-kev electrons to reduce the number of sulfur interstitials, than for 400 μa-hr/cm^2 with 150-kev electrons to produce an excess of sulfur vacancies. At room temperature, photoconductive peaks were observed at 0.67, 0.9, and 1.4 μ. Point-contact rectification was used to determine that the 0.67-μ peak was due to electronic conduction and the 0.9- and 1.4-μ peaks were due to hole conductivity. A "quenching" experiment, i.e., simultaneous irradiation with bandgap light and infrared light of variable wavelength, at room temperature shows the 0.67-μ photopeak and quenching at 0.9 and 1.4 μ. In a separate experiment, the 1.4-μ quenching band was partially removed from a platelet-type crystal by bombarding at 100 kev. This bombardment also removed edge emission from this crystal. The temperature dependence of the 1.4-μ quenching band and of the intensity of edge emission as observed by Reynolds suggests that the centers for edge emission and for the 1.4-μ quenching bands are actually the same center, namely the sulfur interstitial in different ionization states.

INTRODUCTION

In experiments with electron-bombarded CdS, it has been observed that in thin crystals, below the threshold for displacement of the sulfur atom from its lattice point (115 kev),[1] the resistivity usually decreases with bombardment. This has been interpreted as being a result of the removal of sulfur interstitials from the crystal. If the energy of the electrons emerging from the bottom of the crystal is sufficiently high, cadmium interstitials will also be removed.[1,2] Above the threshold for the displacement of the sulfur atom, an equilibrium between the number of interstitials created by the electron beam and the number removed from the bottom of the crystal is achieved, while the number of sulfur vacancies continually increases. By bombarding first below the threshold for the displacement of the sulfur atom, then above the threshold, a crystal should be created which has a large excess of sulfur vacancies and a few sulfur interstitials. If bombardment is long enough, a decomposition of the top surface is possible and some cadmium interstitials will be put into the crystal.

The removal of interstitials and the production of vacancies might be expected to produce changes in the photoconductive spectrum of CdS. It is well known that the photoconductivity in CdS can be quenched by

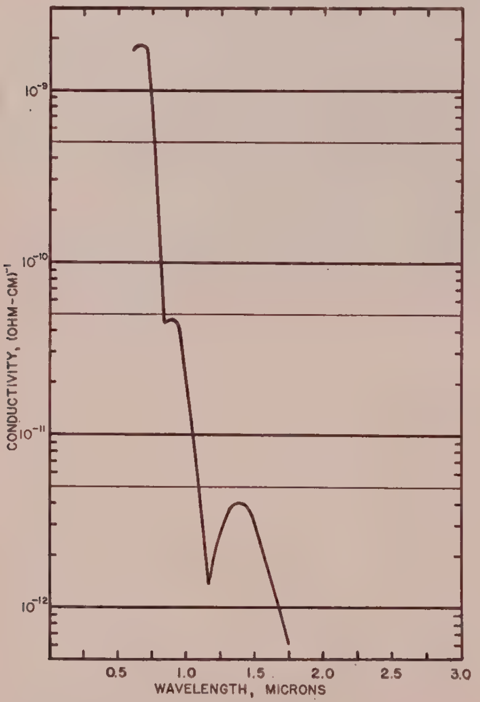

Fig. 1. Photoconductivity of a crystal bombarded with 1.2×10^{19} electrons of 100-kev energy plus 0.8×10^{19} electrons of 150-kev energy. σ dark $<5\text{x}10^{-13}$ (ohm-cm)$^{-1}$. Light intensity 10 μw/cm^2.

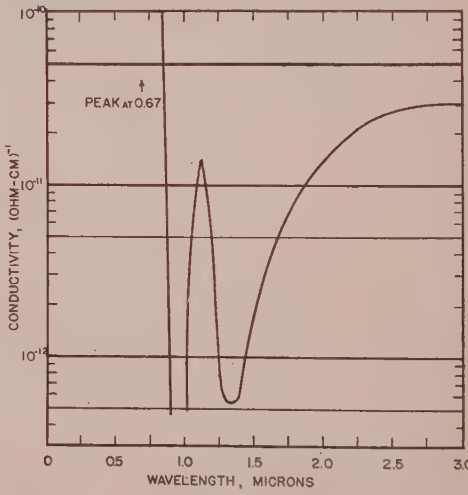

Fig. 2. Quenching of photoconductivity of crystal of Fig. 1. Bandgap light intensity 0.1 μw/cm^2. Infrared light intensity 10 μw/cm^2.

---

[*] Present address: The Ohio State University, Columbus, Ohio.

[1] B. A. Kulp and R. H. Kelley, J. Appl. Phys. 31, 1057 (1960).

[2] B. A. Kulp and R. H. Kelley, Bull. Am. Phys. Soc. 4, 420 (1959).

TABLE I. Rectification ratios using a point contact electrode.

Wavelength band	Rectification ratio	Indicated polarity of carriers
Band gap	>2:1	Negative
0.67 μ	1.5:1	Negative
0.9 μ	3:1	Positive
1.4 μ	7:1	Positive
Dark	3:1	Negative

infrared radiation.[3] Quenching bands have been reported at 0.9, 1.08, 1.35, 1.5, and 1.65 ev corresponding to 1.4, 1.15, 0.9, 0.82, and 0.75 μ, respectively. Bube[4] and Tutihasi[5] have studied the temperature dependence of quenching. They have observed that the 1.4-μ band disappears as the temperature is decreased below −50°C. The experiments described here deal mostly with the 1.4-μ quenching band and note the occurrence of a peak in the photoconductivity at about 0.67 μ.

EXPERIMENTAL

A platelet-type crystal of undoped cadmium sulfide 46 μ thick by 2 mm wide by 10 mm long was bombarded first at 100 kev for 600 μa-hrs/cm², then at 150 kev for 400 μa-hr/cm². (2×10^{19} electrons/cm² total.) The bombardment was at 30°C and at a current level of 8 μa/cm². After bombardment, the surfaces looked as if they had been etched, the top surface much more severely than the bottom. This etching is not a thermal etching since the temperature of the crystal does not exceed 30°C during bombardment. The fluorescence spectrum under uv stimulation at liquid nitrogen temperature showed a broad orange band centering at about 6050 A and a deep red band with a maximum intensity at about 7200 A. The 6050-A band has previously been associated with the cadmium interstitial and the 7200-A band with the sulfur vacancy.[2] The dark conductivity after bombardment was less than 5×10^{-13} (ohm-cm)$^{-1}$. Conductivity measurements were made with sputtered platinum contacts using an electrometer and a battery. Figure 1 shows the photoconductivity as a function of wavelength between 0.54 and 3.0 μ in vacuum at 20°C. The intensity of the light was about 10 μw/cm². Three peaks are observed; one at 0.67 μ, another at 0.9 μ, and a third at 1.4 μ. At −196°C only the 0.67-μ peak is detectable. The lower limit of reliable measurement is about 5×10^{-13} (ohm-cm)$^{-1}$.

Figure 2 shows the quenching of photoconductivity at room temperature by simultaneous irradiation with long wavelength light of variable wavelength and with bandgap light (6000–4700 A, 0.1 μw/cm² intensity). The infrared radiation was supplied by a globar operating at 1500°K through a NaCl prism spectrometer. The intensity at 1.4 μ was 10 μw/cm². The data are plotted on an equal energy basis. The 0.67-μ photopeak is observed as are quenching bands at 0.9 and 1.4 μ. At liquid nitrogen temperature, only the photopeak and the 0.9-μ quenching band are found.

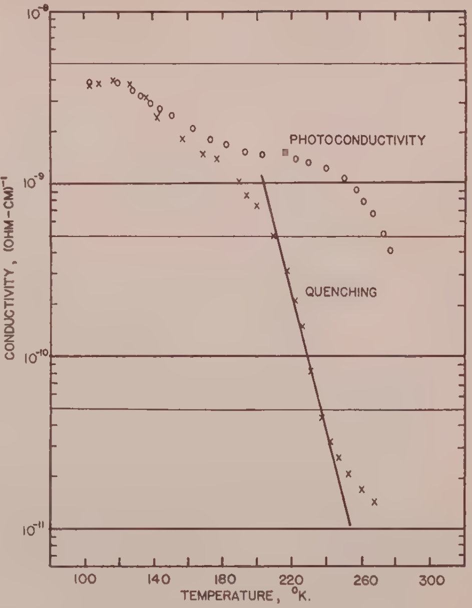

FIG. 3. Quenching of photoconductivity by 1.4-μ radiation vs temperature.

Lambe[6] has previously attempted to observe hole-type conductivity when doped CdS was irradiated with light in a quenching band without success. Table I shows the rectification ratios obtained using a tungsten point contact with silver paint for the other electrode. In the dark, for bandgap and 0.67-μ radiation, maximum current was obtained when the point was positive. For radiation in the quenching bands, the maximum current was obtained with the point negative. These data confirm the model that holes are released when CdS crystals are irradiated with light in the quenching bands.

Figure 3 shows the photoconductivity and quenching by radiation in the 1.4-μ band as a function of temperature between −165°C and 20°C. The solid line is the slope of the data of Reynolds[7] for the temperature dependence of edge emission. The edge emission decreases in intensity as the temperature increases, while the quenching in the 1.4-μ band increases as the temperature rises. The decrease in photoconductivity at the higher temperatures is possibly a result of a decrease in mobility and changes in the recombination processes.

In a second series of experiments, the effect of bombardment below 115 kev on the 1.4-μ quenching band

---

[3] A. E. Hardy, Trans. Electrochem. Soc. **87**, 355 (1945); R. Frericks, Phys. Rev. **72**, 594 (1947); F. C. Herman and C. F. Meyer, J. Appl. Phys. **17**, 743 (1946); E. A. Taft and M. H. Hebb, J. Opt. Soc. Am. **42**, 349 (1952).

[4] R. Bube, Phys. Rev. **99**, 1105 (1955).

[5] S. Tutihasi, J. Opt. Soc. Am. **46**, 446 (1956).

[6] J. Lambe, Phys. Rev. **100**, 1586 (1955).

[7] D. C. Reynolds, Phys. Rev. **118**, 478 (1960).

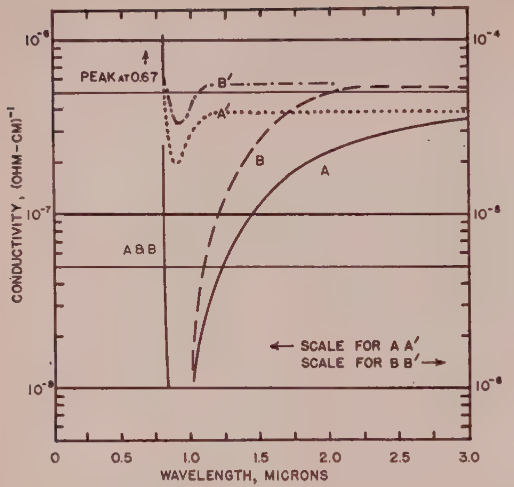

FIG. 4. Change in long-wavelength quenching by bombardment with 2×10^{19} electrons/cm² at 110 kev. *A* and *A′* before bombardment, *B* and *B′* after bombardment. Quenching light intensity 0.1 μw/cm² for *A′* and *B′*, 10 μw/cm² for *A* and *B*. Bandgap light intensity 0.1 μw/cm².

has been studied. Figure 4 shows the quenching spectrum for a 30-μ thick crystal before and after bombardment for 920 μa-hr/cm² at 110 kev. The level of irradiation was 4 μa/cm². The dark conductivity of the crystal increased from 5.2×10^{-10} (ohm-cm)$^{-1}$ to 4.7×10^{-7} (ohm-cm)$^{-1}$ during this time. This increase in conductivity with bombardment below 115 kev is typical of a large group of crystals. Before bombardment there is a photopeak at 0.67 μ and a broad quenching band at longer wavelengths. After bombardment, however, the long wavelength quenching band is definitely changed, while the 0.9-μ band is only slightly different in relative depth before and after bombardment. It was also noted that edge emission was removed by this bombardment (see also reference 1).

Figure 5 shows the quenching spectrum of another crystal 30 μ thick before and after bombardment. After 18 μa-hrs/cm² of bombardment at 100 kev, the 1.4-μ quenching band is greatly reduced in intensity, while the 0.9-μ band appears to be only slightly affected by the bombardment. The dark conductivity of the crystal shown in Fig. 5 before bombardment was 3.8×10^{-9} (ohm-cm)$^{-1}$ and not detectably different after bombardment. The level of bandgap light was reduced 10% after bombardment so that the photoconductivity was the same as before bombardment.

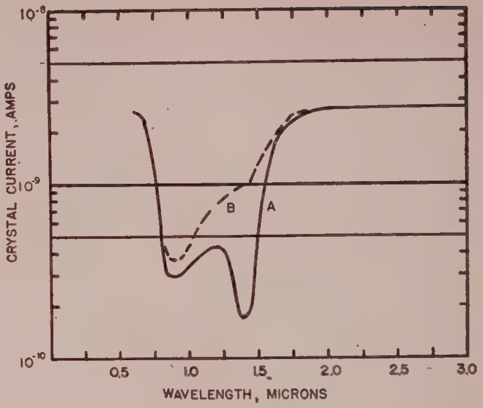

FIG. 5. Decrease in 1.4-μ quenching band by bombardment for 4×10^{17} electrons/cm². *A*, before bombardment; *B*, after bombardment.

DISCUSSION

The measurements on the nature of the current carriers when CdS is irradiated with 0.9- and 1.4-μ light confirm that holes are released from traps at levels of about 1.4 and 0.9 ev above the valence band. Evidence has also been presented which shows that the center for the 1.4-μ quenching band is removed by bombardment of thin crystals below 115 kev. This bombardment has also been shown to remove edge emission. Reynolds has measured the temperature dependence of the intensity of edge emission and finds it to decrease exponentially with temperature over a range of temperatures. The slope of the linear portion of the curve of Fig. 3 of the intensity of quenching in the 1.4-μ band vs temperature is the same as Reynolds', but with the quenching increasing as the temperature increases. If the center for edge emission and the center for the 1.4-μ quenching band were actually the same center in different ionization states, then the rate of depopulation of the edge emission center must equal the rate of population of the quenching center as the temperature increases. It has been previously shown that the center for edge emission is the sulfur interstitial,[1] and the suggestion made that it is the doubly negatively charged sulfur ion that is the actual center. As the temperature increases from liquid nitrogen temperature, the second electron is ionized off and the sulfur interstitial becomes a singly ionized ion. The data presented here indicate that this ion is a hole trap and the centerfor the 1.4-μ quenching band.

JOURNAL OF APPLIED PHYSICS VOLUME 32, NUMBER 7 JULY, 1961

Magnetization of Nickel Single Crystals

LAMBROS TTERLIKKIS AND ALVIN W. JENKINS, JR.
Denver Research Institute, University of Denver, Denver, Colorado

(Received January 30, 1961)

A calculation of the magnetization curves of nickel single crystals is made by the method of Lawton and Steward for arbitrary orientation of the crystal in the field. The anisotropy coefficients are calculated from experimental curves with the applied field in symmetry directions, and it is found that only K_1 can be determined reliably with the data used. The calculated off-axis curves agree well with experimental results. A correcting field determined from the easy-axis magnetization curve is utilized to compensate for internal strain effects. The relation between the calculated field minus the observed field and the easy-axis field suggests a possible method for measuring internal strain energy in ferromagnetic crystals.

IN 1932, Gans and Czerlinski[1] calculated the magnetocrystalline anisotropy coefficients of iron, cobalt, and nickel from the data of Kaya,[2,3] Honda, Masumoto, and Kaya,[4] and Honda and Masumoto.[5] The experimental magnetization curves in the symmetry directions were used together with Akulov's[6] theoretical expression for the magnetocrystalline energy to obtain the first nonzero anisotropy coefficient K_1. Lawton and Steward[7] later extended these results so that the magnetization curves of single crystals of iron in off-axis directions could be calculated in reasonable agreement with experiment.

In this paper, the calculation of Lawton and Steward is extended to describe the magnetization of nickel single crystals, and the effects of internal strain are discussed.

I. CALCULATION OF ANISOTROPY COEFFICIENTS

The equations of the magnetization curves of nickel in the symmetry directions are derived by minimizing the magnetic energy of the single crystal. They are as follows, correct to terms of degree six in direction cosines[8]:

$$\langle 100\rangle:\quad H_eI_s=K_1(\eta-3\eta^3)+K_2(\tfrac{1}{2}\eta-2\eta^3+\tfrac{3}{2}\eta^5), \qquad (1)$$

$$\langle 110\rangle:\quad H_eI_s=K_1(2\eta-3\eta^3)+K_2(\eta^3-\tfrac{3}{2}\eta^5), \qquad (2)$$

$$\langle 111\rangle:\quad \begin{cases} I=I_s; & H_e>0 \\ I=0, & H_e=0. \end{cases} \qquad (3)$$

H_e is the applied field; I_s=saturation magnetization, $\eta=\cos\theta$, where θ is the angle between I and H_e, K_1, K_2 are the first two anisotropy coefficients, defined by the Akulov expression for magnetocrystalline energy:

$$E_K=K_1[\alpha_1^2\alpha_2^2+\alpha_1^2\alpha_3^2+\alpha_2^2\alpha_3^2]+K_2\alpha_1^2\alpha_2^2\alpha_3^2+\cdots, \qquad (4)$$

with the α's the direction cosines of the magnetization referred to the symmetry axes of the cubic crystal. Equation (3) follows from the experimental fact that $K_1<0$.

The K_1 and K_2 may be determined by fitting Eqs. (1) and (2) to experimental data. However, such a fit will surely result in a poor determination of the constants, since the magnetization curves of all real crystals deviate from the theoretical ones because of the effects of imperfections. Gans and Czerlinski[1] showed that the experimental magnetization curve in the [111] direction in nickel (the easy direction of magnetization) was useful for correcting the theoretical curves for internal strain effects. That is, the H in equations (1), (2) should replaced by $H_T-H_{[111]}$, where H_T is the "true" field available for magnetizing the crystal. Gans and Czerlinski, using this approximate correction for internal strain and the experimental data of Kaya,[3] derived a value of $K_1=-5.12\times10^4$ ergs/cm^3. In their calculation, a K_1 was found for each experimental point and these values were averaged. A better procedure might be to make a least-squares fit of the experimental data to Eqs. (1) and (2), and to solve the least-squares equations simultaneously for K_1 and K_2. This later procedure has

TABLE I. Comparison of calculated values of K_1, K_2 with those of Gans and Czerlinski.

	$K_1{}^{[100]}$	$K_1{}^{[110]}$	$\bar{K_1}$	$K_2{}^{[100]}$	$K_2{}^{[110]}$
G and C	$\cdots$	$\cdots$	5.12×10^4	$\cdots$	$\cdots$
J and T	5.04×10^4	4.84×10^4	4.94×10^4	-1.67×10^4	$+5.39+10^4$

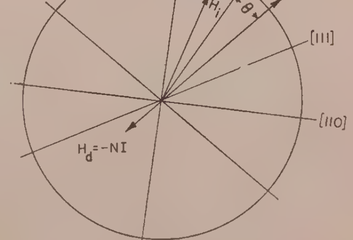

FIG. 1. The (110) plane is nickel, illustrating the relative directions of field quantities.

---

[1] R. Gans and E. Czerlinski, Schriften königsberg. gelehrt Ges. Naturw. Kl. **9**, 1 (1932).

[2] S. Kaya, Sci. Repts. Tohoku Univ. **17**, 1172 (1928).

[3] S. Kaya, Sci. Repts. Tohoku Univ. **17**, 639 (1928).

[4] K. Honda, H. Masumoto, and S. Kaya, Sci. Repts. Tohoku Univ. **17**, 111 (1928).

[5] K. Honda and H. Masumoto, Sci. Repts. Tohoku Univ. **20**, 323 (1931).

[6] N. S. Akulov, Z. Physik **57**, 249 (1929).

[7] H. Lawton and K. H. Steward, Proc. Roy. Soc. (London) **A193**, 72 (1948).

[8] See K. H. Steward, *Ferromagnetic Domains* (Cambridge University Press, New York, 1954), Chap. 2, for a derivation of similar equations for iron.

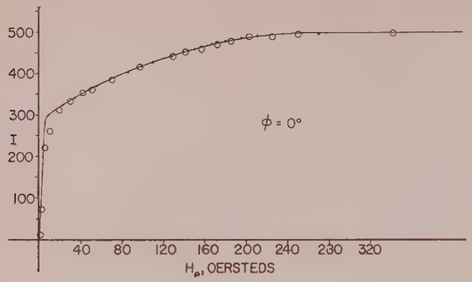

FIG. 2.

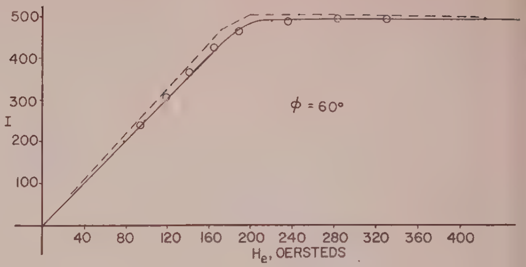

FIG. 6.

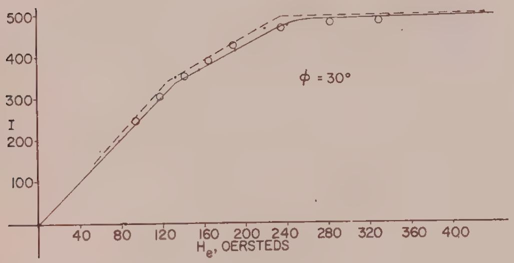

FIG. 3.

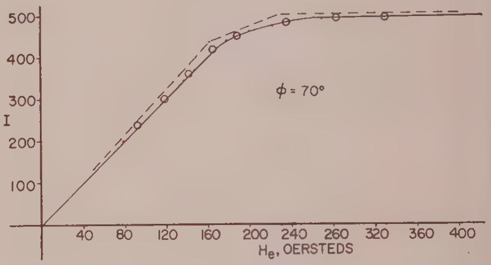

FIG. 7.

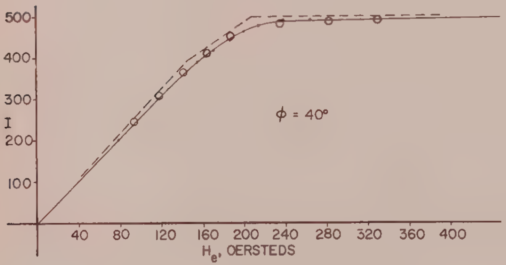

FIG. 4.

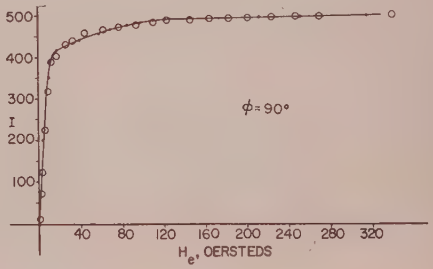

FIG. 8.

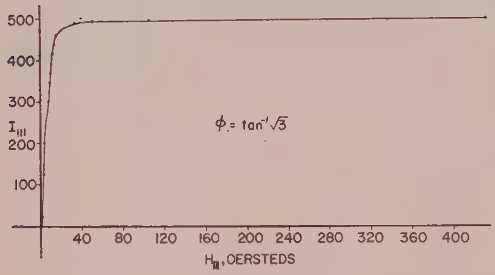

FIG. 5.

FIGS. 2–8. Magnetization curves for nickel in various directions in (110) plane. ϕ is the angle the applied field H_e makes with the [100] axis. The dashed line is the calculated curve without correction; the solid curve is the calculated curve corrected by the addition of $H_{[111]}$; the circles are experimental points (see footnote 3).

been used with Kaya's[3] experimental data to determine the anisotropy coefficients. The mesurements employed were made on a oblate spheroid with principal axis in the [110] direction, carefully cut, filed, and annealed so as to minimize strains due to working the metal.

The results of this calculation, together with those of Gans and Czerlinski, are shown in Table I.

The results calculated for K_2 in the two symmetr directions are so different that no conclusion can b reached. In addition, including the K_2 term changes, th magnetization curves by less than 1%. Hence, K_2 neglected in all that follows. The value adopted f K_1 is 4.94×10^4 ergs/cm^3, the average of the two leas squares values.

In all these calculations, values of $I>498$ were not utilized because of the uncertainty in the corresponding field values. I_s was taken to be 503.

II. CALCULATION OF OFF-AXIS MAGNETIZATION CURVES

The calculation of the magnetization curves for nickel in directions other than symmetry directions differs somewhat from the calculation of off-axis curves for iron samples, and will be described in some detail.

Consider first an oblate spheroid with principal axis in the [110] direction, cut from a nickel crystal, as shown in Fig. 1. The external magnetizing field H_e makes an angle ϕ with the Z axis ([001] axis). The magnetization I lies between H_e and the easy axis, [111]. When H_e is very large, I is equal to I_s. As H_e is reduced, all the domains remain aligned, but rotate away from H_e towards the easy axis, the [111] direction. The direction of magnetization is found by minimizing the energy of the crystal, E.

$$E=-H_eI_s\cos\theta+K_1(\alpha_1^2\alpha_2^2+\alpha_1^2\alpha_3^2+\alpha_2^2\alpha_3^2)+H_dI_s. \quad (5)$$

H_d is the demagnetizing field.

The direction cosines are found in terms of θ, ϕ to be

$$\left.\begin{aligned}\alpha_3&=\cos(\theta+\phi)\\ \alpha_1^2=\alpha_2^2&=\tfrac{1}{2}\sin^2(\theta+\phi)\end{aligned}\right\}. \quad (6)$$

Thus,

$$E=-H_eI_s\cos\theta+H_dI_s +K_1[\tfrac{1}{4}\sin^4(\theta+\phi)+\sin^2(\theta+\phi)\cos^2(\theta+\phi)]. \quad (7)$$

Differentiating E with respect to θ and setting the result equal to zero leads to

$$H_e=-(K_1/I_s)\sin(\theta+\phi)\cos(\theta+\phi) \times[3\cos^2(\theta+\phi)-1]\csc\theta. \quad (8)$$

In order to approximately correct for internal strain effects, the experimental value of $H_{[111]}$ corresponding to a given θ (or to a given $I_{[111]}/I_s=\cos\theta$) is added to the right side of (8).

The portion of the magnetization for which (8) is valid is called the one-vector region. The magnetization obeys Eq. (8) as H_e is reduced until the internal field H_i has rotated to the symmetry axis nearest H_e but on the opposite side from the magnetization. Thus, if $0<\phi<\tan^{-1}\sqrt{3}$, H_i rotates to the [001] axis. At this point, the component of the magnetiztaion in the [001] direction satisfies Eq. (1) with H_e replaced by H_i. As the field H_e is reduced beyond this point, the magnetization varies so as to keep H_i directed along [001]. Hence, since $H_d=NI$, where N is the demagnetizing factor of the sample,

$$H_e\sin\phi-NI\sin(\theta+\phi)=0, \quad (9)$$

$$H_i=H_e\cos\phi-NI\cos(\theta+\phi), \quad (10)$$

$$H_iI_s=-K_1\cos(\theta+\phi)[3\cos^2(\theta+\phi)-1]. \quad (1a)$$

These three equations may be combined into a single equation relating θ and H_e,

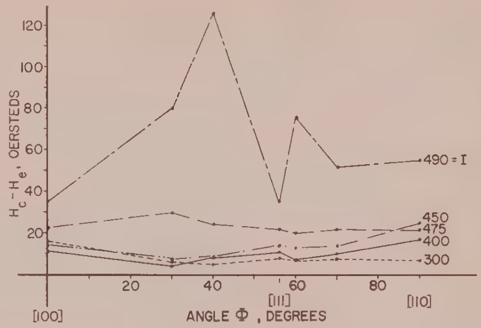

FIG. 9. Variation of the difference between experimental and calculated field values with direction of applied field in the (110) plane.

$$H_e=NI_s\csc\phi\tan(\theta+\phi) \times\{(I_s^2N/3K_1)[\cot\phi\tan(\theta+\phi)-1]+\tfrac{1}{3}\}^{\frac{1}{2}}. \quad (11)$$

Choosing θ, H_e is calculated from (11) and H_e is used in Eq. (9) to find I. This part of the magnetization curve is described as the two-vector region (since the domains lie along the two easy directions, in this case [111] and $[\bar{1}\bar{1}1]$). As H_e is reduced, H_i remains along [001] but decrease to zero. At this point, H_e is exactly equal and opposite to H_d and $\theta=0$. The equation for this part (i.e., $H_i=0$ part) of the curve (the eight-vector region) is thus simply

$$I=H_e/N. \quad (12)$$

The solutions of these equations are plotted in Figs. 2–8 for several values of ϕ. In all cases, H has been corrected for internal strain by use of that value of $H_{[111]}$ which corresponds to the calculated I value. The experimental points are from the work of Kaya and are seen to agree fairly well with calculated values. Since only domain rotation has been assumed, the equations do not accurately represent the magnetization near zero field. However, the results are in approximate agreement at the lowest experimental field values, and the curves are arbitrarily extended through zero.

III. CORRECTION FOR INTERNAL STRAIN

From the agreement between calculated and observed magnetization curves, one sees that the easy-direction curve provides a good correction for the imperfect crystal. Lawton and Steward[7] argue that there is no real justification for the use of the easy-axis values for this purpose; however, their use of the experimental curves in other symmetry directions to obtain better agreement with measured values is hardly better justified. The fact that the $H_{[111]}$ correction holds for all directions in the (110) plane is probably a good indication that the internal strain effects in this sample are isotropic. (This does not imply that the strain itself is isotropic, since magnetostriction varies with direction in the crystal.) This is illustrated in Fig. 9, where the difference in calculated and experimental fields is plotted against direction of applied field in (110) plane. For values of magnetization below 475, the curves do not differ appreciably from horizontal lines through the $H_{[111]}$ values. The curve for $I=490$ is erratic; this might be expected, however, since the magnetization curves here are almost parallel to the H axis.

The variation of the correcting field (the difference between the experimental and the calculated field) with magnetization and with direction of applied field may yield interesting information concerning the state of perfection of the crystal. Investigation of the correcting field for crystals with known internal strain is a planned future study.

ACKNOWLEDGMENT

The authors wish to express their thanks to Dr. E. N. Sickafus for assistance and many valuable discussions in the course of this work.

JOURNAL OF APPLIED PHYSICS VOLUME 32, NUMBER 7 JULY, 1961

Hydromagnet: A Self-Generating Liquid Conductor Electromagnet

Henry H. Kolm
M.I.T. National Magnet Laboratory, Cambridge 39, Massachusetts, and M.I.T. Lincoln Laboratory,† Lexington 73, Massachusetts*

AND

Osman K. Mawardi‡
Case Institute of Technology, Cleveland, Ohio

(Received January 16, 1961)

A novel liquid electromagnet is investigated in which the exciting current is generated within the solenoid by forcing the liquid conductor radially inward through the space between two coaxial cylinders placed in an axial magnetic field. The tangential current thus generated within the flowing conductor adds to the initial applied field so that the device behaves like a self-excited, short-circuited homopolar generator. It is shown theoretically that for low values of the magnetic Reynolds number, the amplification of the magnetic field is a quadratic function of this number and that the total dissipation depends on the square of the amplification and on the cube of the hydrodynamic Reynolds number. The experimental findings are in reasonable agreement with the theory.

INTRODUCTION

THE intensity of magnetic fields for continuous operation is limited to 100 kgauss by present economic restrictions and to about 250 kgauss by the mechanical strength of copper. Stronger alloys have survived short pulses up to 750 kgauss,[1] but their use for steady fields of such magnitudes would entail unreasonably large expenditures of power and also magnets of enormous sizes to meet the requirements of heat removal.

Replacement of the solid conductors in the coil windings of the magnet by liquid metal conductors such as Ag, Na, or the eutectic alloy NaK offers the possibility of appreciably improving the heat transfer. Liquid conductors also have the advantage of allowing the magnetic forces to be compensated by the walls of the container without sacrificing the internal volume of the electromagnet. Consequently, one may expect small liquid conductor magnets to be operable at power dissipation ratings more advantageous than those of stationary conductors.

A particularly attractive arrangement is illustrated in Fig. 1. A current I is induced in the manifold as a result of the inward radial flow of liquid conductor in the presence of an external axial magnetic field. The magnetic field resulting from this azimuthal current adds to the initial applied field so that the hydromagnet in effect represents a self-exciting, internally short-circuited homopolar generator. From the point of view of hydromagnetic theory, the operation of the device can be explained this way. The inward flow of conducting fluid compresses the initial axial magnetic field towards the central region. The amount of compression depends on the relative slip between the fluid and the lines of force. Hence, the strength of the field produced by the hydromagnet will depend strongly on the magnetic Reynolds number of the flow.

An estimate of the order of magnitude of the magnetic fields produced by the method of this paper can be obtained by assuming the liquid conductor to be inviscid and to have a resistivity of about 11×10^{-6} ohm-cm (Na at 150°C or Ag at 1000°C). The character-

---

* Operated with support of the U. S. Air Force Office of Scientific Research.

† Operated with support from the U. S. Army, Navy, and Air Force.

‡ Supported in part by the Geophysics Research Directorate, U. S. Air Force Cambridge Research Center.

[1] S. Foner and H. H. Kolm, Rev. Sci. Instr. 28, 799 (1957).

TABLE I. Summary of feasibility calculations.

Exciting field (kgauss)	B_0	10	10	100	100	60
Flow rate (gal/min)	Q	500	5000	500	5000	3000
Generated voltage (v)	V	0.44	4.4	4.4	44	15.8
Total current (kamp)	J	120	1200	1200	12 000	4300
Power dissipated (Mw)	W	0.053	5.3	5.3	530	69
Back pressure (lb/in.^{2})	P	233	2330	23 300	23 300 000	50 000
Generated field (kgauss)	H	12.4	124	124	1240	450

istic parameters for a hydromagnet of 1 in. i.d., 12 in. o.d., and 3 in. in length are summarized in Table I. The first two variables in the table, viz., the exciting field and the flow rate, are treated as the independent variables. The dependent variables are governed by the following relations:

generated voltage	$V=k_1(QB_0/l)$
total current	$J=k_2(QB_0/2\pi l\rho_e)l_n(r_2/r_1)$
power dissipated	$W=k_3(1/2\pi\rho_e)(QB_0/l)^2$
generated field	$H=k_4W^{\frac{1}{2}}=k_sQB_0$
electromagnetic pressure	$P=W/Q,$

where the k's are constants depending on choice of units, Q is the flow rate, B_0 the applied exciting field, r_2 and r_1 the outer and inner radii, respectively, l the length, and inner radii, respectively, l the length, and ρ_e the resistivity of the liquid conductor. The pressure values in the table represent backpressure for an inviscid fluid and do not include the pressure head required to overcome viscosity.

The first column in Table I represents the mildest operation at an excitation of 10 kgauss and a flow rate of 500 gal/min. It is seen to represent the minimum conditions for self-excitation, the generated field of 12.4 kgauss being just above the exciting field. Actually, of course, the generated field is not constant over the flow volume so that excitation would still have to be maintained. In the second column, the flow rate has been increased by a factor of 10, while in the third column, the excitation has been increased by a factor of 10. Both of these cases are near the limit of feasibility as regards the pressure involved. In the fourth column, both the excitation and the flow rate have been increased tenfold, resulting in a back pressure which cannot be regarded as realistic. The fifth column represents a compromise in which both values have been increased by a factor of 6. The resulting pressure of 50 000 lb/in^2 is approximately the chamber pressure normally contained by small fire arms and, more graphically, corresponds to a standpipe of liquid conductor extending up a 10 000-ft mountain. The resulting field of about half a million gauss can, therefore, be regarded as the maximum possible field achievable by hydromagnets at present.

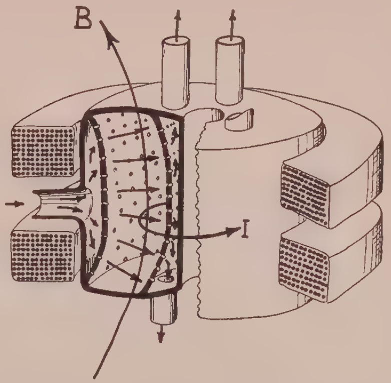

FIG. 1. Principle of the hydromagnet: liquid conductor is forced radially inward through a cylindrical space in which an axial magnetic field is generated by external exciting coils. The induced azimuthal current in the liquid conductor adds to the exciting field, or "compresses flux lines."

Since there is no known way of generating fields of such intensities for more than several milliseconds, the problem appears worth pursuing further. A more detailed theoretical and experimental investigation will have to determine to what extent the approximate limit can actually be approached.

The present paper treats in detail the fluid flow in the hydromagnet. The magnetic compression is derived in Sec. I of the paper, while in Sec. II, the expected energy dissipation in the magnet is estimated. The paper concludes with a preliminary experiment to demonstrate the operation of a hydromagnet.

I. MAGNETIC COMPRESSION

A. Fundamental Equations

In order to obtain the operational characteristics of the hydromagnet, the flow of the liquid metal in the manifold M will have to be studied. For the purpose of stabilizing the flow, the annular space M is divided by a number of radial conducting vanes V (Fig. 2). From symmetry considerations, it is clear that it suffices to determine the flow in a sector bounded by two neighboring vanes.

To simplify the calculations, the coaxial cylinders are considered infinitely long. A cylindrical system of coordinates (z, r, ϕ) is chosen in such a way that the z axis coincides with the axis of the cylinders. Since the conducting fluids that will be used in the hydromagnet are metallic, the assumption of incompressibility is a reasonably good one.

When the flow is purely radial, the components of the fluid velocity along the axial and azimuthal directions vanish. The governing equations for the flow of the

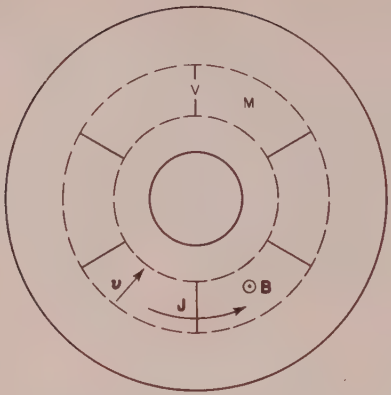

FIG. 2. Schematic diagram of assumed hydromagnet geometry: fluid flow **v** in the infinitely long annular cylinder M is purely radial; magnetic field **B** (out of page) induces azimuthal current **J**; radial vanes V and perforated walls of annulus are ideal conductors.

fluid, at steady state, become

$$u(\partial u/\partial r)=-(1/\rho)(\partial p/\partial r)+\nu[\nabla^2 u-(u/r^2)]+(1/\rho)(\mathbf{J}\times\mathbf{B})_r \quad (1)$$

and

$$0=-(1/r\rho)(\partial p/\partial\phi)+(2\nu/r^2)(\partial u/\partial\phi)+(1/\rho)(\mathbf{J}\times\mathbf{B})_\phi. \quad (2)$$

The symbol u in the above relation stands for the radial component of the velocity **v**, ρ stands for the density of the fluid, and ν for its kinematic viscosity which is the viscosity μ divided by the density ρ. The pressure of the fluid is denoted by p, the current by **J**, and the magnetic field density by **B**.

In addition to the mechanical relations for the fluid, one has to consider Maxwell's equations:

$$\nabla\times\mathbf{B}=\mu_0\mathbf{J}, \quad (3)$$

$$\nabla\times\mathbf{E}=-(\partial\mathbf{B}/\partial t), \quad (4)$$

and

$$\nabla\cdot\mathbf{B}=0. \quad (5)$$

The displacement current does not appear in Ampere's relation, Eq. (3), in accordance with the usual approximation of magnetohydrodynamics.[2] **E** is the electric field and μ_0 is the magnetic permeability of the fluid. The rationalized mks system of units is used throughout this paper. In addition to Maxwell's equations, one introduces Ohm's law.

$$\mathbf{J}=\sigma(\mathbf{E}+\mathbf{v}\times\mathbf{B}), \quad (6)$$

where σ is the electrical conductivity of the fluid. The system of Eqs. (1)–(6) completely describes the flow.

By making use of Eq. (3), the expression for the electromagnetic force per unit volume of the fluid becomes

$$\mathbf{J}\times\mathbf{B}=(1/\mu_0)(\nabla\times\mathbf{B})\times\mathbf{B}=-\nabla(B^2/2\mu_0)+(\mathbf{B}\cdot\nabla)\mathbf{B}. \quad (7)$$

The above expression follows from a well-known identity for the triple vector product. Now, from considerations of symmetry, it is observed that the lines of force are all parallel to the z axis and in view of the hypothesis of infinite length of the container C, the magnetic field **B** is independent of the z coordinate. The immediate consequence of these two properties is that $(\mathbf{B}\cdot\nabla)\,\mathbf{B}$ vanishes. Expressing the gradient in cylindrical coordinates, one finds after substitution of Eq. (7) into Eqs. (1) and (2), that these relations become:

$$u(\partial u/\partial r)=-(1/\rho)(\partial/\partial r)[p+(B^2/2\mu_0]+\nu[\nabla^2 u-(u/r^2)], \quad (8)$$

$$0=-(1/\rho r)(\partial/\partial\phi)[p+(B^2/2\mu_0]+(2\nu/r^2)(\partial u/\partial\phi). \quad (9)$$

Since the flow is purely radial, the equation of continuity; viz.,

$$\nabla\cdot\mathbf{v}=0, \quad (10)$$

is satisfied if the radial velocity is of the form

$$u=f(\phi)/r. \quad (11)$$

When the above expression is substituted into Eqs. (8) and (9), these reduce to:

$$-f^2/r^3=-(1/\rho)(\partial/\partial r)[p+(B^2/2\mu_0]+(\nu f''/r^3), \quad (12)$$

$$0=-(1/\rho r)(\partial/\partial\phi)[p+(B^2/2\mu_0]+(2\nu f'/r^3). \quad (13)$$

The primes above refer to derivatives with respect to the ϕ coordinates. It is deduced from the first of these two equations that $r^3\ (\partial/\partial r)[(p/\rho)+(B^2/2\mu_0\rho)]$ is a function of ϕ only. The second equation gives for the total pressure

$$(1/\rho)[p+(B^2/2\mu_0)]=(2\nu f/r^2)+(K_1\nu/2r^2)+K_2, \quad (14)$$

where K_1 and K_2 are constants. By manipulation of Eqs. (12) and (14), the differential relation for the function $f(\phi)$ is found to be

$$(f')^2=(2/3\nu)(K_3-3\nu K_1 f-6\nu f^2-f^3), \quad (15)$$

where K_3 stands for a new constant of integration. This equation which is identical to that for the flow of a viscous fluid between two nonparallel plane walls, has been studied by a number of authors.[3] Since the flow is purely converging, f is negative. The function f is symmetrical about the plane bisecting the sector, i.e., about $\phi=0$, and vanishes at the walls. If the angle subtended by the sector is $2\,\alpha$, then it can be shown that f is approximately given by[4]

$$f/f_2=3\tanh^2[\tfrac{1}{2}R(\alpha-\phi)^{\frac{1}{2}}+\beta]-2, \quad (16$$

---

[2] See, for instance, T. G. Cowling, *Magnetohydrodynamics* (Interscience Publishers, Inc., New York, 1957), p. 2 ff.

[3] An extensive list of references dealing with this problem i found in S. Goldstein, *Modern Developments in Fluid Dynamic* (Clarendon Press, Oxford, England, 1938), Vol. 1, p. 106.

[4] See p. 109 of reference 2.

where $f_2=-r|u_{\max}|$. The Reynolds number R is defined by $(-f_2/\nu)$, and β is a constant such that $\tanh^2\beta=\frac{2}{3}$. The behavior of f as a function of the angle ϕ is shown in graphical form in Fig. 3.

B. Magnetic Field Configurations

Whereas the expression for the total pressure is given by Eq. (14), that for the magnetic field alone is obtained by combining Eqs. (3)–(6). For steady state, one finds

$$0=\nabla\times(\mathbf{v}\times\mathbf{B})+(1/\mu_0\sigma)\nabla^2\mathbf{B}. \qquad (17)$$

Because the magnetic field is assumed by hypothesis to be axial, the above relation reduces to a single equation, which is:

$$(\partial^2B/\partial r^2)+(1/r)(\partial B/\partial r)+(1/r^2)(\partial^2B/\partial\phi^2)=f(\mu_0\sigma/r)(\partial B/\partial r). \qquad (18)$$

Introducing the change of variable

$$r=\xi r_2, \qquad (19)$$

where r_2 is the outer radius of the hydromagnet, and combining Eq. (16) with Eq. (18), one finds

$$(\partial^2B/\partial\xi^2)+(1/\xi)(\partial B/\partial\xi)+(1/\xi^2)(\partial^2B/\partial\phi^2)=(-FR_m/\xi)(\partial B/\partial\xi), \qquad (20)$$

where R_m, the magnetic Reynolds number, stands for $r|u_{\max}|\sigma\mu_0$, and $F=3\tanh^2\{[\frac{1}{2}R(\alpha-\phi)]^{\frac{1}{2}}+\beta\}-2$.

The electrical conductivity of liquid NaK is 2.7×10^6 mho/m. Assuming a maximum velocity $u_{\max}$ of the order of 0.1 m/sec and an outer radius of the container C of 0.15 m, the resulting R_m is about 0.05. Of course, the velocity may be considerably below 0.1 m/sec, so that R_m, in general, is a small quantity less than 1.

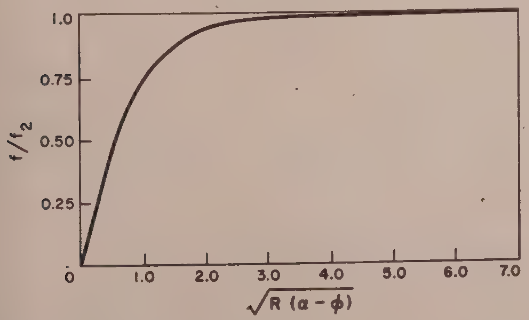

FIG. 3. Normalized distribution fucntion f plotted as a function of the angle measured from the wall. Taken from reference 6, p. 109.

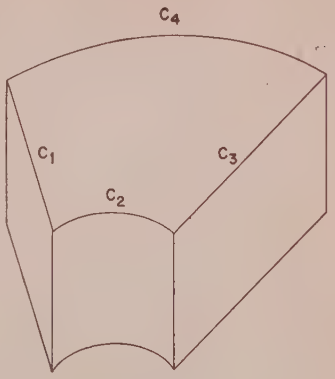

FIG. 4. Domain of integration for Eq. (22). The sector subtends an angle 2 α and is of unit height.

For values of R_m less than unity, a solution can be found in the form of an expansion of powers of R_m. To this effect, the term in R_m is treated as the right-hand side of an inhomogeneous differential equation. A Green's function $G(\xi,\phi;\,\xi',\phi')$ for the homogeneous part is defined by

$$(\partial^2G/\partial\xi^2)+(1/\xi)(\partial G/\partial\xi)+(1/\xi^2)(\partial^2G/\partial\phi^2)=-[\delta(\xi-\xi')/\xi]\delta(\phi-\phi'), \qquad (21)$$

where δ is the usual Dirac function.[5] The left-hand side of Eq. (20) or Eq. (21) is of course the Laplacian of B or G. These two equations are multiplied respectively by G and B and their difference evaluated. On integrating both sides of the difference over a section of C of unit height and bounded by two vanes, it is found that

$$\int_V(B\nabla^2G-G\nabla^2B)d\tau=B(\xi',\phi')-R_m\int_V\frac{FG}{\xi}\frac{\partial B}{\partial\xi}d\tau, \qquad (22)$$

where $d\tau$ is an element of volume and V is the domain of integration (Fig. 4). But by Green's second identity, the volume integral to the left of Eq. (22), in view of G being independent of the z coordinate, reduces to $\oint(B\partial_nG-G\partial_nB)ds$, where the line integral is carried along the contour of C.

The Green's function G is now chosen so that it vanishes on the segments C_2 and C_4 (Fig. 3). In view of the symmetry with respect to the $\phi=0$ plane, G is expected to be an even function in ϕ. The gradient ∂_nB, however, vanishes on C_1 and C_3. This is proved this way: From Ohm's law, the component of the current in the radial direction is

$$J_r=\sigma E_r \qquad (23)$$

since $(\mathbf{v}\times\mathbf{B})_r$ vanishes by virtue of the flow being purely radial by hypothesis. We assume the electrical conductivity of the vanes to be much higher than that of the liquid, so that to a first approximation the vanes and the "rim" are equipotential surfaces $E_r=0$. Consequently the current J_r vanishes on C_1 and C_3. Actually, the vanishing of E_r in the vanes is not such a drastic assumption, in view of the current circulating in *opposite* directions on both sides of the vanes in adjoining sectors, thus tending to reduce the net field and current in the vanes.

But by Ampère's law, the vanishing of J_r implies that

$$J_r=(1/\mu_0r)(\partial B/\partial\phi)|_{\phi=\pm\alpha}=0, \qquad (24)$$

---

[5] P. M. Morse and H. Feshbach, *Methods of Theoretical Physics* (McGraw-Hill Book Company, Inc., New York, 1953), Vol. 1, p. 122 ff.

which shows that $\partial_n B=0$ on C_1 and C_3 as stated above.

The term $G\partial_n B$ in the integrand therefore contributes nothing to the contour integral, which now may be decomposed into

$$\oint B\partial_n G ds=\int_{c1}+\int_{c2}+\int_{c3}+\int_{c4} B\partial_n G ds. \quad (25)$$

Because of the periodic character of B and $\partial_n G$, the integrals on C_1 and C_3 are equal in magnitude but different in signs. The normal pointing in opposite senses their sum will accordingly vanish. Remembering that all quantities are independent of z, so that the volume integral on the right of Eq. (22) becomes a surface integral evaluated over S, this equation becomes:

$$B(\xi',\phi')=\oint B\partial_n G ds+R_m\int_s \frac{FG}{\xi}\frac{\partial B}{\partial \xi}d\sigma, \quad (26)$$

which is a Fredholm integral equation of the second kind if B is prescribed on the segments C_2 and C_4 on which the contour integral is evaluated. The solution of this equation is of the form

$$B(\xi',\phi')=f_0(\xi',\phi')+R_m f_1(\xi',\phi')+R_m^2 f_2(\xi',\phi')+\cdots, \quad (27)$$

where the zeroth order approximation f_0 is the solution of

$$B(\xi',\phi')=\oint B\partial_n G ds, \quad (28)$$

while the remaining functions, f_1, f_2, . . ., are the results of successive iterations.

The appropriate Green's function to use here is found from a well-known theorem of Schmidt[6] which states that the solution of Eq. (21) is

$$G(\mathbf{r},\mathbf{r}')=\sum_{n,m}\frac{\psi_{nm}(\mathbf{r})\psi_{nm}(\mathbf{r}')}{\gamma_{nm}^2}, \quad (29)$$

where $\psi_{nm}(\mathbf{r})$ is the normalized eigenfunction of the homogeneous part of Eq. (21) and γ_{nm} the corresponding eigennumber. Now it can be shown (Appendix A) that the appropriate functions which vanish on part of the contour, as required, are

$$\psi_{nm}=\Lambda_{nm}^{-\frac{1}{2}}[J_{n\pi/\alpha}(\gamma_{nm}\xi)Y_{n\pi/\alpha}(\gamma_{nm})-Y_{n\pi/\alpha}(\gamma_{nm}\xi)J_{n\pi/\alpha}(\gamma_{nm})]\cos(n\pi\phi/\alpha),$$
$$n=0, 1, 2, \ldots, \quad (30)$$

where the dimensionless variable ξ extends from a (the ratio of the inner to outer radius of C) to unity, and γ_{nm} are the roots of the equation

$$J_{n\pi/\alpha}(\gamma_{nm}a)Y_{n\pi/\alpha}(\gamma_{nm})-Y_{n\pi/\alpha}(\gamma_{nm}a)J_{n\pi/\alpha}(\gamma_{nm})=0. \quad (31)$$

These have been tabulated in a number of places.[7] The symbol Λ_{nm} stands for the normalization constant of ψ_{nm} which may be shown to be (Appendix B)

$$\Lambda_{nm}=\int_{-\alpha}^{\alpha}\int_{a}^{1}\xi\psi_{nm}^2 d\xi d\phi$$
$$=\frac{4\alpha}{\pi^2\gamma_{nm}^2}\left(\frac{J_{n\pi/\alpha}^2(\gamma_{nm}a)-J_{n\pi/\alpha}^2(\gamma_{nm})}{J_{n\pi/\alpha}^2(\gamma_{nm}a)}\right). \quad (32)$$

The value of the magnetic field, however, is not known over the segment C_2. In order to solve for f_0, it is assumed that the magnetic field is constant at the periphery, which is a plausible approximation. The derivation is subsequently greatly simplified. In fact, if in the integral equation (28) the value of $\partial_n B$ at $\xi=1$, $\phi=0$, is estimated, then

$$\frac{\partial B}{\partial \xi}(1,0)=B_0\int_{-\alpha}^{\alpha}\partial_\xi\partial_{\xi}'G(\xi,\xi';\phi,0)|_{\xi,\xi'=1}d\phi$$
$$-B_1\int_{-\alpha}^{\alpha}\partial_\xi\partial_{\xi}'G(\xi,\xi';\phi,0)|_{\substack{\xi=a\\ \xi'=1}}\, a d\phi. \quad (33)$$

B_1, the unknown value of the field at $\xi=a$, deduced at once from the above, provided the left-hand side is known. But the latter is, in fact, identified with the azimuthal current as evident from Ampère's relation

$$J_\phi=(1/\mu_0)(\partial B/\partial r)=(1/\mu_0 r_2)(\partial B/\partial \xi). \quad (34)$$

But on the rim, assumed to be an equipotential because of the supposed high conductivity of the wall material, Ohm's law yields at once

$$J_\phi=-\sigma u_{\max}B_0. \quad (35)$$

On combining Eqs. (34) and (35),

$$(\partial B/\partial \xi)|_{\xi=1}=-R_m B_0. \quad (36)$$

One finds in this way that

$$B_1=B_0\left\{R_m+2\sum_m\frac{J_0^2(\gamma_{om}a)}{\gamma_{om}^2[J_0^2(\gamma_{om}a)-J_0^2(\gamma_{om})]}\right\}$$
$$\times\left\{2\sum_m\frac{J_0(\gamma_{om}a)J_0(\gamma_{om})}{\gamma_{om}^2[J_0^2(\gamma_{om}a)-J_0^2(\gamma_{om})]}\right\}^{-1}$$
$$=B_0 A, \quad (37)$$

where the coefficient A depends on R_m and a as shown above. Since the order $(n\pi/\alpha)$ for $n\neq 0$ is much larger than one, the successive terms decrease very quickly in magnitude and only the order $n=0$ needs to be retained. The zeroth-order approximation is

$$f_0(\xi')=B_0[\sum_m\psi_{om}'(1)\psi_{om}(\xi)-Aa\sum_m\psi_{om}'(a)\psi_{om}(\xi)]. \quad (38)$$

---

[6] See Vol. 1, p. 820 ff. of reference 5.

[7] See, for instance, E. Jahnke and F. Emde, *Tables of Functions* (Dover Publications, New York, 1945), p. 204.

This is finally substituted in Eq. (26) to yield to first order

$$B(\xi',\phi')=f_0+R_m\int_{-\alpha}^{\alpha}\int_{a}^{1}F(\phi)G(\xi,\xi';\phi,\phi')\frac{\partial f_0}{\partial \xi}d\xi d\phi. \quad (39)$$

The function $F(\phi)$ is supposed to be developed in a Fourier series:

$$F(\phi)=\sum_n a_n\cos(n\pi\phi/\alpha);\quad n=0,\,1,\,2,\,\cdots. \quad (40)$$

Because of the symmetry of $F(\phi)$, the coefficients of odd rank are not expected to be present. In fact, by means of numerical integration, it is found that

$$\begin{aligned} a_0&=0.644\\ a_2&=-0.397\\ a_4&=-0.171\\ a_6&=-0.076\\ \cdot\cdot\quad&\cdots \end{aligned}$$

and

$$a_1=a_3=\cdots=a_{2n-1}=\cdots=0. \quad (41)$$

Whereas the field distribution inside S is given approximately by Eq. (39), that inside the cylindrical region of the core of C is constant and its value is $B(a,0)$. The "amplification" of the field intensity is thus equal to:

$$\begin{aligned}\frac{B(a,0)}{B_0}=A-\frac{8\times 0.644}{\pi^2}&\times R_m\sum_{n,m}\frac{J_0^2(\gamma_{om}a)}{\gamma_{om}^2[J_0^2(\gamma_{om}a)-J_0^2(\gamma_{om})]}\\ &\times\left[\frac{J_0^2(\gamma_{on}a)-AJ_0(\gamma_{on}a)J_0(\gamma_{on})}{J_0^2(\gamma_{on}a)-J_0^2(\gamma_{on})}\right]\\ &\times\left[1-\frac{J_0(\gamma_{om})}{J_0(\gamma_{om}a)}\frac{J_0(\gamma_{on})}{J_0(\gamma_{on}a)}\right]. \quad (42)\end{aligned}$$

The dependence of this amplification factor on R_m and on a is shown in graphical form in Fig. 5. The arrows on the different curves indicate the place where more than two terms had to be used to compute the series (42).

As R_m approaches unity, the convergence of Eq. (42) becomes very poor. Furthermore, the method of solution discussed here fails for $R_m>1$. Preliminary attempts[8] have been made to solve Eq. (20) by numerical analysis for R_m slightly greater than unity.

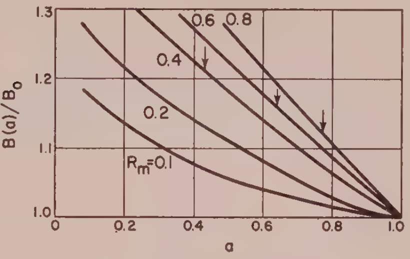

FIG. 5. Dependence of amplification factor on a, the ratio of radii, and R_m, the magnetic Reynolds number.

II. LOSSES IN THE ELECTROMAGNET

One of the operating characteristics of the electromagnet which is of special importance from the design point of view is the amount of losses in the system. The total power dissipated may be estimated by summing the individual contributions of the ohmic and viscous losses. This procedure, however, is very laborious. It is more expedient instead to use an expression derived below.

It can be shown that the energy loss in the electromagnet per unit length and per unit time is

$$W=-(\pi/\alpha)\oint[\rho(v^2/2)+p]\mathbf{v}\cdot\mathbf{n}ds, \quad (43)$$

where the contour integration is along the perimeter C, and $\mathbf{n}$ is a unit vector normal to C and pointing outwards.

The starting point of the proof is the momentum equation for steady state,

$$\rho(\mathbf{v}\cdot\nabla)\mathbf{v}=-\nabla p+\mathbf{J}\times\mathbf{B}+\nu\nabla^2\mathbf{v}. \quad (44)$$

The scalar product of both sides of this equation with $\mathbf{v}$ is now performed and then followed by an integration over the test volume V. This leads to

$$\int_V\nabla\cdot[\rho(v^2/2)\mathbf{v}+p\mathbf{v}]d\tau=\int(\mathbf{v}\cdot\mathbf{J}\times\mathbf{B}+\nu\mathbf{v}\cdot\nabla^2\mathbf{v})d\tau, \quad (45)$$

in which the incompressible property of the fluid has been invoked. But from the triple scalar product and Ohm's law,

$$\begin{aligned}\mathbf{v}\cdot\mathbf{J}\times\mathbf{B}&=-\mathbf{J}\cdot\mathbf{v}\times\mathbf{B}\\ &=\mathbf{J}\cdot\mathbf{E}-(J^2/\sigma). \quad (46)\end{aligned}$$

Hence,

$$\int_s[p+\rho(v^2/2)]\mathbf{v}\cdot\mathbf{n}d\sigma=\int(\mathbf{J}\cdot\mathbf{E})d\tau-\int(J^2/\sigma)d\tau+\nu\int\mathbf{v}\cdot\nabla^2\mathbf{v}d\tau.$$

But

$$\begin{aligned}\int(\mathbf{J}\cdot\mathbf{E})d\tau&=\mu_0\int\nabla\cdot(\mathbf{H}\times\mathbf{E})d\tau\\ &=\mu_0\int_s(\mathbf{H}\times\mathbf{E})\cdot\mathbf{n}d\sigma, \quad (47)\end{aligned}$$

---

[8] L. B. Vaughn and A. M. Schneiderman, thesis, Massachusetts Institute of Technology, 1960.

where Ampère's relation and the steady state form of Faraday's equation,

$$\nabla\times\mathbf{E}=0,$$

have been used. The right-hand side of Eq. (47), however, vanishes since the walls of C are considered equipotentials. But it is well known[9] that $\int\nu(\mathbf{v}\cdot\nabla^2\mathbf{v})d\tau$ represents the negative of the viscous dissipation in the fluid, hence substitution in Eq. (45) leads to the required form.

The result is of course as expected since the work done to overcome the losses in the hydromagnet are completely supplied by the pump. Since the normal component of the velocity vanishes at the vanes, the contour integration of Eq. (43) reduces to integrals along C_2 and C_4. By using the result of Eqs. (14) and (16), the total energy loss W can be found without difficulty. Indeed, this is

$$W=\frac{\pi}{\alpha}\int_{-\alpha}^{\alpha}\frac{\rho f_2^3}{2r_2^2}F^3(\phi)\left(\frac{1}{a^2}-1\right)d\phi+\frac{\pi}{\alpha}\times\int_{-\alpha}^{\alpha}\left[\frac{2\nu f_2^2F^2(\phi)}{r_2^2}+\frac{K_1\nu f_2F(\phi)}{2r_2^2}\right]\left(\frac{1}{a^2}-1\right)d\phi+\frac{\pi}{\alpha}\frac{(B_0^2-B_a^2)f_2}{2\mu_0}\int_{-\alpha}^{\alpha}F(\phi)d\phi. \quad (48)$$

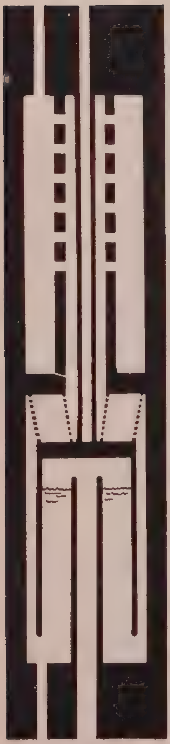

FIG. 6. Schematic diagram of experimental hydromagnet: pressure admitted through bottom riser tube forces surrounding liquid conductor upward, inward through perforated annular chamber, and then upward through upper riser tube. After venting back to atmospheric pressure, the liquid conductor slowly returns to bottom reservoir through small weep hole in preparation for next cycle.

Reference 5 gives the value of $(K_1\nu)$ to be $-(f_2^2/3)$ and that for f_2, $-r|u_{\max}|$. In the above expression, the magnetic field is assumed constant on C_2 and C_4 in accordance with the arguments of the previous section. B_a stands for the value of the field on C_2. It is readily shown by manipulation of the integrand of Eq. (44), together with the expansion, Eq. (41), for $F(\phi)$, that the total loss per unit length is

$$W=\{(\pi/r^2)\mu\nu^2R^2[(1/a^2)-1](2.0308+0.679R)+(0.644\pi R_m/\mu_0^2\sigma)[1-(B_0/B_a)^2]B_a^2\}\ \text{w/m.} \quad (49)$$

The first term of W is associated with the viscous losses. Inspection of Eq. (49) reveals that these losses depend on the third power of the conventional Reynolds' number $(r_2u_{\max}/\nu)$. This dependence of the losses on the cube of the velocity is in accordance with hydrodynamic theory. The second term of Eq. (49), on the other hand, refers to the ohmic losses. In a manner of speaking, the hydromagnet behaves like a one-turn coil. For such an electromagnet, the current is proportional to the magnetic field; hence the Joule losses are like B_a^2. But in the hydromagnet, the induced current varies along the radius; consequently, the mean square value of the current must be used. This explains the form of the second term of Eq. (49).

III. EXPERIMENTAL

In order to obtain some experimental verification of the theoretical predictions at the minimum cost of time and effort, it was decided to take advantage of the very high excitation field available in the 4-in. caliber, 70-kgauss Bitter solenoid magnet in the MIT Magnet Laboratory. This made it possible to generate a measurable field by means of a very simple hydromagnet operating at low pressure.

The device is illustrated schematically in Fig. 6. The actual hydromagnet is a stainless steel chamber bounded by two perforated, coaxial cones and two flat end plates, and divided into six sectors by copper separators. Its average inside and outside diameters are approximately 1 and $2\frac{1}{2}$ in., respectively, and its length is 1 in. This chamber, which is depicted in the photograph of Fig. 7, is mounted at the center of a steel tube

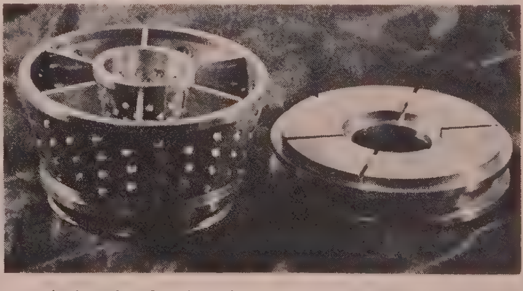

FIG. 7. Annular chamber of experimental hydromagnet: average inside and outside diameters of the slightly conical chamber are 1 and 3 in., respectively.

---

[9] Sir Horace Lamb, *Hydrodynamics* (Dover Publications, New York 1945), p. 580 ff.

of 3 in i.d., 4 in. o.d., and 7 ft. in length. The tube is centered in the 4-in. caliber solenoid magnet so that the chamber is located in the region of maximum field. The assembled installation is shown in Fig. 8.

The hydromagnet is operated by applying the exciting field (64 kgauss) and then opening a solenoid valve which admits nitrogen gas at 2000 lb/in.^{2} from four tanks connected in parallel to a central orifice at the bottom of the hydromagnet tube (Fig. 6). The gas passes upward through a central pipe and exerts pressure on the surface of four liters of NaK located in a reservoir surrounding this central pipe. The NaK is forced downward in the reservoir and then upward in the annular space surrounding it, radially inward through the perforated conical chamber, and then upward again through a vertical outlet tube. The upper half of this outlet tube is perforated to allow the NaK to escape into a surrounding expansion chamber in which the pressure rises until all of the NaK has arrived. The exciting field is then turned off, the gas inlet valve is closed, and the expansion chamber is vented to the atmosphere through a solenoid valve at the top.

After the pressure in the entire system has equalized, the NaK slowly returns to the bottom reservoir through a weep hole at the base of the outlet tube which is sufficiently small to permit only negligible outward flow during operation. The cycle can then be repeated.

To measure the generated field, a suitable sensing coil (2000 turns) is lowered to the center of the hydromagnet chamber through the central $\frac{1}{4}$-in. i.d. access tube. The voltage induced in this coil is integrated electronically by a standard circuit using Philbrick operational amplifiers and is displayed on a Tektronix oscilloscope, triggered simultaneously with the inlet solenoid valve. The photograph of a typical trace is shown in Fig. 9. The system is calibrated by measuring the integrated signal produced by a known change in excitation field, well above the saturation value of the steel tube.

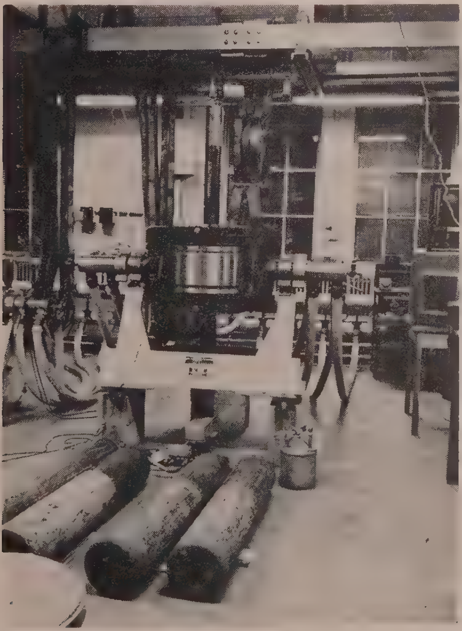

FIG. 8. Experimental hydromagnet installed in 4-in. caliber, 67-kgauss Bitter solenoid. Driving pressure from four nitrogen tanks is admitted by solenoid valve at bottom, system is vented by valve at top.

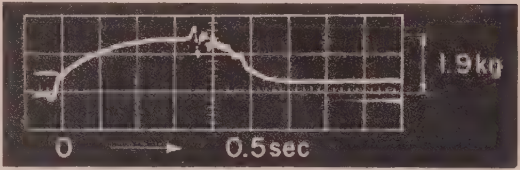

FIG. 9. Oscillogram of transient field generated by hydromagnet. Noise at end of pulse represents arcing due to exhaustion of liquid conductor supply.

In comparing the observed pulse with theory, it was necessary to calculate the flow velocity from the observed pulse duration. On this basis, the observed amplitude of 1.9 kgauss is in good agreement with the value of 2.3 kgauss calculated by simple theory and 2.1 kgauss by the more exact method of Sec. II.

It should be pointed out that the driving pressure was considerably less than the tank pressure of 2000 lb/in^2., probably in the vicinity of 200 lb/in^2. This drop is due to the constriction at the valves of the nitrogen tanks, which was not alleviated substantially despite the fact that four tanks were used in parallel.

ACKNOWLEDGMENTS

We would like to take this opportunity to thank Charles Bir for assisting in the experimental part of this investigation. We are also indebted to D. J. Rose and M. Clark, Jr. for their constructive criticism.

APPENDIX

A. Evaluation of ψ_{nm}

The functions ψ_{nm} are the eigenfunctions of the Helmholz equation

$$(\partial^2\psi/\partial\xi^2)+(1/\xi)(\partial\psi/\partial\xi)+(1/\xi^2)(\partial^2\psi/\partial\phi^2)+\gamma^2\psi=0, \tag{A1}$$

with the boundary conditions that ψ be an even function of ϕ and that it vanishes at $\xi=1$ and $\xi=a$. The function ψ is first developed in a Fourier series:

$$\psi=\sum_n \psi_n(\xi)\cos(n\pi\phi/\alpha), \tag{A2}$$

then substituted in Eq. (A1). The latter equation defines ψ_n by means of the equation

$$(\partial^2\psi_n/\partial\xi^2)+(1/\xi)(\partial\psi_n/\partial\xi)+[\gamma^2-(n^2/\xi^2)]\psi_n=0, \tag{A3}$$

the solution of which can be found at once to be

$$\psi_n = AJ_n(\gamma\xi) + BY_n(\gamma\xi). \qquad \text{(A4)}$$

On introducing the boundary conditions, it is deduced that

$$-B/A = [J_n(\gamma)/Y_n(\gamma)] = [J_n(\gamma a)/Y_n(\gamma a)], \qquad \text{(A5)}$$

while γ_{nm} is the mth root of the equation

$$J_n(\gamma)Y_n(\gamma a) - J_n(\gamma a)Y_n(\gamma) = 0. \qquad \text{(A6)}$$

Manipulation of Eqs. (A2), (A4), and (A5) leads to Eq. (30) to within a constant which is estimated in the following section.

B. Normalization Factor Λ_{nm}

The factor Λ_{nm} is derived from the integral

$$\Lambda_{nm}^{\frac{1}{2}} = \int_{-\alpha}^{\alpha}\int_{a}^{1} \xi\psi_{nm}^2(\gamma_{nm}\xi)\cos^2(n\pi\phi/\alpha)d\xi d\phi$$

$$= \alpha\int_a^1 \psi_n^2 \xi d\xi. \qquad \text{(A7)}$$

A general procedure for the evaluation of such an integral is given in standard texts.[10] It is easier, however, to derive it from first principles. The differential equation for ψ_{nm} is written

$$(1/\xi)(d/d\xi)[\xi(d\psi_{nm}/d\xi)] + [\gamma_{nm}^2 - (n^2/\xi^2)]\psi_{nm} = 0. \qquad \text{(A8)}$$

On multiplying the equation by $2\xi^2(d/d\xi)$, it can be reduced to

$$\frac{d}{d\xi}\{[\xi(d\psi_{nm}/d\xi)]^2\} + \gamma_{nm}^2\xi^2\frac{d\psi_{nm}^2}{d\xi} - n^2\frac{d\psi_{nm}^2}{d\xi} = 0. \qquad \text{(A9)}$$

This is now integrated to yield

$$\gamma_{nm}^2\int_a^1 \xi^2\frac{d\psi_{nm}^2}{d\xi}d\xi + (\xi d\psi_{nm}/d\xi)^2\Big|_a^1 = 0. \qquad \text{(A10)}$$

The third term of Eq. (A9) contributes nothing, since $\psi_{nm}(a) = \psi_{nm}(1) = 0$ from the boundary conditions. Expansion of the integral by parts and further use of the boundary conditions shows that

$$\int_a^1 \xi\psi_{nm}^2 d\xi = \frac{1}{2\gamma_{nm}^2}\left(\xi\frac{d\psi_{nm}}{d\xi}\right)^2\Big|_a^1. \qquad \text{(A11)}$$

But from the previous section,

$$\begin{aligned} \xi d\psi_{nm}/d\xi\,|_{\xi=a} &= a\gamma_{nm}[J_n'(\gamma_{nm}a)Y_{nm}(\gamma_{nm}a) \\ &\qquad - J_n(\gamma_{nm}a)Y_n'(\gamma_{nm}a)] \\ &= -(2/\pi). \end{aligned} \qquad \text{(A12)}$$

The last step follows from the value of the Wronskian. Similarly,

$$\begin{aligned} \xi d\psi_{nm}/d\xi\,|_{\xi=1} &= \frac{\gamma_{nm}J_n(\gamma_{nm}a)}{J_n(\gamma_{nm})} \\ &\qquad \times[J_n'(\gamma_{nm})Y_n(\gamma_{nm}) - Y_n'(\gamma_{nm})J_n(\gamma_{nm})] \\ &= -\frac{2}{\pi}\frac{J_n(\gamma_{nm}a)}{J_n(\gamma_{nm})}. \end{aligned} \qquad \text{(A13)}$$

By substituting (A12) and (A13) in (A11), the result stated in Eq. (32) is obtained.

---

[10] G. N. Watson, *Theory of Bessel Functions* (The Macmillan Company, New York, 1948), p. 134 ff.

JOURNAL OF APPLIED PHYSICS VOLUME 32, NUMBER 7 JULY, 1961

Two-Phase Permalloy for High-Speed Switching

E. A. Nesbitt and E. M. Gyorgy
Bell Telephone Laboratories, Murray Hill, New Jersey

(Received March 22, 1961)

The addition of gold to Permalloy has made it possible to precipitate a second phase in the alloy. As a result it is possible to control the coercive force and, to some degree, the threshold for rotational flux reversal, by appropriate heat treatments. On this basis a series of alloys have been developed by adding 2–14% gold to Permalloy. Some of these alloys have switching times approximately four times faster than that of the standard Permalloy composition. The switching time is defined as the reversal time at twice the coercive force. The alloy is prepared by annealing at the solution temperature of 900°C and then cooling rapidly. This is followed by cold rolling tape from approximately 0.014- to 0.00013-in. thickness, which is the thickness for switching applications. The material is then annealed at 600–650°C. Under these conditions, alloys containing 7% gold and 14% gold yield square hysteresis loops having coercive forces of at least 1.7 and 4.3 oe, respectively. For the 7% gold alloy, the threshold for rotational flux reversal is 2.5 oe.

INTRODUCTION

IN certain applications of magnetic elements for logic and memory purposes, the magnetic flux reversal process must be accomplished with magnetic fields slightly less than twice the coercive force H_c. The utilization of the coincident-current selection technique imposes this field limitation.[1] The switching time which results from an applied field of only $2H_c$ is often longer than is desirable. Providing magnetic materials which switch in shorter times under these conditions is therefore a current problem.

Considerable insight into a solution of this problem is provided by a review of the basic features of the flux reversal process. A schematic plot of the reciprocal switching time as a function of the applied field amplitude is shown in Fig. 1. Curves A, B, and C illustrate different types of magnetic material. The essential features of this plot are characteristic of most soft magnetic materials.[2] Switching occurs only for fields larger than H_c; at a slightly higher field a nonlinear region occurs while at larger fields the plot is linear. The extrapolation of this linear region to the field axis is called the threshold field H_0 for nonuniform rotation. Most experimental evidence indicates that the dominant flux reversal mechanism for fields below H_0 is the motion of domain walls, while above H_0 it is nonuniform rotation. The switching characteristics of most materials are quite similar in the nonuniform rotation region. The inverse slope of the linear region (S_w) is generally about 0.25 oe μsec. This corresponds to a steeper slope than is found in the wall motion region. The values of H_0 and H_c, however, vary widely from one material to another.

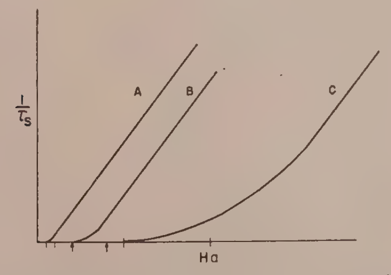

Fig. 1. Reciprocal of the switching time vs applied field for three different types of soft magnetic material.

Since the nonuniform rotation region has the higher slope, it is clear that for a given H_c the minimum switching time at $2H_c$ is obtained if $H_0=H_c$. Under these conditions the switching time is given approximately by $0.25/H_c$. If H_c and H_0 were controllable, the value of H_c would then be determined by the switching time required. Unfortunately, the values of H_c and H_0 are not generally independently controllable. For instance, well-annealed 4–79 Permalloy has H_0 close to H_c (curve A of Fig. 1). However, the coercive force of

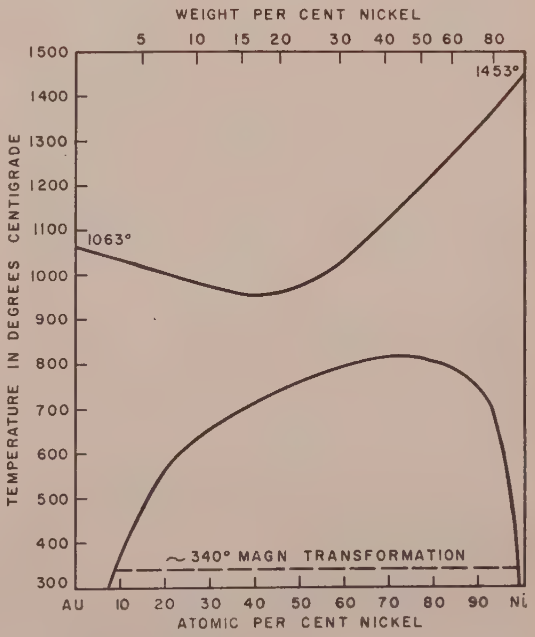

Fig. 2. Equilibrium diagram of the Ni-Au system.

---

[1] J. A. Rajchman, Proc. Inst. Radio Engrs. 41, 475 (1952).
[2] E. M. Gyorgy, J. Appl. Phys,. 31, 110S (1960).

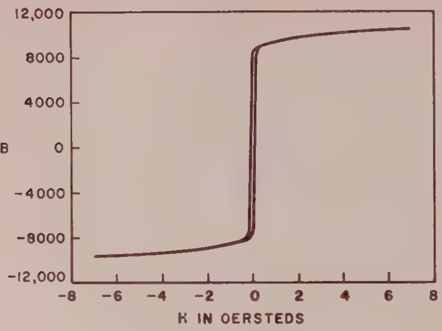

FIG. 3. Hysteresis loop of the toroidal sample for the alloy 77% Ni, 19% Fe, 4% Au after 1000°C anneal and cooling in a magnetic field.

0.06 oe is so low that the switching time is relatively long. Partial cold working of this alloy results in larger values of H_c, but H_0 increases substantially more rapidly than does H_c (curve C of Fig. 1). Consequently, although it is frequently possible to obtain the required switching time at $2H_c$ by increasing H_c without any control of H_0, it is clear that to minimize the applied field needed it is necessary to keep H_0 as close to H_c as possible (curve B of Fig. 1).

Since H_0 of Permalloy-type materials depends sensitively on the amount of strain introduced by cold work, it is attractive to consider a strain-independent means of controlling H_c. Hindering the motion of domain walls by the precipitation of a second phase is a possible way to control H_c. If the second phase is an incoherent precipitate so that the matrix is strain-free, the precipitation process should have little effect on H_0.

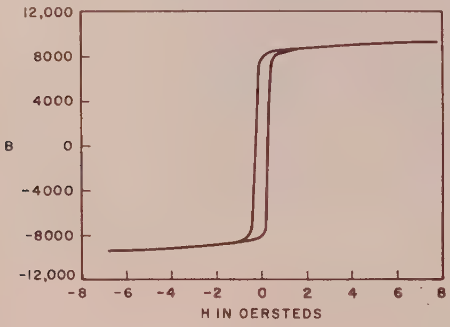

FIG. 4. Hysteresis loop of the toroidal sample for the alloy 77% Ni, 19% Fe, 4% Au after 1000°C anneal and cooling in a magnetic field, plus 550°C for 2 hr in magnetic field.

It is known that a complete series of solid solutions occurs in the nickel-gold system near 900°C. Below this temperature a miscibility gap occurs which results in the alloys' having a heterogeneous structure (Fig. 2). Koster and Dannohl[3] have obtained coercive forces as high as 200 oe in this system. Since the Permalloys are structurally similar to nickel, the addition of gold to Permalloy followed by a suitable heat treatment should result in the precipitation of a second phase in a relatively strain-free matrix. The purpose of this paper is to show that this is in fact the case and to present the switching and other characteristics of material produced in this way.

EXPERIMENT

Nine melts were made in the vicinity of the standard Permalloy composition, with the nickel contents ranging from 71–78%, the iron from 15–20%, and the gold from 2–14% by weight. One additional melt was also made with approximately 4% molybdenum added in order to increase the resistivity. The castings, $2\frac{1}{2}$ in. square by $\frac{1}{2}$-in. thick, were cold rolled to a 0.10-in. thickness. Toroidal rings 2.0 in. i.d., $2\frac{1}{2}$ in. o.d., and 0.10 in. thick were cut from these plates. Tape approximately $\frac{1}{8}$-mil thick and $\frac{1}{8}$-in. wide was also supplied from this material for the switching experiments. This tape was annealed at a thickness of 0.014 in. and then

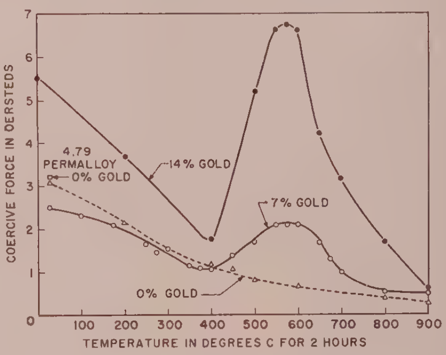

FIG. 5. Coercive force H_c vs temperature of anneal for the alloys (tape 0.125×0.000125 in.) containing 0, 7, and 14% Au by weight. Note absence of age-hardening peak at 575°C for the 0% Au specimens.

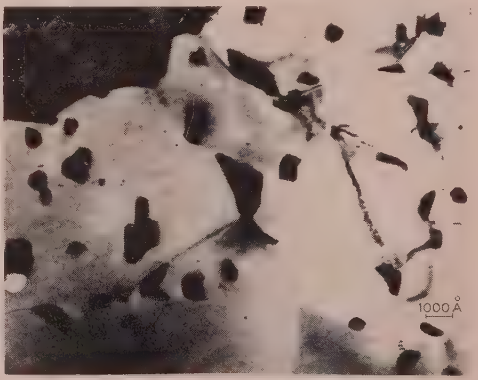

FIG. 6. Electron transmission micrograph by R. D. Heidenreich for tape of the 14% Au alloy after 650°C for 2 hr. The dark areas are regions of precipitated gold-rich phase.

---

[3] W. Koster and W. Dannohl, Z. Metallk. **28**, 248–253 (1936).

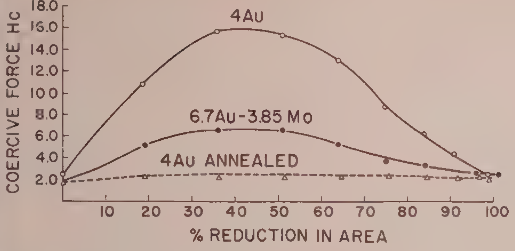

FIG. 7. Coercive force H_c vs degree of cold reduction for the wire samples containing 4% Au and 6.7% Au with 3.85% Mo. Dotted line shows effect of annealing on the 4% Au specimens.

cold rolled to a $\frac{1}{8}$-mil thickness without further annealing. The tape was then insulated and wrapped on a standard ceramic bobbin. In addition, 10 wires with 1- to 10-mil diameters were furnished from each casting. The wires were annealed at 900°C at 10-mil diam and then reduced to their final diameters.

COERCIVE FORCE

Toroidal Samples

Some of the results obtained with the toroidal rings are shown in Figs. 3 and 4. Figure 3 shows a hysteresis loop obtained on a specimen of 77% Ni, 19% Fe, and 4% Au after a 1000°C anneal and cooling in a magnetic field. The loop is reasonably square, and the coercive force is approximately 0.1 oe. Upon aging this specimen at 550°C for 2 hr the coercivity is increased to 0.3 oe and the loop still remains square, as shown in Fig. 4. The alloy containing 75% Ni, 18% Fe, and 7% Au behaved in a similar manner, yielding a final coercivity of 0.6 oe and a reasonably square hysteresis loop. Thus we see that the desired effect of age hardening is operating in these alloys.

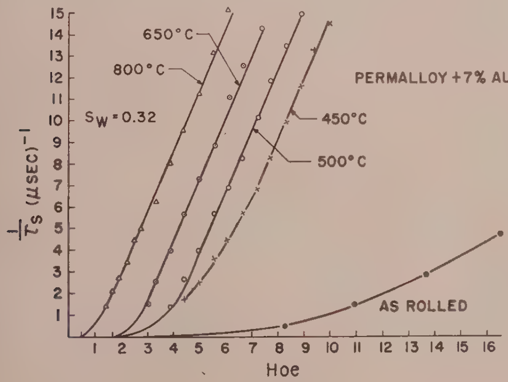

FIG. 8. Reciprocal of the switching time vs applied field for the tape containing 7% Au as rolled and annealed at 450°, 500°, 650°, and 800°C.

Tape Samples

The investigation of the magnetic properties of the thin tape was concentrated on the 7 and 14% gold Permalloys. Hysteresis loops were traced for specimens heat treated at approximately 100° intervals up to 900°C for 2 hr. The coercive force as a function of the temperature of anneal is plotted in Fig. 5 and compared with the standard Permalloy thin tape. For all treatments, the 7% gold alloy had a square hysteresis loop, and therefore it was not necessary to invoke magnetic annealing. In the cold-rolled state, the 7% gold alloy has a coercive force of 2.5 oe, which gradually drops to a minimum value of 1.1 oe after the 400°C heat treatment, probably due to the partial relief of working stresses. The coercivity then rises to a maximum value of 2.2 oe after the 575°C heat treatment and then falls again to a value of 0.5 oe after the 800°C heat treatment. As shown in Fig. 5, the alloy containing 71% Ni, 15% Fe, and 14% Au has a similar behavior but with a much larger peak at 575°C. The two curves for the 7 and 14% gold may be contrasted with the dotted curve of Fig. 5 for 0% gold. For this alloy there is no peak at 575°C, and the coercivity gradually diminishes with annealing from its value in the cold-worked state. The maximum at 575°C for the specimens containing gold is due to the

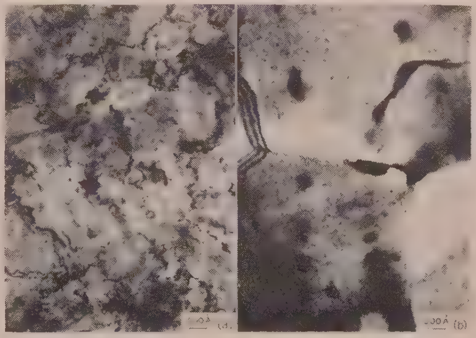

FIG. 9. Electron transmission micrographs by R. D. Heidenreich for the 7% Au tape (a) annealed at 500°C, 2 hr; (b) annealed at 650°C, 2 hr.

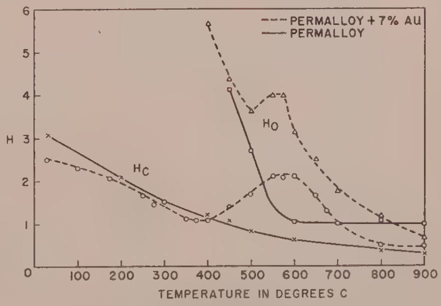

FIG. 10. Threshold field for nonuniform rotation H_0 and coercive force H_c vs temperature of anneal for Permalloy and 7% Au Permalloy tape.

precipitation of a gold-rich phase. The presence of the gold-rich phase has been verified by electron microscope and diffraction photographs obtained by R. D. Heidenreich. Figure 6 shows an electron transmission micrograph of the alloy containing 14% Au after annealing at 650°C for 2 hr. The dark areas are regions of the precipitated gold-rich phase; they have a width of approximately 1000 A which is large enough to hinder domain wall motion. The grain boundaries are also clearly evident, and this indicates that the annealing has relieved some of the strains due to cold working. Micrographs of specimens annealed at a lower temperature (500°C for 2 hr) did not reveal grain boundaries. The difference in the coercive force obtained for the tapes and the thicker toroidal samples may be attributed to the effect of work-induced strains on the precipitation process. In fact, if the strains in the tape are first removed by an anneal at 900°C, the peak at 575°C produced by subsequent heat treatment is reduced to approximately the value obtained for the bulk samples.

Wire Samples

Magnetic measurements were made on wires of 2, 4, 5, 6, 7, and 10% gold Permalloy. The wires had diameters of 0.010–0.0011 in. with varying degrees of cold work. Figure 7 shows a plot of the coercive force H_c vs the degree of cold reduction for the alloys containing 4% Au and 6.7% Au with 3.85% Mo. The coercive force first rises with percent cold reduction to a maximum, and then decreases as the reduction in area approaches 99%. All the wires tested vary in this manner and their values lie between the two curves shown. This behavior is probably due to inhomogeneties in the structure, caused by the cold-working process, which offer impedance to the domain wall motion. Finally, however, the working causes them to be uniformly distributed throughout the material and their effect on the coercivity diminishes. Upon annealing at 500°C for 2 hr the effect of the cold work largely disappears, as shown by the dotted line for the 4% gold alloy. For anneals below this temperature, however, cold work can still exert a large influence on the coercive force of these alloys.

SWITCHING MEASUREMENTS

Systematic high-speed flux reversal measurements have been completed on the $\frac{1}{8}$-mil tape of the 7% gold Permalloy. The reciprocal of the switching time as a function of the applied field is shown in Fig. 8 for some of the samples measured. It may be seen that in the high-drive, or rotational region, all the slopes are equal. The rotational threshold for the cold-rolled sample is too high to be measured. The reciprocal of the slope is defined as the switching coefficient S_w. Simple calculations indicate that reducing the eddy current damping by the addition of molybdenum would lead to a switching coefficient of 0.23 oe μsec. This value has been experimentally verified, and is in good agreement with the value of S_w generally observed for soft magnetic materials at intermediate applied fields.

In Fig. 8 it may be seen that while the 7% gold specimens annealed at 650° and 500°C have the same coercive force, the switching time of the 650°C specimen is about three times faster than that of the 500°C specimen. This greater speed arises from the lower threshold for rotation of the 650°C sample. The electron transmission micrographs shown in Fig. 9 contrast the structure of the 7% gold alloy annealed for 2 hr at (a) 500°C and (b) 650°C. In the 500°C specimen, the crystal boundaries are not evident; the effect of the strain due to cold working is still present. In the 650°C specimen, the grain boundaries are clearly visible as a result of the higher temperature of annealing, and the major effect of the cold working strain has been relieved. In addition, the precipitate has coalesced, which leaves the Permalloy matrix relatively strain free. The difference in the rotational thresholds is consistent with difference in strain between the 500° and 650°C treatments. The values obtained for the rotational thresholds are shown compared to the coercive force in Fig. 10. These data clearly show that with the gold alloy it is possible to have a relatively high H_c with H_0 substantially less than $2H_c$. With standard Permalloy, a high H_c can only be obtained in conjunction with a substantially larger H_0.

CONCLUSIONS

As a result of the present investigation, the value of having a second phase present in Permalloy for switching applications has been demonstrated. The central idea is that the large stresses induced by cold work reduce the switching speed, and therefore another mechanism is necessary to produce the required coercive force. It is desirable to have a strain-free matrix of Permalloy with particles of second phase to inhibit domain wall motion. In this work, a gold-rich phase was precipitated to produce the desired result, but other phases might also be effective. Switching cores of such material were found to be four times faster than standard Permalloy cores.

ACKNOWLEDGMENTS

The authors wish to thank J. K. Galt and F. B. Hagedorn for many valuable ideas and discussions during this investigation. We wish to thank R. C. Sherwood and A. J. Williams for excellent technical assistance. We are indebted to D. H. Wenny for supervision of alloy preparation and to C. V. Wahl for many wire-drawing experiments.

JOURNAL OF APPLIED PHYSICS VOLUME 32, NUMBER 7 JULY, 1961

Helium Diffusion through Glass

V. O. Altemose
Corning Glass Works, Corning, New York

(Received January 23, 1961)

Helium permeation rates have been determined through 20 different glasses using a mass spectrometer to measure the gas flow rates directly. The temperature range investigated was 25°–500°C. Values of diffusion constants and solubilities have been computed for 10 of these glasses. The permeation rate has been related to glass composition. It is felt that a better correlation exists between log permeation rate and mole percent of glass network former (SiO_2, B_2O_3, and P_2O_5) content than exists between log permeation and weight percent of network former as used by previous workers in this field.

INTRODUCTION

The use of glass for vacuum applications, and particularly the recent advent of ultra-high vacuum systems, has produced many inquiries about the helium permeation of the glasses used in these systems.

Numerous references are given in Barrer[1] to earlier diffusion measurements. Several more recent investigators have reported on permeation through Code 7740 glass[2–4] and Vycor Brand glasses.[2,5] Correlations have been made between permeation rates and glass composition,[2,6] particularly with weight percent of glass formers.[2]

It is the purpose of this paper to present helium permeation data for many of the glasses used for vacuum applications. It is also felt that a better correlation exists between permeation rate and mole percent of glass network former rather than weight percent.

PRINCIPLE OF THE EXPERIMENT

Formulation for the diffusion process is given by Fick's Law[1]:

$$\partial C/\partial t = D\nabla^2 C, \qquad (1)$$

where C, the concentration of gas within the solid, varies with time and distance through an element of unit cross section. D is the diffusion constant.

For the permeation of gas through the solid in the steady state, the concentration gradient may be expressed as the pressure gradient, and Eq. (1) becomes

$$K\nabla^2 p = 0, \qquad (2)$$

where K, the permeation constant, is equal to the product of the solubility S and diffusion constant D.

For a plane membrane, with pressure gradient p, cross-sectional area A, and thickness d, the quantity of gas q, per unit time t, to pass through it is given by

$$q = KA\Delta pt/d. \qquad (3)$$

In the case of spherical samples, the solution of Eq. (2) becomes

$$q = 4\pi a^2 Kt\Delta p[b/a(b-a)], \qquad (4)$$

where b and a are outside and inside radii, respectively. As with all the samples used in this experiment, if the thickness d (where $d=b-a$) is small compared to the radius of the sphere, Eq. (4) reduces to Eq. (3).

The time-dependent solutions to Eq. (1) are discussed by Rogers *et al.*[3] The equation applying to very small values of t in the diffusion process is[3]:

$$\frac{dp}{dt} = \frac{2AS}{V}\Delta p\left(\frac{D}{\pi t}\right)^{\frac{1}{2}} \sum_{m=0}^{\infty} \exp[-(d^2/4Dt)(2m+1)^2]. \qquad (5)$$

In this experiment, using the mass spectrometer as the measuring device, we measure the flow rate dq/dt directly instead of the pressure rise dp/dt in a volume V. Since

$$dq/dt = V(dp/dt),$$

Eq. (5) becomes

$$\frac{dq}{dt} = V\frac{dp}{dt} = 2AS\Delta p\left(\frac{D}{\pi t}\right)^{\frac{1}{2}} \sum_{m=0}^{\infty} \exp\left[-\left(\frac{d^2}{4Dt}\right)(2m+1)^2\right]. \qquad (6)$$

For short times, Eq. (6) converges rapidly, and may be written

$$\ln\left(t^{\frac{1}{2}}\frac{dq}{dt}\right) = \ln\left[2AS\Delta p\left(\frac{D}{\pi}\right)^{\frac{1}{2}}\right] - \frac{d^2}{4Dt}. \qquad (7)$$

By plotting the left side of Eq. (7) vs reciprocal time, values of the diffusion constant D can be obtained from the line slope.

EXPERIMENTAL ARRANGEMENT

The mass spectrometer used here as the detecting instrument is of the same type as the one described by Norton.[2] His description of the instrument operation is adequate and need not be repeated. Spectrometer flow sensitivity throughout all the experiments has been better than 1 $\mu\mu$l/sec or 10^{-6} cc-mm Hg/sec for helium gas.

---

[1] R. M. Barrer, *Diffusion in and through Solids* (Cambridge University Press, New York, 1941).

[2] F. J. Norton, J. Am. Ceram. Soc. **36**, 90 (1953).

[3] W. A. Rogers, R. S. Buritz, and D. Alpert, J. Appl. Phys. **25**, 868 (1954).

[4] N. W. Taylor and W. Rast, J. Chem. Phys. **6**, 612 (1938).

[5] C. C. Leiby and C. L. Chen, J. Appl. Phys. **31**, 268 (1960).

[6] C. C. Van Voorhis, Phys. Rev. **A23**, 557 (1927).

TABLE I. Approximate glass compositions.

Glass code No.	Wt. % of $SiO_2+B_2O_3+P_2O_5$	Mole %			
		$SiO_2+B_2O_3+P_2O_5$	Sum of $Na_2O+Li_2+K_2O$	PbO	Other oxides
7900	99	99	...	...	1
7230	96	96	...	...	4
Fused silica	...	100	...	...	...
7240	99	98	2	...	...
7070	99	98	2	...	...
7160	98	98	1	...	1
7740	94	94	5	...	1
7720	88	93	4	2	1
7052	83	86	6	...	5
7040	91	92	7	...	2
7050	91	92	7	...	1
7056	86	90	8	...	1
0010	61	77	14	8	1
9010	68	75	14	...	8
8160	56	74	12	8	5
0120	56	76	12	11	1
0080	74	73	16	...	11
1715	66	72	...	...	28
1720	64	66	1	...	33
1723	62	65	...	...	35

Figure 1 is a schematic of the vacuum system employed in the experiment. The portion of the system to the right of the sample consists of the gas lecture bottle (Matheson Company) from which gas is admitted, a mercury manometer to measure the gas pressure outside the sample, and a cold trap (*CT*) on which is kept dry ice slush to eliminate manometer errors due to small amounts of water vapor which may be driven off the sample jacket at high temperatures. The stopcock S_2 allows one to evacuate this part of the system.

AV_1 and AV_2 are Alpert-type high-vacuum valves (Consolidated Electrodynamics Corporation) capable of holding the high vacuum of the mass spectrometer against an atmosphere of pressure. AV_2 permits evacuation of the sample before opening AV_1 to the mass spectrometer. The ion gauge aids in determining any leaks in the system as well as in depicting a satisfactory vacuum.

The gas flow through the sample to be measured is run directly to the source of the mass spectrometer. The conventional gas sampling system of the spectrometer is utilized to calibrate the instrument in terms of ion current per unit flow rate for the gas to be used. At any time during the experiment this calibration can be made simply by putting a known pressure of the gas behind the capillary leak *C* via S_1 with AV_1 closed. *C* is a capillary of 0.0336 cm diam and has a conductance of 2.0×10^{-4} l/sec for helium.

It was possible to bake out the entire system from the sample to AV_1, including AV_2 and the ion gauge.

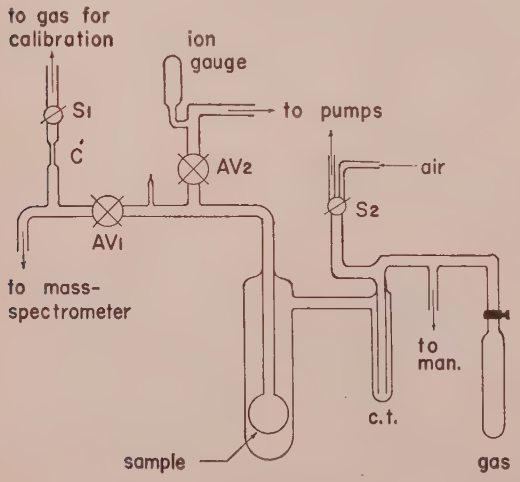

FIG. 1. Schematic diagram of vacuum system used.

EXPERIMENTAL PROCEDURE

After being formed, each sample bulb was sealed to a piece of thick Code 7740 glass tubing which in turn was sealed into the jacket as shown in Fig. 1. The neck of the sample bulb was kept very thick (1.5–2.0 mm) compared to the bulb thickness itself (about 0.1 mm) to eliminate the necessity of accounting for diffusion through the part of the neck which was in the furnace.

After placing the furnace around the sample jacket, the temperature was raised to the desired point and controlled with a Leeds and Northrup Micromax temperature controller. While the helium peak was monitored with the mass spectrometer, the gas was admitted to the sample. With the spectrometer acting as a continuous flowmeter, the transient curve and the steady state flow rates are readily and directly determined. Flow calibrations were taken immediately before and after each reading to be sure of no sensitivity shift.

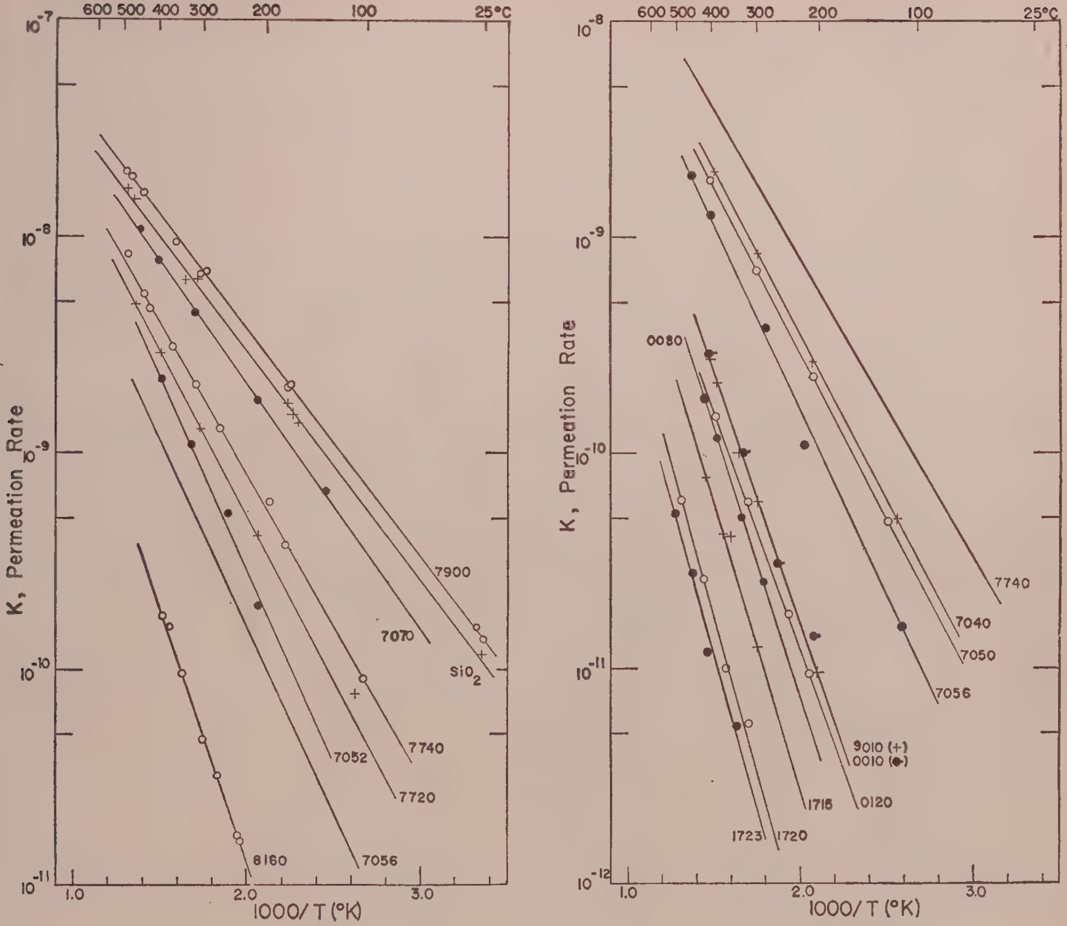

(a) (b)

FIG. 2. Permeation rate K of helium through various glasses. Log$K$ is plotted vs reciprocal of absolute temperature, $1000/T$°K. Units of K are cc(STP)/sec/cm^2 area/mm thickness/cm Hg pressure difference.

Steady state conditions were monitored for several hours in each case to ensure no change in flow rate.

Furnace temperatures were checked with a Chromel-Alumel thermocouple. The temperatures were steady to ±5°C. As the temperature swung through minimum and maximum values, the spectrometer was sensitive enough to record minimum and maximum flow rates. The average values of both temperature and flow rates were used to minimize errors in computing permeation constants.

To measure the area and thickness of the samples, they were filled with mercury, immersed in mercury, and the capacitance was measured. Knowing the dielectric constant of each glass, the ratio of A/d could be computed. It is estimated that the maximum uncertainly in this measurement is ±10%.

TYPES OF GLASS USED

Table I lists the types of glass used in the experiment in a general order of decreasing permeation rates along with their approximate composition in mole percent. The weight percent of network formers is also listed for comparison. The fused silica was General Electric and Amersil clear fused silica. All other glasses are made by Corning Glass Works.

EXPERIMENTAL RESULTS

The units chosen to express the permeation constant K in this report are those used by Norton,[2] Barrer,[1] and Leiby and Chen.[5] Units of K are cubic centimeters of gas at STP/sec/cm^2 area/mm thickness/cm Hg pressure difference.

TABLE II. Permeation rates for helium gas.

T(°C)	K^{a}
Code 7900 glass	
25	1.4×10^{-10}
358	9.5×10^{-9}
449	1.6×10^{-8}
28	1.6×10^{-10}
175	2.0×10^{-9}
307	6.8×10^{-9}
481	1.9×10^{-8}
171	2.1×10^{-9}
293	7.1×10^{-9}
−78	2.4×10^{-12}
Code 7230 glass	
96	6.2×10^{-10}
145	1.4×10^{-9}
261	5.0×10^{-9}
338	8.9×10^{-9}
419	1.4×10^{-8}
Fused silica (Amersil)	
25	1.2×10^{-10}
169	1.5×10^{-9}
313	6.4×10^{-9}
470	1.5×10^{-8}
25	1.2×10^{-10}
175	1.7×10^{-9}
Fused silica (GE)	
25	1.0×10^{-10}
161	1.3×10^{-9}
333	6.4×10^{-9}
485	1.7×10^{-8}
Code 7240 glass	
186	2.2×10^{-9}
309	6.9×10^{-9}
378	1.2×10^{-8}
432	1.8×10^{-8}
Code 7070 glass	
135	6.8×10^{-10}
215	1.8×10^{-9}
317	4.5×10^{-9}
396	7.8×10^{-9}
450	1.1×10^{-8}
Code 7160 glass	
28	5.7×10^{-11}
215	1.8×10^{-9}
311	4.4×10^{-9}
397	8.1×10^{-9}
445	1.1×10^{-8}
Code 7740 glass	
101	9.1×10^{-11}
180	3.8×10^{-10}
273	1.3×10^{-9}
369	3.1×10^{-9}
441	5.5×10^{-9}
197	6.0×10^{-10}
311	2.1×10^{-9}
427	4.7×10^{-9}
492	8.4×10^{-9}
Code 7720 glass	
109	7.7×10^{-11}
213	4.3×10^{-10}
305	1.3×10^{-9}
392	2.9×10^{-9}
464	4.9×10^{-9}
Code 7052 glass	
131	4.7×10^{-11}
212	2.0×10^{-10}
257	5.4×10^{-10}
321	1.1×10^{-9}
388	2.2×10^{-9}
Code 7040 glass	
122	4.9×10^{-11}
215	2.7×10^{-10}
302	8.3×10^{-10}
394	2.0×10^{-9}
Code 7050 glass	
125	4.9×10^{-11}
210	2.3×10^{-10}
301	7.0×10^{-10}
399	1.9×10^{-9}
Code 7056 glass	
115	1.6×10^{-11}
216	1.1×10^{-10}
284	3.9×10^{-10}
403	1.3×10^{-9}
453	2.0×10^{-9}
Code 0010 glass	
218	1.4×10^{-11}
264	3.1×10^{-11}
335	1.0×10^{-10}
408	2.9×10^{-10}
Code 9010 glass	
207	9.7×10^{-12}
302	6.0×10^{-11}
339	1.0×10^{-10}
391	2.1×10^{-10}
404	2.8×10^{-10}
Code 8160 glass	
236	1.6×10^{-11}
273	3.2×10^{-11}
342	9.5×10^{-11}
387	1.8×10^{-10}
200	5.6×10^{-12}
239	1.7×10^{-11}
299	4.8×10^{-11}
369	1.6×10^{-10}
Code 0120 glass	
214	9.4×10^{-12}
246	1.8×10^{-11}
319	6.0×10^{-11}
382	1.5×10^{-10}
Code 0080 glass	
291	2.5×10^{-11}
334	5.1×10^{-11}
393	1.2×10^{-10}
421	1.8×10^{-10}
Code 1715 glass	
298	1.25×10^{-11}
371	4.2×10^{-11}
412	7.7×10^{-11}
489	2.0×10^{-10}
491	2.0×10^{-10}
349	4.1×10^{-11}
Code 1720 glass	
315	5.6×10^{-12}
363	1.0×10^{-11}
420	2.6×10^{-11}
490	6.0×10^{-11}
Code 1723 glass	
339	5.4×10^{-12}
414	1.2×10^{-11}
451	2.8×10^{-11}
517	5.3×10^{-11}

[a] Units of permeation rate: cc(STP)/sec/cm² area/mm thickness/cm Hg pressure difference.

TABLE III. Diffusion constants and solubilities.

Glass code No.	T(°C)	D(cm²/sec)	S(cc/cc-atm)
7740	199	5.4×10^{-7}	0.0084
7740	310	3.8×10^{-6}	0.0038
7740	492	1.4×10^{-5}	0.0046
7720	109	6.8×10^{-8}	0.0086
7720	392	2.2×10^{-6}	0.010
7052	388	6.2×10^{-7}	0.027
7040	393	2.7×10^{-6}	0.005
7050	400	2.7×10^{-6}	0.005
7056	115	3.1×10^{-8}	0.0039
7056	402	1.7×10^{-6}	0.0059
9010	393	7.2×10^{-7}	0.0022
8160	369	5.6×10^{-7}	0.0022
8160	342	4.2×10^{-7}	0.0017
0080	394	7.6×10^{-7}	0.0012
1723	414	5.7×10^{-8}	0.0016

The values of permeation constants K obtained for helium through the various glasses are shown in Table II. The curves of log$K$ vs reciprocal temperature for these same glasses are shown in Fig. 2(a) and (b); Codes 7740 and 7056 glass are shown in both (a) and (b) for comparison. Codes 7230 and 7240 glass almost coincide with the Code 7900 glass curve. The curve of Code 7160 glass coincides with the curve of Code 7070 glass.

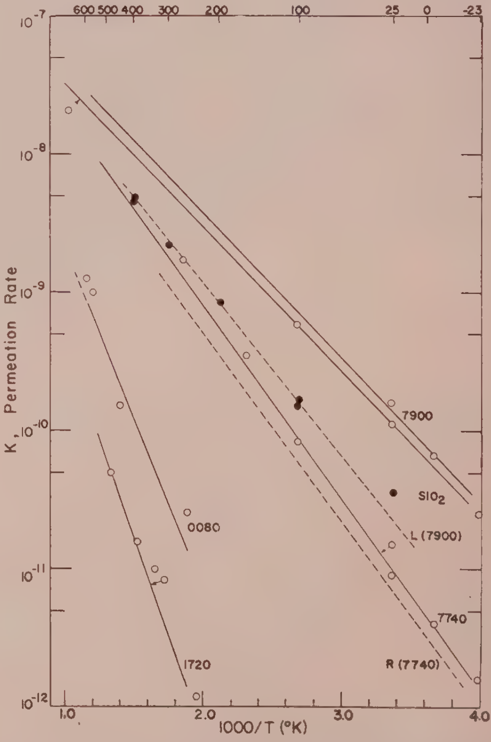

FIG. 3. Comparison of helium permeation rates as a function of $1/T$(°K) with results of other recent investigations. Solid lines denote the present work, circles the results of Norton[2] for the five glasses shown. Line L shows results of Leiby and Chen[5] for Vycor Brand glass. Line R(7740) denotes results of Rogers *et al.*[3] for Code 7740 glass.

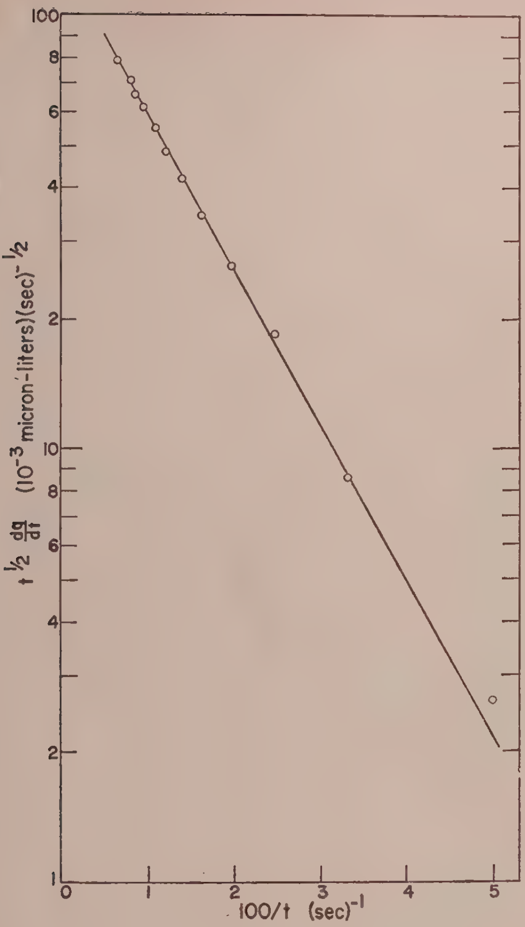

FIG. 4. Plot of "early time" transient data for helium through Code 0080 glass at 394°C.

Figure 3 shows the excellent agreement between these results and those of Norton.[2] Both experiments have five glasses in common. It should be pointed out that Norton also used a mass spectrometer in his work.

Diffusion coefficients were computed from the initial transient flow rates for 10 of the commercial glasses. Table III lists the glasses, temperature, diffusion constants, and solubilities. The flow rates dq/dt were replotted as shown in Fig. 4 for Code 0080 glass at 394°C. From the slope of these curves the diffusion constants were computed by Eq. (7). The solubilities were then computed from $S=K/D$. The average solubility for Code 7740 glass was 0.0056 cc/cc/atmosphere pressure as compared to the average value of 0.0065 quoted by Rogers *et al.*[3]

ACTIVATION ENERGIES

The permeation velocity is related to the temperature by the relation

$$K=Ae^{-Q/RT}, \qquad (8)$$

where A is a constant, Q is the activation energy (cal/mole), R the gas constant (1.986 cal/mole°C), and T the absolute temperature. Thus, from the plot of ln K vs reciprocal temperature, the temperature coefficient or activation energy can be computed.

Table IV lists the activation energies for the glasses investigated, with some comparisons with values by recent authors. The glasses are listed in order of decreasing permeation rates. In general, with one exception, the activation energy increases with decreasing values of K.

RELATION TO GLASS COMPOSITION

An attempt was made by Norton[2] to correlate permeation rate and activation energy with percentage of glass formers present in the glass. The most important glass-forming oxides[7] are SiO_2, B_2O_3, and P_2O_5. Figure 5 is a plot of permeation vs weight percent of these three

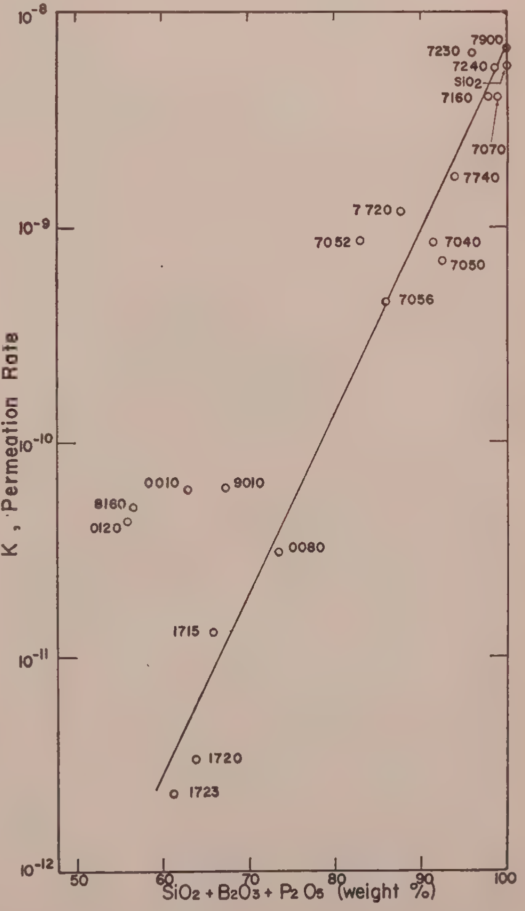

FIG. 5. Log plot of permeation rate K vs weight percent of network formers ($SiO_2+B_2O_3+P_2O_5$) for helium at 300°C.

---

[7] J. E. Stanworth, *Physical Properties of Glass* (Oxford University Press, New York, 1950).

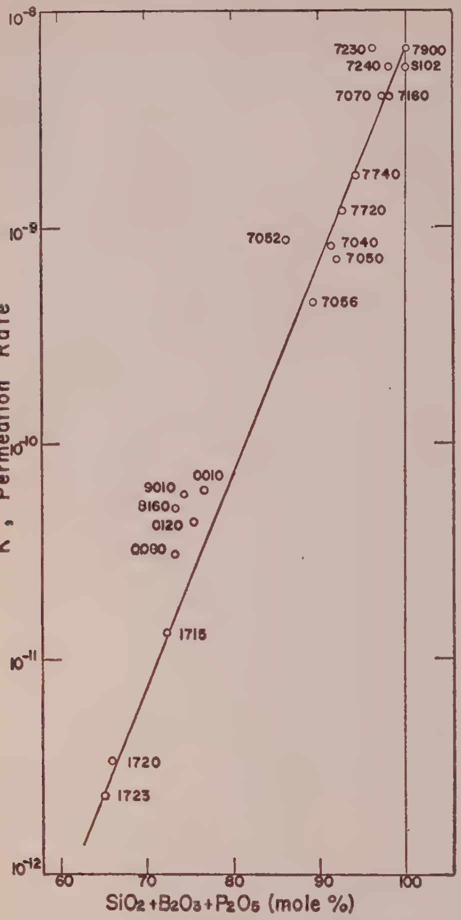

FIG. 6. Log plot of permeation rate K vs mole percent of network formers ($SiO_2+B_2O_3+P_2O_5$) for helium at 300°C.

TABLE IV. Activation energies for helium gas.

Glass code No.	Q(cal/mole)	Observer
7900 (Vycor Brand)	4800	Present experiment
7900	4900	Norton[2]
7900	5900	Leiby and Chen[5]
7230	4900	Present experiment
Fused silica	4800	Present experiment
Fused silica	4900	Norton
7240	5300	Present experiment
7070	5090	Present experiment
7160	5300	Present experiment
7740	6400	Present experiment
7740	6400	Norton
7740	6400	Rogers *et al.*[3]
7720	6770	Present experiment
7052	7860	Present experiment
7040	7100	Present experiment
7050	7100	Present experiment
7056	7930	Present experiment
0010	10 600	Present experiment
9010	10 600	Present experiment
8160	10 500	Present experiment
0120	9900	Present experiment
0080	11 060	Present experiment
0080	11 000	Norton
1715	12 400	Present experiment
1720	12 000	Norton
1720	12 000	Present experiment
1723	12 000	Present experiment

oxides at 300°C. There is a considerable spread among the points shown with the glasses of higher density farthest from the curve.

We shall assume an irregular glass lattice as shown by Zachariasen[8] and quoted by Norton.[2] The glass-forming oxides, or network formers, complete a chain-like network with openings large enough for small gas molecules to permeate. Addition of alkali oxides and alkaline earth oxides is pictured as plugging or blocking these openings. With this picture in mind, one would feel that the important factor in determining permeation rates would be the effective size or number of modifier particles rather than their weight. As an example, the effective size of a heavy Pb^{2+} ion is not much different from the effective size of the lighter Na^+ or K^+ ions[9] and should have about the same effect on permeation rate. This would suggest a plot of log permeation vs mole percent of the network formers rather than weight percent.

Figure 6 is such a plot involving mole percent of the three primary network formers, SiO_2, B_2O_3, and P_2O_5.

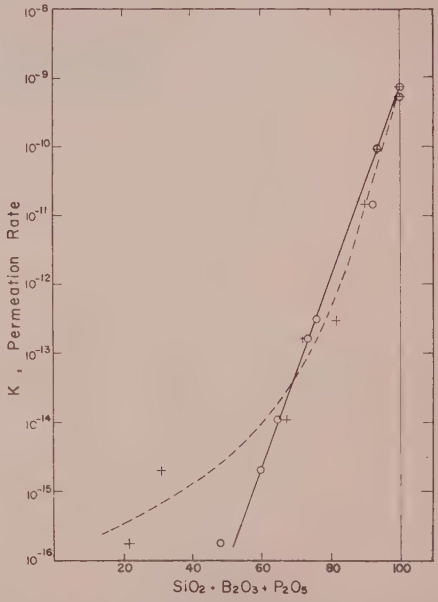

FIG. 7. Permeation rate K vs percentage of network formers ($SiO_2+B_2O_3+P_2O_5$). Dashed line (+) is a curve from Norton[2] comparing log$K$ (at 100°C) with weight percent of network formers. Solid line (○) denotes the same data of Norton replotted vs mole percent of network formers.

---

[8] W. H. Zachariasen, J. Am. Chem. Soc. 54, 3841 (1932).

[9] *Handbook of Chemistry and Physics*, edited by C. D. Hodgman, R. C. Weast, and S. M. Selby (Chemical Rubber Publishing Company, Cleveland, Ohio, 1949), 31st ed.

There now seems to be a better correlation between log permeation rate and network former content. The heavy, lead-containing glasses are now brought much nearer to the curve than in Fig. 5, suggesting that alkali ions inhibit gas permeation as much as the heavier lead ions. Thus, density plays a role in permeation only as it pertains to closeness of packing of the network and not as weight density.

To further illustrate the point discussed above, let us take Norton's data,[2] which cover many orders of magnitude, and replot them. Figure 7 is a reproduction of his curve (dashed line) of log permeation at 100°C vs weight percent of network formers. Along with this, in Fig. 7, the same data is then replotted (circles-solid line) as a function of mole percent of the network formers.

One of the striking differences in the two curves of Fig. 7 is that the curve considering weight percent suggests a lower limit of about 10^{-16} cc helium (STP)/sec/cm^2 area/mm thickness/cm Hg pressure difference at 100°C for 0% of network former, while the curve considering mole percent suggests a lower limit of about 10^{-23}. In the same manner, the limit for 0 mole % of glass former at 300°C would be about 10^{-18} (from Fig. 6).

In the temperature range considered, the activation energy appeared to remain constant for each glass over the entire range. Figure 8 shows these energies plotted as a function of mole percent formers for the various glasses. As in the case of the permeation rate curves already discussed, the same scattering of points is observed when weight percent is plotted.

From Fig. 6, the plot of K vs M, where M is mole percent of network former, one arrives at the equation

$$K=1.8\times10^{-18}e^{0.22M} \qquad (T=300°\text{C}). \qquad \text{(9a)}$$

Similarly, from plots at other temperatures (not shown),

$$K=1.1\times10^{-16}e^{0.20M} \qquad (T=400°\text{C}), \qquad \text{(9b)}$$

$$K=5.8\times10^{-25}e^{0.35M} \qquad (T=100°\text{C}). \qquad \text{(9c)}$$

TABLE V. Permeation constants (K) for other gases.[a]

Glass	Gas	T(°C)	$K(\times10^{10})$	Observer
Vycor Brand	Hydrogen	400	1.32–1.39	Leiby and Chen[5]
		450	2.98–3.39	Leiby and Chen[5]
		200	0.61	Present report
		400	7.8	Present report
		600	33.0	Present report
	Neon	490	2.6	Present report
		400	0.50	Leiby and Chen[5]
		450	0.90	Leiby and Chen[5]
	Argon	490	under 0.00003	Present report
	Methane	490	under 0.00004	Present report
	Nitrogen	490	under 0.00004	Present report
		400	0.0063	Leiby and Chen[5]
Fused silica	Hydrogen	600	12.5	Norton[2]
		700	21.0	Norton[2]
		200	0.38	Present report
		400	5.3	Present report
		600	23.0	Present report
	Neon	600	2.8	Norton[2]
		700	4.2	Norton[2]
	Argon	700	under 0.00001	Norton[2]
	Nitrogen	700	under 0.00001	Norton[2]

[a] Units of K are as in Table II.

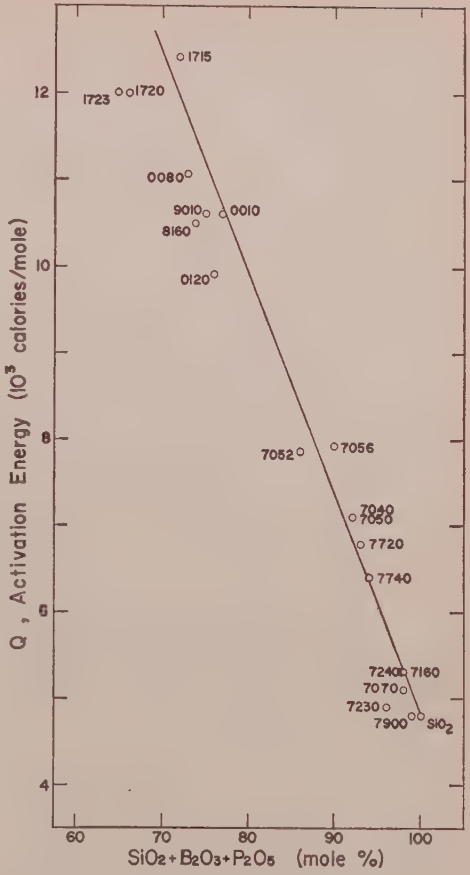

FIG. 8. Activation energy Q as a function of mole percent of the network formers.

From Figs. 2(a) and (b), for all the glasses considered, the average value of the constant A in Eq. 8 is 4.8×10^{-7}. Thus,

$$K=4.8\times10^{-7}e^{-Q/RT} \qquad (\text{for all } T). \qquad (10)$$

By combining Eqs. (9) and (10), in each case one obtains to two significant figures

$$Q=260M+30\times10^{3}\ \text{cal/mole}. \qquad (11)$$

Equation (11) is the expression that is plotted in Fig. 8, and it fits the plotted points quite well.

PERMEATION OF OTHER GASES

A few measurements were taken for hydrogen and neon through Code 7900 glass (Vycor Brand) and fused silica. Attempts were made to measure the flow of methane, argon, and nitrogen through Code 7900 glass, but no flow of these gases was observed. Table V summarizes the measurements made in the present experiment and those of other recent observers.

Since no flow of methane, argon, or nitrogen was observed, the maximum values given are based on the sensitivity of the mass spectrometer employed.

It is felt that the simplicity, accuracy, and selectivity of the mass spectrometer for permeation measurements again deserves mention. In practically all high vacuum work, especially where temperature variations are used, there will generally be a certain amount of system outgassing. The presence of these extra gases are not easy to account for when using an ion gauge or other pressure gauge to determine permeation rates by measuring pressure rises in a known volume. The mass spectrometer, however, is used independent of, and in the presence of, these other gases. Thus, where no detectable background is observed for the particular gas of interest after the sample is up to the desired temperature, the need for a lengthy bakeout is eliminated.

ACKNOWLEDGMENT

The writer wishes to thank Dr. B. J. Todd of this laboratory for helpful advice and discussion.

JOURNAL OF APPLIED PHYSICS VOLUME 32, NUMBER 7 JULY, 1961

Temperature-Dependent Bismuth-Cesium Photosurfaces

R. J. Zollweg and C. R. Taylor
Westinghouse Research Laboratories, Pittsburgh 35, Pennsylvania

(Received February 14, 1961)

The yield of bismuth-cesium photosurfaces is sometimes strongly temperature dependent. We have investigated this effect and found it to be dependent upon the presence of oxygen and upon the size of the aggregates making up the photosurface. The photoelectron energy spectra are also examined. It is concluded that the temperature dependence probably arises from a change in escape depth with temperature because of phonon collisions, but that the principal photoelectron energy loss may occur at oxygen impurity sites.

INTRODUCTION

Harper and Choyke[1] found that semitransparent Bi-Cs photosurfaces prepared on a tin oxide on a glass substrate exhibited a marked increase in photoemissive yield when cooled below −90°C. The yield was usually rather insensitive to temperature between room temperature and −60°C to −90°C, at which point it began to increase roughly linearly with a decrease in temperature and then flattened out near liquid nitrogen temperature. On some surfaces the yield at liquid nitrogen temperature was found to be a factor of 15 higher than that at room temperature. The effect was present over a wide wavelength range as shown by Fig. 1 (obtained by Harper and Choyke). This contrasts with the 10–30% increase in photoemission in the ultraviolet sometimes observed for Sb-Cs photosurfaces. It should be noted, however, that even at low temperatures the quantum yield is not so high as that of Sb-Cs.

This remarkable property of Bi-Cs photosurfaces proved to be reversible and stable in properly prepared tubes, but difficult to reproduce. Still it held considerable promise as the key temperature-dependent element for a thermal-radiation image converter[2] under development at these laboratories. We have investigated the various parameters of the processing necessary for enhancing the effect and have performed additional experiments to help elucidate the source of the temperature dependence.

PROCESSING AND SURFACE STRUCTURE

The Bi-Cs photosurfaces were prepared by evaporation of the bismuth film on Pyrex and other substrates to a white-light transmission of about 30%, followed by heating in cesium vapor but with subtle changes of some of the processing parameters. Oxygen was admitted at the appropriate time, sometimes before and sometimes after reacting with cesium. After processing, the tubes were usually sealed off using a previously torched glass constriction. Our results confirmed the suspicion of Harper and Choyke that oxygen was a necessary (though not sufficient) ingredient to produce the desired effect. Best results were obtained by allowing the oxygen to react with the bismuth film before introduction of cesium (preoxidation). The reaction could be detected by about a 10% increase in transmission of the bismuth films. When oxygen was admitted after reaction with cesium (postoxidation), the amount was carefully controlled while monitoring the changes in photo-emissive response. Associated with the introduction of oxygen was an increased response to the red end of the spectrum relative to the unfiltered light from a tungsten ribbon source. The precise red threshold varied greatly with the amount of oxygen and processing history.

Measurements of the optical transmittance vs wavelength were made at room temperature and at liquid nitrogen temperature of Bi-Cs photosurfaces showing the large temperature-dependent effect. No differences were observed aside from the somewhat increased sharpness of the rather indistinct structure in the optical absorption.

---

[1] W. J. Harper and W. J. Choyke, Rev. Sci. Instr. **27**, 966 (1956).

[2] M. Garbuny, T. P. Vogl, and J. R. Hansen, J. Opt. Soc. Am. **51**, 261 (1961).

The magnitude of the temperature-dependent effect was found to vary with the rate of evaporation of the bismuth and the temperature of the Pyrex substrate during the evaporation. Best results were obtained with the substrate heated to 55°C and evaporation times of the order of $\frac{1}{2}$ hr as opposed to 1–2 min. This suggested that the structure of the bismuth was involved, and that its influence was preserved in the subsequent swelling of the film which occurred during the reaction with cesium. To verify that the bismuth films would be sensitive to these conditions, we prepared several films in a bell-jar vacuum system at pressures of 10^{-6} mm Hg with room temperature and heated substrates, and long and short evaporations. These films were immediately replicated in vacuum with SiO_2 and the replicas examined by electron microscopy. The results, shown in Fig. 2, reveal that there is a change in size of the aggregations associated with the time and temperature of evaporation.

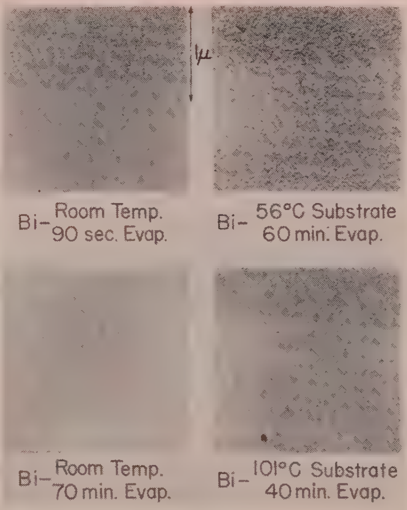
1μ
Bi– Room Temp. 90 sec. Evap.
Bi– 56°C Substrate 60 min. Evap.
Bi– Room Temp. 70 min. Evap.
Bi– 101°C Substrate 40 min. Evap.

FIG. 2. Electron microscope pictures of SiO_2 replicas of bismuth films. Substrate temperature and evaporation times are indicated.

After measuring the photoemissive response at room temperature and liquid nitrogen temperature, several of the Bi-Cs photosurfaces were replicated with SiO_2 directly in the evacuated tube.[3] To utilize tubes made previously without provision for evaporating SiO_2 inside the tube, we developed a technique for breaking the tubes inside a bell-jar vacuum system and evaporating the SiO_2 immediately at pressures of 10^{-6} mm Hg. These replicas were examined by electron microscopy, and some of the results are shown in Fig. 3 arranged in order of the ratio of the yield at liquid nitrogen temperature to that at room temperature. While the textures of the photosurfaces vary considerably, a correlation is observed between the aggregate size and the magnitude of the temperature dependence. For the surfaces exhibiting the stronger temperature dependence, the aggregates appear to have sharper corners, as in a greater tendency toward crystallinity. The diameters of several aggregates from each picture were measured to determine an "average" diameter, which is plotted in Fig. 4 vs the magnitude of the temperature dependence. The various symbols indicate the processing method used.

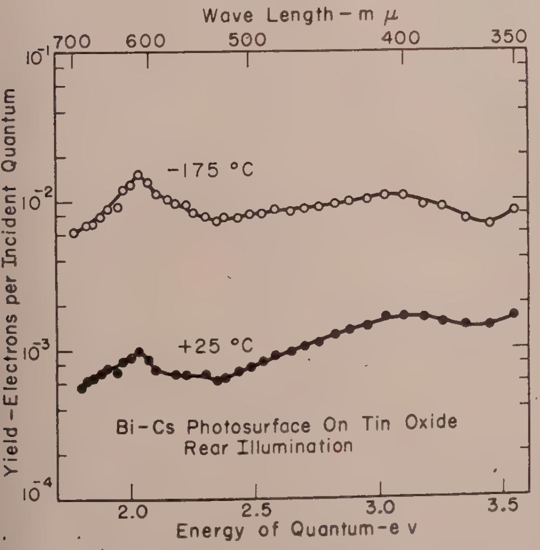

FIG. 1. Photoelectron yield at 25°C and -175°C vs photon energy for Bi-Cs photosurface on tin oxide.

INTERPRETATION

An increase in photoemissive yield when a photosurface is cooled might be accounted for in a variety of ways:

(a) as an increase in escape depth for photoelectrons arising because of an increase in photoelectron mfp between inelastic collisions,
(b) as an increased efficiency of excitation of photoelectrons associated with an increased occupancy of certain electronic energy states at lower temperature,
(c) as an increased escape of photoelectrons through the surface barrier associated with a change in the surface configuration,
(d) as one of other more complicated processes such as energy transfer by excitons and creation of defect energy states by the incident radiation.

The observed dependence of the magnitude of the temperature-dependent effect with Bi-Cs on the structure suggests a volume effect and that the first of these possibilities is more nearly correct. The relative inde-

---

[3] A. I. Frimer and A. M. Gerasimova, Zhur. Tekh. Fiz. **26**, 726 (1956).

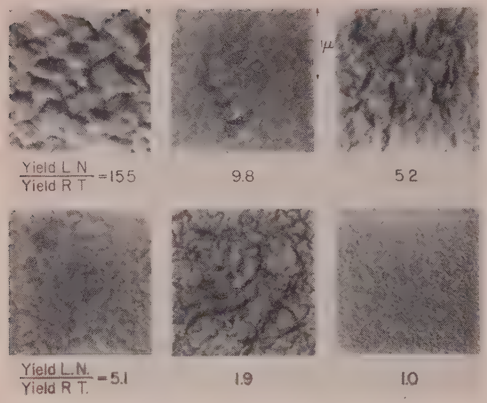

FIG. 3. Electron microscope pictures of SiO_2 replicas of Bi-Cs photosurfaces. The ratio of the yield at liquid nitrogen temperature to room temperature is indicated below each picture.

pendence of the effect upon wavelength and the lack of significant change with temperature in the optical absorption appear to rule out (b) and (d). The precise form of the photoelectron escape probability is unknown at the present time. Hebb[4] considered both an escape probability of the form $e^{-(x/\lambda)}$, where x is the distance from the surface and λ is the electron mfp, and an escape probability involving simultaneous diffusion and gradual energy loss of the photoelectrons, which he treated using the "age theory" of Fermi. The latter treatment results in a more rapid decrease in escape probability beyond a certain depth.

Morgulis *et al.*,[5] in studies of photoemission from Sb-Cs photosurfaces in which the thickness varied with position as in a wedge, found their experimental results more closely approximated by a model assuming gradual loss of photoelectron energy in small amounts, as in collisions between photoelectrons and phonons. This was approximated by using a precise cutoff depth for photoelectron escape. Regardless of which model is used, if one assumes hemispherical aggregates with uniform excitation of photoelectrons and assumes that the mfp at liquid nitrogen temperature is at least 10 times that at room temperature, then one will obtain substantially the same straight line as that shown in Fig. 4 upon attempting to fit the experimental data. Using the exponential escape probability, we obtain from Fig. 4 a photoelectron mfp at room temperature for Bi-Cs of 36 A, which might be compared with 100–250 A given for Cs_3Sb.[5,6]

Such a temperature dependence of the photoelectron mfp is reasonable if it is associated with phonon collisions. As the photosurface is cooled below the Debye temperature, photoelectron-phonon scattering decreases sharply as a result of the decreased phonon population. The photoelectron energy may be degraded in small steps as a result of the collisions with phonons, perhaps with an assist through scattering from the oxygen impurity sites. An alternative explanation would involve the oxygen impurity sites as recombination centers, with the phonon scattering increasing the average electron path required to reach the surface and hence increasing the chance of collision with such impurity sites. Although we do not know the Debye temperature for Cs-Bi photosurfaces, it is probably in this temperature range.[7] If phonons were not involved but the photoelectrons were lost at impurity atom sites, one would not expect the observed temperature dependence unless the impurity site were to change its charge with temperature and hence its effectiveness as a recombination center.

The assumption that the photoelectron energy is degraded by interaction with phonons would appear to be in conflict with the results of Apker *et al.*[8] for Cs_3Sb and Cs_3Bi, which emphasized the onset of photoelectron-valence electron collisions when the photon energy became equal to twice the band gap energy. With most photosurfaces of Cs_3Sb and Cs_3Bi, however, especially the more sensitive ones, the aggregate size is sufficiently small that photoelectron-phonon collisions would be relatively unimportant.

In order to look more closely for any surface structure change with temperature, several spherical retarding potential tubes were made with the photosurface prepared on the inner 1-in. diam sphere which could be cooled with liquid nitrogen. The differential photoelectron

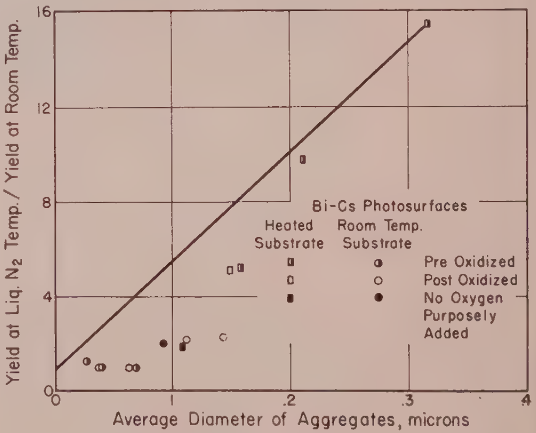

FIG. 4. Ratio of photoelectron yield at liquid N_2 temperature to yield at room temperature vs "average" diameter of aggregates in film determined from electron microscope pictures. Symbols indicate whether substrate was heated and when oxygen was introduced. The solid line is discussed in text.

---

[4] M. Hebb, Phys. Rev. **81**, 702 (1951).

[5] N. D. Morgulis, P. G. Brozyak, and B. I. Dyatlavitskaya, Izvest. Akad. Nauk S.S.S.R. **12**, 126 (1948); R. I. Dyatlavitskaya, Zhur. Tekh. Fiz. **22**, 84 (1952).

[6] J. A. Burton, Phys. Rev. **72**, 531A (1947).

[7] K. H. Jack and M. M. Wachtel, Proc. Roy. Soc. (London) **A239**, 46 (1957).

[8] L. Apker, E. Taft, and J. Dickey, J. Opt. Soc. Am. **43**, 78 (1953).

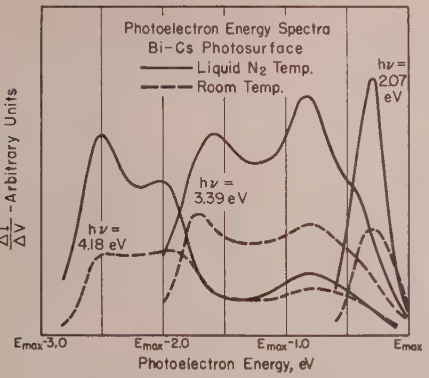

FIG. 5. Photoelectron energy spectra of Bi-Cs photosurface at oom and liquid nitrogen temperatures. $E_{\max}$ is the maximum hotoelectron energy in each case.

energy curves were obtained directly using a 0.05-v ac quare wave signal in series with the dc retarding potenial.[9] Although we were unsuccessful in preparing photourfaces having the very large temperature-dependence roperty in tubes of this geometry, some photosurfaces howed a photoemission at liquid nitrogen temperature hat was two to three times that at room temperature. Figure 5 shows the photoelectron energy spectra for uch a situation, with results for three different photon energies; the curves are displaced by the difference in hoton energy so that the maximum electron energy is epresented by $E_{\max}$ in each case.

If a change in surface structure had been important, ve would have expected much more profound differnces with temperature, such as a shift in the threshold or photoelectrons or a more complete change in the nergy spectra. The purpose of displacing the energy pectra curves in proportion to photon energy is so that hotoelectrons which originate from given energy states and escape without energy loss appear at the same positions in the figure. Thus one can detect groups of photoelectrons with energies of 0.4, 0.9, and 1.9 ev less than the maxima,[10] which appear to originate from energy levels located at these positions below the top of the valence band. At room temperature the peaks are appreciably broadened over their appearance at liquid nitrogen temperature, but it is difficult to obtain a quantitative measure of the broadening since the structure and background are poorly resolved.

If all of the photoelectron energy loss were associated with collisions with phonons, then the peaks at room temperature would probably be broadened even more. The photoelectron energy loss associated with each phonon collision is small, yet at room temperature only about half as many photoelectrons escape as at liquid nitrogen temperature. Thus a very large number of phonon collisions and a large average energy loss would be required if phonon collisions were principally responsible for the energy loss. It appears more likely that impurity sites associated with the oxygen act as recombination centers. Such a conclusion must be considered tentative at best since these photoelectron energy spectra were obtained from photosurfaces that did not have the very large temperature dependence, and the amount of structure observed was not always so distinct, depending upon the processing. The liquid nitrogen curve in Fig. 5 for $h\nu = 4.18$ ev shows a relatively large increase in the number of "slow" electrons, which probably arise from collisions with valence band electrons as observed by Apker *et al.*[8] These "slow" electrons are less prominent at room temperature.

ACKNOWLEDGMENT

We wish to thank G. H. Glade for taking the electron photomicrographs of our replicas.

---

[9] L. B. Leder and J. A. Simpson, Rev. Sci. Instr. **29**, 571 (1958).

[10] E. Taft has found similar groups of photoelectrons in Bi-Cs [L. Apker (private communication)].

JOURNAL OF APPLIED PHYSICS VOLUME 32, NUMBER 7 JULY, 1961

Nonohmic Behavior in Near-Stoichiometric Rutile (TiO_2)†

E. H. Greener* and D. H. Whitmore
Department of Materials Science, Northwestern University, Evanston, Illinois

(Received January 19, 1960)

Experimental observations of the isothermal current-voltage relationships in rutile (TiO_2) over the temperature range 632°–908°C have shown that currents in excess of ohmic currents can be drawn through small, single crystals of near-stoichiometric composition. These currents have been identified as space-charge-limited currents analogous to those observed in the case of a vacuum diode. An increase in the ambient specimen temperature had the effect of displacing the potential for transition from ohmic to nonohmic behavior to greater values so that, at 908°C, near-stoichiometric rutile exhibited only ohmic currents even at the largest fields employed.

INTRODUCTION

In his investigation of the electrical properties of rutile, Cronemeyer[1] found that the isothermal resistance of single-crystal rutile specimens heated in air to temperatures below 900°C ceased to be independent of applied field and decreased with increasing field strength at fields greater than approximately 8 v/cm. This effect was attributed to the "injection" of carriers into the conduction band. Since Cronemeyer was interested only in ohmic phenomena in rutile, no further explanation of this resistance dependency was given.

There are three mechanisms by which additional "carriers," that is, carriers in excess to those present in thermal equilibrium, may be either injected into the conduction band or made to play a role in the conduction process. These are field emission, field-enhanced ionic conductivity, and space-charge-limited currents.

It is the purpose of this study to attempt to determine the mechanism responsible for the nonohmic behavior observed in rutile and to evaluate the important parameters associated with this phenomenon.

EXPERIMENTAL DETAILS

Specimens approximately 0.50×0.020×0.10 in. were cut from a single-crystal boule of rutile obtained from the Linde Company. The specimens were ground through 420-grit carborundum paper to facilitate electrical contact. During measurement the specimen was held in a Lavite jig, and platinum electrodes were placed against the specimen by means of stainless steel screws bearing against Lavite pressure plates (see Fig. 1). Resistance measurements were made by conventional four-probe techniques, with the potential drop across the specimens being measured by means of a Keithley Model 610 electrometer and that across a standard resistance (either 10^3 or 10^4 ohms) with a Rubicon Type B potentiometer. To avoid any contribution to the measured potential from thermally generated emf's, readings were taken in both forward and reverse directions and averaged. The specimen jig was placed in a Vycor tube surrounded by an electrical resistance furnace, the temperatures of which were held to ±1°C by means of a saturable reactor temperature controller.

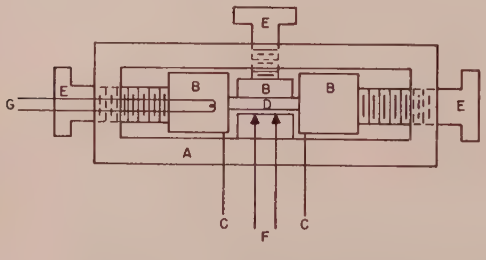

Fig. 1. Schematic diagram of specimen jig. A, body of Lavite jig; B, Lavite pressure plates; C, platinum electrodes; D, specimen; E, stainless steel screw; F, potential probes; G, thermocouple.

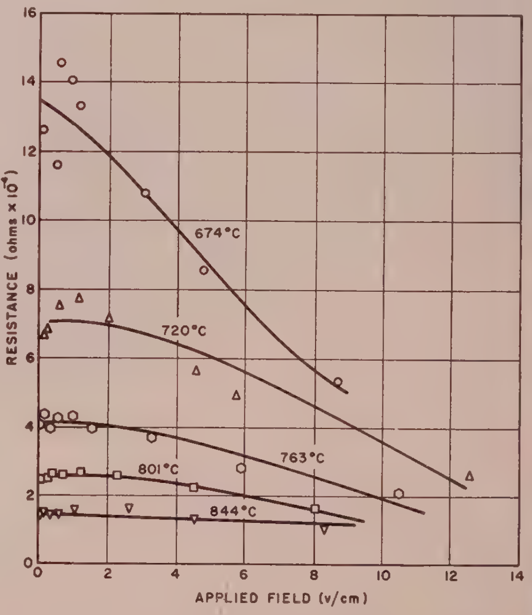

Fig. 2. Isothermal resistance of a rutile single crystal as a function of the applied field.

[†] This research was supported in part by the U. S. Office of Naval Research under contract with Northwestern University.

[*] Present address: Marquette University, Milwaukee, Wisconsin.

[1] D. C. Cronemeyer, Phys. Rev. 87, 1876 (1952).

EXPERIMENTAL RESULTS AND DISCUSSION

Figures 2 and 3 are plots of a typical family of curves which result when resistance, as measured in air, is plotted as a function of temperature and applied voltage. The curves can be broken down into two parts: a region of low applied field, $E\lesssim 2$ v/cm, where resistance is independent of the magnitude of the applied field (ohmic behavior); and a region where resistance is field dependent with a decrease in measured resistance accompanying an increase in applied field.

As shown in Fig. 4, the temperature dependence of the ohmic resistance obeys an exponential relation of the type

$$R=\text{const}\cdot\exp\epsilon/kT \quad (\epsilon=1.45\pm0.1\text{ ev}), \tag{1}$$

where ϵ is an activation energy, k is Boltzmann's constant, and T is the absolute temperature. Under similar conditions, Cronemeyer[1] observed an activation energy of 1.50 ev, in good agreement with the value of ϵ in Eq. (1).

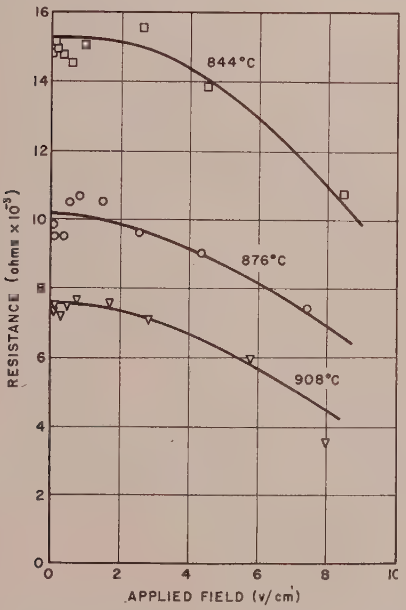

Fig. 3. Isothermal resistance of a rutile monocrystal as a function of the applied field.

In addition, it should be noted, from Figs. 2 and 3, that the degree of field dependency of the resistance (i.e., the extent of the nonohmic effect) becomes greater as the temperature is decreased.

It is probable that the fields employed here are too small to cause field emission. Furthermore, because no direct evidence for ionic motion in rutile has ever been reported[1,2] and because the nonohmic effects occur at such low fields and are inversely related to temperature, it is not likely that the extra source of charge carriers is due to a field-enhanced ionic conductivity. Moreover, the use of separate potential probes across the bulk of the specimen indicates that the extra carriers are not confined to the specimen/contact interface, but actually exist within the bulk of the material.

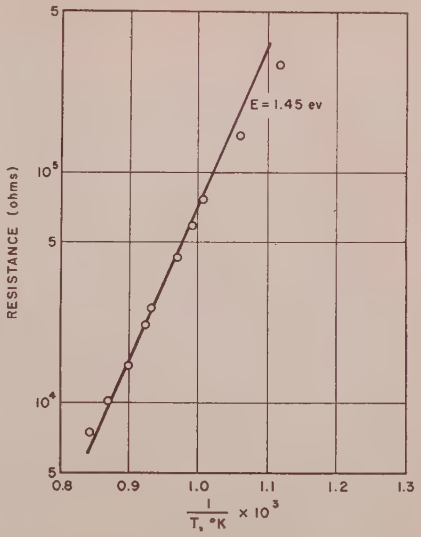

Fig. 4. Temperature dependence of the resistance of a near-stoichiometric rutile single crystal.

For these reasons, it is attractive to invoke the concept of space-charge-limited currents to explain the observed effects in rutile (TiO_2) at low fields. As first formulated by Mott and Gurney[3] and further elaborated by Rose[4] and Lampert[5] for the case of CdS, it is quite possible for space-charge-limited currents to exist in an insulator or an insulator containing shallow traps. The criterion for the existence of these currents is that the difference between the work function of contact ϕ (the energy necessary to remove an electron from the top of the Fermi surface to vacuum) and the electron affinity of the insulator χ (the work required to remove an electron from the lowest level in the conduction band and put it into vacuum) is of the order of the available thermal energy. This may be expressed as

$$(\phi-\chi)\approx kT, \tag{2}$$

where k is Boltzmann's constant and T is absolute temperature.

The quantity $(\phi-\chi)$ represents, therefore, the energy to remove an electron from the metal electrode and place it in the lowest-lying states of the insulator. Thus, if Eq. (2) holds, it would be quite possible to "boil" off electrons from the cathode into the insulator by thermionic emission.

---

[2] M. D. Earle, Phys. Rev. **61**, 56 (1942).

[3] N. F. Mott and R. W. Gurney, *Electronic Processes in Ionic Crystals* (Oxford University Press, New York, 1940), p. 172.

[4] A. Rose, Phys. Rev. **97**, 1538 (1955).

[5] M. A. Lampert, Phys. Rev. **103**, 1648 (1956).

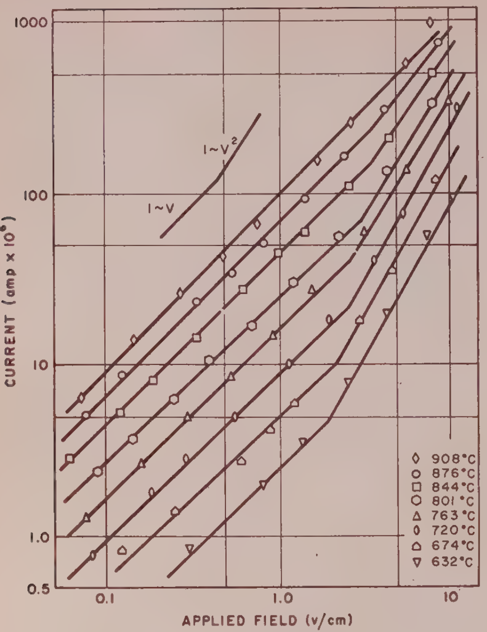

Fig. 5. Experimental current–applied field characteristics at various ambient temperatures for a single crystal of near-stoichiometric rutile.

According to the ideas of Mott and Gurney[3] and Rose,[4] if space charges are limiting, the current I is no longer proportional to the first power of the applied voltage V, as demanded by Ohm's Law, but becomes in absolute units

$$I=10^{-13}\mu k_0 V^2/d^3 \tag{3}$$

or, in terms of the applied field E,

$$I=10^{-13}\mu k_0 E^2/d, \tag{4}$$

where μ is the drift mobility, k_0 is the dielectric constant, and d is the electrode spacing.

Accordingly, if the logarithm of the current through the specimen is then plotted against the logarithm of the applied voltage across the specimen, a linear plot of a unity slope should be expected if Ohm's Law is applicable, and a slope of two would be obtained if space-charge currents were limiting. The current-voltage data presented in Figs. 2 and 3 have been replotted in Fig. 5 on a log-log basis. It is evident that the data can best be represented by two straight lines: one at low fields with a slope of unity (indicating ohmic behavior), and one at higher fields with a slope approximating 2, in agreement with predictions of a controlling space-charge-limited current.

As the temperature is increased, the transition from ohmic to nonohmic behavior is shifted to higher applied voltages. The change in transition potential as a function of temperature is shown in Fig. 6. It is noteworthy that as the temperature is increased, the slopes of the nonohmic portion of the $\log I$ vs $\log V$ curve shift from a slope approximating a value of 2 to lower values. Finally, at approximately 910°C, the material shows essentially only ohmic behavior at the highest fields employed. Consequently, an extremely high potential would be needed to cause a transition ohmic to nonohmic behavior at these high temperatures.

At the higher applied voltages, transient effects in both the potential and current are observed (Fig. 7). These effects have been also tentatively identified with the existence of space-charge-limited currents in the conduction band. At the higher applied voltages, both polarization and annihilation of carriers (that is, a decrease in potential across specimen as a function of time) were observed. Although both the current through the specimen and the potential across the potential probes change, these change in the same direction and are of the same order of magnitude so that the resistance remains essentially the same. Consequently the transient phenomena are believed to originate at the metal/insulator contact and arise from distortion of the charge distribution at that point.

The nonohmic behavior which has been observed can therefore be explained by a model which considers the existence of two sources of charge carriers in the conduction band at a given temperature.

The first type of charge carrier can be considered to be those electrons normally present in the conduction band at thermal equilibrium. For rutile in the temperature range investigated, this result may be expressed as[1,2,6]

$$n_c=KP_{\mathrm{O}_2}^{-1/n}\exp(-E/kT) \tag{5}$$

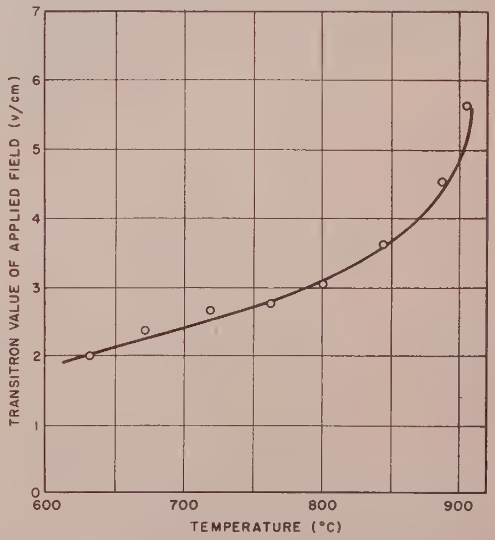

Fig. 6. Temperature dependence of the applied field at which transition occurs from ohmic to nonohmic behavior in a rutile monocrystal.

---

[6] R. G. Breckenridge and W. R. Hosler, Phys. Rev. 91, 793 (1953).

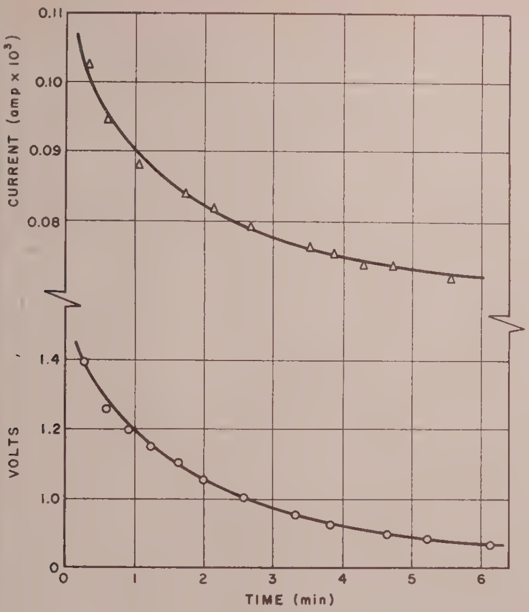

FIG. 7. Typical transient current and potential effects in a rutile single crystal at 820°C.

where K is constant, k is Boltzmann's constant, T is absolute temperature, $E \approx 3.0$ ev, P_{O_2} is oxygen partial pressure, $n \approx 4$. It is apparent that, in this instance, the concentration of conduction-band carriers in thermal equilibrium is not field dependent.

The second type of charge carrier has been identified with the existence of space-charge-limited currents within the material resulting from electrons forced into the insulator by thermionic emission at the electrode/insulator interface. The concentration of electrons n_{sc} which may be forced into the insulator may be expressed as

$$n_{sc} = CV, \tag{6}$$

where C is the capacitance of the material and V is the applied voltage.

It seems reasonable that the total number of charge carriers n_t in the conduction band may be expressed as the sum of Eqs. (5) and (6). Accordingly, n_t is given by

$$\begin{aligned} n_t &= K \exp(-3/kT) P_{O_2}{}^{-\frac{1}{4}} + CV \\ &= K P_{O_2}{}^{-\frac{1}{4}} \exp(-3/kT) + V k_0 \cdot 10^{-12}/4\pi d. \end{aligned} \tag{7}$$

At low fields, the concentration of charge carriers in the conduction band will be given the temperature-dependent, field-independent term which would, of course, yield ohmic behavior. As the applied voltage across the specimen is increased, more charge is forced into the conduction band of the insulator and a critical voltage would be reached where the contribution of charge carriers from Eqs. (5) and (6) would be equal. Finally, if the applied voltage across the crystal is increased still further, one would expect Eq. (6) to become limiting.

The process described above would certainly occur if both the ohmic current due to thermally excited charge carriers and the space-charge currents existed in parallel, but physically separate, paths. However, in fact, the two different types of current, each having its own potential distribution, move in the same volume. It seems logical, though, to assume that the mechanism which produces the greater carrier density would also control the potential distribution since the presence of carriers resulting from the minority process could then be neglected as a first approximation.

As the temperature of the specimens is increased, the contribution of thermally excited charge carriers to the conduction band might be expected to increase according to Eq. (5). Thus, higher applied voltages would be necessary to cause a transition from ohmic to space-charge-limiting behavior. This is exactly the situation in the case of rutile (see Fig. 7). Furthermore, a temperature could be reached where the contribution to conduction band carrier density from thermally excited carriers is large enough to mask any space-charge-limited currents in the voltage ranges investigated. The behavior of the material would then be essentially ohmic. This is seen to occur in rutile at temperatures greater than 910°C for the fields employed in this investigation.

An attempt was made to evaluate the μk_0 product for TiO_2 as given in Eq. (3), where μ is the drift mobility and k_0 is the dielectric constant for space-charge-limited currents, with the result that μk_0 equals 10^7. Substitution of the room-temperature dielectric constant[7] would lead to mobility values of 10^5 cm^2/v-sec. There are indications that the dielectric constant of TiO_2 above 600°C may be 10 or 100 times greater than the room-temperature value. According to several investigators,[7,8] the dielectric constant first decreases slightly with temperature, and then goes through a minimum at about 150°–200°C, after which it begins to rise extremely rapidly. No published values for the dielectric constant of rutile exist above 300°C, and there are insufficient data above the minimum for accurate extrapolation to 650°C. An increase in the dielectric constant by a factor of 10 or 100 would result in electron mobilities of 10^3–10^4 cm^2/v-sec. By comparison, the electron mobilities in Si and Ge have been found to be of the order of 10^3 cm^2/v-sec, while those[9] in ZnO and those[10] in NiO have been found to be of the order of 10^2 and 10^3 cm^2/v-sec, respectively.

---

[7] A. Von Hippel, R. G. Breckenridge, F. G. Chelsea, and L. Tisza, Ind. Eng. Chem. **38**, 1097 (1946).

[8] A. Eucken and A. Buchner, Z. physik Chem. (Leipzig) **B27**, 32 (1935).

[9] E. Mullwo, G. Heiland and F. Stockmann, *Solid State Physics*, edited by F. Seitz and D. Turnbull (Academic Press, Inc., New York, 1953), Vol. 8, p. 191.

[10] F. J. Morin, Bell System Tech. J. **37**, 1047 (1958).

There are no values for the electron mobility in rutile of near-stoichiometric composition. Values for the electron mobility in reduced samples of this material obtained from Hall effect measurements have been reported[6] to be of 1–10 cm^2/v-sec. The magnitude of the electron mobility which has been deduced from analysis of the space-charge-limited currents is at least a factor of a 10^2 larger than the aforementioned Hall mobility values.

At least two possible explanations may be offered for this discrepancy in mobility values. First, the Hall effect studies were made on reduced rutile at low temperatures where the carrier concentration in the conduction band is due to donor excitation. A rather high concentration of carriers is expected to exist in the conduction band for these specimens. If this were the case, the highest-energy electrons would lie near the edge of the band and thus might be expected to have a high effective mass and low mobility. In the case of the material in the near-stoichiometric condition, since there would be only a small number of carriers present, as is illustrated by the high values of resistance, the highest-energy electrons would lie at the bottom of the band and thus might be expected to have a higher mobility. Secondly, there is the possibility that when space-charge-limiting currents are observed, the potential distribution associated with this type of carrier may make it possible for electrons to exist in high-energy bands; in, for example, the 4*s* band in the cation lattice, where mobilities of the order of 10^3 cm^2/v-sec are possible.

JOURNAL OF APPLIED PHYSICS VOLUME 32, NUMBER 7 JULY, 1961

Analysis of Photojunctions Formed by Diffusing Copper into Insulating Cadmium Sulfide Crystals

Robert R. Bockemuehl, James E. Kauppila, and David S. Eddy
General Motors Research Laboratories, Warren, Michigan

(Received March 6, 1961)

A study of the observed photovoltaic, photorectification, and field effect modulation properties of junctions formed by diffusing copper into photoconductive, dark-insulating CdS crystals shows that two potential barriers are produced, one at the surface, the other in the crystal bulk. A transition from a double space charge dipole to a single separated dipole occurs at a reverse bias of less than 1 v. A corresponding transition from a primary to a secondary photocurrent process results. Values for the drift mobility of holes ranging from 10^{-5}–10^{-2} cm^2/v-sec were derived from field effect measurements and found to be proportional to illumination intensity at the infrared quenching wavelengths.

INTRODUCTION

COPPER is known to produce a rectifying barrier when applied to a cadmium sulfide crystal. This is to be expected since the work function of copper is greater than that of CdS and the copper impurity in CdS is an acceptor center. The properties of copper to CdS junctions may differ greatly, depending upon the impurity content and whether the copper is diffused into the crystal. Analyses of the physical processes have been made by Williams and Bube[1] on undiffused copper to CdS junctions and by Reynolds *et al.*[2] on junctions formed by diffusing copper into low-resistance CdS. These analyses were based on the measurement of photovoltaic and conductance properties as a function of light intensity, wavelength, and direction of illumination. Although similar physical processes occur in a junction formed by diffusing copper into dark-insulating CdS, those which principally determine the junction properties may differ considerably. For example, in dark-insulating CdS the conductance is dependent on illumination, and if the carrier density is relatively low, the space charge formed at the junction produces a relatively thick depletion layer for a given reverse bias voltage. Such junctions permit the realization of a photoconductive field effect transistor.[3]

This paper considers a physical model of a junction formed by diffusing copper into one surface of a photoconductive CdS crystal plate. The model is derived from measurements of the photovoltaic, photorectification, field effect modulation, and junction capacitance characteristics of the more than one hundred junctions of this type. The results of this experimental study support the previously reported theoretical analysis[4] of the field effect modulation of photoconductance.

SAMPLE PREPARATION

The crystals were grown from the vapor phase from luminescent grade CdS powder. The furnace and general technique used was that of Boyd and Sihvonen[5] except that the CdS vapor was transported to the condensing

---

[1] R. Williams and R. H. Bube, J. Appl. Phys. **31**, 968 (1960).

[2] D. C. Reynolds, L. C. Green, and L. L. Antes, J. Chem. Phys. **25**, 1177 (1956).

[3] R. R. Bockemuehl, Proc. Inst. Radio Engrs. **48**, 875 (1960).

[4] R. R. Bockemuehl, J. Appl. Phys. **31**, 2255 (1960).

[5] D. R. Boyd and Y. T. Sihvonen, J. Appl. Phys. **30**, 176 (1959).

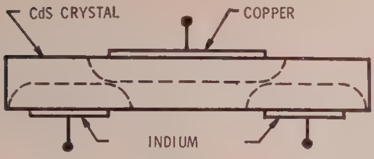

FIG. 1. Sample configuration.

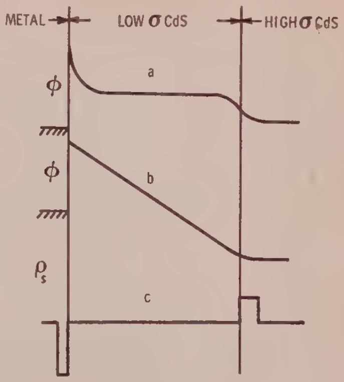

FIG. 2. Idealized electron energy profiles, (a) low bias voltage; (b) high reverse bias; (c) space charge distribution for high reverse bias.

region of the furnace by a slow flow of helium gas.[6] The gas-flow technique favored the growth of thin plates.

The crystal plates ranged in thickness from 40–100 μ and in area from 0.3–1 cm^2. All of the crystals selected for tests were free from visible defects, and most of them exhibited green luminescence at room temperature with ultraviolet excitation. Dark resistances were all greater than 10^{10} ohms.

Crystals were cleaned in dilute HCl and rinsed with distilled water prior to contact applications. Semitransparent bands of copper and indium were formed on the crystal surfaces by conventional vacuum deposition techniques. The copper and indium were then diffused into the crystal by heating at 400°C for periods ranging from 5–15 min. Connection wires were cemented to the contacts with conducting silver paint. The contact configuration shown in Fig. 1 permits convenient measurement of junction current, junction capacitance, and field effect modulation of photoconductance. All three contacts extend the full width of the crystal. The length of the copper barrier junction and the distance between the indium ohmic contacts are both approximately 0.1 cm.

PHYSICAL MODEL

Free electrons in a dark-insulating photoconductor result primarily from photon absorption, and their density is equal to the product of the electron-hole pair generation rate and the free electron lifetime. If a free electron density gradient exists, electron diffusion transfers charge which establishes an equilibrium potential gradient. Previous observations[7] have shown that the addition of copper impurity to CdS can decrease the lifetime and the resulting electron density by several orders of magnitude. Furthermore, the change in lifetime occurs abruptly at a particular value of copper concentration. Therefore, when copper is diffused into one surface of a CdS crystal, a potential barrier is formed in the region of the crystal where the abrupt change in lifetime occurs. If the copper penetration is relatively deep, the barrier location may be well into the crystal bulk.

A metal to semiconductor potential barrier also exists at the metallic copper to CdS:Cu crystal surface discontinuity. The energy profile of the resulting double barrier is similar to that obtained in a metal to n to $n+$ junction[8] and is of the form shown in Fig. 2(a). Two space-charge dipoles exist, one at each junction, as indicated by the curvature of the energy profile. When a sufficient reverse bias voltage is applied, the portions of the two barriers which exist in the low-conductivity region merge and effectively cancel, producing the barrier energy profile shown in Fig. 2(b). In the latter case a single, separated space-charge dipole results as shown in Fig. 2(c). The transition which occurs at low-bias voltages from the case in Fig. 2(a) to that of Fig. 2(b) is accompanied by a transition in the electrical characteristics of the junction.

When the reverse-bias voltage is increased, a net negative charge is transferred from the space-charge layer boundary in the conductive region to the metal surface. This produces an increase in the thickness of the space-charge layer and a corresponding reduction of the junction capacitance from the metal surface to the charge neutral portion of the high-conductivity region. If the charge transfer process is such that a redistribution of free charge carriers results, the current-voltage characteristics of the junction will be influenced accordingly. Furthermore, if free charge carriers are transferred from the conductive region to the metal, the conductance will diminish. This influence of applied voltage on the conductance of the high-conductivity region satisfies the requirements for the field effect modulation of conductance.

The quantitative properties of these various electrical characteristics are determined primarily by the relationship between the positive space charge and the transfer of free charge. Virtually all of the carriers in the system are produced by photogeneration of electron-hole pairs. In the junction represented by Fig. 2(c), the electrons generated in the positive space-charge layer drift toward the high-conductivity region and are effectively carried by external circuitry to the copper metal. The generated holes drift toward the metal surface. Thus both positive and negative charges are transferred from the positive space-charge layer to the metal surface. A net transfer of negative charge results because the electron mobility is much greater than the hole mobility. An equilibrium value of positive space charge density is reached when the free hole density in the space-charge layer is such that the holes drift out of that region at the same rate they are generated. An analysis of this effect[4] shows that the equilibrium space-charge density ρ_s is a function of the charge generation rate qf (coul/cm^3-sec), dielectric constant k (farads/cm), and the drift mobility of the holes μ_{dp} (cm^2/v-sec):

---

[6] H. Sainte-Claire-Deville, and M. L. Troost, Compt. rend. **52**, 920 (1861).

[7] R. H. Bube and S. M. Thomsen, J. Chem. Phys. **23**, 15 (1955).

[8] H. K. Henisch, *Rectifying Semiconductor Contacts* (Clarendon Press, Oxford, England, 1957), p. 191.

$$\rho_s = (qfk/u_{dp})^{\frac{1}{2}} \text{ coul/cm}^3. \qquad (1)$$

The equilibrium charge density ρ_f of the free electrons in the high-conductivity region is proportional to the free electron lifetime τ_n (sec):

$$\rho_f = -qf\tau_n \text{ coul/cm}^3. \qquad (2)$$

Therefore, unlike the conventional semiconductor junction, the photojunction exhibits a net transfer of charge from the positive space-charge layer to the metal surface which can be either greater or less than the free electron charge which is transferred.

Both charge densities are dependent on absorbed excitation radiation which determines qf. They are also influenced by infrared quenching[9] intensity. The reduction of free electron lifetime by low-energy photon absorption has been explained by Rose[10] on the basis of a resulting transfer of holes from class II centers, which have a low electron capture probability, to class I centers which have a high electron capture probability. This process involves liberating a hole trapped in a class II center into a free state where it remains until it is recaptured by a class I or class II center. Therefore, an increase in the fraction of the total generated holes which are free is obtained. This effectively increases the drift mobility of the hole. Experimental results indicate that the fractional change of hole drift mobility produced by a change in incident quenching intensity is much greater than that of the free electron lifetime, and that the relationship between that hole mobility and quenching intensity is approximately linear.

INFLUENCE OF IMPURITIES

Although copper is the principal impurity in the junctions studied, its effect is dependent on the residual impurities or vacancies in the as-grown crystal. By influencing the recombination processes, copper can either increase or decrease the free electron lifetime in CdS.[11] When copper is substituted for cadmium, a deep acceptor state is produced. If the acceptor states are compensated by donor states already in the crystal, class II or sensitizing centers are formed. Such a center has a relatively small capture cross section for electrons. The density of these centers can be made sufficient to shift the recombination process to the smaller cross section centers and thereby increase the electron lifetime and the corresponding photosensitivity. However, if the copper acceptor is not compensated, it behaves as an additional class I center which decreases the lifetime and desensitizes the photoconductivity.

Diffusion of the copper into one surface of a CdS crystal produces an acceptor concentration which decreases with distance from that surface. The density of copper impurities near the surface is much greater than any of the other donor or recombination center densities in the crystal. The region near the surface has very low conductivity. As the copper concentration diminishes, one of two conditions may result during the transition to the original crystal properties further into the crystal. First, if the original crystal was already sensitized by class II centers, a sharp transition from low- to high-carrier lifetime would occur in the region where the copper density becomes low enough for recombination to shift from the uncompensated copper centers to the original sensitizing centers. The boundary of the sensitized region is the other surface of the crystal. However, if class I centers dominated the original recombination process and if sufficient donors are present to compensate some of the added copper acceptors, a transition from the low-conductivity region near the surface to a sensitized high-conductivity region occurs where the copper density is of the same magnitude as the available donor density. A second transition occurs deeper in the crystal from the sensitized region to the portion of the crystal which retains its original desensitized properties. The junction is essentially the same as in the first example except that the effective boundary of the sensitized region does not extend to the opposite surface. This produces a system whose effective thickness is less than the crystal thickness.

Both types of conductivity profiles have been observed for junctions made from as-grown CdS. Additional control over the type of profile formed can be achieved by adding suitable impurities during growth

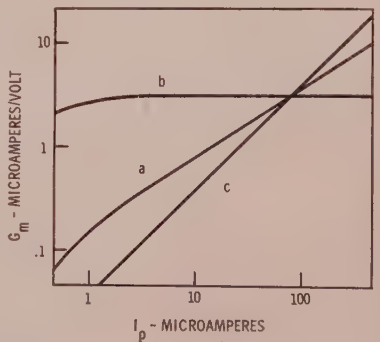

FIG. 3. Relationships between mutual transconductance G_m an channel current I_p with (a) excitation intensity P varied an quenching intensity S constant, (b) S varied and P constan (c) both varied but P/S constant.

---

[9] R. H. Bube, Phys. Rev. **99**, 1105 (1955).

[10] A. Rose, Phys. Rev. **97**, 322 (1955).

[11] R. H. Bube and L. A. Barton, RCA Rev. **20**, 564 (1959).

or by diffusing impurities into the surface opposite the copper junction. The high-conductivity regions of the junctions tested were found to be sensitized, often to a greater extent than the original crystal. This was made evident by the relatively long carrier lifetimes (10^{-3}–10^{-2} sec) and the infrared quenching of photoconductivity which were observed.

FIELD EFFECT MODULATION

The configuration of the experimental device shown in Fig. 1 is that of a conventional field effect transistor.[12] However, differences exist which involve the dependence of terminal characteristics on illumination parameters and the more complex relationship between free charge density and space-charge density. Observations of the influence of illumination on the modulation properties were analyzed to determine this relationship.

When the voltage between the ohmic contacts of a field effect transistor exceeds a certain value, the current through them approaches a constant value I_p. The influence of junction bias voltage is also constant in that operating condition and is represented by a mutual transconductance G_m. An analysis[4] has shown that G_m and I_p are related to the free and space-charge densities ρ_f and ρ_s which are in turn dependent on pair production rate f, free electron lifetime τ_n, and hole drift mobility μ_{dp} from Eqs. (1) and (2):

$$G_m \propto \rho_f \propto f\tau_n, \tag{3}$$

$$I_p \propto \rho_f \rho_s \propto \tau_n f^{\frac{3}{2}} \mu_{dp}^{-\frac{1}{2}}. \tag{4}$$

Relationships between G_m and I_p were obtained under various conditions of illumination by two independent light sources. One source produced excitation wavelengths which generate electron-hole pairs, the other produced quenching wavelengths in the infrared region. Figure 3 shows representative examples of the experimentally obtained relationships. The logarithmic plots are seen to be linear over most of the range but have different slopes. The empirical relationships between the terminal characteristics G_m and I_p obtained under various conditions of excitation intensity P and quenching intensity S can be analyzed on the basis of Eqs. (3) and (4) to yield an indication of the influence of intensities P and S on the carrier properties f, τ_n, and μ_{dp}. The results obtained may be summarized as follows:

(a) With P varied and S held constant, $G_m \propto I_p^{\frac{2}{3}}$. This indicates that the product $\tau_n \mu_{dp}$ is not a function of P while f increases with P.

(b) With S varied and P held constant, G_m is constant although I_p decreases with S. This indicates that the product $f\tau_n$ is not a function of S, while μ_{dp} increases with S.

(c) With both P and S varied but with the ratio P/S held constant, G_m is directly proportional to I_p. This indicates that the ratio f/μ_{dp} is constant under these conditions.

Other tests showed that the excitation intensity range used was sufficiently low to yield linear photoconductivity[10]; that is, τ_n is not a function of P, and f is directly proportional to P. A simple argument based on the preceding summary indicates that the drift mobility of the hole μ_{dp} is directly proportional to quenching intensity S. Therefore, the charge densities in Eqs. (1) and (2) are related to P and S in the following manner:

$$\rho_f \propto P \quad \text{and} \quad \rho_s \propto (P/S)^{\frac{1}{2}}. \tag{5}$$

Other factors which influence field effect modulation include the geometry of the junction, free electron mobility, and the dielectric constant. These are not expected to change appreciably with illumination. Although infrared quenching of photoconductivity was observed in all crystals, it was not appreciable over most of the intensity range used for the data in Fig. 3. The departure from linearity of curves 3(a) and 3(b) at low values of I_p can be explained on the basis of reduction of lifetime by infrared quenching. The influence of optical absorption on carrier distribution was minimized by using relatively long wavelength excitation illumination. Comparison of the field effect observed with either surface illuminated showed that only a very small portion of the electron concentration gradient resulted from the absorption coefficient of the wavelengths used.

The influence of quenching illumination on hole mobility is also shown by the observed frequency dependence of the field effect illustrated in Fig. 4. Two flat-response regions exist, separated by a transition region. The low-frequency amplification increases as S increases. However, the high-frequency amplification is independent of S. The space charge density ρ_s given by Eq. (1) is an equilibrium value which depends on the drift mobility of the hole and, therefore, on S. However, at higher signal frequencies the time between cycles is insufficient for the equilibrium hole density to be established, and the space charge formed in the modulated region is equal to the free charge removed from that region. Inasmuch as the equilibrium time is related to the transit time of the holes through the space-charge region, the transition frequency increases with hole mobility. The resulting

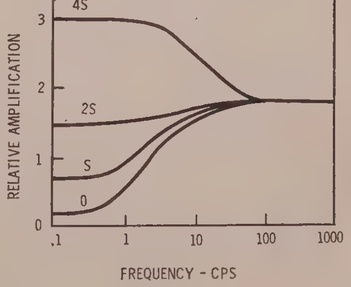

FIG. 4. Variation of amplification frequency response with quenching intensity S.

---

[12] W. Shockley, Proc. Inst. Radio Engrs. 40, 1365 (1952).

increase in transition frequency with quenching intensity can be seen in Fig. 4.

The positive space-charge density given by Eq. (1) results from the assumption that electron contribution to the charge density is negligible and that generated holes are extracted by the field rather than recombined with electrons in the space-charge region.[4] The results of field effect experiments support these assumptions by showing that the equilibrium hole density in the space charge region can be less than that which existed prior to space-charge formation. The transit time of an electron through the space charge region is about 10^{-8} sec. This is much shorter than the free electron lifetimes (of the order of 10^{-3} sec) in the conductive regions of the crystals tested. In order for appreciable recombination to take place in the space-charge region, the electron and hole densities would have to readjust to produce an electron lifetime of the order of the transit time. This would require a significant increase in hole density which is contrary to the field effect results.

The positive space charge includes both free and trapped holes. The effective mobility can be represented as the product of the free hole mobility and the fraction of the total hole density which is free. This is the conventional definition of drift mobility.[13] Values of hole drift mobility estimated from field effect experiments varied greatly between crystals. Maximum values obtained during quenching illumination were of the order of 10^{-2} cm^2/v-sec and were proportional to quenching illumination intensity. This mobility continues to increase at higher quenching intensities, but evaluations cannot be made because of the complicated dependence of electron lifetime on these higher intensities. Evaluation of hole mobility at extremely low quenching intensities was limited to values of the order of 10^{-5} cm^2/v-sec. The positive space charge density resulting from lower mobilities is too high to permit accurate measurement of field effect modulation without exceeding the electrical breakdown field of the material.

Only two of the more than one hundred junctions tested exhibited field effect modulation at low frequencies in the absence of quenching illumination. Furthermore, with no quenching illumination, junction capacitance modulation was negligible and linear junction current—voltage characteristics were observed. This indicates the importance of quenching illumination in the modulation of the space-charge layer boundary.

The manner in which the conducting channel current is influenced by the junction bias voltage is also dependent on the geometry of the junction. Three general forms are summarized in Fig. 5. Figure 5(a) represents the case where the low-conductivity region is very thin relative to the thickness of the higher-conductivity region. As the space-charge layer thickness increases, the effect of bias current diminishes and a curved relationship results. However, if the conductive region is concentrated near the surface opposite the copper surface, their separation is determined mainly by the thickness of the desensitized region and the linear relationship shown in Fig. 5(b) results. The abrupt change in modulation characteristic shown in Fig. 5(c) results when the high-conductivity region is highly sensitized near the copper surface and diminishes to a lower conductivity farther into the crystal.

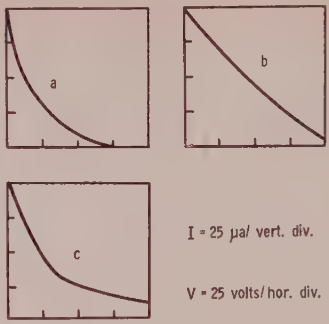

FIG. 5. Modulation of photoconductance with bias voltage with (a) thin low-conductance region, (b) thick low-conductance region, (c) thin, centrally located high-conductance region.

Short-circuit current amplification in the field effect device can be shown to be proportional to the ratio of the electron lifetime in the sensitized region to that in the desensitized region. The measured current amplification values, of the order of 10^3, indicate that the ratio of lifetimes is about 10^5.

JUNCTION CAPACITANCE

The small signal junction capacitance is effectively represented by a capacitor in which the two plates are the copper metal and the conducting portion of the sensitized region. The plate separation includes the thickness of the desensitized region and the positive space charge layer. Maximum capacitance occurs at zero bias voltage and is limited by the thickness of the desensitized region. This thickness also determines the $C{:}V$ relationship. As the thickness of the desensitized region approaches zero, a $C\propto V^{\frac{1}{2}}$ relationship is approached. When the desensitized region thickness approaches the crystal thickness, the capacitance becomes independent of voltage.

Estimates based on capacitance measurements indicate that for an appreciable field effect to be observed, the copper diffusion must form a desensitized region at least 10 μ thick. This limit may result from the influence of surface states when the positive space-charge forms too near the surface. The expected correlation between diffusion time and desensitized layer thicknesses was observed, although significant differences between crystals resulted from uncontrolled impurity and stoichiometric defects in the as-grown crystal. The magnitude of the thicknesses of the desensitized layers compare favorably with those predicted from published diffusion coefficients for copper in CdS.[14]

---

[13] W. Shockley, *Electrons and Holes in Semiconductors* (D. Van Nostrand Company, Inc., Princeton, New Jersey, 1950), p. 211.

[14] R. L. Clarke, J. Appl. Phys. **30**, 957 (1959).

JUNCTION CURRENT

The minimum reverse-bias junction current is limited by the equilibrium condition which requires that carriers be removed from the space charge layer at the same rate they are generated.[4] The generated carrier travels through the circuit but once. This primary photocurrent density is proportional to the space-charge layer thickness and would be expected to increase with quenching illumination intensity because of the corresponding reduction in space-charge density. This relationship is observed when reverse bias is less than 1 v. However, at higher voltages the magnitudes of the observed reverse current are much greater than can be attributed to a primary photocurrent process. Furthermore, this current decreases when quenching illumination is increased. In fact, at the higher bias voltages the junction current is influenced by excitation and quenching illumination in exactly the same manner as the conducting channel current I_p in the field effect experiments.

These observations indicate that at voltages greater than a volt or so the reverse current is dominated by a secondary photocurrent process. The relationship of the reverse current to field effect characteristics is satisfied by a reverse current density of the form $J=\sigma E$, where the conductivity σ is proportional to excitation illumination intensity and the electric field E is equal to, or at least proportional to, the constant field in the desensitized region as shown in Fig. 2(b). This can result from a conventional photoconductive process in the low lifetime region, but requires that the copper metal freely replenish electrons. Although the processes which establish the necessary equilibrium between the desensitized region and the metal are not clearly understood, secondary photocurrents in a reversed biased Cu—CdS junction have been observed previously.[2]

The shape of the junction current–voltage relationship is determined by the junction geometry. Two representative cases are shown in Fig. 6. If the desensitized region is thick relative to the sensitized region, both the forward and reverse currents are limited by the low-conductivity region. A similar linear $I:V$ relationship exists in both directions, as shown in Fig. 6(a). However, as the thickness of the densitized region approaches zero, the reverse current approaches an $I \propto V^{\frac{1}{2}}$ relationship, Fig. 6(b). The forward current is again limited by the conductivity of the desensitized region and is linear at low voltages. However, many of the junctions studied exhibited an abrupt increase in forward current at voltages greater than 4–5 v. Inasmuch as the thickness of the desensitized region in this case is of the order of 10 μ, space charge limited current through that region can be expected.[15] Space-charge limited current is proportional to voltage to a power greater than two, depending on the properties of the electron traps within the material. It is inversely related to the cube of the thickness and in thin low-conductivity regions it can greatly exceed the current due to the ohmic conduction process at moderate voltages.

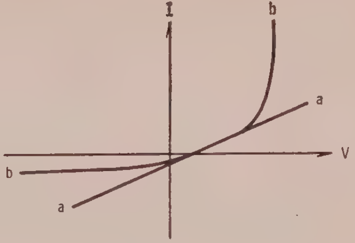

FIG. 6. Typical junction current-voltage characteristics with (a) thick low-conductance region, (b) thin low-conductance region.

PHOTOVOLTAIC PROPERTIES

Junctions of this type are not efficient photoelectric energy convertors because the photocurrent is limited by relatively low conductance regions. However, the measurement of open circuit photovoltage and short-circuit photocurrent provides further information concerning the junction processes.

The open-circuit photovoltage tends to approach a constant value at high light intensities. The maximum photovoltage of all the junctions tested ranged from 0.2–0.4 v when illumination was limited to excitation wavelengths. This value increased to 0.5 or 0.6 v when quenching illumination was added. Short circuit currents varied from 10^{-9}–10^{-6} amp and always increased when quenching illumination intensity was increased.

Quenching illumination *increases* the short-circuit photocurrent but *decreases* the reverse bias current of the junction. The transition between these two opposite effects occurs at reverse bias voltages of the order of 1 v. This apparently corresponds to a transition of the energy profile of the junction from that shown in Fig. 1(a) to that of Fig. 1(b). In the first case, at low bias voltage, the field in the desensitized region is nearly zero and the photocurrent results from the primary process of collection of carriers generated in the space-charge regions. By increasing the drift mobility of the hole with quenching illumination, the space-charge densities decrease and the space-charge layer thicknesses increase accordingly. The increased photocurrent corresponds to the increase of the carrier collection volume of the junction.

In the second case, at high bias voltage, a high field exists in the desensitized region; the reverse current is dominated by the previously discussed secondary photocurrent process determined by the conductivity of the desensitized region. Quenching illumination decreases the charge density in the space charge layer, increasing the thickness of that layer and thereby reduces the field in the desensitized region and the corresponding current.

The open-circuit photovoltage is such that the copper metal becomes positive with respect to the crystal bulk. The spectral response of the photocurrent is shown in Fig. 7. The shape of the spectral response is the same

---

[15] R. W. Smith and A. Rose, Phys. Rev. **97**, 1531 (1955).

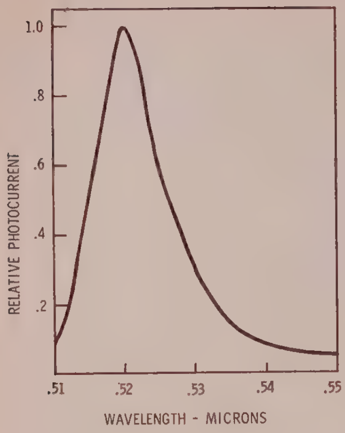

FIG. 7. Spectral response is essentially the same for photoconductance, short-circuit photocurrent, and reverse current.

as that obtained for the bulk conductance of the crystal and the reverse bias junction current. Very little dependence of spectral response on direction of illumination is exhibited, which indicates that the dominant photocurrent and photoconductance processes occur in the crystal bulk. No evidence was obtained which suggested photoemission of electrons from the copper metal to the CdS.[1] Furthermore, the similarity between the spectral response of the photoconductance and that of the reverse bias current indicates that, although the copper concentration in the desensitized region is sufficient to reduce electron lifetime four to five orders of magnitude, the spectral response of that region is not significantly different from that of the sensitized region.

The tests which derived the relationships between junction parameters and quenching illumination utilized an incandescent source with a suitable color filter. However, tests made with a monochromatic source showed that all of the observed influences of quenching intensity on field effect, photovoltage, photocurrent, reverse current, and junction capacitance occur only at the commonly observed infrared quenching wavelengths (0.9 and 1.4 μ[9]). Furthermore, the relationships of the junction properties to the quenching intensity is independent of which of the two wavelengths is used.

SUMMARY

The properties and processes of a junction formed by diffusing copper from 10–100 μ into a dark-insulating CdS crystal are summarized as follows:

1. The diffusion of copper into one surface of a crystal produces a low electron lifetime region near that surface and a relatively abrupt transition to a sensitized region further into the crystal.

2. Potential barriers exist at the copper metal to CdS junction and in the desensitized to sensitized transition region.

3. Positive-negative space-charge dipoles form at both barriers when reverse bias is less than about 1 v. At higher reverse bias, a single separated dipole forms in which the metal surface becomes negatively charged and a positive space charge forms in the sensitized region of the crystal.

4. Reverse current is dominated by a primary photocurrent process when the double dipole exists but is transferred to a secondary process at reverse bias voltages which produce the single separated dipole.

5. The magnitude of the forward current is similar to that of the reverse current except in the case where the desensitized region is sufficiently thin to permit an appreciable space-charge limited current.

6. The equilibrium positive space-charge density is a function of pair generation rate and the drift mobility of the hole. It may be either greater or less than the original charge density of the free electrons removed during the formation of the space-charge layer.

7. The drift mobility of the holes in the positive space charge region is proportional to quenching intensity (0.9- and 1.4-μ wavelengths) over the range which is defined by the measurement limits from 10^{-5}–10^{-2} cm^2/v-sec.

ACKNOWLEDGMENTS

The crystals studied were grown by Dr. C. E. Bliel and F. D. Bosco. The contacts were prepared by J. W. Bergstrom and P. W. Wood who also assisted in experimental evaluations.

JOURNAL OF APPLIED PHYSICS VOLUME 32, NUMBER 7 JULY, 1961

Formation Conditions and Structure of Thin Epitaxial Silver Films on Rocksalt*

BILLY W. SLOOPE AND CALVIN O. TILLER
Virginia Institute for Scientific Research, Richmond, Virginia

(Received February 15, 1961)

A comprehensive experimental investigation of the effects of formation conditions on the structural characteristics of thin, single-crystal Ag films vapor deposited onto synthetic NaCl single crystals is reported. Formation conditions studied include: preannealing heat treatment of the substrate, postheat treatment of film and substrate, substrate temperature during deposition, and the rate of deposition. It is shown that an epitaxial temperature as such does not exist, and that the minimum deposition temperature for the formation of single-crystal films is rate dependent. Crystalline structure, porosity, and stacking fault density of the films are related to the rate of deposition, deposition temperature, and thickness.

INTRODUCTION

THE growth, structure, and physical properties of evaporated films have been, and continue to be, the subject of many investigations. Recently, many of these have involved the use of single-crystal metal films formed by deposition onto single-crystal substrates, a process called "epitaxy." Reference has been made by many authors to the fact that thin films are dependent upon their conditions of formation and that the properties of thin films as deposited in a vacuum are influenced by their structural form. There has, however, been no comprehensive study of the effects of the formation conditions on the resultant film. It is important, therefore, to investigate the effects of formation conditions on epitaxially grown thin metallic films and to characterize the films in terms of these conditions. In this manner one may then prepare films of controlled characteristics so that consistent measurements may be made on various physical properties.

Among the factors to be considered are the preannealing treatment of the substrate upon which the film is to be formed, the temperature of the substrate during the deposition of the film, the rate at which the material is deposited, the postannealing treatment of the film after formation, and the film thickness. The work reported herein presents the results of an experimental investigation of the effects of these formation conditions on the character of thin films of Ag vapor deposited onto freshly cleaved single-crystal surfaces of synthetic NaCl.

The classical nucleation theory of Frenkel (1923) suggested a mechanism for the formation of surface layers which resulted in a temperature-dependent, critical rate of deposition. In addition to the formation of a continuous layer, the requirement of orientation must be included when epitaxial films are desired. It is very likely that the mode of nucleation and the growth of the nuclei determine to a great extent the structural characteristics of the resulting film. In general, a slow rate of evaporation favors the occurrence of orientation, whereas a fast rate favors the formation of a continuous layer. On the other hand, a low temperature favors the continuous film while a high temperature favors orientation. Thus the temperature of the support and the rate of deposition act in opposite sense, and the formation of a film with the desired orientation and continuity must be a compromise between these factors. Early work by Brück[1] indicated that there existed a substrate temperature, the so-called epitaxial temperature, above which a single-crystal film could be formed. This temperature was dependent upon the material deposited and the substrate used. Later work appeared to confirm this idea, and theories of epitaxial growth have attempted to predict this temperature. None of these have been completely successful, and more recently the idea of an epitaxial temperature has come to be doubted.

While this work has not been directed toward the subject of the mechanism of the oriented overgrowth per se, the characterization of the films with respect to orientation, continuity, and possibly stacking fault density and dislocations is discussed qualitatively in terms of nucleation and growth after the experimental results have been presented.

EXPERIMENTAL

Film Preparation

The Ag films formed for this study were prepared by vacuum deposition onto heated single-crystal NaCl surfaces. Pressures of the order of 10^{-5} mm Hg were maintained during the evaporation. The NaCl substrates, freshly cleaved along a (100) plane, were 2 mm thick by 10 mm square.

Films were prepared by evaporating 99.999% pure Ag downward through the hole in the bottom of an electrically heated, 20-mil, conical W basket. The evaporation rate was controlled by the current to the basket. The thickness of the deposited film was controlled by the use of a predetermined amount of Ag. Consistent rates of evaporation and thicknesses were possible for this manner of control, and were determined from the evaporation times and thickness measurements using the Fizeau multiple-beam interference technique.

Several hot-plate-type arrangements were used as the substrate holder and heater; however, the most reliable system was the oven-type heater as shown in Fig. 1. It

---

* Supported by the Department of Defense.

[1] L. Brück, Ann. Physik **26**, 233 (1936).

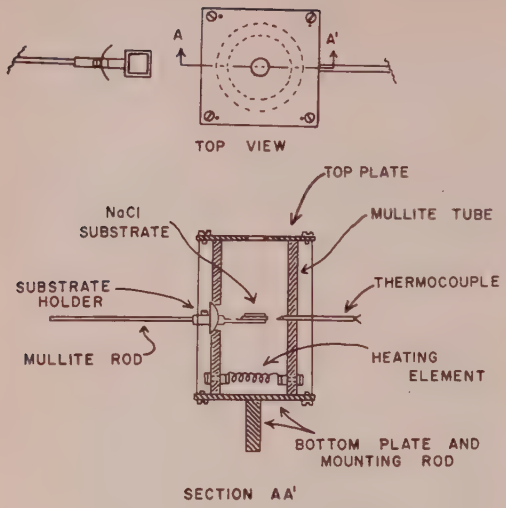

FIG. 1. Substrate holder and oven.

consists of a mullite tube 3 in. high and $1\frac{1}{2}$ in. in diameter with top and bottom plates of $\frac{1}{16}$-in. Ta. The top plate contains a 1-cm hole centered on the axis of the tube. The substrate holder, made of Ta and approximately 1 cm square, fits into an opening in the side of the mullite tube. The shield on the mullite arm closes this opening when the substrate is centered below the hole in the top. Deposition onto the substrate is accomplished through the hole using a source-to-substrate distance of 7.5 cm. A thermocouple is introduced into the oven opposite the substrate holder so that the sensing element is adjacent to the substrate. This thermocouple was compared with a thermocouple introduced through the hole in the top and placed in contact with the substrate surface. Agreement between the two was good over the range from room temperature to 500°C. The oven is heated by 10-mil Ta coils mounted just above the bottom plate.

After each evaporation the oven is removed from the vacuum system, washed in a 35% nitric acid solution, rinsed in distilled water, dried, and stored in a desiccator until mounted in the vacuum system for use. Under proper conditions of formation, good single-crystal films are produced each time following the cleaning process. However, without this process, films formed by subsequent evaporations contained polycrystalline traces which increased with use.

Film Analysis

Characterization of the films was made using electron transmission diffraction, electron microscopy, and x-ray diffraction. Samples of each film were removed from the substrate by dissolving the NaCl in water and were supported on copper screens for observation in the electron microscope. In order to compare the crystalline structure of the entire film with that obtained from the electron diffraction patterns, a glancing-angle, x-ray diffraction pattern was obtained for the remainder of the film. A 4° glancing angle was used in order to allow the x-ray beam to pass through the optimum specimen distance for maximum diffraction intensity. In addition to giving indications of polycrystalline and textured-type orientations, the x-ray pattern also indicates twinning on (111) planes since some of the planes of the twin, particularly (100) planes, are in position to diffract the x rays. Therefore, if the information from electron and x-ray diffraction patterns are combined, the films can be studied for perfection of crystalline structure. Electron microscopy was used to investigate structural features such as continuity, stacking faults, and dislocations.

All films classified as single crystals herein are those for which the electron and x-ray diffraction patterns indicated the (001)Ag//(001)NaCl and[100]Ag//[100] NaCl orientation with twinning.

Heat Treatment

Various preannealing treatments of the substrate and postannealing treatments of the deposited film on the substrate were made to determine conditions which would be effective in allowing single-crystal films to be produced. These heat treatments were of interest because it had been reported that a preannealing treatment improved the smoothness of the substrate surface and that poorly oriented films could be converted into relatively well-oriented films by postheat treatment.

Substrate preannealing treatments varied from room temperature to above 600°C, initially for 3-hr periods. At 600°C an appreciable amount of the substrate evaporated and the surface was not smoother as reported by Shirai.[2] Metallographic investigation of the surface of the film formed on these substrates showed many octahedral faces as seen in Fig. 2. Even at a preannealing temperature of 450°C, the substrates were noticeably "heat etched" and the resultant films often porous.

Postannealing treatments were made at 500° and 200°C for periods up to 15 min. Films made under various preannealing temperatures were compared for no heat treatment, for a heat treatment after short exposure to the atmosphere, and for an immediate heat treatment before exposure to the atmosphere. Except for very few cases, the heat treatment after exposure to air produced little or no observable improvement in film orientation, even for treatments at 500°C. On the other hand, structural perfection was improved for those films given an immediate postheat treatment at 200°C.

The effects of postheat treatments were not independent of thickness and time. Films 500–700 A thick were given a 200°C, 15-min heat treatment, but these did not retain the metallic shine characteristic of 1000 A

---

[2] S. Shirai, Proc. Phys.-Math. Soc. Japan **20**, 65 (1935).

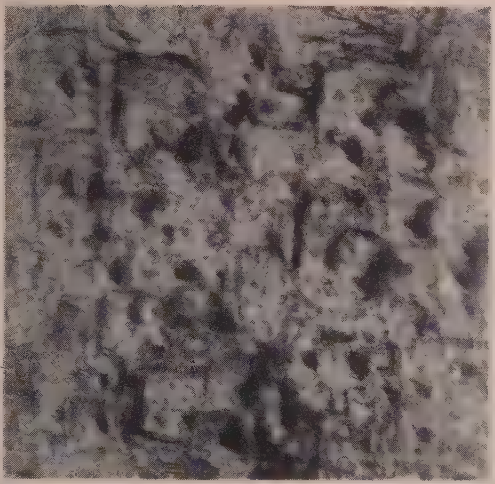

FIG. 2. Metallographic photograph of the surface of a Ag film on a NaCl substrate which was preannealed above 600°C prior to deposition of the film. Heat etching at this temperature produced many octahedral faces on the surface. Magnification 250×.

films after a 500°C, 15-min treatment. For these thinner films, postannealing caused agglomeration in varying degrees. For the case in which the heat treatment produced small holes, the electron diffraction pattern indicated the film was still single crystalline. As the agglomeration increased, the structural perfection decreased, and when the films became lacelike, the electron diffraction pattern was characteristic of a (100)-textured orientation with some traces of polycrystallinity. However, for a 5-min postheat treatment at 200°C, the films retained their metallic shine and had markedly improved crystalline structure. Therefore, while a postheat treatment improves the structure of the film, the time must not be such as to allow agglomeration. These results are in general agreement with the work of Johnson,[3] although the annealing temperatures are somewhat lower for these single-crystal films which are annealed before, rather than after, atmospheric exposure.

The most important results of the heat treatment studies and their relation to the formation of single-crystal Ag films on NaCl were:

(1) Single-crystal films were formed for substrate preannealing up to 450°C but, at this and higher temperatures, the substrate appeared "heat etched" and the films often porous.
(2) If the preannealing treatment was omitted from those conditions which otherwise produced single crystals, the films were not so perfect structurally.
(3) A 1-hr preanneal treatment was as effective as a 3-hr treatment for temperatures as low as 125°C.
(4) No completely single-crystal films were produced without an immediate postheat treatment.

Deposition Rate, Deposition Temperature, and Thickness

The major portion of the work on epitaxial formation of Ag films on NaCl involved the investigation of the relationship of the rate of deposition, the deposition temperature, and the thickness to the structure of the films. All films for these experiments were formed as follows: the NaCl substrate preannealed at 125°C for 1 hr, the substrate taken to the desired deposition temperature, Ag deposited at the determined rate and thickness, and the resultant film immediately postannealed at 200°C for 15 min.

Three groups of films were prepared, the groups having thicknesses of 900, 1200, and 1650 A. Each group consisted of three sets of films, each set for a different deposition rate which ranged from 10 A/min to 1000 A/min. Each set was a series of films made at deposition temperatures varying from room temperature to 400°C. The entire range was not used for all series, only enough to establish the upper and lower temperature limits for which single-crystal films were produced.

RESULTS

Using the analysis already described, the films were compared for perfection of orientation, continuity, and the occurrence of stacking faults, if possible. The films were classified generally as continuous or not continuous and as single crystals or not single crystals. These features were then compared with regard to rate of deposition, deposition temperature, and thickness. These results are illustrated by a plot of the logarithm of the deposition rate against the reciprocal of the deposition temperature in degrees absolute. Such a plot is shown in Fig. 3 for each of the three thicknesses. The films are indicated as not single crystals, continuous single crystals, or noncontinuous single crystals, and are located on the appropriate plot according to their formation conditions and thickness.

Lines are drawn on the plots to indicate generally the upper and lower temperature limits for the formation of single-crystal films, hence defining a range of deposition temperatures for each deposition rate. It is immediately obvious that the minimum deposition temperature for the production of single-crystal films increases with increasing rate of deposition. Also, it is observed that there is little variation in the lower temperature limits for the different thicknesses. Within the region corresponding to single-crystal films, it is observed that at higher temperatures the films are not continuous. The degree of continuity is not indicated on the graph, and some of the films shown as noncontinuous actually contain only a few small holes. As the temperature increased the holes increased in size, becoming more ribbonlike until, at the higher temperatures, the films are extremely porous and contain many isolated nuclei. The continuity of the films is rate

---

[3] G. W. Johnson, J. Appl. Phys. 21, 449 (1950).

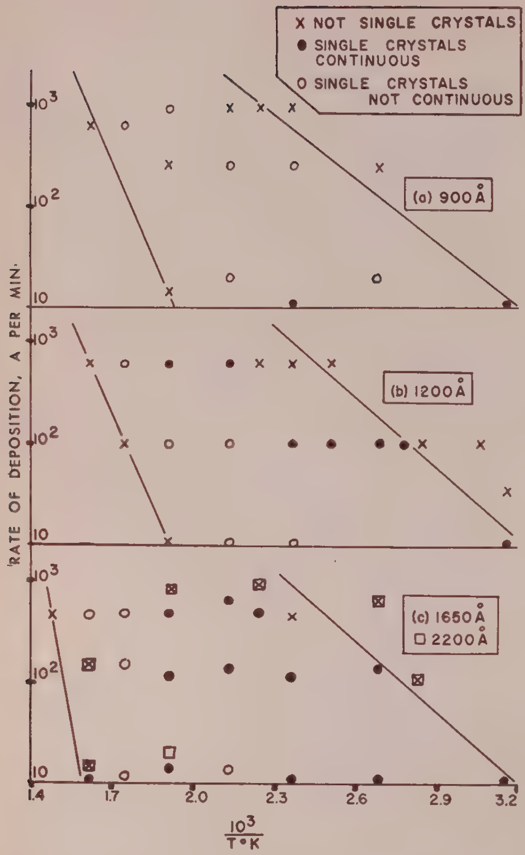

FIG. 3. Logarithm of the deposition rate vs the reciprocal of the deposition temperature in degrees absolute for films of various thicknesses. The regions bounded by the lines on the plots indicate the range of conditions for the formation of single-crystal films.

dependent, being more continuous at higher rates of deposition.

The plots of Fig. 3 are divided into three regions: continuous nonsingle crystals, single crystals, and highly porous nonsingle crystals. The graph does not make distinction between those films marked as not single crystals. However, the type of crystalline structure, or perfection of structure, of any film is characteristic of the region for which the formation conditions apply. Transmission electron diffraction patterns typical of those regions, for all thicknesses, are shown in Fig. 4 and are arranged so as to follow the general order of Fig. 3. In Fig. 4, low temperature refers to 30–100°C and high temperature to 350°C or above. It is observed that there are three distinct patterns, one corresponding to each of the three regions. Those films formed in the region at, or below, the lower temperature limit are strongly (100) oriented and all contain the double-positioned (111) orientation, polycrystallinity, and twinning. The lower the temperature, the weaker the (100) orientation. The diffraction patterns of the central region have the characteristic square array of the (100) orientation, with twinning, regardless of whether or not the films are continuous. However, as the porosity increases to the point that the film becomes lacelike, at or above the upper temperature limit, the strong (100) spots become arced, characteristic of misalignment. At the higher temperatures and rates where the films consist of a larger number of smaller aggregates, or nuclei, the diffraction pattern is similar to that shown with the addition of more (111)-oriented, but misaligned, nuclei. These films do not give any indication of polycrystallinity as do those at the much lower temperature.

The degree of continuity was obtained from electron micrographs, and additional micrographs of the films, made at higher magnification, gave evidence of microstructure such as stacking faults and dislocations. Comparison of these micrographs with regard to deposition rate, deposition temperature, and thickness indicated that the porosity and microstructure of the films are related to the formation conditions. The results concerning porosity have already been mentioned in connection with Figs. 3 and 4. Comparisons of the microstructure with respect to formation conditions and thickness are shown in Figs. 5, 6, and 7.

Figure 5 shows electron micrographs of 900-A-thick Ag films for 600-A/min and 10-A/min deposition rates as a function of deposition temperature. For both of

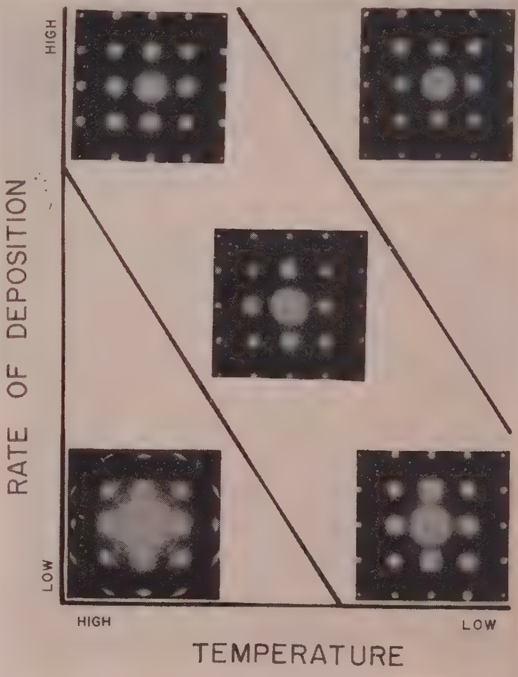

FIG. 4. Typical transmission electron diffraction patterns comparing the crystalline structure of films formed in the three regions of Fig. 3.

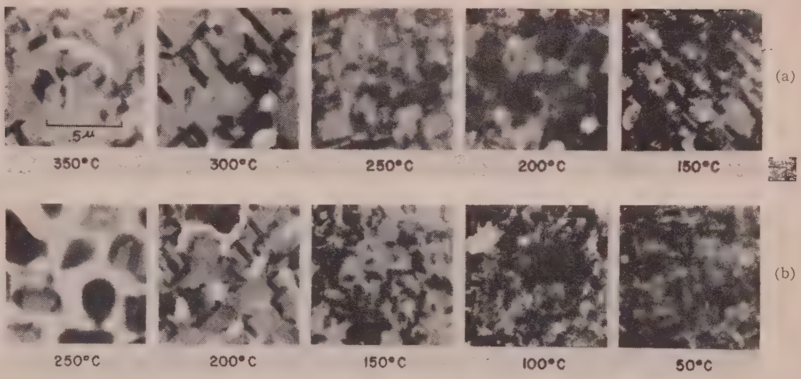

FIG. 5. Electron micrograph of 900-A-thick Ag films deposited on NaCl showing microstructure as a function of deposition temperature for deposition rates of (a) 600 A/min and (b) 10 A/min.

these rates it is seen that the stacking fault density decreases as the deposition temperature increases. This is also characteristic for other rates and thicknesses. It is observed that, for those nonsingle crystalline films at lower temperatures, the microstructure is much more complex and grains are apparent. On the other hand, for the high-temperature films which consist essentially of isolated nuclei, a few stacking faults are evident in the individual nuclei and some of these are misaligned with respect to others. Both these conditions agree with the type of electron diffraction patterns shown for these two regions in Fig. 4.

The fact that the stacking fault density increases as the deposition rate increases can be seen in Fig. 5, but this is more clearly shown in Fig. 6. These micrographs are for 1200-A films, and compare the stacking fault density as a function of deposition rate for the deposition temperatures of 200° and 250°C. This order holds for other temperatures and thicknesses. The 10-A/min, 250°C film of Fig. 6 is comparable to the 900-A film formed under the same conditions and shown in Fig. 5. Both these films contain essentially isolated nuclei, some having observable stacking faults, which indicate misalignment. The electron diffraction pattern of the 1200-A film, characteristic of both, is that shown at the lower left of Fig. 4. Except for the misalignment, all the films of Fig. 6 are single crystals.

The stacking fault density for various thicknesses is shown in the micrographs of Fig. 7. As expected, the width of the stacking faults increases with film thickness. Also, there may be some decrease in stacking fault

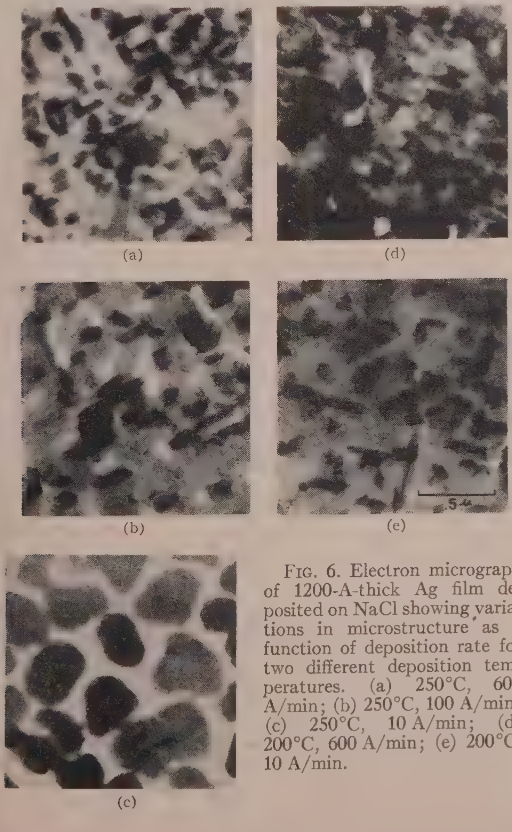

FIG. 6. Electron micrograph of 1200-A-thick Ag film deposited on NaCl showing variations in microstructure as a function of deposition rate for two different deposition temperatures. (a) 250°C, 600 A/min; (b) 250°C, 100 A/min; (c) 250°C, 10 A/min; (d) 200°C, 600 A/min; (e) 200°C, 10 A/min.

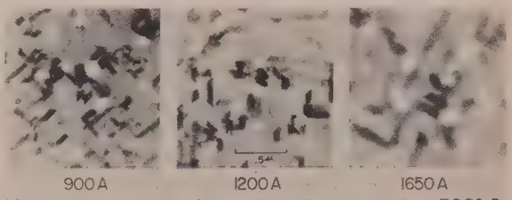

(a) Deposition rate 600A/min, deposition temperature 300° C

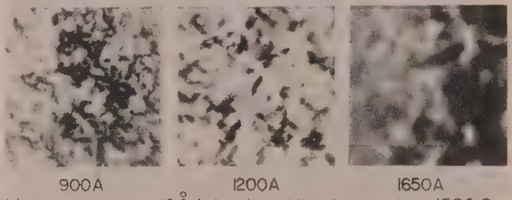

(b) Deposition rate 10Å/min, deposition temperature 150° C

FIG. 7. Electron micrograph of Ag films deposited on NaCl comparing the microstructure for different thicknesses.

density as the thickness increases, though the difference is not great. It is obvious, however, that the stacking fault density at a high temperature–high rate is less than that at a low temperature–low rate.

DISCUSSION

If the results shown in Figs. 4–7 are compared with the plots in Fig. 3, it is seen that the characteristics of a film with respect to crystalline structure, continuity, and microstructure can be fairly well predicted from a knowledge of the conditions of formation. The observed variations of these characteristics with rate of deposition and deposition temperature is that which would be expected generally from nucleation theory. These experiments show that, for a given deposition rate, the films are continuous at lower temperatures, but as the deposition temperature is increased the films contain holes, and at sufficiently high temperatures the films are essentially isolated aggregates. This is more pronounced at low rates than at high rates. Conversely, for a given temperature, at low deposition rates the film may be porous, but as the rate is increased the films are more continuous. Hence, low temperature and high deposition rate favor continuity. In the case of orientation, an increase of deposition temperature for a given deposition rate gives improved orientation, whereas for a given temperature, orientation improves as the rate of deposition is lowered. Hence, orientation is favored for low rates and high temperature.

These results are in general agreement with various investigations of initial nucleation and growth. Sennett and Scott,[4] investigating the deposition of Ag on glass, found that the aggregates of the films formed for slow evaporations tended to grow in height and hence required thicker films before joining together; whereas, for faster rates, the aggregates remained thin and grew over the substrate. At higher temperatures the films showed greater aggregation. The films studied here followed this pattern in that at lower temperatures the holes were small. Also, at high temperatures and low rates the aggregates were larger than those at high temperatures and high rates. Bassett and Pashley[5] studied growth and structure in more detail, and the structure of the Ag films, as reported herein, are very similar to those for Au on NaCl and Ag on mica described by these authors. Stacking faults as observed by Phillips[6] in thin Ag films deposited on NaCl at 300°C are in agreement with those reported here at the same temperature, but only for a deposition rate of 600 A/min.

Matthews[7] presents evidence that stacking faults are the result of two or more nuclei growing together in such a way that there may be mismatching of the lattice spacing at the junction region. Thus a large number of junction regions would introduce a large number of stacking faults. This might be expected for the case where film growth occurs from many small nuclei. Comparing stacking fault features as in Fig. 5 with those of porosity, one can see that the films having a high density of stacking faults are those formed under the rate of deposition and temperature conditions which generally favor nucleation and growth from many small nuclei. On the other hand, for those conditions which might favor growth from large initial nuclei, hence greater porosity if the thickness is not sufficient, films would be formed with fewer junctions and likewise fewer stacking faults. The introduction of stacking faults at junction regions as described by Matthews, and which can be used to explain the results here, are in accord with the findings of Bassett[8] on the growth of evaporated films. He observed that, at the stage of growth where the film is made up of large aggregates separated by small channels, the mismatch between adjacent islands could not be taken care of by rotation on the substrate, and faults are then necessarily built into the films.

CONCLUSIONS

The investigation of the relationship of rate of deposition, deposition temperature, and thickness to the formation of single-crystal thin Ag films deposited on NaCl has shown that an epitaxial temperature per se does not exist, but that the minimum temperature of deposition is dependent on the rate of deposition. Likewise, structural characteristics of the films are quite dependent on these formation conditions. The characterization of thin films as to crystalline structure, continuity, and stacking faults is possible in terms of the conditions of formation.

In the region of low rate–low temperature up through high rate–high temperature, or some proper compromise between the two, single crystals are formed whose crystalline structures as shown by electron diffraction are similar. However, the mode of nucleation and growth can explain the observed differences in porosity and microstructure for those films formed in that region corresponding to proper conditions for the deposition of single-crystal Ag films. The differences in these films as evidenced by porosity and microstructure may be significant in determining their physical properties, and the effects of these differences may now be studied.

ACKNOWLEDGMENT

The authors are indebted to E. M. Gentry of this laboratory for technical assistance in the experimental work of this paper.

---

[4] R. S. Sennett and G. D. Scott, J. Opt. Soc. Am. 40, 203 (1950).

[5] G. A. Bassett and D. W. Pashley, J. Inst. Metals **87**, 449 (1958–59).

[6] V. A. Phillips, Gen. Elec. Research Lab. Rept. No. 60-R6-2443M (May, 1960).

[7] J. W. Matthews, Phil. Mag. **4**, 1017 (1959).

[8] G. A. Bassett, paper presented at the Fifth International Congress of the International Union of Crystallography, Cambridge, England, August, 1960.

JOURNAL OF APPLIED PHYSICS VOLUME 32, NUMBER 7 JULY, 1961

Growth of Single-Crystal Calcium Fluoride with Rare-Earth Impurities

H. Guggenheim
Bell Telephone Laboratories, Inc., Murray Hill, New Jersey

(Received March 13, 1961)

The preparation of large single crystals of CaF$_2$ by the zone melting and the pulling techniques is reported. Many crystals were doped with rare-earth elements. The ingots showed high optical perfection; they could be used in optical maser studies. The annealing of such crystals is discussed.

INTEREST in single-crystal calcium fluoride has increased recently because it is a favorable host lattice for use in solid state research, particularly in optical maser work.[1]

For many years large single crystals of optical quality CaF$_2$ have been grown exclusively from the melt using the Bridgman-Stockbarger[2] technique. For the present application to solid solutions, this method has several disadvantages: (a) a uniform distribution of impurities is difficult to achieve because of segregation during normal freezing; (b) the crystals are in most cases not visible for inspection and correction during growth; (c) slow growth rates (days) are necessary; (d) the most favorable and frequently used crucible material, graphite, reacts with certain doping elements.

In this article we wish to report on two techniques, which were in the past considered unfeasible[3] for the preparation of CaF$_2$ crystals; these are the horizontal zone[4] and the vertical pulling[5] techniques. Preliminary pulling experiments were made with Nassau.[6] With the procedures described here, it was found that both methods can provide single crystals of CaF$_2$ of high crystalline perfection free from flaws and inclusions. The crystals can easily be observed and doped during the preparation. In the pulling process, various crucible materials (carbon, platinum, iridium) were used successfully.

The following two points are of utmost importance for the preparation of good CaF$_2$ crystals:

(1) The starting material has to be thoroughly dry and free of surface oxide. This was accomplished by holding CaF$_2$ powder at 800°C in an atmosphere of dry HF for 18 hr before melting the sintered ingot in the crucible. Pieces of CaF$_2$ crystals obtained from the Harshaw Chemical Company (grown by the Bridgman-Stockbarger method) were also found to be suitable as a starting material.

(2) The ambient inert gas has to be carefully freed of oxygen and water vapor. Good results in the purification of the gas were obtained by passing it through an all-metal trap containing a Linde molecular sieve and cooled by liquid nitrogen.

The importance of the preparation of pure starting material and the dryness of the ambient gas was best illustrated in the case of samarium-doped calcium fluoride. Samarium in CaF$_2$ gives an intensely green color even at low concentrations (below 0.05 mole %) when in the divalent state. However, if the system is contaminated with oxidizing reagents, the Sm^{2+} will be converted to Sm^{3+} which results in colorless CaF$_2$ crystals. Therefore, the intensity of the Sm^{2+} absorption serves as a sensitive indicator for trace quantities of oxidizing reagents.

Large single crystals of CaF$_2$ were prepared in a horizontal boat by zone melting. Growth rates from 1–12 in./hr were used. The size of the crystals (up to $1\times1\times10$ in.) was determined only by the length and width of the carbon container. Ordinary graphite was used, but it was found not to give reproducible results because of difficulty in outgassing it before charging. A graphite boat coated with Pyrolytic[7] graphite worked quite satisfactorily.

Crystal pulling from the melt (Czochralski technique) resulted in long single crystals several millimeters in diameter. In preliminary experiments, it was found that the growing crystal cracked after several centimeters were withdrawn from the melt due to thermal strains resulting from the large temperature gradient. Strains were also introduced by the impurity concentration gradient between the undoped seed and the doped growing crystal. This problem was eliminated by attaching an afterheater ($\sim$800°C) around the growing crystal directly above the crucible level. A seed rotation of 36 rpm and pull rates of 1 to 6 in./hr were used frequently.

As mentioned above, both techniques provide CaF$_2$ single crystals of high perfection. There were no inclusions, as judged by the absence of Tyndall scattering (which would be indicative of such things as CaO precipitation). Optical absorption measurements at 2000 A showed no selective[8,9] absorption characteristic for oxygen impurities.

---

[1] P. P. Sorokin and M. J. Stevenson, Phys. Rev. Letters **5**, 557 (1960).

[2] D. C. Stockbarger, J. Opt. Soc. Am. **39**, 731 (1949).

[3] V. Stepanov and P. P. Feofilov, *Reports at the First Conference on Crystal Growth* (U.S.S.R. Academy of Sciences Press, Moscow, 1957).

[4] W. G. Pfann, Trans. Am. Inst. Mining Met. Engrs. **197**, 1441 (1953).

[5] J. Czochralski, Z. physik. Chem. **92**, 219–221 (1918).

[6] K. Nassau (to be published).

[7] Obtained from High Temperature Materials Company, Brighton, Massachusetts.

[8] D. Messner and A. Smakula, Phys. Rev. **120**, 1162 (1960).

[9] W. Bontinck, Physica **24**, 639 (1958).

Ordinarily CaF_2 can be annealed by heating the crystal uniformly in dry air to a high temperature below its melting point for a period of time (the number of hours depending on the size of the crystal) and slowly cooling. However, in the case of CaF_2 with rare-earth impurities capable of exhibiting more than one oxidation state, e.g., Eu and Sm, special precautions are necessary in the annealing. If the specimen contains surface oxide or if the ambient contains even trace quantities of oxygen, then a change to the higher valence state of the rare-earth impurity could be observed; e.g., deep green CaF_2 doped with Sm^{2+} could be "bleached" by high-temperature treatment with dry oxygen or dry hydrogen fluoride. From such measurements a diffusion coefficient for oxygen was estimated to be 10^{-7} cm²/sec at 1200°C.

The best conditions for annealing CaF_2 containing Sm^{2+} were as follows: (a) The sample was kept in a desiccant for several days prior to the annealing. (b) The sample was completely enclosed in a previously outgassed graphite tube and heated uniformly by induction *in vacuo* and then slowly cooled. At 1200°C a sample of 5 mm diam could be annealed in 16 hr.

Many crystals were doped with various rare-earth elements in concentrations of 0.01–5 mole % and a high degree of uniformity was obtained. This fact was manifested by optical absorption and luminescence studies of various parts of the ingot.

Crystals prepared by the above techniques were used successfully in optical masers.[10]

The author is greatly indebted to W. Kaiser for many helpful discussions and suggestions during the course of this work. Thanks are also due to K. Nassau for his cooperation during the preliminary experiments using the pulling technique and D. L. Wood for optical absorption measurements.

---

[10] C. G. B. Garrett, W. Kaiser, and D. L. Wood (to be published).

JOURNAL OF APPLIED PHYSICS VOLUME 32, NUMBER 7 JULY, 1961

Electroluminescence at *p-n* Junctions in Gallium Phosphide†

M. Gershenzon and R. M. Mikulyak
Bell Telephone Laboratories, Inc., Murray Hill, New Jersey

(Received February 20, 1961)

Both diffused and alloyed junctions were prepared from single crystals of GaP cut from ingots grown near the melting point, as well as from crystals grown at lower temperatures. The diodes were characterized by their current-voltage relationship and their capacity at reverse bias. Anomalies in both the forward and the reverse currents, an excess capacity, and a hysteresis effect are attributed to the presence of deep centers in the depletion layer, particularly in the alloyed structures. A nearly compensated layer was found at the junction of the diffused diodes. The spectra, bias dependences, decay times, and efficiences of the electroluminescence emitted at these junctions at both forward and reverse bias were studied and correlated with the diode models. At reverse bias, radiative intraband relaxation was due to carriers excited during avalanche breakdown (diffused diodes), by internal field emission (alloyed diodes), and from carriers thermally generated within the depletion layer (all diodes). At forward bias, only the diffused junctions exhibited light emission and this was of two types: (1) a band-to-band recombination with phonon cooperation, whose recombination kinetics depended on whether or not the process occurred within the depletion layer, and (2) recombination through a deep level which may be associated perhaps with a vacancy.

INTRODUCTION

Because of its large band gap, 2.2 ev,[1] gallium phosphide offers an environment favorable for the study of semiconductor luminescence which falls in this case in the highly accessible visible region of the spectrum. Electroluminescent radiation from GaP has been reported by several observers.[2–8] The materials investigated were either polycrystalline or consisted of fairly small single crystals, and the essential physical parameters—carrier densities, mobilities, etc., were not known. It has become clear, however, that the existence of a rectifying barrier—grain boundary, surface barrier, or point contact—is a prerequisite for electroluminescence. Accordingly, with the availability of large single crystals of uniform high purity[9] and

---

† Portions of this paper were presented orally at the Electrochemical Society, Spring Meeting, Chicago, Illinois, 1960), Electronics Division, Abstract 98.

[1] O. G. Folberth and F. Oswald, Z. Naturforsch. **9a**, 1050 (1954).

[2] G. A. Wolff, R. A. Hebert, and J. D. Broder, Phys. Rev. **100**, 1144 (1955); *Proceedings of the International Colloquium on Semiconductors and Phosphors in Garmisch* (Interscience Publishers, Inc., New York, 1958).

[3] D. B. Hold, G. F. Alfrey, and C. S. Wiggins, Nature **181**, 109 (1958); G. F. Alfrey and C. S. Wiggins, *International Congress on the Physics of Solid State, Brussels, 1958* (Academic Press, Inc., New York, 1960), Vol. 2, Part 2, p. 747.

[4] E. E. Loebner and E. W. Poor, Bull. Am. Phys. Soc. **4**, 4 (1959).

[5] E. E. Loebner and E. W. Poor, Phys. Rev. Letters **3**, 23 (1959

[6] H. G. Grimmeiss and H. Koelmans, Philips Research Rept **15**, 290 (1960).

[7] M. Kikuchi and T. Iizuka, J. Phys. Soc. Japan **15**, 935 (1960

[8] J. W. Allen and P. E. Gibbons, J. Electronics and Contr **7**, 518 (1959).

[9] C. J. Frosch and L. Derick, J. Electrochem. Soc. **108**, 2 (1961).

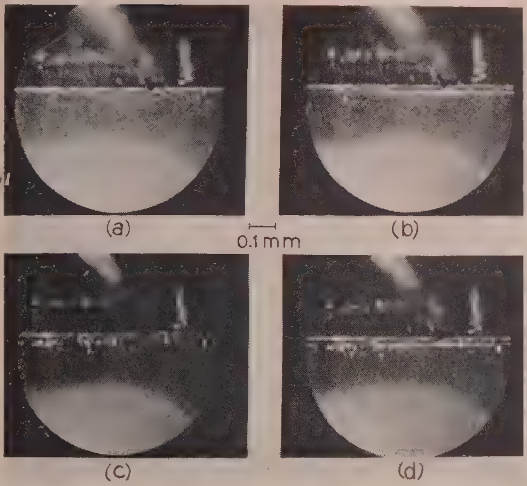

FIG. 1. Light emission from a zinc-diffused, single-crystal diode. The point shown near the top of the photographs serves as the ohmic contact to the highly doped zinc layer. The contact to the n-type substrate is made by an alloyed ohmic Ag:Te dot not shown. The junction itself is horizontal, perpendicular to the plane of the photograph and about 25 μ below the top edge of the crystal. (a) Zero bias; (b) forward dc bias; (c) reverse dc bias above breakdown. (d) ac excitation.

whose semiconductor properties have been described,[10,11] it has been possible to fabricate reproducible p-n junctions whose electroluminescent properties could be investigated readily. It is shown that a consequence of the large energy gap of GaP is the introduction of two classes of deviations from ideal p-n junction behavior due to the inclusion of deep levels in the depletion layer and to a strong tendency toward compensation. At reverse bias light emission is associated with avalanche breakdown, Zener breakdown, and thermally generated currents below breakdown. At forward bias both intrinsic and extrinsic radiation is observed and can be related to the physical properties of the junctions.

EXPERIMENTAL

The diodes were fabricated from crystals prepared either by the lengthwise solidification of gallium-phosphorus melts at 1500°C and at a phosphorus pressure of 15–20 atm,[10] by the floating-zone recrystallization of such ingots under similar conditions,[9] by the vapor phase reaction of gallium suboxide and phosphorus at 900°–1000°,[12] or by crystallization from gallium-rich solutions.[13] Both n-type and p-type crystals were obtained. Free carrier concentrations ranged from 5×10^{17} to $\sim10^{14}$ cm^{-3} for n-type samples and from 3×10^{17} to 5×10^{16} cm^{-3} for p-type samples, while the room temperature mobilities were 110 and 70 cm^2/v sec, respectively.[11] Compensation of from 5×10^{15} to 1×10^{17} cm^{-3} was present in both instances. Since grain boundaries are generally regions of very high resistivity along which enhanced diffusion and precipitation occur during processing, it was essential to use only single crystals for the preparation of these diodes.

The junctions were made either by diffusion or by alloying. The acceptor, zinc or cadmium, was diffused into n-type material at 800°C under its own vapor pressure for $\frac{1}{2}$ to 24 hr, corresponding to junction depths of 20 to 200 μ as determined from the position of light emission at forward bias. Alloyed junctions were prepared by melting dots of a 1% zinc-silver alloy or a 1% tellurium-silver mixture on n-type and on p-type material, respectively, whose surfaces had been cleaned by an aqua regia etch and by subsequent reduction at 700°–1000°C in hydrogen. Regrowth layer thicknesses of ~1 μ were indicated by visual observations on sectioned samples and by the spectral distribution of the light emitted from the immediate vicinity of the junction and transmitted through the regrowth layer. The latter measurement will be considered in greater detail later. The alloyed diodes were divided into two types depending upon the rate of cooling of the molten phase during their preparation. Those which were quenched to room temperature in 10–20 sec are called "rapidly alloyed" diodes, while those cooled in a matter of several minutes are the "slowly alloyed" diodes.

The ohmic contacts to all the diode structures were either alloyed dots of the same composition as those used in the manufacture of the junctions on material of opposite carrier sign, or zinc or tellurium plated points "formed" by a current pulse. The points were useful only on low resistivity material ($<\sim1$ Ω cm).

Each diode was characterized by its rectification behavior, its transition layer capacity at reverse bias, and its pattern of light emission both as a function of bias and of temperature. Three types of diode structure were prepared to facilitate the detection of the luminescence. The first geometry, exemplified in Fig. 1, was that of a junction intersecting the surface and was used with both classes of diodes. The second structure, which has already been mentioned, consisted of etching back most of the metallic contact to an alloyed junction leaving only the regrowth layer between the junction and the surface. The third type, used in connection with many of the diffused diodes, had a junction well below the crystal surface, so that access from the junction to the surface was only through a substantial thickness of undiffused material.

The spectral distribution of the emitted radiation was analyzed by a double-pass Perkin-Elmer monochromator with fused-silica optics and was detected either by a photomultiplier (RCA 7362, 7265; Du Mont

---

[10] C. J. Frosch, M. Gershenzon, and D. F. Gibbs, Symposium on Preparation of Single Crystals of the III–V Compounds, Battelle Memorial Institute, Columbus, Ohio, 1959.

[11] M. Gershenzon and R. M. Mikulyak (to be published).

[12] M. Gershenzon and R. M. Mikulyak, J. Electrochem. Soc. **108** (June, 1961).

[13] G. A. Wolff, P. H. Keck, and J. D. Broder, Phys. Rev. **94**, 753 (1954).

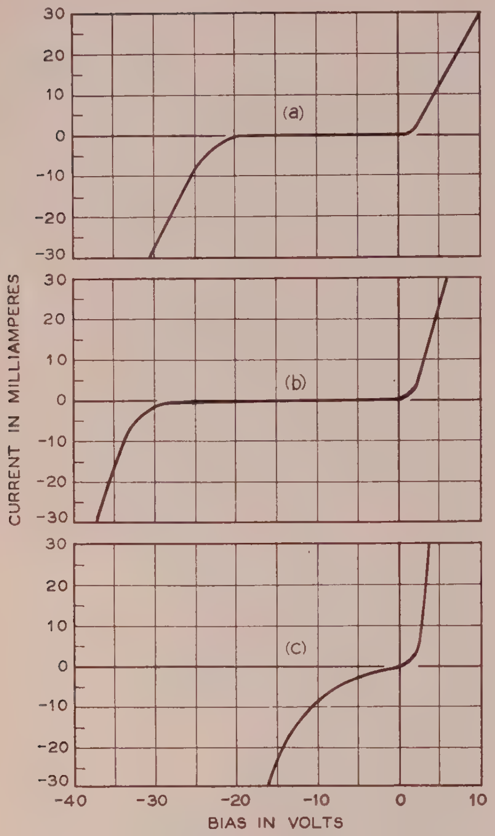

FIG. 2. Typical diode characteristics. (a) Diffused diode; (b) slowly alloyed diode; (c) rapidly alloyed diode.

6911) or by a cooled PbS cell. Detector wavelength sensitivity was normalized to a thermocouple. The electroluminescence was excited by a dc source and the observed bands were always significantly broader then the spectral slit widths used. Total radiative efficiencies were determined by intercepting a portion of the light by a photomultiplier through a known aperture after passage through a series of calibrated filters. The photomultiplier was used both to compare the light with that from a radiation-phosphor standard, and as an absolute detector after calibration against a standard lamp and thermocouple. The efficiencies are reported only in terms of the light intensity external to the crystal and assuming that it is spatially uniform.

RESULTS

A. Voltage-Current Characteristics

The characteristics of several typical diodes are shown in Fig. 2 on a linear scale, and in Figs. 3 and 4 on a semi-logarithmic scale. Reverse breakdown was highest and hardest in the diffused diodes with maximum breakdown potentials of about 40 v. Much higher breakdown voltages have been observed on alloyed diodes made from crystals grown from the vapor phase and having much higher resistivities, about 1000 Ω cm.[12] The diffused diodes exhibited the highest rectification ratios, up to 3×10^6. Although the rectification characteristics persisted to much higher temperatures, the high diffusion constant of zinc, about 10^{-7} cm^2/sec at 800°C, resulted in noticeable junction degradation between 400° and 500°. Moreover, reversible changes in the reverse characteristic which occurred in this temperature range were probably due to ion transport caused by the junction fields as has been noted in silicon.[14]

At high forward bias the current in all cases was limited by a series resistance, resulting in a linear dependence at high bias. The resistance varied inversely with the junction area, but was otherwise independent of the geometry of the junction. Potential probes across the face of the diode indicated that the entire *IR* drop occurred at the junction itself and not elsewhere in the base material. This resistance was present only when a p-n junction was produced, either by diffusion or alloying, never when the contact was ohmic. The conductance was about 1 mho cm^{-2} for the diffused junctions, and somewhat greater than this for the

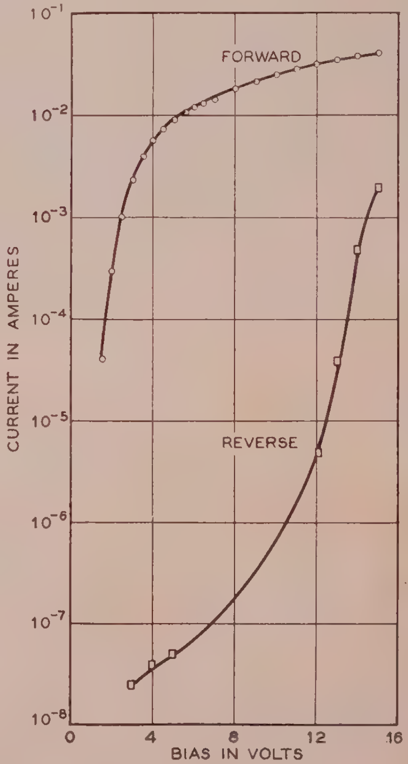

FIG. 3. Diffused diode characteristic on a semilogarithmic scale.

---

[14] E. M. Pell, J. Appl. Phys. 31, 291 (1960).

TABLE I. Current below breakdown as a function of bias (V) and temperature (T).

$I=kV^n\exp(-\theta/T)$	θ °K	n	k amp cm^{-1} v^{-n}
Diffused diode	180	3.0	0.0001
Slowly alloyed diode	3170	2.6	0.5
Rapidly alloyed diode	6600	1.3	3000

alloyed diodes. Between 80° and 700°K the resistance of the diffused diodes decreased exponentially with temperature with an activation energy of approximately 0.07 ev. The true forward current-voltage characteristics, obtained by subtracting the series IR drops, showed that the current increased as $\exp(eV/nkT)$ with n varying from 2 to 3 for the diffused diodes and ranging up to 15 for rapidly alloyed diodes. For example, n is equal to 5 for the slowly alloyed diode shown in Fig. 4.

Reverse breakdown in all the diodes was manifested by the abrupt change in functional relationship between current and voltage, and by a simultaneous change in the rate of light production as a function of current or voltage as discussed later. If the diodes were ideal, the reverse current below breakdown would have saturated at a value approximately 10^{-37} amps because of the large energy gap of GaP. However, the current continued rising until breakdown was reached. This excess current is empirically related to the bias, V and the temperature, T by $I=kV^n\exp-(\theta/T)$. Typical values for the constants k, n, and θ are shown in Table I. The highest currents were exhibited by the rapidly alloyed diodes. This current was not due to surface leakage which was usually observed at the lowest voltages giving a linear current-voltage relation that was highly dependent upon surface treatment and that usually corresponded to a surface conductivity of about 10^{-9} mhos per square.

The breakdown potential, which is defined here as the zero-current intercept of the extrapolated linear portion of the current-voltage characteristic, decreased with increasing temperature much more quickly in the case of the rapidly alloyed diodes than in the diffused diodes. As in the forward direction, the reverse current at high bias approached linearity, yielding a differential resistivity equal to, or somewhat less than, the limiting resistance in the forward direction.

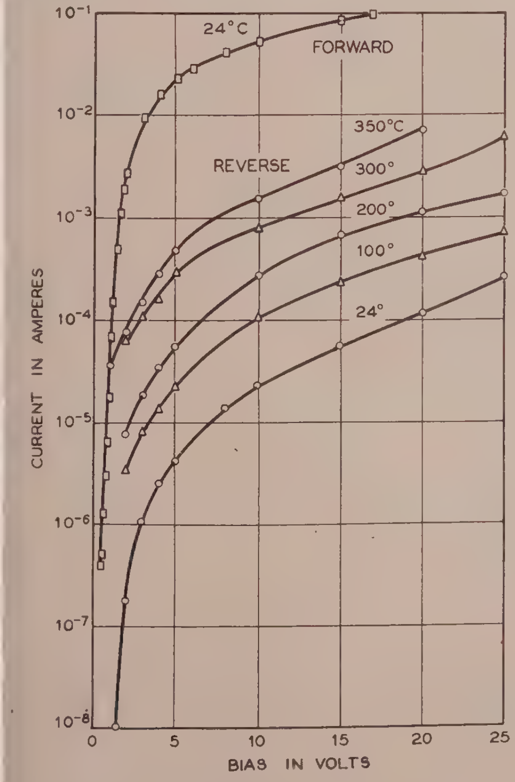

FIG. 4. Characteristic of a slowly alloyed diode at several temperatures.

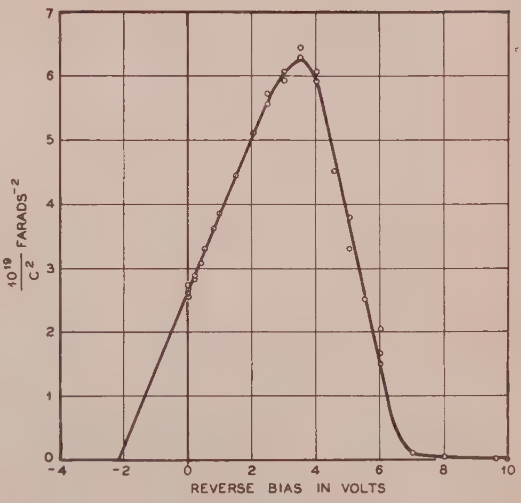

FIG. 5. Depletion layer capacity.

B. Capacity at Reverse Bias

The capacity of all the diodes decreased normally with increasing reverse bias, and then suddenly began rising rapidly beyond a critical threshold as shown for a single diode in Figs. 5 and 6. In the first region the behavior of the capacity corresponds to the normal depletion layer capacitance. It depends inversely on the $1/n$ power of the bias, with n equal to 2.0 ± 0.8 for all the diodes, the uncertainty being due to the limited accessible voltage range before the increasing capacity component begins to dominate. In the case of the diffused diodes, the built-in potentials obtained by extrapolating to infinite capacity lie in a very narrow range, which is itself a function of n. This potential is

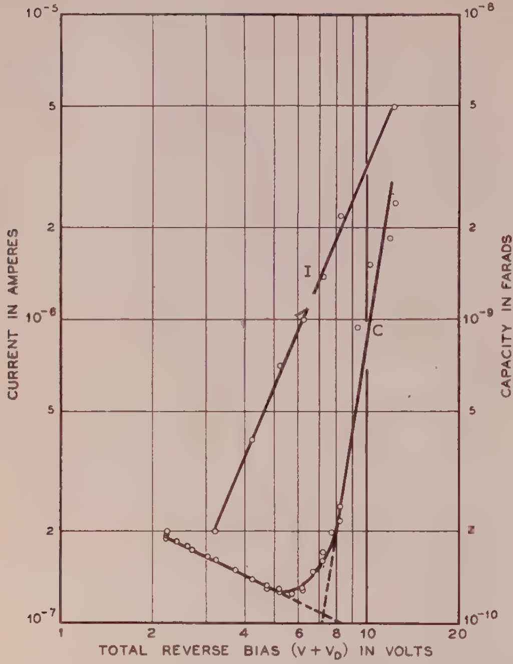

FIG. 6. Reverse current and capacity of a slowly alloyed diode as a function of total bias.

essentially a measure of the band-gap energy but may lie somewhat below this value. Equating the upper value of this cluster of points with the band gap 2.2 v requires that n be 2.0±0.1. (The lowest value in the group is then 1.9 v.) The capacities of the diffused diodes, therefore, fall off inversely as the square root of the bias, so that they, as well as the alloyed diodes, are characterized by step junctions. The depletion layer widths determined for zero external bias fell between 150 and 2000 A, with the diffused diodes corresponding to the widest junctions. These widths correspond to a total donor (or acceptor) concentration of 10^{15} to 10^{18} cm^{-3} for a step junction, the lower values corresponding to the diffused structures. If it is assumed that the diffused sides of the junction in the case of the diffused diodes, or the regrowth-layer sides in the case of the alloyed diodes, were the more heavily doped sides, then the measured widths and the concentrations determined from them are properties of the base sides of the junctions, i.e., they correspond to the material before diode fabrication. For the alloyed junctions the total donor or acceptor density indicated, agrees within an order of magnitude with the results of Hall effect measurements on the undoped crystals.[11] The values deduced for the diffused diodes, however, fall one to two orders of magnitude beneath the Hall values.

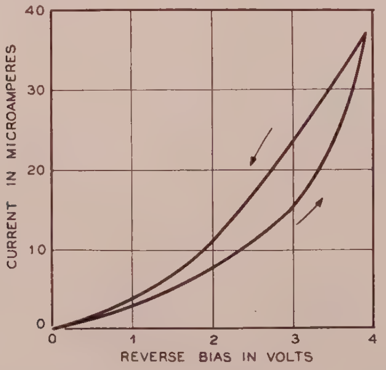

FIG. 7. Hysteresis of the reverse current of a rapidly alloyed diode. Tracing time: 1 minute.

The anomalous rise in capacity was most prominent in the rapidly alloyed diodes, where it commenced at very low reverse bias. The thresholds lay well below the breakdown region. Neither the reverse current nor its first derivative exhibited any discontinuity at this threshold as seen in Fig. 6. While the normal transition region capacity was independent of frequency, the anomalous component was not; the threshold moved to lower bias as the frequency of measurement decreased. The threshold behaved similarly as the temperature was increased.

C. Transient Behavior of the Current-Voltage Characteristic

When an abrupt change in bias was made on any of the diodes, the current decayed to its new steady-state value in a period of up to a minute. These slow recovery times were most prominent in the case of the rapidly alloyed diodes, as exhibited by the hysteresis in the current-reverse voltage curve traced in Fig. 7. Figure 8 is an oscilloscopic presentation of the reverse characteristic of a rapidly alloyed diode at 60 cps, upon which a dc bias has been superimposed. Upon abruptly reversing the polarity of the dc component, the trace decayed to curve b in a matter of half a minute.

D. Reverse Bias Electroluminescence

Light emission in the reverse direction was observed in the diffused diodes and in the alloyed diodes, both above and below breakdown. The spectra were al identical, exhibiting a single broad maximum a photon energies just below the band gap and slowl dropping off in both directions as seen in Fig. 9. Th short wavelength cutoff is due to the band-edg absorption of gallium phosphide.[15] The shoulder is du to the transition from absorption to the indirect edg to absorption to the $k=0$ conduction band minimum. In the alloyed diodes whose metallic contacts had bee etched back, absorption occurred only in the regrowt layer whose thickness ($\sim 1\ \mu$) was obtained by assumin that the cutoff was due only to the known bulk absorption. Because of the rapid variation of the absorption coefficient with wavelength near the edge it was difficult to establish the wavelength dependence of the emission with any accuracy in this region, except to note that it was not changing very rapidly.

---

[15] W. G. Spitzer, M. Gershenzon, C. J. Frosch, and D. F. Gibb J. Phys. Chem. Solids 11, 339 (1959).

Although the photon energy distribution was not a function of the current, the dependence of the total light yield upon the junction current exhibited a singularity at a current which was identified from the current-voltage characteristics with reverse breakdown. (See Fig. 10.)

The light emitted by the diffused diodes biased above breakdown originated from small spots lying near the junction. The spots were all less than 10 000 A in size, the resolution of the microscope through which they were observed, and they appeared one by one as the bias was increased. Near breakdown the individual intensities appeared to be invariant to bias changes, and an increase in current corresponded to an increase in the number of light-emitting spots. In this range, the total breakdown current divided by the number of visible spots was roughly constant and equivalent to about 100 μa per spot. The total light yield was always linear in current between 80° and 300°K as shown in Fig. 10. Just above breakdown the light output varied directly with the number of visible light spots which in turn was linearly related to the total current. At higher current, although the total radiative yield remained linear with current, the intensities of the individual spots began to increase. The density of spots per unit junction area was greatest near the intersection of the junction with either a surface or a grain boundary. Although radiation emitted during forward bias was always sharply situated at the junction, the reverse breakdown spots were distributed over a range starting at the junction and extending toward the less heavily doped side of the junction, as seen in Fig. 1. The total visible radiation actually leaving the sample under these conditions of bias indicated an over-all photon yield of 10^{-5} to 10^{-7} per injected carrier, with a decay time of less than 1.5×10^{-8} sec, the limit of detectibility. A decay time of about a third this value has been measured by Allen and Gibbons.[8]

The light emission accompanying breakdown in the alloyed diodes originated in small irregular areas, larger in size than in the previous case. The intensity of each area increased with bias even near breakdown and the total light yield depended superlinearly upon the breakdown current.

Below breakdown in either the diffused or the alloyed diodes the total light output varied as the first to the third power of the current as shown in Fig. 10. Its spectrum was identical with those discussed above, but light emission was too feeble to permit detailed microscopic examinations as in the previous cases.

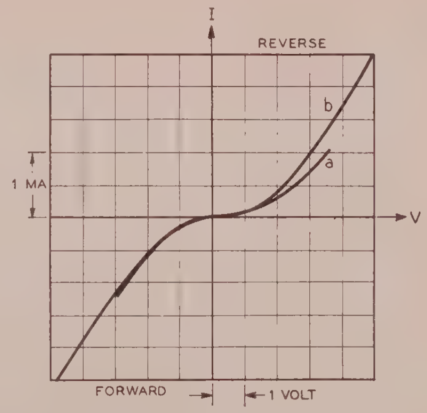

Fig. 8. Transient behavior of a rapidly alloyed diode. (a) Forward dc bias; (b) reverse dc bias.

E. Forward Bias Electroluminescence

Light emission at forward bias was always observed in the diffused diodes but never in the case of the alloyed structures. Two spectral bands were always present, one in the green and one in the red as shown in Fig. 11, where the intensities have been normalized relative to the red peak. The red band became more efficient at lower temperatures. In the temperature range investigated, 80° to 300°K, the green band fell always 0.04 ev below the band gap and its half-width was always

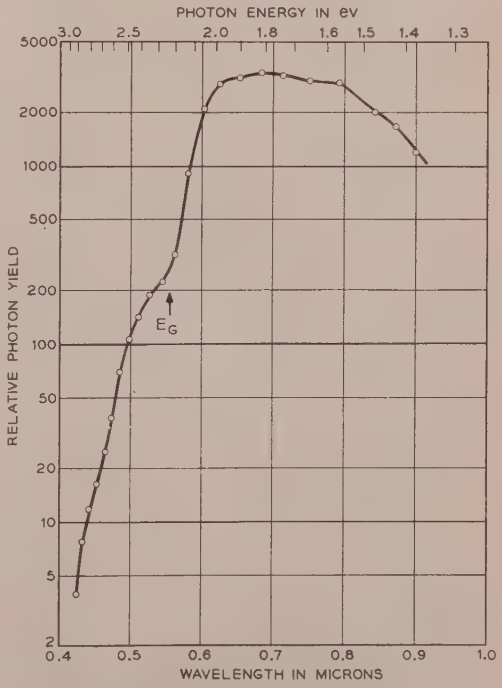

Fig. 9. Electroluminescence spectrum of a slowly alloyed diode above breakdown at 300°K.

Table II. Photon energies and bandwidths of forward bias luminescence compared with the energy gap.[1] Energies in ev.

		Band-to-band			Via centers		
T °K	E_G	$h\nu$	$E_G-h\nu$	Width	$h\nu$	$E_G-h\nu$	Width
300	2.25	2.21	0.04	0.08	1.83	0.42	0.20
200	2.30	2.27	0.03	~0.06	1.90	0.40	0.20
80	2.36	~2.30	~0.06	?	1.96	0.40	0.20

approximately 3 kT. (See Table II.) Its quantum efficiency was 10^{-6} to 10^{-8} per injected carrier, based only on the light actually leaving the sample. The light output varied quadratically with current at the lower biases but approached linearity at higher injection levels and before sample heating became appreciable, as shown in Fig. 12.

The red band fell about 0.4 ev below the band gap and was usually about 0.2 ev wide independent of temperature, as indicated in Table II. Small spectral shifts of about 0.02 ev have been observed in both the peak and the half-width as a function of bias, with the peak moving toward shorter wavelengths with increasing bias. Variations of up to 0.05 ev in the position of the peak have been noted for different samples. Despite the reports in the literature indicating that this peak may extend into the infrared,[2,4] careful observations with the cooled PbS cell offered no trace of any further emission out to 2 μ. The red peak was observed in junctions prepared by diffusing cadmium, as well as in the zinc-diffused diodes. Its over-all quantum efficiency at room temperature ranged from 10^{-4} to 10^{-6} and its decay was about 2×10^{-8} sec. The photon yield was linear with current at the lower temperatures and became superlinear above room temperature. It sometimes exhibited complete saturation at biases where the green band was still in the quadratic region.

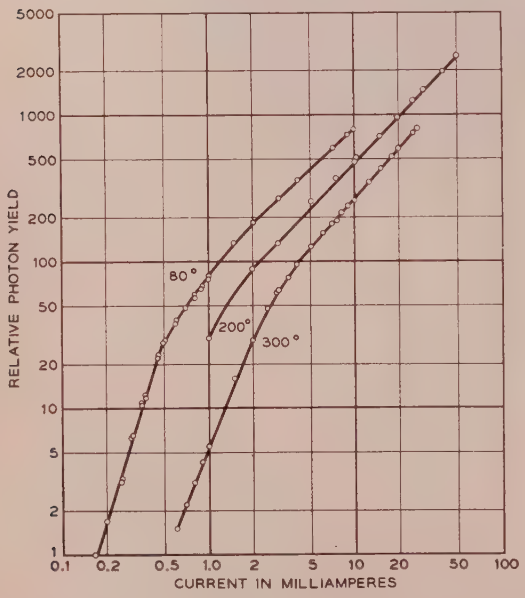

Fig. 10. The current dependence of the reverse bias radiation from a diffused diode both below and above breakdown at three temperatures.

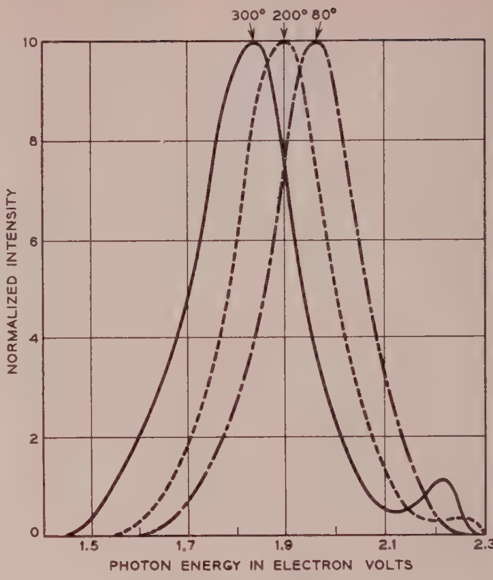

Fig. 11. Normalized spectra of radiation emitted by a diffused diode at forward bias.

DISCUSSION

The electrical behavior of the diodes clearly indicates gross deviations from the ideal Shockley junction.[16] Although each GaP diode exhibited all the deviations described here, it is possible to correlate the major departures from ideality with the method of junction fabrication. Thus, the series junction resistance is the dominant characteristic of the diffused structures, while the excess reverse and forward currents, the anomalous capacity and the hysteresis effects are peculiar to the rapidly alloyed diodes. The slowly alloyed junctions, presumably due to the small amount of inevitable diffusion, from a class whose behavior bridges the other two groups.

A. Diode Anomalies

1. Rapidly Alloyed Diodes

From photoconductivity and photoluminescence data,[17] from the presence of the extrinsic electroluminescence discussed below, and from an analysis of the compensation levels deduced from Hall measurements,[1] it has been demonstrated that the GaP crystals used in the preparation of the diodes contained 10^{15} to 10^{1}

---

[16] W. Shockley, Bell System Tech. J. 28, 435 (1949).

[17] L. F. Johnson (private communication).

deep centers per cm^3 at a number of energies. The presence of such centers in the transition region of a p-n junction should lead to departures from the ideal diode characteristics in both the forward and the reverse currents due to recombination and thermal generation, respectively, at these centers.[18] The observed deviations are in the correct directions. The oppositely directed flow of electrons and holes across the depletion layer at reverse bias may lead to a voltage dependent, steady-state separation of charge, i.e., a frequency dependent capacity in parallel with the normal depletion layer capacity. This is presumably the observed excess capacity. When the bias is altered abruptly, the potential distribution at the junction and hence the quasi-Fermi levels must change. Since the latter determine the occupancy of the deep-lying levels, these populations must be redistributed. However, this can be done only with the relaxation times characteristic of the levels themselves. These may be relatively long[17] and hence can give rise to the transient effects and hysteresis loops observed in the measured current-voltage characteristics.

2. *Diffused Diodes*

The second type of anomalous behavior is exemplified by the presence of the series resistance, which is most predominant in the diffused diodes. This is attributed to the presence at the junction of a compensated layer of high resistivity which arises because the diffusion is performed at temperatures well below the onset of intrinsic conduction in the gallium phosphide crystal, where both the solubility and the effective diffusion constant are enhanced before the carrier type becomes inverted by the diffusing species,[19] and where the large numbers of deep donors and acceptors can themselves lead to a compensated region in the diffusion tail. This resistive layer appears only when the diffusion leads to an inversion of carrier type. It occurs only in the immediate vicinity of the junction. It was noted that while the total donor or acceptor concentration deduced from the measured capacities at reverse bias agreed with those determined from Hall measurements in the case of the alloyed diodes, the results were one to two orders of magnitude below the Hall densities deduced for the diffused diodes. Since the depletion layer lies in the compensated region, the capacity data measure the difference between the original total donor concentration and the density of diffused acceptors, while the Hall results give only the original density of donors. Thus, in the region of the depletion layer, the donors have been compensated to within 1 to 10%.

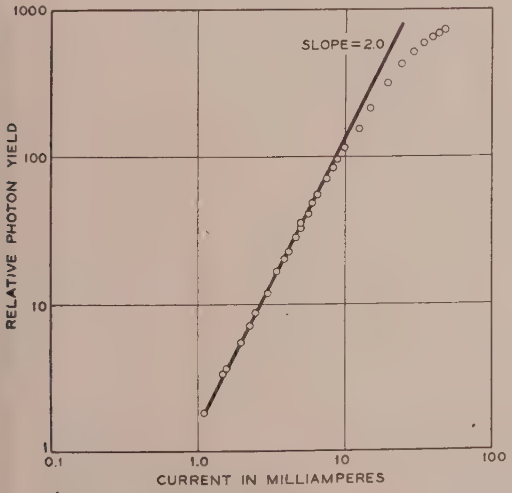

FIG. 12. The dependence of the peak intensity of the band-to-band recombination radiation upon junction current at 300°K.

From the temperature dependence of the resistance of this layer, an ionization energy of approximately 0.07 ev is deduced, provided that it is assumed that the region of the sample giving rise to this resistance is compensated and that in the temperature range measured the resistivity is far more sensitive to the ionization of donors or acceptors than to any variations in mobility. This measured ionization energy is consistent with that characteristic of the donor in the undiffused material as determined from Hall measurements, 0.08 ev.[11] Therefore, in accord with the diffusion model the compensated layer remains n type. Since the voltage dependence of the capacity indicated that the junction was a step junction even in the case of the diffused diodes, the difference between total donor and acceptor concentrations must have been approximately constant in the experimentally observed range of the depletion layer. This range was limited by the onset of the excess capacity component. In terms of distance from the junction, the density difference was constant starting from 1000 to 2000 A (the depletion layer without external bias) to up to about twice this distance (the width corresponding to swamping by the excess capacity).

It is thus possible to assign models which qualitatively predict the correct behavior of the two classes of diodes. These models will now be used to discuss the observed electroluminescence. The radiation emitted at reverse bias is considered first and distinctions are drawn between the light emitted below breakdown in all diodes, that emitted above breakdown by the diffused diodes, and that corresponding to the alloyed diodes. Finally, the forward bias luminescence of the diffused diodes is considered.

B. Reverse Bias Luminescence

The spectra of the reverse bias luminescence characteristic of all the diodes, both above and below breakdown, were identical, indicating that although the mechanism for the excitation of carriers may be different in each case, the radiative emission step was always the same. The spectral distribution in the present case is peaked below the band gap, although the geometries used led to strong reabsorption of photons that may have been generated with energies above the band gap. Two processes may be considered. In the first, the field accelerated carriers lose energy by intraband, radiative relaxation processes. For this process photon energies from thermal energies up to the pair production threshold are possible. In the second process, interband radiative recombination of energetic carriers may occur via the center responsible for the red band at forward bias. A spectrum from 1.80 ev to the sum of the pair production threshold and 1.80 ev is expected. Since the experiments give no indication of any inflection near 1.80 ev it is inferred that the first mechanism dominates and any radiation above the band gap is masked by the band-edge absorption. Because of this absorption, it is difficult to ascertain whether any other processes producing photons of larger than band-gap energy become important at the shorter wavelengths.

---

[18] C. T. Sah, R. N. Noyce, and W. Shockley, Proc. I. R. E. 45, 1228 (1957).

[19] C. S. Fuller, *Semiconductors*, edited by N. B. Hannay (Reinhold Publishing Corporation, New York, 1959), p. 192 ff.

1. *Avalanche Breakdown*

The avalanche breakdown mechanism is invoked to account for reverse breakdown in the diffused diodes exhibiting the high breakdown potentials. The observed breakdown characteristic is hard and the breakdown fields obtained by extrapolating the depletion layer width through the region of the excess capacity to the breakdown potential are 10^5 to 5×10^6 v-cm^{-1}. The small spots of light are compared with the discrete microplasmas studied in silicon.[20] As they are in silicon, these spots are less than 10 000 A in size, they are concentrated near surfaces or crystal defects,[21] and they appear and disappear reproducibly with voltage.[7,8,20] The total light yield near breakdown is linearly proportional to the number of microplasmas. If all the current is channeled through the visible microplasmas, each spot is equivalent to about 100 μa. In silicon this figure has been variously reported between 25 and 100 μa.[20,22] At potentials well above breakdown, the total light emission increases without the formation of new spots. However, the total light intensity remains a linear function of the total current as it does in silicon.[23] The observed spectrum is almost independent of temperature as it is in silicon[20] because the carrier temperatures far exceed the normal lattice temperatures in both materials. The breakdown noise previously reported in GaP diodes[7,8] is also characteristic of avalanche breakdown.[24]

2. *Zener Breakdown*

The breakdown mechanism to be associated with the alloyed diodes must be altogether different. Since the junctions are narrow, internal field emission may become significant before the bias is large enough to cause avalanche breakdown.[25] Unlike the previous case, the breakdown is now relatively soft and the light is emitted from large areas whose brightness is dependent upon current. Since the crystal structure and alignment of the regrowth layers associated with the alloyed diodes, and particularly with those alloyed rapidly, is not uniform, the space charge field in turn may not be homogeneous. Hence, breakdown will occur at specific regions of greatest field intensity-the areas from which the light originates. The tunneling probability varies as $\exp(\alpha-\beta/E)$, where E is the field strength.[25] The parameter β which is predicted from the band gap (2.2 ev) and the effective mass ratio (~1) is $\sim10^8$ v-cm^{-1}. It may be determined experimentally from the slope of a log-log plot of current vs voltage above breakdown combined with the value of the breakdown field, provided the dependence of the field upon the bias is known.[26] The latter is known from the fact that the diode behaves as a step junction and the breakdown fields have been evaluated previously. Thus, from the current-voltage characteristic of the alloyed diodes above breakdown the parameter β has been determined as $1-3\times10^8$ v-cm^{-1}, in good agreement with the predicted value.

3. *Prebreakdown Emission*

Below breakdown a third carrier excitation mechanism must be invoked because the dependence of light emission upon bias changed abruptly at breakdown in both classes of diodes. The thermal generation of carriers at the deep centers within the depletion layer, which has already been proposed to account for one of the classes of diode anomalies, provides the free carriers which are excited by the field and these thereupon decay radiatively in the manner discussed above. It has not been possible so far to verify that the light is emitted uniformly over the entire junction area as the model presupposes. Thus localized prebreakdown processes are not ruled out.[23] The change in bias dependence at breakdown may be associated with the rapid variation of the quasi-Fermi levels. Below this threshold, the strong dependence of the light upon the current suggests that nonradiative relaxation is far more important at lower bias.

---

[20] A. G. Chynoweth and K. G. McKay, Phys. Rev. **102**, 369 (1956).

[21] A. G. Chynoweth and G. L. Pearson, J. Appl. Phys. **29**, 1103 (1958).

[22] K. S. Champlin, J. Appl. Phys. **30**, 1039 (1959).

[23] A. G. Chynoweth and K. G. McKay, J. Appl. Phys. **30**, 1811 (1959).

[24] A. G. Chynoweth and K. G. McKay, Phys. Rev. **106**, 418 (1957).

[25] A. G. Chynoweth, *Progress in Semiconductors* (John Wiley & Sons, Inc., New York, 1960), Vol. 4, p. 97.

[26] K. B. McAfee, E. J. Ryder, W. Shockley, and M. Sparks, Phys. Rev. **83**, 650 (1951).

C. Forward Bias Luminescence

The radiation emitted at forward bias is seen only in the diffused specimens. Since the compensated layer is the feature which distinguishes the diffused diodes, it is concluded that the presence of this layer is in some way a necessary condition for luminescence at forward bias. Its effect may be twofold. First, the minority carrier lifetime is enhanced resulting in an increased luminescent efficiency. Second, the Fermi level lies deep in the forbidden gap so that the populations of the deep centers which may participate in the luminescent processes are altered significantly from those in an uncompensated region.

1. Band-to-Band Recombination

The green band lies so close to the reported band edge that it must be identified with the band-to-band recombination which is optically active in other semiconductors.[27] It has been so identified by Loebner from a detailed-balance analysis.[5] Its energy is too low for it to result from the direct transition involving no net change in crystal momentum. It is therefore associated with the recombination of a hole with an electron from the (100) minimum which is probably the lowest conduction band minimum in GaP.[28] This process must involve the simultaneous emission or absorption of phonons. The phonon spectrum in GaP encompasses the energy range 0.008 to 0.047 ev and multiphonon processes have been reported with energies of 0.05 to 0.10 ev.[29] Since the green peak persists at 80°K where the thermal distribution of these phonons is severely attenuated, the luminescent process must involve the emission rather than the absorption of phonons. The required phonon energies are obtained by subtracting the observed photon energy at the radiation maximum from the energy difference between an electron and a hole, each possessing their mean thermal energy $3/2\ kT$.[30] The phonon energies deduced are 0.06 to 0.07 ev using Spitzer's value of the band gap (2.20 ev)[15] and 0.11 to 0.12 ev using Folberth's value (2.25 ev).[1] Such phonons are included in the phonon spectrum of GaP,[29] but they are about twice as energetic as those deduced by Loebner from analysis of the absorption edge.[5]

The width of the green peak should be $\sim 3\ kT$ reflecting the thermal distribution of carriers before recombination. The measured half-width at 300°K is 0.08 ev where $3\ kT$ is 0.078 ev, and at 200° $3\ kT$ is 0.051 ev where ~ 0.06 ev is measured.

The fact that the intensity of the green peak depends quadratically upon current over a wide range has been noted by Loebner[5] and is evidence that the recombination obeys second-order kinetics. However, at higher injection levels the dependence approaches linearity. It is suggested that at small forward bias the recombination occurs within the depletion layer which is still present. To maintain space charge neutrality a majority carrier must re-enter the depletion layer for each minority carrier injected. Since the rate of recombination depends upon the product of majority and minority carriers present and since the injected minority carriers are directly related to the current, the recombination rate should depend upon the square of the current as is observed. As the forward bias increases, however, the depletion layer becomes narrower, so that if the minority carrier diffusion length remains constant, the recombination process will begin to occur outside the space charge region. Because of the large densities of majority carriers there, the kinetics become first order. For this mechanism to account for the observed change in the light intensity-current relationship, the depletion layer width at moderate forward bias must equal the diffusion length. The width of the space charge layer at zero bias has been given as 1000–2000 A for the diffused structures. Utilizing the Einstein-Nernst relation and the previously reported electron mobility-110 $\mathrm{cm}^2\ V^{-1}\ \mathrm{sec}^{-1}$,[11] a diffusion constant of $\sim 2\ \mathrm{cm}^2\ \mathrm{sec}^{-1}$ is obtained. For the diffusion length to match the depletion layer width requires a minority carrier lifetime of $\sim 10^{-10}$ sec, which as will be seen is not unlikely.

Although the energy balance calculation to obtain the phonon energies implicitly ignored the participation of excitons in the recombination mechanism, exciton processes are in no way ruled out by the experimental data as indeed they seem to be involved in the recombination process in other semiconductors.[31]

2. Recombination through Centers

The energies of the photons appearing in the red band always fall ~ 0.4 ev below the band gap, indicating that a radiative recombination center lying 0.4 ev from one of the band edges is involved. Since the recombination occurs in the n-type compensated layer the mechanism must involve the capture of an injected hole by a filled electron trap. Since the layer is heavily compensated but not quite intrinsic, the Fermi level lies deep in the forbidden gap but remains above the radiative center. The center is then always occupied while the shallow donor levels are substantially empty.

If the measured decay time is identified with the lifetime of some intermediate step in the recombination process, then, since saturation has been observed in some cases as mentioned earlier, the density of centers can be calculated from the saturation current, the radiative efficiency, and the volume in which recombination occurs—the product of the junction area and the diffusion length which was estimated earlier. A density of about 5×10^{13} per cc which seems unreasonably small is obtained.

---

[27] T. S. Moss, *Optical Properties of Semiconductors* (Academic Press, Inc., New York, 1959), Chap. 6.

[28] A. L. Edwards, T. E. Slykhouse, and H. G. Drickamer, J. Phys. Chem. Solids **11**, 140 (1959).

[29] D. A. Kleinman and W. G. Spitzer, Phys. Rev. **118**, 110 (1960).

[30] J. R. Haynes and W. C. Westphal, Phys. Rev. **102**, 1676 (1956).

[31] J. R. Haynes, M. Lax, and W. F. Flood, J. Phys. Chem. Solids **8**, 394 (1959).

The identity of this center has not been established. A red band in the electroluminescence spectrum of GaP has previously been associated with copper,[4] with zinc[2] and with a vacancy.[6] In the present investigation, the red band appeared in junctions prepared both by zinc and by cadmium diffusion into *n*-type material. Moreover, the band could not be identified with photoluminescent peaks characteristic of samples heavily doped with zinc, or cadmium, or copper.[17] However, it could be associated with a red band appearing in the photoluminescence spectrum of many undoped crystals.[17] It must be concluded, therefore, that the center responsible for the red band in electroluminescence is present in the gallium phosphide before the diodes are fabricated, and may be associated with a vacancy since its photoluminescence counterpart is enhanced by the presence of excess Ga.[17]

The large width of this band 0.20 ev, independent of temperature, deserves attention. If it were due to a strain-induced distribution of levels arising from a single center it is not immediately obvious why the band edges themselves should not be diffuse, resulting also in an increase in the width of the band-to-band recombination peak. The latter shows only the expected thermal widths. If the center is a structure whose energy is related to its exact constitution or configuration, such as in a cluster, and if the energy separations of the individual levels are within the resolution of the spectrometer, such a wide band might be observed. The specific distribution of such centers and the position of the quasi-Fermi levels would then determine the exact shape of the emission band. As was noted earlier, shifts in both width and peak intensity with bias and from sample to sample were noted. The red band described by Wolff[2] and by Loebner,[4] possessed a sizable fraction of its energy in the wavelength region between 1 and $2\,\mu$. Careful search in the present investigation revealed no trace of any emission in this region. Most of the diodes used here, however, were prepared from crystals grown from a near-stoichiometric melt,[9] whereas those used by the former investigators were grown from gallium-rich melts. The red band reported by Grimmeis and Kohlmans is intermediate in wavelength as are correspondingly the crystal growth conditions.[6]

The red band is thus attributed to recombination at a set of centers whose total density in the crystal is 10^{13} to 10^{14} cc^{-1} and whose distribution as a function of energy is determined by the stoichiometry or the growth conditions of the crystals which were subsequently used to fabricate the diodes.

SUMMARY

The principal conclusions drawn are:

(1) The rapidly alloyed diodes exhibit anomalies due to the presence of deep-lying centers in the depletion layer, which result in recombination at forward bias and thermal generation in the reverse direction. The latter leads to an excess junction capacity component and to hysteresis in the current-voltage characteristic.

(2) The diffused diodes contain a compensated region near the junction which adds a series resistance term and results also in a step junction.

(3) At reverse bias radiative intraband relaxation is observed for three cases:

(a) Avalanche breakdown in the diffused diodes.
(b) Breakdown by internal field emission in the narrow alloyed junctions.
(c) Below breakdown, where the carriers are thermally generated within the depletion layer.

(4) Luminescence at forward bias appears only in the diffused structures. It is attributed to the nearly intrinsic layer and consists of:

(a) Band-to-band recombination with simultaneous phonon emission. The kinetics depend upon the location of the recombination process.
(b) Extrinsic radiation due to recombination via a deep-lying level which was not added intentionally.

ACKNOWLEDGMENTS

The authors are indebted to C. J. Frosch and L. Derick for preparing most of the crystals and to W. S. Boyle, A. G. Chynoweth, C. J. Frosch, D. F. Gibbs, J. R. Haynes, L. F. Johnson, D. A. Kleinman and D. F. Nelson for many fruitful discussions.

JOURNAL OF APPLIED PHYSICS VOLUME 32, NUMBER 7 JULY, 1961

Propagation in Periodic Electron Beams

W. M. Mueller
Microwave Tube Division, Hughes Aircraft Company, Los Angeles, California

(Received December 12, 1960)

A small-signal analysis of smooth electron beams with periodic variations in their dc parameters reveals the existence of infinite sets of space harmonics of the fast and slow space-charge waves. For a finite beam coupling between the space-charge waves and field waves exists at an infinite number of frequencies. The periodicity of a beam has a very small effect on the space-charge wave propagation constants. Velocity-jump, rippled-stream, and rippled-wall amplification are shown to result from coupling between fast and slow space-charge waves of adjacent harmonics. The periodicity of an electron beam will have negligible effect on most conventional traveling-wave devices. Although the frequency dependence of the amplitudes of the beam harmonics may introduce difficulties in some devices, this dependency may also be made use of in a variety of ways. Beam harmonics make millimeter-wave interactions possible in smooth circuits, but practical devices at these frequencies will probably be limited to those employing positional periodicity of the beam.

I. INTRODUCTION

With the advent of electronic devices making use of transit-time and velocity-modulation effects, attention was focused on the problem of analyzing the electromagnetic wave behavior of electron streams under small-signal conditions. Since the now-familiar analyses of Hahn[1] and Ramo[2] which revealed the existence of the pair of space-charge waves, a number of other writers have investigated propagation in drifting beams flowing in infinite, finite, and zero magnetic fields.

Consideration of nondrifting beams began with studies of accelerated beams.[3–6] During the course of one of these studies,[4] the velocity-jump amplifier was discovered. It led eventually to other forms of what might be called the reduced plasma-wave number-jump amplifier.[7]

The periodic nature of the beams used in these amplifiers and the application of periodic focusing to traveling-wave devices suggested studies of wave propagation on periodic beams. Bloom, Peter, and Ruetz[8,9] formulated the transmission-line analog and recognized the filter properties of such beams. Their work was followed by that of Agdur and Rydbeck,[10] whose determination of the conditions for space-charge wave gain and expressions for maximum gain have been verified experimentally by Mihran.[11]

Periodicity of an electron beam suggests the existence of space harmonics corresponding to the space harmonics of other periodic wave-propagating structures. A number of authors[12–22] have shown theoretically that these waves should exist, and experimental verification of their existence has been reported.[21,22] It is the purpose of this paper to display in rigorous fashion the space harmonics which exist in periodic beams and to discuss the consequences of their existence in practical beam-type devices.

II. SMALL-SIGNAL EQUATION FOR ARBITRARY VELOCITY VARIATION

Appendix A contains the details of a small-signal analysis of a cylindrical beam constrained by an infinite magnetic field to flow in the axial direction. Essential to this analysis are the restrictions that dc quantities are assumed to be uniform over any cross section of the beam; however, no restriction is placed on the axial variation of these quantities.

The result of this analysis is an expression for the ac radial magnetic field for modes of any number of circumferential variations. For the case of most general interest, that of no circumferential variations of ac quantities, the ac radial magnetic field is zero. However, the ac circumferential magnetic field exists, and if separation of variables is assumed, the solution for this field is

---

[1] W. C. Hahn, Gen. Elec. Rev. **42**, 258–270 (1939).

[2] S. R. Ramo, Phys. Rev. **56**, 276–283 (1939).

[3] L. D. Smullin, J. Appl. Phys. **22**, 1496–1499 (1951).

[4] L. M. Field, P. K. Tien, and D. A. Watkins, Proc. I.R.E. **39**, 194 (1951).

[5] R. Müller, Arch. Elektrischen. Übertragung **9**, 505–512 (1955).

[6] P. Parzen, J. Appl. Phys. **23**, 215–219 (1952).

[7] C. K. Birdsall, Tech. Memo No. 346, Electron Tube Laboratory, Hughes Aircraft Company (1954).

[8] S. Bloom and R. W. Peter, RCA Rev. **15**, 95–112 (1954).

[9] S. Bloom, R. W. Peter, and J. A. Ruetz, RCA Rev. **15**, 113–120 (1954).

[10] B. Agdur and O. E. H. Rydbeck, L'Onde elec. **34**, 499–507 (1954).

[11] T. G. Mihran, IRE Trans. on Electron Devices **ED-3**, 32–39 (1956).

[12] H. Kleinwächter, Elektrotech. Z. **72**, 714–717 (1951).

[13] H. Kleinwächter, Arch. Elektrischen. Übertragung **6**, 376–378 (1952).

[14] W. Beaver, Varian Associates (1954, unpublished).

[15] R. Müller, Arch. Elektrischen. Übertragung **10**, 505–511 (1956).

[16] P. V. Bliokh and Ya. B. Fainberg, Soviet Phys.–Tech. Phys. **1**, 510–516 (1956).

[17] P. V. Bliokh, Radiotekh. i Elektron. **2**, 92–103 (1957).

[18] G. A. Bernashevskii, Radiotekh. i Elektron. **2**, 124–125 (1957).

[19] W. M. Mueller, Ph. D. thesis in Electrical Engineering, University of California, Berkeley, California (1958), pp. 144–167.

[20] R. Müller, *Proceedings of the Symposium on Electronic Waveguides* (Polytechnic Press, Brooklyn, New York, 1958), pp. 353–365.

[21] W. M. Mueller and A. Staprans, "Propagation in periodic electron beams," Sixteenth Annual Electron Tube Research Conference, Quebec, Canada, June 27, 1958.

[22] A. Staprans, Univ. Calif. Electronics Research Lab. Rept. Ser. **60**, issue 225 (June, 1959).

$$H_{\theta 1}=J_1(Kr)G(z), \tag{A.34}$$

where K is the radial propagation constant and $G(z)$ is given by

$$K^2=\frac{[1+(\partial/\partial z)(\beta_p{}^2)^{-1}(\partial/\partial z)]\exp\left[j\int(\omega/v_z)dz\right][k^2+(\partial^2/\partial z^2)]G(z)}{(\partial/\partial z)(\beta_p{}^2)^{-1}(\partial/\partial z)\exp\left[j\int(\omega/v_z)dz\right]G(z)}. \tag{A.32}$$

Here k is the wave number associated with the velocity of light and β_p is the plasma wave number of the electron stream. The modes of propagation can be found for a given velocity variation by assuming a particular value of K and solving this last equation.

III. INFINITE BEAM

Equation (A.32) can be solved conveniently only when $K=0$; i.e., for an infinite beam. In this case $H_{\theta 1}$ is zero, and the only component of the field which exists is E_{z1}, which can be shown from Eq. (A.11) to be identical to $k^2+(\partial^2/\partial z^2)G(z)$. For this case the definition

$$P_zG(z)\equiv\exp\left[-j\int(\omega/v_z)dz\right]\mathcal{H}(z), \tag{1}$$

where

$$P_z=k^2+(\partial^2/\partial z^2), \tag{A.19}$$

is convenient, reducing Eq. (A.32) to

$$[1+(d/dz)(\beta_p{}^2)^{-1}(d/dz)]\mathcal{H}=0. \tag{2}$$

which is the same as the equation obtained by Smullin from a one-dimensional analysis.[3]

Equation (2) may be integrated if $\mathcal{H}$ is defined by

$$\mathcal{H}=(d/dz)\phi_1, \tag{3}$$

the result being

$$(d^2\phi_1/dz^2)+\beta_p{}^2(\phi_1+C_1)=0, \tag{4}$$

where C_1 is an arbitrary constant. On defining

$$\phi_1+C_1=\phi, \tag{5}$$

Eq. (4) reduces to the very simple form

$$(d^2\phi/dz^2)+\beta_p{}^2\phi=0. \tag{6}$$

While the assumption of an infinite magnetic field and the restriction on the variation of dc quantities in the transverse directions which led to this last equation are unrealistic, meaningful conclusions may still be drawn from it and Eq. (1). Certainly the general character of periodic beams may be extracted from the present analysis.

When $\beta_p{}^2$ can be expressed as

$$\beta_p{}^2=\alpha+\gamma f(z), \tag{7}$$

where $f(z)$ is an arbitrary periodic function of z, Eq. (6) assumes the standard form of Hill's equation:

$$(d^2\phi/dz^2)+[\alpha+\gamma f(z)]\phi=0. \tag{8}$$

This equation has been studied extensively and the following conclusion set down.[23]

When $f(z)$ is a real periodic function with period 2π, twice differentiable, and with

$$\int_0^{2\pi}f(z)dz=0, \tag{9}$$

the general solution of Eq. (8) is of the form

$$\phi=K_1e^{\mu z}F(z)+K_2e^{-\mu z}F(-z), \tag{10}$$

where K_1 and K_2 are arbitrary constants, $F(z)$ is a periodic function with period 2π, and μ is purely real, purely imaginary, or complex depending upon the relationship existing between α and γ. Plotting α vs γ allows the definition of eight regions, as shown in Fig. 1.

Since $\beta_p{}^2$ may never be negative for electron beams, the following restrictions must be met by α:

$$\alpha\geqq\gamma|f(z)\text{ min}|\quad\text{for}\quad\gamma>0 \tag{11}$$

$$\alpha\geqq-\gamma|f(z)\text{ max}|\quad\text{for}\quad\gamma<0. \tag{12}$$

Thus all of the possible combinations of α and γ lie in regions Ia and IVa of Fig. 1. In these regions μ generally is purely imaginary, but there are narrow bands which go out from the points $\alpha=n^2$, n being an integer, on the positive α axis in which μ may be complex or purely real. The existence of these bands implies the possibility of gain due to periodic variation of $\beta_p{}^2$.

Space harmonics in the periodic beam are revealed by the form of Eq. (10). Since $F(z)$ is a periodic function with the same period as $\beta_p{}^2$, it may be written as

$$F(z)=\text{Re}\sum_{n=-\infty}^{\infty}a_n\exp\left(j\frac{2n\pi z}{d}\right), \qquad (13$$

where the a_n are real constants and d is the period o $\beta_p{}^2$. Now, if

$$\mu=j\mu_1, \qquad (14$$

---

[23] M. J. O. Strutt, Math. Ann. **101**, 559–569 (1929).

can be expressed as

$$= \mathrm{Re}\left\{K_1 \sum_{n=-\infty}^{\infty} a_n \exp\left[j\left(\mu_1+\frac{2\pi n}{d}\right)z\right]\right.$$

$$\left. + K_2 \sum_{n=-\infty}^{\infty} a_n \exp\left[-j\left(\mu_1+\frac{2\pi n}{d}\right)z\right]\right\}. \quad (15)$$

More harmonics are revealed when a solution is ought for Eq. (1). It has been pointed out[22] that the actor $\exp[-j\int(\omega/v_z)dz]$ can be expanded as

$$\mathrm{xp}\left(-j\int\frac{\omega}{v_z}dz\right)$$

$$= \sum_{m=-\infty}^{\infty} b_m \exp\left[-j\left(\beta_{e0}+\frac{2\pi m}{d_1}\right)z\right], \quad (16)$$

vhere $\beta_{e0}=\omega/v_{z0}$, v_{z0} being the average velocity, the $_m$ are constants, and d_1 is the period of the velocity ariation. In the present mathematical stream

$$\beta_p^2 = -\eta I/\epsilon v_z^3, \quad (17)$$

vhere I is the current density. The period of the ariation in β_p^2 will, therefore, be the same as that of he variation in v_z so that $d_1=d$.

The constants b_m can be found from the Fourier ntegral, and are

$$_m = \frac{1}{d}\int_{-d/2}^{d/2} \exp\left(-j\int\frac{\omega}{v_z}dz\right)$$

$$\times \exp\left[j\left(\beta_{e0}+\frac{2\pi m}{d}\right)z\right]dz. \quad (18)$$

t can be demonstrated easily that when

$$v_z = \frac{v_{z0}}{1+\delta\cos(2\pi z/d)}, \quad (19)$$

$$b_m = J_m\left(\frac{\beta_{e0}\delta d}{2\pi}\right) \quad (20)$$

or

$$b_m = J_m\left(\delta\frac{c}{v_{z0}}\frac{d}{\lambda}\right), \quad (21)$$

vhere c is the velocity of light and λ is the free-space vavelength. Thus the b_m are frequency dependent in his simple case and presumably also when v_z is a more complicated periodic function.

By proceeding from Eq. (15), the complete solution of Eq. (1) may be found. The details of this procedure are to be found in Appendix B. The result is that $G(z)$ s the sum of a number of modes of the form $e^{-j\beta z}$. Two of these have

$$\beta = \pm k \quad (22)$$

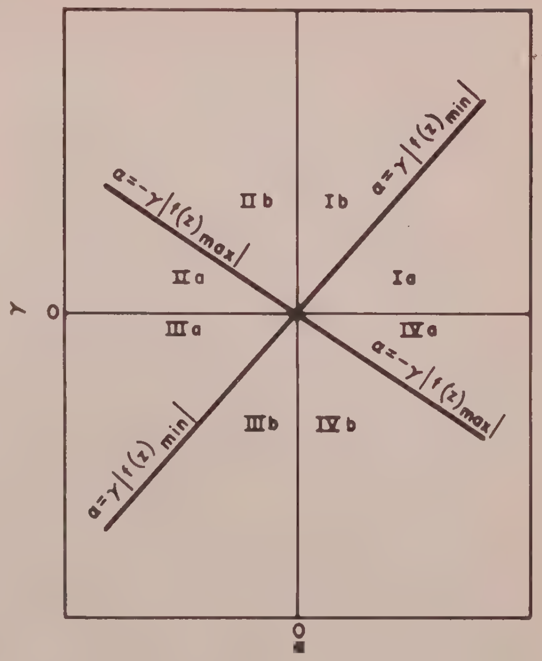

FIG. 1. Regions of the $\alpha-\gamma$ plane.

and are the free-space or field modes. For the others,

$$\beta_\nu = \beta_{e0} + \mu_1 + (2\pi\nu/d) \quad (23)$$

and

$$\beta_\Omega = \beta_{e0} - \mu_1 + (2\pi\Omega/d), \quad (24)$$

where $\nu=m+n$ and $\Omega=m-n$.

The solution of Hill's equation is such that when μ is imaginary it is approximately equal to $j\sqrt{\alpha}$ or

$$\mu_1 = \beta_{p0}' \cong \sqrt{\alpha}. \quad (25)$$

The phase velocities of the slow waves can therefore be written as

$$v_\nu = \frac{v_{z0}}{1+(\beta_{p0}'/\beta_{e0})[(\nu\lambda_{p0}'/d)+1]} \quad (26)$$

and

$$v_\Omega = \frac{v_{z0}}{1+(\beta_{p0}'/\beta_{e0})[(\Omega\lambda_{p0}'/d)-1]}. \quad (27)$$

Thus, there are pairs of waves corresponding to the single pair of space-charge waves in the uniform beam case. The Ω waves are the fast space-charge waves and the ν waves the slow space-charge waves.

Equations (23) and (24) indicate that all of the space-charge waves have a group velocity equal to v_{z0}. As a consequence, in Fig. 2, an $\omega-\beta$ plot for a beam with $\lambda_{p0}'/d=10$ and $c/v_{z0}=10$, all of the space-charge waves are lines parallel to v_{z0}. The values of ν or Ω for each wave are indicated. Each wave is made up of an infinite number of harmonics corresponding to the

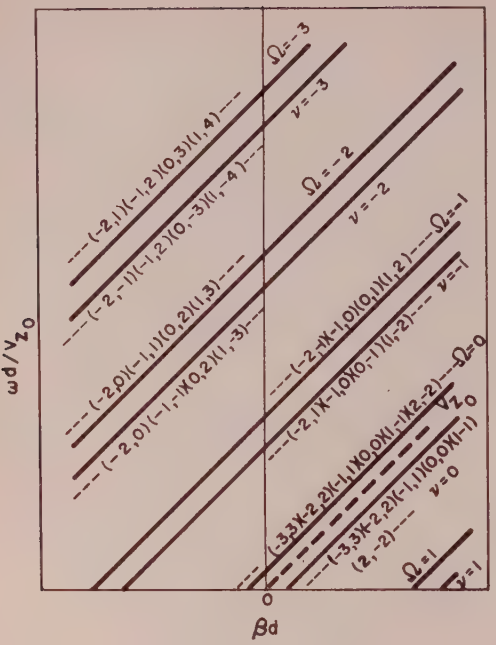

FIG. 2. $\omega-\beta$ diagram for infinite beam, $\lambda_{p0}'/d=10$, $c/v_{z0}=10$.

values of $\nu=m+n$ or $\Omega=m-n$. Some of the values of m, n for each wave are shown in parentheses.

It can be demonstrated from Maxwell's equations and Eq. (A.14), and also from Eq. (B.7) and the equivalence between E_{z1} and $P_zG(z)$ that the only field component of the slow or space-charge waves which exists in the infinite beam case is E_{z1}, and that for the free-space modes $E_{z1}=0$. Any free-space waves existing must be *TE* waves, as indicated by Eq. (A.17).

IV. FINITE BEAM

For a finite electron beam, the results found above will be modified slightly. In this case, all field components except H_{z1} will exist and will contain both field and space-charge waves.

As for the finite uniform beam, plasma-frequency reduction factors may be defined. These may be found by considering Eq. (A.32), which can be written as

$$K^2\frac{d}{dz}\frac{1}{\beta_p{}^2}\frac{d^2}{dz^2}\int\exp\left(j\int\frac{\omega}{v_z}dz\right)Gdz$$

$$=\frac{d}{dz}\int\exp\left(j\int\frac{\omega}{v_z}dz\right)P_zGdz$$

$$+\frac{d}{dz}\frac{1}{\beta_p{}^2}\frac{d^2}{dz^2}\int\exp\left(j\int\frac{\omega}{v_z}dz\right)P_zGdz. \quad (28)$$

Integrating this, setting the constant of integration equal to zero, and multiplying the resulting equation by $\beta_p{}^2$ yields

$$\frac{d^2}{dz^2}\left[K^2\int\exp\left(j\int\frac{\omega}{v_z}dz\right)Gdz\right.$$

$$\left.-\int\exp\left(j\int\frac{\omega}{v_z}dz\right)P_zGdz\right]$$

$$=\beta_p{}^2\int\exp\left(j\int\frac{\omega}{v_z}dz\right)P_zGdz. \quad (29)$$

If K is equal to zero, this becomes Hill's equation, as was demonstrated earlier in the solution for the infinite beam. The form of Eq. (29) suggests that the same method of solution be tried as is used in solving Hill's equation. $\beta_p{}^2$ and ω/v_z can be written as

$$\beta_p{}^2=\sum_{n=-\infty}^{\infty}d_n'\exp\left(j\frac{2\pi n}{d}z\right) \quad (30)$$

and

$$\frac{\omega}{v_z}=\sum_{n=-\infty}^{\infty}d_n''\exp\left(j\frac{2\pi n}{d}z\right). \quad (31)$$

Now, considering only the $\nu=m+n$ proton of the solution, it can be written as

$$G(z)=\exp\left(-j\int\frac{\omega}{v_z}dz\right)\sum_{n=-\infty}^{\infty}d_n$$

$$\times\exp\left[-j\left(R\mu_1+\frac{2\pi n}{d}\right)z\right]. \quad (32)$$

Use of this last expression and Eqs. (30) and (31) in Eq. (29) results in an infinite set of equations for the coefficients d_n in terms of $R\mu_1$ and the coefficients d_n', d_n'', corresponding to the infinite set of equations obtained in solving Hill's equation. The procedures followed in obtaining the exponent in the solution of Hill's equation from its infinite set of equations can be paralleled to find $R\mu_1$, which will be a function of K. When K is zero, R will be unity, and the expression for μ_1 in this case can be used with the expression for $R\mu_1$ to obtain an expression for R in terms of K.

The central portion of the infinite set of equations for the coefficients has been derived for the case in which v_z is given by Eq. (19). The coefficient of the central term in the set of equations resulting in this case is

$$a_1\frac{\beta_{p0}{}^2}{\beta_{e0}{}^2}\Gamma^4+\frac{\beta_{p0}}{\beta_{e0}}(2\alpha_1-\alpha_2\delta^2)\Gamma^3+\left[\alpha_1\left(1+\frac{\delta^2}{2}-\frac{k^2}{\beta_{e0}{}^2}+\frac{K^2}{\beta_{e0}{}^2}\right)\right.$$

$$\left.-a_2\delta^2+\frac{a_2\delta^4}{2}-\frac{\beta_{p0}{}^2}{\beta_{e0}{}^2}\right]\Gamma^2-2\frac{\beta_{p0}}{\beta_{e0}}\left(\alpha_2\delta^2\frac{\pi^2}{\beta_{p0}{}^2d^2}+1\right)\Gamma$$

$$-\left(1+\frac{\delta^2}{2}-\frac{k^2}{\beta_{e0}{}^2}\right)=0, \quad (33$$

where

$$\Gamma = R\mu_1/\beta_{p0},$$

$$\alpha_1 = 1+3\delta^2+\frac{45}{8}\delta^4+\frac{35}{4}\delta^6+\frac{1575}{128}\delta^8+\cdots \tag{34}$$

$$\alpha_2 = 3+\frac{15}{2}\delta^2+\frac{105}{8}\delta^4+\frac{315}{16}\delta^6+\frac{3465}{128}\delta^8+\cdots.$$

When δ is zero, Eq. (33) reduces to the familiar equation for the propagation constants of a beam of uniform velocity.

μ_1 can be found by examining Eq. (33) when $K=0$. It has already been demonstrated that for this case the spacing of the space-charge modes is independent of β_{e0}. Therefore the solutions of Eq. (33) for $\beta_{e0}=0$ and $\beta_{e0}=\infty$ should yield μ_1 to the approximation provided by consideration of the central coefficient in the infinite set of equations. The solutions for $\beta_{e0}=0$ are

$$\Gamma = \pm\frac{1}{(\alpha_1)^{\frac{1}{2}}}, \quad \pm\frac{k}{\beta_{p0}}, \tag{35}$$

so that

$$\mu_1 = \pm\frac{\beta_{p0}}{(\alpha_1)^{\frac{1}{2}}}, \quad \pm k. \tag{36}$$

At $\beta_{e0}=\infty$ for either a finite or an infinite beam, the asymptotic value of μ_1 is

$$\mu_1 = \frac{\pm\beta_{p0}}{\{\alpha_1-\alpha_2\delta^2[(1-\delta^2/2)/(1+\delta^2/2)]\}^{\frac{1}{2}}}. \tag{37}$$

It will be shown in the next section that the result of a periodicity in the plasma wave number is an increase in the effective plasma wave number. Both Eqs. (36) and (37) predict decreases in this quantity with increasing δ, but Eq. (37) predicts the smallest decrease. Therefore Eq. (37) is a better approximation to μ_1 than Eq. (36), and the solutions of Eq. (33) become less inaccurate as β_{e0} becomes larger.

As K is increased from zero, the plasma wave number of the space-charge modes is reduced at values of β_{e0} near zero until finally $R\mu_1$ becomes zero at $\beta_{e0}=0$. The behavior of these modes is very similar to that revealed by Gould and Trivelpiece[24] for the uniform beam.

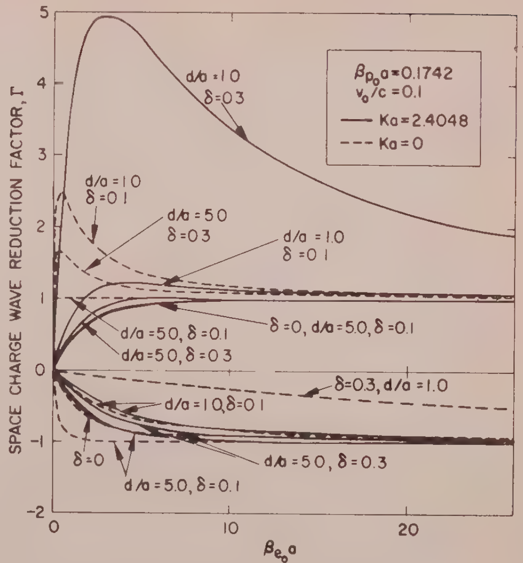

FIG. 3. Space-charge wave reduction factor Γ.

Figure 3 is a plot of the two values of Γ given by Eq. (33) for the space-charge modes for several sets of parameters. Γ is actually a reduction factor including the effects of periodicity and finite geometry. The solutions plotted for $K=0$ indicate that Eq. (33) is a reasonable approximation to the correct equation for the propagation constants only for small δ and large d/a. For large δ and small d/a, the infinite beam solution of Eq. (33) is no longer independent of β_{e0}, as is required by the results of the previous section. Physically, the same fact influences both the behavior of the reduction factors as a function of $\beta_{e0}a$ and as a function d/a. When the beam diameter is small compared to the distance between bunches, the external electric flux leakage of the beam results in reduced electric field between bunches. This situation exists at low frequencies, and thus all of the reduction factors are most strongly affected in the low-frequency range and tend to become asymptotic at high frequencies to the values given by Eq. (37). At high values of d/a the force reduction due to external electric flux leakage is more important than the force change due to the dc velocity variation, and as d/a goes to infinity the reduction factor curves approach the curves for a uniform beam. As d/a is reduced the forces due to dc velocity variation become more important, but the effect on the reduction factors appears to be very small. As δ goes to zero the reduction factors approach those calculated for the uniform beam by Branch and Mihran.[25] The principal feature of the curves of Fig. 3 for small δ and large d/a, the situation for most periodic beams, is a very slight increase in the nonsymmetry of the space-charge wave propagation constants over that which exists for $\delta=0$. There are also two fast or field-wave solutions of Eq. (33) which are similar to those of the uniform stream.

In the periodic beam there are an infinite number of sets of four waves corresponding to the infinite number of harmonics. Figure 4 is an exaggerated $\omega-\beta$ diagram for a finite periodic beam in a cylindrical waveguide. Coupled-mode interaction between modes is assumed

---

[24] R. W. Gould and A. W. Trivelpiece, J. Appl. Phys. **30**, 1784–1793 (1959).

[25] G. M. Branch and T. G. Mihran, IRE Trans. on Electron Devices **ED-2**, 3–11 (1955).

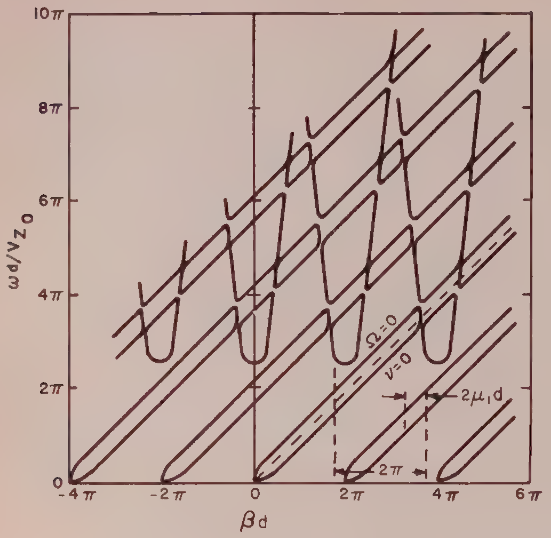

FIG. 4. $\omega-\beta$ diagram for periodic beam.

according to the theory of Pierce and Tien.[26] Floquet's Theorem requires that all of the patterns be identical.

Since both space-charge and field modes may exist, there is the possibility of interaction between these modes. If the lines $\beta=\pm k$ were drawn in Fig. 2, they would intersect the space-charge mode lines at points corresponding to frequencies at which the denominators of Eqs. (B.8) and (B.9) are zero. For the ν mode, these frequencies are

$$\omega=\frac{(2\pi v_{z0}\nu/d)-\omega_{p0}'}{(1\pm v_{z0}/c)}, \tag{38}$$

and for the Ω mode they are

$$\omega=\frac{(2\pi v_{z0}\Omega/d)+\omega_{p0}'}{(1\pm v_{z0}/c)}, \tag{39}$$

where

$$\omega_{p0}'=\mu_1 v_{z0}. \tag{40}$$

Note that v_{z0}/d is the frequency of the force an electron feels due to the periodic dc velocity and charge density of the beam. The frequencies found above are thus Doppler-shifted beat frequencies between the equivalent plasma frequency and the harmonics of the dc driving frequency.

In the case of the finite beam, the frequencies near which interaction is likely to occur will correspond to the intersections of the space-charge wave and field-wave lines as modified by the reduction factors. The expressions for the amplitudes of the field components will contain factors very much like those in the denominators of Eqs. (B.8) and (B.9). Thus these amplitudes will become large for frequencies at which coupling between the modes occurs, and the possibility of useful interaction will be great. In theory, at least, it should be possible to construct oscillators and amplifiers for use at very high frequencies. These possibilities will be discussed briefly later.

V. CONSEQUENCES OF PERIODICITY IN BEAMS

A. Velocity Jump Amplification

The exponent μ_1 for the slow waves can be thought of as an equivalent plasma wave number related to an equivalent plasma wavelength. In reference to Fig. 4, Mueller and Staprans[21,22] have pointed out that when

$$2\mu_1 d=2\pi, \tag{41}$$

or when

$$\frac{2d}{\lambda_p'}=1, \tag{42}$$

the fast space-charge wave of each harmonic coincides with the slow space-charge wave of an adjacent harmonic. Coupling can then occur between these modes to produce gaining interaction. This is velocity-jump gain. This can be further understood by considering a stability chart for the solution of Hill's equation, Fig. 5. In Fig. 5 the solid curve marking the boundary between the first stable and unstable regions and the dotted lines running parallel to it are lines along which μ_1 is constant and has the values β_{p0} corresponding to the points at which these curves intersect the axis $\alpha=0$. As α is increased, μ_1 increases until the boundary of the unstable region is reached. At this point gain will result, a condition which corresponds to the coinciding lines on the $\omega-\beta$ chart. As α is increased further, the real part of μ_1 remains unchanged, but the imaginary part increases and thus gain increases.

From another point of view it is apparent, as Bliokh[17] has pointed out, that condition (42) is that for parametric resonance. This type of resonance is possible whenever the period of the driving force is equal to one-half an integral number of periods of the natural frequency of the system. For the periodic beam this will occur whenever $2\mu_1 d=2n\pi$, or whenever coupling between slow and fast space-charge waves occurs.

B. Rippled-Stream Amplification

Although the present analysis does not apply to a rippled stream, because of the restriction to axial velocities only, such a stream can be approximated by a stream with axial velocities only and a charge density which varies periodically in the axial direction. The $\omega-\beta$ diagram for this case is the same as that of Fig. 4, and rippled-stream gain is due to a coincidence of slow and fast space-charge wave harmonics.

---

[26] J. R. Pierce and P. K. Tien, Proc. I.R.E. 42, 1389–1396 (1954).

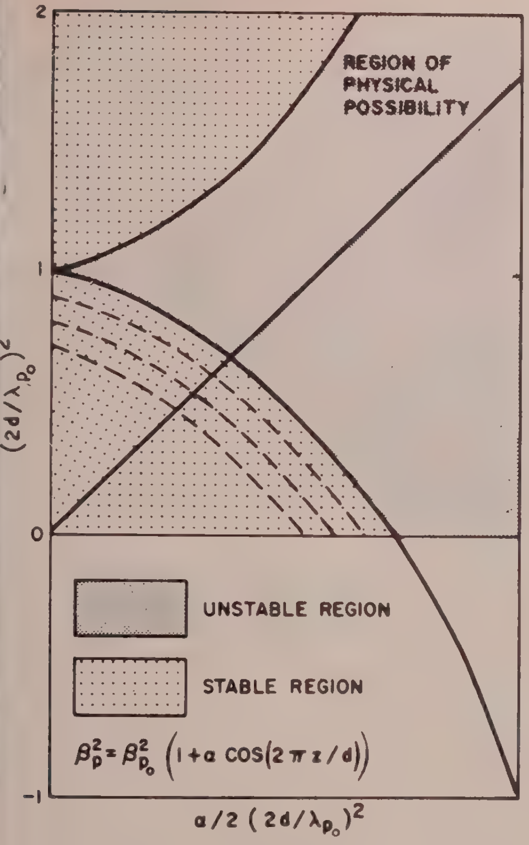

FIG. 5. Stability chart for field solutions of periodic beam.

C. Rippled-Wall Amplification

For the case of a uniform beam inside a cylinder with a rippled wall, the assumption that the solutions of Eq. (28) have the form $e^{-j\beta z}$ reduces that equation to

$$K^2 = -(\beta^2 - k^2)\left[1 - \frac{\beta_p^2}{(\beta_{e0}-\beta)^2}\right], \qquad (43)$$

the familiar equation for the propagation constants of a uniform stream.

Satisfaction of the boundary condition at the rippled wall requires that the field exterior to the beam be the sum of space-harmonic fields. Each of these space harmonics will vary in a different manner radially, and thus will have a different radial propagation constant K. For each value of K, Eq. (43) yields four waves, so that there is again an infinite set of patterns of four waves and Floquet's Theorem again specifies that all of the patterns must be identical. The $\omega-\beta$ diagram is again that of Fig. 4, and the coinciding space harmonic argument may again be applied to explain rippled-wall gain. The amplitudes of the various space harmonics are determined in this case by the wall geometry.

If all three types of variation are present with different periods, three infinite sets of space-harmonic fields are required and the $\omega-\beta$ diagram can be constructed from the diagrams for each of the types of periodicity. When the periods of all the variations are the same, the $\omega-\beta$ diagram of Fig. 4 holds. The amplitudes of the space harmonics in this case depend upon both the wall geometry and the beam parameters.

D. Effects of Beam Periodicity on Traveling-Wave Devices

Other than in a few devices in which periodic beams may be employed to take advantage of the unique propagation characteristics of such beams, they generally occur as a result of the use of a periodic focusing system. These beams generally have scalloping boundaries and periodic charge densities which can, of course, affect their rf behavior. In addition, periodic velocity variations may be such that the fundamental beam-harmonic amplitude will be appreciably reduced, resulting in poor performance. A large body of experience with periodically focused devices has revealed no such effects. The following arguments will illustrate why this is so.

The phase characteristics of the space harmonics of a periodic propagating structure are given by

$$\beta_m = \beta_0 + (2\pi m/p), \qquad (44)$$

where β_m is the phase shift of the mth circuit space harmonic at a given frequency, β_0 is the phase shift of the fundamental circuit space harmonic at the same frequency, p is the period of the structure, and m is an integer. The phase velocity of a given space harmonic is

$$v_m = \omega/\beta_m = 2\pi f p/(\beta_0 p + 2m\pi), \qquad (45)$$

where $\omega = 2\pi f$. Thus the argument of the Bessel function involved in the harmonic amplitudes is

$$\theta = \delta(c/v_m)(d/\lambda) = \delta(d/p)[(\beta_0 p + 2m\pi)/2\pi]. \qquad (46)$$

For the helix in the nondispersive region,

$$\beta_0 p = 2\pi k a, \qquad (47)$$

where a is the helix radius and $k = w/c$, and

$$\theta = (\delta d/p)[(ka + mD)/D], \qquad (48)$$

where D is the dielectric loading factor.

From Eq. (48) and the fact that $ka = D/2$ represents the upper frequency limit for almost all traveling-wave devices, it is apparent that

$$[(2m-1)/2]\delta(d/p) \leq \theta \leq [(2m+1)/2]\delta(d/p). \qquad (49)$$

Since δ will usually be small and operation is generally practical only for $m=0$ or -1, the only possible source of difficulty in practical devices occurs when $d \gg p$. For electrostatically focused bifilar helices and interdigital lines and coupled-cavity circuits employing periodic magnetic focusing, d is generally equal to p, and effects due to periodic velocity will be negligible.

One typical situation in which the focusing period and the circuit period can be quite different is periodic magnetic focusing when the circuit is a helix. An approximate derivation of θ for this case given in Appendix C indicates that the likelihood of any measurable effect exists only for low-velocity devices. For forward-wave tubes the effect of a periodic velocity variation ought to appear as a decrease in gain at the high-frequency end of the passband.

E. Possible Uses of Periodic Beams

The utility of the beam-space harmonics depends, as for the circuit-space harmonics, upon the possibility of enhancing their amplitudes. From the value of θ calculated in Appendix C it is apparent that it is possible to produce appreciable amplitudes for the various beam space harmonics in helix tubes employing periodic magnetic focusing. Appreciable harmonic amplitudes can also be generated in devices employing electrostatic focusing schemes for which d/p is large. One example this is a string of short sections of helix operated at potential alternately above and below the average beam potential. Of course, if focusing by uniform magnetic field is provided, then many schemes are possible in which the velocity is varied by electrostatic means and d/p is large.

Suppression of Backward-Wave Oscillations

One useful byproduct of velocity variation is the possibility of increasing the backward-wave oscillation-starting current of a low-velocity traveling-wave tube employing periodic magnetic focusing. If parameters are such that $\theta = 2.4048$ at the frequency of the intersection of the phase velocity curves of the fundamental and first backward space harmonics of the circuit, backward-wave oscillations would be impossible at that point. However, in order to attain this value of θ, a large value of d/p would be necessary and, consequently, the higher beam harmonics of the slow space-charge wave would interact with the backward circuit harmonic at frequencies near the crossover. At these frequencies the beam harmonic amplitudes would not be zero. These interactions would take place at

$$ka/D = (ka/D)_c[1 \pm n(p/d)], \tag{50}$$

where the subscript c denotes the value at the crossover point of the fundamental and first backward space harmonics of the circuit, and m is the number of the beam harmonic. The value of θ at these intersections would be

$$\theta_n = \theta_c[1 \pm n(p/d)]. \tag{51}$$

From the start-oscillation characteristics of the helix and Eqs. (50) and (51), the optimum value of θ_c can be chosen.

As an example of what might be accomplished, assume that the start-oscillation current for a uniform beam is the same at $(ka/D)_c$ and $(ka/D)_c[1 \pm (p/d)]$, and choose θ_c such that $J_0(\theta_c) = J_1(\theta_c)$. Then the ratio of the start-oscillation current to the operating current at a frequency one-third of f_c would be increased by a factor of 3 from that of a uniform beam.

Active Microwave Filter

Equation (48) suggests that a low-voltage, forward-wave amplifier could be made into a single-frequency rejection filter by adjusting the parameters correctly. The frequency of rejection could be tuned by varying δ. A device consisting of a number of short helix sections could be used for this purpose by maintaining the average beam velocity near the phase velocity of the helices while the difference in helix potential was varied to change the frequency at which the amplitude of the fundamental beam harmonic went to zero. To first order, the gain of this device would vary as $J_0^{2/3}(\theta)$, so that the filter characteristic would not be particularly sharp. However, the cutoff could be considerably sharpened if the helices were designed to give dispersive gain with the peak of gain centering around the notch. In this case both the average voltage and the voltage difference would be tuned.

Multiple Frequency Interactions

By adjusting the various parameters so that several beam harmonics have appreciable amplitudes where their phase velocities are the same as that of the helix backward wave, several oscillation frequencies, all tunable, could be obtained at the same time. This situation might be combined with a dispersive forward-wave amplifier to yield a tunable amplified signal and several tunable oscillations or, with a nondispersive forward-wave amplifier, to amplify over a broad band while generating several fixed-frequency oscillations. This last scheme might be useful in broad-band detection systems or multichannel communication systems.

Millimeter-Wave Generation and Amplification

Several authors[12,15,21,22] have suggested the possibilit of interaction between a smooth waveguide and a spac harmonic of a periodic electron beam. From Fig. 4 i can be seen that for interaction between the $-n$th harmonic of the slow space-charge wave and th fundamental harmonic of the waveguide mode,

$$\omega_c d/v_0 \leq 2n\pi - \mu_1 d, \qquad (52$$

where ω_c is the radian frequency at the cutoff of th waveguide. When this condition is satisfied,

$$\theta_n \leq \delta[n - (\mu_1 d/2\pi)]. \qquad (53$$

Since the maximum practical value of δ is of the order of 0.2 for periodic magnetic focusing, θ_n will always be much smaller than the value for which $J_n(\theta_n)$ is a maximum. Consequently, the $-n$th space harmonic will have a small amplitude at the interaction frequency.

The impedance of the waveguide mode is infinite at cutoff and falls off rapidly for frequencies above cutoff, while the waveguide wall losses are large near cutoff and decrease at higher frequencies. Thus, interaction will be possible only in a narrow range of frequencies just above the waveguide-cutoff frequency where the combination of waveguide impedance and loss is favorable. Staprans[22] has discussed this situation in considerable detail, and has found that the useful operating bandwidth of a device of this kind would be of the order of 1%. The voltage and current required would both be large and the period of the velocity variation very short.

A confined flow beam in which velocity variation is obtained by electrostatic means might allow a higher value of δ, but the formidable probablem of providing insulation of the order of tens of kilovolts in a configuration in which the period is of the order of 1 mm (for 100-kMc operation) would be introduced.

In spite of an advantage in terms of larger size for a given wavelength, a device of this sort seems to be a less practical solution to the problem of millimeter-wave generation than other more conventional approaches now being pursued.[27,28] A related device making use of a helical beam in a waveguide is enjoying some success at lower frequencies.[29] However, since it makes use of a beam spiraling at the cyclotron frequency, it will probably be limited to frequencies below the millimeter-wave range because of the difficulty in obtaining extremely high magnetic fields. Other devices making use of smooth circuits and electrostatically focused helical or meandering beams have been proposed to obtain interaction at millimeter waves.[30,31] These do not have the disadvantage of requiring either extremely high voltages or magnetic fields, and thus give more promise of success.

VI. CONCLUSIONS

A small-signal analysis of smooth electron beams with periodic variations in their dc parameters reveals the existence of infinite sets of space harmonics of the fast and slow space-charge waves. For a finite beam, coupling between the space-charge waves and field waves exists. Plasma-frequency reduction factors can be defined as for the uniform stream. The periodicity of the beam causes an increase in the effective plasma wave number and a very slight increase in the nonsymmetry of the space-charge wave propagation constants.

Velocity-jump, rippled-stream, and rippled-wall amplification are shown to result from coupling between fast waves and slow waves of adjacent harmonics.

The periodicity of the beam will have negligible effect on most conventional traveling-wave devices. Difficulties due to the frequency dependence of the amplitudes of the beam harmonics may be experienced in low-voltage tubes using periodic permanent magnet focusing.

One possible use of the beam harmonics is to increase the starting current of backward-wave oscillations in traveling-wave amplifiers. This use would be limited to low-voltage, periodically focused tubes. An electronically tunable, single-frequency rejection filter could be constructed, making use of the frequency-dependent harmonics, and a variety of multiple-frequency interactions can be imagined.

Millimeter-wave generation and amplification by interaction between a beam space harmonic of a beam with varying velocity and the fields in a wave guide appears to be impractical because of the high voltages and short periods required and the narrow bandwidths which could be obtained. Other schemes which make use of electrostatically focused helical beams at low velocities and smooth wave guides appear to have some promise for very high frequencies.

ACKNOWLEDGMENTS

The author is indebted to Dr. J. R. Whinnery of the University of California and Dr. Armand Staprans of Varian Associates for many stimulating discussions of the work presented here.

APPENDIX A

Small-Signal Analysis of Periodic Beams

If it is assumed that all quantities in an electron beam can be represented as the sum of a dc and an ac quantity,

$$f_t = f + f_1 e^{j\omega t}, \tag{A.1}$$

where lack of subscript refers to the dc quantity, the subscript 1 refers to the ac quantity, $q_1 \ll q$, and all ac quantities vary as $e^{j\omega t}$, then the ac parts of Maxwell's Equations can be written as

$$\nabla \times \mathbf{E}_1 = -j\omega\mu \mathbf{H}_1, \tag{A.2}$$

$$\nabla \times \mathbf{H}_1 = \mathbf{i}_1 + j\omega\epsilon \mathbf{E}_1, \tag{A.3}$$

$$\nabla \cdot \mathbf{D}_1 = \rho_1, \tag{A.4}$$

$$\nabla \cdot \mathbf{B}_1 = 0. \tag{A.5}$$

---

[27] W. E. Danielson, H. L. McDowell, and E. D. Reed, Proc. I.R.E. **48**, 321–328 (1960).

[28] G. Convert, T. Yeou, and B. Pasty, *Proceedings of the Symposium on Millimeter Waves* (Polytechnic Press, Brooklyn, New York, 1959), pp. 313–339.

[29] R. H. Pantell, Proc. I.R.E. **47**, 1146 (1959).

[30] R. Müller (private communication).

[31] L. Haas (private communication).

These last four equations can be combined with the definition of ac current,

$$\mathbf{i}_1=\rho\mathbf{v}_1+\rho_1\mathbf{v}, \tag{A.6}$$

which neglects the second order product $\rho_1\mathbf{v}_1$, to give the wave equation for a region containing currents and charges:

$$(\nabla^2+k^2)\mathbf{E}_1=j\omega\mu(\rho\mathbf{v}_1+\rho_1\mathbf{v})+\nabla(\nabla\cdot\mathbf{E}_1), \tag{A.7}$$

where $k^2=\omega^2\mu\epsilon$.

The ac force equation, again neglecting second-order quantities, is

$$\begin{aligned}-\eta[\mathbf{E}_1+\mathbf{v}\times\mathbf{B}_1+\mathbf{v}_1\times\mathbf{B}]&\\ =j\omega\mathbf{v}_1+(\mathbf{v}_1\cdot\nabla)\mathbf{v}+(\mathbf{v}\cdot\nabla)\mathbf{v}_1,&\end{aligned} \tag{A.8}$$

where $\eta=e/m$, the charge-to-mass ratio of the electron. A definition of $\mathbf{v}_1$ available from Eq. (A.7) is

$$\begin{aligned}\mathbf{v}_1=(-j/\omega\mu\rho)[(\nabla^2+k^2)\mathbf{E}_1-\nabla(\nabla\cdot\mathbf{E}_1)&\\ -j\omega\mu\epsilon\mathbf{v}\nabla\cdot\mathbf{E}_1].&\end{aligned} \tag{A.9}$$

This, together with Eq. (A.2) when substituted into Eq. (A.8), yields the equation for electric field:

$$\begin{aligned}-\eta\Big\{\mathbf{E}_1+\frac{j}{\omega}\mathbf{v}\times\nabla\times\mathbf{E}_1-\frac{j}{\omega\mu\rho}[(\nabla^2+k^2)\mathbf{E}_1&\\ -\nabla(\nabla\cdot\mathbf{E}_1)-j\omega\mu\epsilon\mathbf{v}\nabla\cdot\mathbf{E}_1]\times\mathbf{B}\Big\}&\\ =[j\omega+\mathbf{v}\cdot\nabla]\Big\{\frac{j}{\omega\mu\rho}[(\nabla^2+k^2)\mathbf{E}_1-\nabla(\nabla\cdot\mathbf{E}_1)&\\ -j\omega\mu\epsilon\mathbf{v}\nabla\cdot\mathbf{E}_1]\Big\}-\frac{j}{\omega\mu\rho}[(\nabla^2+k^2)\mathbf{E}_1-\nabla(\nabla\cdot\mathbf{E}_1)&\\ -j\omega\mu\epsilon\mathbf{v}\nabla\cdot\mathbf{E}_1]\cdot\nabla\mathbf{v}.&\end{aligned} \tag{A.10}$$

For general electron flow, Eq. (A.10) yields a system of three simultaneous scalar equations to be solved for the three components of electric field.

Consider a cylindrically symmetric electron beam in which both ac and dc velocities are restricted to the axial direction by an infinite magnetic focusing field. In this case Eq. (A.10) reduces to the single equation

$$\begin{aligned}-\eta E_{z1}=\frac{-j}{\omega\mu}\left(j\omega+\frac{\partial v_z}{\partial z}+v_z\frac{\partial}{\partial z}\right)\Big\{\frac{1}{\rho}\Big[(\nabla^2+k^2)E_{z1}&\\ -\frac{\partial}{\partial z}(\nabla\cdot\mathbf{E}_1)-j\omega\mu\epsilon v_z\nabla\cdot\mathbf{E}_1\Big]\Big\}.&\end{aligned} \tag{A.11}$$

Now since v_r and v_{r1} are equal to zero, the r component of Eq. (A.3) is

$$E_{r1}=(j/\omega\epsilon)(\partial H_{\theta1}/\partial z), \tag{A.12}$$

and the θ component of Eq. (A.2)

$$-(\partial E_{z1}/\partial r)+(\partial E_{r1}/\partial z)=-j\omega\mu H_{\theta1} \tag{A.13}$$

is thus

$$\partial E_{z1}/\partial r=(j/\omega\epsilon)[k^2+(\partial^2/\partial z^2)]H_{\theta1}. \tag{A.14}$$

Because of the vector identity

$$\nabla^2\mathbf{E}_1-\nabla(\nabla\cdot\mathbf{E}_1)=-\nabla\times\nabla\times\mathbf{E}_1, \tag{A.15}$$

$$\nabla^2E_{z1}-\frac{\partial}{\partial z}(\nabla\cdot\mathbf{E}_1)=j\omega\mu\left[\frac{1}{r}\frac{\partial}{\partial r}(rH_{\theta1})-\frac{1}{r}\frac{\partial H_{r1}}{\partial\theta}\right]. \tag{A.16}$$

Applying this same vector identity to $\mathbf{H}_1$ and remembering that Eq. (A.5) must be satisfied and that only axial current is allowed leads to

$$(\nabla^2+k^2)H_{z1}=0. \tag{A.17}$$

This is a statement that only free-space wave solutions are possible with finite H_{z1}, or that H_{z1} must be zero for space-charge wave solutions.

With this in mind, and making the restrictions $\partial\rho/\partial r=0$, $\partial v_z/\partial r=0$, i.e., that current density and velocity be uniform over any cross section of the beam, Eq. (A.11) can be differentiated with respect to r and combined with Eqs. (A.12), (A.14), (A.16), and the θ-component of Eq. (A.3) to yield

$$\begin{aligned}P_zH_{\theta1}=\frac{\epsilon}{\eta\rho}\left(j\omega+\frac{\partial v_z}{\partial z}-\frac{v_z}{\rho}\frac{\partial\rho}{\partial z}+v_z\frac{\partial}{\partial z}\right)\Big[\left(j\omega+v_z\frac{\partial}{\partial z}\right)&\\ \times\left(P_zH_{\theta1}+P_rH_{\theta1}-\frac{\partial}{\partial r}\frac{1}{r}\frac{\partial H_{r1}}{\partial\theta}\right)\Big],&\end{aligned} \quad \text{(A.18}$$

where

$$P_z\equiv k^2+(\partial^2/\partial z^2) \quad \text{(A.19}$$

and

$$P_r\equiv(\partial/\partial r)r^{-1}(\partial/\partial r)r.$$

When H_{z1} is zero, Eq. (5) states that

$$\partial H_{\theta1}/\partial\theta=-(\partial/\partial r)(rH_{r1}). \quad \text{(A.2}$$

If $\partial v_z/\partial\theta=0$, $\partial\rho/\partial\theta=0$, then Eq. (A.18) can be differentiated with respect to θ and combined with Eq. (A.2 to produce

$$\begin{aligned}P_z\frac{\partial}{\partial r}(rH_{r1})=\frac{\epsilon}{\eta\rho}\left(j\omega+\frac{\partial v_z}{\partial z}-\frac{v_z}{\rho}\frac{\partial\rho}{\partial z}+v_z\frac{\partial}{\partial z}\right)&\\ \cdot\Big\{\left(j\omega+v_z\frac{\partial}{\partial z}\right)\Big[P_z\frac{\partial}{\partial r}(rH_{r1})+P_r\frac{\partial}{\partial r}(rH_{r1})&\\ +\frac{\partial}{\partial r}\frac{1}{r}\frac{\partial^2H_{r1}}{\partial\theta^2}\Big]\Big\}.&\end{aligned} \quad \text{(A.2}$$

ow let

$$P_z\frac{\partial}{\partial r}(rH_{r1})\equiv\exp\left(-j\int\frac{\omega}{v_z}dz\right)A_1$$

$$P_r\frac{\partial}{\partial r}(rH_{r1})\equiv\exp\left(-j\int\frac{\omega}{v_z}dz\right)A_2 \qquad (A.22)$$

$$\frac{\partial}{\partial r}\frac{1}{r}\frac{\partial^2 H_{r1}}{\partial\theta^2}\equiv\exp\left(-j\int\frac{\omega}{v_z}dz\right)A_3.$$

ubstitution of these definitions into Eq. (A.21) esults in

$${}_1=\frac{\epsilon}{\eta\rho}\left[\frac{\partial v_z}{\partial z}-\frac{v_z}{\rho}\frac{\partial\rho}{\partial z}+v_z\frac{\partial}{\partial z}\right]\left[v_z\frac{\partial}{\partial z}(A_1+A_2+A_3)\right]. \qquad (A.23)$$

se of the continuity equation

$$(\partial/\partial z)(\rho v_z)=0 \qquad (A.24)$$

nd the definition

$$\beta_p{}^2=-(\eta\rho/\epsilon v_z{}^2) \qquad (A.25)$$

educes Eq. (A.23) to

$$A_1=-\frac{\partial}{\partial z}\frac{1}{\beta_p{}^2}\frac{\partial}{\partial z}(A_1+A_2+A_3) \qquad (A.26)$$

or

$$-\frac{\partial}{\partial z}\frac{1}{\beta_p{}^2}\frac{\partial}{\partial z}\exp\left(j\int\frac{\omega}{v_z}dz\right)\left[P_r\frac{\partial}{\partial r}(rH_{r1})+\frac{\partial}{\partial r}\frac{1}{r}\frac{\partial^2 H_{r1}}{\partial\theta^2}\right]$$

$$=\left(1+\frac{\partial}{\partial z}\frac{1}{\beta_p{}^2}\frac{\partial}{\partial z}\right)\exp\left(j\int\frac{\omega}{v_z}dz\right)P_z\frac{\partial}{\partial r}(rH_{r1}), \qquad (A.27)$$

which reduces to the equation of Agdur and Rydbeck[10] when there are no circumferential variations.

Assuming separation variables,

$$H_{r1}=G(z)F(r)L(\theta), \qquad (A.28)$$

let

$$L(\theta)=e^{jm\theta} \qquad (A.29)$$

and

$$F(r)=[F_1(r)]/r. \qquad (A.30)$$

Then the equation for $F_1(r)$ is

$$\frac{d^3F_1}{dr^3}+\frac{1}{r}\frac{d^2F_1}{dr^2}+\left[K^2-\frac{(m^2+1)}{r^2}\right]\frac{dF_1}{dr}+\frac{2m^2}{r^3}F_1=0, \qquad (A.31)$$

where

$$K^2=\frac{[1+(\partial/\partial z)(\beta_p{}^2)^{-1}(\partial/\partial z)]\exp\left[j\int(\omega/v_z)dz\right][k^2+(\partial^2/\partial z^2)]G(z)}{(\partial/\partial z)(\beta_p{}^2)^{-1}(\partial/\partial z)\exp\left[j\int(\omega/v_z)dz\right]G(z)}. \qquad (A.32)$$

Equation (A.31) is just the derivative of Bessel's quation, so that

$$F(r)=[J_m(Kr)]/r, \quad m\neq 0. \qquad (A.33)$$

When $m=0$, Eq. (A.20) requires that if H_{r1} is not to e infinite at the center of the stream it must be zero verywhere. In this case a solution for $H_{\theta 1}$ can be found rom Eq. (A.18). Following the procedure outlined in qs. (A.22)–(A.27) and assuming separation of varibles, it can be shown that

$$H_{\theta 1}=J_1(Kr)G(z), \qquad (A.34)$$

here Eq. (A.32) again defines the relationship between and $G(z)$.

APPENDIX B

Complete Solution of Eq. (1)

Since

$$\mathcal{H}=d\phi/dz, \qquad (B.1)$$

$$\mathcal{H}=\operatorname{Re}\sum_{n=-\infty}^{\infty}ja_n\left(\mu_1+\frac{2\pi n}{d}\right)\left\{K_1\exp\left[j\left(\mu_1+\frac{2\pi n}{d}\right)z\right]\right.$$

$$\left.-K_2\exp\left[-j\left(\mu_1+\frac{2\pi n}{d}\right)z\right]\right\}. \qquad (B.2)$$

The right-hand side of Eq. (1) is thus

$$\exp\left(-j\int\frac{\omega}{v_z}\right)\mathcal{H}$$

$$=\operatorname{Re}\left[\left\{\sum_{m=-\infty}^{\infty}b_m\exp\left[-j\left(\beta_{e0}+\frac{2\pi m}{d_1}\right)z\right]\right\}\right.$$

$$\times\sum_{n=-\infty}^{\infty}\left(ja_n\left(\mu_1+\frac{2\pi n}{d}\right)\left\{K_1\exp\left[j\left(\mu_1+\frac{2\pi n}{d}\right)z\right]\right.\right.$$

$$\left.\left.\left.-K_2\exp\left[-j\left(\mu_1+\frac{2\pi n}{d}\right)z\right]\right\}\right)\right], \qquad (B.3)$$

or

$$\exp\left(-j\int\frac{\omega}{v_z}dz\right)\mathcal{H}$$

$$=\mathrm{Re}\left\{\sum_{\nu=-\infty}^{\infty}C_\nu\exp\left[-j\left(\beta_{e0}+\mu_1+\frac{2\pi\nu}{d}\right)z\right]\right.$$

$$\left.+\sum_{\Omega=-\infty}^{\infty}C_\Omega\exp\left[-j\left(\beta_{e0}-\mu_1+\frac{2\pi\Omega}{d}\right)z\right]\right\}, \quad \text{(B.4)}$$

where $\nu=m+n$, $\Omega=m-n$,

$$C_\nu=K_1\sum_{n=-\infty}^{\infty}ja_n\left(\mu_1+\frac{2\pi n}{d}\right)b_{\nu-n}, \quad \text{(B.5)}$$

$$C_\Omega=-K_2\sum_{n=-\infty}^{\infty}ja_n\left(\mu_1+\frac{2\pi n}{d}\right)b_{\Omega+n}. \quad \text{(B.6)}$$

The solution to Eq. (1) is

$$G=\mathrm{Re}[C_2e^{jkz}+C_3e^{-jkz}]$$

$$+\mathrm{Re}\left\{\sum_{\nu=-\infty}^{\infty}K_\nu\exp\left[-j\left(\beta_{e0}+\mu_1+\frac{2\pi\nu}{d}\right)z\right]\right.$$

$$\left.+\sum_{\Omega=-\infty}^{\infty}K_\Omega\exp\left[-j\left(\beta_{e0}-\mu_1+\frac{2\pi\Omega}{d}\right)z\right]\right\}, \quad \text{(B.7)}$$

where

$$K_\nu=\frac{-C_\nu}{[\beta_{e0}+\mu_1+(2\pi\nu/d)]^2-k^2} \quad \text{(B.8)}$$

and

$$K_\Omega=\frac{-C_\Omega}{[\beta_{e0}-\mu_1+(2\pi\Omega/d)]^2-k^2}. \quad \text{(B.9)}$$

APPENDIX C

Derivation of θ for Periodic Magnetic Focusing of Helix Tubes

To a first approximation,

$$v_z^2=v_{z0}^2[1-(\eta B_z^2r^2/2V)], \quad \text{(C.1)}$$

where r is the beam radius, B_z is the axial magnetic field, V is the beam voltage, and

$$v_{z0}^2=2\eta V. \quad \text{(C.2)}$$

If

$$B_z=B_0\cos(2\pi z/L), \quad \text{(C.3)}$$

then

$$v_z\simeq v_{z0}\left(1-\frac{\eta B_0^2r^2}{8V}-\frac{\eta B_0^2r^2}{8V}\cos\frac{4\pi z}{L}\right) \quad \text{(C.4)}$$

or

$$\delta=\frac{-\eta B_0^2r^2}{8V}\Big/1-\frac{\eta B_0^2r^2}{8V}. \quad \text{(C.5)}$$

Now Eq. (46) can be written as

$$\theta=\frac{1}{2\pi}\delta\frac{c}{v_0}\frac{d}{r}\frac{r}{a}\frac{ka}{D} \quad \text{(C.6)}$$

or, inserting the definition of δ from Eq. (C.5),

$$\theta=\frac{-1}{2\pi}\frac{c}{v_0}\frac{r}{a}\frac{ka}{D}\frac{(\eta B_0^2d^2/8V)(r/d)}{1-(\eta B_0^2d^2/8V)(r/d)^2}. \quad \text{(C.7)}$$

In order to avoid the first focusing stop-band, it is necessary[32] to operate such that

$$\eta B_0^2d^2/V\leq 418, \quad \text{(C.8)}$$

and to avoid difficulties due to rf defocusing, the limit stated should be reduced by a factor of at least 5. In addition, it has been estimated[32] that for practical designs,

$$r/d<\tfrac{1}{8}. \quad \text{(C.9)}$$

Thus, in practice $B_0^2r^2/8V$ must be less than 0.16 and δ less than 0.195. Assuming $r/a=0.7$ and a dielectri loading factor of 0.9,

$$\theta\leq 0.202ka(c/v_0). \quad \text{(C.10)}$$

---

[32] J. T. Mendel, C. F. Quote, and W. H. Yocum, Proc. Ins Radio Engrs. 42, 800–810 (1954).

OURNAL OF APPLIED PHYSICS VOLUME 32, NUMBER 7 JULY, 1961

Anodic Oxidation of Germanium

T. Gabor
Westinghouse Research Laboratories, Pittsburgh 35, Pennsylvania

(Received February 10, 1961)

On anodic polarization of etched samples of *n*-type or near-intrinsic *p*-type germanium, striations are formed. The periodic depletion of holes is advanced as a tentative explanation of the phenomenon.

INTRODUCTION

ACCORDING to Brattain and Garrett,[1] on anodic oxidation of germanium, holes are removed from he valence band and electrons are supplied to the onduction band. Gerischer and Beck[2] have shown that n the case of ready availability of holes, the latter rocess was negligible, while in case of dissolution imited by the availability of holes, somewhat more than wo out of four positive charges necessary for oxidation vere made available by the transfer of electrons to the onduction band.

A phenomenon thought to be partly caused by the lepletion of holes in germanium will be described in the resent paper. The work consisted of the examination f the anodic dissolution of germanium in aqueous $HClO_4$. When CP4-etched samples of *n*-type or near-ntrinsic *p*-type were used, striations were formed. First, dark line appeared at the level of the meniscus. Following this, at intervals of a few seconds, new lines ppeared, each line running approximately parallel to he line above it. As the lines gradually covered the urface, a white precipitate (GeO_2) became visible at he level of the meniscus and was extending downwards.

EXPERIMENTAL

The anodes were partly immersed into aqueous erchloric acid (35%) in an open beaker. The cathode vas a platinum disk, about 2 cm away, which had about 1 cm² of its area immersed into the electrolyte. About 45 v were used. Figure 1 shows part of a circular, 1-mm hick, etched electrode (near intrinsic, *n* type). In the ase of Fig. 1(a), electrolysis was started at room temperature and a reading of 55°C was obtained at the end, vhile in the case of Fig. 1(b), electrolysis was begun at 75°C, and the temperature rose to near the boiling point n the end. In the first case, only about 0.01 amp was btained initially, and it took about 4 min before 0.6 mp was reached; at this current the first line appeared. In the other case, the current in the beginning was 0.2–0.3 amp, rising to 0.6 amp in <1 min. In both cases, he current remained at about 0.5–0.6 amp while the ines were forming, the latter taking about 15 sec in the hot electrolyte and about 2 min in the cold electrolyte.

The white precipitate that was formed on continued electrolysis (34 Ω cm, *n*-type germanium) is shown in Fig. 2(a). This photo shows a dark and a white line. Figure 2(b) shows two lines after removal of the GeO_2 by aqueous HF. Figure 3 shows the surface after 10 min of electrolysis. The GeO_2 was peeling off in places.

Figure 4 shows a sample of near-intrinsic germanium that was lapped and the right half of which was etched in CP4. After anodic oxidation and treatment with HF, the photograph was taken with the sample immersed into water; this made the lines more clearly visible. Electrolysis started over the lapped area. That part of the dark coating that was formed above the meniscus (where the electrolyte has crept up) did not oxidize to

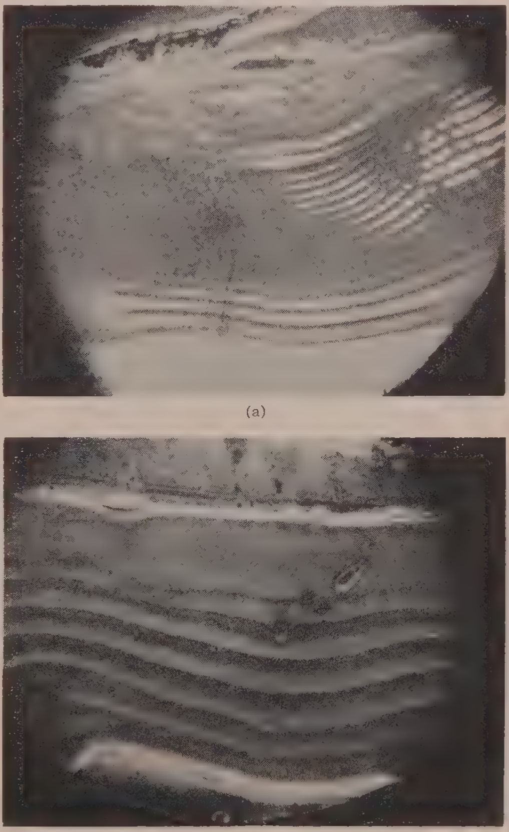
(a)

(b)

Fig. 1. Striations on a germanium anode. Electrolysis started at (a) 25°C, (b) 75°C. Magnification 2.5×.

---

[1] W. H. Brattain and C. G. B. Garrett, Bell System Tech. J. 34, 129 (1955).

[2] H. Gerischer and F. Beck, Z. physik. Chem. (Frankfurt) 24, 378 (1960).

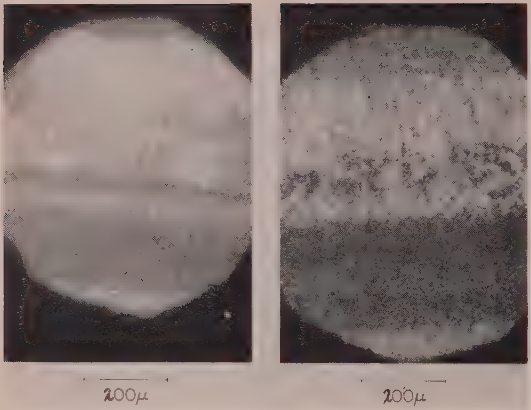

(a) (b)

FIG. 2. Dark and light line on germanium after (a) anodization, (b) anodization and treatment with aqueous HF. Magnification 50×.

the dioxide and can be seen on the photo. The lines on the etched surface now started forming not only from the top downwards, but also parallel to the lapped surface.

It was shown that the formation of the lines was not connected with the presence of atmospheric oxygen at the meniscus. Contact was made with the bottom of the electrode by an insulated lead. Even though the top of the electrode was protruding into the atmosphere, the lines now started forming from the bottom upwards.

DISCUSSION

Results thus far obtained do not allow a rigorous explanation. As work on this subject has, at least temporarily, been discontinued, it was thought desirable to describe the existence of the phenomenon. A tentative explanation will be offered, however.

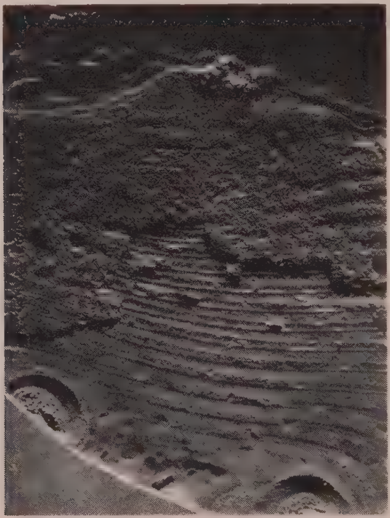

FIG. 3. Coating formed on prolonged anodization. Magnification 4×.

The low value of the current density that was obtained before the lines started forming shows that a barrier existed at the electrode-electrolyte interface. At the same time that the lines started appearing, a considerable increase in current density took place. This suggests that at this stage the barrier was considerably decreased. The observation that the striations always started appearing along the highest equipotential line shows that a minimum voltage was required for their formation. The near absence of lines on lapped and on strongly p-type etched samples suggests that holes or dislocations may facilitate the extension of the reaction along the electrode. On the other hand, on etched n-typ or near-intrinsic samples, the electrode reaction ma require a higher potential and hole concentration.

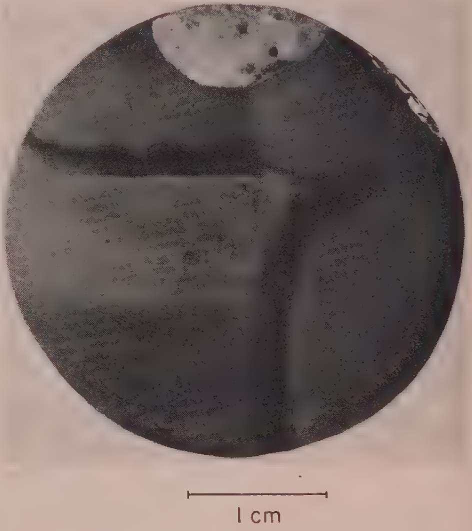

FIG. 4. Germanium electrode after anodization and treatmen with aqueous HF. Whole electrode was originally lapped but onl right side was etched (CP4). Magnification 2×.

It was found on lapped samples that the first step wa the formation of a dark film with a simultaneou decrease in current density. This film showed simila properties to the "monoxide film" that was obtained b Ellis[3] by the chemical etching of germanium. On furth electrolysis, the film became white (oxidized to GeO and the current density increased. Evidently, t monoxide has a higher electric resistance than t dioxide. Consequently, if on etched n-type samples t reaction $Ge^{2+} \rightarrow Ge^{4+}$ requires higher potential or ho concentration than the reaction $Ge \rightarrow Ge^{2+}$, the e planation of the appearance of the dark lines may that in between the dark lines the reaction $Ge^{2+} \rightarrow Ge$

---

[3] S. G. Ellis, J. Appl. Phys. 28, 1262 (1957).

ook place, resulting in a band where little or no resistance remains at the electrode-electrolyte interface. Consequently, in the vicinity of the band, a potential gradient and a hole-concentration gradient must exist which may limit the reaction in the neighboring band to Ge $\rightarrow$ Ge^{2+}. Along a line further down the electrode, both the potential and the concentration of holes may be of suitable value to allow the oxidation to the tetravalent germanium, etc. The increased width of the bands at higher temperatures (see Fig. 2) may thus be explained by an increase in the concentration of holes.

Striations similar in appearance to the ones shown in this paper were found by English.[4] Those striations were caused by some periodicity introduced into the germanium during the growth of the crystal. This can definitely not be the explanation in case of the present work, as the lines always started forming at the meniscus (when electric contact was made at the top) whatever the position of the sample.

ACKNOWLEDGMENTS

Thanks are due to S. Barnartt, J. P. McKelvey, and P. Schmidt for their interest in the present work.

---

[4] A. C. English, J. Appl. Phys. **31**, 1498 (1960).

JOURNAL OF APPLIED PHYSICS VOLUME 32, NUMBER 7 JULY, 1961

Proposed Method of Measuring Thermal Diffusivity at High Temperatures*

Robert D. Cowan
University of California, Los Alamos Scientific Laboratory, Los Alamos, New Mexico

(Received January 3, 1961)

A method is proposed for determining the thermal diffusivity α of a thin solid plate, mounted in a vacuum and heated to incandescence by means of a high-energy electron beam impinging on one face of the plate, or heated by thermal radiation from an arc-imaging furnace. The beam energy is to be modulated by either a square wave or a sine wave, and the resulting temperature modulation of the faces is to be observed photoelectrically. A theoretical study is made of the possibility of deducing the thermal diffusivity of the solid from amplitude and/or phase measurements. The most practical method seems to be that which involves sine wave modulation, and measurement of the phase difference between the temperatures of the two faces of the plate. With a plate thickness of about 1 mm and frequencies of the order of 0.01–300 cps (depending on the value of α), it should be possible to measure thermal diffusivities, especially of the poorer conductors (α less than about 0.1 cm^2/sec), for temperatures from 1000°K or less to the point where sublimation becomes troublesome.

I. INTRODUCTION

Accurate experimental measurement of the thermal conductivity k or of the thermal diffusivity $\alpha = k/c_p\rho$ of solids is very difficult at high temperatures, especially with samples of small size. This paper deals with a possible method[1] of measuring α at temperatures above about 1000°K, using small samples in the form of a slab perhaps a centimeter square and a millimeter thick (such as might be produced by rolling and sintering a powdered sample, for example). In this method, the sample is mounted in a vacuum and bombarded more or less uniformly on one face by a beam of electrons from an electron gun. The power deposited on the near face of the slab by this beam is adjusted to heat the solid to the temperature at which α is to be measured, and the intensity of the beam is then modulated so as to produce corresponding fluctuations in the temperatures of the faces of the slab. The resulting fluctuations in intensity of thermal radiation are observed photoelectrically, and used to deduce α from equations to be derived below. The physical setup is shown schematically in Fig. 1; it may be necessary to observe both faces of the slab, but only one phototube setup is shown.

The sample must of course be mounted in such a way that the electron beam current i can be conducted away, but with minimum heat conduction through the mounts. This indicates a small current and hence a high accelerating potential V for the electron gun—perhaps 5000 v or more.

It will be assumed that the energy which the solid acquires from the beam electrons is deposited instantaneously at the near face, $x=l$. These conditions are satisfied so long as V is less than 10 kv or so, since the electrons are then stopped within a negligible fraction of the slab thickness, and since heating by the x rays produced is negligible.[2] However, it is also necessary that the i^2R heating in the slab be less than, say, 1%

---

* Work performed under the auspices of the U. S. Atomic Energy Commission.

[1] The method was suggested to the author by R. D. Reiswig, P. E. Armstrong, and R. B. Gibney. The theory outlined in this paper is treated in greater detail in Los Alamos Sci. Lab. Rept. LA-2460, August 1, 1960.

[2] R. D. Evans, *The Atomic Nucleus* (McGraw-Hill Book Company, Inc., New York, 1955), pp. 615, 622 ff.

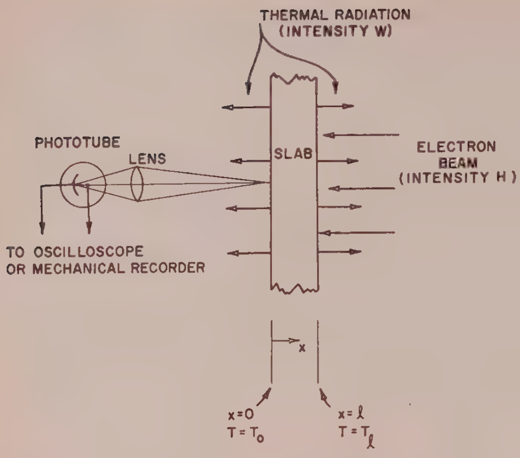

FIG. 1. Schematic drawing of experimental arrangement.

of the beam power $P=Vi\cong A\epsilon\sigma T^4$ (where $\epsilon\sigma T^4$ is the rate of thermal radiation loss per unit area of sample, and $A\cong 2$ cm² is the total surface area of the slab). With the electron current conducted out one edge of the slab, $R\cong\rho/l$. Assuming $l\cong 0.1$ cm, $V\cong 5000$ v, and an emissivity $\epsilon\cong 0.5$, this leads to the following limitation on the resistivity of the sample[3]:

$$\rho<\frac{0.01lV^2}{P}\cong\frac{5\cdot 10^{15}}{T^4}\cong\begin{cases}5000\text{ ohm-cm}, & T=1000^\circ\text{K},\\ 300\text{ ohm-cm}, & T=2000^\circ\text{K},\\ 60\text{ ohm-cm}, & T=3000^\circ\text{K}.\end{cases}\qquad(1)$$

Obviously this method of heating cannot be used with good electrical insulators. However, many materials of interest are semiconductors, and have adequate conductivity at high temperatures. For example, the resistivity of UO_2 is about 10^5 at room temperature, but drops to about 1 ohm-cm at 1000°K.[4] This is more than adequate, though a supplementary heater may be required initially to bring the material up to conducting temperatures where the electron beam heating can take over.

These restrictions on resistivity can of course be eliminated by using thermal radiation from an arc-imagining furnace in place of the electron beam; the latter is, however, more easily controlled and modulated. The theoretical treatment of the heat flow problem given below is of course applicable to either type heating.

II. SOLUTION OF EQUATION OF THERMAL CONDUCTIVITY

The temperature distribution within the slab (neglecting thermal conduction in directions parallel to the faces) is given by the solution of the one-dimensional differential equation

$$\alpha(\partial^2T/\partial x^2)=\partial T/\partial t,\qquad(2)$$

(where T is temperature, t is time, and x is the distance from the slab face farther from the incident electron beam), which satisfies the boundary conditions

$$\begin{aligned}(k\partial T/\partial x)_0&=W_0,\\(k\partial T/\partial x)_l&=H-W_l,\end{aligned}\qquad(3)$$

where $H=H(t)$ is the power per unit area deposited by the electron (or thermal radiation) beam, and $W_x=W(T_x)$ is the power radiated per unit area at the face $x=0$ or l.

It will be assumed that $H(t)$ has been constant for a long time previous to $t=0$, so that immediately before $t=0$, the temperature $T(x,t)$ in the slab has reached a steady state distribution $T_x{}^0$. The solution of Eqs. (2) and (3) is easily seen to be

$$\begin{aligned}T_x{}^0&=T_0{}^0+(T_l{}^0-T_0{}^0)x/l,\\k_x\partial T_x{}^0/\partial x&=(T_l{}^0-T_0{}^0)k_x/l=W_0{}^0=H^0-W_l{}^0.\end{aligned}\qquad(4)$$

It is also assumed that at $t=0$ a modulation is superimposed on H^0; this may consist of a change in H to some new constant value, or superposition of a square wave or sine wave, etc. If the change in temperature distribution which results is denoted by $\theta(x,t)\equiv T(x,t)-T_x{}^0$, then Eqs. (2) and (3) may be replaced by

$$\begin{aligned}\alpha(\partial^2\theta/\partial x^2)&=\partial\theta/\partial t,\\(\partial\theta/\partial x)_0&=c_0\theta(0,t),\\(\partial\theta/\partial x)_l&=F(t)-c_l\theta(l,t),\end{aligned}\qquad(5)$$

where

$$\begin{aligned}c_x&=[(\partial W/\partial T)/k]_{T_x{}^0},\quad x=0,l,\\F(t)&=[H(t)-H^0]/(k)_{T_l{}^0},\end{aligned}\qquad(6)$$

and it has been assumed that $F(t)$ is such that $\theta(x,t)$ is sufficiently small that $W_x-W_x{}^0$ can be represented by the first term in a Taylor series expansion.

The solution of the boundary value problem [Eqs. (5)] can be carried out by a straightforward application of the theory of Laplace transforms.[5] The transformed equations have the same form as Eqs. (5), except that $\theta(x,t)$ is replaced by its Laplace transform $\bar{\theta}(x,s)$; $F(t)$ is replaced by its transform $\bar{F}(s)$, and $\partial\theta/\partial t$ becomes $s\theta$. The solution of the transformed equations is easily found to be

$$\begin{aligned}\bar{\theta}(x,s)&=l\bar{F}(s)\left[\frac{(z+lc_0)e^{zx/l}+(z-lc_0)e^{-zx/l}}{(z^2+az+b)e^z-(z^2-az+b)e^{-z}}\right]\\&=l\bar{F}(s)\left[\frac{y\cos(yx/l)+lc_0\sin(yx/l)}{ay\cos y+(b-y^2)\sin y}\right],\end{aligned}\qquad(7$$

---

[3] This use of the symbol ρ should of course not be confused with that in the definition of α, where it represents the density of the material in question.

[4] R. K. Willardson, J. W. Moody, and H. L. Goering, J. Inorg. and Nuclear Chem. **6**, 19 (1958).

[5] See, for example, R. V. Churchill, *Operational Mathematic* (McGraw-Hill Book Company, Inc., New York, 1958), 2nd ed. Chaps. 1, 2, 4, 6; or H. S. Carslaw and J. C. Jaeger, *Conduction* *Heat in Solids* (Oxford University Press, New York, 1959), 2nd ed., Chap. 12.

where

$$z=iy=l(s/\alpha)^{\frac{1}{2}}, \tag{8}$$

$$a=l(c_0+c_l)=lc_0(1+r), \quad r=c_l/c_0, \tag{9}$$

$$b=l^2c_0c_l=ra^2/(1+r)^2\leqq a^2/4. \tag{10}$$

It will be shown in Sec. VI that the physically interesting ranges of the heat loss parameters a and r are

$$a\leqq\sim 3, \quad 1\leqq r\leqq\sim 2. \tag{11}$$

The solution of Eqs. (5) themselves is given by the inverse transform of Eq. (7), which may be written[5]

$$\theta(x,t)=\sum\left[\text{residue of } e^{st}\bar{\theta}(x,s)\right]_{s=s_n}, \tag{12}$$

the summation being over all singular points s_n of $\bar{\theta}(x,s)$.[6]

In addition to any singular points of $\bar{F}(s)$, whose values will of course depend on the form assumed for $F(t)$, there are also the singular points of the quantity in brackets in Eq. (7); these latter points are given by $s=-\alpha y^2/l^2$, where y is a solution of the equation

$$\cot y=y/a-b/ay. \tag{13}$$

All solutions of Eq. (13) can be shown to be real[7]; we need consider only the positive ones because corresponding positive and negative solutions represent the same value of s. It is easily seen [by drawing graphs of the functions on either side of Eq. (13)] that there is one positive solution y_n in each interval $n\pi<y<(n+1)\pi$, $n\geqq 0$. Because of the factor $\exp(-\alpha y_n^2t/l^2)$ in Eq. (12), the only solution of interest at large t is y_0; a series solution of Eq. (13) gives the following expression, accurate to better than $\frac{1}{2}\%$ over the range (11):

$$\begin{aligned} y_0^2 &\cong 3(a+b)/(3+a)-3a(a+b)^2/[5(3+a)^3], \\ &\qquad\qquad a\leqq 3; \qquad (14) \\ &\cong a(1-a/12), \quad a\leqq 0.2. \end{aligned}$$

Discussion of the solution (12) will be continued for three special forms of the electron beam modulation function $F(t)$.

III. STEP FUNCTION CHANGE

The first case considered is that in which the electron beam intensity is suddenly changed at $t=0$ from the constant value H^0 to some new constant value H.

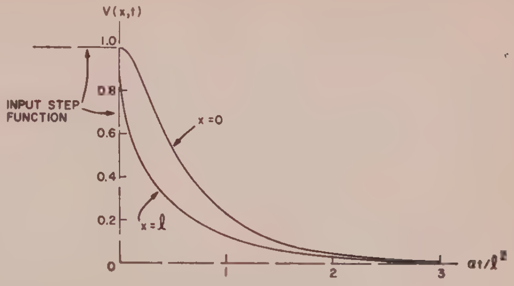

FIG. 2. Temperature changes at the surfaces of the slab, on a temperature scale of zero to one, when the irradiating-beam power is changed suddenly at $t=0$. (The case drawn is for $a=2$, $r=1$.)

From Eq. (6) it follows that $F(t)$ has the form

$$F(t)=\begin{cases}0, & t\leqq 0\\ F=\text{const}, & t>0,\end{cases} \tag{15}$$

for which the Laplace transform is $\bar{F}(s)=F/s$. This adds the singular point $s=0$ to the points $s_n=-\alpha y_n^2/l^2$ already discussed. Evaluation of the necessary residues at these points gives, from Eq. (12),

$$\frac{\theta(x,t)}{lF}=\frac{1+c_0x}{a+b}-2\sum_{n=0}^{\infty}\frac{\cos(y_nx/l)+(lc_0/y_n)\sin(y_nx/l)}{D_n} \times\exp\left(-\frac{\alpha y_n^2}{l^2}t\right), \tag{16}$$

where

$$D_n(a,b)=y_n(\sin y_n)\left(1+a-\frac{2b}{a}+\frac{y_n^2}{a}+\frac{b}{y_n^2}+\frac{b^2}{ay_n^2}\right). \tag{17}$$

It can be verified by numerical evaluation that $\theta(x,0)\equiv 0$, and it is easily seen that the limiting form of Eq. (16) as t tends to infinity is the correct (new steady state) solution of Eqs. (5).

To see how this result might be used to deduce a value of α, it is convenient to define a new function

$$V(x,t)=1-[(a+b)/(1+c_0x)lF]\theta(x,t). \tag{18}$$

This is simply the temperature change on a scale in which the initial steady state temperature is unity and the final steady state temperature is zero. The general forms of the functions $V(0,t)$ and $V(l,t)$ are shown in Fig. 2. These functions are readily measured experimentally without necessity of absolute temperature calibration; the only requirements are that the temperature-sensing device give a response which is a linear (or at least a known) function of temperature, and that observation be continued long enough to ascertain the asymptote of the observed curve (i.e., a time long compared with $l^2/\alpha y_0^2\cong l^2/\alpha a$).

For sufficiently large values of t, only the term $n=0$ in Eq. (16) contributes appreciably to V. If this

---

[6] Since distribution of the original report on which this treatment is based, the author has been informed that a solution of Eq. (5) identical in principle to that discussed here has been given by A. Hirschman (New York Naval Shipyard Material Laboratory project 5046-3, Part 121, Rept. DASA-1167, December 9, 1959). Hirschman's treatment is, however, much more limited in that he considers only the case $r=1$ with $F(t)$ a sinusoidal function, does not consider the amplitude of the temperature changes $\theta(x,t)$, considers the phase only at the face $x=0$, and discusses the result in detail only in the limit $a=0$.

[7] The proof given by Carslaw and Jaeger (Sec. 3.9 of reference 5) is unnecessarily complicated. A simple proof consists in setting $y=u+iv$ and expanding the cotangent into a real and an imaginary part; it is immediately seen that the imaginary part of Eq. (13) is satisfied only for $v=0$.

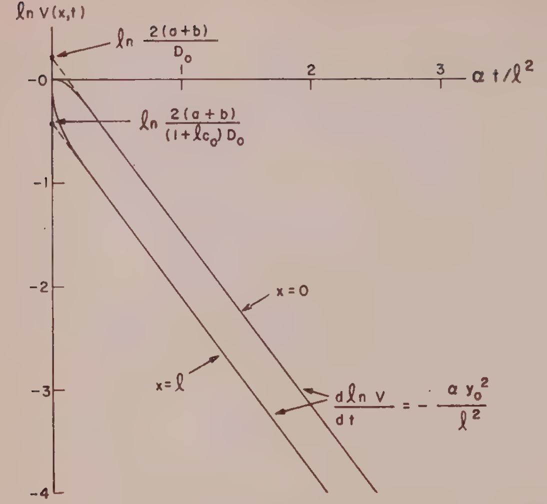

FIG. 3. Temperature changes of Fig. 2 drawn on a semilog plot. [The expression shown for the $x=l$ intercept is correct only for $r=1$; see Eq. (19).]

contribution is denoted by V_0, the value of V_0 at the two faces of the slab may be written

$$V_0(0,t)=[2(a+b)/D_0]\exp(-\alpha y_0^2 t/l^2),$$

$$V_0(l,t)=\frac{2(a+b)}{(1+lc_0)D_0}\left[\frac{(1+r)^2y_0^2+a^2}{(1+r)^2y_0^2+r^2a^2}\right]^{\frac{1}{2}}e^{-\alpha y_0{}^2t/l^2}, \quad (19)$$

where the expression at $x=l$ has been simplified with the aid of Eqs. (13), (9), and (10). Thus, on a semilog plot, both $V(0,t)$ and $V(l,t)$ tend asymptotically to straight lines with slope $-\alpha y_0^2/l^2$; this is shown in Fig. 3. Numerical evaluation of Eq. (16) shows that for all a and r satisfying Eq. (11), V becomes essentially identical with V_0 by the time V has decreased to about 0.7; thus there should be no difficulty in determining this slope experimentally.

In order to obtain a value of α from the experimental slope, it is necessary to know the value of $y_0=y_0(a,r)$. In some cases this can be found from the intercepts obtained by extrapolating to $t=0$ the straight-line parts of the $(\ln V,t)$ curves—i.e., from $\ln V_0(0,0)$ and/or $\ln V_0(l,0)$—since these depend on (a,r) but not on α. In fact, on using Eqs. (9), (10), and (14) it can easily be shown that Eqs. (19) reduce for small a (and any r) to

$$\begin{aligned} V_0(0,0)&\cong 1+a/6\cong 1+y_0^2/6,\\ V_0(l,0)&\cong 1-a/3\cong 1-y_0^3/3. \end{aligned} \quad (20)$$

These results are not valid when V_0 differs from unity by more than about 0.08, but general results obtained by numerical evaluation of Eqs. (19) are given in Fig. 4. It may be seen that $V_0(0,0)$ is essentially a unique function of y_0^2, being nearly independent of r, so that

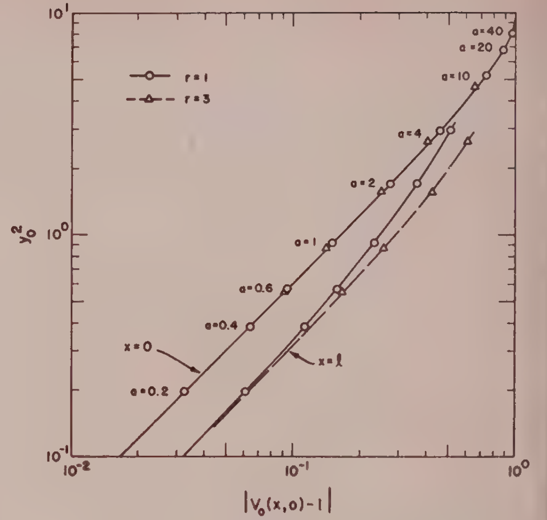

FIG. 4. Graph for determining y_0^2 from the extrapolated intercepts of experimental $\ln V$ vs t curves (step function change in irradiating-beam power).

y_0^2 can be found without ambiguity from measurements on the face $x=0$. However, this method of finding y_0^2 (and thereby α) is limited to values of a greater than about 0.1 because of difficulty in obtaining an accurate experimental value of the difference between $V_0(0,0)$ and unity [or between $V_0(0,0)$ and $V_0(l,0)$ for small a]. In spite of this seriously restricted range of values of a, the square wave method may be of value in supplementing the sine wave method to be described next, since for maximum accuracy the latter method requires approximate knowledge of a if $a>0.1$, and this is precisely the information obtainable from Fig. 4.

IV. SINE WAVE MODULATION

The case will now be considered in which the electron beam power is modulated with a sine wave of amplitude kF, where k is the thermal conductivity of the sample and F is some constant. Then, from Eq. (6),

$$F(t)=[H(t)-H^0]/k=\begin{cases}0, & t\leqq 0,\\ F\sin\omega t, & t\geqq 0,\end{cases} \quad (21)$$

which has a Laplace transform

$$\bar{F}(s)=F\omega/(s^2+\omega^2). \quad (22)$$

The singular points of Eq. (7) are now $s=\pm i\omega$, $-\alpha y_n^2/l^2$. The contributions to Eq. (12) at the points y_n decay exponentially with time, as before; we will consider only times $t\gg l^2/\alpha y_0^2$, so that all transients have died out and we need consider only the contributions to Eq. (12) at the points $s_\pm=\pm i\omega$. Then the sum of the residues of $e^{st}\bar{\theta}(x,s)$ at s_+ and s_- is just twice the real part of the residue at s_+, so that, writing $z=B(1+i)$ in

Eqs. (7) and (8), we find

$$\frac{\theta(x,t)}{lF}=\Re\frac{e^{i\omega t}}{i}\,\frac{(B+lc_0+iB)e^{C+iC}+(B-lc_0+iB)e^{-C-iC}}{(b+aB+2iB^2+iaB)e^{B+iB}-(b-aB+2iB^2-iaB)e^{-B-iB}},\tag{23}$$

where

$$B=l(\omega/2\alpha)^{\frac{1}{2}},\quad C=Bx/l.\tag{24}$$

This expression is of the form

$$\frac{\theta}{lF}=\Re\frac{e^{i\omega t}}{i}\left(\frac{j+ik}{m+in}\right)$$
$$=\frac{(jm+kn)(\sin\omega t)+(km-jn)(\cos\omega t)}{m^2+n^2},\tag{25}$$

where j and k are real functions of B and x, and m and n are real functions of B. This may be condensed to the form

$$\begin{aligned}\theta/lF&=P_x\sin(\omega t-\delta_x)\\&=P_x[(\cos\delta_x)(\sin\omega t)-(\sin\delta_x)(\cos\omega t)],\end{aligned}\tag{26}$$

where the amplitude P_x and phase lag δ_x are given by

$$P_x^2=(j^2+k^2)/(m^2+n^2),\qquad \tan\delta_x=(jn-km)/(jm+kn).$$

Obtaining the functions j, k, m, and n by comparing Eqs. (25) and (23), and introducing the abbreviations

$$\begin{aligned}Q_0&=\cosh^2B\cos^2B+\sinh^2B\sin^2B,\\Q_1&=\cosh B\sinh B+\cos B\sin B,\\Q_2&=\cosh^2B\sin^2B+\sinh^2B\cos^2B,\\Q_3&=\cosh B\sinh B-\cos B\sin B,\end{aligned}\tag{27}$$

one finds after a somewhat long but straightforward calculation:

$$P_l^2=\frac{2B^2Q_0+2aBQ_1/(1+r)+bQ_2/r}{2a^2B^2Q_0+2abBQ_1+(4B^4+b^2)Q_2+4aB^3Q_3},\tag{28}$$

$$P_0^2=\frac{2B^2}{2a^2B^2Q_0+2abBQ_1+(4B^4+b^2)Q_2+4aB^3Q_3},\tag{29}$$

$$\tan\delta_l=\frac{2B^3Q_1+2B^2aQ_2/(1+r)+bBQ_3/r}{2aB^2Q_0+b(1+2r)BQ_1/r+abQ_2/(1+r)+2B^3Q_3},\tag{30}$$

$$\tan\delta_0=\frac{b(\tan B-\tanh B)+2aB\tan B\tanh B+2B^2(\tan B+\tanh B)}{b(\tan B+\tanh B)+2aB-2B^2(\tan B-\tanh B)}.\tag{31}$$

These expressions are functions of the frequency ω and the thermal diffusivity α through the quantity $B=l(\omega/2\alpha)^{\frac{1}{2}}$, and depend also on the heat loss parameters a and r [Eqs. (9) and (10)]. The dependence of amplitude and phase on these quantities is obviously rather complicated, and can be studied satisfactorily only by numerical evaluation for various values of the parameters. This has been done with the aid of digital computers, and the results are given in Figs. 5–9. Figure 5 shows the amplitude of the temperature fluctuations at the irradiated face in arbitrary units (conversion to an absolute temperature scale is discussed in Sec. VIII), and Fig. 6 shows the attenuation of the temperature wave in passing through the slab. Figures 7 and 8 give the phase lag of the temperature wave (relative to the phase of the irradiating beam) for the irradiated face and for the far face of the slab, respectively; Fig. 9 shows the phase difference between the two faces. The possibility of determining α from experimental measurements corresponding to each of these figures will be discussed briefly in turn.

Amplitude Measurement aP_l at Input Face

This possibility seems definitely excluded because of extreme sensitivity to the value of the heat loss parameter a, the necessity of an absolute temperature change calibration, and the difficulty in making an accurate correlation between aP_l and an absolute temperature scale [Eq. (40) below].

Ratio P_0/P_l of Temperature Amplitudes at the Two Faces

For the parameter range (11), the relation between B and P_0/P_l is fairly insensitive to the value of a for $B>\sim 0.6\pi$, so that B (and thereby α) could in principle be found from a measurement of the ratio P_0/P_l; however, the necessity of calibrating even the relative response of two temperature sensing elements (possibly working at somewhat different mean temperatures) introduces additional uncertainty. The need for this relative-response calibration could be eliminated by measuring experimentally the *slope* of the $\ln(P_0/P_l)$

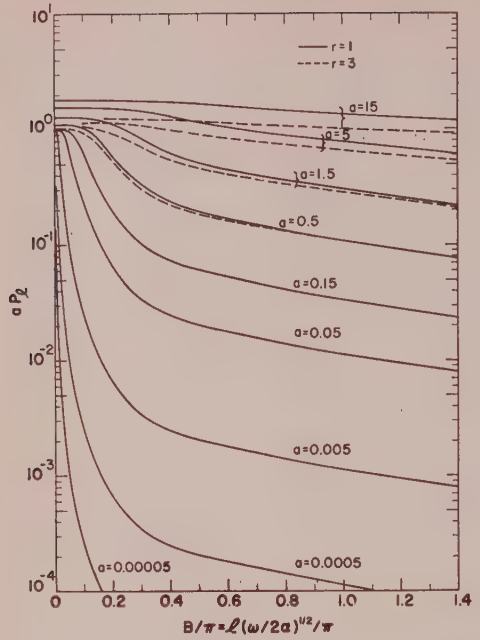

FIG. 5. Amplitude of the temperature change at the irradiated face of the slab for sine wave modulation of the irradiating beam. The relation of aP_l to an absolute temperature scale is given by Eq. (40).

vs B curve; however, this requires measurements at two or more frequencies, which is not only time consuming, but also introduces the possibility of error from change with time of a or of sensing-element response. In either case, it may not always be possible to work at sufficiently large B (high frequency) because of insufficient amplitude of the temperature wave (see Fig. 5 and Sec. VIII).

Phase Lag δ_l at Input Face

Phase comparisons are much easier to make than amplitude measurements, but use of δ_l does not seem feasible because of high sensitivity to a at low frequencies, and low sensitivity of δ_l to B at high frequencies.

Phase Lag δ_0 at Output Face

Since the δ_0 vs B relation is relatively insensitive to a, this approach appears feasible provided a is known approximately, and/or amplitude restrictions permit measurement at sufficiently large values of B.[8]

Phase Difference $\delta_0-\delta_l$ at the Two Faces

This method is rather insensitive to a even for small values of B. It would appear to be the most satisfactory of all with electron beam irradiation. With thermal irradiation, measurement of δ_l would probably be affected by reflected incident radiation, so that the δ_0 method might be preferable.

V. SQUARE WAVE MODULATION

Especially in the case of thermal irradiation, square wave modulation (chopping) of the irradiating beam may be much simpler than sine wave modulation. Theoretical results for this case can of course be obtained by analyzing the input wave form in a Fourier series, applying the sine wave theory to each term, and combining the results. Because of the high attenuation of the harmonics (Figs. 5 and 6), the output tends to be a pure sine wave and the phase relations are almost those given in Sec. IV, expecially if the output phase (δ_0) method is used, or if the harmonics are electrically filtered from the temperature signals.[8]

VI. PARAMETER VALUES

In order to use any of the above methods of finding α with maximum accuracy it is necessary to know at least approximately the values of the heat loss parameters a and r, defined in Eq. (9). These values can be estimated as follows if the sample is mounted in a vacuum so that the only heat loss is that resulting

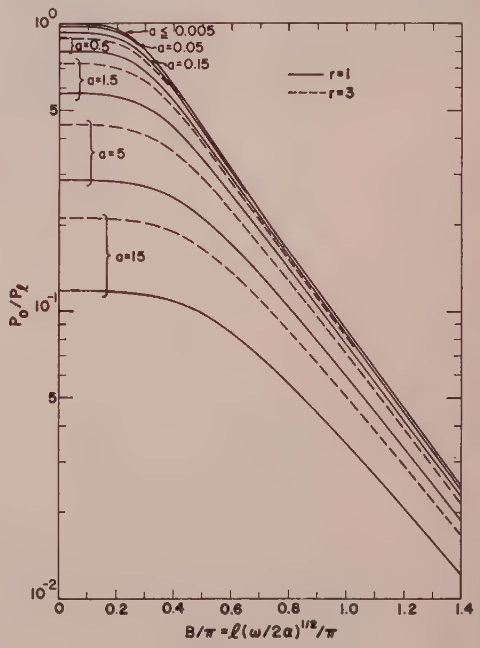

FIG. 6. Ratio of temperature amplitude at the output face to that at the input face for sine wave modulation.

---

[8] This method has been applied successfully by J. E. Dennis, A. Hirschman, W. L. Derksen, and T. I. Monahan (New York Naval Shipyard Material Laboratory project 5046-3, Part 123, Rept. DASA-1187, June 14, 1960), who used metal samples in air ($400<T<1100$°K), carbon-arc irradiation with square wave chopping, thermocouple sensing, and $\delta_0=\pi$. Amplitude restrictions were apparently not serious even though a was presumably as small as 10^{-3} for the cases which they investigated. The method has also been used with electron-beam heating in work sponsored by Materials Central, Wright Air Development Division, Air Research and Development Command, U. S. Air Force.

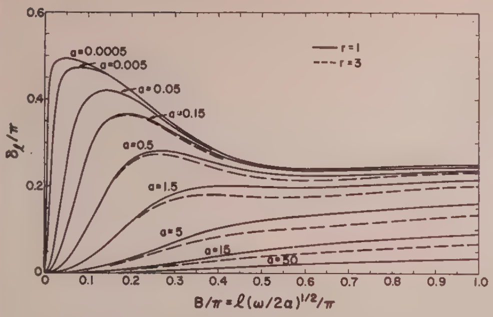

FIG. 7. The phase lag δ_l of the temperature wave at the irradiated face of the slab for sine wave modulation.

from thermal radiation. Over the limited range of the temperature fluctuations, $T = T^0 + \theta$, the total emissivity $\epsilon(T)$ of the sample may be assumed to vary as some power $m-4$ of the temperature. Thus

$$W = \epsilon\sigma T^4 \cong \sigma' T^m, \qquad (32)$$

where σ' is a constant (for given T^0), and m is known empirically[9] to have a value between about 4 and 5. From Eq. (6),

$$c_x \cong (mW/kT)_{T_x^0} \cong 5.7\times10^{-5}(m\epsilon T^3/k)_{T_x^0}, \qquad (33)$$

the numerical coefficient being for T and k in cgs units. Since k varies with temperature[10] no faster than about $T^{\pm1}$, then from Eqs. (9), (32), and (33),

$$r \cong (T_l^0/T_0^0)^{m-1\pm1}, \qquad (34)$$

and by also using Eq. (4),

$$a \equiv lc_0(1+r) = m(1+r)(T_l^0 - T_0^0)/T_0^0 \qquad (35)$$

$$\cong 5.7\times10^{-5} l(1+r)(m\epsilon T^3/k)_{T_0^0}. \qquad (36)$$

[Since the temperatures of the two faces cannot be allowed to differ by more than 10 or 20% at most, if α is to be measured as an average value over a fairly limited temperature range, Eqs. (34) and (35) lead immediately to the restrictions (11).] Since values of k for solids range from about 10^5 to 4×10^7 erg/sec-cm-°K, then for $l = 0.1$ cm, $r = 1$, and $m = 4$, the corresponding range of values of a is (for T in °K):

$$a \cong (0.5 \text{ to } 0.001)\epsilon(T/1000)^3. \qquad (37)$$

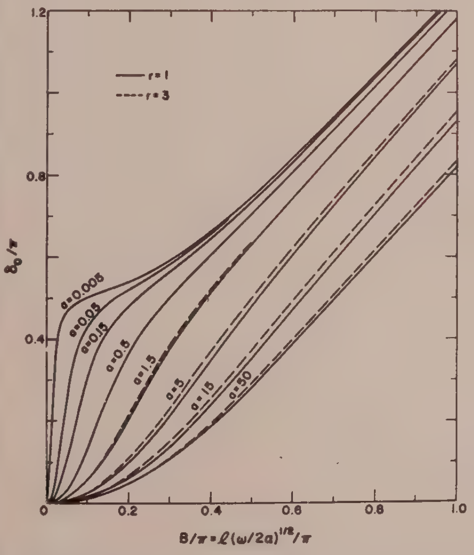

FIG. 8. The phase lag δ_0 of the temperature wave at the output face of the slab, relative to the phase of the sine wave modulation of the irradiating beam.

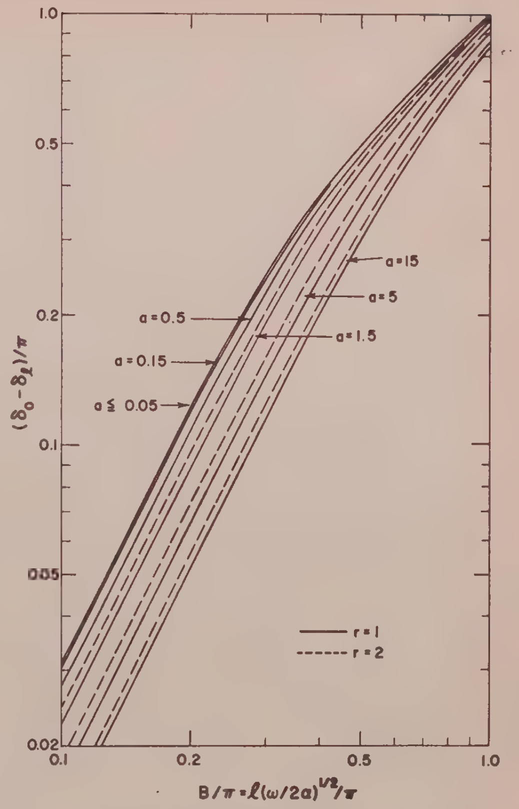

FIG. 9. The phase difference $\delta_0 - \delta_l$ between the temperature fluctuations at the two faces of the slab for sine wave modulation of the irradiating beam. (Note that unlike the other figures, curves are given here for $r=1$ and $r=2$.)

If the sample is heated by thermal radiation rather than by electron bombardment and is not mounted in a vacuum, then an additional term must be added to W in Eq. (32) to represent heat loss by convection to the surrounding gas. This additional term varies with a power of T little greater than unity[11]; hence it tends to make the effective value of m for use in Eqs. (33)–(35) more nearly unity, and makes r more nearly equal to 1. A corresponding term must be added to Eq. (36); this term is dominant below about 1000°K, especially for metals, for which ϵ is very low.

---

[9] See, for example, M. Jakob, *Heat Transfer* (John Wiley & Sons, Inc., New York, 1949), Vol. I, Chaps. 4 and 7.

[10] M. Jakob and G. A. Hawkins, *Elements of Heat Transfer and Insulation* (John Wiley & Sons, Inc., New York, 1950), 2nd ed., p. 26.

In any case, Eqs. (34) and (35)—with an estimated effective value of m—can be used to estimate a and r from experimentally observed values of the surface temperatures. Or a can be estimated by using the step function method described in Sec. III. Either approach should be sufficiently accurate for use with Fig. 8 or Fig. 9.

VII. TIME AND FREQUENCY REQUIREMENTS

As mentioned above, both the step function and the sine wave method involve times long compared with $l^2/\alpha y_0^2 \cong l^2/\alpha a$. Using (36) for a sample mounted in a vacuum, this implies

$$t \gg \frac{l c_p \rho}{5.7\times 10^{-5}(1+r)m\epsilon T^3} \cong 40\left(\frac{1000}{T}\right)^3 \text{ sec}, \qquad (38)$$

where the values $l \cong 0.1$ cm, $c_p\rho \cong 4\times 10^7$ erg/cc-°K, $r \cong 1$, and $m\epsilon \cong 1$ have been used. Such times should not be prohibitive for $T \gtrsim 1000$°K. For samples mounted in a gas, convection losses increase a, and hence the times required are smaller than indicated by relation (38).

From Figs. 8 and 9 it may be seen that the sine wave method requires values of B/π of about 0.1–1.0. The corresponding frequencies are (for $l \cong 0.1$).

$$f = \omega/2\pi = (\alpha\pi/l^2)(B/\pi)^2 \cong 3\alpha \text{ to } 300\alpha. \qquad (39)$$

With experimental diffusivities covering a range of about $0.002 < \alpha < 1.0$ cm²/sec, the corresponding frequency range is about 0.01–300 cps. The low frequencies are probably most easily produced and recorded mechanically, the high frequencies electronically.

VIII. AMPLITUDE CONSIDERATIONS

An expression for the ratio of the temperature modulation of the input face ($x=l$) to the (sine wave) modulation of the irradiating beam follows from Eqs. (26), (21), (4), (33), and (9):

$$\frac{(\text{ampl}\,\theta_l)/T_l^0}{(\text{ampl}\,H)/H^0} = \frac{lP_lH^0}{kT_l^0} \cong \frac{lP_l}{k}\left(\frac{W_0^0}{T_0^0}+\frac{W_l^0}{T_l^0}\right) = \frac{aP_l}{m}. \qquad (40)$$

Since the modulation of the irradiating beam cannot be greater than unity (and still remain a sine wave),

$$(\text{ampl}\,\theta_l)/T_l^0 \leqq aP_l/m \cong aP_l/4. \qquad (41)$$

It is clear from Figs. 5 and 6 that the temperature amplitudes are very small for small values of a, except at low frequencies (small B, and correspondingly small phase shifts). No experiments have been made in this laboratory, and it is uncertain how serious phototube noise, etc., would be in setting lower limits on workable values of a. However, amplitude restrictions do not appear serious for semiconducting samples (which have low thermal conductivity and therefore relatively large a), nor for metals mounted in gas[8] or examined at sufficiently high temperatures ($T > \sim 1000$°K).

IX. CONCLUSIONS

The step function method is probably of little practical value, since by itself it gives a value of α only over the rather limited parameter range $0.1 < a < 3$. However, it might be of some interest in checking the theory, or in providing a check on the sine wave method in special cases.

The sine wave method, which uses a measurement of the phase of the temperature wave at the output face relative to that at the input face (or relative to the phase of the irradiating beam), requires a somewhat complicated experimental arrangement, but is simple in principle and appears to be perfectly feasible. It should be especially suitable for low thermal-conductivity materials at high temperatures, where the loss parameter a is relatively large and amplitudes of the temperature waves are correspondingly conveniently large; this is just the case in which most methods tend to be least satisfactory.

For high-conductivity metals at low temperatures, sufficient amplitude may be obtainable only if the loss parameter a is increased by putting the sample in a gaseous environment rather than in a vacuum. This would of course necessitate thermal irradiation of the input face rather than electron beam heating, and would probably necessitate measuring the phase of the irradiating beam rather than that of the temperature of the input face.

The method is applicable only to materials which are essentially opaque to thermal radiation, since it is assumed that all heat loss by radiation occurs at the sample surfaces.

ACKNOWLEDGMENT

The author wishes to thank R. D. Reiswig for suggesting this theoretical investigation, and for numerous helpful discussions.

---

[11] See Chaps. 22 and 25 of reference 9.

JOURNAL OF APPLIED PHYSICS VOLUME 32, NUMBER 7 JULY, 1961

Paramagnetic Maser Oscillator Analysis*

S. WANG AND J. R. SINGER†
University of California, Berkeley, California

(Received December 27, 1960)

A physical and mathematical description of maser oscillator is given with particular emphasis upon explaining the structure of the output line shape. Several approaches to the problem are taken. A qualitative description of the motion of the spin vector is followed by a derivation of the equations pertinent to the interaction of a tuned circuit (microwave cavity) and precessing spins. The resultant equation is nonlinear. Approximate solutions are given and these are plotted as output amplitude vs time. In addition, the equations are solved with numerical solutions for specific experimental conditions by means of a digital computer. The numerical results are compared with experimental data including that taken in our laboratory. The field-swept oscillator line shapes are explained by the analysis, and the steady state oscillator is described as well.

I. INTRODUCTION

A NUMBER of approximate analyses[1–4] to the problem of understanding the shape of maser oscillator output have shown rough agreement with some of the data. Reference should also be made to an earlier work by Bloembergen and Pount[5] concerning the interaction between radiation field and spin system. In this paper, the analysis is extended to include more realistic experimental conditions, and an IBM 704 computer has been utilized to obtain a more exact solution to the pertinent nonlinear differential equation. The solutions are plotted for the various conditions and compared with maser experiments using different materials which were carried out in various laboratories, including ours. Theoretical agreement is very satisfactory for both the static experiment and the field-swept maser oscillator experiment.

We shall first qualitatively describe the physics of the spin system coupled to a resonator in general terms, and show why the spin system behaves as a damped oscillator. In a later section we shall quantitatively analyze the spin system coupled to the resonating circuit and derive the pertinent descriptive equations. Finally, we will compare our theoretical analysis with the experimental data.

II. QUALITATIVE DESCRIPTION OF THE SPIN VECTOR MOTION

In the initial description we assume, following a treatment of Bloch,[6] that the net magnetization, due to spins polarized in a magnetic field, be considered as a vector **M**. In the conventional two-level maser, the population inversion of the upper and lower energy levels (by adiabatic fast passage or 180° pulse) may be considered as a reversal of the magnetization (or spin) vector direction relative to the magnetic field. The inverted vector may then be conveniently treated by a modified set of Bloch equations to describe its motion.

Consider the spin vector inverted in a resonant structure. The vector precesses in a magnetic field and satisfies the Larmor relation $\omega=\gamma H_0$ where ω is the angular frequency, γ is the magnetogyric ratio of the spins, and H_0 is the static magnetic field. Suppose that ω, the precession frequency, equals the angular frequency to which the resonant structure is tuned. The oscillation condition, first derived by Combrission *et al.*,[7] is

$$N\geqslant\frac{kTV_c(\Delta H)}{4\pi\mu_B{}^2H_0FQ}, \tag{1}$$

where N is the total number of spins, k is Boltzmann's constant, T is the temperature, V_c is the cavity volume, ΔH is the resonant linewidth of the crystal, μ_B is a Bohr magneton, F is the filling factor of the cavity, and Q is the loaded Q of the cavity. We suppose that this equation is satisfied, and consider the motion of the spin vector.

The classical description of a magnet precessing while coupled to a resonant circuit will be adequate for this description. The spin vector is never completely aligned along the direction of H which we call the z axis, but has a component in the x and y directions. This component induces a voltage in the resonant circuit which is oriented as shown in Fig. 1.

The initial voltage induced in the coil L is due to the y component of changing flux, which is

$$(d/dt)(M\sin\theta\cos\omega t) =-M\omega\sin\theta\sin\omega t+\dot{\theta}M\cos\theta\cos\omega t, \tag{2}$$

providing M were constant and not a function of time.

---

* This research was supported in part by the Office of Scientific Research through a contract, and by the Miller Institute for Basic Research in Science, University of California, Berkeley, California.

† Miller Institute for Basic Research in Science.

[1] J. R. Singer in *Quantum Electronics*, edited by C. H. Townes (Columbia University Press, New York, 1960), p. 525.

[2] H. Statz and G. deMars in *Quantum Electronics*, edited by C. H. Townes (Columbia University Press, New York, 1960), p. 530.

[3] J. C. Kemp, Ph.D. dissertation, University of California, Berkeley, California (1959, unpublished).

[4] A. Yariv, J. R. Singer, and J. Kemp, J. Appl. Phys. **30**, 265 (1959).

[5] N. Bloembergen and R. V. Pound, Phys. Rev. **95**, 8 (1954).

[6] F. Bloch, Phys. Rev. **70**, 460 (1946).

[7] J. Combrisson, A. Honig, and C. H. Townes, Compt. rend. **242**, 2451 (1956).

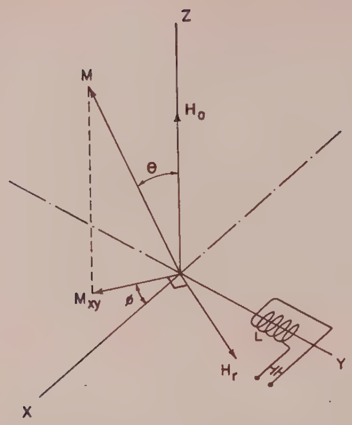

FIG. 1. Qualitative description of the precessing motion of the magnetization vector **M** in a two-level maser oscillator.

(Later we shall consider a more detailed analysis where $|M|$ varies with time.) The current flowing in the coil gives rise to a magnetic field H_r (the reaction field) which can best be described by solving the resonant circuit equation without losses (initially).

We defer the quantitative analysis but note that the current flowing in the coil and H_r are (to first order) 90° behind the magnetization vector due to the fact that the voltage induced is given by Eq. (2). We may draw the respective orientation of the vectors M and H_r as shown in Fig. 1 in a reference frame rotating with angular frequency ω.

The effect of H_r is to induce an increase in the angle which M makes with the z axis; that is, θ will increase. The physical reason for the increase is the torque **T** which $\mathbf{H}_r$ exerts upon **M**,

$$\mathbf{T}=\mathbf{M}\times\mathbf{H}_r, \tag{3}$$

which leads to the Larmor equation for the precession frequency ω_1 of **M** about $\mathbf{H}_r$ in a reference frame rotating with angular frequency ω. The angular precession frequency is

$$\omega_1=\gamma H_r. \tag{4}$$

It must be noted, however, that H_r is not constant but is rather a function of time. Consequently the rate at which M precesses from the $+z$ to the $-z$ direction varies. Initially the angle θ is small, the voltage induced in the resonant circuit is small, and the current with its attendant field H_r is small. After H_r appears, the torque on **M** becomes larger and increases θ, leading to a larger H_r which in turn increases θ again through the torque exerted on **M**. The buildup of a reaction field and the precession of **M** is very rapid in the maser oscillator since the processes of increasing θ and H_r provide mutually positive feedback. When **M** precesses in the $x-y$ plane the value of H_r is a maximum and the angular velocity $\dot{\theta}$ is also a maximum. As **M** continues precessing and becomes aligned in the $-z$ direction, the value of H_r depends only upon the Q of the resonant circuit relative to the precession time of **M** for $\pi/2$ rad.

If the usual experimental conditions for oscillation are satisfied as per Eq. (1), then the Q of the cavity is generally the order of 10^4. Hence the ringing time (Q/ω) is about a microsecond. Therefore the reaction field will continue to derive the vector **M** past the $-z$ direction and up towards the $x-y$ plane. When the magnetization vector goes past the $-z$ direction, there is a change in direction in the phase of the induced voltage.

The voltage and current flow in the new direction is π rad out of phase with the ringing current of the resonant cavity. The necessity of this phase shift may be realized by considering that the reaction field must lag the magnetization vector which induces it. The rotation of **M** through the $-z$ axis results in the resonant circuit having a reaction field which leads **M** in the rotating frame. Consequently **M** is driven past $-z$ by the ringing of the cavity, but as θ becomes greater than 180° the voltage induced in the resonant circuit by **M** is π rad out of phase with the ringing voltage. The two voltages therefore cancel at some time after **M** goes past the $-z$ axis. H_r continues building up in the cavity and produces a torque on **M** which drives **M** back towards the $-z$ direction again. The effect of the reaction field is to drive the magnetization vector back through the $-z$ direction, where **M** builds up a reaction field in the opposite direction again. Thus there is a pendulum motion of **M** in the rotating reference frame of our observation.

Three mechanisms will reduce the energy of the spin system. First, there is the fact that energy is lost from the resonant circuit, and the vector **M** will be driven less far from the $-z$ direction on each swing. Second, there is a dephasing effect on the spins so that they may act independently and reduce the magnitude of **M** (T_2 effects). Third, the value of **M** is reduced by thermal relaxation (T_1 effects). The processes have been listed in their order of importance for most of the experimental data available. In some cases this order may be changed.

Another possibility for the motion of the spin vector should be discussed. We ask if the Q of the cavity and the stored energy may be sufficient to drive the magnetization vector completely through π rad and back to the initial condition. This can be proven to be impossible, as we now argue. Suppose that **M** has reached the negative z direction. The energy in the circuit continues to drive **M** around. If **M** remains a coherent collection of spins, the driving field will be exactly opposed by the oppositely oriented reaction field when **M** reaches $\pi/2$ rad past the $-z$ direction. On the other hand, if **M** had decreased in magnitude due to relaxation processes, it might be possible to drive the reduced **M** to the $+z$ direction. In the physical cases considered, the latter situation was very unlikely because the ringing time of the cavity was insufficient relative to the time for **M** to precess about H_r.

One must also ask what determines the coherence of the spin vector **M**. If **M** were to become incoherent in a time T_2, then the analysis would only be valid for that time. However, the fact that a field H_r exists will tend to produce coherence of the vector **M** for a time much longer than T_2. The only time that H_r is zero is when the ringing field of the cavity and the reaction field are opposed. At other times coherence is self-sustaining. Thus one expects that the vector **M** will be coherent for a much longer time than T_2.

III. QUANTITATIVE ANALYSIS

The interaction between the spin system and the external magnetic field can be described by a set of the celebrated Bloch equations[6]:

$$(dm_x/dt)-\gamma(m_yH_z-m_zH_y)+(m_x/T_2)=0, \quad (5)$$

$$(dm_y/dt)-\gamma(m_zH_x-m_xH_z)+(m_y/T_2)=0, \quad (6)$$

$$(dm_z/dt)-\gamma(m_xH_y-m_yH_x)-[(m_0-m_z)/T_1]=0. \quad (7)$$

In the above equations, T_1 is the spin-lattice relaxation time and T_2 is the spin-spin relaxation time. These equations have been successfully applied to paramagnetic resonance experiments, including both absorption and induction types, and need no further explanation. In a resonance experiment, one applies a constant ac magnetic field H_1 to the spin system and solves for m_x or m_y as a function of H_1. For a maser oscillator, however, the amplitude of the ac magnetic field, and hence those of m_x and m_y, can no longer be considered as constants. For the sake of simplicity, complex notation will be used in the following analysis.

Let

$$H^+=H_x+jH_y, \quad H^-=H_x-jH_y$$

$$m^+=m_x+jm_y, \quad m^-=m_x-jm_y$$

in order to transform in a convenient way to a rotating coordinate system. Then Eqs. (5) and (6) can be written as

$$\begin{aligned}(dm^+/dt)&=[(T_2)^{-1}+j\gamma H_z]m^+=j\gamma m_zH^+,\\(dm^-/dt)&+[(T_2)^{-1}-j\gamma H_z]m^-=-j\gamma m_zH^-.\end{aligned} \quad (8)$$

Since a linearly polarized field can always be resolved into two circularly polarized components, there is no loss of generality to assume

$$H^+=H_1(t)\exp(-j\omega t),$$

$$H^-=H_1(t)\exp(j\omega t),$$

$$m^+=[u(t)+jv(t)]\exp(-j\omega t),$$

and

$$m^-=[u(t)-jv(t)]\exp(j\omega t).$$

In the above equations, $H_1(t)$, $u(t)$, and $v(t)$ are slowly varying functions of time as compared with $\exp j\omega t$, and they are also real. Substituting H^+, H^-, m^+, and m^- into Eq. (8), and separating the real and imaginary parts, one obtains

$$(dv/dt)+(v/T_2)+(\gamma H_z-\omega)u=\gamma m_zH_1, \quad (9)$$

$$(du/dt)+(u/T_2)-(\gamma H_z-\omega)v=0. \quad (10)$$

At resonance, one has $\omega=\gamma H_z=\gamma H_0$, where H_0 is the dc magnetic field, and thus

$$(dv/dt)+(v/T_2)=\gamma m_zH_1. \quad (11)$$

Let us now turn our attention to the interaction between the cavity and the spin system. Because of induced transitions by the microwave field, the spin system steadily loses its energy to the cavity. Classically, one can write the rate of change of stored energy in a cavity as

$$\frac{d}{dt}\left[\frac{1}{4\pi}\int_{v_c}\mu H_1^2dv\right]$$

$$=\frac{-1}{4\pi}\int_{v_c}\frac{\omega}{Q}\mu H_1^2dv+\frac{d}{dt}\int_{v_s}\mu H_0m_zdv, \quad (12)$$

where Q is the load quality factor, v_c the volume of the cavity, and v_s the volume of the sample. In the above equation, the first term on the right-hand side represents power delivered to external load plus ohmic loss inside the cavity, while the second term represents power transfer from the spin system to the cavity. Using the definition of a filling factor F, one can rewrite the above equation as

$$(dH_1^2/dt)+(\omega/Q)H_1^2=4\pi FH_0(dm_z/dt). \quad (13)$$

The average rate of change in the z component of magnetization can be obtained from Eq. (7). In Eq. (7), $(m_0-m_z)/T_1$ represents the change in m_z due to spin-lattice interaction, while $(m_xH_y-m_yH_x)$ represents the change in m_z due to induced transitions by the microwave field. For efficient operation of a two-level maser oscillator, the former process is insignificant as compared with the latter process. Therefore, one can write the average rate of change in m_z as

$$dm_z/dt=\langle(m_xH_y-H_xm_y)\rangle_{\text{av}}=-\gamma v(t)H_1(t)$$

or

$$m_z=-m_0-\int_0^t\gamma v(t)H_1(t)dt. \quad (14)$$

One can also rewrite Eq. (13) as

$$(dH_1/dt)+(\omega/2Q)H_1=-2\pi F\omega v(t) \quad (15)$$

and then Eq. (14) as

$$m_z=-m_0+\frac{\gamma}{2\pi F\omega}\left(\frac{1}{2}H_1^2+\frac{\omega}{2Q}\int_0^tH_1^2dt\right). \quad (16)$$

Equations (11), (15), and (16) are three fundamental equations which describe the behavior of $H_1(t)$, $v(t)$, and $m_z(t)$ as a function of time. On eliminating $v(t)$ from Eqs. (11) and (15) and using the value of m_z from Eq. (16), one obtains an integral-differential equation for H_1 as follows:

$$\frac{d^2H_1}{dt^2}+\left(\frac{\omega}{2Q}+\frac{1}{T_2}\right)\frac{dH_1}{dt}-\left(\omega 2\pi F m_0-\frac{\omega}{2Q}\frac{1}{T_2}\right)H_1 = -\frac{\gamma^2 H_1^3}{2}-\frac{\gamma^2\omega H_1}{2Q}\int_0^t H_1^2 dt. \quad (17)$$

Initially, $H_1=0$; therefore, for oscillation to build up, the following condition has to be satisfied:

$$\omega 2\pi F\gamma m_0 > \omega/2QT_2.$$

The above condition for spontaneous radiation was first established by Combrisson *et al.*[7] in a different form; it is the same as Eq. (1).

IV. IDEAL CASE

Equation (17) is nonlinear and is best solved by numerical procedrures; however, it will be useful to first examine the qualitative behavior of the various quantities $H_1(t)$, $v(t)$, and $m_z(t)$ for an ideal case where there is no spin dephasing, i.e., $1/T_2=0$, and no loss in the cavity, i.e., $1/Q=0$. From Eqs. (11) and (14), one finds that $m_z^2(t)+v^2(t)$ is a constant of motion, and further that

$$m_z(t)=-m_0\cos\int_0^t \gamma H_1(t)dt, \quad (18)$$

$$v(t)=-m_0\sin\int_0^t \gamma H_1(t)dt. \quad (19)$$

From Eq. (16) one obtains

$$m_z=-m_0+\gamma H_1^2(t)/4\pi F\omega. \quad (20)$$

In other words, the energy of the whole system is oscillating back and forth between the spin system and the cavity, and the magnetization vector m continuously makes spiral precessions about the z axis. In the rotating coordinate system, if one chooses the y' axis as the direction of the reaction field, then the magnetization vector m will precess continuously in the $x'-z$ plane. The qualitative behavior of $H_1(t)$, $v(t)$, and $m_z(t)$ is illustrated in Fig. 2.

One can clearly see from Fig. 2 that $H_1(t)$ is amplitude modulated, while both $m_z(t)$ and $v(t)$ are phase modulated. Furthermore, if one expresses $H_1(t)$ in terms of its Fourier components

$$H_1(t)=h_0+h_1\cos\beta t+h_2\cos 2\beta t+\cdots$$

and uses the following expansion:

$$\cos(x\cos\phi)=J_0(x)+2J_2(x)\cos 2\phi+2J_4(x)\cos 4\phi+\cdots$$

$$\sin(x\sin\phi)=2J_1(x)\sin\phi+2J_3(x)\sin 3\phi+\cdots,$$

one can easily show that the fundamental oscillation frequency β is equal to γh_0, where $h_0=(4\pi F\omega m_0/\gamma)^{\frac{1}{2}}$.

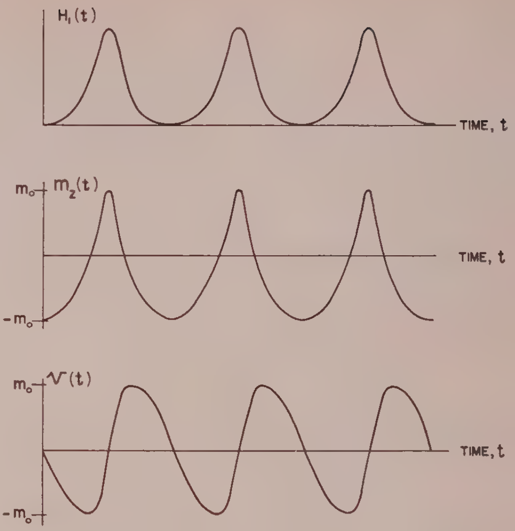

FIG. 2. Qualitative behavior of the amplitude of the microwave field $H_1(t)$ and the amplitudes of the x and the z component of magnetization, $v(t)$ and $m_z(t)$, as functions of time for an ideal two-level maser oscillator without any cavity loss and spin dephasing.

It should be mentioned that Eq. (17), by setting $1/Q=0$ and $1/T_2=0$, is very similar to the pendulum equation. The more exact value of β can be found by successive approximation as carried out in the analysis[8] of a nonlinear problem of this type. However, for the present purpose, the analysis is semiquantitative, and the value of β given above is considered to be accurate enough.

In Fig. 3, the numerical solution of $H_1(t)$, calculated from Eq. (17) with the aid of an IBM 704 computer,[9] is plotted as a function of time for the ideal case with $1/T_2=0$, $1/Q=0$, and $\omega 2\pi F\gamma m_0=1\times 10^{14}$ sec^2. Thus, the maximum amplitude of the microwave magnetic field should be about 1.1 oe as calculated from Eq. (20), and this value agrees well with the computed value shown in Fig. 3. The average amplitude h_0 of the ac field which can be estimated from Fig. 3 is around 0.4 oe. This value of h_0 corresponds to an amplitude-modulation period of $t_1=2\pi/\gamma\ h_0=0.9\times 10^{-6}$ sec, which agrees well with the value of 10^{-6} sec as shown in Fig. 3.

V. OSCILLATION ENVELOPE IN PRACTICAL MASERS

In Fig. 4, the computed solution of Eq. (17) is plotted as a function of time for two cases: $2\pi F\omega\gamma m_0$

---

[8] See, for example, W. J. Cunningham, *Nonlinear Analysis* (McGraw-Hill Book Company, Inc., New York, 1958), Chap. 6.

[9] We are indebted to the University of California Computer Center and the Faculty Research Committee for assistance in programing the problem on the computer.

$=10\times10^{13}$ and $15\times10^{14}/\text{sec}^2$. In both cases the values of $\omega/2Q=3\times10^6/\text{sec}$ and $1/T_2=5\times10^6/\text{sec}$ were chosen. The amplitude of the microwave magnetic field is again amplitude modulated, indicating that the stored energy is oscillating back and forth from the spin system to the cavity. The amplitude-modulation period t_1, which can be obtained from Fig. 4 directly, agrees well with the value computed from the formula $t_1=2\pi/\gamma h_0$, where h_0 is the average value of the microwave magnetic field. For example, in Fig. 4(a), $h_0=0.3$ oe; this corresponds to a value of $t_1=1\times10^{-6}$ sec, while Fig. 4(a) gives a value of $t_1=0.8\times10^{-6}$ sec. In Fig. 4(b), $h_0=1.4$ oe; this corresponds to a value of $t_1=2.4\times10^{-7}$ sec, while Fig. 4(b) gives a value of $t_1=2\times10^{-7}$ sec.

The introduction of cavity loss and spin dephasing does not change the basic picture presented in the preceding discussion. The stored energy in a two-level maser system oscillates back and forth from the spin system to the cavity with an angular frequency $\beta=\gamma h_0$. Further, in a lossy cavity, the total energy in a maser system will decay with a characteristic time Q/ω. This is obvious from the following equation:

$$\frac{\omega}{2Q}\int_0^t H_1^2 dt=2\pi F H_0 m_0,$$

which says that the total energy dissipated in the microwave system should be equal to the total energy stored originally in the spin system. From Eq. (20), $H_1^2=4\pi F H_0 m_0$. Thus, the duration of the microwave oscillation due to maser section will be of the order

$$4\pi Q F H_0 m_0/\omega H_1^2=(Q/\omega)\text{ sec}.$$

The curves shown in Fig. 4 indeed bear out the above reasoning.

So far, our discussion has been based on the assumption that the oscillation condition $\omega=\gamma h_0$ is suddenly established and that the total energy stored in the spin system is all of a sudden ready for maser action. In a practical maser, however, the dc magnetic field is swept at a finite rate through the resonance condition. Because of inhomogeneous broadening of the resonance line, maser action may take place when the dc magnetic field H_0 is still slightly off the resonance condition.

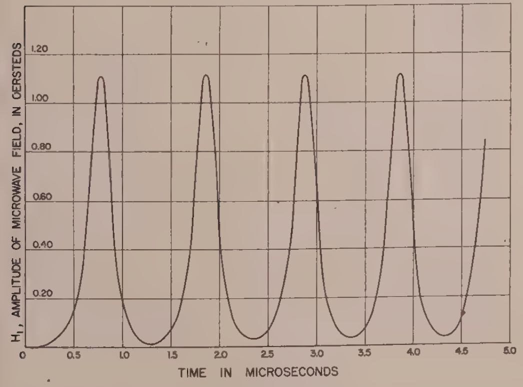

FIG. 3. Computed curve of the amplitude of the microwave field $H_1(t)$ as a function of time from Eq. (17) for an ideal two-level maser oscillator with $1/T_2=0$, $1/Q=0$, and

$$2\pi F\omega\gamma m_0=1\times10^{14}/\text{sec}^2.$$

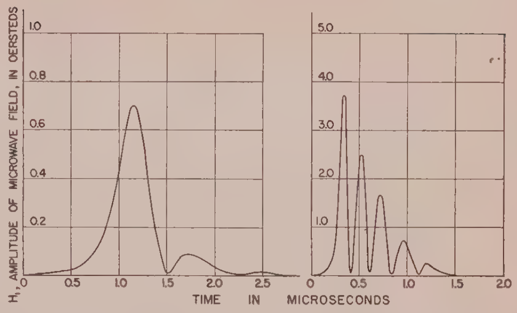

FIG. 4. Computed curves of the amplitude of the microwave field $H_1(t)$ as functions of time from Eq. (17) for two cases: (a) $2\pi F\omega\gamma m_0=1\times10^{14}/\text{sec}^2$ and (b) $2\pi F\omega\gamma m_0=1.5\times10^{15}/\text{sec}^2$. In both cases, $\omega/2Q=3\times10^6/\text{sec}$ and $1/T_2=5\times10^6/\text{sec}$.

Different spins in a solid see a different local field due to hyperfine structure and spin-spin interaction. This will result in the inhomogeneous broadening of the resonance line; in other words, the spin system has a distribution of resonance frequencies. As the dc magnetic field is swept through the resonance line, only that part of the spin system which has the proper resultant field, $H_0+H_{\text{local}}=\omega/\gamma$, is able to interact strongly with the microwave field. Therefore, the spin system releases its stored energy to the cavity system in a time τ, the time required for the dc magnetic field to be swept through the resonance line of the spin system. If ΔH is the linewidth in oersteds of the resonance line and α is the swept rate of the dc magnetic field in oe/sec, then $\tau\approx\Delta H/\alpha$. It is expected that experimentally, τ will be about equal to the duration of the microwave pulse resulted from maser oscillation.

The amplitude of the microwave magnetic field can again be calculated from the energy balance equation given below:

$$\frac{\omega}{Q}\int_0^\tau H_1^2 dt=4\pi F H_0 m_0. \tag{21}$$

For a cavity operated in $(TE)_{101}$ mode,[10] $F=(8V_s/V_c)\times(\lambda/\lambda g)^2$, where V_s and V_c are the volume of the sample and the cavity, respectively, and λ and λg are the free-space and guided wavelength, respectively. If N is the total number of spins used in a given experiment, the total energy W stored in the spin system is given by $W=gN\mu_B{}^2H_0{}^2/kT=4\pi H_0 m_0 V_s$. Knowing N and the maser oscillation envelope, one can estimate the amplitude of the microwave field.

---

[10] S. Ramo and J. R. Whinnery, *Fields and Waves in Modern Radio* (John Wiley & Sons, Inc., New York, 1953), p. 370.

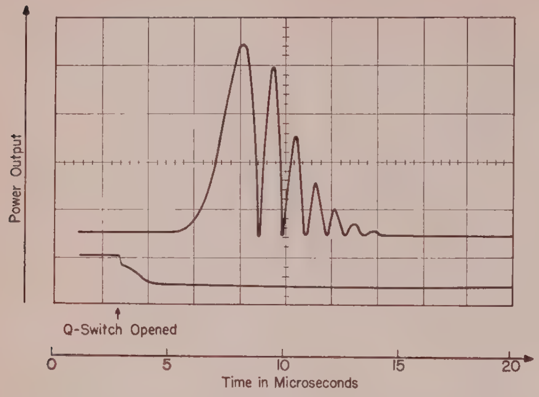

FIG. 5. This is a previously unpublished drawing of the power output $H_1^2(t)$ of a nonfield swept two-level (irradiated quartz) microwave maser. The experimental work is due to P. F. Chester, P. E. Wagner, and J. G. Castle, Jr. The drawing was kindly supplied by Dr. Castle.

Approximately, one has

$$H_1^2=(32\pi Q/\omega\tau V_c)(\lambda/\lambda g)^2 H_0 M_0, \qquad (22)$$

where $M_0=m_0V_s$. From the average value of the microwave field h_0, one can compute the period of the amplitude-modulation wiggles appearing in the oscillation envelope. A typical picture of such oscillation envelope taken from Kemp's work[3] is shown in Fig. 5. For any quantitative analysis, one has to take into consideration the shape of the oscillation envelope. That means, in Eq. (22), that τ should be interpreted as the effective pulse duration during which a microwave field of h_0 was assumed to exist in the cavity.

First, let us examine qualitatively three available sets of experimental data on a two-level maser by Chester,[11] Feher,[12] and Kemp.[3] The number of total spins, N, used in the experiments are respectively 10^{18}, 1.2×10^{16}, and 2×10^{16}; the effective pulse durations, τ, are respectively 4×10^{-6} sec, 16×10^{-6} sec, 30×10^{-6}; the operating temperatures T in these experiments are respectively 4.2°, 1.2°, and 1.5°K, and the loaded Q of their respective cavities are 6000, 20 000, and 18 000. Therefore, the microwave fields h_0 which are proportional to $(NQ/T\tau)^{\frac{1}{2}}$ are expected to be in the ratio 5.3:1:1.3 in the three experiments. The periods of the wiggles appearing in the oscillation envelope should be in the ratio 1:5.3:4. The experimental values are estimated to be 0.7×10^{-6} sec, 3×10^{-6} sec, and 2.5×10^{-6} sec, respectively. The result of this qualitative analysis is very encouraging.

Let us now check quantitatively the period of the wiggles from available experimental data. Discussion of one set of experimental data will suffice. Let us take Feher's result. It was quoted that the amplitude of the microwave field was about equal to the linewidth, 0.22 oe. A more reliable value can be calculated from Eq. (22). Assuming that the cavity was made out of a standard waveguide section, the value of $V_c(\lambda g/\lambda)^2$ was found to be 9 cm³. Using Eq. (22) and an effective τ value of 16×10^{-6} sec, one finds $h_0=0.12$ oe and $t_1=2\pi/\gamma h_0=3\times10^{-6}$ sec. This value of t_1 agrees well with the experimental value of around 3×10^{-6} sec. Since the estimation of h_0 was quite rough, we should not put too much emphasis on the exact agreement of those two values, and we should accept an agreement within 50% as a valid test of our foregoing discussion.

To make an exact analysis of the oscillation envelope in a two-level maser is rather difficult because the envelope obviously depends upon the sweep rate in relationship to the decay time Q/ω of the cavity and the reciprocal of the linewidth measured in terms of T_2. However, some general remarks can still be made. The faster the sweep rate, the closer the actual situation to sudden establishment of the resonance condition. Not only will the pulse duration be shorter, but the amplitude of the wiggles will be larger (that is, larger percentage of amplitude modulation). The qualitative difference between the envelopes shown in Chester's and Feher's paper can be accounted for if $\Delta H/\alpha$ is much shorter in the former than in the latter, where ΔH is the linewidth and α is the sweep rate.

VI. CONCLUSION

The wiggles or amplitude modulations appearing in the oscillation envelope of a two-level maser can be explained on the basis of energy exchange between the spin system and the cavity. In a rotating coordinate system, the magnetization vector is precessing around the resultant microwave magnetic field with an average precession frequency γh_0, where h_0 is the average amplitude of the microwave field. The period of the amplitude-modulated envelope is found to be equal to $2\pi/\gamma h_0$. If the time τ required to sweep the dc magnetic field through the resonance line is short compared with the cavity decay time, one expects that the pulse duration of maser oscillations will be of the order Q/ω, and that the amplitude modulation of the oscillation envelope will be almost 100%. For slower sweep rates, the pulse duration is determined by τ, and not by Q/ω. Further, as the dc magnetic field is swept through the resonance line, part of the spin system newly reaching the resonance condition is ready to give up its stored energy to the cavity, while that part of the spin system already passing the resonance condition is about to receive its lost energy back from the cavity. Under such circumstances, the total energy will at no time be stored either completely in the spin system or completely in the cavity. Consequently, the oscillation envelope will only be partly amplitude modulated.

---

[11] P. F. Chester, P. E. Wagner, and J. G. Castle, Jr., Phys. Rev. **110**, 281 (1958).

[12] G. Feher, J. P. Gordon, E. Buehler, E. A. Gere, and C. D. Thurmond, Phys. Rev. **109**, 221 (1958).

JOURNAL OF APPLIED PHYSICS VOLUME 32, NUMBER 7 JULY, 1961

Spectral Response of Solar Cells

BRIAN DALE AND F. P. SMITH*
Transitron Electronic Corporation, Wakefield, Massachusetts

(Received October 24, 1960)

An analysis of the spectral response of a solar cell is given which includes the effect of the electric field present in the diffused surface region. Results are presented which show the variation of response with junction depth and with carrier lifetime in both surface and bulk regions. By curve fitting, it is found that in a typical silicon cell the bulk lifetime is in the range 1–15 μsec, while the surface region lifetime is between 10^{-9} and 10^{-10} sec. Bombardment with a total flux of 3.3×10^{14} electrons/cm^2 of 2-Mev electrons reduced the n region lifetime by a factor of 300, and the p region lifetime by a factor of 6 in a particular case.

I. INTRODUCTION

SEVERAL analyses have been made concerning the spectral response of a solar cell on the assumption that the minority carriers move only by diffusion.[1–3] For the bulk region, assumed here to be n type, this is a valid assumption. However, in the p-type material there is a very large impurity gradient which results from the very heavy surface concentration and the shallow junction depth. This causes an electric field to exist throughout the p-type region. The physical reason for the existence of the field is that a gradient of majority carriers exists due to the impurity gradient. This would give a diffusion current of majority carriers unless an electric field were set up to restrain the majority carriers. This field aids the flow of minority carriers from the surface towards the junction.

The value of the field is given by

$$E=-\frac{kT}{q}\frac{1}{N(x)}\frac{dN}{dx},$$

where $N(x)$ is the impurity concentration at x. The variation of impurity concentration with position is determined by the diffusion procedure used in the manufacture of the cell. If the variation followed the complementary error function, the field would vary with x and the solution of the continuity equation would be rather complex. The problem may be simplified greatly by assuming that the impurity concentration is an exponential function of position, in which case the field E is constant. This assumption involves a rather small error and is frequently made in the analysis of minority carrier transport through the base of a diffused base transistor.[4]

The value of the field strength can be obtained from the total potential drop across the p region and the junction depth. The potential drop is

$$V=(kT/q)\log(N_s/N_J),$$

where N_s and N_J represent impurity concentrations at the surface and the junction. Taking typical values for a solar cell, a field of about 2000 v/cm is found to exist in the p region. If the velocity with which minority carriers drift in this field is compared with the velocity at which they can diffuse towards the junction, it is found that the drift velocity is the greater unless the lifetime is exceptionally short, of the order of 10^{-10} sec. However, since the results indicate that lifetimes in the p region are quite short, both drift and diffusion terms must be included.

An analysis has been made recently of the response of a solar cell, in which the effect of the electric field has been considered.[5] In this analysis it was assumed that bulk recombination in the surface region was negligible, whereas in the present work the lifetime in this region is considered to be so low that the efficiency of the cell is considerably reduced.

In Sec. II an analysis is given of the response of the p region including the effects of drift, diffusion, and surface recombination. Also given briefly is the analysis for the n region in which diffusion only is considered. In Sec. III the theoretical response curves are presented, and Sec. IV gives practical results on a solar cell before and after electron bombardment.

II. ANALYSIS

A. p-Type Surface Region Response

The continuity equation for the p region is

$$\frac{dn}{dt}=\alpha He^{-\alpha x}-\frac{n-n_p}{\tau_n}-\frac{1}{q}\frac{dI_n}{dx}, \tag{1}$$

where n is the electron density, n_p its thermal equilibrium value, τ_n the lifetime, I_n the electron current, α the absorption coefficient, H the photon flux which generates electron hole pairs, and q the electronic charge.

The current equation including both diffusion and drift is

$$I_n/q=-D_n(dn/dx)+\mu_n nE, \tag{2}$$

where D_n is the electron diffusion coefficient and μ_n is the electron mobility.

---

* F. P. Smith now associated with Laboratory for Electronics, Inc., Boston, Massachusetts.

[1] W. G. Pfann and W. Van Roosbroeck, J. Appl. Phys. **25**, 1422 (1954).

[2] P. Rappaport, J. J. Loferski, and E. G. Linder, RCA Rev. **17**, 100 (1956).

[3] M. Wolf, Proc. Inst. Radio Engrs. **48**, 1246 (1960).

[4] H. Krömer in *Transistors I* (Radio Corporation of America Laboratories, Princeton, New Jersey, 1956), p. 202.

[5] A. G. Jordan and A. G. Milnes, IRE Trans. on Electron Devices **ED-7**, 242 (1960).

Combining Eqs. (1) and (2) and letting $dn/dt=0$, one obtains

$$\frac{d^2n}{dx^2}-\frac{\mu_nE}{D_n}\frac{dn}{dx}-\frac{n-n_p}{D_n\tau_n}+\frac{\alpha He^{-\alpha x}}{D_n}=0. \tag{3}$$

The boundary conditions to be applied are:

$$\text{at } x=0, \text{ the surface, } I_n/q=-nS, \tag{4}$$

which gives

$$D_n(dn/dx)=n(\mu_nE+S). \tag{5}$$

At $x=x_J$, the junction,

$$n=n_p\doteq 0. \tag{6}$$

Equation (4) represents the recombination current into the surface in terms of a recombination velocity S. Equation (6) expresses the fact that under short-circuit conditions minority carrier density at the juntion is close to zero.

On using the Einstein relationship connecting mobility and diffusion constant

$$\mu_n=qD_n/kT, \tag{7}$$

the required solution of Eq. (3) can be written

$$n-n_p=A[Be^{-x(M-m)}+Ce^{+x(M+m)}-e^{-\alpha x}], \tag{8}$$

where

$$m=qE/2kT,\quad L=(D_n\tau_n)^{\frac{1}{2}},\quad M=[m^2+(L^2)^{-1}]^{\frac{1}{2}} \tag{9}$$

and

$$A=\frac{H}{D_n[\alpha+2m-(\alpha L^2)^{-1}]} \tag{10}$$

$$B=\frac{[\alpha+2m+(S/D_n)]-[m-M+(S/D_n)]e^{-x_J(M+m+\alpha)}}{[(m+M+(S/D_n)]-[m-M+(S/D_n)]e^{-2x_JM}} \tag{11}$$

$$C=\frac{[m+M+(S/D_n)]e^{-x_J(m+M+\alpha)}-[\alpha+2m+(S/D_n)]e^{-2x_JM}}{[m+M+(S/D_n)]-[m-M+(S/D_n)]e^{-2x_JM}}. \tag{12}$$

These expressions can be simplified by noting that

$$\exp(-mx_J)=\exp[-(qV/2kT)]\sim\exp(-4)\ll 1,$$

where V is the potential across the p region. Equations (11) and (12) then become

$$B=\frac{\alpha+2m+(S/D_n)}{m+M+(S/D_n)} \tag{13}$$

$$C=e^{-x_J(m+M+\alpha)}-\frac{\alpha+2m+(S/D_n)}{m+M+(S/D_n)}e^{-2x_JM}. \tag{14}$$

To obtain the short-circuit current at x_J, Eqs. (2) and (6) give

$$I_n/q=-D_n(dn/dx)\big|_{x=x_J} \tag{15}$$

$$I_n/q=-D_nA[\alpha e^{-\alpha x_J}-B(M-m)e^{-x_J(M-m)}+C(M+m)e^{x_J(M+m)}]. \tag{16}$$

Substitution of A, B, and C from Eqs. (10), (13), and (14) yields

$$\frac{I_n}{q}=\frac{H}{\dfrac{\alpha+2m}{\alpha+2m+(S/D_n)}-\{\alpha L^2[\alpha+2m+(S/D_n)]\}^{-1}}\times\left(2e^{-x_J(M-m)}\Big/\left[1+\frac{m+(S/D_n)}{M}\right]-e^{-\alpha x_J}\frac{(\alpha+m+M)}{[\alpha+2m+(S/D_n)]}\right). \tag{17}$$

The term involving surface recombination S/D_n will usually be much smaller in magnitude than m. For example, if S is taken as 2000 cm per sec, S/D_n will be $\sim$1000 cm^{-1}, whereas m will be of the order of 40 000 cm^{-1}. This indicates that surface recombination has little effect on the response from the p region unless exceptionally high values of S occur. Neglecting S, Eq. (17) simplifies to

$$\frac{I_n}{q}=\frac{H}{1-[\alpha L^2(\alpha+2m)]^{-1}}\times\left[\frac{2e^{-x_J(M-m)}}{1+(m/M)}-e^{-\alpha x_J}\frac{\alpha+m+M}{\alpha+2m}\right]. \tag{18}$$

If the lifetime in the p material were very long, $L\to\infty$; then

$$I_n/q\to H[1-e^{-\alpha x_J}], \tag{19}$$

which indicates that all charges liberated in the p region would be collected at the junction.

B. *n*-Type Bulk Region Response

The continuity equation for the n region is

$$\frac{dp}{dt}=\alpha He^{-\alpha(x+x_J)}-\frac{p-p_n}{\tau_p}-\frac{1}{q}\frac{dI_p}{dx}, \tag{20}$$

where x_J is the junction depth and the origin of x is at the junction. The current equation is

$$I_p/q = -D_p(dp/dx), \tag{21}$$

giving, when $dp/dt=0$,

$$\frac{d^2p}{dx^2} - \frac{p-p_n}{D_p\tau_p} + \frac{\alpha H e^{-\alpha(x+x_J)}}{D_p} = 0. \tag{22}$$

The boundary conditions for the cell short-circuited are

$$p = p_n \quad \text{for} \quad x=0 \quad \text{and} \quad x=\infty. \tag{23}$$

Then

$$p - p_n = \frac{H}{\alpha D_p[1-(\alpha^2L^2)^{-1}]} e^{-\alpha x_J}[e^{-(x/L)} - e^{-\alpha x}] \tag{24}$$

and

$$\frac{I_p}{q} = \frac{H}{1+(\alpha L)^{-1}} e^{-\alpha x_J} \quad \text{at } x=0 \tag{25}$$

(that is, at the junction).

If $L \to \infty$,

$$I_p/q \to He^{-\alpha x_J}. \tag{26}$$

The total current response of the cell with infinite lifetime is therefore the sum of Eqs. (19) and (26), and equals the photon flux.

The analysis for the n region has been carried through for the case of an infinitely thick cell, as indicated by the boundary condition in Eq. (23). In a practical cell the minority carrier density must be zero at the back contact, and so the result given in Eq. (25) is not completely accurate. However, the error is very small if the cell thickness is large compared to a diffusion length. In the cells on which measurements were made by the authors, the thickness was of the order of five times the diffusion length, so the error incurred by assuming an infinite specimen was negligible. In the general case, the boundary condition (23) can be replaced by

$$p = p_n \quad \text{for} \quad x=0 \quad \text{and} \quad x=W, \tag{27}$$

from which it follows that

$$\frac{I_p}{q} = \frac{H}{1+(\alpha L)^{-1}} e^{-\alpha x_J} \left(1 - 2\frac{[1-e^{-(w/L)(\alpha L-1)}]}{(\alpha L-1)[e^{(2w/L)}-1]}\right) \tag{28}$$

The second term, which distinguishes (28) from (25), represents the effect of finite thickness of the cell and reduces to zero for $w \gg L$.

C. Validity of the Theory

Since most previous authors have neglected the effect of the electric field in the surface region, some comments may be made on the necessity of including it in the analysis. The form of the spectral response curve for the surface region can be adequately explained in several ways. For example, the loss of response at short wavelengths can be attributed to a very high surface recombination velocity, or alternatively to a very low bulk lifetime in the surface material. The inclusion of the electric field term modifies the values of these parameters which must be assumed to obtain a good fit between theoretical and practical curves, but does not alter very appreciably the shape of the curves. Since the lifetime of the surface material is not readily obtainable by any other technique, there appears to be no independent means of checking the validity of the results. However, the following facts indicate the basic correctness of the analysis. First, it seems unlikely that the dominant recombination is on the surface. In order to explain the experimental results, very large recombination velocities, of the order of 10^5 cm/sec, would be needed. However, after etching the surface of the cells lightly with an $HF-HNO_3$ mixture, very little change in spectral response was obtained. The small change which occurred could be attributed solely to a slight reduction in thickness of the surface region. Such etches are known to produce recombination velocities of the order of 10^3 cm/sec on silicon. Second, sheet resistance measurements show that the surface concentration of impurity in the diffused layer of our cells is greater than 10^{20} atoms/cc. Since the bulk impurity concentration is about 10^{16} atoms/cc, an average electric field of the order of 2000 v/cm must exist in the surface region. The effect of this field can be obtained by investigation of the full solution, Eq. (17), using the constants defined by Eqs. (10), (11), and (12). For a junction depth of 10^{-4} cm and an absorption coefficient of 10^4 cm^{-1}, the electron current has been calculated as a function of lifetime for the two cases $E=0$ and $E=2000$ v/cm. It was found that the lifetime required with diffusion only was a factor of 4.5 longer for the same current than if the field term were included in addition. This factor applies to lifetimes in the range actually observed. If larger lifetimes were obtainable, the factor would be greater, since the collection efficiency asymptotes towards unity more quickly in the presence of the electric field than with diffusion alone. It is felt that this factor is large enough to warrant the inclusion of the field.

III. PRESENTATION OF THE THEORETICAL RESULTS

Equations (18) and (25) contain several variables. Some examples of the results obtained for particular choices of these variables are shown in Figs. 1–5. In Figs. 1 and 2, the effect of the bulk lifetime on the n and p response curves is illustrated for a particular value of junction depth, 1.5μ. The choice of values for the other quantities in the equations is given in the legend.

Also included in Fig. 2 for comparison is the n-region response curve for a lifetime of 10 μsec, taken from Fig. 1. In Fig. 3 this curve is combined with the p-layer

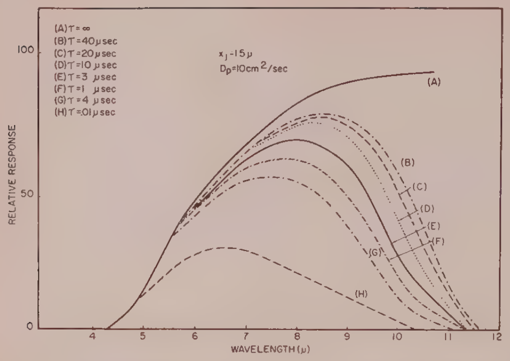

FIG. 1. n-region spectral response as a function of lifetime.

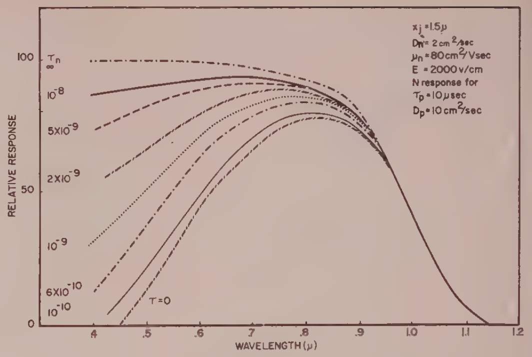

FIG. 3. Total spectral response as a function of p-region lifetime.

response curves of Fig. 2 to give the total response as a function of p-layer lifetime. The figure of 10 μsec has been found to be a fairly typical value for the n-region lifetime.

Figure 4 shows the total response for two different junction depths, 0.4 μ and 1.5 μ. Also shown is the n-layer response alone for each case, indicating that the large improvement in short wavelength response for the shallow junction is to be attributed mainly to an increased contribution from the n side. The interpretation is that the surface region produces marked attenuation of the light which penetrates to the n region, and that a considerable proportion of the absorbed energy is wasted because of the low p-region lifetime.

Figure 5 shows the shift in spectral response which would result from using low-lifetime n material. The solid lines are n-material responses only, the other curves show the added contributions from the p region for two different lifetimes in the region of interest. The curves indicate the change in spectral response which would occur if the lifetime were degraded by irradiation, as discussed in the next section.

The absorption coefficient as a function of wavelength for silicon is from data given by Braunstein *et al.*[6] and by Dash and Newman.[7]

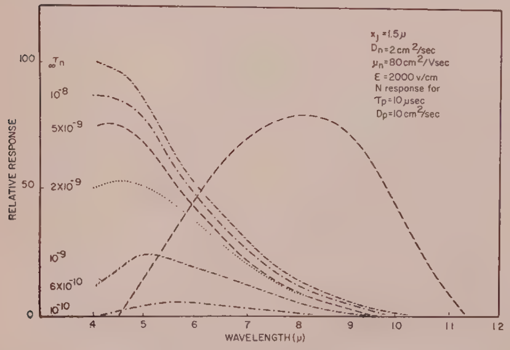

FIG. 2. p-region spectral response as a function of lifetime.

IV. ELECTRON BOMBARDMENT

As an example of the agreement obtained between the theoretical and practical response curves, an analysis was made of a solar cell before and after electron bombardment. The junction depth was 1.5 μ, and the bombardment dosage was 3.3×10^{14} electrons/cm² of 2-Mev particles. The practical response curves before and after bombardment are given in Fig. 6, together with fitted theoretical curves. Before bombardment the best fit was obtained with $\tau_p=3\mu$sec, $\tau_n=6\times10^{-10}$ sec. After bombardment the best values of these parameters were $\tau_p=0.01$ μsec, $\tau_n=10^{-10}$ sec. As expected, the bombardment produced a much larger change in the bulk lifetime than in the surface region lifetime.

The value of n-region lifetime was considered to be reasonably accurate since the response curves are quite sensitive to lifetime. However, the response from the p region of these cells was quite small, consequently the

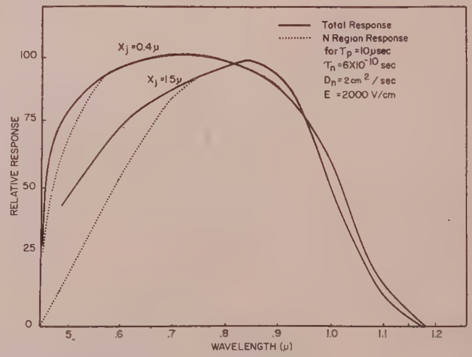

FIG. 4. Effect of junction depth on total spectral response.

---

[6] R. Braunstein, A. Moore, and F. Herman, Phys. Rev. 109, 695 (1958).

[7] W. C. Dash and R. Newman, Phys. Rev. 99, 1151 (1955).

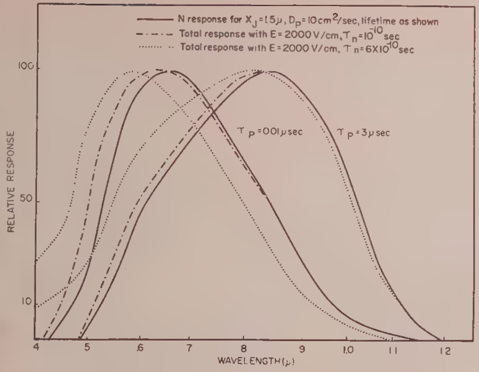

FIG. 5. Shift in spectral response due to *n*-region lifetime.

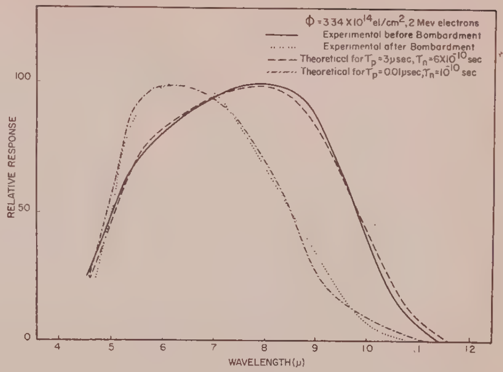

FIG. 6. Effect of electron bombardment on spectral response.

lifetime determination was subject to considerable error. No great significance is therefore to be attached to the reduction of *p*-region lifetime.

Reduction of lifetime in *n*-type silicon by bombardment with 700-kev electrons has been reported by Wertheim.[8] He obtained a capture cross section $\sigma_p = 2.8 \times 10^{-14}$ cm², and a rate of production of centers of 0.18 per electron cm. Assuming the same capture cross section, the number of recombination centers required to reduce the lifetime to 0.01 μsec is 2×10^{14}/cc. With a flux of 3.3×10^{14} electrons per cm,² this corresponds to a rate of production of 0.6 center per electron cm. This higher value may be expected in view of the fact that we used 2-Mev electrons. The apparent, almost-linear relationship between the energy and the rate of production of centers may be quite fortuitous, but the general agreement with the results of Wertheim is considered to be satisfactory.

The photoconversion efficiency for an artificial light source producing an incident energy of 85 mw/cm² on the cell surface was reduced by a factor of 2 due to the irradiation.

SUMMARY

An electric field exists in the surface region of a solar cell of such magnitude that carrier drift is at least as important as diffusion. An analysis has been given which includes the effects of both drift and diffusion. Theoretical response curves are given for both *p* and *n* regions, with lifetime as a parameter. By curve fitting, lifetimes of the order of several microseconds are found for the bulk regions of typical silicon solar cells. The lifetimes in the surface regions are less than 10^{-9} sec. Bombardment with 2-Mev electrons drastically reduces the bulk region lifetime, but has a comparatively small effect on the surface region lifetime.

ACKNOWLEDGMENTS

The work covered in this paper was made possible by the support of the Advanced Research Projects Agency through the U. S. Army Signal Research and Development Laboratory, and by the Air Force Cambridge Research Center, under contract.

---

[8] G. K. Wertheim, Phys. Rev. **105**, 1730 (1957).

JOURNAL OF APPLIED PHYSICS VOLUME 32, NUMBER 7 JULY, 1961

Perfection of the Lattice of Dislocation-Free Silicon, Studied by the Lattice-Constant and Density Method

M. E. Straumanis, P. Borgeaud, and W. J. James
University of Missouri School of Mines and Metallurgy, Departments of Metallurgical and of Chemical Engineering, Rolla, Missouri

(Received March 10, 1961)

The lattice-constant and density method revealed that a high-purity silicon crystal free of dislocations has a perfect lattice without an excess of vacant sites or interstitials ($n'=8.0000_4$) within the limits of error, in agreement with the results obtained with the decoration method. The lattice constant of vacuum heated silicon powder of semiconductor purity was 5.43070±0.00004 A; that of the nonheat-treated powder was 5.43081 A at 25°C. The constants determined from crystal chips by the rotating crystal method were lower: between 5.43028–5.43048 A at 25°C. As the constants of each series of measurements could be reproduced very well ($s=\pm 0.00004$ A), the lower values suggested the presence of some unknown systematic errors, the magnitude of which is outside the scope of errors due to absorption. The thermal expansion coefficients of all samples between 10°–60°C were $(2.6\pm 0.4)\times 10^{-6}/°\text{C}$. The average density of etched crystal chips was 2.3289±0.0001 g/cm³. The lower density of the nonetched chips indicated the presence of microcracks, removable by etching, within the distorted surface layers. There was no significant difference in density of bars sawed, or of chips broken from the crystal and etched.

INTRODUCTION

SILICON of high (semiconductor) purity, free of dislocations,[1] can be used to check the exactitude of the method of n' determination[2] from the expression

$$n'=vdN_0/A, \tag{1}$$

where v is the volume of the unit cell, N_0 is Avogadro's number, d the density, and A the atomic weight of Si. n', the actual number of atoms per unit cell, should then approach the ideal value of $n=8.0000$, meaning that the lattice of the Si mentioned is perfect,[3,4] free of an excess of vacant sites, interstitials, and other imperfections within the limits of error.

Further objectives of the present work were to find the expansion coefficients of Si, in the form of small crystal fragments and of a powder; the experimental densities of the unetched and etched fragments; the lattice parameters of crystal chips and of powder, and to draw conclusions concerning the applicability of the absorption correction for lattice constants determined from rotation patterns of tiny crystal fragments.

MATERIALS USED, SAMPLES, AND MEASUREMENTS

High-purity single silicon crystals, obtained from Dr. W. C. Dash of the General Electric Company, were used for the study.[1] The major impurities were probably carbon and oxygen, present to no greater extent than 10^{-7} (in atom fraction). Because of the high purity of the crystals, no chemical analysis was available nor could one be made. Etching and copper decoration techniques[5] revealed that the crystals grown by the method of Dash in an argon atmosphere do not contain observable dislocations.[1]

Samples for x-ray single-crystal rotation photographs and powder patterns were made of this material. A multitude of small crystal fragments was obtained by breaking an end of a crystal with pliers. Needle-shaped fragments with the appropriate crystallographic directions along the needle axis were chosen for the studies. However, since the fragments probably contained dislocations and microcracks on their surface as a result of deformation, the distorted layers were removed by etching (one part of concentrated pure HF in three parts of concentrated HNO_3).

To exclude, as much as possible, distortion in the interior of the crystal fragments, further samples were prepared as follows. Several leaflets about 0.5 mm thick were cut approximately parallel to the (111) plane from a crystal by means of a diamond saw blade. They were again cut perpendicularly to the surface into roughly rectangular 0.5×0.5×4-mm bars, then were etched down to needles about 2 mm long and 0.07 mm in diam. For powder mounts, fragments of the fairly brittle crystal were ground and the powder passed through a 350-mesh screen. To detect the influence of cold work on the lattice constant, one part of the powder was heated in vacuum (about 10^{-5} mm) at 600°C for 1 hr. It was assumed that by this treatment stresses were released and a part of the dislocations and other imperfections was annealed out.

For the determination of lattice parameters, asymmetric rotation crystal and powder photographs at a constant temperature of the sample (±0.1°) were made.[6,7] The constants were calculated from the density peaks of back-reflection lines, $444_{\alpha 1}$, which appeared under a Bragg angle of about 80° on the films.[8] Copper radiation was used ($\lambda_{\alpha_1}=1.537395\times 1.00202$ A). The time of exposure in 64-mm precision cameras was 15–30 min for the single-crystal patterns, and 120–15 min for the powder photographs. As the diameter of he powder mounts was less than 0.2 mm, no correcions, except for refraction, were applied.[9] An amount of .00040 kX was added to all constants to allow for efraction. Although the crystal fragments for rotation hotographs had diameters between 0.07–0.2 mm, the ecessity of an absorption correction was considered.

---

[1] W. C. Dash, J. Appl. Phys. **29**, 736 (1958).

[2] M. E. Straumanis, Chimia (Switz.) **12**, 136 (1958).

[3] M. E. Straumanis and T. Ejima, J. Chem. Phys. **32**, 629 (1960); Z. physik. Chem. **23**, 440 (1960).

[4] M. E. Straumanis, Phys. Rev. **92**, 1155 (1953); **95**, 1157 (1954).

[5] W. C. Dash, J. Appl. Phys. **23**, 1193 (1956); **31**, 2275 (1960).

[6] M. E. Straumanis, J. Appl. Phys. **23**, 330 (1952); Anal. Chem. **25**, 700 (1952).

[7] L. V. Azaroff and M. T. Buerger, *The Powder Metho* (McGraw-Hill Book Company, Inc., New York, 1958), p. 233.

[8] M. E. Straumanis and E. Z. Aka, J. Appl. Phys. **23**, 330 (1952)

The thermal expansion coefficients were calculated rom constants obtained at sample temperatures etween +10 and 60° in increments of 10°.

The density (reduced to vacuum) of the etched nd nonetched fragments was determined by the mproved suspension method,[10] using tetrabromethane s a heavy liquid. To adjust the density of this liquid o that of the crystals, bromobenzene was used as a iluting agent and finally temperature changes were nade.

In order to establish the significance of a measured ifference, the standard deviation s was calculated rom each series of experimental determinations.[2,10] The least-squares method[11] was used for computation f the lattice parameter at 25°C (a_{25}) from the values a_t obtained between 10 and 60°, and for the determinaion of the thermal expansion coefficient.

EXPERIMENTAL RESULTS

Lattice Constants

Table I shows the reproducibility of the lattice onstant of a nonetched fragment (split from the ilicon crystal), adjusted and centered by the goniometer ead of the camera. From the mean values at each emperature, the expansion coefficient was calculated nd then used to reduce all the lattice constants to 5°C. Using the deviations of these constants from the verage value, the standard deviation corresponding to 50% confidence limit was calculated.

Table II lists the lattice parameters and expansion oefficients of two other Si crystal fragments (one cut rom the crystals) both deeply etched.

Although sharp, narrow, and hence easily measurable, pots were obtained on the films, there is still some oubt concerning the reliability of lattice constants alculated from rotation crystal patterns, especially f the axis of rotation of the crystal is not the simplest (like 001). The authors observed that the lattice onstants in some cases appeared smaller than calulated from powder photographs. Powder methods are egarded as being more reliable. Because of this reason ragments of single Si crystals were pulverized and owder patterns were made. For the latter, lattice neasurements at various temperatures resulted in the xpansion coefficient and the lattice constant of the powder (at 25°C) (see Table II). The increased value of the lattice constant, as compared with those obtained from rotation photographs, was not unexpected because of strains (or interstitials) introduced into the lattice by the severe deformation process (crushing). The expansion coefficient of the material was approximately the same.

TABLE I. Lattice constants of a nonetched Si crystal fragment at various temperatures. Rotation axis 110, thermal expansion coefficient calculated from the a_t constants,

$$\alpha = (2.8 \pm 0.4) \times 10^{-6}/°\text{C}.$$

Temp. (°C)	a_t (A)	a_{25} (A)
11.0	5.42993	5.43014
11.0	5.43001	22
21.0	29	35
21.0	12	18
31.0	41	32
31.0	47	38
41.0	52	28
41.0	33	09
51.0	64	24
51.0	57	17
61.0	77	22
61.0	85	29
	Average	5.43024
	Refraction corr.	0.00004
	$a_{25}=$	5.43028 ±0.00004 A

It was expected that the increased lattice constant could be reduced by the heat treatment mentioned above; the constant indeed decreased (see Table II), but did not reach as low a value obtained from rotation photographs. There was still a possibility that the low value from rotation patterns could be explained by the shift of the spots due to absorption (which was disregarded). However, calculations gave for a completely opaque sample (0.1–0.2 mm in diam) an absorption correction of only 0.00004–0.00007 A. If the absorption shift is interpreted according to Warren, then the correction is larger but still insufficient to explain the low value of constants obtained from rotation crystal photographs.[9,12] Thus this question has

TABLE II. Lattice constants, expansion coefficients α, densities d, and perfection of the lattice n', of silicon free of dislocations.

Sample	a_{25} (A)	$\alpha(\times 10^6/°\text{C})$	d_{25} (g/cm^3)	n' (atoms/unit cell)
Crystal fragments, unetched	5.43028[a]	2.8±0.2	2.3287[b]	7.9975±0.0009
Crystal fragments, unetched	5.43030	3.4	2.3291	7.9989
Crystal bar, sawed, etched	5.43048	2.5	2.3289	7.9990
Powder (2 samples)	5.43081	2.5	...	...
Powder heated (2 samples)	5.43070	2.0	...	8.00004[c]
	Averages	2.6±0.4	2.3289±0.0001	

[a] ±0.00004
[b] ±0.00004
[c] Using the average density.

---

[9] M. E. Straumanis, J. Appl. Phys. **30**, 1965 (1959); Acta ryst. **13**, 818 (1960).

[10] M. E. Straumanis, Am. Mineralogist **38**, 662 (1953).

[11] B. Ostle, *Statistics in Research* (Iowa State College Press, mes, Iowa, 1954), pp. 117–173.

[12] B. E. Warren, J. Appl. Phys. **16**, 614 (1945).

yet to be answered, and the lattice constant from powder photographs has to be regarded as the most reliable value.

Density Measurements

Four determinations of density were made for each of nine crystal fragments. For example, the densities found for one etched fragment were: 2.32915, 2.32916, 2.32908, and 2.32903 g/cm^3 at 25°C. An average $d=2.32910\pm0.00003$ was obtained. The pieces cut from the single crystal and etched exhibited a slightly lower density; still lighter were the unetched fragments broken from the crystal (see Table II). The differences may be explained by the formation of dislocations, vacant sites, and even of microcracks[13] on the surface layers during deformation. By etching, the layers are removed and the core shows a higher density then the fragments as a whole. Because only small amounts of Si powder were available, no density determinations were made with it but preliminary measurements showed a lower value.

Calculation of n' and Discussion

The actual number of atoms n' per unit cell can now be computed from Eq. (1), substituting for N_0 the value[2,4] of $(6.02403\pm0.00030)10^{23}$ and for A (28.0875 ± 0.0005).[14] The results are summarized in Table II. To decide whether a deviation of n' from the theoretical value $n=8$ is significant or not, an estimation of the propagated error was made. The latter was calculated as previously described[2,10] assuming that the standard deviation of the lattice constant is ±0.00004 A and that of the density measurements is ±0.0001 g/cm^3. To take care of the systematic errors which possibly were made in these measurements, the error in the lattice constant was increased by a factor of 3, the density error by a factor of 2, and the factor 1 was used for A and N_0, thus assuming that all errors were covered by the deviations given. For the lowest value of N_0 $(=6.0237\times10^{23})$,[14] n' diminishes by 0.00044.

Table II clearly shows that for all three groups of single crystals, n' is significantly lower than 8. On comparing the respective lattice parameters, it can be seen that the low value of n' is explained mainly by the low value of the a constant, which because of unknown reasons deviates from that calculated from patterns of heated silicon powder. On the other hand, using for n' calculations the most reliable values, e.g., the a constant from heated powders and densities as determined from etched chips of silicon suspended in a heavy liquid, an n' is obtained which is very close to the theoretical value and completely within the limits of error, ±0.0009, calculated. The n' value obtained with the etched crystal bar is also very close to 8. Therefore, the conclusion drawn is that the dislocation-free silicon crystal has a perfect lattice without a measurable excess of interstitials or vacant sites. This agrees with the results obtained by the decoration method.[1]

CONCLUSIONS

The lattice-constant and density method can be used to determine the excess of one kind of imperfections in a crystalline substance.

For lattice-constant determination, the powder method is more reliable than the rotation-crystal method.

Crushed silicon powder has a slightly larger lattice constant than that heated in vacuum. The thermal expansion coefficients do not change appreciably from sample to sample near room temperature.

Breaking of the brittle silicon introduces vacancies and probably microcracks into the surface of the chips. This layer of lower density can be removed by etching. The core has a higher density. The densities of the cores of various chips differed by amounts outside the limits of error which suggested incomplete removal of the deformed surface layer by etching in some cases.

ACKNOWLEDGMENTS

We thank Dr. W. C. Dash, General Electric Company, Schenectady, New York, for the silicon crystals and for his helpful suggestions. This investigation was sponsored by the National Science Foundation under contract.

---

[13] W. C. Dash, J. Appl. Phys. **29**, 228 (1958); G. R. Pulliam, J. Am. Ceram. Soc. **42**, 477 (1959); J. R. Bristlow, Brit. J. Appl. Phys. **11**, 81 (1960); K. A. Bendler and W. A. Wood, Acta Met. **8**, 494 (1960).

[14] A. Smakula, J. Kalnajs, and V. Sils, Phys. Rev. **99**, 1747 (1955).

JOURNAL OF APPLIED PHYSICS VOLUME 32, NUMBER 7 JULY, 1961

Charged Cylindrical Tube*

T. R. Ferguson and R. H. Duncan
Physical Science Laboratory, New Mexico State University, University Park, New Mexico

(Received September 9, 1960; in final form, March 6, 1961)

The Fourier series for the charge density on a hollow tube of finite length is found in such a way that the Fourier coefficients are the unknowns of a system of linear equations. A machine method is used to solve the set of equations in finite order. The leading coefficient is the most accurately known at any order, and solely determines the capacitance of the tube. Capacitances are determined for various ratios of half-length to radius to an accuracy of better than 0.02%. The technique of solving the integral equation for charge density is useful in other physical problems.

INTRODUCTION

A METALLIC right-circular cylindrical tube without end caps is held at constant potential. The Fourier series representation of the charge density is developed, with a calculation of the capacitance of the tube. Smythe has solved the corresponding problem with end caps by a different method.[1] The technique employed in this paper is useful for developing a numerical solution to an integral equation on a finite range when the Fourier transform of the kernel contains transcendental functions or branch points. It has recently been applied in the solution of Hallen's integral equation.[2]

The cylinder has a total length $2h$ and radius a, with center at the origin. The technique is valid for any ratio of h to a, though calculations are easiest for $h \gg a$, and may be made as accurate as desired.

METHOD OF SOLUTION

In the geometry considered, the equation to be solved is

$$4\pi\epsilon V_s = \int_{-h}^{+h} \sigma(\zeta) g(z-\zeta) d\zeta, \tag{1}$$

where

$$2\pi g(z-\zeta) = \int_{-\pi}^{\pi} [4a^2 \sin^2(\phi/2) + (z-\zeta)^2]^{-\frac{1}{2}} d\phi. \tag{2}$$

An expansion of $g(z-\zeta)$ is desired on the ranges $-h \leq z, \zeta \leq h$. A double Fourier series on z, ζ is difficult to accomplish because of the integration one must perform to find the coefficients. However, it is only necessary to note that $g(z-\zeta)$ is an even function of the difference in z and ζ to realize that a single series expansion is adequate. A suitable form is

$$g(z-\zeta) = \frac{D_0}{2} + \sum_{m=1}^{m=\infty} D_m \cos\left[\frac{m\pi(z-\zeta)}{2h}\right]. \tag{3}$$

The fundamental formula for any coefficient D_m in Eq. (3) is

$$D_m = (2h)^{-1} \int_0^{2h} g(\xi) \cos(m\pi\xi/2h) d\xi, \tag{4}$$

where $\xi = z - \zeta$. Direct integration of Eq. (4) is difficult. An indirect method may be constructed by writing

$$g_1(\xi) = g(\xi) - g_2(\xi), \tag{5}$$

where $g_1(\xi)$ is equal to $g(\xi)$ in the range $0 \leq \xi \leq 2h$, and is zero outside this range; $g_2(\xi)$ is equal to $g(\xi)$ in the range $2h \leq \xi < \infty$, and is zero outside this range. The symbolic cosine transformation of Eq. (5) is

$$G_1(\alpha) = G(\alpha) - G_2(\alpha). \tag{6}$$

The transformations of $g_1(\xi)$ and its inverse are given by

$$g_1(\xi) = (2/\pi)^{\frac{1}{2}} \int_0^\infty G_1(\alpha) \cos(\alpha\xi) d\alpha \tag{7}$$

and

$$G_1(\alpha) = (2/\pi)^{\frac{1}{2}} \int_0^{2h} g_1(\xi) \cos(\alpha\xi) d\xi. \tag{8}$$

Comparison of Eqs. (4) and (8) shows that the coefficients of the cosine series expansion of $g_1(\xi)$ are proportional to sample values of its cosine transform, $G_1(\alpha)$. Thus

$$D_m = h^{-1}(\pi/2)^{\frac{1}{2}} G_1(m\pi/2h). \tag{9}$$

It follows that

$$D_m = h^{-1}(\pi/2)^{\frac{1}{2}} [G(m\pi/2h) - G_2(m\pi/2h)]. \tag{10}$$

One immediately obtains $G(\alpha)$ from the identity[3]

$$g(\xi) = 2/\pi \int_0^\infty \cos(\alpha\xi) I_0(\alpha a) K_0(\alpha a) d\alpha. \tag{11}$$

By performing a series expansion of the kernel distance in negative odd powers of ξ, one may obtain $G_2(\alpha)$ in the form

$$G_2(\alpha) = \int_{2h}^\infty (A\xi^{-1} + B\xi^{-3} + \cdots) \cos(\alpha\xi) d\xi, \tag{12}$$

---

* Supported by Sandia Corporation, P. O. No. 15-0079.

[1] W. R. Smythe, J. Appl. Phys. **27**, 917 (1956).

[2] R. H. Duncan and F. A. Hinchey, J. Research Natl. Bur. Standards **64D**, 569 (1960).

[3] P. M. Morse and H. Feshbach, *Methods of Theoretical Physics* (McGraw-Hill Book Company, Inc., New York, 1953), p. 1263.

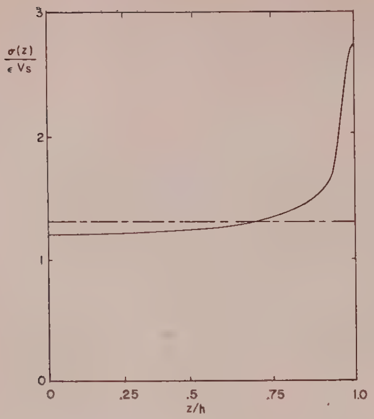

FIG. 1. Charge density vs z/h for $h/a=25\pi$.

where the ϕ integration (involving only powers of $\sin\phi/2$) has been performed and included in A, B, and the ξ integrations involve sine and cosine integral functions. The coefficients D_m may be calculated from sample values of $G(\alpha)$ and $G_2(\alpha)$.

The charge density is now expanded as

$$\sigma(\zeta)=\sum_{n=0}^{n=\infty}\sigma_n\cos\left(\frac{n\pi\zeta}{h}\right). \tag{13}$$

If the leading coefficient in the expansion of $g(z-\zeta)$ is redefined so that it may be included under the summation sign, and the series for $g(z-\zeta)$ and $\sigma(\zeta)$ are substituted into Eq. (1), there results

$$\sum_{n=0}^{n=\infty}\sum_{m=0}^{m=\infty}\sigma_nD_m\gamma_{nm}\cos\left(\frac{m\pi z}{2h}\right)=4\pi\epsilon V_s, \tag{14}$$

where the expansion of $\cos[m\pi(z-\zeta)/2h]$ degenerates to cosine terms since $\sigma(\zeta)$ is an even function of ζ, and

$$\gamma_{nm}=\int_{-h}^{h}\cos(n\pi\zeta/h)\cos(m\pi\zeta/2h)d\zeta. \tag{15}$$

An infinite set of linear simultaneous equations is obtained by multiplying both sides of Eq. (14) by $\cos[(2p+1)\pi z/2h]$ and integrating on z from $-h$ to $+h$. The result is

$$\sum_{n=0}^{n=\infty}\sum_{m=0}^{m=\infty}\sigma_nD_m\gamma_{nm}\beta_{pm}=4\pi\epsilon V_sv_p, \tag{16}$$

where

$$\beta_{pm}=2\int_0^h\cos[(2p+1)\pi z/2h]\cos(m\pi z/2h)dz \tag{17}$$

and

$$v_p=2\int_0^h\cos[(2p+1)\pi z/2h]dz. \tag{18}$$

TABLE I. Calculated capacitances.

h/a	$C/a\times10^{-10}$ (farad)
5	2.7518
10	4.1920
15	5.4867
20	6.6045
25	7.8910
25π	18.586

The matrix of coefficients of the σ_n is given by

$$T_{pn}=\sum_{m=0}^{m=\infty}D_m\gamma_{nm}\beta_{pm}. \tag{19}$$

If Eq. (19) actually contained an infinite number of terms, the present theory would be laborious. However, maximum use has been made of orthogonality in the choice of the indexing function $\cos[(2p+1)\pi z/2h]$, for it and the set $\cos(n\pi z/h)$ are two disjoint complete subsets of $\cos(m\pi z/2h)$ in the range $-h\leq z\leq h$. From the forms for γ and β, one may see that each element of the matrix is given by a sum of two terms.

CALCULATED RESULTS

When Eqs. (16) and (19) are combined and written in matrix form, and the system is truncated to finite order, a square matrix formed from the elements T_{pn} must be inverted by computer methods. The T_{pn} involve calculation of the D_m, which depend on a/h, and the matrices β and γ, which are independent of a/h. The sample values of $G(\alpha)$ and $G_2(\alpha)$ involve looking up the table of the Bessel functions and of sine and cosine integral functions respectively. As the form for $G_2(\alpha)$ converges most rapidly for $h\gg a$, calculations for this paper were made for $h/a=5$, 10, 15, 20, 25, and 25π. Calculations were made at 25th order, with a calculation at 24th order to examine stability. Elements of the matrix were carried to five figures, the last being subject to errors due to roundoff. For the purpose of calculation the product ϵV_s was set equal to unity.

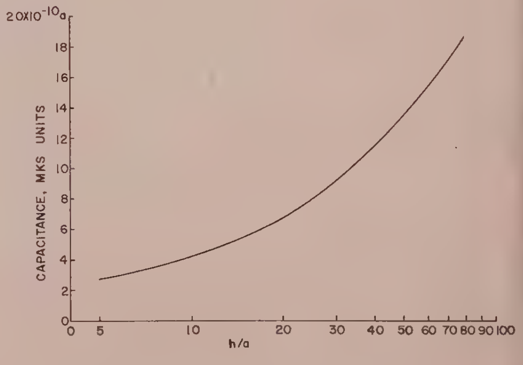

FIG. 2. Capacitance vs h/a.

The charge density near the ends of the tube must nust approximate that near the edge of a semi-infinite lane. This requires a singularity of the form $\delta^{-\frac{1}{2}}$, vhere δ is the distance from the edge. At 25th order the ourier series does begin to develop this singularity, s may be seen in Fig. 1, which shows the charge lensity on a cylinder with $h/a=25\pi$.

An estimate of the accuracy of the solution is found y examining Eq. (14) at 25th order:

$$4\pi(\epsilon V_s)=\sum_{n=0}^{n=24}\sigma_n\sum_{m=0}^{m=\infty}D_m\gamma_{nm}\cos\frac{m\pi z}{2h}. \qquad (21)$$

The sum on m was run to $m=24$, which introduces some rror in the calculation of (ϵV_s). Numerical results vere 0.9996 at the equator and 0.8062 at the ends for $/a=25\pi$, compared to the assumed unity.

The coefficients σ_n were calculated at both 24th and 5th order for the thick cylinder with $h/a=5$, and for he thin cylinder with $h/a=25\pi$. Each coefficient becomes increasingly stable with the addition of higher-order terms. The leading coefficient is then the most stable.

The capacitance is found by integration of Eq. (14) over the cylinder to find the total charge, and division by V_s. The orthogonality of the expansion terms leaves the capacitance in terms of the leading coefficient: $C=2h\sigma_0/V_s$. Since σ_0 changes by no more than 0.02% from 24th to 25th order for all the h/a ratios considered, the capacitances are likewise accurate. If one desired only the capacitance and not the charge distribution, the sequence of values of σ_0 at much lower orders could be extrapolated to obtain the same accuracy.

The calculated capacitances of Table I were used in constructing Fig. 2, which shows the variation of capacitance with h/a ratio.

ACKNOWLEDGMENT

Assistance with the computations was provided by the New Mexico State University Computing Center.

OURNAL OF APPLIED PHYSICS VOLUME 32, NUMBER 7 JULY, 1961

Piezoelectricity of Quartz for Finite Strain*

S. Machlup
Electronic Research Division, Clevite Corporation, and Western Reserve University, Cleveland, Ohio

AND

M. E. Christopher
Electronic Research Division, Clevite Corporation, Cleveland, Ohio

(Received January 11, 1961)

In order to obtain an estimate of the maximum piezoelectric polarization possible for alpha quartz, the principal piezoelectric coefficient is calculated on the basis of a hard-sphere, rigid-ion model. The result, obtained by purely geometrical reasoning (including an *ad hoc* geometrical constraint), fits the measured value of e_{11} with an "effective ionic charge" of one-sixth the free ionic charge. Extension of the calculation to finite compressive strain yields a maximum polarization of 3.4 μcoul/cm^2 at a 34% strain. (Compare with $e_{11}=16.7$ μcoul/cm^2 per unit strain.) For higher strains the polarization drops off rapidly, but the model becomes inconsistent for strains greater than 43%. A test for more general validity of the model, by obtaining directly the ratio of the two independent piezoelectric coefficients, e_{14}/e_{11}, yields seven times the measured ratio.

I. HISTORICAL

THE crystal structure of alpha quartz was determined by Bragg and Gibbs[1] in 1925. In reference (b), Gibbs calculated the principal piezoelectric oefficient (Mason's[2] d_{11}) on the assumption that each ilicon ion has a charge of 4+ (his geometrical reasoning vill be reviewed in Sec. III). Noting that his value was bout four times the measured value, one may conclude that the binding forces are not entirely ionic but largely covalent. Gibbs states his assumptions but does not present the calculation. It is repeated in Sec. III of this paper, with a result more than half again as large.

The earliest calculation of the piezoelectricity of quartz appears to have been by Lord Kelvin.[3] Working before the days of x-ray diffraction, he did not know the crystal structure, only the crystal class (point group). He somewhat imaginatively considered the behavior of a "crystalline molecule" Si_3O_6, ascribing the piezoelectricity to the distortion of the silicon triangle. Kelvin also had to guess at the ionic charge,

---

* Supported in part by Sandia Corporation.

[1] W. Bragg and R. E. Gibbs, (a) Proc. Roy. Soc. (London) **09**, 405–27 (1925); (b) R. E. Gibbs, *ibid.* **110**, 443–55 (1926).

[2] W. P. Mason, *Piezoelectric Crystals and Their Applications to ltrasonics* (D. Van Nostrand Company, Inc., Princeton, New ersey, 1950), p. 39.

[3] Lord Kelvin, Phil. Mag. **36**, 331 (1893).

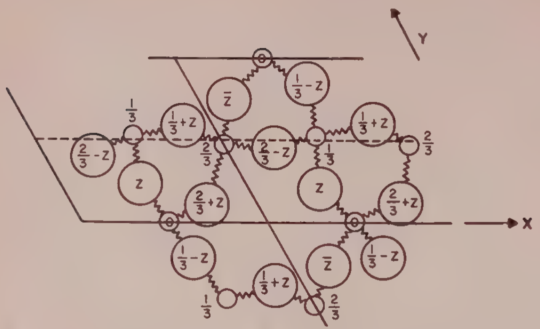

FIG. 1. XY projection of the structure of α quartz based on values in Table I.[5] The Z coordinates are written in, with the parameter $z=0.12$. Nearest neighbors are formed by wiggly-line bonds.

but had to do so before Millikan had measured the electronic charge (i.e., before the oil drop experiment gave us a good value for Avogadro's number).

II. CRYSTAL STRUCTURE OF α QUARTZ

The low-temperature modification of quartz is a trigonal crystal, class 32 (trigonal hemihedral, trigonal holoaxial, or trapezohedral, Schoenflies symbol D_3). It is enantiomorphous, and both the left-handed and right-handed forms occur. The space groups are $D_3^{(4)}$ and $D_3^{(6)}$, respectively (newer notation: $P3_121$ and $P3_221$). Using the notation of the *International Tables for Determination of Crystal Structures*,[4] the silicon ions occupy the (a) positions and the oxygen ions the (c) positions. Wyckoff's[5] values for the ion positions are given in Table I. Here the X and Y coordinates are measured in units of a_0 and the Z coordinates in units of c_0, where a_0 and c_0 are the lattice constants (a_0 measured along a twofold axis, c_0 along the threefold). Note that the Z axis is the threefold axis, and X and Y are twofold axes making a 120° angle. In discussing piezoelectricity it will be more useful to use Cartesian (rectangular) coordinates (to be denoted by lower-case letters). The z axis will still be the threefold axis, the x axis any twofold axis, and the y axis will be normal to both such as to form a right-handed system.

If we revert to the oblique axes, Fig. 1 is an XY projection with the Z coordinate written into the circle representing the atom (small circles denote silicon and large, oxygen). The configuration shown is left-handed, in the sense that if one follows the helix of nearest neighbor bonds along the Z axis, one turns left as one proceeds. This is the configuration of "right" (dextrorotatory) quartz; i.e., to the observer facing the light, the plane of polarization of light traveling along the Z axis appears to rotate in a clockwise sense.[6]

The exercise of following such a spiral staircase of nearest neighbor bonds is useful in visualizing the structure. Note that while every such helix, by definition, consists of alternate silicons and oxygens, each Si participates in two such helices and each O belongs to only one. The unit cell (a rhombohedron) consists of two adjoining helices sharing one Si, three rungs long along the Z axis. Note that all the six oxygens are inside the cell, as is the central silicon, but the other four silicons are each shared with a neighboring cell, so the unit is, indeed, Si_3O_6.[7]

The packing is best visualized by noting that each silicon is tetrahedrally surrounded by four oxygen nearest neighbors. The ionic radii are such that these four oxygens may be considered as tangent, with the (much smaller) silicon nestled in the center of the tetrahedron. The space group symmetry does not require that the tetrahedron be regular. The oxygen positions in Wyckoff (given to ±0.003) are, however, consistent with such an assumption to ±0.5%.[8]

TABLE I.

A. Atom positions, according to Wyckoff,[a] given in the oblique coordinate system, X, Y, Z.[b] Si-O distance = 1.61 A; O-O distance = 2.60 A.

Silicon	X[c]	Y[c]	Z[d]
No. 0	u	0	0
No. 1	1−u	1−u	$\frac{1}{3}$
No. 2	1	u	$\frac{2}{3}$
Oxygen			
No. 0	1+y−x	1−x	$\frac{1}{3}$+z
No. 1	1−y	x−y	$\frac{2}{3}$+z
No. 2	x	y	z

B. Transform to Cartesian coordinates, with $c_0/a_0=1.099938$. The values for ζ (the z coordinate of the oxygens) have been computed using 0.11946 instead of 0.120 for the fourth parameter (z) above. This makes the oxygen tetrahedron regular, a symmetry not required by the space group.

Silicon	x	y	z
No. 0	0.465	0	0
No. 1	0.2675	0.463324	0.366646
No. 2	0.7675	0.402702	0.733292
Oxygen	ξ	η	ζ
No. 0	0.5645	0.506625	0.498041
No. 1	0.6565	0.123842	0.864694
No. 2	0.2790	0.235559	0.131399

[a] Reference 5.
[b] In part A, u = 0.465, x = 0.415, y = 0.272, z = 0.120. Values are claimed good to ±0.003; these parameters are not to be confused with Cartesian coordinates in part B of the table.
[c] $a_0=4.913$ A.
[d] $c_0=5.404$ A.

---

[4] Edited by K. Lonsdale *et al.* (Kynoch Press, Birmingham, England, 1952).

[5] R. W. G. Wyckoff, *Crystal Structures* (Interscience Publishers, Inc., New York, 1948), Vol. I, Chap. 4, p. 26. In making a drawing or model based on these data one must be careful to use a right-handed coordinate system with a 120° angle between the positive X and Y axes.

[6] A. deVries, Nature **181**, 1193 (1958). The light seems to follow the spiral staircase in its rotation.

[7] This last fact was understood by Kelvin (reference 3).

[8] The structure is described by five parameters (see Table II) u, x, y, z, and the axial ratio c_0/a_0. In the calculation the parameter z, given as 0.120 by Wyckoff,[5] is taken as 0.1195, making the tetrahedron regular.

III. PIEZOELECTRIC CONSTANTS

For theory based on geometrical rather than dynamical consideration, the indicated piezoelectric constants are the *e* constants, defined as the differential electric polarization per unit strain for given applied electric field:

$$e_{mi}=(\partial P_m/\partial S_i)_E, \quad m=1 \text{ to } 3, \quad i=1 \text{ to } 6.$$

The point symmetry leaves only two independent constants, giving the e_{mi} matrix[9]:

$$\begin{pmatrix} e_{11} & -e_{11} & 0 & e_{14} & 0 & 0 \\ 0 & 0 & 0 & 0 & -e_{14} & -e_{11} \\ 0 & 0 & 0 & 0 & 0 & 0 \end{pmatrix}.$$

Some of its features are (a) no piezoelectric polarization along the *z* (threefold) axis, (b) no polarization along he *y* axis for a pure tensile (or compressive) strain along the *x*, *y*, or *z* axis, and (c) no polarization along he *x* axis for pure tensile (or compressive) strain along he *z* axis.

The calculation of the constants is based on the following assumptions, whose validity must be subjected to close scrutiny:

(1) The strain is considered as applied to the silicon lattice, and the concomitant relaxation of the oxygen lattice gives rise to the piezoelectric polarization. This relaxation is determined by the purely geometrical constraints (2) and (3).
(2) The nearest neighbor bond length remains constant.
(3) The inclination with respect to the *z* axis of the normal to the plane of each adjoining Si-O-Si group remains constant.
(4) The effective charges of all ions remain constant, and are considered point charges.

Assumption (2) is equivalent to taking a hard-sphere nteraction between nearest neighbor Si-O pairs. Coupled with assumption (4), it is equivalent to the statement that the polarization may be described entirely as the *reorientation* of a lattice of dipoles (whose *magnitude* remains constant). This assumption eems to be the basis for the work of von Hippel.[10]

For a two-dimensional lattice, assumption (2) would uffice to determine the oxygen position for given train applied to the silicon lattice.[11] In three dimensions, one more condition is needed to remove the one remaining degree of freedom. If it is to be, as assumed, a purely geometrical constraint, it must be one which provides only *one* equation in the *three* coordinates of each oxygen; otherwise the system will be overdetermined. It is likely that Bragg and Gibbs chose condition (3) because it was the simplest available, and not for good physical reasons. Certainly both (2) and (3) should be replaced by some minimum principle involving bond energies. This would imply the assumption of a "bond stiffness" (bond energy as a function of bond angle), and presents a more complicated problem.

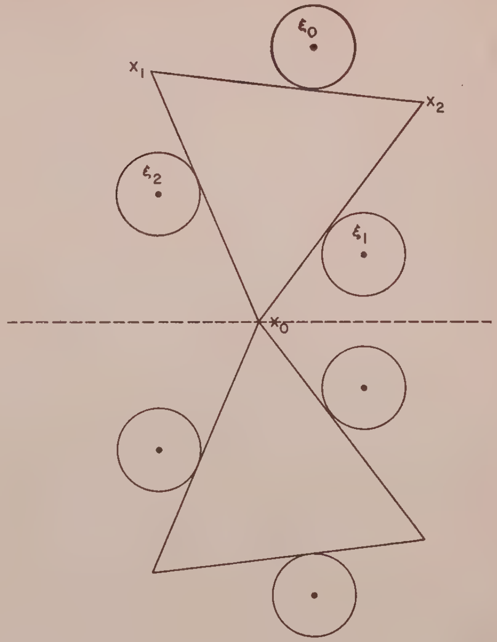

FIG. 2. *xy* projection of a unit cell. The vertices of the triangles represent silicons (Roman letters), the circles represent oxygens (Greek letters). The dotted horizontal line is a twofold (*x*) axis.

Analytical Geometry of the Oxygen Positions

Schematically, the problem may be represented by the *xy* projection of a unit cell shown in Fig. 2.[1] The vertices of the triangles represent silicon positions (coordinates given in Roman letters), the centers of the intervening circles, oxygen positions (coordinates given in Greek letters).

Henceforth, attention will be focused on only one Si-O-Si group at a time; take, for example, Si^1-O^0-Si^2, and solve for the oxygen position $(\xi_0\eta_0\zeta_0)$ as the silicon positions are varied (as the crystal is strained). The oxygen remains on the plane which bisects normally the line joining the two silicons, and is restricted to a circle of radius ρ on this plane [assumption (2)]. Letting b be the (constant) bond length (silicon-oxygen distance), and $2r$ the silicon-silicon distance, we have

$$\rho^2=b^2-r^2. \tag{1}$$

Since the analysis is so easy in the plane determined by the three atoms, a simple rotation of coordinates is

---

[9] W. G. Cady, *Piezoelectricity* (McGraw-Hill Book Company, nc., New York, 1956), p. 191.

[10] A. von Hippel, Z. Physik **133**, 158 (1952).

[11] This is easily seen by replacing a Si_3O_3 helix by, for example, hree pennies and three silver dollars lying tangent on the table.

TABLE II. Transformation matrix for rotation by the Euler angles.[a,b]

Let the transformation be $\mathbf{x}=\mathbf{A}^{-1}\mathbf{x}'$. Then

$$\mathbf{A}^{-1}=\begin{pmatrix} \cos\psi\cos\varphi-\gamma\sin\psi\sin\varphi & -\sin\psi\cos\varphi-\gamma\cos\psi\sin\varphi & (1-\gamma^2)^{\frac{1}{2}}\sin\varphi \\ \cos\psi\sin\varphi+\gamma\sin\psi\cos\varphi & -\sin\psi\sin\varphi+\gamma\cos\psi\cos\varphi & -(1-\gamma^2)^{\frac{1}{2}}\cos\varphi \\ (1-\gamma^2)^{\frac{1}{2}}\sin\psi & (1-\gamma^2)^{\frac{1}{2}}\cos\psi & \gamma \end{pmatrix}$$

[a] Reference 12.
[b] Here $\gamma=\cos\theta$, where θ = angle made by $x'y'$ plane with z axis.

suggested, in which this becomes the $x'y'$ plane, with the line joining the two silicons as the x' axis.

Such a rotation can best be described in terms of the Euler angles; i.e., as three successive rotations. First, there is a rotation about the z axis through an angle φ, which brings the x axis into the plane. Next, a rotation about this "temporary" x axis makes the z axis into a z' axis normal to the plane; i.e., a rotation through that angle θ which is the inclination of the plane to the z axis, and which is to remain constant according to assumption (3). Finally, a rotation about this new z' axis through an angle ψ aligns the x axis with the silicon-silicon axis, the new x' axis. The matrix of the resulting rotation is given in Table II.[12]

In the $x'y'z'$ coordinates, if the midpoint between the silicons is taken as origin, the coordinates of the oxygen are simply $(0,\rho,0)$. Letting $(\mathrm{x},\mathrm{y},\mathrm{z})$ and $(-\mathrm{x},-\mathrm{y},-\mathrm{z})$ be the silicon coordinates relative to this origin, i.e.,

$$\mathrm{x}_0=\tfrac{1}{2}(x_2-x_1),\quad \mathrm{y}_0=\tfrac{1}{2}(y_2-y_1),\quad \mathrm{z}_0=\tfrac{1}{2}(z_2-z_1),\tag{2}$$

we have

$$\xi_0-\tfrac{1}{2}(x_1+x_2)=-\rho(\sin\psi\cos\varphi_0+\gamma\cos\psi\sin\varphi_0),\tag{3}$$

where

$$\begin{aligned}\gamma&=\cos\theta,\\ \tan\psi&=\mathrm{z}/[r^2(1-\gamma^2)-\mathrm{z}^2]^{\frac{1}{2}},\\ r^2&=\mathrm{x}^2+\mathrm{y}^2+\mathrm{z}^2,\\ \tan\varphi&=(\mathrm{y}-\mathrm{x}\gamma\tan\psi)/(\mathrm{x}+\mathrm{y}\gamma\tan\psi),\\ \rho^2&=b^2-r^2.\end{aligned}$$

$$\eta_0-\tfrac{1}{2}(y_1+y_2)=\rho(-\sin\psi\sin\varphi_0+\gamma\cos\psi\cos\varphi_0),\tag{4}$$

$$\zeta_0-\tfrac{1}{2}(z_1+z_2)=\rho(1-\gamma^2)^{\frac{1}{2}}\cos\psi.\tag{5}$$

Only the angle φ need have a subscript, since $\gamma=\cos\theta$ and ψ are the same for all the oxygens by virtue of the threefold symmetry.[13]

Dipole Moment

The electric dipole moment per unit cell is given by the "effective ionic charge" times the vector drawn from the center of mass of the three silicons in the triangle to that of the three oxygens. Thus, for the x component,

$$p_x=2\epsilon[(x_0+x_1+x_2)-(\xi_0+\xi_1+\xi_2)].\tag{6}$$

The factor 2 takes account of the lower triangle in Fig. 2; ϵ is half the effective charge of a silicon ion, or minus the effective charge of an oxygen. ($\epsilon=2e$ for 100% ionic binding.) Use of the expression for ξ_0 above and the similar ones for ξ_1 and ξ_2 gives

$$p_x=2\epsilon\sum_{i=0}^{2}\rho(\sin\psi\cos\varphi_i+\gamma\cos\psi\sin\varphi_i).\tag{7}$$

Coefficient for Small Strain

The dielectric polarization $\mathbf{P}$ is the dipole moment of a unit cell divided by the cell volume. The change of cell volume with strain will introduce a second-order contribution to the piezoelectric coefficients and will be neglected. The task is then only to find the variation of $\mathbf{p}$ with strain. Thus, for the principal e coefficient,

$$e_{11}=\text{cell volume}^{-1}(\partial p_x/S_1).\tag{8}$$

The differentiation with respect to compressional strain is performed by replacing x by $x(1+S_1)$ throughout and differentiating with respect to S_1. Performing the differentiation yields

$$\begin{aligned}\tfrac{1}{2}\epsilon^{-1}(\partial p_x/\partial S_1)=+\tfrac{1}{2}\epsilon^{-1}(\partial/\partial S_1)\textstyle\sum_i\rho(\sin\psi\cos\varphi_i\\ +\gamma\cos\psi\sin\varphi_i)=-0.3495a_0.\end{aligned}\tag{9}$$

Note that all quantities having the dimensions of length are thus stated in units of the lattice constant a_0.[14]

If one takes the point of view that the effective charge is unknown and the principal piezoelectric

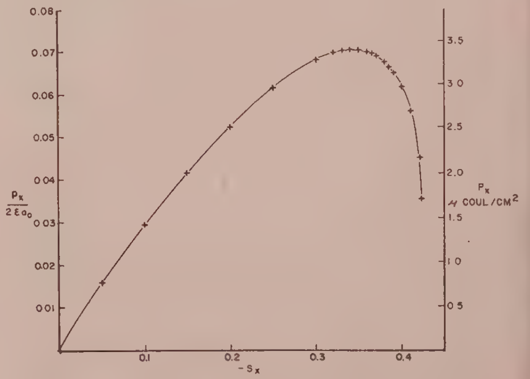

FIG. 3. Calculated polarization vs strain for α quartz.

---

[12] See, for example, H. Goldstein, *Classical Mechanics* (Addison-Wesley Publishing Company, Inc., Reading, Massachusetts, 1950), p. 109.

[13] In working out the position of oxygen No. 1, the z coordinate of silicon No. 0 must, of course, be taken as unity, not zero as in Table I.

[14] Only the Z coordinate in the oblique coordinate representation given at the top of Table I is in units of c_0. The Cartesian coordinate z at the bottom is again in units of a_0.

coefficient is known, the equation for e_{11} can be written

$$e_{11}=2\epsilon(-0.3495a_0)/(\tfrac{1}{2}\sqrt{3}a_0^2c_0)$$
$$=(-\epsilon/2e)(29.184\times10^4\ \text{statcoul/cm}^2). \quad (10)$$

Comparison with the experimental value,[15] $e_{11}=-5.022\times10^4$ statcoul/cm², gives a fractional effective charge of $\epsilon/2e=0.1721$; i.e., about one-sixth of pure ionic binding. This is to be compared with the value one-fourth, given by Gibbs.[1b]

Finite Strain

The relative x displacement $p_x/2\epsilon a_0$ of the two centers of charge (positive relative to negative) has been calculated as a function of the compressional strain $-S_1$ and is plotted in Fig. 3. The right-hand scale reads the polarization P_x directly, using the effective charge ϵ of the previous paragraph. The curve is almost linear up to about 10% compressive strain, then flattens out to reach a maximum at 34%, from which it falls sharply. For compressions greater than 42.3% the assumed constraints can no longer be satisfied, so the calculation breaks down.

For handy conversion from the characteristic length $p_x/2\epsilon$ to polarization P_x, the formula

$$P_x=\left(\frac{5.022\times10^4\ \text{statcoul/cm}^2}{0.3495a_0}\right)\left(\frac{p_x}{2\epsilon}\right) \quad (11)$$

readily gives away its ancestry. Converting to practical units, the theoretical maximum corresponds, as shown, to 3.4 μcoul/cm².

e_{14} Coefficient

As there is a second independent piezoelectric constant, it would seem to be a reasonable test of the assumptions used above to compute the other one using the same effective charge. The coefficient connecting an x polarization with a shear in the yz plane can be written, corresponding to Eq. (8),

$$e_{14}=\text{cell volume}^{-1}(\partial p_x/\partial S_4). \quad (12)$$

Thus, in the expression for p_x [Eq. (7)] the coordinates x, y, z are replaced as follows:

$$x\rightarrow x$$
$$y\rightarrow y+\tfrac{1}{2}S_4z$$
$$z\rightarrow z+\tfrac{1}{2}S_4y.$$

The differentiation with respect to S_4 yields

$$\tfrac{1}{2}\epsilon^{-1}(\partial p_x/\partial S_4)=+0.4719a_0. \quad (13)$$

The calculated ratio of the two piezoelectric coefficients is thus $e_{14}/e_{11}=-1.35$, in contrast to the observed ratio[15] of -0.19. This discrepancy casts doubt on the assumptions, particularly on (3) and (4), the geometric constraint and the point charge approximation, to which e_{14} would seem to be very sensitive.

APPENDIX

An evaluation of $\gamma=\cos\theta$, where θ is the angle made by the normal to a Si-O-Si plane (the z' axis) with the Z axis, is needed for Eq. (9).

Let (α,β,γ) be the direction cosines of this normal. It is normal, for example, to the Si¹-O⁰ line:

$$\alpha(x_1-\xi_0)+\beta(y_1-\eta_0)+\gamma(z_1-\zeta_0)=0$$

and to the Si²-O⁰ line:

$$\alpha(x_2-\xi_0)+\beta(y_2-\eta_0)+\gamma(z_2-\zeta_0)=0.$$

Since they are direction cosines,

$$\alpha^2+\beta^2+\gamma^2=1,$$

one can solve for γ:

$$\frac{1-\gamma^2}{\gamma}=\frac{[(y_1-\eta_0)(z_2-\zeta_0)-(y_2-\eta_0)(z_1-\zeta_0)]^2+[(x_1-\xi_0)(z_2-\zeta_0)-(x_2-\xi_0)(z_1-\zeta_0)]^2}{[(y_1-\eta_0)(x_2-\xi_0)-(y_2-\eta_0)(x_1-\xi_0)]^2}.$$

Cyclical permutation of the subscripts 0, 1, 2 should, of course, give the same value of γ, because of the threefold symmetry. The result is $\gamma=0.626477$, $\theta=51.2°$.

---

[15] W. P. Mason (see p. 85 of reference 2) gives the piezoelectric d coefficients [corrected for 1949 sign conventions; see Proc. I.R.E. **37**, 1384 (1949)]:

$$d_{11}=-6.76\times10^{-8}\ \text{statcoul/d},$$
$$d_{14}=-2.56\times10^{-8}\ \text{statcoul/d},$$

and the elastic constants at constant electric field:

$$c_{11}=86.05\times10^{10}\ \text{d/cm}^2,$$
$$c_{12}=4.85\times10^{10}\ \text{d/cm}^2,$$
$$c_{14}=-18.25\times10^{10}\ \text{d/cm}^2,$$
$$c_{44}=58.65\times10^{10}\ \text{d/cm}^2,$$

from which (see p. 40 of reference 2)

$$e_{11}=d_{11}(c_{11}-c_{12})+d_{14}c_{14}=-5.022\times10^4\ \text{statcoul/cm}^2.$$
$$e_{14}=2d_{11}c_{14}+d_{14}c_{44}=+0.96\times10^4\ \text{statcoul/cm}^2.$$

Note that "right" quartz (see reference 6) has negative e_{11} and positive e_{14}, according to the 1949 sign conventions.

JOURNAL OF APPLIED PHYSICS VOLUME 32, NUMBER 7 JULY, 1961

Texture Transition in High-Purity Silver and Its Correlation with Stacking Fault Frequency

HSUN HU, R. S. CLINE, AND S. R. GOODMAN
Edgar C. Bain Laboratory for Fundamental Research, United States Steel Corporation Research Center, Monroeville, Pennsylvania

(Received January 30, 1961)

The rolling texture of high-purity silver is found to change gradually from the common *silver type* to the *copper type* as the temperature of deformation increases. The transition is completed in the temperature range 150°–200°C. There is a general correlation between the texture transition and the change in stacking fault frequency as a function of rolling temperature. On the basis of such a correlation, the texture transition produced by varying the temperature of deformation, or by alloy additions, can be consistently interpreted in terms of a change in the stacking fault energy, a change in the dislocation density, or both.

INTRODUCTION

IN a previous paper[1] it was reported that the rolling texture of high-purity silver (total metallic impurities spectrographically detected, <2 ppm; O_2, 2 ppm) was the common *silver type*; i.e., $(110)\ [\bar{1}12]$, when the specimen was rolled 91% at 0°C. A rolling texture of predominantly $(124)\ [21\bar{1}]$ plus $(146)\ [21\bar{1}]$, which is very similar to the texture of cold-rolled copper, was obtained when the specimen was rolled at 200°C. Thus, a change in texture from the common *silver type* to the *copper type* can be effected in high-purity silver by merely raising the temperature of rolling. Conversely, Müller[2] has observed a change in the rolling texture of electrolytic copper from the usual *copper type* to the *silver type* by lowering the rolling temperature. The effect of temperature of deformation on the formation of rolling textures is thus very similar to that produced by alloy additions. Smallman[3] has suggested that the "overshooting" phenomenon,[4] which is commonly observed in copper alloys but not in pure copper specimens, may be responsible for the difference in the rolling textures. According to Piercy *et al.*,[5] "overshooting" is a result of a high rate of hardening on the latent slip system, since the dislocations in the conjugate slip planes have difficulty cutting through the partial dislocations in the primary slip planes. As a consequence, the amount of overshooting would depend on the separation between the partials or the width of the stacking faults, which, in turn, depends on the stacking fault energy. Brown,[6] incorporating the ideas of Seeger and of Hirsch, has also suggested the dependence of wire textures on the stacking fault energy. In connection with these ideas, the texture transition in high-purity silver as a function of rolling temperature was studied in more detail. The change in texture, as expressed quantitatively by various selected parameters, was correlated with the stacking fault frequency determined from peak shift measurements.

EXPERIMENTAL PROCEDURE

Specimen Preparation

The same high-purity silver used previously was remelted and processed in exactly the same manner as described in a previous paper,[1] except that a slightly higher remelting temperature was employed, and the piece was remelted three times. The oxygen content was reduced to less than 1 ppm, as compared with 2 ppm in the previous specimens. The total metallic impurities remained the same; i.e., less than 2 ppm. Three intermediate rolling temperatures between 0°–200°C at intervals of every 50° were added to the previous investigation. Since the rolls could be preheated to the desired temperatures by using a gas burner, the specimens were rolled without sandwiching blocks. The temperature of the rolls was frequently checked with a thermocouple after one or two passes, and the rolls were reheated to temperature when necessary. Because of the lack of accuracy in such temperature measurements, the exact temperature of rolling was likely subject to some slight deviations. However, for the purpose of the present work, such temperature deviations are thought to be insignificant. The specimens were etched slightly (from 0.004 to 0.003 in. thick) to remove the surface irregularities before exposure to x rays. For the series rolled at 0°C and at 50°C, specimens were stored in liquid nitrogen. Those rolled at 100°C and above were stored at room temperature.

X-Ray Measurements

The stacking fault frequency was determined from peak-shift measurements of the first four reflections {111}, {200}, {220}, and {311}. Theoretical treatment for small stacking fault probabilities (or frequencies)[7] in a cold-worked specimen of an fcc metal have been given by Paterson[8] and Warren.[9] From the change in the peak eparations of two neighboring reflections from a cold-orked specimen, as compared with that for a fully nnealed specimen, the stacking fault probability α can e calculated from one of the following equations:

---

[1] H. Hu and R. S. Cline, J. Appl. Phys. **32**, 760 (1961).

[2] H. Müller, Österr. Akad. Wiss. Math-naturw. Kl. Anz. **7**, 117–119 (1958).

[3] R. E. Smallman, J. Inst. Metals **84**, 10 (1955–56).

[4] The tendency for slip to continue on the initial slip system even after an alternate slip system has rotated into a favorable orientation for slip to occur.

[5] G. R. Piercy, R. W. Cahn, and A. H. Cottrell, Acta Met. **3**, 331 (1955).

[6] N. Brown, Trans. AIME **221**, 236 (1961).

[7] "Stacking fault frequency" and "stacking fault probability" are used synonymously in this paper.

[8] M. S. Paterson, J. Appl. Phys. **23**, 805 (1952).

[9] B. E. Warren, Progr. in Metals Phys. **8**, 178 (1959); B. E. Warren and E. P. Warekois, Acta Met. **3**, 473 (1955).

$$\Delta(2\theta_{200}{}^{\circ}-2\theta_{111}{}^{\circ})=-(45\sqrt{3}\alpha/\pi^2)(\tan\theta_{200}+\tfrac{1}{2}\tan\theta_{111}),$$

$$\Delta(2\theta_{220}{}^{\circ}-2\theta_{200}{}^{\circ})=(45\sqrt{3}\alpha/\pi^2)(\tfrac{1}{2}\tan\theta_{220}+\tan\theta_{200}),$$

$$\Delta(2\theta_{311}{}^{\circ}-2\theta_{220}{}^{\circ})=-(90\sqrt{3}\alpha/\pi^2)\times[(1/11)\tan\theta_{311}+\tfrac{1}{4}\tan\theta_{220}].$$

s pointed out by Warren[9] (and Warren and Warekois[9]), hese derivations are made on the assumption that de-ormation faulting occurs independently and on only ne set of (111) planes, but it is considered to be a good pproximation that α so calculated is equal to the sum f the probabilities for different sets of active (111) lanes in drastically cold-worked specimens. In the resent work, the specimens were all in sheet form, and highly preferred orientation existed in each specimen. ence, strictly speaking, a direct application of these erivations does not seem to be completely justified. owever, on the basis of the fact that no significant ifference was detected in the peak separations of the rst four reflections in a substantially recrystallized heet specimen as compared with that in a fully annealed owder specimen, the errors introduced by using a sheet pecimen are probably small. The stacking fault proba-ility determination will be discussed further in the text.

The peak-separation measurements were made at -40°C for the specimens rolled at 0° and 50°C. For the pecimens rolled at higher temperatures, measurements ere made at room temperature immediately after olling. A GE XRD-5 x-ray spectrometer with filtered u K_α radiation was used. Intensity measurements were aken at every 0.02 or 0.05° in 2θ, and the first four eflections were completed in a single run for each speci-nen to minimize positioning errors. The individual eaks were then plotted on graph paper, and the exact osition of $K_{\alpha 1}$ reflection was located by the graphical echnique of Papoulis.[10] The peak positions could be etermined with an accuracy of 0.005° from the graph. he angular separation between each pair of adjacent eaks was then compared with that of a fully annealed owder specimen measured at the same temperature. s shown by the above three equations, the peak shifts ue to deformation faulting should be negative between he {111} and {200} reflections, positive between the 200} and {220} reflections, and negative between the 220} and {311} reflections. Shifts of the proper signs ere considered a criterion that the peak shifts were due o stacking faults.

After the peak-shift measurements were completed, he same specimens were used for texture determina-ions. The same general procedures described in a pre-ious paper[1] were followed, except that only transmis-ion data were recorded. Hence, the central portion of the pole figure within a radius of 25° was not obtained. For the purpose of orientation analysis, these transmission pole figures were found to be adequate. Textures for all the specimens rolled at temperatures higher than room temperature were determined at room temperature. However, it was found later that progressive recrystallization took place slowly at room temperature even in the specimens rolled at 150°C. This finding was quite unexpected.

EXPERIMENTAL RESULTS

Rolling Textures

Figures 1 and 2 are the (111) and (200) pole figures, respectively, of the specimen rolled at 50°C. The main orientation is (110) [$\bar{1}12$], and the pole figures are almost exactly the same as those of a specimen rolled at

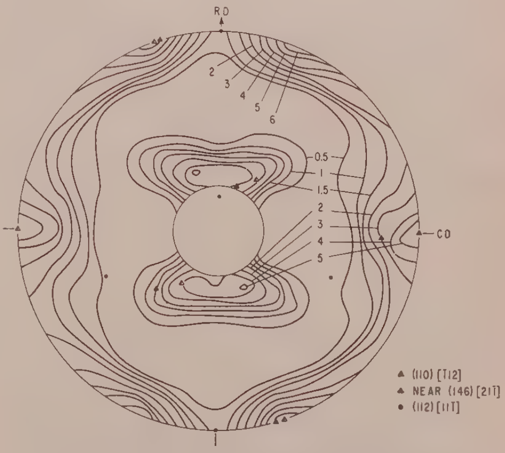

FIG. 1. (111) pole figure of high-purity silver rolled 91% at 50°C.

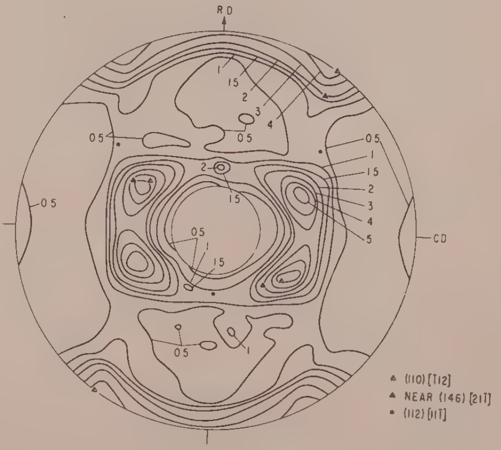

FIG. 2. (200) pole figure of high-purity silver rolled 91% at 50°C. Some recrystallization has taken place, as shown by the extra peaks.

---

[10] A. Papoulis, Rev. Sci. Instr. **26**, 423 (1955).

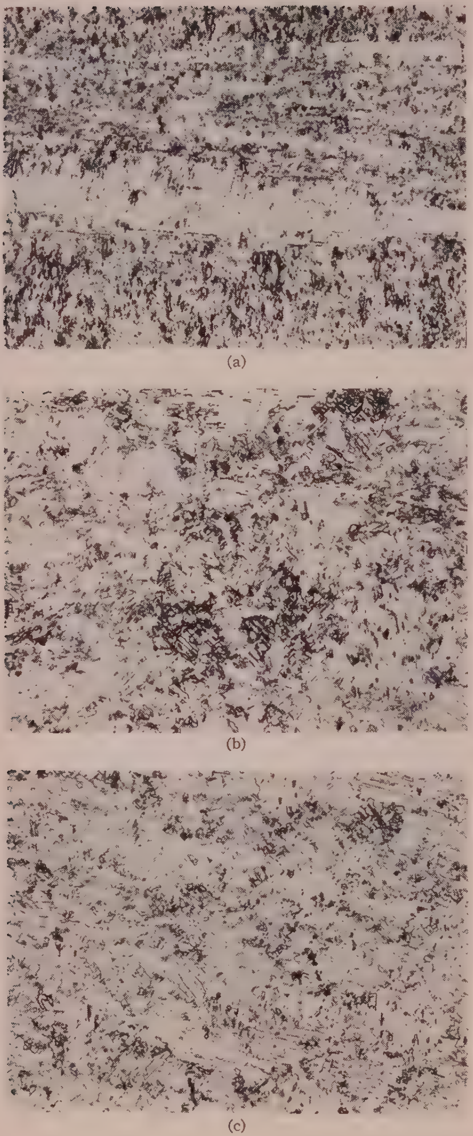

(a)

(b)

(c)

Fig. 3. Microstructure of the specimen rolled 91% at 50°C (a) immediately after rolling, (b) after 1 wk at room temperature, and (c) after 3 wk at room temperature. 160×.

0°C (see Figs. 1 and 2 in a previous paper[1]). The (200) pole figure was determined immediately after the {111} reflections were recorded. Nonetheless, some recrystallization had taken place in the specimen during that period of time, as suggested by the extra peaks of weaker intensities in the (200) pole figure (Fig. 2). Microscopic examination[11] showed the presence of a few small recrystallized grains in the specimen [Fig. 3(a)]. The same specimen was reexamined after one weak and after three weeks at room temperature. The microstructures are shown in Figs. 3(b) and (c). It can be seen that recrystallization had taken place quite extensively after one week at room temperature [Fig. 3(b)]. After that, no appreciable further changes in the microstructure were noted [Fig. 3(c)]. The texture of the specimen rolled at 100°C is shown in Figs. 4 and 5, which are the (111) and (200) pole figures, respectively. Because of some unexpected delay in the texture determinations on this specimen, considerable recrystallization had taken place before the {200} reflections were recorded. However, a major part of the deformation texture still remained. From the (111) pole figure as shown in Fig. 4, definite changes in texture from a (110) $[\bar{1}12]$, the common *silver type*, towards the *copper type* can be noted. Ideal orientations of the two different types of textures are indicated in the pole figure by various triangular symbols. The ideal orientation of (112) $[11\bar{1}]$ (as designated by the black dots) is also indicated, since it is believed that this particular orientation probably played an important role in the texture transition. A discussion of the fine details of the texture changes will be given in the next section. No attempt will be made in the present paper to analyze the *recrystallized* texture components in the (200) pole figure (Fig. 5), because the recrystallization textures of these specimens will be considered in a subsequent presentation.

Figures 6 and 7 are, respectively, the (111) and (200) pole figures of the specimen rolled at 150°C. This texture is essentially of the *copper type*, as shown by the ideal orientations of (124) $[21\bar{1}]$ and (146) $[21\bar{1}]$ (indicated by the open and filled triangles respectively). Being similar to the texture of the specimen rolled at 200°C, there is also a (100) [001] cube texture component (as

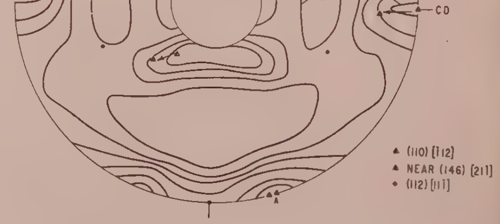

Fig. 4. (111) pole figure of high-purity silver rolled 91% at 100°C. Arrows indicate a rotation of 12.5° from the (110) $[\bar{1}12]$ orientation to the near (146) $[21\bar{1}]$ orientation around the approximately common (111) pole at *A*.

---

[11] Specimens were electrolytically polished in a solution of 4% KCN, 4% K_2CO_3, and 4% AgCN, and etched in a solution of 100 ml saturated $K_2Cr_2O_7$, 2 ml saturated NaCl and 10 ml conc. H_2SO_4.

indicated by the open squares) due to partial recrystallization during rolling, although the intensity of this cube texture component is considerably weaker in the present specimen. (Compare the present Figs. 6 and 7 with Figs. 3 and 4 of the previous paper.[1]) A main difference between the texture of the specimen rolled at 150°C and that rolled at 200°C is obviously in the separation of the two intensity maxima near the rolling direction in the (111) pole figures. As shown in Fig. 6, these two intensity maxima for the specimen rolled at 150°C are not well separated. A survey of the average pole density of the (112) [11$\bar{1}$] component in both textures indicates that the percentage contribution of the (112) [11$\bar{1}$] orientation in the specimen rolled at 150°C is approximately 50% greater than in the specimen rolled at 200°C. Hence, the apparent merging of the two intensity maxima near the rolling direction in Fig. 6 is actually caused by overlapping with the intensity peaks of the (112) [11$\bar{1}$] components. In the third week after rolling, the specimen was briefly rechecked for its preferred orientation. It was found that a few new peaks appeared. The fact that further recrystallization can take place at room temperature after the specimen was previously deformed at a temperature as high as approximately 150°C is really astonishing! However, no such phenomenon was observed in a previous specimen rolled at 200°C. Perhaps the difference in oxygen contents of the specimens is responsible. In the previous specimens, the oxygen content is 2 ppm, whereas in the present specimens it is less than 1 ppm.

Stacking Fault Frequencies

Wagner studied deformation faulting in alpha brass[12] and in silver (99.95% pure)[13] by measuring the peak shifts between pairs of the first four or five reflections. He found that the reciprocal stacking fault probability values α^{-1} computed from the change in separation of the (200)–(111) and (311)–(220) reflection pairs agree very well, whereas the values of α^{-1} obtained from (220)–(200) are always larger. These discrepancies were considered by him as due to nonrandom faulting in the filings.[12] Presumably, there is the possibility of some preferred orientation in the packed powder, as the shape of the filed particles is not spherical. In the present work, we observed a similar effect; i.e., the α^{-1} values calculated from the peak shifts of the (220)–(200) pair were always greater. While each of our specimens had a highly preferred orientation, the actual effect of a particular

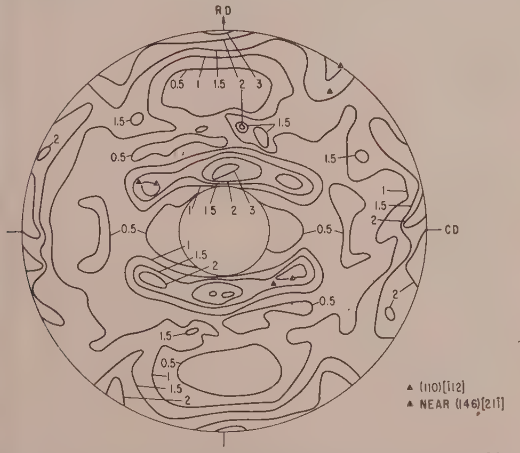

Fig. 5. (200) pole figure of high-purity silver rolled 91% at 100°C. Considerable recrystallization has taken place in the specimen as a result of unexpected delay in pole figure determinations. A large portion of the deformation texture, as indicated by the triangular symbols, still remains.

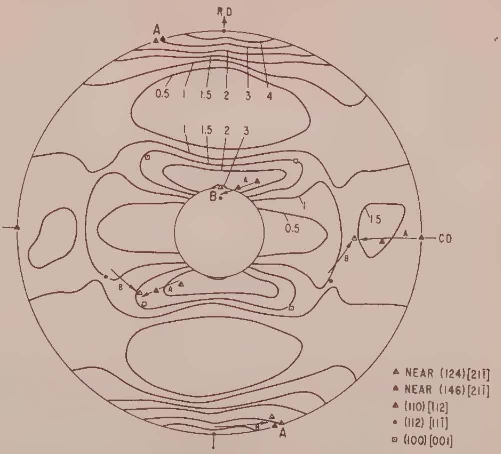

Fig. 6. (111) pole figure of high-purity silver, rolled 91% at 150°C. Arrows *A* indicate rotation of approximately 22° from the (110) [$\bar{1}$12] orientation to near (124) [21$\bar{1}$] orientation around the approximately common (111) pole at *A*. Arrows *B* indicate rotation of approximately 21° from the (112) [11$\bar{1}$] orientation to near (124) [21$\bar{1}$] orientation around the approximately common (111) pole at *B*.

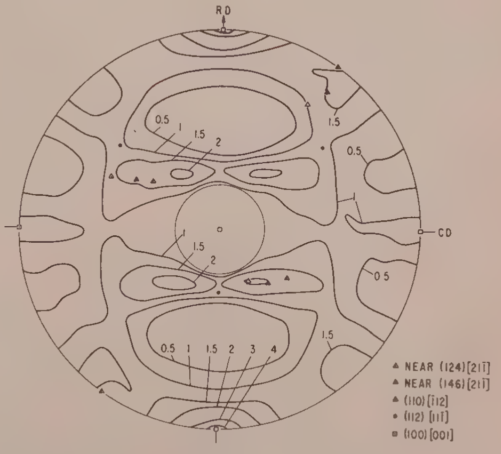

Fig. 7. (200) pole figure of high-purity silver rolled 91% at 150°C.

---

[12] C. N. J. Wagner, Acta Met. **5**, 427 (1957).
[13] C. N. J. Wagner, Acta Met. **5**, 477 (1957).

TABLE I. Peak shifts, calculated stacking fault frequency α, and α^{-1} in number of $d_{(111)}$ spacings in high-purity silver.

Rolling temp. (°C)	Peak shifts Reflection pairs	$\Delta 2\theta$°	α	α^{-1}	$\langle\alpha^{-1}\rangle$
0	(200)–(111)	−0.048	0.0104	96	120 (280 A)
	(220)–(200)	+0.028	0.0049	204	
	(311)–(220)	−0.060	0.0164	61	
50	(200)–(111)	−0.022	0.0048	208	230 (500 A)
	(220)–(200)	+0.014	0.0024	416	
	(311)–(220)	−0.052	0.0142	70	
100	(200)–(111)	−0.015	0.0033	303	320 (750 A)
	(220)–(200)	...	...	...	
	(311)–(220)	−0.011	0.0030	333	
150	(200)–(111)	−0.003	0.0007	1430	1430 (3360 A)
	(220)–(200)	...	...	...	
	(311)–(220)	...	...	...	
200	(200)–(111)	cannot be measured accurately			
	(220)–(200)				
	(311)–(220)				

orientation on the discrepancy of the α^{-1} values is not at all clear. Most of the reflection peaks were fairly symmetrical. Only the (220) peaks showed a very slight asymmetry. A summary of the results from the peak shift measurements is given in Table I.

As mentioned earlier, specimens rolled at 0°–50°C were stored in liquid nitrogen, and their peak-separation measurements were completed at −40°C. For the other specimens, measurements were made at room temperature immediately after rolling. No detectable peak shifts were observed in the specimen rolled at 200°C, in which substantial recrystallization was found to have taken place. For specimens rolled at 100° and 150°C, one or two of the peak shifts of the three reflection pairs were too small to be measured accurately. Extensive recovery and partial recrystallization in these specimens may have been responsible for these discrepancies. The average reciprocals of the stacking fault frequencies $\langle\alpha^{-1}\rangle$, as shown in the last column of Table I, do indicate a general trend for the average interval (expressed as number of $d_{(111)}$ spacings) between faulted planes to increase as the temperature of deformation increases. These results are in comparable agreement with the results of Wagner,[13] who has determined the values of $\langle\alpha^{-1}\rangle$ for filed silver powder specimens after annealing at various temperatures.

DISCUSSION OF RESULTS

Characteristics of the Rolling Textures

It is seen that the change in texture from the common *silver type* to the *copper type*, as the rolling temperature increases from 0° to 200°C, takes place rather continuously and gradually. The details of this texture transition can be described as follows: At low rolling temperatures, e.g., 0° and 50°C, the texture is (110) $[\bar{1}12]$. To be more precise, this ideal orientation does not quite coincide with the high intensity maxima of the texture as shown by the pole figures (Figs. 1 and 2, and Figs. 1 and 2 in the previous paper). The orientation spread actually includes the (146) $[21\bar{1}]$ orientation, which is indicated by the solid triangles in Figs. 1 and 2. The (112) $[11\bar{1}]$ orientation makes a negligible contribution to the texture. At a somewhat higher rolling temperature, e.g., 100°C, the change in orientation takes place in such a direction that the (110) $[\bar{1}12]$ orientation shifts towards the (146) $[\bar{2}\bar{1}1]$ orientation. Evidence indicating such a shift is shown by the disappearance of the (110) $[\bar{1}12]$ intensity maxima near the center of the (111) pole figure, and the shape of the intensity contour lines at the cross direction (Fig. 4). Such an orientation shift can be expressed as a rotation around the common (111) poles of these two ideal orientations (indicated as *A*) near the rolling direction, as shown by the arrows in Fig. 4. In the meantime, the (112) $[11\bar{1}]$ orientation, indicated by the black dots in Fig. 4, becomes stronger than that in Fig. 1. Upon rolling at a still higher temperature (e.g., 150°C), the shift in orientation extends to the (124) $[21\bar{1}]$ ideal orientation as shown by the open triangles and the *A* arrows in Fig. 6. The (112) $[11\bar{1}]$ orientation becomes even stronger than that in Fig. 4. It will be noted that the (124) $[21\bar{1}]$ and (112) $[11\bar{1}]$ orientations have a (111) pole approximately in common, which is located on the N-S axis near the center of the pole figure. When the specimen is rolled at a still higher temperature, such as 200°C, the (124) $[21\bar{1}]$ type orientation becomes the most stable; some of the (112) $[11\bar{1}]$ type components shift into the (124) $[21\bar{1}]$ type orientation by rotation around the common (111) pole *B*, as shown by the *B* arrows in Fig. 6. As a consequence, the intensity of the (124) $[21\bar{1}]$ type orientation increases at the expense of the (112) $[11\bar{1}]$ type components. (Compare Fig. 6 with Fig. 3 of the previous paper.[1])

There is another distinguishing feature among the rolling textures of high-purity silver rolled at various temperatures. The (111) pole figures determined for specimens rolled at a low temperature show considerable orientation spread along the periphery between the rolling and cross directions. Several low-intensity contour lines are continuous through those regions (see Fig. 1, and Fig. 1 of the previous paper[1]). These orientation spreads decrease as the rolling temperature increases. For specimens rolled at 150° and 200°C, a clear separation between the high-intensity maximum near the rolling direction and that at the cross direction can be noted (see Fig. 6, and Fig. 3 of the previous paper[1]).

Texture Transition as Expressed by Certain Quantitative Parameters

In order to study the texture transition quantitatively, some arbitrary parameters can always be used. However, as can be realized from the complexities of the pole figures, it is quite difficult to show the differences adequately between two textures by using a simple arbitrary parameter. Smallman,[3] in his studies of texture transition in fcc alloys, has used the ratios between the intensity maxima on the vertical center line (the N-S axis) of the (111) pole figure and that on the diameter 25 or 30° to the N-S axis to indicate the relative amounts of the *copper-type* and the *brass-type* textures. Liu and Richman[14] used the ratios of the peak height at the cross direction to the peak height at 20° from the rolling direction on the periphery of a (111) pole figure to indicate the texture transition as a function of solute concentration, and found these to be satisfactory. In the present work, we have chosen and measured a number of parameters in order to see how the texture transition will be indicated by each arbitrarily selected parameter.

Based on the analysis of the rolling textures given in the previous section, the texture transition from the common *silver type* to the *copper type* can be expressed quantitatively in terms of the decrease in the (110) $[\bar{1}12]$ orientation with increasing rolling temperature. The integrated intensity of the (220) reflection parallel to the rolling plane can be readily obtained from the peak-separation measurements. Instead of measuring the intensity of the (224) reflection in the rolling direction, the intensity of the (111) reflection in the cross direction is used. After the intensities are converted into multiples of the corresponding reflection intensities of a random powder sample, and with the values of the 0°C rolled specimen taken as unity, the change in the intensity of the (110) $[\bar{1}12]$ orientation as a function of rolling temperature is shown in Fig. 8. From this figure, we see that the change in intensities is not exactly the same for these two reflections. Thus, the change in texture, which was described in the previous section as a rotation of the (110) $[\bar{1}12]$ orientation around the (111) pole *A*, on the periphery near RD, is but a simplified analysis of the apparent results. The reduction of the (111) reflection intensity at the cross direction begins to take place at a much lower rolling temperature than does that for the (220) reflection in the rolling plane; also, the residual intensity of the (220) reflection in the rolling plane is considerably higher than that of the (111) reflection in the cross direction after the texture transition is virtually complete. Complete transition, as shown by these two parameters, corresponds to a rolling temperature of approximately 150°–160°C. However, if a 50% transition is considered, these two parameters actually indicate two different rolling temperatures (vertical lines in Fig. 8).

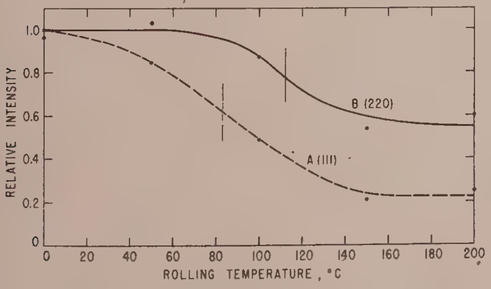

FIG. 8. Texture transition as shown by the change in the relative intensity of the (111) reflection at the cross direction (curve A) and that of the (220) reflection from the rolling plane (curve B). Vertical lines indicate temperatures corresponding to 50% transition.

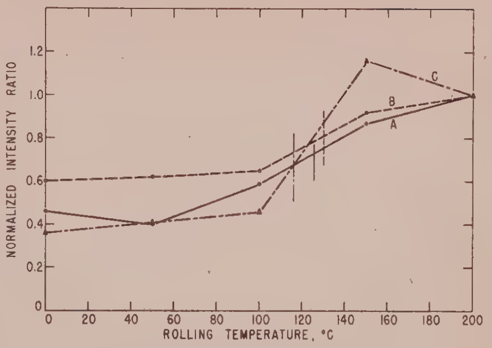

FIG. 9. Texture transition as shown by various intensity ratios. Vertical lines indicate temperature corresponding to 50% transition. Curve A: I (maxima near RD/(45° from RD and CD). Curve B: I (maxima near RP on N-S axis)/I (maxima near RP on diameter 20° with N-S axis). Curve C: I (maxima near RD)/I (CD).

In Fig. 9, three normalized intensity ratios are plotted vs the rolling temperature. All these intensities refer to the (111) reflections, and the intensity ratio determined for the specimen rolled at 200°C is taken as unity. Curve A represents the ratio of the peak intensities near the rolling direction to the intensities measured at 45° from the rolling direction (or the cross direction) on the periphery of a (111) pole figure. The intensity ratios in curve B are those measured from the intensity maxima near the rolling plane on the N-S axis to those on a diameter 20° with the N-S axis. This parameter is the same as that used by Smallman.[3] Curve C represents the ratios of the intensity maxima measured near the rolling direction to those in the cross direction. As shown in Fig. 9, these parameters do not indicate the texture transition in exactly the same manner, but a general trend is approximately followed. There is an exceptionally high point on curve C at 150°C, which is probably due to the high intensities near the rolling direction as a result of overlapping of the (112) $[11\bar{1}]$ and (124) $[21\bar{1}]$ orientations (see Fig. 6). At 50% transition, each parameter corresponds to a slightly different rolling temperature. However, essentially complete transition is indicated by all three curves to take place around 150°–160°C, which is in agreement with the other two parameters shown in Fig. 8. Among all these parameters, the change in the (111) reflection intensity at the cross direction (curve A in Fig. 8) appears to be the most sensitive in showing the texture

---

[14] Y. C. Liu and R. H. Richman, Trans. AIME **218**, 688 (1960).

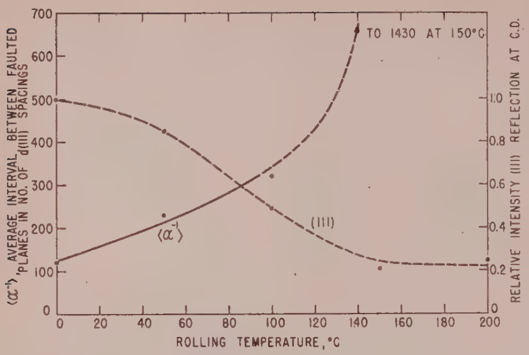

FIG. 10. Correlation of texture transition and the stacking fault frequency as a function of rolling temperature (the average reciprocal stacking fault frequency is actually plotted).

transition of this kind. For this reason, this parameter will be used in the following discussions.

Correlation of Texture Transition with Stacking Fault Frequency

In order to compare the texture transition with the stacking fault frequency, curve A of Fig. 8 is replotted in Fig. 10, where the average interval between faulted planes in number of $d_{(111)}$ spacings $\langle\alpha^{-1}\rangle$ is plotted against the rolling temperature. For the specimens rolled at 100°C and above, peak shifts were obtained from only one or two reflection pairs (see Table I). Their $\langle\alpha^{-1}\rangle$ values were therefore considered to be less certain; hence that portion of the curve is drawn as a dashed line. Figure 10 shows that there is a general correspondence between the texture transition and the reciprocal stacking fault frequency for the temperature range studied. At low rolling temperatures where the texture is of the common *silver type*, the stacking fault frequency is high (α values in Table I), or the average interval between faulted planes in number of $d_{(111)}$ spacings $\langle\alpha^{-1}\rangle$ is small. On the other hand, at high rolling temperatures, faulting occurs at greater intervals, and the texture is of the *copper type*. The change in $\langle\alpha^{-1}\rangle$ at intermediate rolling temperatures follows roughly the change in the texture transition parameter.

As mentioned previously, the values of α^{-1} are interpreted as the number of $d_{(111)}$ spacings between faulted planes. If ρ is the dislocation density, r the width of the stacking fault separated by the two partial dislocations, and $d_{(111)}$ the spacing between slip planes, then

$$\alpha^{-1}=[\rho r d_{(111)}]^{-1}. \tag{1}$$

The energy per unit area of the fault γ which is equal to the elastic repulsion per unit length between the two partial dislocations, is given by Cottrell[15] as

TABLE II. Fractional change in density δ, dislocation density ρ, and stacking fault energy γ at different rolling temperatures.

Rolling temp. (°C)	$\langle\alpha^{-1}\rangle$	δ	ρ (lines/cm²)	γ (erg/cm²)
0	120	3.46×10^{-4}	1.3×10^{12}	24
50	230	1.82×10^{-4}	6.8×10^{11}	24
100	320	0.72×10^{-4}	2.7×10^{11}	...
150	1430	0.15×10^{-4}	5.7×10^{10}	...
200	...	cannot be accurately measured		

approximately

$$\gamma=G(\mathbf{b}_2\cdot\mathbf{b}_3)/2\pi r=Ga^2/24\pi r, \tag{2}$$

where G is the shear modulus, $\mathbf{b}_2$ and $\mathbf{b}_3$ are the Burgers vectors of the [112] partial dislocations, r is the equilibrium distance between the two partials, and a is the lattice constant. Hence,[16]

$$\alpha^{-1}=24\sqrt{3}\pi/Ga^3\cdot\gamma/\rho. \tag{3}$$

The shear modulus G changes very little with temperature. The change in lattice parameter a at 0° and 200°C is less than 0.5%. If these changes within the temperature range 0°–200°C are neglected, then

$$\alpha^{-1}\simeq\text{const}(\gamma/\rho). \tag{4}$$

The dislocation density in each of the as-rolled specimens was obtained from the fractional change in density by using the technique of Clarebrough, Hargreaves, and West.[17] For the specimens rolled at 0° and 50°C, the specimens were taken out from the liquid nitrogen and were allowed to recover at room temperature for 2–3 hr before density measurements. Thus, the change in density due to vacancies should be largely reduced. From the fractional change in density $\delta=\Delta D/D$, where D is the density of a fully annealed sample, the dislocation density ρ was calculated from the equation[18] $\rho=4\sqrt{2}\delta/0.9a^2$, where a is the lattice parameter. With both α^{-1} and ρ values known, the stacking fault energy γ was approximated by using Eq. (3), taking $G=2.9\times10^{11}$ d cm^{-2}, $a=4.09\times10^{-8}$ cm, and their temperature dependence neglected. The results are summarized in Table II.

The stacking fault energy obtained for specimens rolled at 0° and 50°C is the same; i.e., ~24 erg/cm². This value is in fair agreement with the value given by Thornton and Hirsch[19] ($\gamma_{\text{Ag}}=26$–58 erg/cm²), and with that calculated from twinning shear stress by Suzuk and Barrett[20] ($\gamma_{\text{Ag}}=21$ erg/cm²). The γ values obtained from specimens rolled at 100° and 150°C are not listed. These specimens, as mentioned previously, were partially recrystallized after rolling; further recrystallization was found to take place after long-time exposure at room temperature. Thus, their dislocation densities as determined later during this work were likely too low, and the stacking fault energies obtained from the above calculations will be meaningless.

---

[15] A. H. Cottrell, *Dislocations and Plastic Flow in Crystals* (Clarendon Press, Oxford, England, 1956), p. 74.

[16] R. E. Smallman and H. H. Westmacott [R. E. Smallman an H. H. Westmacott, Phil Mag. 2, 669 (1957)] have given a simila equation, $\alpha=Ga^3\rho/24\sqrt{2}\pi\gamma$, in which $\sqrt{2}$ was probably misprinted

[17] L. M. Clarebrough, M. E. Hargreaves, and G. W. West Phil. Mag. 1, 528 (1956).

[18] W. Boas in *Dislocations and Mechanical Properties of Crystal* (John Wiley & Sons, Inc., New York, 1956), p. 333.

[19] P. R. Thornton and P. B. Hirsch, Phil. Mag. 3, 738 (1958) M. J. Whelan and P. B. Hirsch, *ibid.* 2, 1121 (1957).

[20] H. Suzuki and C. S. Barrett, Acta Met. 6, 156 (1958).

The above results indicate that the stacking fault energy of high-purity silver, as calculated from Eq. (3), is independent of temperature. This appears to be certain at least within the temperature range of 0°–50°C. Swann and Nutting[21] have recently reported that the stacking fault energy in a Cu-Al (15 at.% Al) alloy increases rapidly with temperature in the range 360°–400°C. This can be explained, however, as due to a reduction of the solute segregation in the stacking faults at higher temperatures.

From a rolling temperature of 0°–50°C, there is some change in texture as shown by the most sensitive parameter [the change in the (111) reflection intensity at CD; see Fig. 8 or Fig. 10], but the amount of change is too small to be considered as significant. Since a complete texture transition takes place at 150°–200°C, where the stacking fault energies cannot be obtained accurately due to experimental difficulties, the present results cannot lead to a definite conclusion that the stacking fault energy contributes significantly to texture transition. However, on the basis of the relationship shown in Eq. (4), and the correlation of α (or α^{-1}) with the texture transition, the change in texture produced by either varying the temperature of deformation or the addition of alloying elements can be qualitatively but consistently explained in terms of the change in either stacking fault energy or in density of dislocations. When the stacking fault energy is constant, an increase in the density of dislocations will decrease the value of α^{-1}, and a *silver-type* texture will be obtained. As shown by the results of the present investigation and by others,[16] the density of dislocations can be raised considerably by lowering the temperature of deformation. The results of Müller[2] that a *brass-type* (or *silver-type*) texture was obtained in copper after rolling at a very low temperature (−183°C) can probably be explained on this basis. It has been known that the stacking fault energy can be lowered by solute additions. The dislocation density of powder specimens was reported to be higher in alloys than in pure metals,[16] and it is reasonable to believe that the same is true in deformed bulk specimens. Thus, by making alloy additions to a pure metal, the stacking fault energy will be reduced and the dislocation density will be increased. Both of these changes will reduce the value of α^{-1}; hence a *silver type* texture will be strongly favored.

SUMMARY AND CONCLUSION

(1) The rolling texture transition from the common *silver type* to the *copper type* in high-purity silver takes place gradually as the rolling temperature is increased. Complete transition occurs within the temperature range of 150°–200°C.

(2) There is a general correlation between the temperature dependence of the rolling texture transition and of stacking fault frequency. The common *silver-type* texture is associated with high stacking fault frequencies or small α^{-1} values, whereas the *copper-type* texture is associated with low stacking fault frequencies or large α^{-1} values.

(3) The calculated stacking-fault frequency can be expressed as a function of stacking fault energy and dislocation density. The stacking fault energy of high-purity silver so calculated is about 24 erg/cm^2, which is in reasonable agreement with those given in the literature.

(4) Based on the correlation between texture transition and the stacking fault frequency, the change in texture as produced by varying the deformation temperature or by the addition of alloying elements can be interpreted consistently by either a change in stacking fault energy, or a change in dislocation density, or both.

ACKNOWLEDGMENT

The authors wish to thank Professor P. A. Beck for his advice and helpful discussions, and Dr. C. S. Barrett for his interest and comment. Some helpful discussions from Dr. J. C. M. Li on part of this work are sincerely acknowledged. The high-purity silver was zone melted by E. W. Troy, the analysis for oxygen was done by J. F. Martin, and the spectrographic analysis was done by J. K. Hurwitz. Their assistance is sincerely appreciated.

---

[21] P. R. Swann and J. Nutting, J. Inst. Metals (to be published).

JOURNAL OF APPLIED PHYSICS VOLUME 32, NUMBER 7 JULY, 1961

Letters to the Editor

Guidance and Collimation of Sputtered Tungsten Particles

CARL A. LUDEKE
Graduate School of Arts and Sciences, University of Cincinnati, and Large Jet Engine Department, General Electric Company, Cincinnati, Ohio

(Received January 30, 1961)

IT is the purpose of this paper to report on the results of some experiments designed to determine the feasibility of sputtering tungsten into very tiny holes in stainless steel. The problem is one of guiding or collimating the tungsten particles onto the sides of the hole.

The sputtering phenomenon at the cathode of a glow discharge was discovered by Grove in 1852. Since then, all theories developed to explain the mechanism of sputtering have depended upon the energy of a sufficient number of gas ions. The pressure of the glow discharge may range from 1 down to 0.01 mm; below this value the gas ions are too few in number for successful sputtering.

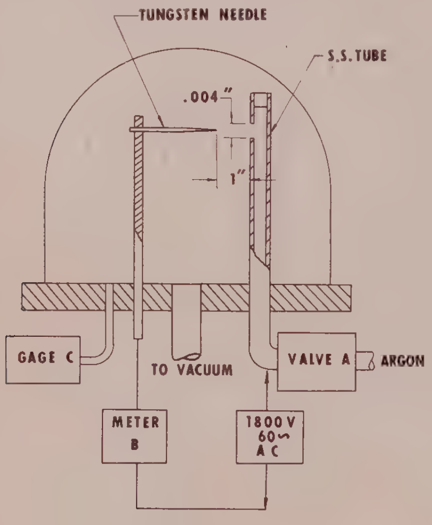

FIG. 1. Diagram of the apparatus.

Since the relatively high pressure of 10^{-2} mm is needed for successful sputtering, it seems feasible to start with a system evacuated to a pressure of 10^{-5} mm and then introduce a tiny stream of argon from a hole in the anode. Although the pressure of the system as a whole might then rise to 10^{-4} mm, this would still be too low for over-all sputtering. However, the local pressure within the stream of argon might well be of the order of 10^{-2} mm or more, and hence sufficient for sputtering.

Once introduced into the system, the argon ions will rapidly diffuse in all directions but can be collimated by a highly directional electric field. This type of field can be obtained by using a sharply pointed tungsten needle as the cathode and the sharp edges of the hole as the anode. Thus the glow discharge is directed primarily by the electric field, and the tungsten needle is not required to be directly in front of the hole in the anode.

In order to test these concepts, the apparatus shown in Fig. 1 was constructed. It consisted of a $\frac{1}{4}$-in. diam stainless steel tube closed at the top end but having a 0.004-in. diam hole in its side, and a tungsten needle having a tip diameter of 0.0004 in. In the first experiment the tip of the needle was located 1 in. away and directly in front of the 0.004-in. hole. The needle and the tube were mounted under a bell jar and the pressure was reduced to 1.5×10^{-5} mm. A potential difference of 1800 v, 60 cycle ac was maintained between the needle and the tube. Argon at 15.7 psi absolute was then introduced into the tube by opening valve A, whereupon argon escaped from the 0.004-in. hole, a current registered on meter B, and a slight increase in pressure registered on gauge C. Soon, however, the current ceased and the pressure reading on gauge C returned to its original value. Upon opening the system, the 0.004-in. hole was found to be completely sealed. This seal could be accomplished in about 10 sec and did not leak when tested with compressed air at 150 psi.

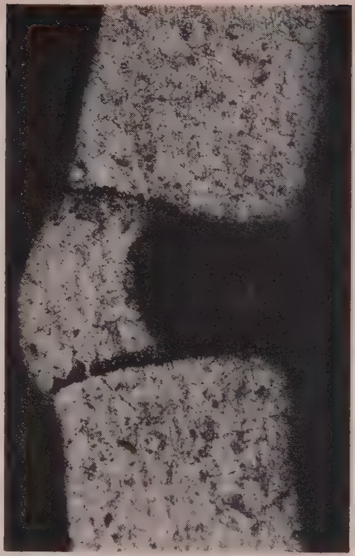

FIG. 2. A section (enlarged 200 ×) through the axis of the hole and perpendicular to the axis of the tube.

The above experiment was repeated with the tube rotated through 90° so that the axis of the 0.004-in. hole was at 90° to the axis of the needle. The results were the same.

In order to see how well the sputtered particles were collimated, the tube was sectioned through the 0.004-in. hole. The resulting circular section was then photographed. Figure 2 shows a 200 ×

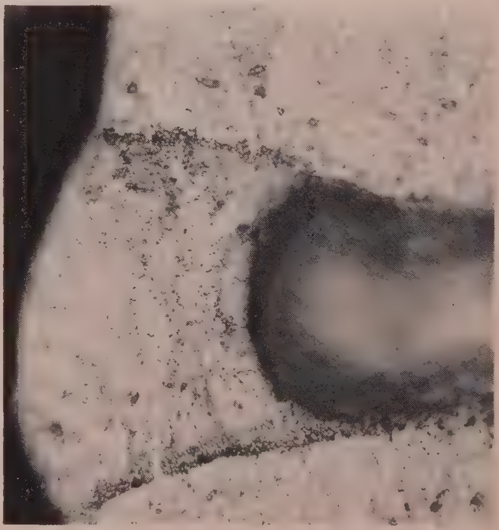

FIG. 3. The section of Fig. 2 enlarged 400 ×.

enlargement of the portion containing the hole. We note first that there seems to be no deposit of material except in the hole. Secondly, we note that the deposited material is approximately 0.003 in. thick. Thus, in approximately 10 sec, a cylinder of tungsten 0.004 in. in diameter and 0.003 in. long was deposited in the hole from which the argon emerged. Figure 3 is a 400 × enlargement and clearly shows the diffusion zone between the tungsten and the stainless steel tubing.

It has been experimentally shown that sputtered particles can be directed to a small opening in the anode.

It was observed that a glow discharge existed between the needlelike cathode and the hole in the anode while the sputtering was in progress. Since the stream of ions was not necessarily directed toward the cathode, the gas ions are directed by the field.

After the gas ions strike the cathode and the tungsten particles are emitted, they too must be directed by the field because they strike the anode only at the hole. Thus the sputtered particles follow the path of the glow discharge and the particles can be directed by directing the glow discharge.

Multiple Shock Wave Structures in Polycrystalline Ferroelectrics*

C. E. Reynolds and G. E. Seay
Los Alamos Scientific Laboratory, University of California, Los Alamos, New Mexico

(Received February 13, 1961)

NEILSON and co-workers[1] have made electrical measurements with piezoelectric shock detectors which indicated the presence under explosive loading of two-wave shock structures in three ferroelectric ceramics: (1) $Pb(Zr_{0.52}, Ti_{0.48})O_3$ with a 1 wt.% addition of Nb_2O_5, (2) pure $BaTiO_3$, and (3) 95% $BaTiO_3$ and 5% $CaTiO_3$. The authors have confirmed the existence of these shock structures optically with a streak camera, and measured free-surface and shock velocities of the waves by use of both optical and electrical techniques.

An explosive-driven, impedance-mismatch attenuator system,[2] sketched in Fig. 1, was used to transmit a planar shock into a $\frac{1}{2}$ in. thick by 2-in. diam ceramic specimen. The strength of the shock was varied by changing the nonexplosive material X. The ferroelectric ceramic was oriented in such a way that the shocks traveled in the direction of negative polarization. In order to provide a short circuit for the electrical charge released, each ceramic piece was covered with a conducting material. One flat surface and the cylindrical surface were painted with Dupont 4929 silver paint; the other flat surface was polished and coated with evaporated silver to complete the short circuit and at the same time provide a reflecting surface for free-surface velocity measurements by the knife-edge technique.[3] In this technique the image of a knife-edge reflected from a polished surface is observed as it moved due to the shock-induced motion of the surface. Shock velocities were determined using transit times measured with (a) shock-detecting ferroelectric wafers by which arrival of shock fronts were recorded as voltage pulses on an oscilloscope with a calibrated sweep speed, and (b) a streak camera observing the emergence of a shock front from the inclined surface of a ceramic wedge.[4]

Figure 1 also shows a streak camera record of the free-surface motion typical of any one of the ceramics. It is clear that a two-wave structure exists. The "interaction zone" is believed to be the result of successive reflections of disturbances between the moving surface and the second shock before arrival of the latter at the surface. The velocity of the surface resulting from the first shock is time dependent. The pressure behind the first shock may be calculated using the expression $P_s = \frac{1}{2}\rho_0 U_s u_{fs}$ where, ρ_0, U_s, and u_{fs} are, respectively, the initial density, the shock velocity, and the initial free-surface velocity. The free-surface velocity resulting from the second shock remains constant.

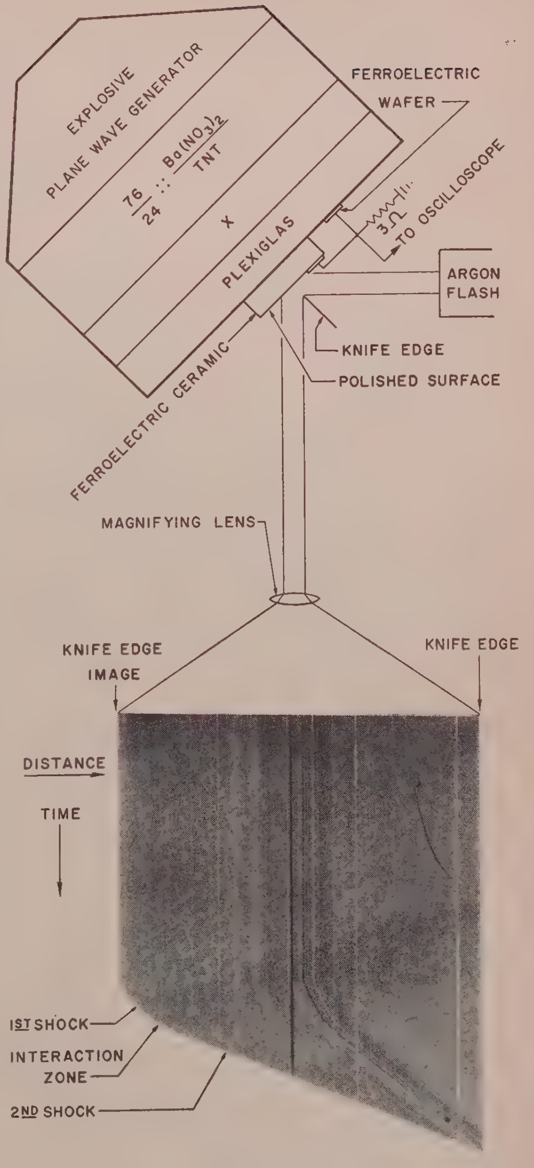

Fig. 1. Schematic of (a) the explosive-attenuator system used to generate shocks in ferroelectric ceramics, (b) the optical arrangement for measurement of free-surface velocity and a typical streak camera record, and (c) the location of ferroelectric wafers used to obtain shock velocity.

For the Pb(Zr, Ti)O_3 ceramic it was found that while the velocity of the first shock was independent of the pressure of the second shock, the initial free-surface velocity varied slightly. The time separation of the two shocks decreased as the strength of the shock was increased. The approximate pressure and velocity of the first shock were 19 kbar and 4.1 mm/μsec, respectively. The pressure above which a single shock wave exists was found to be approximately 250 kbar. At a second-wave pressure of about 80 kbar the pure $BaTiO_3$ ceramic and the $BaTiO_3$ ceramic with the $CaTiO_3$ additive exhibited first-wave pressures and velocities of 24 kbar and 5.8 mm/μsec, and 28 kbar and 6.1 mm/μsec, respectively.

The authors would like to express appreciation to various persons at the Sandia Corporation for many helpful discussions, and to D. L. Wilson for valuable assistance in the execution of the experiments.

---

* This work was performed under the auspices of the U. S. Atomic Energy Commission.

[1] F. W. Neilson, W. B. Benedick, and R. A. Graham (private communication).

[2] J. M. Walsh, M. H. Rice, R. G. McQueen, and F. L. Yarger, Phys. Rev. **108**, 196 (1957).

[3] B. G. Craig and W. C. Davis (to be published).

[4] T. E. Holland, A. W. Campbell, and M. E. Malin, J. Appl. Phys. **28**, 1217 (1957).

New, Thermally Variable Bead Resistor

Victor J. Tennery and Russell G. West
Motorola Research Laboratory, Scottsdale, Arizona

(Received January 20, 1961)

The electrical and thermal properties of temperature-sensitive semiconducting bead resistors or thermistors possessing negative temperature coefficients of resistance (NTC) are well categorized in the literature. These thermistors often are composed of manganese, cobalt, and nickel oxides which upon sintering form solid solutions of nickel and cobalt manganite. The resistance of these units decreases with temperature because of the presence of a thermal activation of charge carriers into the conduction band of the oxide comprising the bead.

It has been demonstrated[1] that when ferroelectric $BaTiO_3$ is doped with the proper ions, such as La^{3+}, Sm^{3+}, Gd^{3+}, Ho^{3+}, and Nb^{5+}, the titanate becomes a semiconductor with a room temperature resistivity varying between 20 and several thousand ohm-cm, depending upon the impurity ion used, the impurity concentration, and certain processing variables. The semiconducting titanate exhibits an anomalous increase in the resistivity and a positive temperature coefficient of resistivity (PTC) when it is heated through the tetragonal-cubic transition temperature. This behavior is demonstrated in Fig. 1. The tetragonal-cubic transition can be moved to higher or lower temperatures by partially substituting Pb^{++} or Sr^{++}, respectively, for Ba^{++}.

Bead thermistors have been fabricated of this semiconducting oxide and found to possess unique voltage-current characteristics. The beads were formed by placing a small quantity of slurry consisting of water and doped titanate powder onto two 0.010-in. diam parallel platinum wires. After drying, the beads were sintered in air at 1375°C; specimens of ~0.075 in. in diameter were obtained. The voltage-current characteristic for the composition $Ba_{0.850}Sr_{0.147}La_{0.006}TiO_3$ is shown in Fig. 2 for still air conditions.

The unique overlapping characteristic results from the thermistor operating in the positive temperature coefficient region (PTC) of resistivity at low applied power but operating in the negative temperature coefficient region (NTC) of resistivity at higher dissipated power. This device may therefore be denoted as a (PN)TC thermistor. At least three properties of this thermistor are unique in that they are not found in commercially available NTC thermistors.

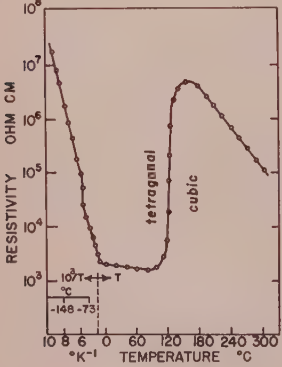

FIG. 1. Variation of resistivity with temperature for a typical doped barium titanate composition.

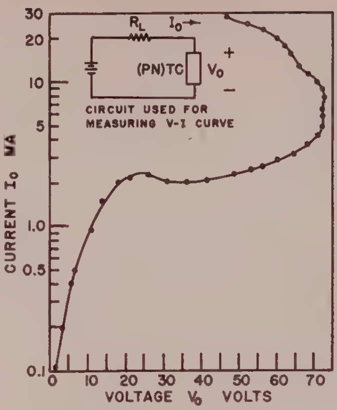

FIG. 2. Voltage-current characteristic of a 0.075-in. diam (PN)TC bead thermisotor.

In the PTC region of operation the doped barium titanate thermistor is voltage stable. A duality exists between NTC and PTC thermistors in that $V=f(I)$ in the NTC case, while $I=f(V)$ for a PTC thermistor.

The very rapid increase of resistivity as a function of temperature at the tetragonal-cubic transition gives rise to a large energy work function which manifests itself as a large negative ac resistance in the PTC region (~−20 000 ohm in Fig. 2). A value of ac negative resistance typical of NTC thermistors is observed in the high-power region (~−1400 ohm in Fig. 2).

Enough energy must be dissipated in the doped $BaTiO_3$ thermistor to increase its temperature to about 180°C before the commencement of operation in the NTC region. The resistivity at this temperature is typically 10^6 ohm-cm. This high resistivity at elevated temperatures gives rise to a large power handling capacity in a bead of small mass. For example, when biased to 200 ohm in still air, one experimental unit dissipated 1.5 w of power.

---

[1] H. A. Sauer and S. S. Flaschen, Ceram. Ind. **66**, 95 (1956); G. G. Harmon, Phys. Rev. **106**, 1358 (1957); O. Saburi, J. Phys. Soc. Japan **14**, 1159 (1959); V. J. Tennery, Ph.D. dissertation, University of Illinois, Urbana, Illinois (June, 1959) [J. Am. Ceram. Soc. (to be published)].

Field-Enhanced Donor Diffusion in Degenerate Semiconductor Layers*

W. Shockley
Shockley Transistor, Unit of Clevite Transistor, Stanford Industrial Park, Palo Alto, California

(Received March 20, 1961)

It has been shown that in a nondegenerate extrinsic semiconductor, the apparent diffusion constant of donors or acceptors will be enhanced, owing to the electric field that exists in order to distribute the current carriers so that they neutralize the donors or acceptors. The effective diffusion constant[1] when only donors at density N_d and carriers are present is D^*.

$$D^*/D=1+[N_d/(4n_i^2+N_d^2)^{\frac{1}{2}}], \tag{1}$$

where the diffusion current is

$$F=-D^*\nabla N_d. \tag{2}$$

D is the diffusion constant in zero electric field and n_i is the intrinsic electron or hole concentration.

It is the purpose of this communication to point out that if the material is degenerate with $N_d>N_c$, where N_c is the effective concentration of states in the conduction band, then

$$D^*/D=1+(\pi/6)^{\frac{1}{3}}(N_d/N_c)^{\frac{2}{3}}. \tag{3}$$

This result is readily obtained by noting that the Fermi level E_F

lies above the conduction band by[2]

$$E_F - E_c = kT(N_d/N_c)^{\frac{2}{3}}(9\pi/16)^{\frac{1}{3}}, \tag{4}$$

and the donor flux is given by

$$F = -D\nabla N_d + (qD/kT)N_d\nabla(E_c/q), \tag{5}$$

where the donor mobility is qD/kT and the electrostatic potential varies as $-E_c/q$.

Equation (3) does not limit the enhancement of the D^* to $2D$ as does Eq. (1).

---

* Research supported by the U. S. Air Force Cambridge Research Laboratories.

[1] The limiting form $D^* = 2D$ for $N_d > n_i$ was published by J. Bardeen, W. H. Brattain, and W. Shockley, J. Chem. Phys. **14**, 714 (1946). Equation (1) was published by F. M. Smits, Proc. I.R.E. **46**, 1049 (1958).

[2] See W. Shockley, *Electrons and Holes in Semiconductors* (D. Van Nostrand, Company, Inc., Princeton, New Jersey, 1950), p. 242.

Deformation-Produced Point Defects*

HOWARD K. BIRNBAUM
University of Chicago, Chicago, Illinois
AND
FLOYD R. TULER
University of Illinois, Urbana, Illinois

(Received March 14, 1961)

CONSIDERABLE experimental information is available which indicates that point defects are generated during plastic deformation of fcc metals. However, little is known about the nature of these defects (whether they are of the vacancy or interstitial type) or about their motion energy. The present communication describes preliminary results of an investigation of the interaction of deformation-produced point defects with dislocations in high-purity copper (99.999% Cu). Analysis of the kinetics of this interaction leads to an evaluation of the activation energy for diffusion of the point defects and to the conclusion that an appreciable concentration of interstitials are produced by plastic deformation.

The experimental procedure was to strain the fine-grained polycrystalline specimens in tension at 77°K to a prestrain ϵ_p, age the specimens at a temperature T_a for a time t_a and then continue the tensile deformation at 77°K. (The stress was reduced to 90% of the flow stress during aging to prevent plastic flow and creep when the temperature was raised. This amount of unloading did not result in the small yield effect which is caused by a more complete removal of the applied stress.[1]) A yield point was observed upon continuing deformation after aging,[2] as shown in Fig. 1, which also illustrates the test procedure and defines the magnitude of the yield point $\Delta\sigma$.

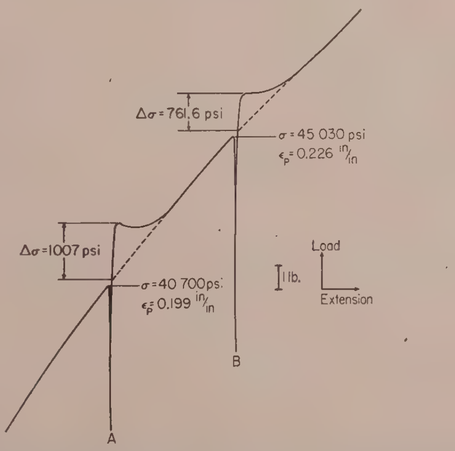

FIG. 1. Load-extension curve showing the yield point obtained on aging after low-temperature deformation. Temperature of prestrain, 77°K; temperature of test after aging, 77°K. At points A and B the specimen was aged at 200°K for 20 min.

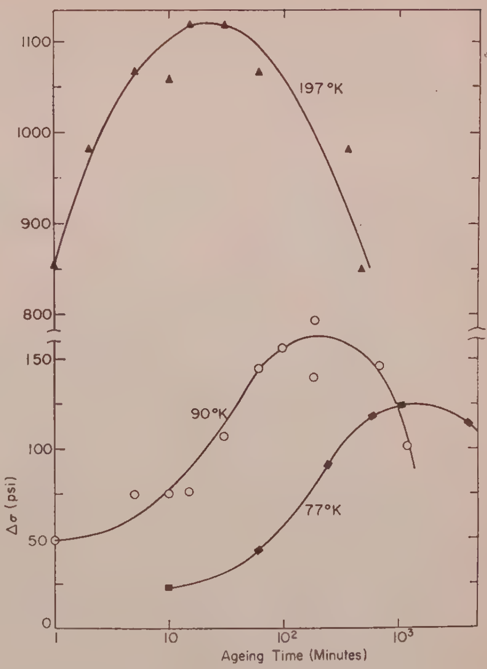

FIG. 2. Typical isothermal aging curves showing the variation of $\Delta\sigma$ with aging time and temperature. Specimens prestrained 0.25 in./in. at 77°K. Temperature of test after aging, 77°K.

$\Delta\sigma$ was observed to depend on T_a and t_a in the manner shown in Fig. 2 for several aging temperatures in the range 77°–273°K. After a constant prestrain of $\epsilon_p = 0.25$, the magnitude of the yield initially increased to a maximum and then decreased as the aging time was increased. The value of t_a at the maximum ($t_a^{\max}$) was observed to decrease and the value of $\Delta\sigma$ at the maximum ($\Delta\sigma^{\max}$) to increase as the aging temperature was increased. For constant aging treatment, the value of $\Delta\sigma$ increased linearly with the amount of prestrain up to a value of $\epsilon_p \approx 0.30$. These results indicate that the yield point resulted from diffusion of deformation-produced point defects to dislocations during the aging treatment since dislocation pinning due to impurities would not exhibit the decrease in $\Delta\sigma$ at long aging times nor the linear dependence on prestrain. The point defect nature of the pinning points was confirmed by the observation that, subsequent to the yield point, the flow curve was identical to that obtained in the absence of aging; i.e., upon continuous deformation, and by the observation that $\Delta\sigma$ (after a constant aging treatment) was strongly temperature dependent. $\Delta\sigma$ varied as T_t^{-3} (T_t is the testing temperature after aging) in very good agreement with the calculations of Haasen,[3] which were based on the expected $1/r$ distance dependence of the elastic interaction between the interstitials and the dislocation. The decrease in $\Delta\sigma$ for $t_a > t_a^{\max}$ indicates that the pinning point density decreased on prolonged aging. This was confirmed by the data shown in Fig. 1. After $\epsilon_p = 0.199$ in./in. and aging at 200°K for 20 min, $\Delta\sigma$ was 1007 psi. Upon a further strain of 0.027 in./in., the aging treatment was repeated and resulted in $\Delta\sigma = 761.6$ psi, thus indicating that the number of available pinning points decreased during the first aging treatment.

Good agreement is obtained between the experimental data and calculations based on a simple model of the aging process[4] if $\Delta\sigma$ is assumed proportional to the concentration of point defect pinning points along the dislocations. Two processes have been considered: (1) an increase in the concentration of pinning points at the dislocations as a result of diffusion of point defects to the dislocations, and (2) a decrease in pinning point concentration as a result of diffusion of point defects along the dislocations to sinks which are taken to be existing jogs in the dislocations.[5] Using this model, the number of defects per atom distance along the dislocation (N_d) for $t_a \ll t_a^{\max}$ is calculated to be

$$N_d = \text{const}\,(Dt_a/T_a)^{\frac{2}{3}},$$

where D is the diffusion coefficient of the point defects. The data for $t_a \ll t_a^{\max}$ exhibits the $t_a^{\frac{2}{3}}$ dependence, and from the temperature dependence of dN_d/dt_a the activation energy for volume diffusion of the defects is calculated to be 0.10 ev. The expression for $t_a^{\max}$ which results from the theory[4, 5] is

$$t_a^{\max} = \text{const}\,(l_j^2/D'),$$

where D' is the diffusion coefficient of the point defects along the dislocation and l_j is the distance between sinks. The experimental values for $t_a^{\max}$ exhibit the expected temperature dependence from which an activation energy of 0.06 ev for diffusion along the dislocations is calculated. $\Delta\sigma^{\max}$ is given by an expression of the form[5]

$$\Delta\sigma^{\max} = \text{const}\,(D/T_a)^{\frac{2}{3}}(t_a^{\max})^{\frac{2}{3}},$$

which is in good agreement with the experimental values. Using the experimental values of $\Delta\sigma^{\max}$ and $t_a^{\max}$, the point defect volume diffusion activation energy is calculated to be 0.14 ev, in good agreement with the result obtained from the values of $\Delta\sigma$ at $t_a \ll t_a^{\max}$.

Comparison of the activation energy for volume diffusion of the mobile defect in these experiments with the calculated and experimental values previously reported[6] indicates that the defect causing the strain aging is the interstitial. The activation energy of 0.10–0.14 ev agrees very well with the value associated with interstitial migration during the 30°K annealing step after radiation damage of copper, and is considerably lower than that expected for either vacancy or divacancy migration in copper. In addition to the interstitials, it is expected that appreciable vacancy concentrations will be produced by deformation. Interaction between the dislocations and vacancies may lead to yield effects similar to those observed for the interstitial–dislocation interactions. However, because of the larger energy of motion of vacancies and divacancies this effect is expected to be observable only at considerably longer aging times. Some evidence for this vacancy–dislocation interaction has been obtained and will be reported in a subsequant publication.

---

[*] This work was partially supported by the U. S. Atomic Energy Commission.

[1] A. R. C. Westwood and T. Broom, Acta Met. 5, 77 (1957).

[2] A similar yield effect during low-temperature strain aging of aluminum has been previously reported by Westwood and Broom.[1]

[3] P. Haasen, *Internal Stresses and Fatigue in Metals* (Elsevier Publishing Company, Inc., New York, 1959), p. 205.

[4] H. K. Birnbaum and F. R. Tuler (to be published).

[5] A treatment based on a similar model has been given by P. Coulomb and J. Friedel [*Dislocations and Mechanical Properties of Crystals* (John Wiley & Sons, Inc., New York, 1957), p. 555]. This analysis is in agreement with ours for short aging times and deviates from the experimental data for $t_a \ll t_a^{\max}$.

[6] J. S. Koehler, J. W. Henderson, and J. H. Bredt in *Dislocations and Mechanical Properties of Crystals* (John Wiley & Sons, Inc., New York, 1957), p. 587.

Nuclear Magnetic Resonance in Flowing Fluids

Louis R. Hirschel and Louis F. Libelo
U. S. Naval Ordnance Laboratory, White Oak, Silver Spring, Maryland

(Received February 17, 1961)

EXPERIMENT shows that the steady state nuclear magnetic resonance signal for a flowing fluid varies from that when the sample is stationary. The effect may be simply explained by noting that when the liquid is flowing, saturated portions of the sample are being replaced by unsaturated portions. The result is a larger signal. In general, the signal is a complicated function of the time spent by the sample in the static magnetic field, the time spent in the rf field, the velocity of fluid flow, and the degree of saturation. The signal response when exhibited as a function of velocity may exhibit an initial linear rise and a subsequent hyperbolic falloff as the velocity is increased from zero. An analysis is made employing the Bloembergen equations.

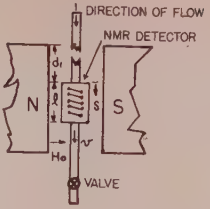

FIG. 1. Path of flowing fluid in static and rf fields.

Referring to Fig. 1, the results of Bloembergen[1] are used to obtain the rate of change of excess spins in the lower energy state, so that for a small volume element of fluid in the static magnetic field,

$$dn/dt = [(n_0 - n)/T_1], \quad 0 \le t \le d_1/v, \tag{1}$$

where n_0 is the excess spins at equilibrium, T_1 is the spin-lattice relaxation time, and v is the velocity of the fluid. In the region where the static magnetic field and the radiation field both exist, we may write

$$dn/dt = [(n_0 - n)/T_1] - 2nP, \quad d_1/v \le t \le l/v, \tag{2}$$

where P is the probability per unit time of a transition by the nucleus under the influence of the rf field.

The solution corresponding to Eq. (1) at the entrance of the sample into the rf region is

$$n_H = n_0 - (n_0 - n_E)\exp[-(d_1/vT_1)], \tag{3}$$

where n_E is the initial excess in the earth's magnetic field and d_1/v is the time spent by the sample in the static magnetic field. In the region where the rf field is present, the solution corresponding to Eq. (2) is

$$n\lambda = n_0 - (n_0 - n_H\lambda)\exp[-(\lambda t/T_1)], \tag{4}$$

where λ replaces the quantity $1+2PT_1$. Substituting from Eq. (3) for n_H into Eq. (4) and neglecting n_E, we may write

$$\frac{n}{n_0}\lambda = 1 - \left\{1 - \lambda\left[1 - \exp\left(-\frac{d_1}{vT_1}\right)\right]\right\}\exp\left(-\frac{\lambda s}{vT_1}\right), \tag{5}$$

where the variable t has been changed to s/v.

Equation (5) is valid for an elementary volume of fluid. In practice, because of the finite length l of the rf unit ($l < d_1$), Eq. (5) must be integrated over the length l so that

$$\frac{n}{n_0}\lambda = 1 + \frac{T_1 v}{l}\left[\left(\frac{1}{\lambda} - 1\right) + \exp\left(-\frac{d_1}{vT_1}\right)\right]\left[\exp\left(-\frac{\lambda l}{vT_1}\right) - 1\right]. \tag{6}$$

Equation (6) adequately explains the observed phenomena over the entire range of velocities. For the simple case in which $v=0$, we see immediately that

$$n/n_0 = 1/\lambda. \tag{7}$$

When v is very large relative to d_1/T_1, and $\lambda l/T_1$, the signal falls off with velocity such that

$$n/n_0 = d_1/vT_1. \tag{8}$$

In general, Eq. (6) possesses a maximum. Of particular interest is the value of the signal response when the velocity is small with respect to d_1/T_1 and l/T_1. Equation (5) then reduces to

$$n/n_0 = (1/\lambda) + (1/\lambda)(T_1 v/l)[1 - (1/\lambda)], \tag{9}$$

which may be put into the form

$$(R - R_0)/R_0 = (T_1 v/l)(1 - R_0). \tag{10}$$

When in addition $1/\lambda \ll 1$, we may write

$$(R - R_0)/R_0 = T_1 v/l. \tag{11}$$

Equation (11) is a particularly simple relation which yields information concerning T_1 or velocity. Equation (11) is in agreement with the results obtained by Suryan[2] in the limited range of velocities reported on. Equation (6) is valid for the entire range of velocities.

---

[1] N. Bloembergen, E. M. Purcell, and R. V. Pound, Phys. Rev. **73**, 679 (1948).
[2] G. Suryan, Proc. Indian Acad. Sci. **A33**, 107 (1951).

Useful Technique for Growing Large, Single-Crystal YIG*

Don Barry and Roy W. Roberts
Melabs, Palo Alto, California
(Received January 27, 1961)

THE following technique has proven useful in growing large, single crystals of YIG from a 100-ml platinum crucible. The method used is one introduced by Nielsen.[1] The technique used consists of melting the powdered charge at 1250°C, cooling rapidly to room temperature, and then recharging the crucible with more of the powdered mixture and again heating to soak temperature. By recharging the curcible several times a larger mass is built up in the crucible, making the effective melt volume larger, and thus enhancing growth of larger crystals.

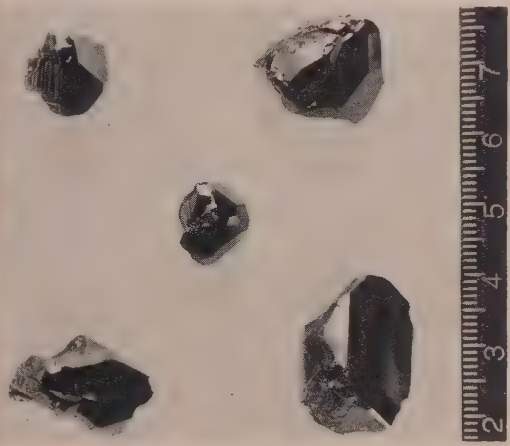

Fig. 1. Single-crystal YIG obtained with the technique, measurement in cm.

Results obtained using this technique are pictured in Fig. 1. The total mass introduced was 387 g, which was cooled at 2°C/hr from 1250°C. The total yield of crystals weighed 53.7 g and the largest single crystal weighed 9.2 g.

It is believed that the technique described here will be useful for those laboratories with limited facilities to grow large single-crystal YIG.

---

* This research was supported by the U. S. Signal Corps, Fort Monmouth, New Jersey, under contract.
[1] J. W. Nielsen, J. Appl. Phys. **31**, 51S (1960).

Elastic Constants of TiC and TiB_2

J. J. Gilman* and B. W. Roberts
General Electric Research Laboratory, Schenectady, New York
(Received February 23, 1961)

MONOCRYSTALS of two compounds that are second only to diamond in their extreme hardness have recently become available: titanium carbide and titanium diboride. They are grown by means of an arc-fusion process by the Linde Company, the source of the specimens used in this work. It was of interest to measure their elastic constants in order to compare them with those of diamond and other hard compounds, to learn how much anisotropy these compounds possess, and to see whether their elastic properties correlate with their high hardness.

Table I. Microhardness and elastic constants.

Microhardness (kg/mm²)	Diamond[a] 9000	TiC 3200	TiB_2 3400	Al_2O_3[b] 2000
C_{11} (10^{12} d/cm²)	10.8	5.00	6.9	4.65
C_{33}	...	...	4.4	5.63
C_{44}	5.8	1.75	2.5	2.33
C_{12}	1.3	1.13	4.1	1.24
C_{13}	...	...	3.2	1.17
C_{14}	...	...	...	1.01

[a] H. J. McSkimin and W. L. Bond, Phys. Rev. **105**, 116 (1957).
[b] J. Bhimasenachar, Proc. Natl. Inst. Sci. India **16**, 241 (1950).

Crystals of TiC were received in the form of $\frac{1}{2}$-in. diam cylinders about 1 in. long. This crystal has the cubic rocksalt structure,[1] so specimens with parallel faces perpendicular to [100] and [111] directions were prepared. This was done by means of x-ray orientation, diamond sawing, and diamond polishing. The ease with which these crystals cleave along {100} planes caused difficulty, but satisfactory specimens were obtained. The elastic constants were measured by the pulse-echo method; that is, by measuring the velocities of transverse and longitudinal sound waves in the ⟨100⟩ and ⟨111⟩ directions. Standard equations[2] were used to calculate the elastic constants from the sound velocities. The density was assumed to be the theoretical one[1]; measurements by the Linde Company confirm this assumption.

One crystal of TiB_2 was received in the form of a $\frac{1}{4}$-in. diam cylinder about $\frac{5}{8}$ in. long. This crystal has a hexagonal structure in which the small boron atoms are located in all of the interstices between layers of titanium atoms that are arranged on a simple hexagonal lattice. In this case parallel faces were ground perpendicular to the c and a axes of the lattice. Fortunately, this was possible because the specimen's rod axis was parallel to the a axis of the crystal lattice. Again transverse and longitudinal sound velocities were measured, and the theoretical density was assumed in calculating the elastic constants. Four of the five constants were measured: C_{11}, C_{44}, C_{33}, and C_{12}. The value for C_{13} was only estimated because the crystal was neither large enough, nor of sufficient perfection, to allow a significant measurement to be made.

Table I lists the results of the measurements together with values for diamond and sapphire. It may be seen that both TiC and TiB_2 have very high elastic constants consistent with their high hardnesses. TiB_2 approaches diamond in its resistance to dilational strains, but has considerably less resistance to shearing strains. This reflects its metallic binding compared with the covalent binding of diamond.

TiC is nearly elastically isotropic. Not only is the Cauchy relation, $C_{12}=C_{44}$, approximately obeyed, but Zener's anisotropy parameter, $2C_{44}/(C_{11}-C_{12})=0.91$, is nearly equal to unity.

An estimate[3] of the surface energies for TiC yields a minimum value for the {100} planes consistent with the observed cubic cleavage. The magnitude of the {100} surface energy is estimated to be 2500 erg/cm².

---

* Present address: Division of Engineering, Brown University, Providence, Rhode Island.
[1] R. Kieffer and P. Schwarzkopf, *Hartstoffe und Hartmetalle* (Springer-Verlag, Vienna, 1953).
[2] W. P. Mason, *Physical Acoustics and the Properties of Solids* (D. Van Nostrand Company, Inc., Princeton, New Jersey, 1958), p. 370.
[3] J. J. Gilman in *Fracture*, edited by Averbach, Felbeck, Hahn, and Thomas (John Wiley & Sons, Inc., New York, 1959), p. 204.

Erratum: Oblique-Incidence Anisotropy in Evaporated Films

[J. Appl. Phys. **31**, 1755 (1960)]

M. S. Cohen, D. O. Smith, and G. P. Weiss
Massachusetts Institute of Technology, Lincoln Laboratory, Lexington, Massachusetts

THE values of the ordinate plotted in Fig. 10 should be multiplied by 0.5.

Errata: Microwave Propagation through a Magnetoplasma

[J. Appl. Phys. **31**, 552 (1961)]

R. L. Phillips, R. G. De Losh, and D. E. White
Bendix Systems Division, Ann Arbor, Michigan

FIGURES 2 and 3 are printed upside down. Each figure must be rotated 180° to be read properly.

Erratum: Growth Twins in Indium Antimonide

[J. Appl. Phys. **32**, 550 (1961)]

R. K. Mueller and R. L. Jacobson
Mechanical Division, General Mills, Inc., Minneapolis, Minnesota

THE accompanying photograph was inadvertently omitted from the subject paper. It forms the third part of Fig. 1.

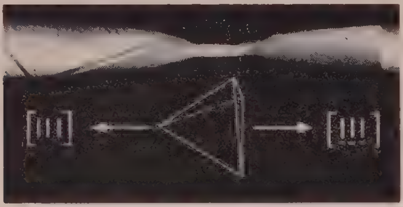

Fig. 1. InSb crystals grown in opposite ⟨111⟩ crystallographic directions demonstrate the preferential occurence of twinning on *B* (111) faces. The tetrahedron faces correspond to the *B* faces of the seed.

Announcements

U. S. National Congress of Applied Mechanics

The Fourth U. S. National Congress of Applied Mechanics, sponsored by the U. S. National Committee on Theoretical and applied Mechanics, a joint committee of the American Institute of Chemical Engineers, the American Mathematical Society, the American Physical Society, the American Society of Civil Engineers, the American Society of Mechanical Engineers, the Institute of the Aerospace Sciences, and the Society of Experimental Stress Analysis, will be held at the University of California (Berkeley) from June 18 to 21, 1962. These Congresses are planned to supplement the International Congresses of Applied Mechanics but not to compete with them. Accordingly, no effort is made to attract papers from outside the U. S. and Canada, although there is no rule against their presentation.

To be considered for presentation at the Congress, complete papers and manuscripts must be submitted to the Chairman of the Editorial Committee before January 1, 1962; to be scheduled for presentation the final manuscript of a paper must have been accepted before May 1, 1962. Inquiries regarding the Congress and preparation of manuscripts should be addressed to the secretary of the Congress, W. Goldsmith, at the University of California, Applied Mechanics, Berkeley 4, California.

Symposium on Aerospace Nuclear Propulsion

An International Symposium on Aerospace Nuclear Propulsion will be held in Las Vegas, Nevada, October 23–26, 1961. This symposium is jointly sponsored by the IRE Professional Group on Nuclear Science, the AEC, and the NASA. The meeting will be unclassified and include, among other topics, a review of the Rover, Pluto, and ANP programs.

Crystal Lattice Defects Conference

An International Conference on Crystal Lattice Defects will be held in Kyoto, Japan, from Friday, September 7, 1962, to the following Wednesday, September 12. The conference is being organized by the Physical Society of Japan. The International Union of Pure and Applied Physics is considering sponsorship of the conference.

The aim of the conference is to obtain a clearer understanding of lattice defects. In order to maintain a high scientific standard throughout the conference, attendance will be limited to research workers who are actually active in the field of lattice defects, and others who may be preparing to enter work in this field. The meeting will be arranged to reserve ample time for discussions. The language used will be English.

The conference will cover point defects in metals, semiconductors, and ionic crystals, as well as extended defects closely related to point defects. Suggested items of discussion are electronic processes in imperfect crystals, properties of single and multiple point defects, radiation damage, association, dissociation, and diffusion of point defects. Purely phenomenological studies will not be included, nor work that is ambiguous from the viewpoint of lattice defects.

For further information, contact the Lattice Defects Conference Sectetariat, ℅ Professor R. R. Hasiguti, Department of Metallurgy, University of Tokyo, Bunkyo-ku, Tokyo, Japan.

Technical Journal Donation Plan

A program has been organized by the Division of Scientific Development of the Pan American Union, General Sectetariat, to provide a way for United States scientists to donate unwanted technical journals to understocked libraries in Latin America. The transfer is being accomplished through the U. S. Book Exchange, Inc., in Washington, D. C.

Further information about the program is available from the U. S. Book Exchange, 3335 V Street, N. E., Washington 18, D. C., or from the Division of Science Development, Pan American Union, Washington 6, D. C.

Conference on Chemical Physics of Nonmetallic Crystals

The 1961 International Conference on Chemical Physics of Nonmetallic Crystals will be held from August 28 to 31, 1961, at Northwestern University, Evanston, Illinois. Sponsors are the Divisions of Chemical Physics and Solid State Physics of the American Physical Society and the Division of Physical Chemistry of the American Chemical Society.

Subjects of major interest will include: quantum theory of nonmetallic crystals, characterization of point defects in crystals, equilibrium properties of dilute solid solutions, and transport processes and point defects.

AIME Semiconductor Conference

The Third Annual AIME Semiconductor Conference will be held from August 30 to September 1, 1961, at the Ambassador Hotel in Los Angeles, California. Contributed papers will be considered; 250-word abstracts should be sent by April 15, 1961 to the Program Chairman, W. V. Wright, Electro-Optical Systems, Inc., 125 N. Vinedo Avenue, Pasadena, California.

Kodak reports on:

anthracene: decent, pure, purest, hyper-pure . . . special plates, backyard telescopes, and the infrared . . . x-ray film like tape

Infiltrated by solid-staters

An oldtimer from the coal pits has been cleaned up with a vengeance, to the accompaniment of long thoughts about "purity" in organic chemistry. (The word is becoming almost useless as a good, all-purpose shibboleth.) You can now buy *Anthracene* as Eastman H480 for $1200 per kilogram.

The prefix "H" stands for hyper-pure. Replace the "H" by "P" for Practical, and the price drops to $6.70 per kg. With "X" prefixed, the price shoots up again to $25.75 for 100 grams because the product is then purified to exhibit a proper blue-green fluorescence. Leave off all prefixes and you get the Eastman Grade at $10.85 for 100g. This is defined as "essentially free from isomers, homologs, and impurities." That "essentially" leaves a little essential room for maneuver. If say 99% of the organic molecules in a bottle are of identical species, most organic chemists would consent to labeling it essentially pure.

But now there has sprung up a breed of organic chemists who work in solid-state physics; or perhaps they are really solid-state physicists extending their realm beyond metals and semiconductors. To them a substance that is only 99% pure is like a pail of garbage. Some of them are even to be found in the Kodak Research Laboratories, which is (or are) where Eastman Organic Chemicals are made.

At their behest *o-Benzoylbenzoic Acid* (Eastman 2242) was cyclized with sulfuric acid to make anthraquinone, that reduced with tin and HCl to anthrone, and *that* reduced with zinc and dilute NaOH to anthracene. This, with much purification and repurification along the way, we call Eastman H480.

For the solid-staters it was only the beginning. They recrystallized it from toluene, got rid of the toluene by a special technique, and zone-refined a dozen times or so. Then by Bridgeman technique in a two-zone furnace they made a large single crystal of the hyper-hyper-pure anthracene. They sandwiched little slices of the crystal between transparent electrodes, applied voltage, and illuminated with an air spark of microsecond duration and very high intensity. They compared current vs. time oscillograms for illumination of the positive side with those for illumination of the negative side. The curves told how long an electron or a hole could drift in the crystal lattice between being set loose by the flash and being trapped by an irregularity or impurity in the lattice. Both electrons and holes showed lifetimes of about 200 microseconds. It is very unusual to have long-lived electrons and holes in the same organic photoconductor. Not only is this very interesting, but long lifetimes permit accurate measurements of the mobility of electrons and holes.

What is happening to organic chemistry?

Whatever is happening, we are continuing the sale of some 3900 Eastman Organic Chemicals from Distillation Products Industries, Rochester 3, N. Y. (Division of Eastman Kodak Company). Write for a copy of List No. 42.

Our connections with the heavens

We have three connections with the heavens:

1. Years ago we threw our weight on the side of the angels by a Good Deed. We went to work for the astronomers, a group noted for the slimness of their budgets. We made them the special photographic plates needed for all the projects that have seemed pressing to them, like measuring the angular momentum of galaxies. This work has netted us a medal or two but no wealth. That's all right. Questions about these plates are answered by Eastman Kodak Company, Special Sensitized Products Division, Rochester 4, N. Y. Professional astronomers know that address very well.

2. Amateur astronomers are among the most numerous of scientific-type hobbyists. Many thousands of persons who have to deal all day with tiresome human affairs like to reach out toward the ultimate verities through a backyard telescope. But, being human themselves, they hanker for tangible trophies of the sport. These photography can provide. To guide, we provide a free booklet, "Astrophotography with Your Camera," from the same address the professionals know. The amateur astronomers far outnumber the professionals and buy standard Kodak films at popular prices.

3. A protostar evolving from clouds of dust a million light-years away and an ICBM a thousand miles from the U. S. border have a certain resemblance in the infrared. At Ohio State University we have some astronomers working for us on an astronomical job which lack of suitable equipment has long delayed—preparation of an atlas of infrared emitters on the celestial sphere to 13.5 microns. We made them the missing equipment. We need the atlas. We have our reasons. The equipment includes a drift-free homodyne amplifier which takes a signal from our liquid-helium-cooled copper-doped germanium detector on the 69-inch Perkins Observatory telescope. It can cramp down to a .0011 cycle/sec scanning bandwidth so that in 20 minutes it can distinguish the emission of a single star from intergalactic infrared noise. Those who have need and funds for such up-to-date infrared systems should get in touch with Eastman Kodak Company, Apparatus and Optical Division, Rochester 4, N. Y.

Why snip in the dark?

The "cultural lag" they talk about in sociology serves in simple ways to restrain technology from advancing too fast.

X-rays were discovered through their effect on the photographic emulsion. Photographic emulsion comes on photographic film. Photographic film is mostly used to take pictures by visible light. Visible light won't pass through paper. Paper therefore protects from light. The converse yields the principle that a sheet of film must be extracted from its paper protection before use. This principle seems sort of fundamental to photography. Though modern radiography employs a different kind of film and even omits a camera, the principle of transferring the film from its package to a separate exposure holder before use has been respectfully preserved (except by dentists who seem, in this respect at least, a little brighter than the rest of us).

The chains that bind have now been sundered. *Kodak Industrial X-ray Film* in sheets has been available for some little time now in a *Ready Pack* form, enclosed in individual lighttight packets. Now one can also buy a 200-foot roll of 70mm, 35mm, or 16mm x-ray film with a paper skin on it. One cuts off what one needs, seals the end with opaque tape, and strips off the paper just before processing.

You can get Kodak Industrial X-ray Film, Type AA *and* Type M *this way. (Type M is the one that trades speed for maximum resolution.) Eastman Kodak Company, X-ray Division, Rochester 4, N. Y. can supply the name of the nearest dealer.*

Prices subject to change without notice.

Kodak
TRADE MARK

This is another advertisement where Eastman Kodak Company probes at random for mutual interests and occasionally a little revenue from those whose work has something to do with science

ELECTROMAGNETIC SYSTEMS

Division of Space Technology Laboratories, Inc.

*Offers Immediate Assignments
in Southern California*

The continuing growth and diversification of Space Technology Laboratories, Inc. creates immediate career openings in the Radio Physics and Signal Equipment Laboratories of STL's Electromagnetics Division, located in the community of Canoga Park in Los Angeles' San Fernando Valley.

This division is engaged in developing advanced communication, radio direction finding, electro-optical, and penetration and reconnaissance systems; and in investigating advanced signal processing, electronic and anti-submarine warfare techniques.

Outstanding engineers and scientists who can qualify to perform advanced work in these areas are invited to communicate with Dr. R. C. Potter, Manager of Professional Placement and Development. All qualified applicants considered regardless of race, creed, color or national origin.

SPACE TECHNOLOGY LABORATORIES, INC.

a subsidiary of Thompson Ramo Wooldridge, Inc.

P. O. Box 95005AA, Los Angeles 45, California

ILFORD

industrial "G" X-ray film for crystallography

If you are seeking a superior film for X-ray diffraction studies, Ilford Industrial "G" X-ray Film will meet your requirements. This film combines the advantages of maximum speed and medium grain with extremely low background fog and relatively high contrast. It is manufactured to close tolerances to simplify standardization of X-ray reflection intensities.

Industrial "G" and other Ilford X-ray films are available from General Electric, Keleket, Picker, Westinghouse and their authorized dealers.

For further details write to:

ILFORD INC. 37 WEST 65th STREET, NEW YORK 23, N.Y.

ARMA ARMA ARMA ARMA ARMA

senior solid state scientist

ARMA has immediate need for a Senior Solid State Scientist to participate in an advanced and challenging research program.

The man selected will have a strong background in theory and application of solid state physics, with emphasis on molecular phenomena. He probably will have experience in molecular theory of gases and liquids.

His assignment: He will conduct independent investigations in thin film and surface physics and some aspects of electro-optical properties of ferroelectrics.

Most important, he will be a creative—perhaps presently stifled—physicist with wide scientific interests and a desire to advance the frontiers of research.

Salary is open.

If you fit the above description, phone Mr. E. C. Lester at PIoneer 2-2000 in Garden City, L.I. Or send your résumé in confidence to Mr. Lester, professional placement supervisor, address below.

EQUAL JOB For All Qualified Applicants OPPORTUNITY

ARMA DIVISION
AMERICAN BOSCH ARMA CORPORATION
ROOSEVELT FIELD, GARDEN CITY, LONG ISLAND, N. Y.

8407

ARMA ARMA ARMA ARMA ARMA

CENCO® HYVAC
GAS BALLAST PUMPS

For vacuum applications plant and laboratory. Eliminates use of oil separators, centrifuges, refrigerated traps. Wide range of capacities.

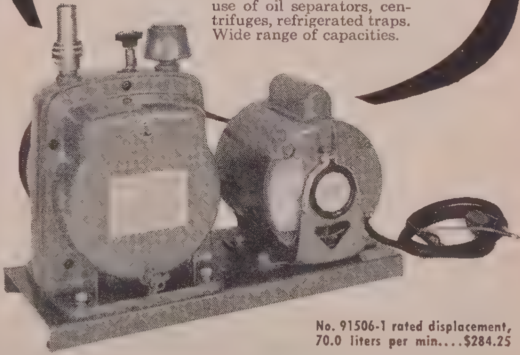

No. 91506-1 rated displacement, 70.0 liters per min....$284.25

to simplify vacuum control . . .

NEW CENCO DISCHARGE GAGE AND CONTROLLER

A gage and automatic controller that continuously reads from 0.001 to 20 microns total pressure of all condensable vapors and gases in your system. Starts instantly at any pressure. Controller provides automatic on-off switching at pre-set pressures—transistorized amplifier opens or closes contacts of relay to control up to 1 amp.

No. 94183 $249.50

cenco
Quality since 1889

CENTRAL SCIENTIFIC
A Division of Cenco Instruments Corporation
1700 Irving Park Road • Chicago 13, Illinois
Mountainside, N. J. Montreal Santa Clara
Somerville, Mass. Toronto Los Angeles
Birmingham, Ala. Ottawa Vancouver Houston
Cenco S.A., Breda, The Netherlands Tulsa

CORRELATION SYSTEM

for direct readout of correlation number

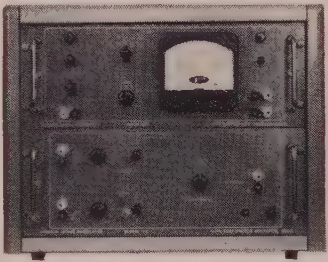

A new analog computing system for measuring the normalized cross correlation between any two signals.

featuring

Frequency response: 2 cps to 250 kc, ±0.4 db
Input signal range: 20mv rms to 40v peak to peak, each channel
Time constant: .... 16 seconds
Peak factor: .... 10 or more

WRITE FOR BULLETIN 58

FLOW CORPORATION
11 Carleton Street · Cambridge 42, Mass. · TR 6-9843

ASSOCIATE EDITORS

To review foreign technical and scientific literature, select articles and prepare brief summaries for engineering studies. A basic competence in 2 or more of the following disciplines or arts is necessary:

Automation/Astronomy/Bionics/Crystallography/Electronics/Metallurgy/Nucleonics/Organic Chemistry/Physical Chemistry/Solid State Physics/Spectroscopy/Telemetering.

A thorough knowledge of both Russian and English technical terminology are required. Understanding of other Slavic languages is desirable. These positions will prove rewarding to qualified men with initiative and some editorial experience.

Send resume and salary requirements to:

McGRAW-HILL
BOOK COMPANY, INC.
P. O. Box 269, Times Square Station
New York 36, N. Y.

PERIODICAL PUBLICATIONS
OF THE
INSTITUTE OF PHYSICS AND
THE PHYSICAL SOCIETY

●

Journal of Scientific Instruments

A monthly publication dealing with the principles, construction and use of scientific instruments.
£6 per annum

British Journal of Applied Physics

A monthly publication dealing with applications of physics, especially in industry.
£6 per annum

Proceedings of the Physical Society

A monthly publication containing papers describing original work in physics.
£12 12*s.* per annum

Reports on Progress in Physics

An annual publication containing comprehensive reviews—issued in April.
£4 4*s.* per annum

Available from:

The Institute of Physics and The Physical Society
47 Belgrave Square, London S.W.1

announcing

1" & 2" ULTRA-HIGH VACUUM VALVES

and COMPLETE LINE of MATCHED FITTINGS

- Bakeable to 450° C
- Useful to 10^{-10} mm Hg or lower
- Conductance variable from 60 liter/sec to 10^{-13} liter/sec with 2" valve; from 10 liter/sec to less than 10^{-14} liter/sec with 1" valve
- Constructed entirely of low vapor pressure metals insuring minimum contamination
- Available from stock

WRITE OR PHONE FOR COMPLETE SPECIFICATIONS

GP **Granville-Phillips Company**

P. O. Box J-198 Pullman, Washington • telephone LOgan 4-1130

EPLAB **EPPLEY PRECISION VOLTAGE STANDARD AND ASSOCIATED EQUIPMENT**

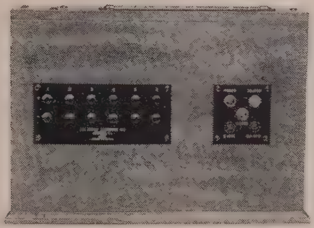

THE EPPLEY PRECISION VOLTAGE STANDARD

Consisting of six Eppley saturated standard cells, mounted in a Constant Temperature Air Bath for laboratories desiring to maintain a primary reference standard eligible for certification by the National Bureau of Standards. This combination provides an extremely reliable and accurate reference for use in calibrating unsaturated standard cells in accordance with specifications requiring "traceability" to NBS standards.

Send for Bulletin #1 (Standard Cells) and #12 (Constant Temperature Box)

THE EPPLEY STANDARD CELL POTENTIOMETER

A precision potentiometer designed especially for the rapid and accurate measurement of standard cell voltages. For use where routine calibrations must be made in quantity without sacrifice of accuracy.

Send for Bulletin No. 7

THE EPPLEY STANDARD CELL COMPARATOR

Provides a means of comparing accurately, to tenths of microvolts, the electromotive forces of two standard cells, by a measurement of the difference between the two forces. Designed primarily for the intercomparison of saturated, primary reference standards.

Send for Bulletin No. 11

The Eppley Laboratory, Inc. 6 SHEFFIELD AVENUE NEWPORT, R. I., U.S.A. **EPLAB**

45-1

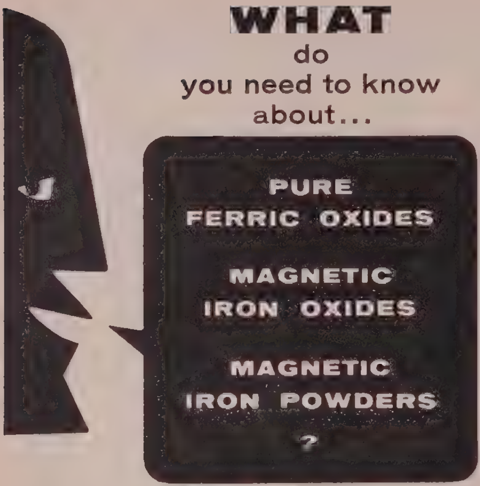

Since final quality of your production of ferrites, electronic cores, and magnetic recording media depends on proper use of 3 specialized groups of magnetic materials . . . you'll find it mighty helpful to have all the latest, authoritative technical data describing the physical and chemical characteristics of each. This information is available to you just for the asking. Meanwhile, here are highlights of each product group.

PURE FERRIC OXIDES—For the production of ferrite bodies, we manufacture a complete range of high purity ferric oxide powders. These are available in both the spheroidal and acicular shapes, with average particle diameters from 0.2 to 0.8 microns. Impurities such as soluble salts, silica, alumina and calcium are at a minimum.

MAGNETIC IRON OXIDES—For magnetic recording—audio, video, instrumentation etc.—we produce a group of special magnetic oxides with a range of controlled magnetic properties. Both the black ferroso-ferric and brown gamma ferric oxides are available.

MAGNETIC IRON POWDERS—For the fabrication of magnetic cores in high-frequency, tele-communication, and other magnetic applications, we make a series of high purity iron powders.

If you have problems involving any of these materials, please let us go to work for you. We maintain fully equipped laboratories for the development of new and better inorganic materials. Write . . . stating your problem . . . to C. K. Williams & Co., Dept. 38, 640 N. 13th St., Easton, Penna.

WILLIAMS
COLORS & PIGMENTS

C. K. WILLIAMS & CO.
E. ST. LOUIS, ILL. • EASTON, PA. • EMERYVILLE, CAL.

TRANSLATIONS OF . . . .
SOVIET JOURNALS

Published by the American Institute of Physics with the cooperation of the National Science Foundation.

SOVIET PHYSICS—JETP

Monthly. Translation of *Zhurnal Eksperimental'noi I Teoreticheskoi Fiziki* of Academy of Sciences, USSR.

SOVIET PHYSICS—SOLID STATE

Monthly. Translation of *Fizika Tverdogo Tela* of Academy of Sciences, USSR.

SOVIET PHYSICS—TECHNICAL PHYSICS

Monthly. Translation of *Zhurnal Tekhnicheskoi Fiziki* of Academy of Sciences, USSR.

SOVIET PHYSICS—DOKLADY

Bimonthly. Translation of the Physics Section of Proceedings of Academy of Sciences, USSR.

SOVIET PHYSICS—ACOUSTICS

Quarterly. Translation of *Akusticheskii Zhurnal* of Academy of Sciences, USSR.

SOVIET PHYSICS—CRYSTALLOGRAPHY

Bimonthly. Translation of *Kristallografiya* of Academy of Sciences, USSR.

SOVIET PHYSICS—USPEKHI

Bimonthly. Translation of *Uspekhi Fizicheskikh Nauk* of Academy of Sciences, USSR.

SOVIET ASTRONOMY—AJ

Bimonthly. Translation of *Astronomicheskii Zhurnal* of Academy of Sciences, USSR.

Send orders and inquiries to:

American Institute of Physics
335 East 45 Street, New York 17, N. Y.

High Performance ELECTROMAGNETS and Power Supplies

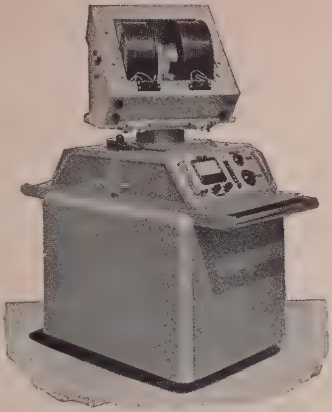

ECONOMY
7″ Electromagnet Type E (7″ pole diameter). Fields up to 8,000 gauss. Homogeneity of at least 4 parts in 10^5 in ½ cc.

ROTATION
Rotating Base Type AE. 360° scale. Positive friction lock.

STABILITY
Current-Stabilized Power Supply Unit Type B.

Also available:—
1½″ Electromagnet Type C—for Teaching purposes.
4″ Electromagnet Type A—for all purposes.
8″ Electromagnet Type D—for Electron Resonance and Nuclear Magnetic Resonance work.
Direct Reading Magnetometer Type G.
Proton Resonance Magnetometer Type P.

NEWPORT INSTRUMENTS
(Scientific & Mobile) Ltd
10 CRAWLEY ROAD, NEWPORT PAGNELL, BUCKS
Telephone: NEWPORT PAGNELL 401/2

MEASURE VACUUM
10^{-3} to 10^{-10} Torr ACCURATELY
... with NRC's Nottingham Vacuum Gauge

NRC Equipment Corp.'s ultra-high vacuum gauge is the only unit which permits you to know—accurately—the actual pressures being measured in the ultra-high vacuum range.
NRC Model 751A provides a grounded shield coating which prevents space charge build-up, giving you uniform stability at low pressures. Grid structure closures at both ends of gauge prevent end-loss of ions ... results in more uniform sensitivity over a wider pressure range.
Two separate filaments enable you to measure pressures below normal gauge range—to 10^{-12} Torr. Low amplifier sensitivity with 100% negative feedback provides stable, 100% linear amplification ... eliminates effect of stray signals.

For pressure readings down to 10^{-12} Torr, use the NRC Nottingham vacuum gauge.

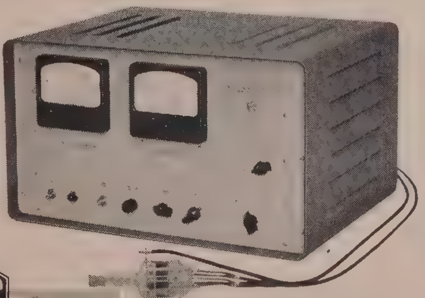

NRC
EQUIPMENT CORPORATION

For data sheet, specs or a quote, write:
Dept. 20G, 160 Charlemont St.,
Newton 61, Mass., or any
NRC Sales Office. DEcatur 2-5800

A Subsidiary of
National Research Corporation

ARMA ARMA ARMA ARMA ARMA

senior theoretical physicist

ARMA has an immediate need for a Senior Theoretical Physicist to participate in an advanced and challenging research program.

The man selected will be responsible for advanced theoretical studies in several new areas contemplated by the Company. A PhD in Theoretical Physics or Applied Mathematics, and some degree of scientific accomplishment are required. He should be conversant, in a general way, with various problems and theoretical techniques of classical physics and be capable of adapting these techniques to new problems.

Most important, he will be a creative—perhaps presently stifled—physicist with wide scientific interests and a desire to advance the frontiers of research.

Salary is open.

If you fit the above description, phone Mr. E. C. Lester at PIoneer 2-2000 in Garden City, Long Island, N. Y. Or send your résumé to Mr. Lester, professional placement supervisor, address below.

ARMA DIVISION
AMERICAN BOSCH ARMA CORPORATION
ROOSEVELT FIELD, GARDEN CITY, LONG ISLAND, N. Y.

EQUAL JOB OPPORTUNITY

8408

ARMA ARMA ARMA ARMA ARMA

Name	*Page*
AEROSPACE CORPORATION	iv
ARMA, AMERICAN BOSCH ARMA CORP.	xxvii, xxxi
ASARCO, AMERICAN SMELTING & REFINING COMPANY	xv
BELL TELEPHONE LABORATORIES	v
CENTRAL RESEARCH LABS., INC.	xvii
CENTRAL SCIENTIFIC CO.	xxvii
Manufacturers of Cenco physical apparatus and instruments to meet all requirements of University, College and High School Physics Laboratories. Specializing in high vacuum pumps and development of instruments and apparatus for various sciences.	
EASTMAN KODAK COMPANY	xxv
THE EPPLEY LABORATORY, INC.	xxix
FISHER SCIENTIFIC COMPANY	ix
FLOW CORPORATION	xxviii
GENERAL RADIO CO.	Cover 4
Manufacturers of electronic measuring instruments; vacuum-tube voltmeters, amplifiers, and oscillators; wave analyzers, noise meters and analyzers, stroboscopes, laboratory standards of capacitance; inductance and frequency; impedance bridges, decade resistors and condensers, air condenser and variable inductors; rheostats, variacs, transformers; other laboratory accessories.	
GENERAL TELEPHONE & ELECTRONICS LABORATORIES	xvi
GRANVILLE-PHILLIPS COMPANY	xxix
HAMNER ELECTRONICS CO., INC.	xxxiv
THE HARSHAW CHEMICAL CO.	Cover 2
HARVEY-WELLS CORP.	xi
HUGHES AIRCRAFT COMPANY	xix
ILFORD INC.	xxvi
ILIKON CORPORATION	xiii
LINCOLN LABORATORY, M.I.T.	viii
LOS ALAMOS SCIENTIFIC LAB.	xii
McGRAW-HILL BOOK CO., INC.	xxviii
NRC EQUIPMENT CORP.	xxxi
Manufacturers of standard and special high vacuum components, equipment, and systems including mechanical booster, and diffusion pumps; gauges; valves; seals; connectors; melting and heat-treating furnaces; coaters; impregnators; gas in metal analyzers; driers and freeze driers; altitude chambers and leak detectors.	
NEWPORT INSTRUMENTS LTD.	xxxi
OPERATIONS EVALUATION GROUP, M.I.T.	vi
RADIO CORP. OF AMERICA	vii

Name *Page*

SANYO ELECTRIC CO., LTD. xxii

SPACE TECHNOLOGY LABORATORIES, INC. .. xxvi, Cover 3

SYLVANIA ELECTRONIC SYSTEMS, AMHERST LABORATORIES x

TECHNICAL MEASUREMENT CORP. xxiii

Nuclear instrumentation—single and multichannel pulse height analyzers, liquid scintillation beta spectrometers, reactor flux plotting systems, sealers, precision high voltage power supplies, ratemeters, linear amplifiers and custom nuclear system design.

TESLA, REP., NATIONAL INSTRUMENTS LABORATORIES, INC. xiv

VARIAN ASSOCIATES

INSTRUMENT DIVISION .... xx, xxi

VACUUM DIVISION iii

WELCH SCIENTIFIC CO., W. M. xxiv

Manufacturers of high-vacuum pumps, both mechanical and diffusion; vacuum gauges; electrical measuring instruments; physics equipment; and other items for the physical and chemical laboratories.

C. K. WILLIAMS & CO. xxx

TUBULAR SLIDE CONTACT RHEOSTATS
RESISTORS
Toroidal Winding Machines
REX RHEOSTAT CO.
149-a Babylon Tpke. Roosevelt, L. I., N. Y.

PHYSICAL METALLURGIST

Experienced in semiconductors with a knowledge of intermetallics desirable. Work with the most rapidly growing group in the thermoelectric field on problems of bonding, impurity doping, diffusion, etc. Graduate degrees desirable, but not required. U.S. citizen.

Send resume & salary expected, directly
to M. Barmat, Manager

GENERAL INSTRUMENT CORP.
Thermoelectric Division
65 Gouverneur St. Newark, N.J.

ELECTRO-OPTICS

Corning Electronic Components, Corning Glass Works, needs men with the following qualifications:

1. **Postgraduate study in EE, Physics, or Math**
2. **Two or more years experience**
3. **A desire to contribute to the development of light modulating devices and electro-optical systems.**

Corning Electronic Components is situated in Bradford, Pa., adjacent to Allegheny State Park, near Chautauqua Lake and 80 miles south of Buffalo, N. Y.

Please write R. J. Stone or call collect: FO 2-5571.

CORNING ELECTRONIC COMPONENTS
CORNING GLASS WORKS,
BRADFORD, PA.

IONOSPHERE PHYSICIST

Requires demonstrated ability in the characteristics of and interactions with the Ionosphere. Should be familiar with the advanced technique of measurement as well as the physics of the Ionosphere.

Must have capability to handle advanced design and analysis of Ionosphere measurement techniques and equipment. Knowledge of flight hardware desired.

Send resume in confidence to
Professional Placement Office
Electro-Optical Systems, Inc.
125 No. Vinedo Ave.
Pasadena, California

PROGRAMMED NUCLEAR COUNTING SYSTEMS

CUSTOM-ENGINEERED BY **HAMNER**

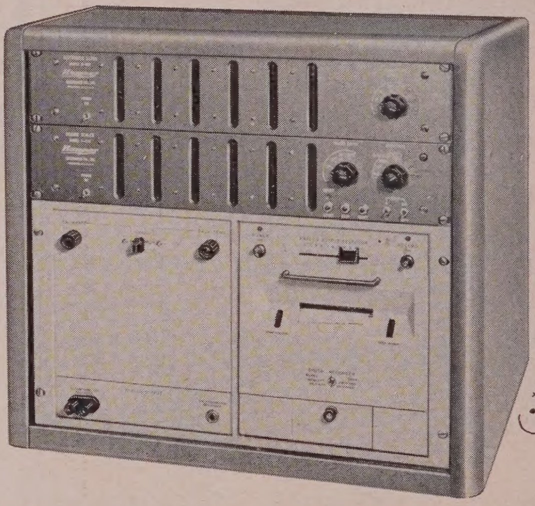

There is a growing demand by the researcher for programmable nuclear counting systems, with outputs suitable for automatic handling of data. To serve these demands, Hamner added specialists to their engineering staff and developed a line of instruments suitable for filling this need.

Requirements for systems of this type are individual in nature, and each system is custom-engineered, to some extent. Through the use of highly versatile "Building Block" instruments, some of which are described below, costs for this type of system are kept to an absolute minimum.

Input—Signals from any type nuclear detector(s)

Output

- Electric Typewriter
- Parallel Entry Printer
- Punched Tape
- Punched Cards
- Relay closure or electronic gate for actuation of auxiliary equipment
- Combinations of above

The S-4000 System is an example of the "Building Block" philosophy previously mentioned. This System consists of a high speed printing scaler, a crystal control printing timer and a high speed digital printer. Standard modes of operation include preset time, with 15 selectable preset times, preset count with a choice of 15 settings, or combined preset time-preset count with any combination of these two settings. Either counts or time or both may be printed out at the rate of 5 lines per second.
Similar systems may be built up with typewriter, punched card or punched tape output and may involve many scaling and timing units, programmed as required.

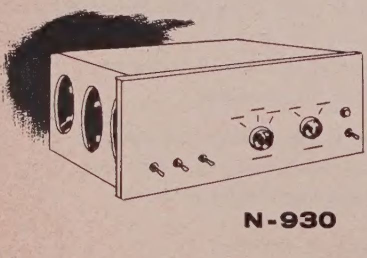

N-930

This unit is designed to couple conventional electronic scalers or timers to a tape punch, typewriter or other serial entry type equipment. It accepts any binary coded decimal input (4 line) in parallel, converts this to serial form, translates to any other binary coded decimal form (4 line code), and also presents decimal code at the same time. It contains output circuitry suitable for actuating punch solenoids in any standard paper tape or card punch. A three position selector switch permits tape punch and typewriter to be operated simultaneously or separately. Units with 25 or 50 information point capacity are available. Hamner also has available an N-950 Parallel Binary/Decimal Register for use with 4 line coded equipment and a similar unit, the N-970, for use with Staircase coded equipment.

Inquire about solid state versions of these items.

Your Hamner representative is anxious to work with you in translating system requirements into instrument requirements. Hamner sales engineers will then offer proposals outlining possible methods of doing the job.

Hamner

HAMNER ELECTRONICS CO., IN

Dept. 7AP, P. O. Box 531, Princeton, New Jersey, PEnnington 7-13

Careers in a New Era of Space Technology Leadership

OGO • ADVENT • ATLAS TITAN • MINUTEMAN

Today Space Technology Laboratories, Inc., is engaged in a program of diversification and planned growth.

Programs. Research, development, design, and construction of three Orbiting Geophysical Observatories for NASA. Systems engineering support and technical consulting services for the Army Advent program. Systems engineering and technical direction of the Atlas, Titan, and Minuteman weapon systems for the Air Force. Original and applied research in a broad spectrum of disciplines: particle physics, solid state theory, guidance, space physics, communication theory, propulsion and power, and electromagnetic systems in the infrared, ultraviolet and microwave regions.

Facilities. Presently under construction on a 110-acre site at Redondo Beach, near Los Angeles International Airport, is the STL Space Technology Center comprising ten buildings specially designed for research and development in missile and space systems, for the fabrication and environmental test of subsystems and components, and for the production of scientific and technical devices derived from STL's sustained research program. These new facilities will be augmented by the STL research and fabrication installation at Canoga Park, California.

Immediate Opportunities at STL exist for qualified engineers and scientists at all levels of experience, in the following activities:

BALLISTIC MISSILE PROGRAM MANAGEMENT (Los Angeles, Vandenberg AFB, Norton AFB—San Bernardino). Responsible for systems engineering and technical direction for the Air Force ICBM Weapon Systems Programs—Atlas, Titan, and Minuteman—including achievement of all technical objectives of these programs.

MECHANICS DIVISION (Los Angeles). Responsibilities of the Propulsion, Engineering Mechanics, and Aerosciences Laboratories within this division include: analyzing and evaluating performance of rocket engines, propellants and propulsion subsystems and components; conception, design, development, and evaluation of ballistic missile and space vehicle systems; development and implementation of structural, dynamic, aerodynamic, and re-entry vehicle research and development concepts for both ballistic missile and space vehicle programs; and development of new subsystems for missile and spacecraft applications.

SYSTEMS RESEARCH AND ANALYSIS DIVISION (Los Angeles). *Systems Research Laboratory* activities include: management of complete space and missile systems studies including initial design; operations analysis; preliminary design in such areas as structures and aeromechanical and electromechanical systems; trajectory and error analysis; space navigation; and communication systems. *Computation and Data Reduction Center* performs the following functions: numerical analysis; applied mathematics; statistical analysis; scientific programming; computational systems programming; data processing analysis; and test evaluation programming and analysis.

ELECTRONICS DIVISION (Los Angeles). The Communication, Electromechanical, Guidance, and Space Physics Laboratories of this division are responsible for analysis, design, and development of advanced guidance, control, and communications systems for ballistic missiles and space vehicles—from applied research to electronic product and ground support equipment design. Disciplines include the physical, electronic, and electromechanical aspects of guidance, tracking, control, communication, and computer systems, geophysics, and space physics.

RESEARCH LABORATORY (Los Angeles and Canoga Park, California). Fields of interest include: physical studies of gaseous electronics, artificial meteors, reactor kinetics, microwave electronics; studies of quantum chemistry, thin film applications, electron and ion dynamics, and theoretical physics; heavy particle studies; ion propulsion research including neutralization and beam diagnostics, emitters, acceleration and ion optics, and engine design.

FABRICATION, INTEGRATION & TEST DIVISION (Los Angeles). Incorporates the areas of mechanical and electronic fabrication and assembly, environmental test, mechanical and electrical integration of spacecraft, integrated subsystems and systems checkout, and launch operations.

ELECTROMAGNETIC SYSTEMS DIVISION (Canoga Park, California). The Radio Physics and Signal Equipment Laboratories of this division are engaged in developing advanced communication, radio direction finding, electro-optical, and penetration and reconnaissance systems; and in investigating advanced signal processing, electronic and anti-submarine warfare techniques.

FLIGHT TEST OPERATIONS (Cape Canaveral). Responsible for directing systems test programs and for supplying technical leadership to contractors conducting flight testing of ballistic missiles, space programs, and vehicles modified for special development purposes.

Resumes and Inquiries from engineers and scientists, at all levels of experience, will receive prompt and careful attention. All qualified applicants, regardless of race, creed, color or national origin, are invited to communicate with Dr. R. C. Potter, Manager of Professional Placement and Development, for opportunities in Southern California or at Cape Canaveral.

SHARE IN THE GROWTH OF SPACE TECHNOLOGY LEADERSHIP

CE TECHNOLOGY LABORATORIES, INC.
iary of Thompson Ramo Wooldridge Inc.
es • Vandenberg AFB • Canoga Park • Norton AFB, San Bernardino

P.O. BOX 95005AA, LOS ANGELES 45, CALIFORNIA
P.O. BOX 4277AA, PATRICK AFB, FLORIDA
Dayton • Cape Canaveral • Washington D.C. • Boston • Huntsville

R-L-C Standards and Components . . . No. 1 of a Series

Resistance...

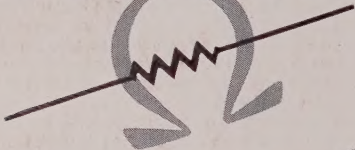

These resistance standards incorporate optimum construction for wide-band applications (useful to several hundred kc, as well as dc) . . . low residual reactance . . . preaged at high temperatures to insure excellent stability . . . 100% inspection.

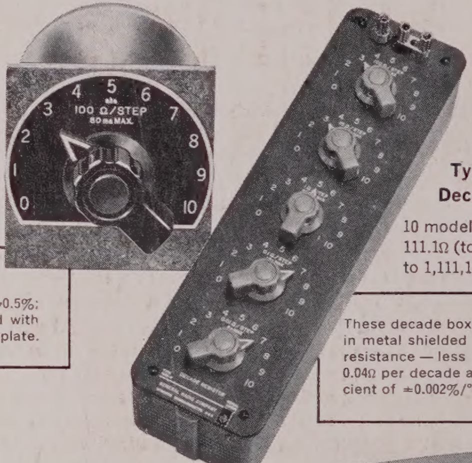

Type 510
Decade Resistance Units

9 models in ranges from 0.1Ω (total) to 1.0 MΩ (total) — $14 - $35.

Accuracy of ±0.05% for most units, except 10Ω (total) decade which is ±0.15%; 1Ω decade ±0.5%; and 0.1Ω decade ±2%. Supplied with aluminum shield can, knob, dial plate.

Type 1432
Decade Resistance Boxes

10 models in ranges from 111.1Ω (total) to 1,111,100Ω (total) — $95-$160.

These decade boxes are assemblies of 510 models in metal shielded cabinets. They feature low zero resistance — less than 0.002Ω per decade at dc, 0.04Ω per decade at 1 Mc. Low temperature coefficient of ±0.002%/°C, except for 0.1Ω decade.

Type 500
Fixed Precision Resistors

18 models in ranges from 10Ω to 1 MΩ in 1-2-5 sequence; 1Ω and 600Ω units also available — $6-$27.

±0.05% accuracy for all but 1Ω unit (±0.15%). Sealed from moisture in phenolic case — banana plugs permit direct connection to standard ¾"-spaced terminals.

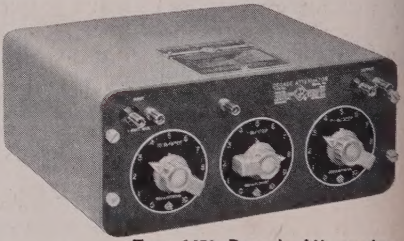

Type 1450 Decade Attenuators

2 models: 110-db total in 1-db steps, $285; and 111-db total in 0.1-db steps, $390.

These are 600Ω, T-section attenuators for power-level, gain, loss, or transmission efficiency measurements. Low-frequency error is less than +0.006 db ±0.25% of dial reading for 1-db-per-step decade; less than +0.009 db ±0.25% for 0.1 db-per-step decade.

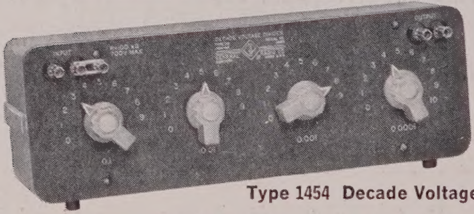

Type 1454 Decade Voltage Dividers

2 models provide voltage ratios from 0.0001 to 1.0000 in 0.0001 steps — $150 each.

Accuracy is 0.04% of ratio at input voltages below 120v . . . negligible thermal emf . . . valuable for linearity measurements, meter calibration, and in determining voltage transmission ratios . . . constant input 10kΩ for 1454-A, 100kΩ for 1454-AH.

Special units
can be
custom built

Write For Complete Information

GENERAL RADIO COMPANY
WEST CONCORD, MASSACHUSETTS

The Best Instruments In Electronics

NEW YORK, WOrth 4-2722
NEW JERSEY, Ridgefield, WHitney 3-3140

CHICAGO
Oak Park
Village 8-9400

PHILADELPHIA
Abington
HAncock 4-7419

WASHINGTON, D.C.
Silver Spring
JUniper 5-1088

SAN FRANCISCO
Los Altos
WHitecliff 8-8233

LOS ANGELES
Los Angeles
HOllywood 9-6201

IN CANADA
Toronto
CHerry 6-2171